Physics of Atomic Nuclei, Vol. 68, No. 1, 2005, pp. 1–2. Translated from Yadernaya Fizika, Vol. 68, No. 1, 2005, p. 3.

Fortieth Anniversary of the Journal *Physics of Atomic Nuclei*

This year marks the 40th anniversary of the starting of the journal *Yadernaya Fizika* (translated into English under the title *Physics of Atomic Nuclei*, formerly known as the *Soviet Journal of Nuclear Physics*). The need for a specialized journal on nuclear and elementary-particle physics was felt because of the rapid development of these fields in this country in the 1960s. Major nuclear research centers were created: the Joint Institute for Nuclear Research (JINR) in Dubna, the Institute of Theoretical and Experimental Physics (ITEP) in Moscow, the Institute for High Energy Physics (IHEP) near Serpukhov, the Institute of Nuclear Research at Moscow State University, Institute for Nuclear Research in Troitsk, nuclear research institutes in Novosibirsk and Gatchina, and the Institute for Physics and Power Engineering in Obninsk. Nuclear physics research was done at large departments of the Kurchatov Institute of Atomic Energy and the Lebedev Institute of Physics in Moscow, and the Institute for Physics and Technology in Kharkov. Important independent schools evolved in theoretical and experimental nuclear physics. Typically, it was around accelerators, newly built or under construction, at nuclear centers that experimental schools sprung up. The relaxation of secrecy conditions went a long way toward the proliferation of nuclear physics papers. This stream of papers overwhelmed the *Journal of Experimental and Theoretical Physics*, which covered a wide range of physics subjects. As it branched from the *JETP*, which was directed by P.L. Kapitsa at that time, the new journal, *Physics of Atomic Nuclei*, has retained the splendid traditions of the leading national physics journal—namely, high professionalism, scientific objectivity, and adherence to principle. The first editorial board was headed by V.I. Veksler (editor in chief), V.V. Vladimirsky (deputy editor in chief), and Ya.A. Smorodinsky (executive editor). The editorial board has included some of the nation's leading names in nuclear physics: S.T. Belyaev, D.I. Blokhintsev, N.N. Bogolyubov, G.I. Budker, S.N. Vernov, A.S. Davydov, B.S. Dzhelepov, V.G. Kirillov-Ugryumov, A.A. Logunov, M.G. Meshcheryakov, A.B. Migdal, B.M. Pontecorvo, R.M. Sulyaev, I.E. Tamm, G.N. Flerov, and I.M. Frank. The editorial staff, led by T.G. Bychkova, maintained high publishing standards. With time, V.I. Veksler was replaced by V.V. Vladimirsky as editor in chief, who was in turn replaced by Yu.G. Abov at a later date. The composition of the editorial board and staff varied, but the principles that underlay the journal at its founding were carefully preserved, turning into traditions.

Since 1965, the journal *Physics of Atomic Nuclei* has appeared in an English version. It is distributed by the American Institute of Physics among libraries outside Russia, which, naturally, broadens its readership and increases its communication potential.

Many eminent scientists have been published in this journal—among them, I.Ya. Pomeranchuk, V.Z. Gribov, Ya.B. Zeldovich, A.B. Migdal, G.N. Flerov, S.T. Belyaev, B.I. Ioffe, L.B. Okun, K.A. Ter-Martirosyan. The list can be made much longer.

Many papers that appeared in the journal are widely known and quoted.

The current phase in nuclear physics research is marked by broad international cooperation. This trend is reflected in the coverage of the journal, which often carries papers coauthored by Russian and foreign scientists. Not infrequently, it prints independent foreign papers generated at leading research centers in Europe and the United States (Saclay, Princeton, and others).

Papers printed in the *Physics of Atomic Nuclei* more than once took the first prize in the annual best paper competition started by IAPC Nauka/Interperiodica in 1995, which is a testimony to their high quality. Over the intervening ten years, authors from the *Physics of Atomic Nuclei* captured the first prize four times, which is a record among the journals in this field! The winners (listed chronologically) are Yu.A. Simonov, ITEP (for a set of papers proposing a new approach to the description of nonperturbative phenomena in quantum chromodynamics); members of two groups at the Institute for High Energy Physics headed by L.G. Landsberg and A.M. Zaitsev (for a set of papers devoted to the search for, and systematic study of, the properties of exotic baryon and meson resonances); Yu.D. Prokoshkin, IHEP [for a set of papers on hadron spectroscopy (the award was given posthumously)];

1063-7788/05/6801-0001$26.00

and Yu.Ts. Oganesyan, JINR (for a set of papers devoted to the discovery of the stability island).

The journal held out through a period of hard times for science in this country—the late 1980s and the 1990s. It is busy developing new publishing methods and keeping a firm hold on its bridgehead. Over the intervening years, the *Physics of Atomic Nuclei* citation index has quadrupled.

We are confident that the journal will continue to appear and develop together with Russian nuclear physics and, while changing in a rapidly changing world, maintain its high standards.

Editorial Board

Physics of Atomic Nuclei, Vol. 68, No. 1, 2005, pp. 104–113. From Yadernaya Fizika, Vol. 68, No. 1, 2005, pp. 106–115.

ELEMENTARY PARTICLES AND FIELDS
Theory

Off-Mass-Shell Dual Amplitude with Mandelstam Analyticity*

V. Magas**

Departament de Física Teórica, Universitat de Valéncia, Valéncia, Spain

Received December 1, 2003; in final form, April 28, 2004

Abstract—A model for the Q^2-dependent dual amplitude with Mandelstam analyticity (DAMA) is proposed. The modified DAMA (M-DAMA) preserves all the attractive properties of DAMA, such as its pole structure and Regge asymptotics, and leads to a generalized dual amplitude $A(s,t,Q^2)$. This generalized amplitude can be checked in the known kinematical limits; i.e., it should reduce to the ordinary dual amplitude on mass shell and to the nuclear structure function when $t=0$. In such a way, we complete a unified "two-dimensionally dual" picture of strong interaction. By comparing the structure function F_2, resulting from M-DAMA, with phenomenological parametrizations, we fix the Q^2 dependence in M-DAMA. In all studied regions, i.e., in the large- and low-x limits as well as in the resonance region, the results of M-DAMA are in qualitative agreement with the experiment. © *2005 Pleiades Publishing, Inc.*

1. INTRODUCTION

About thirty years ago, Bloom and Gilman [1] observed that the prominent resonances in inelastic electron–proton scattering (see Fig. 1) do not disappear with increasing photon virtuality Q^2 with respect to the "background" but, instead, fall at roughly the same rate as the background. Furthermore, the smooth scaling limit proved to be an accurate average over resonance bumps seen at lower Q^2 and s; this is so-called Bloom–Gilman or hadron–parton duality.

For the inclusive e^-p reaction, we introduce virtuality Q^2, $Q^2=-q^2=-(k-k')^2\geq 0$, and Bjorken variable x. These variables x, Q^2 and Mandelstam variable s (of the γ^*p system), $s=(p+q)^2$, obey the relation

$$s=Q^2(1-x)/x+m^2, \qquad (1)$$

where m is the proton mass.

Since its discovery, hadron–parton duality has been studied in a number of papers [2] and new supporting data has come from recent experiments [3, 4]. These studies were aimed mainly at answering the questions: In which way can a limited number of resonances reproduce the smooth scaling behavior? The main theoretical tools in these studies were finite energy sum rules and perturbative QCD calculations, whenever applicable. Our aim, instead, is the construction of an explicit dual model combining direct channel resonances, Regge behavior typical for hadrons and scaling behavior typical for the partonic picture. Some attempts in this direction have already been made in [5–8], which we will discuss in more detail below.

The possibility that a limited (small) number of resonances can build up the smooth Regge behavior was demonstrated by means of finite energy sum rules [9]. Later it was confused by the presence of an infinite number of narrow resonances in the Veneziano model [10], which made its phenomenological application difficult, if not impossible. Similar to the case of resonance–Reggeon duality [9], hadron–parton duality was established [1] by means of finite energy sum rules, but it was not realized explicitly like the Veneziano model (or its further modifications).

The first attempts to combine resonance (Regge) behavior with Bjorken scaling were made [11–13] at low energies (large x), with the emphasis on the right choice of the Q^2 dependence, such as to satisfy the required behavior of form factors, vector meson

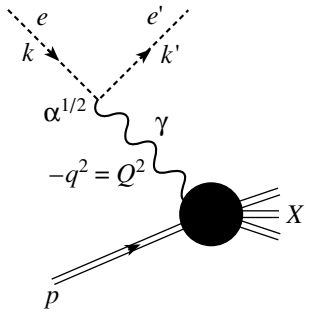

Fig. 1. Kinematics of deep inelastic scattering.

*This article was submitted by the author in English.

**e-mail: Volodymyr.Magas@ific.uv.es

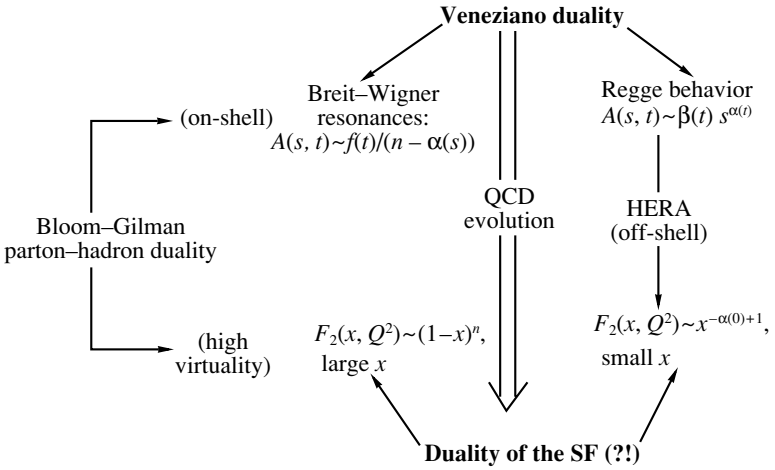

Fig. 2. Veneziano (or resonance–Reggeon) duality [10] and Bloom–Gilman (or hadron–parton) duality [1] in strong interactions. From [6].

dominance [the validity (or failure) of the (generalized) vector meson dominance is still disputable] with the requirement of Bjorken scaling. Similar attempts in the high-energy (low-x) region became popular recently, stimulated by the HERA data. These are discussed in Section 6.

Recently, in a series of papers [5–8], the authors made attempts to build a generalized Q^2-dependent dual amplitude $A(s,t,Q^2)$. This amplitude, a function of three variables, should have correct known limits; i.e., it should reduce to the on-shell hadronic scattering amplitude on the mass shell and to the nuclear structure function (SF) when $t=0$. In such a way, we could complete a unified "two-dimensionally dual" picture of strong interaction [5–8]—see Fig. 2.

In [5, 6], the authors tried to introduce Q^2 dependence in the Veneziano amplitude [10] or more advanced Dual Amplitude with Mandelstam Analyticity (DAMA) [14]. The Q^2 dependence can be introduced either through a Q^2-dependent Regge trajectory [5], leading to a problem of physical interpretation of such an object, or through the g parameter of DAMA [5, 6]. This last way seems to be more realistic [6], but it is also restricted due to the DAMA model requirement $g>1$ [14]. The authors [5–8] relate the imaginary part of amplitude to the total cross section and then to the nucleon SF: $F_2(x,Q^2)\sim\sigma_{\rm tot}\sim \mathrm{Im}A(s(x,Q^2),t=0,Q^2)$, which was compared to the experimental data (we shall discuss this chain in more detail in Section 6). In this way, the low-x behavior of F_2 prescribed a transcendental equation for $g(Q^2)$ (see [6] for more details), which led to $g(Q^2\to\infty)\to 0$, forbidden by DAMA definition. Therefore, such an identification of $g(Q^2)$ is allowed only in the limited range of Q^2, as was actually stressed by the authors.

Recently, this problem was also studied in the framework of field theory. In [15], the off-shell continuation of the Veneziano formula was derived in the Moyal star formulation of Witten's string field theory.

In [7, 8], the authors went in an opposite direction—they built a Regge-dual model with Q^2-dependent form factors, inspired by the pole series expansion of DAMA, which fits the SF data in the resonance region. The hope was to reconstruct later the Q^2-dependent dual amplitude, which would lead to such an expansion. It is important that DAMA not only allows but rather requires nonlinear complex Regge trajectories [14]. Then the trajectory with a restricted real part leads to a limited number of resonances.

A consistent treatment of the problem requires taking into account the spin dependence. This was done in [8], and a substantial improvement of the fit, in comparison to earlier works [7] ignoring the spin dependence, was found. Nevertheless, the applicability range of the above model [8] is limited to the resonance region, as was actually discussed by the authors. For the sake of simplicity, we ignore spin dependence in this paper. Our goal is rather to check qualitatively the proposed new way of constructing the "two-dimensionally dual" amplitude.

2. MODIFIED DAMA MODEL

The DAMA integral is a generalization of the integral representation of the B function used in the

Veneziano model [14]:[1)]

$$D(s,t)=\int\limits_0^1 dz\left(\frac{z}{g}\right)^{-\alpha_s(s')-1}\left(\frac{1-z}{g}\right)^{-\alpha_t(t'')-1}, \tag{2}$$

where $a'=a(1-z)$, $a''=az$, and g is a free parameter ($a=s,t$), $g>1$, and $\alpha_s(s)$ and $\alpha_t(t)$ stand for the Regge trajectories in the s and t channels.[2)]

In this paper, we propose a modified definition of DAMA (M-DAMA) with Q^2 dependence [17]. It also can be considered as a next step in generalization of the Veneziano model. M-DAMA preserves the attractive features of DAMA, such as pole decompositions in s and t and Regge asymptotics, yet it gains the Q^2-dependent form factors, correct $Q^2\to\infty$ limit for $t=0$ ($F_2(x,Q^2)$ at large x), etc.

The proposed M-DAMA integral reads

$$D(s,t,Q^2)=\int\limits_0^1 dz\left(\frac{z}{g}\right)^{-\alpha_s(s')-\beta(Q^{2\prime\prime})-1} \times\left(\frac{1-z}{g}\right)^{-\alpha_t(t'')-\beta(Q^{2\prime})-1}, \tag{3}$$

where $\beta(Q^2)$ is a smooth dimensionless function of Q^2, which will be specified later on from studying different regimes of the above integral.

The on-mass-shell limit, $Q^2=0$, leads to the shift of the s- and t-channel trajectories by a constant factor $\beta(0)$ (to be determined later), which can be simply absorbed by the trajectories, and, thus, M-DAMA reduces to DAMA. In the general case of the virtual particle with mass M, we have to replace Q^2 by (Q^2+M^2) in the M-DAMA integral.

Now all the machinery developed for the DAMA model (see, for example, [14]) can be applied to the above integral. Below, we shall report briefly only some of its properties, relevant for further discussion.

3. SINGULARITIES IN M-DAMA

The dual amplitude $D(s,t,Q^2)$ is defined by integral (3) in the domain $\mathrm{Re}(\alpha_s(s')+\beta(Q^{2\prime\prime}))<0$ and $\mathrm{Re}(\alpha_t(t'')+\beta(Q^{2\prime}))<0$. For monotonically decreasing function $\mathrm{Re}\beta(Q^2)$ (or nonmonotonic function with maximum at $Q^2=0$) and for increasing or constant real parts of the trajectories, the first of these equations, applied for $0\le z\le 1$, means

$$\mathrm{Re}(\alpha_s(s)+\beta(0))<0. \tag{4}$$

Similarly, the second one leads to

$$\mathrm{Re}(\alpha_t(t)+\beta(0))<0. \tag{5}$$

To enable us to study the properties of M-DAMA in the domains $\mathrm{Re}(\alpha_s(s')+\beta(Q^{2\prime\prime}))\ge 0$ and $\mathrm{Re}(\alpha_t(t'')+\beta(Q^{2\prime}))\ge 0$, which are of the main interest, we have to make an analytical continuation of M-DAMA. It can be done in the same way as for DAMA [14]—basically, we need to transform the integration contour in the complex z plane in such a way that $z=0$ and $z=1$ will no longer be the end points of the integration contour; instead, the contour will run around these points at an arbitrarily close distance. The important thing here is that such a procedure will lead to an extra factor

$$\{\exp[-2\pi i(\alpha_s(s')+\beta(Q^{2\prime\prime}))]-1\} \times\{\exp[-2\pi i(\alpha_t(t'')+\beta(Q^{2\prime}))]-1\}$$

in the denominator of the M-DAMA integrand [14], which generates two moving poles z_n and z_m from zeros of the denominator:[3)]

$$\alpha_s(s(1-z_n))+\beta(Q^2z_n)=n, \quad n=0,1,2,\ldots, \tag{6}$$

$$\alpha_t(tz_m)+\beta(Q^2(1-z_m))=m, \quad m=0,1,2,\ldots. \tag{7}$$

The motion of the poles z_n and z_m with s, t, and Q^2 depends on the particular choice of the trajectories and function $\beta(Q^2)$. The integrand (3) also has two fixed branch points at $z=0$ and $z=1$. If the trajectories $\alpha_s(s)$, $\alpha_t(t)$ or function $\beta(Q^2)$ have thresholds and correspondingly their own branch points, then these also generate the branch points of the M-DAMA integrand. For example, z_s generated by the threshold s_{th} in α_s trajectory will be given by $s(1-z_s)=s_{\mathrm{th}}\Rightarrow z_s=1-s_{\mathrm{th}}/s$. Similarly, the threshold Q^2_{th} in $\beta(Q^2)$ will generate $z^1_Q=1-Q^2_{\mathrm{th}}/Q^2$ and $z^2_Q=Q^2_{\mathrm{th}}/Q^2$ branch points. In this work, we are not going to discuss the threshold behavior of M-DAMA, but we assume that the trajectory $\alpha_s(s)$ has a threshold and an imaginary part above it, and

[1)]There are several integral representations of DAMA [14]; here, we shall use the most common one.

[2)]In [14], the authors use the same trajectories in s and t channels. This is easy to generalize—see, for example, [16].

[3)]Of course, the above denominator has zeros for $n,m=-1,-2,\ldots$ also, but, as we said above, we need to make an analytical continuation only in the region where $\mathrm{Re}(\alpha_s(s')+\beta(Q^{2\prime\prime}))\ge 0$ and $\mathrm{Re}(\alpha_t(t'')+\beta(Q^{2\prime}))\ge 0$. This point is not clearly described in [14]—there are no poles in DAMA for $\mathrm{Re}\alpha(s)<0$ (or $\mathrm{Re}\alpha(t)<0$).

correspondingly dual amplitude $D(s,t,Q^2)$ also has an imaginary part above the threshold.

The singularities of the dual amplitude are generated by pinches which occur in the collisions of the above-mentioned moving and fixed singularities of the integrand.

(1) The collision of a moving pole $z = z_n$ with the branch point $z = 0$ results in a pole at $s = s_n$, where s_n is defined by

$$\alpha_s(s_n) + \beta(0) = n. \tag{8}$$

Please note the presence of an extra (in comparison to DAMA) term $\beta(0)$. It can be considered as a shift of the trajectory. If $\beta(0)$ is an integer number, then the modification is trivial.

(2) The collision of a moving pole $z = z_n$ with the branch point $z = 1$ results in a pole at $Q^2 = Q_n^2$, defined by

$$\alpha_s(0) + \beta(Q_n^2) = n. \tag{9}$$

In this sense, we can think of $\beta(Q^2)$ as a kind of trajectory, but we do not mean that it describes real physical particles. Also, we will see later that, with a proper choice of $\beta(Q^2)$, we can avoid these unphysical poles, and $\beta(Q^2)$ required by the low-x behavior of the nucleon SF is exactly of this type.

(3) Similarly, the collision of a moving pole $z = z_m$ with the branch point $z = 1$ results in a pole at $t = t_m$, defined by

$$\alpha_t(t_m) + \beta(0) = m. \tag{10}$$

(4) The collision of a moving pole $z = z_m$ with the branch point $z = 0$ results in a pole at $Q^2 = Q_m^2$, defined by

$$\alpha_t(0) + \beta(Q_m^2) = m. \tag{11}$$

Note that, if $\alpha_s(0) = \alpha_t(0)$, the poles in Q^2 will be degenerate.

Generally, since poles in s, t, and Q^2 arise when pairs of different singularities collide, the amplitude is free of terms like $\sim 1/[(s - s_n)(t - t_m)]$ or $\sim 1/[(s - s_n)(Q^2 - Q_m^2)]$, which would possess poles simultaneously in two variables (similarly, there are no terms possessing the poles simultaneously in all three variables). Although in some degenerate cases this could happen—for example, if $\beta(x) = \alpha_s(x)$ and $\alpha_t(0) = \alpha_s(0)$, then we could have terms like $\sim 1/[(s - s_n)(Q^2 - Q_n^2)^2]$ coming from Eqs. (8), (9), and (11). For further discussion, we shall consider a nondegenerated case.

4. POLE DECOMPOSITIONS

Let us consider the pinch resulting from the collision of a pole at $z = z_n$ with the branch point $z = 0$. The point z_n is a solution of Eq. (6):

$$\alpha_s(s(1 - z_n)) + \beta(Q^2 z_n) = n, \quad n = 0, 1, 2, \ldots.$$

For $z_n \to 0$, it becomes

$$\alpha_s(s) - s\alpha_s'(s) z_n + \beta(0) + \beta'(0) Q^2 z_n = n \tag{12}$$

and so

$$z_n = \frac{n - \alpha_s(s) - \beta(0)}{\beta'(0) Q^2 - s\alpha_s'(s)}. \tag{13}$$

We see that $z_n \to 0$ when $s \to s_n$ given by Eq. (8). The residue at the pole z_n (see [14] for more details) is equal to

$$\begin{aligned} 2\pi i \mathrm{Res}_{z_n} &= \frac{1}{\beta'(0) Q^2 - s\alpha_s'(s)} \left(\frac{z_n}{g}\right)^{-n-1} \\ &\times \left(\frac{1 - z_n}{g}\right)^{-\alpha_t(tz_n) - \beta(Q^2(1-z_n)) - 1} \\ &= \frac{g^{n+1} [\beta'(0) Q^2 - s\alpha_s'(s)]^n}{[n - \alpha_s(s) - \beta(0)]^{n+1}} \\ &\times \left(\frac{1 - z_n}{g}\right)^{-\alpha_t(tz_n) - \beta(Q^2(1-z_n)) - 1}. \end{aligned} \tag{14}$$

It contains a pole at $s = s_n$ of order of $n + 1$. By expanding the nonpole cofactor in (14), we obtain

$$\begin{aligned} &\left(\frac{1 - z_n}{g}\right)^{-\alpha_t(tz_n) - \beta(Q^2(1-z_n)) - 1} \\ &= \sum_{l=0}^{n} C_l(t, Q^2) z_n^l + F_n(t, Q^2, z_n), \end{aligned} \tag{15}$$

where

$$\begin{aligned} C_l(t, Q^2) &= \frac{1}{l!} \frac{d^l}{dz^l} \\ &\times \left[\left(\frac{1 - z}{g}\right)^{-\alpha_t(tz) - \beta(Q^2(1-z)) - 1}\right]_{z=0}, \end{aligned} \tag{16}$$

$$\frac{F_n(t, Q^2, z)}{z^{n+1}} \to \text{const}, \quad z \to 0. \tag{17}$$

Finally, inserting (15) into (14), we end up with the following expression for the pole term:

$$\begin{aligned} D_{s_n}(s, t, Q^2) &= g^{n+1} \\ &\times \sum_{l=0}^{n} \frac{[\beta'(0) Q^2 - s\alpha_s'(s)]^l C_{n-l}(t, Q^2)}{[n - \alpha_s(s) - \beta(0)]^{l+1}}. \end{aligned} \tag{18}$$

Formula (18) shows that our $D(s,t,Q^2)$ does not contain ancestors and that an $(n+1)$-fold pole

emerge on the nth level. The crossing-symmetric term can be obtained in a similar way by considering the case 3 from the list above (see Section 3).

The modifications with respect to DAMA are (i) the shift of the trajectory $\alpha_s(s)$ by the constant factor of $\beta(0)$ (we can easily remove this shift including $\beta(0)$ in the trajectory); (ii) the coefficients C_l are now Q^2-dependent and can be directly associated with the form factors. The presence of the multipoles [Eq. (18)] does not contradict the theoretical postulates. On the other hand, they can be removed without any harm to the dual model by means of the so-called Van der Corput neutralizer.[4)] This procedure [14] seems to work for M-DAMA equally well as for DAMA and will result in a "Veneziano-like" pole structure:

$$D_{s_n}(s,t,Q^2) = g^{n+1}\frac{C_n(t,Q^2)}{n-\alpha_s(s)-\beta(0)}. \qquad (19)$$

The Q^2-pole terms can be obtained by considering cases 2 and 4 from Section 3, but as we shall see later in Section 7, with our choice of $\beta(Q^2)$, we avoid Q^2 poles.

5. ASYMPTOTIC PROPERTIES OF M-DAMA

Let us now discuss the asymptotic properties of M-DAMA. For this purpose, we rewrite the M-DAMA expression (3) in the following way:

$$D(s,t,Q^2) = \int_0^1 dz e^{-W(z;s,t,Q^2)}, \qquad (20)$$

where

$$W(z;s,t,Q^2) \qquad (21)$$
$$= \ln\left(\frac{z}{g}\right)(\alpha_s(s') + \beta(Q^{2\prime\prime}) + 1)$$
$$+ \ln\left(\frac{1-z}{g}\right)(\alpha_t(t'') + \beta(Q^{2\prime}) + 1).$$

Below, a simplified notation $W(z)$ will be used instead of $W(z;s,t,Q^2)$.

The calculations in this section will be done through the saddle-point method, and we will care only about the leading-order term, although the method allows one to derive subleading terms to any order. If z_0 is the saddle point, then the leading term is given by

$$D(s,t,Q^2) = \sqrt{\frac{2\pi}{W''(z_0)}}e^{-W(z_0)}. \qquad (22)$$

Let us prove the Regge asymptotic behavior of M-DAMA ($s\to\infty$, $t, Q^2 = \text{const}$). First, we consider the behavior of $D(s,t,Q^2)$ for $s\to-\infty$ and fixed Q^2 and t such that $\mathrm{Re}(\alpha_t(t)+\beta(0))+1<0$. In this case, analytical continuation is not needed. The first term of the integrand (3) is a decreasing function of s for any $0\le z<1$; it vanishes for $z=0$. The second term vanishes at the opposite end of the integration region. As is easy to see, the integrand has a maximum somewhere in the middle, i.e., a saddle point, which can be found from the equation

$$W'(z) = \ln\left(\frac{z}{g}\right) \qquad (23)$$
$$\times(-s\alpha_s'(s(1-z)) + Q^2\beta'(Q^2z))$$
$$+\frac{1}{z}(\alpha_s(s(1-z)) + \beta(Q^2z) + 1)$$
$$+\ln\left(\frac{1-z}{g}\right)(t\alpha_t'(tz) - Q^2\beta'(Q^2(1-z)))$$
$$-\frac{1}{1-z}(\alpha_t(tz) + \beta(Q^2(1-z)) + 1) = 0.$$

Since t and Q^2 are constants, the saddle point approaches $z=1$ as $s\to-\infty$. For large $|s|$ and near $z=1$, there are only two important terms in Eq. (23); the rest can be neglected:

$$-s\alpha_s'(s(1-z))\ln\left(\frac{z}{g}\right) \qquad (24)$$
$$-\frac{1}{1-z}(\alpha_t(tz) + \beta(Q^2(1-z)) + 1) = 0$$
$$\Rightarrow 1 - z_0 = \frac{a}{s} + O\left(\frac{1}{s^2}\right),$$

where

$$a = \frac{\alpha_t(t) + \beta(0) + 1}{\alpha_s'(0)\ln g}. \qquad (25)$$

Since we are interested now only in the leading term, we can neglect all the corrections and write

$$W''(z_0) \approx -s^2\alpha_s''(0)\ln g \qquad (26)$$
$$-\left(\frac{s\alpha_s'(0)\ln g}{\alpha_t(t)+\beta(0)+1}\right)^2(\alpha_t(t)+\beta(0)+1)$$
$$= s^2\left(-\alpha_s''(0)\ln g - \frac{\alpha_s'(0)\ln g}{a}\right).$$

And finally,

$$D|_{s\to-\infty} \approx -s^{\alpha_t(t)+\beta(0)} \qquad (27)$$

[4)] In brief, the procedure [14] is to multiply the integrand of (3) by a function $\phi(z)$ which has the following properties: $\phi(0)=0$, $\phi(1)=1$, $\phi^n(1)=0$, $n=1,2,3,\ldots$. The function $\phi(z) = 1-\exp(-z/(1-z))$, for example, satisfies the above conditions.

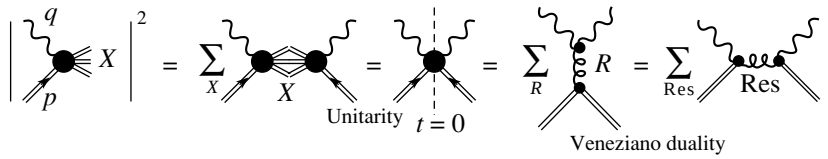

Fig. 3. According to Veneziano (or resonance–Reggeon) duality, a proper sum of either t-channel or s-channel resonance exchanges accounts for the whole amplitude. From [6].

$$\times g^{\alpha_t(t)+\alpha_s(a)+\beta(Q^2)+\beta(0)+2} a^{-\alpha_t(t)-\beta(0)-1} \times \sqrt{\frac{2\pi}{-\alpha_s''(0)\ln g - (\alpha_s'(0)\ln g)/a}}.$$

Thus,

$$D(s,t,Q^2) \sim s^{\alpha_t(t)+\beta(0)} g^{\beta(Q^2)}, \quad s \to -\infty. \tag{28}$$

Now, what happens if we enter into the physical region of the s channel? In this case, we have to use the analytical continuation of M-DAMA. Using exactly the same method as in [14], it is possible to show that, if the trajectory satisfies some restriction on its increase, then the Regge asymptotic behavior (28) holds for $s \to \infty$. Of course, $D(s,t,Q^2)$ becomes a complex function, due to complex trajectory $\alpha_s(s)$, and Eq. (28) gives the asymptotics for both real and imaginary parts.

Thus, in the Regge limit, M-DAMA has the same asymptotic behavior as DAMA (except for the shift $\beta(0)$). It is more interesting to study the new regime, which does not exist in DAMA—the limit $Q^2 \to \infty$, with constant s, t. We assume that $\beta(Q^2) \to -\infty$ for $Q^2 \to \infty$. From Eq. (23), we can easily find that, in this limit, $z_0 = 1/2$. Then

$$\begin{aligned} W''(z_0) &= 2Q^4\beta''(Q^2/2) \\ &+ 8(Q^2\beta'(Q^2/2) - \beta(Q^2/2)) \\ &+ 4(s\alpha_s'(s/2) - \alpha_s(s/2) - t\alpha_t'(t/2) - \alpha_t(t/2)) \\ &- \ln(2g)(s^2\alpha_s''(s/2) - t^2\alpha_t''(t/2)) - 8 \end{aligned} \tag{29}$$

and

$$D(s,t,Q^2)|_{Q^2\to\infty} \approx (2g)^{2\beta(Q^2/2)+\alpha_s(s/2)+\alpha_t(t/2)+2} \sqrt{\frac{2\pi}{W''(z_0)}}. \tag{30}$$

For deep inelastic scattering (DIS), as we shall see below, if s and t are fixed and $Q^2 \to \infty$, then $u = -2Q^2 \to -\infty$, as follows from the kinematic relation $s + t + u = 2m^2 - 2Q^2$. So, we also need to study the $D(u,t,Q^2)$ term in this limit. If $|\alpha_u(-2Q^2)|$ grows slower than $|\beta(Q^2)|$ or terminates when $Q^2 \to \infty$, then the previous result [Eq. (30), s to be changed to $u = -2Q^2$] is still valid. We shall come back to these results in the next section to check the proposed form of $\beta(Q^2)$.

6. NUCLEON STRUCTURE FUNCTION

The kinematics of inclusive electron–nucleon scattering, applicable to both high energies, typical of HERA, and low energies, as at JLab, is shown in Fig. 1. And Fig. 3 shows how DIS is related to the forward elastic ($t = 0$) $\gamma^* p$ scattering, and then the latter is decomposed into a sum of the s-channel resonance exchanges.

The total cross section is related to the SF by

$$F_2(x,Q^2) = \frac{Q^2(1-x)}{4\pi\alpha(1+4m^2x^2/Q^2)}\sigma_t^{\gamma^* p}, \tag{31}$$

where α is the fine structure constant. In Eq. (31), we neglected $R(x,Q^2) = \sigma_L(x,Q^2)/\sigma_T(x,Q^2)$, which is a reasonable approximation.

The total cross section is related to the imaginary part of the scattering amplitude,

$$\sigma_{\rm tot}^{\gamma^* p}(x,Q^2) = \frac{8\pi}{P_{\rm c.m.}\sqrt{s}}{\rm Im}A(s(x,Q^2),t=0,Q^2), \tag{32}$$

where $P_{\rm c.m.}$ is the center-of-mass momentum of the reaction,

$$P_{\rm c.m.} = \frac{s-m^2}{2(1-x)}\sqrt{\frac{1+4m^2x^2/Q^2}{s}}, \tag{33}$$

for DIS. Thus, we have

$$F_2(x,Q^2) = \frac{4Q^2(1-x)^2}{\alpha\,(s-m^2)\,(1+4m^2x^2/Q^2)^{3/2}} \times {\rm Im}A(s(x,Q^2),t=0,Q^2). \tag{34}$$

The minimal model for the scattering amplitude is a sum [18]

$$A(s,0,Q^2) = c(s-u)(D(s,0,Q^2) - D(u,0,Q^2)), \tag{35}$$

providing the correct signature at the high-energy limit, where c is a normalization coefficient (u is not

an independent variable, since $s+u=2m^2-2Q^2$ or $u=-Q^2(1+x)/x+m^2$). As was said at the beginning, we disregard the symmetry properties of the problem (spin and isospin), concentrating on its dynamics.

In the low-x limit: $x\to 0,\ t=0,\ Q^2=\text{const}$, $s=Q^2/x\to\infty$, $u=-s$, we obtain, with the help of Eqs. (28) and (35),

$$\mathrm{Im}A(s,0,Q^2)|_{s\to\infty}\sim s^{\alpha_t(t)+\beta(0)+1}g^{\beta(Q^2)}. \quad (36)$$

Our philosophy in this section is the following: we specify a particular choice of $\beta(Q^2)$ in the low-x limit and then we use M-DAMA integral (3) to calculate the dual amplitude and, correspondingly, SF in all kinematical domains. We will see that the resulting SF has qualitatively correct behavior in all regions. Even more—our choice of $\beta(Q^2)$ will automatically remove Q^2 poles.

According to the two-component duality picture [19], both the scattering amplitude A and the structure function F_2 are the sums of the diffractive and nondiffractive terms. At high energies, both terms are of the Regge type. For γ^*p scattering, only the positive-signature exchanges are allowed. The dominant ones are the Pomeron and f Reggeon, respectively. The relevant scattering amplitude is as follows:

$$B(s,Q^2)=iR_k(Q^2)\Big(\frac{s}{m^2}\Big)^{\alpha_k(0)}, \quad (37)$$

where α_k and R_k are Regge trajectories and residues and k stands either for the Pomeron or for the Reggeon. As usual, the residue is chosen "by hand" to satisfy approximate Bjorken scaling for the SF [20, 21]. From Eqs. (34) and (37), SF is given as

$$F_2(x,Q^2)\sim Q^2R_k(Q^2)\Big(\frac{s}{m^2}\Big)^{\alpha_k(0)-1}, \quad (38)$$

where $x=Q^2/s$ in the limit $s\to\infty$.

It is obvious from Eq. (38) that Regge asymptotics and scaling behavior require the residue to fall like $\sim(Q^2)^{-\alpha_k(0)}$. Actually, it could be more involved if we require the correct $Q^2\to 0$ limit to be respected and the observed scaling violation (the "HERA effect") to be included. Various models to cope with the above requirements have been suggested [20–22]. At HERA, especially at large Q^2, scaling is so badly violated that it may not be explicit anymore.

Data show that the Pomeron exchange leads to a rising structure function at large s (low x). To provide for this, we have two options: either to assume a supercritical Pomeron with $\alpha_{\mathrm{P}}(0)>1$ or to assume a critical ($\alpha_{\mathrm{P}}(0)=1$) dipole (or higher multipole) Pomeron [22–24]. The latter leads to the logarithmic behavior of the SF,

$$F_{2,\mathrm{P}}(x,Q^2)\sim Q^2R_{\mathrm{P}}(Q^2)\ln\Big(\frac{s}{m^2}\Big), \quad (39)$$

which proves to be equally efficient [22, 24].

Let us now come back to M-DAMA results. Using Eqs. (34) and (36), we obtain

$$F_2\sim s^{\alpha_t(0)+\beta(0)}Q^2g^{\beta(Q^2)}. \quad (40)$$

Choosing

$$\beta(0)=-1, \quad (41)$$

we restore the asymptotics (38) and this allows us to use trajectories in their commonly used form. It is important to find such $\beta(Q^2)$ which can provide for Bjorken scaling (if one also wants to take into account the scaling violation, then the problem just gets more technical). If we choose $\beta(Q^2)$ in the form

$$\beta(Q^2)=d-\gamma\ln(Q^2/Q_0^2), \quad (42)$$

with

$$\gamma=(\alpha_t(0)+\beta(0)+1)/\ln g=\alpha_t(0)/\ln g, \quad (43)$$

where d and Q_0^2 are some parameters, we get the exact Bjorken scaling.

Actually, expression (42) might cause problems in the $Q^2\to 0$ limit. To avoid this, it is better to use a modified expression

$$\beta(Q^2)=\beta(0)-\gamma\ln\left(\frac{Q^2+Q_0^2}{Q_0^2}\right) \quad (44)$$
$$=-1-\frac{\alpha_t(0)}{\ln g}\ln\left(\frac{Q^2+Q_0^2}{Q_0^2}\right).$$

This choice leads to

$$F_2(x,Q^2)\sim x^{1-\alpha_t(0)}\Big(\frac{Q^2}{Q^2+Q_0^2}\Big)^{\alpha_t(0)}, \quad (45)$$

where the slowly varying factor $(Q^2/[Q^2+Q_0^2])^{\alpha_t(0)}$ is typical for the Bjorken scaling violation (see, for example, [21]).

Now let us turn to the large-x limit. In this regime, $x\to 1$, s is fixed, $Q^2=(s-m^2)/(1-x)\to\infty$, and, correspondingly, $u=-2Q^2$. Using Eqs. (30), (34), and (35), we obtain

$$F_2\sim(1-x)^2Q^4g^{2\beta(Q^2/2)} \quad (46)$$
$$\times\sqrt{\frac{2\pi}{W''(z_0)}}(g^{\alpha_s(s/2)}-g^{\alpha_u(-Q^2)}).$$

For $Q^2\to\infty$, factors $(g^{\alpha_s(s/2)}-g^{\alpha_u(-Q^2)})$ and $W''(z_0)\approx 8\gamma\ln(Q^2/Q_0^2)$ are slowly varying functions

of Q^2 under our assumption about $\alpha_u(-Q^2)$. Thus, we end up with qualitatively correct behavior,

$$F_2 \sim \left(\frac{2Q_0^2}{Q^2}\right)^{2\gamma \ln(2g)} \sim (1-x)^{2\alpha_t(0)\ln(2g)/\ln g}. \quad (47)$$

Let us now study F_2 given by M-DAMA in the resonance region. The existence of resonances in SF at large x is not surprising by itself: as follows from (32) and (34), they are the same as in the $\gamma^* p$ total cross section, but in a different coordinate system.

For M-DAMA, the resonances in the s channel are defined by condition (8). For simplicity, let us assume that we performed the Van der Corput neutralization and, thus, the pole terms appear in the form (19). In the vicinity of the resonance $s = s_{\rm res}$, only the resonance term $D_{\rm res}(s, 0, Q^2)$ is important in the scattering amplitude and correspondingly in the SF.

The complex pattern of the nucleon SF in the resonance region was developed a long time ago (see, for example, [25]). There are several dozen resonances in the $\gamma^* p$ system in the region above the pion–nucleon threshold, but only a few of them can be identified more or less unambiguously for various reasons. Therefore, instead of identifying each resonance, phenomenologists frequently consider a few maxima (usually three) above the elastic scattering peak, corresponding to some "effective" resonance contributions. In the Regge-dual model [7, 8], it was shown that, for a reasonable fit, it is enough to take into account three resonance terms, corresponding to "effective"[5] Δ, N, N^* trajectories with one resonance on each, plus the background. As was already discussed in the introduction, in the Regge-dual model, the Q^2 dependence was introduced by hand. Let us now check what we get from M-DAMA.

Using $\beta(Q^2)$ in the form (44), which gives Bjorken scaling at large s, we obtain from Eq. (16)

$$C_1(Q^2) = \left(\frac{gQ_0^2}{Q^2+Q_0^2}\right)^{\alpha_t(0)} \quad (48)$$
$$\times \left[\alpha_t(0) + \ln g \frac{Q^2}{Q^2+Q_0^2} - \frac{\alpha_t(0)}{\ln g}\ln\left(\frac{Q^2+Q_0^2}{Q_0^2}\right)\right].$$

[5] By "effective" trajectory, the authors mean that, in the fitting procedure, the parameters of these trajectories were allowed to differ from their values at the physical trajectories. In this way, the authors tried to account for the contributions from the other resonances. The "effective" trajectories did not move far from the physical ones, thus giving a posteriori justification for this approach.

The term $(Q_0^2/[Q^2+Q_0^2])^{\alpha_t(0)}$ gives the typical Q^2 dependence for the form factor (the rest is a slowly varying function of Q^2).

If we calculate higher orders of C_n for subleading resonances, we will see that the Q^2 dependence is still defined by the same factor $(Q_0^2/[Q^2+Q_0^2])^{\alpha_t(0)}$. Here comes the important difference from the Regge-dual model [7, 8] motivated by introducing Q^2 dependence through the parameter g. As we see from Eq. (19), g enters with different powers for different resonances on one trajectory—the powers are increasing with the step 2. Thus, if $g \sim (Q_0^2/[Q^2+Q_0^2])^{\Delta}$, then the form factor for the first resonance ($n = 0$) is $\sim (Q_0^2/[Q^2+Q_0^2])^{\Delta}$, and for the second one ($n = 2$) it is $\sim (Q_0^2/[Q^2+Q_0^2])^{3\Delta}$, etc. As discussed in [4], the present accuracy of the data does not allow one to discriminate between the constant powers of form factor (for example, [3, 4, 25, 26] and this work) and increasing ones.

7. HOW TO AVOID Q^2 POLES?

General study of the M-DAMA integral allows the Q^2 poles (see cases 2 and 4 in Section 3), which would be unphysical. The appearance and properties of these singularities depend on the particular choice of the function $\beta(Q^2)$, and for our choice, given by Eq. (44), the Q^2 poles can be avoided.

We have chosen $\beta(Q^2)$ to be a decreasing function; then, according to conditions (9) and (11), there are no Q^2 poles in M-DAMA in the physical domain $Q^2 \geq 0$ if

$$\mathrm{Re}\beta(0) < -\alpha_s(0), \quad \mathrm{Re}\beta(0) < -\alpha_t(0). \quad (49)$$

We have already fixed $\beta(0) = -1$ [Eq. (41)], and thus we see that, indeed, we do not have Q^2 poles, except for the case of a supercritical Pomeron with the intercept $\alpha_{\rm P}(0) > 1$. Such a supercritical Pomeron would generate one unphysical pole at $Q^2 = Q^2_{\rm pole}$ defined by the equation

$$-1 - \frac{\alpha_{\rm P}(0)}{\ln g}\ln\left(\frac{Q^2+Q_0^2}{Q_0^2}\right) + \alpha_{\rm P}(0) = 0 \quad (50)$$
$$\Rightarrow Q^2_{\rm pole} = Q_0^2(g^{(\alpha_{\rm P}(0)-1)/\alpha_{\rm P}(0)} - 1).$$

Therefore, we can conclude that M-DAMA does not allow a supercritical trajectory—which is good from the theoretical point of view, since such a trajectory violates the Froissart–Martin limit [27].

As was discussed above, there are other phenomenological models which use a dipole Pomeron with the intercept $\alpha_{\rm P}(0) = 1$ and also fit the data (see,

for example, [18]). This is a very interesting case—($\alpha_t(0) = 1$)—for the proposed model. At first glance, it seems that we should anyway have a pole at $Q^2 = 0$. It should result from the collision of the moving pole $z = z_0$ with the branch point $z = 0$, where $\alpha_t(0) + \beta(Q^2(1 - z_0)) = 0$ in our case. Then, checking the conditions for such a collision,

$$\alpha_t(0) - t\alpha_t'(0)z_0 + \beta(Q^2) - \beta'(Q^2)Q^2 z_0 = 0$$
$$\Rightarrow z_0 = \frac{-\alpha_t(0) - \beta(Q^2)}{t\alpha_t'(0) - Q^2\beta'(Q^2)},$$

we see that, for $t = 0$ and for $\beta(Q^2)$ given by Eq. (44), the collision is simply impossible, because $z_0(Q^2)$ does not tend to 0 for $Q^2 \to 0$. Thus, for the Pomeron with $\alpha_{\rm P}(0) = 1$, M-DAMA does not contain any unphysical singularity.

On the other hand, a Pomeron trajectory with $\alpha_{\rm P}(0) = 1$ does not produce rising SF (38), as required by the experiment. So, we need a harder singularity and the simplest one is a dipole Pomeron. A dipole Pomeron produces poles of the second power:

$$D_{\rm dipole}(s, t_m) \propto \frac{C(s)}{(m - \alpha_{\rm P}(t) + 1)^2}; \qquad (51)$$

usually, the simple pole is also taken into account (we write a sum of simple pole and dipole)—see, for example, [23] and references therein. Formally, such a dipole Pomeron can be written as

$$\frac{\partial}{\partial\alpha_{\rm P}}\frac{C(s)}{(m - \alpha_{\rm P}(t) + 1)},$$

and generalizing this

$$D_{\rm dipole}(s, t) = \frac{\partial}{\partial\alpha_{\rm P}}D(s, t), \qquad (52)$$

where $D(s, t)$ can be given for example by DAMA or M-DAMA. Applying this expression to the asymptotic formula of M-DAMA [Eq. (28)], we obtain a term $g^{\beta(Q^2)}s^{\alpha_t(t)+\beta(0)}\ln s$, which then leads to a logarithmically rising SF (for $\alpha_{\rm P}(0) + \beta(0) = 0$)—the one given by Eq. (39).

For $\beta(Q^2)$ in the form (44), M-DAMA will generate an infinite number of the Q^2 poles concentrated near the "ionization point" $Q^2 = -Q_0^2$. Although these are in the unphysical region of negative Q^2, such a feature of the model (i) makes us think of $\beta(Q^2)$ as a kind of trajectory, which is not the case, as was stressed above, and (ii) might create a problem for a general theoretical treatment, for example, for making an analytical continuation in Q^2. To avoid this, we can redefine $\beta(Q^2)$ in the nonphysical Q^2 region, for example, in the following way:

$$\beta(Q^2) \qquad (53)$$
$$= \begin{cases} -1 - \dfrac{\alpha_t(0)}{\ln g}\ln\left(\dfrac{Q^2 + Q_0^2}{Q_0^2}\right), & \text{for } Q^2 \geq 0, \\ -1 - \dfrac{\alpha_t(0)}{\ln g}\ln\left(\dfrac{Q_0^2 - Q^2}{Q_0^2}\right), & \text{for } Q^2 < 0. \end{cases}$$

This function has a maximum at $Q^2 = 0$, $\beta(0) = -1$. M-DAMA with $\beta(Q^2)$ given by Eq. (53) preserves all its good properties discussed above and does not contain any singularity in Q^2 (except for the supercritical Pomeron case, which we do not allow).

8. CONCLUSIONS

A new model for the Q^2-dependent dual amplitude with Mandelstam analyticity is proposed. The M-DAMA preserves all the attractive properties of DAMA, such as its pole structure and Regge asymptotics, but it also leads to generalized dual amplitude $A(s, t, Q^2)$ and in this way realizes a unified "two-dimensionally dual" picture of strong interaction [5–8] (see Fig. 2). This amplitude, when $t = 0$, can be related to the nuclear structure function. In Section 6, we compare the SF generated by M-DAMA with phenomenological parametrizations, and in this way we fix the function $\beta(Q^2)$, which introduces the Q^2 dependence in M-DAMA [Eq. (3)]. The conclusion is that, for both large- and low-x limits as well as for the resonance region, the results of M-DAMA are in qualitative agreement with the experiment.

General study of the M-DAMA integral tells us about the possibility of having poles in Q^2. These singularities may be avoided with our choice of $\beta(Q^2)$ and also by putting a restriction on the physical trajectories—the use of a supercritical trajectory would lead to one Q^2 pole.

In the proposed formulation, a Q^2 dependence is introduced into DAMA through the additional function $\beta(Q^2)$. Although in the integrand this function stands next to Regge trajectories, this, as was stressed already, does not mean that it also corresponds to some physical particles. There is no qualitative difference between the two ways of introducing Q^2 dependence into DAMA: through the Q^2-dependent parameter g, i.e., function $g(Q^2)$ [5, 6], or through the function $\beta(Q^2)$. On the other hand, the second way, i.e., M-DAMA, is applicable for all range of Q^2 and it results in physically correct behavior in all tested limits.

ACKNOWLEDGMENTS

I thank L.L. Jenkovszky for fruitful and enlightening discussions. Also, I acknowledge the support by INTAS under grant no. 00-00366.

REFERENCES

1. E. D. Bloom and E. J. Gilman, Phys. Rev. Lett. **25**, 1149 (1970); Phys. Rev. D **4**, 2901 (1971).
2. A. De Rujula, H. Georgi, and H. D. Politzer, Ann. Phys. (N.Y.) **103**, 315 (1977); C. E. Carlson and N. Mukhopadhyay, Phys. Rev. D **41**, 2343 (1990); P. Stoler, Phys. Rev. Lett. **66**, 1003 (1991); Phys. Rev. D **44**, 73 (1991); I. Afanasiev, C. E. Carlson, and Ch. Wahlqvist, Phys. Rev. D **62**, 074011 (2000); F. E. Close and N. Isgur, Phys. Lett. B **509**, 81 (2001); N. Isgur, S. Jeschonnek, W. Melnitchouk, and J. W. Van Orden, Phys. Rev. D **64**, 054004 (2001); F. Gross, I. V. Musatov, and Yu. A. Simonov, nucl-th/0402097.
3. I. Niculescu *et al.*, Phys. Rev. Lett. **85**, 1182 (2000); **85**, 1186 (2000).
4. M. Osipenko *et al.*, Phys. Rev. D **67**, 092001 (2003); hep-ex/0309052.
5. R. Fiore, L. L. Jenkovszky, and V. Magas, Nucl. Phys. B (Proc. Suppl.) **99A**, 131 (2001).
6. L. L. Jenkovszky, V. K. Magas, and E. Predazzi, Eur. Phys. J. A **12**, 361 (2001); nucl-th/0110085; L. L. Jenkovszky and V. K. Magas, hep-ph/0111398.
7. R. Fiore *et al.*, Eur. Phys. J. A **15**, 505 (2002); hep-ph/0212030.
8. R. Fiore *et al.*, Phys. Rev. D **69**, 014004 (2004); A. Flachi *et al.*, Ukr. Fiz. Zh. **48**, 507 (2003).
9. A. A. Logunov, L. D. Soloviov, and A. N. Tavkhelidze, Phys. Lett. B **24B**, 181 (1967); R. Dolen, D. Horn, and C. Schmid, Phys. Rev. **166**, 1768 (1968).
10. G. Veneziano, Nuovo Cimento A **57**, 190 (1968).
11. M. Damashek and F. J. Gilman, Phys. Rev. D **1**, 1319 (1970).
12. A. Bramon, E. Etim, and M. Greco, Phys. Lett. B **41B**, 609 (1972).
13. E. Etim and A. Malecki, Nuovo Cimento A **104**, 531 (1991).
14. A. I. Bugrij *et al.*, Fortschr. Phys. **21**, 427 (1973).
15. I. Bars and I. Y. Park, Phys. Rev. D **69**, 086007 (2004).
16. A. I. Bugrij, Z. E. Chikovani, and L. L. Jenkovszky, Z. Phys. C **4**, 45 (1980).
17. L. L. Jenkovszky, V. K. Magas, and E. V. Vakulina, in *Proceedings of the 4th International Workshop on Very High Multiplicity Physics, Alushta, Crimea, Ukraine, May 31–June 4, 2003;* L. L. Jenkovszky, V. I. Kuvshinov, and V. K. Magas, in *Proceedings of the 8th International School–Seminar on The Actual Problems of Microworld Physics, Gomel, Belarus, July 28–Aug. 8, 2003.*
18. A. I. Bugrij, Z. E. Chikovani, and N. A. Kobylinsky, Ann. Phys. (Leipzig) **35**, 281 (1978).
19. P. Freund, Phys. Rev. Lett. **20**, 235 (1968); H. Harari, Phys. Rev. Lett. **20**, 1395 (1968).
20. M. Bertini, M. Giffon, and E. Predazzi, Phys. Lett. B **349**, 561 (1995).
21. A. Capella, A. Kaidalov, C. Merino, and J. Tran Thanh Van, Phys. Lett. B **337**, 358 (1994); L. P. A. Haakman, A. Kaidalov, and J. H. Koch, Phys. Lett. B **365**, 411 (1996).
22. P. Desgrolard, A. Lengyel, and E. Martynov, Eur. Phys. J. C **7**, 655 (1999).
23. A. N. Wall, L. L. Jenkovszky, and B. V. Struminsky, Fiz. Élem. Chastits At. Yadra **19**, 180 (1988) [Sov. J. Part. Nucl. **19**, 77 (1988)].
24. P. Desgroland *et al.*, Phys. Lett. B **459**, 265 (1999); O. Schildknecht and H. Spiesberger, hep-ph/9707447; D. Haidt and W. Buchmuller, hep-ph/9605428; P. Desgroland *et al.*, Phys. Lett. B **309**, 191 (1993).
25. S. Stein *et al.*, Phys. Rev. **12**, 1884 (1975).
26. V. V. Davydovsky and B. V. Struminsky, Ukr. Fiz. Zh. **47**, 1123 (2002); hep-ph/0205130.
27. M. Froissart, Phys. Rev. **123**, 1053 (1961); A. Martin, Phys. Rev. **129**, 1432 (1963).

Physics of Atomic Nuclei, Vol. 68, No. 1, 2005, pp. 114–118. From Yadernaya Fizika, Vol. 68, No. 1, 2005, pp. 116–120.

ELEMENTARY PARTICLES AND FIELDS
Theory

Magnetic Moment of the ρ Meson in QCD Sum Rules*

A. V. Samsonov**

Institute of Theoretical and Experimental Physics,
Bol'shaya Cheremushkinskaya ul. 25, Moscow, 117259 Russia

Received June 23, 2003; in final form, February 18, 2004

Abstract—The magnetic moment μ of the ρ meson is calculated in the framework of QCD sum rules in external fields. Bare-loop calculations (parton model) give $\mu_{\text{part}} = 2.0$ (in units $e/(2m_\rho)$). The contribution of operators of dimension 6 reduces this value: $\mu = 1.5 \pm 0.3$. © *2005 Pleiades Publishing, Inc.*

1. INTRODUCTION

Investigation of the static properties of vector mesons provides an important information about strong interaction of hadrons. In particular, the vector dominance hypothesis (VDM) supposes that the interaction of a real or virtual photon with hadrons proceeds in such a way that the photon first transforms into vector mesons ρ, ω, ϕ, which then undergo interaction with hadrons. In the consistent Lagrangian formulation of VDM, it is assumed [1] (for a review, see [2]) that ρ mesons are Yang–Mills vector bosons. In the framework of this hypothesis, the ρ-meson magnetic moment is equal to 2 (in units $e/(2m_\rho)$), at least if strong interaction is neglected.

The goal of this paper is to calculate the ρ-meson magnetic moment in QCD using the method of QCD sum rules in external fields [3, 4].

In [5], the ρ-meson form factors were found at intermediate momentum transfer by QCD sum rules. By extrapolation of the ρ-meson magnetic form factor to the point $Q^2 = 0$ (outside the applicability domain of the technique), it was found that the ρ-meson magnetic moment μ is close to 2. However, this result cannot be considered as conclusive; the direct calculation of μ in QCD in a model-independent way is still absent. The ρ-meson magnetic moment was calculated in models based on the Dyson–Schwinger equation [6, 7] and in the framework of relativistic quantum mechanics [8].

Here, we work in the limit of zero quark masses; α_s corrections are neglected.

2. PHENOMENOLOGICAL PART OF THE SUM RULE

We consider the correlator of two vector currents in the external electromagnetic field:

$$\Pi_{\mu\nu}(p) = i\int d^4x e^{ipx}\langle T(j_\mu(x)j_\nu^+(0)\rangle_F. \quad (1)$$

Here, subscript F denotes the presence of the external electromagnetic field with strength $F_{\rho\lambda}$ and j_μ is the vector current with ρ-meson quantum numbers: $j_\mu = \overline{u}\gamma_\mu d$. Its matrix element is

$$\langle\rho^+|j_\mu|0\rangle = (m_\rho^2/g_\rho)e_\mu, \quad (2)$$

where m_ρ is the ρ-meson mass, g_ρ is the $\rho-\gamma$ coupling constant, $g_\rho^2/(4\pi) = 1.27$, and e_μ is the ρ-meson polarization vector.

In the limit of a weak external field, we consider only terms linear in $F_{\rho\lambda}$ in the correlator $\Pi_{\mu\nu}$ (1):

$$\Pi_{\mu\nu} = \Pi^0_{\mu\nu} + i\sqrt{4\pi\alpha}\Pi_{\mu\nu\chi\sigma}F_{\chi\sigma}. \quad (3)$$

We find the magnetic moment from the sum rule for the invariant function $\Pi(p^2)$ at a certain kinematical structure of $\Pi_{\mu\nu\chi\sigma}$ (3). To obtain this sum rule, we calculate Π at $p^2 < 0$ as the operator product expansion series. On the other hand, we saturate dispersion relation for Π by the contributions of physical states. After equating these representations, the required sum rule appears.

Therefore, first of all, one should choose a kinematical structure.

The electromagnetic vertex of the ρ meson has the following general form [5]:

$$\langle\rho(p+q,e^{r'})|j_\chi^{\text{el}}|\rho(p,e^r)\rangle \quad (4)$$
$$= -e_\sigma^{r'}e_\rho^r\Big(((2p+q)_\chi g_{\rho\sigma} - (p+q)_\rho g_{\chi\sigma}$$
$$- p_\sigma g_{\rho\chi})F_1(-q^2) + (g_{\chi\rho}q_\sigma - g_{\chi\sigma}q_\rho)F_2(-q^2)$$

*This article was submitted by the author in English.

**e-mail: sams@heron.itep.ru

$$+\frac{1}{m_\rho^2}(p+q)_\rho p_\sigma (2p+q)_\chi F_3(-q^2)\Big).$$

In (4), $j_\chi^{\rm el} = e_u\overline{u}\gamma_\chi u + e_d\overline{d}\gamma_\chi d$ is electromagnetic current; e_u, e_d are u- and d-quark charges; and F_1, F_2, and F_3 are electric, magnetic, and quadrupole form factors, respectively,

$$F_1(0)=1, \quad \mu = 1 + F_2(0), \tag{5}$$

μ being the ρ-meson magnetic moment.

Using (2) and (4), we obtain for the $\langle 0|j_\mu|\rho\rangle\langle\rho|j_\chi^{\rm el}|\rho\rangle\langle\rho|j_\nu|0\rangle\epsilon_\chi$ transition

$$\begin{aligned}
&-i\sum_{r,r'}\langle 0|j_\mu|\rho^{r'}\rangle\langle\rho^{r'}|j_\chi^{\rm el}|\rho^r\rangle\langle\rho^r|j_\nu|0\rangle\epsilon_\chi \qquad (6)\\
&= i\frac{m_\rho^4}{g_\rho^2}\sum_{r,r'} e_\mu^{r'}e_\sigma^{r'}e_\rho^r e_\nu^r\epsilon_\chi\Big(((2p+q)_\chi g_{\rho\sigma}\\
&\quad -(p+q)_\rho g_{\chi\sigma} - p_\sigma g_{\rho\chi})F_1(-q^2)\\
&\quad +(g_{\chi\rho}q_\sigma - g_{\chi\sigma}q_\rho)F_2(-q^2) + \frac{1}{m_\rho^2}(p+q)_\rho\\
&\quad \times p_\sigma(2p+q)_\chi F_3(-q^2)\Big).
\end{aligned}$$

Here, ϵ_χ is photon polarization, and r, r' are the ρ-meson polarization indices. Let us consider in this expression the terms linear in q_σ. We sum over ρ-meson polarizations, retain the antisymmetric over χ,σ part, introduce $F_{\chi\sigma} = i(\epsilon_\chi q_\sigma - \epsilon_\sigma q_\chi)$, and obtain for (6)

$$\begin{aligned}
&-\frac{m_\rho^4}{2g_\rho^2}F_{\chi\sigma}\Big(\Big(F_2+\frac{1}{2}F_1\Big)\frac{1}{p^2}(p_\nu(p_\chi g_{\mu\sigma} - p_\sigma g_{\mu\chi})\\
&\quad -p_\mu(p_\chi g_{\nu\sigma} - p_\sigma g_{\nu\chi})) + \frac{1}{2}F_1\frac{1}{p^2}\\
&\times(p_\nu(p_\chi g_{\mu\sigma} - p_\sigma g_{\mu\chi}) + p_\mu(p_\chi g_{\nu\sigma} - p_\sigma g_{\nu\chi}))\\
&\quad +(F_2+F_1)(g_{\mu\chi}g_{\nu\sigma} - g_{\mu\sigma}g_{\nu\chi})\Big).
\end{aligned}$$

Form factor F_3 does not give a contribution linear in q_σ.

Thus, we choose the structure

$$p_\nu(p_\chi g_{\mu\sigma} - p_\sigma g_{\mu\chi}) - p_\mu(p_\chi g_{\nu\sigma} - p_\sigma g_{\nu\chi}). \tag{7}$$

In comparison with another possible structure, $g_{\mu\chi}g_{\nu\sigma} - g_{\mu\sigma}g_{\nu\chi}$, (7) contains two additional powers of momentum in the numerator, which result in better convergence of the operator expansion series.

It should be noted here that, as follows from the vector current conservation, the structure antisymmetric over field indices χ, σ in $\Pi_{\mu\nu\chi\sigma}$ (3) is antisymmetric over ρ-meson indices μ, ν too.

From (5), one can see that $F_2(0) + (1/2)F_1(0) = \mu - 1/2$.

Thus, one should calculate the invariant function $\Pi(p^2)$ at the structure (7) in $\Pi_{\mu\nu\chi\sigma}$. In the dispersion relation for Π, we use the simplest model of a physical spectrum, which contains the lowest resonance and continuum. The phenomenological representation of Π has the form

$$\begin{aligned}
\Pi(p^2) &= \int ds\frac{\rho_L(s)}{(s-p^2)^2} + \ldots,\\
\rho_L(s) &= -\frac{m_\rho^4}{2g_\rho^2}\frac{1}{s}\left(\mu - \frac{1}{2}\right)\delta(s-m_\rho^2)\\
&\quad + f(s)\theta(s-s_\rho).
\end{aligned}$$

Here, dots mean the contributions of nondiagonal transitions (for example, $\langle 0|j_\mu|\rho^*\rangle\langle\rho^*|j_\chi\epsilon_\chi|\rho\rangle\langle\rho|j_\nu|0\rangle$, where ρ^* is the excited state with the same quantum numbers as ρ), function f represents the continuum contribution, and s_ρ is the continuum threshold for the ρ meson.

Retaining only the terms which do not vanish after Borel transformation, we obtain

$$\begin{aligned}
\Pi(p^2) &= -\frac{m_\rho^2}{2g_\rho^2}\frac{\mu - 1/2}{(m_\rho^2 - p^2)^2} \qquad (8)\\
&\quad + \frac{\tilde{C}}{m_\rho^2 - p^2} + \int\limits_{s_\rho}^{\infty} ds\frac{f(s)}{(s-p^2)^2},
\end{aligned}$$

where $\tilde{C}$ appears due to nondiagonal transitions.

3. CALCULATION OF THE VECTOR CURRENT CORRELATOR

Now let us calculate $\Pi(p^2)$, based on the operator product expansion in QCD.

The quark propagator in the external electromagnetic field $F_{\mu\nu}$ in the fixed-point gauge $x_\mu A_\mu = 0$, $A_\mu = -(1/2)F_{\mu\nu}x_\nu$, can be found in [3]:

$$\begin{aligned}
&\langle Tq_\alpha^a(x)\overline{q}_\beta^b(0)\rangle_F\\
&= \frac{i\delta^{ab}(\hat{x})_{\alpha\beta}}{2\pi^2x^4} - \frac{\delta^{ab}g_{\alpha\beta}}{12}\langle\overline{q}q\rangle\\
&\quad -\frac{i\delta^{ab}\langle\overline{q}\sigma_{\rho\lambda}q\rangle_F}{48}(\gamma_\rho\gamma_\lambda - \gamma_\lambda\gamma_\rho)_{\alpha\beta}\\
&\quad -\frac{\delta^{ab}\sqrt{4\pi\alpha}e_qF_{\rho\lambda}}{32\pi^2x^2}(\hat{x}\gamma_\rho\gamma_\lambda + \gamma_\rho\gamma_\lambda\hat{x})_{\alpha\beta}.
\end{aligned}$$

Here, e_q is the quark charge; α, β are spinor indices; a, b are color indices; and (see [3]) $\langle\overline{q}\sigma_{\rho\lambda}q\rangle_F = \sqrt{4\pi\alpha}e_q\chi F_{\rho\lambda}\langle\overline{q}q\rangle$, χ being the quark condensate magnetic susceptibility.

The expression for the quark propagator in the external electromagnetic and soft gluon fields $\hat{S}_{FG}$ has the following form in momentum representation [3]:

$$\hat{S}_{FG} = -\frac{ige_q\sqrt{4\pi\alpha}F_{\rho\lambda}G^n_{\sigma\tau}t^n}{2p^6}$$
$$\times\left(\gamma_\lambda\gamma_\tau\gamma_\rho\gamma_\sigma\hat{p} - 2p_\lambda\gamma_\tau\gamma_\sigma\gamma_\rho - 2p_\tau\gamma_\lambda\gamma_\rho\gamma_\sigma\right.$$
$$\left. - \frac{8p_\rho p_\tau g_{\lambda\sigma}}{p^2}\hat{p} + 2g_{\lambda\tau}\gamma_\sigma\gamma_\rho\hat{p} - 2g_{\lambda\tau}g_{\rho\sigma}\hat{p}\right).$$

Here, $G^n_{\sigma\tau}$ is the gluon field strength and t^n are the color matrices.

The contribution of the loop diagrams to $\Pi(p^2)$ is equal to

$$-\frac{3}{16\pi^2}\int\limits_0^\infty\frac{ds}{(s-p^2)^2}. \qquad (9)$$

According to the quark–hadron duality, the continuum contribution in the interval of $P^2 = -p^2$ from s_ρ to infinity is determined by the bare loop in this interval. Therefore, function f in (8) is constant: $f = -3/(16\pi^2)$.

The loop diagrams correspond to the operator of the lowest dimension $F_{\rho\lambda}$. Operators of dimension 4 are absent. As was shown in [3], operator $\overline{q}(D_\mu\gamma_\nu - D_\nu\gamma_\mu)q$ has opposite C parity with respect to the electromagnetic field and cannot be induced by them, while operator $\epsilon_{\mu\nu\rho\lambda}\overline{q}\gamma_5\gamma_\rho D_\lambda q$ vanishes due to the equation of motion for massless quarks.

There are a number of vacuum expectation values of operators of dimension 6: $\langle\overline{q}\sigma_{\rho\lambda}q\rangle_F\langle\overline{q}q\rangle$, $\langle G^n_{\sigma\tau}G^n_{\sigma\tau}\rangle F_{\mu\nu}$, and

$$g\langle\overline{q}((G^n_{\mu\lambda}D_\nu - \overleftarrow{D}_\nu G^n_{\mu\lambda}) \qquad (10)$$
$$-(G^n_{\nu\lambda}D_\mu - \overleftarrow{D}_\mu G^n_{\nu\lambda}))\gamma_\lambda t^n q\rangle_F,$$
$$\epsilon_{\mu\nu\rho\lambda}g\langle\overline{q}(G^n_{\rho\xi}D_\lambda + \overleftarrow{D}_\lambda G^n_{\rho\xi})\gamma_\xi\gamma_5 t^n q\rangle_F,$$
$$d^{ikl}\langle(G^i_{\mu\lambda}G^k_{\lambda\rho}G^l_{\rho\nu} - G^i_{\nu\lambda}G^k_{\lambda\rho}G^l_{\rho\mu})\rangle_F,$$

where D_μ is the covariant derivative and d^{ikl} are $SU(3)$ structure constants.

The diagrams corresponding to the operator $\langle G^n_{\sigma\tau}G^n_{\sigma\tau}\rangle F_{\mu\nu}$ have infrared divergence. We introduce the cutoff over transversal momenta λ and obtain their contribution into $\Pi(p^2)$:

$$-\frac{1}{36}\left\langle\frac{\alpha_s}{\pi}G^2\right\rangle\left(\frac{1}{2\lambda^4p^2} - \frac{1}{6\lambda^2p^4} + \frac{3}{p^6}\right). \qquad (11)$$

As for vacuum expectation values (10), usually such operators can be calculated by constructing the corresponding sum rules. An example of such an approach can be found in [9] for dimension-4 operators and symmetric tensor field. But for operators (10), this approach is inapplicable because of their high dimension. However, the first and second vacuum expectation values in (10) are suppressed by the factor N_c^{-1} (N_c is the color number) as compared with $\langle\overline{q}\sigma_{\rho\lambda}q\rangle_F\langle\overline{q}q\rangle$, while the third contains the factor g^3. So we can expect that they are rather small and disregard them.

The dominating contribution appears from no-loop diagrams with hard gluon exchange. In our case, such diagrams contain the operator $\langle\overline{q}\sigma_{\rho\lambda}q\rangle_F\langle\overline{q}q\rangle$. They give

$$\frac{2}{9}\frac{g^2\langle\bar{q}q\rangle\chi}{p^6}. \qquad (12)$$

It should be noted here that the quark condensate magnetic susceptibility χ is negative.

Collecting expressions (9), (11), and (12), one can find the operator product expansion part of the sum rule:

$$\Pi(p^2) = -\frac{3}{16\pi^2}\int\limits_0^\infty\frac{ds}{(s-p^2)^2} \qquad (13)$$
$$+\frac{2}{9}\frac{g^2\langle\bar{q}q\rangle\chi}{p^6} - \frac{1}{36}\left\langle\frac{\alpha_s}{\pi}G^2\right\rangle$$
$$\times\left(\frac{1}{2\lambda^4p^2} - \frac{1}{6\lambda^2p^4} + \frac{3}{p^6}\right).$$

4. RESULTS AND DISCUSSION

After Borel transformation

$$\hat{B}(M^2) = \lim_{\substack{P^2,n\to\infty\\ P^2/n=M^2}}\frac{(P^2)^{n+1}}{n!}\left(-\frac{d}{dP^2}\right)^n,$$
$$P^2 = -p^2 > 0,$$

we equate the phenomenological (8) and operator product expansion (13) parts of sum rule and obtain (M^2 is the Borel mass)

$$\mu - \frac{1}{2} + CM^2 \qquad (14)$$
$$= \frac{3g_\rho^2M^2}{8\pi^2m_\rho^2}(1 - e^{-s_\rho/M^2})e^{m_\rho^2/M^2} - \frac{g_\rho^2}{m_\rho^2}e^{m_\rho^2/M^2}$$
$$\times\left(-\frac{2g^2\langle\bar{q}q\rangle^2\chi}{9M^2} + \frac{1}{36}\left\langle\frac{\alpha_s}{\pi}G^2\right\rangle\right.$$
$$\left.\times\left(\frac{M^2}{\lambda^4} + \frac{1}{3\lambda^2} + \frac{3}{M^2}\right)\right),$$

C appears due to nondiagonal transitions.

We use the following values of parameters:

$m_\rho = 0.77$ GeV is the ρ-meson mass,

$g_\rho^2/(4\pi) = 1.27$ is the $\rho-\gamma$ coupling constant,

$s_\rho = 1.5\ \mathrm{GeV}^2$ is the continuum threshold for ρ meson,

$\langle(\alpha_s/\pi)G^2\rangle = 0.009 \pm 0.007\ \mathrm{GeV}^4$ is the gluon condensate [10],

$g^2\langle\bar{q}q\rangle^2 = (0.28 \pm 0.09) \times 10^{-2}\ \mathrm{GeV}^6$ is the quark condensate [10],

$\chi = -(5.7 \pm 0.6)\ \mathrm{GeV}^{-2}$ is the quark condensate magnetic susceptibility [11],

$\lambda^2 = 0.8\ \mathrm{GeV}^2$ is the cutoff over transversal momenta.

First of all, let us consider the contribution of the bare loop (and continuum). It is given by the first term in the right-hand side of (14). In [12], the following relation for g_ρ can be found:

$$\frac{g_\rho^2 M^2}{4\pi^2 m_\rho^2}(1 - e^{-s_\rho/M^2})e^{m_\rho^2/M^2} = 1. \qquad (15)$$

Substituting (15) into (14) and omitting for a while the terms with quark and gluon condensates, one can obtain a very simple answer:

$$\mu_{\mathrm{part}} - \frac{1}{2} = \frac{3}{2}.$$

We see that, in the parton model approximation, the ρ-meson magnetic moment is equal to 2. This result agrees with the prediction of the vector dominance hypothesis.

Now let us analyze the whole Eq. (14). In order to find the value of magnetic moment, we approximate the right-hand side of (14) (see figure) by a straight line in the interval $0.9 \le M^2 \le 1.3\ \mathrm{GeV}^2$ and find its ordinate at zero Borel mass.

Thus, we obtain

$$\mu = 1.5. \qquad (16)$$

The contribution of the operators of dimension-6 to this value does not exceed 20%.

The contribution of the terms which contain λ^2 is not more than 20% of the total contribution of dimension-6 operators. That is why variation of λ^2 within the interval $0.6 \le \lambda^2 \le 1.0\ \mathrm{GeV}^2$ does not change the value of magnetic moment.

The variations of the values of the quark and gluon condensates within the given limits change the value of magnetic moment by $\lesssim 10\%$ each.

The uncertainty in the value of the quark condensate magnetic susceptibility results in an error of a few percent in the value of the magnetic moment.

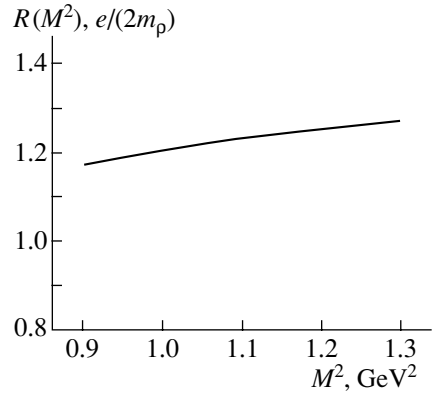

The right-hand side of Eq. (14) $R(M^2)$ as a function of M^2.

Variation of the continuum threshold s_ρ for the ρ meson within reasonable limits gives the same effect.

Supposing that the contribution of vacuum expectation values (10) does not exceed 50% of that from diagrams with hard gluon exchange (12), we obtain after collecting all uncertainties

$$\mu = 1.5 \pm 0.3.$$

This is our final result.

In [13], it was shown that the approximation procedure is correct (nonlinear terms can be safely neglected) when $\mu \gg CM^2$. In our case, $CM^2/\mu \approx 0.2-0.3$.

Thus, we find that, in the parton model (bare-loop) approximation, the ρ-meson magnetic moment $\mu_{\mathrm{part}} = 2$, whereas the nonperturbative interactions decrease this quantity by a quarter: $\mu = 1.5 \pm 0.3$. It is important to mention that all considered operator product expansion corrections are negative, i.e., result in a decrease in μ in comparison with $\mu_{\mathrm{part}} = 2$. Since the effective values of the Borel parameter M^2 are about $1\ \mathrm{GeV}^2$, one may expect that perturbative corrections are remarkable and can reach $\sim 20\%$.

The value of the ρ-meson magnetic moment was calculated in a number of papers within models based on the Dyson–Schwinger equation. In [6], the value $\mu = 2.69$ was found. In [7], several results are compared, and the values of μ lie between 2.5 and 3.0. The relativistic quantum mechanics model gives [8] $\mu = 2.23 \pm 0.13$. Recently, the value of the magnetic moment was found in the light cone QCD sum rule technique [14]. The result is $\mu = 2.2 \pm 0.2$. Unfortunately, while α_s corrections are not calculated (we plan to do this in the next paper), it is hard to say with certainty if this discrepancy is real or not.

ACKNOWLEDGMENTS

The author is grateful to B.L. Ioffe for posing the problem and valuable discussions and to A.G. Oganesian for helpful discussions.

This work is supported in part by grant from CRDF (grant no. RP2-2247), INTAS 2000 (project no. 587), and the Russian Foundation for Basic Research (project no. 00-02-17808).

REFERENCES

1. N. Kroll, T. Lee, and B. Zumino, Phys. Rev. **157**, 1376 (1967).
2. B. Ioffe, V. Khoze, and L. Lipatov, *Hard Processes* (North-Holland, Amsterdam, 1984), Part 5.
3. B. Ioffe and A. Smilga, Nucl. Phys. B **232**, 109 (1984).
4. I. Balitsky and A. Yung, Phys. Lett. B **129B**, 328 (1983).
5. B. Ioffe and A. Smilga, Nucl. Phys. B **216**, 373 (1983).
6. F. Hawes and M. Pichowsky, Phys. Rev. C **59**, 1743 (1999).
7. M. Hecht and B. H. J. McKellar, Phys. Rev. C **57**, 2638 (1998).
8. J. P. B. C. de Melo and T. Frederico, Phys. Rev. C **55**, 2043 (1997).
9. A. Oganesian and A. Samsonov, JHEP **0109**, 002 (2001).
10. B. L. Ioffe, Yad. Fiz. **66**, 32 (2003) [Phys. At. Nucl. **66**, 30 (2003)].
11. V. M. Belyaev and Ya. I. Kogan, Yad. Fiz. **40**, 1035 (1984) [Sov. J. Nucl. Phys. **40**, 659 (1984)].
12. M. Shifman, A. Vainshtein, and V. Zakharov, Nucl. Phys. B **147**, 385, 448 (1979).
13. B. L. Ioffe, Yad. Fiz. **58**, 1492 (1995) [Phys. At. Nucl. **58**, 1408 (1995)].
14. T. Aliev, I. Kanik, and M. Savci, hep-ph/0303068.

Physics of Atomic Nuclei, Vol. 68, No. 1, 2005, pp. 119–123. From Yadernaya Fizika, Vol. 68, No. 1, 2005, pp. 121–125.

ELEMENTARY PARTICLES AND FIELDS
Theory

QCD and Hybrid NBD on Oscillating Moments of Multiplicity Distributions in Lepton- and Hadron-Initiated Reactions*

I. M. Dremin**

Lebedev Physical Institute, Russian Academy of Sciences, Leninskiĭ pr. 53, Moscow, 119991 Russia

Received January 29, 2004

Abstract—QCD predictions for moments of multiplicity distributions are compared with experimental data on e^+e^- collisions and their two-NBD fits. Moments of the multiplicity distribution in a two-NBD model for 1.8-TeV pp collisions are considered. Three-NBD model predictions and fits for pp at LHC energies are also discussed. Analytic expressions for moments of hybrid NBD are derived and used to get insight into jet parameters and multicomponent structure of the processes. Interpretation of observed correlations is proposed. © *2005 Pleiades Publishing, Inc.*

Multiplicity distributions are the integral characteristics of multiparticle production processes. They can be described either in terms of probabilities $P_n(E)$ to create n particles at energy E or by the moments of these distributions. It has been found that their shapes possess some common features in all reactions studied. At comparatively low energies, these distributions are relatively narrow and have sub-Poissonian shapes. With energy increase, they widen and fit a Poisson distribution. At even higher energies, the shapes become super-Poissonian; i.e., their widths are larger than for a Poisson distribution. The width increases with energy and, moreover, some shoulder-like substructures appear.

Their origin is usually ascribed to multicomponent contents of the process. In a QCD description of e^+e^- processes, these could be subjets formed inside quark and gluon jets (for reviews, see, e.g., [1, 2]). In phenomenological approaches, the multiplicity distribution in a single subjet is sometimes approximated by a negative binomial distribution (NBD) first proposed for hadronic reactions in [3]. For hadron-initiated processes, these peculiarities are also explained by the multicomponent structure of the process. This is either multiladder exchange in the dual parton model [4, 5], varying number of clans [6], or multiparton interactions [7, 8]. These subprocesses are related to the state of matter during the collision (e.g., there are speculations about a nonhomogeneous matter distribution in impact parameters [9], not to speak of quark–gluon plasma [10] behaving as a liquid [11], etc.).

Such evolution of the multiplicity distributions can be quantitatively described by the energy behavior of their moments. These moments reveal the correlations inherent for the state of matter formed during the collision. Similarly to virial coefficients in statistical physics, they can tell us about the equation of state of this matter. To introduce them, let us write the generating function of the multiplicity distribution as

$$G(E,z)=\sum_{n=0}^{\infty}P_n(E)(1+z)^n. \qquad (1)$$

In what follows, we will use the so-called unnormalized factorial $\mathcal{F}_q$ and cumulant $\mathcal{K}_q$ moments defined according to the formulas

$$\mathcal{F}_q=\sum_n P_n n(n-1)\dots(n-q+1) \qquad (2)$$
$$=\left.\frac{d^qG(E,z)}{dz^q}\right|_{z=0},$$

$$\mathcal{K}_q=\left.\frac{d^q\ln G(E,z)}{dz^q}\right|_{z=0}. \qquad (3)$$

They correspondingly define the total and genuine correlations among the particles produced (for more details, see [2, 12]). These cumulant moments could be considered as the direct analogies of virial coefficients of statistical physics since both are related to genuine (irreducible) correlations. In particular, the first moments describe the mean multiplicity $\langle n\rangle$:

$$\mathcal{F}_1=\mathcal{K}_1=\langle n\rangle, \qquad (4)$$

and the second moments are related to the dispersion D of the distribution P_n:

$$\mathcal{K}_2=\mathcal{F}_2-\langle n\rangle^2=D^2-\langle n\rangle. \qquad (5)$$

*This article was submitted by the author in English.

**e-mail: dremin@lpi.ru

The higher rank moments reveal other asymmetries of distributions, such as skewness. Since both $\mathcal{F}_q$ and $\mathcal{K}_q$ strongly increase with their rank and energy, their ratio

$$H_q = \mathcal{K}_q/\mathcal{F}_q, \tag{6}$$

first introduced in [13], is especially useful due to partial cancellation of these dependences. The factorial moments $\mathcal{F}_q$ are always positive by definition [Eq. (2)], while the cumulant moments $\mathcal{K}_q$ can change sign. Again, let us recall that the changing-sign second virial coefficient in statistical physics implies the liquid state with the van der Waals equation corresponding to repulsion at small distances and attraction at large distances. Cooper pair formation is also related to similar behavior of correlations.

Here, we compare QCD and NBD approaches to the description of multiplicity distributions. We argue that H_q values are more sensitive to minute details of the distributions than their direct χ^2 fits and reveal differences between proposed fits of e^+e^- and $pp(p\bar{p})$ processes. Some estimates for LHC energies will be provided.

The generating functions for quark and gluon jets satisfy definite equations in perturbative QCD (see [2, 14]). It has been analytically predicted in gluodynamics [13] that, at asymptotically high energies, H_q moments are positive and decrease as q^{-2}, but at present energies up to 200 GeV, they become negative at some values of q and reveal the negative minimum at

$$q_{\min} = \frac{1}{h_1\gamma_0} + 0.5 + O(\gamma_0), \tag{7}$$

where $h_1 = b/(8N_c) = 11/24$, $b = 11N_c/3 - 2n_f/3$, $\gamma_0^2 = 2N_c\alpha_s/\pi$, α_s is a coupling strength, and N_c and n_f are the numbers of colors and flavors. At Z^0 energy, $\alpha_s \approx 0.12$, and this minimum is at about $q \approx 5$. It moves to higher ranks with energy increase because the coupling strength decreases. Some hints to possible oscillations of H_q vs. q at higher ranks at LEP energies were obtained in [13]. Then the approximate solution of the gluodynamics equation for the generating function [15] agreed with this and predicted the oscillating behavior at higher ranks. These oscillations were confirmed by experimental data for e^+e^- and hadron-initiated processes first in [16], later in [17], and most recently in [18]. The same conclusions were obtained from an exact solution of equations for quark and gluon jets in the framework of fixed coupling QCD [19]. The physics interpretation of these oscillations as originating from multisubjet structure of the process is related to the (multi)fractal behavior of factorial moments, found also in QCD [20–22]. The asymptotic disappearance of oscillations can be ascribed to the extremely large number of subjets at very high energies.

A recent exact numerical solution of the gluodynamics equation in a wide energy interval [23] coincides with the qualitative features of multiplicity distributions described above. In terms of moments, they correspond to the values of H_q changing sign at each subsequent q (with $H_2 < 0$) at low energies (narrow shapes[1)]), the approach of H_q to zero at the Poisson transition point about 20 GeV for e^+e^- processes, and the positive second moment H_2 with oscillations of higher rank cumulants at Z^0 which disappear asymptotically. At Z^0, the first minimum appears at $q \approx 5$. This confirms earlier exact QCD results [24] at Z^0. It moves to higher ranks with a steadily decreasing amplitude when energy increases. The only free parameter is the QCD cutoff, which is, however, approximately fixed by the coupling strength and does not strongly influence the results.

In parallel, the NBD fits of multiplicity distributions were attempted [6, 25]. The single NBD parametrization is

$$P_n(E) = \frac{\Gamma(n+k_1)}{\Gamma(n+1)\Gamma(k_1)}\left(\frac{n_1}{k_1}\right)^n\left(1+\frac{n_1}{k_1}\right)^{-n-k_1}, \tag{8}$$

where Γ denotes the gamma function. This distribution has two adjustable parameters $n_1(E)$ and $k_1(E)$ which depend on energy. Such a formula happened to describe low-energy data with negative values of k_1 that correspond to binomial fits. At the Poisson transition point, $k_1^{-1} = 0$. The parameter k_1 becomes positive at higher energies. However, the simple fit by formula (8) is valid until the shoulders appear. In that case, this formula is replaced by the hybrid NBD which combines two or more expressions like (8). Each of them has its own energy-dependent parameters n_i, k_i. These distributions are weighted with the energy-dependent probability factors α_i which sum up to 1. Correspondingly, the number of adjustable parameters drastically increases.

A single NBD (8) has positive cumulants for $k_1 > 0$ ($\mathcal{K}_q = \Gamma(q)n_1^q/k_1^{q-1}$) and thus positive $H_q = \Gamma(q)\Gamma(k_1+1)/\Gamma(k_1+q)$. For hybrid NBD, negative H_q can exist. The traditional procedure to calculate higher rank moments is by the iterative relations

$$H_q = 1 - \sum_{m=1}^{q-1}\frac{\Gamma(q)}{\Gamma(m+1)\Gamma(q-m)}H_{q-m}\frac{\mathcal{F}_m\mathcal{F}_{q-m}}{\mathcal{F}_q}. \tag{9}$$

[1)]Narrow distributions always have such cumulants as shown, e.g., in [2].

Table 1

	QCD	L3, untr. data	L3, tr. data	2NBD (OPAL)
H_2	3.9×10^{-2}	$(4.42 \pm 0.11) \times 10^{-2}$	$(4.41 \pm 0.10) \times 10^{-2}$	4.4×10^{-2}
H_3	7.4×10^{-3}	$(7.40 \pm 0.38) \times 10^{-3}$	$(7.20 \pm 0.35) \times 10^{-3}$	7.4×10^{-3}
H_4	4.0×10^{-4}	$(9.69 \pm 2.56) \times 10^{-4}$	$(7.17 \pm 1.42) \times 10^{-4}$	4.9×10^{-4}
H_5	-2.2×10^{-4}	$-(1.30 \pm 1.59) \times 10^{-4}$	$-(3.95 \pm 0.53) \times 10^{-4}$	-2.4×10^{-4}

Strong compensations are inherent in Eq. (9). This calls for high accuracy of numerical calculations. More importantly, the formula does not give any direct insight into the physical reasons for such compensations. Therefore, it is instructive to write the analytic formulas for moments of hybrid NBD which provide a clear interpretation of negative values of cumulants. We have derived these expressions for the two-NBD parametrization (2NBD) given by a sum of two expressions like (8) with two sets of adjustable parameters n_1, k_1, n_2, k_2 weighted with energy-dependent factors α and $1-\alpha$, respectively. 2NBD describes the process with two independent NBD components of mean multiplicities n_i and widths k_i created with probabilities α and $1-\alpha$. The factorial moments for any rank q are given by the simple formula

$$\mathcal{F}_q = \alpha \frac{\Gamma(k_1+q)}{\Gamma(k_1)} \frac{n_1^q}{k_1^q} + (1-\alpha) \frac{\Gamma(k_2+q)}{\Gamma(k_2)} \frac{n_2^q}{k_2^q} \quad (10)$$
$$(0 \le \alpha \le 1).$$

The cumulant moments are more complicated and should be calculated separately for each rank. The first five moments are

$$\mathcal{K}_1 = \mathcal{F}_1 = \langle n \rangle = \alpha n_1 + (1-\alpha) n_2, \quad (11)$$

$$\mathcal{K}_2 = \frac{\alpha n_1^2}{k_1} + \frac{(1-\alpha) n_2^2}{k_2} + \alpha(1-\alpha)(n_1-n_2)^2, \quad (12)$$

$$\mathcal{K}_3 = \frac{2\alpha n_1^3}{k_1^2} + \frac{2(1-\alpha) n_2^3}{k_2^2} + \alpha(1-\alpha)(n_1-n_2)[3(n_1^2/k_1 - n_2^2/k_2) + (1-2\alpha)(n_1-n_2)^2], \quad (13)$$

$$\mathcal{K}_4 = \frac{6\alpha n_1^4}{k_1^3} + \frac{6(1-\alpha) n_2^4}{k_2^3} + \alpha(1-\alpha) \times [(n_1-n_2)^4(1-6\alpha(1-\alpha)) + 11(n_1^2/k_1 - n_2^2/k_2)^2 - 8 n_1 n_2 (n_1/k_1 - n_2/k_2)^2 + 6(1-2\alpha)(n_1-n_2)^2(n_1^2/k_1 - n_2^2/k_2)], \quad (14)$$

$$\mathcal{K}_5 = \frac{24\alpha n_1^5}{k_1^4} + \frac{24(1-\alpha) n_2^5}{k_2^4} + 5\alpha(1-\alpha) \times [6(n_1-n_2)(n_1^4/k_1^3 - n_2^4/k_2^3) + 4(n_1^3/k_1^2 - n_2^3/k_2^2)(n_1^2/k_1 - n_2^2/k_2) + (1-2\alpha)(n_1-n_2)(7(n_1-n_2)(n_1^3/k_1^2 - n_2^3/k_2^2) + 3 n_1 n_2 (n_1/k_1 - n_2/k_2)^2) + 2(1-6\alpha(1-\alpha))(n_1-n_2)^3(n_1^2/k_1 - n_2^2/k_2) + 0.2(1-2\alpha)(1-12\alpha(1-\alpha))(n_1-n_2)^5]. \quad (15)$$

For $\alpha = 0$ or 1, they reduce to one-NBD formulas with one of the first two terms surviving. This term is always positive for positive k_i. Therefore, as expected, the distributions show no oscillations if considered individually. For 2NBD, there is a symmetry in replacing indices 1 to 2 together with α to $1-\alpha$. Negative $\mathcal{K}_2$ can be obtained only if $k_i < 0$. For positive k_i, one always gets positive $\mathcal{K}_2$. Its value depends on the difference $n_1 - n_2$. $\mathcal{K}_3$ can become negative depending on the values of the last two terms. These cancellations of positive and negative contributions in expressions (13)–(15) are not so drastic as in Eq. (9), especially for large q, because the leading contributions to H_q are strongly decreasing with q in (13)–(15), and not of the order of 1, as in (9). Therefore, they do not require very high precision and, moreover, clearly display the origin of each term and its dependence on fitted parameters.

Actually, five moments determine quite well the shape of the distribution if they are calculated with high enough accuracy. Since these shapes are qualitatively similar in different reactions, it is especially instructive to compare their H_q moments. In Table 1, the H_q moments for e^+e^- annihilation at Z^0 are shown. Their values according to the solution of the gluodynamics equations [23] are in the second column. In the third and fourth columns, the experimental results of the L3 Collaboration [18] are represented for full phase space, respectively, with all measured multiplicities included and with some very high multiplicities truncated (because of large error bars). Next follow H_q values restored from 2NBD fits of OPAL [26] results done in [27]. They are similar

Table 2

	2NBD fit, 1.8 TeV	3NBD fit, 14 TeV	Pythia, 14 TeV
H_2	0.2279	0.8754	0.4224
H_3	0.0988	0.9703	0.3387
H_4	0.0414	0.9737	0.2683
H_5	0.0120	0.9742	0.1877

to directly measured L3 values. The errors in fitted parameters are omitted since they are also close to those for L3.

The overall qualitative agreement is rather good. Quite impressive is the fact that, in all cases, the fifth cumulant moment is negative. However, somewhat surprising is the difference of the theoretical and experimental widths (H_2 values). The widths are determined quite precisely both experimentally and theoretically. The only reason to which such disagreement could be ascribed is the incomplete treatment with quarks omitted in [23]. More complete theoretical calculations will shed some light on this problem.

One cannot blame the so-called truncation effect for this disagreement. The analytical QCD predictions deal with an infinitely long tail of the distribution. In experiment, the final statistics prevent measuring very high multiplicities, and the tail is truncated. Some additional truncation can be imposed to avoid data with large errors. However, this is not very important for low-rank moments if done at high multiplicities. This is seen from comparison of L3 results for untruncated (actually, truncated only by statistics of experiment) and truncated (with highest multiplicity data omitted because of poor statistics) data in the first row of Table 1. Additional truncation does not change the results qualitatively even for H_5 (the last row). The negative sign and decrease compared to H_4 persist. That is why, to minimize the role of the tail of the distribution, we consider only the five lowest rank moments.

Comparing QCD predictions with experiment at higher rank moments, one can hope to reveal new qualitative features. This happened with oscillating moments whose amplitudes do not necessarily agree because of truncation of experimental data. However, this effect can be fully taken into account in cutoff NBD fits and in Monte Carlo models with a sample of the same size.

The comparison of e^+e^- and $pp(p\bar{p})$ data turns out to be especially interesting. While both show qualitative similarity of the shapes of multiplicity distributions, the corresponding H_q values are quite distinctive. In Table 2, we show H_q values for $p\bar{p}$ data at 1.8 TeV [7] (Tevatron) and interpolations to 14 TeV (LHC), both obtained from NBD fits elaborated in [6, 25]. The 2NBD fit at 1.8 TeV corresponds to the parameters $\alpha = 0.62$, $n_1 = 30$, $n_2 = 61.6$, and $k_1 = k_2 = 7$, which are approximately equal to average values for the 2.A model considered in [6]. However, even this extreme model underestimates high multiplicities and, therefore, H_q values in Table 2 should be treated as lower bounds to experimental ones, which are unknown, unfortunately. The extrapolated values at 14 TeV have been calculated using the parameters of 3NBD fits and the Pythia model, both considered in [25].

Quite impressive are much larger values of H_q in hadron-initiated reactions (Table 2) as compared to e^+e^- results (Table 1). They strongly increase with energy. Moreover, the drastic difference is clearly displayed by H_q between 3NBD interpolations and Pythia at 14 TeV. This demonstrates the extremely high sensitivity of H_q analysis because both approaches provide a similar two-shoulder structure of multiplicity distributions as seen in Fig. 2 of [6]. At 14 TeV, the predictions are given for full phase space. For the rapidity interval $|\eta| < 0.9$, the H_q values become larger than those in Table 2. H_q for the 3NBD model of [6] become almost indistinguishable from 1 (above 0.99). Pythia values increase by about 1.4 times. No oscillations are seen at these high energies, while they are present at energies below 1 TeV [16]. Surely, LHC experiments will give their decisive conclusion.

To conclude, we have shown that H_q moments of the multiplicity distribution are extremely sensitive to minute details of its shape. They can resolve the differences between various fits even if those are not clearly seen in the traditional representation. H_q values obtained from experimental data can be compared with analytical QCD results (if the size of the sample is large enough), NBD fits, and Monte Carlo model predictions. Truncation of the tail is not crucial for lower rank moments. Nevertheless, it can be accounted for in the NBD and Monte Carlo approaches (not in analytical QCD), so that higher rank moments are incorporated as well and provide additional information. For e^+e^-, slight disagreement on theoretical and experimental widths is embarrassing and must be further studied. For hadron- and nuclei-initiated reactions, H_q values are much larger than in e^+e^-. Two attempts demonstrated in Table 2 to extrapolate to LHC energy give rise to completely different values of the moments even though the shapes of the multiplicity distributions do not differ much. Thus, it has been shown that moments can be used to discriminate between various phenomenological fits and models. RHIC and LHC data are awaited for

better insight. The energy dependence of H_q and of the relative weights of various NBD components can provide some hints on the state of matter during the collision and its energy evolution.

ACKNOWLEDGMENTS

I am grateful to A. Giovannini and W. Metzger for correspondence.

This work has been supported in part by the Russian Foundation for Basic Research, project nos. 02-02-16779, 03-02-16134, and NSh-1936.2003.2.

REFERENCES

1. V. A. Khoze and W. Ochs, Int. J. Mod. Phys. A **12**, 2949 (1997).
2. I. M. Dremin and J. W. Gary, Phys. Rep. **349**, 301 (2001).
3. A. Giovannini, Nuovo Cimento A **10**, 713 (1972).
4. A. Capella, U. Sukhatme, C. I. Tan, and J. Tran Thanh Van, Phys. Lett. B **81B**, 68 (1979).
5. A. B. Kaidalov, Phys. Lett. B **116B**, 459 (1982).
6. A. Giovannini and R. Ugoccioni, Phys. Rev. D **59**, 094020 (1999).
7. E735 Collab. (T. Alexopoulos *et al.*), Phys. Lett. B **435**, 453 (1998).
8. S. G. Matinyan and W. D. Walker, Phys. Rev. D **59**, 034022 (1999).
9. C. Bourelly *et al.*, in *Proceedings of the VI Blois Workshop on Frontiers in Strong Interactions,* Ed. by J. Tran Thanh Van (Editions Frontiére, Gif-sur-Yvette, 1995), p. 15.
10. L. McLerran, Rev. Mod. Phys. **58**, 1021 (1986).
11. E. Shuryak, hep-ph/0312227.
12. E. A. De Wolf, I. M. Dremin, and W. Kittel, Phys. Rep. **270**, 1 (1996).
13. I. M. Dremin, Phys. Lett. B **313**, 209 (1993).
14. Yu. L. Dokshitzer, V. A. Khoze, A. H. Mueller, and S. I. Troyan, *Basics of Perturbative QCD*, Ed. by J. Tran Thanh Van (Editions Frontiére, Gif-sur-Yvette, 1991).
15. I. M. Dremin and V. A. Nechitailo, Mod. Phys. Lett. A **9**, 1471 (1994); Pis'ma Zh. Éksp. Teor. Fiz. **58**, 945 (1993) [JETP Lett. **58**, 881 (1993)].
16. I. M. Dremin, V. Arena, G. Boca, *et al.*, Phys. Lett. B **336**, 119 (1994).
17. SLD Collab. (K. Abe *et al.*), Phys. Lett. B **371**, 149 (1996).
18. L3 Collab. (P. Achard *et al.*), Phys. Lett. B **577**, 109 (2003).
19. I. M. Dremin and R. C. Hwa, Phys. Rev. D **49**, 5805 (1994); Phys. Lett. B **324**, 477 (1994).
20. W. Ochs and J. Wosiek, Phys. Lett. B **289**, 159 (1992); **304**, 144 (1993).
21. Yu. L. Dokshitzer and I. M. Dremin, Nucl. Phys. B **402**, 139 (1993).
22. Ph. Brax, J. L. Meunier, and R. Peschanski, Z. Phys. C **62**, 649 (1994).
23. M. A. Buican, C. Förster, and W. Ochs, Eur. Phys. J. C **31**, 57 (2003).
24. S. Lupia and W. Ochs, Phys. Lett. B **418**, 214 (1998); Nucl. Phys. B (Proc. Suppl.) **64**, 74 (1998).
25. A. Giovannini and R. Ugoccioni, Phys. Rev. D **68**, 034009 (2003).
26. OPAL Collab. (P. D. Acton *et al.*), Z. Phys. C **53**, 539 (1992).
27. A. Giovannini, S. Lupia, and R. Ugoccioni, Phys. Lett. B **374**, 231 (1996).

Physics of Atomic Nuclei, Vol. 68, No. 1, 2005, pp. 124–130. Translated from Yadernaya Fizika, Vol. 68, No. 1, 2005, pp. 126–133.

ELEMENTARY PARTICLES AND FIELDS
Theory

Magnetic Catalysis of Stability of Quark Matter in the Nambu–Jona-Lasinio Model

K. G. Klimenko[1] and D. Ebert[2]

Received July 1, 2003; in final form, November 20, 2003

Abstract—The effect of an external magnetic field H on the stability of quark matter is studied on the basis of the Nambu–Jona-Lasinio model. It is shown that, at $H = 0$, droplets of quark matter are stable only in the case where the coupling constant G is greater than some value G_{bag}. If $H \neq 0$, stable multiquark formations may exist even for $G \leq G_{\text{bag}}$ (magnetic catalysis of stability). For $G > G_{\text{bag}}$, a magnetic field facilitates the formation of stable quark matter. © *2005 Pleiades Publishing, Inc.*

1. INTRODUCTION

In recent years, physicists have given much attention to dense quark–hadron matter, which is present in neutron stars and which can arise in relativistic heavy-ion collisions. Strictly speaking, QCD, which is a theory of strong interactions, is a theoretical basis for studying this object. The majority of QCD predictions are based on the use of the perturbation-theory method, which is inapplicable at comparatively low baryon densities. In such cases, use is usually made of effective models that, to some extent, are adequate to QCD at low energies, as well as at baryon densities ρ_B commensurate with the baryon density ρ_o in conventional nuclear matter ($\rho_o = 0.16$ fm^{-3}). Among such effective models, those that involve four-fermion interactions—that is, models of the Nambu–Jona-Lasinio type [1]—are very popular. Since it is assumed that a stable quark-matter droplet—that is, a droplet that does not tend to contract into a point or to extend over the entire space—is formed for a short time in heavy-ion processes, any realistic effective model must predict the existence of stable multiquark objects featuring a large baryon number (we will refer to them as baryon droplets). Within Nambu–Jona-Lasinio models, quarks are usually considered as pointlike particles, while mesons are collective quark–antiquark excitations of the vacuum. Within such models, one can also describe an octet and a decuplet of the simplest baryons. Finally, it was shown in [2, 3] that stable multiquark formations are also present in the mass spectrum of Nambu–Jona-Lasinio models. In this case, however, the domain of admissible values of model parameters (coupling constants and so on) is constrained significantly, while such quark droplets can be stable only if they consist of massless quarks (we discuss here the case of chiral-invariant Nambu–Jona-Lasinio models).

As was indicated above, there exist, in nature, objects whose physics is determined to a considerable extent by the properties of dense quark–gluon matter. These are neutron stars. Their surface is formed by ordinary nuclei, electrons, and so on. The pressure in a star and its density grow toward its interior. Therefore, nuclei and thereupon constituent nucleons can merge, forming quark droplets. According to some modern concepts, the core of a neutron star consists of quark matter whose density is severalfold greater than ρ_o. A superstrong magnetic field—according to some estimates, its strength may reach values on the order of 10^{18} G [4]—is an indispensable feature of neutron stars. In this connection, some aspects of the external-magnetic-field effect on dense quark–hadron matter were previously investigated in [5–8].

In the present study, the problem of stability of quark matter is considered within the simplest chiral-invariant Nambu–Jona-Lasinio model and, in contrast to what was done in [2, 3], with allowance for a constant uniform magnetic field H. We will prove the following statements: (i) In an external magnetic field, stable droplets of quark matter can also be formed by massive quarks. (ii) For model-parameter values at which stability is impossible at $H = 0$, quark droplets are stabilized for $H \neq 0$ (magnetic catalysis of stability of quark matter).

2. NAMBU–JONA-LASINIO MODEL AND STABILITY CONDITION

The problem of the external-magnetic-field effect on the stabilization of quark matter will be considered here within the simplest Nambu–Jona-Lasinio

[1]Institute for High Energy Physics, Protvino, Moscow oblast, 142284 Russia; e-mail: kklim@mx.ihep.su

[2]Institut für Physik, Humboldt-Universität zu Berlin, D-10115 Berlin, Germany; e-mail: debert@physik.hu-berlin.de

1063-7788/05/6801-0124$26.00

model [1] featuring quarks that have three colors and the same electric charge q. In Minkowski space, the Lagrangian of the model has the form

$$L = \bar{\psi}[i\gamma^\nu(\partial_\nu - iqA_\nu) + \mu\gamma^0]\psi + G[(\bar{\psi}\psi)^2 + (\bar{\psi}i\gamma^5\psi)^2], \quad (1)$$

where $\mu \geq 0$ is the chemical potential and $A_\nu = \delta_{\nu 2}x^1 H$ is the vector potential of a constant and uniform magnetic field H (we consider here the case of zero temperature). The Lagrangian in (1) is invariant under the continuous chiral transformation group $U(1)_L \times U(1)_R$.

In order to solve the problem of stability of quark matter, we will rely, as in [2, 3], on the thermodynamic approach within which a quark-matter droplet can be interpreted as a dense-phase droplet surrounded by a phase of zero baryon density, a vacuum. The condition under which there emerge stable multiquark droplets is then the condition of coexistence of these two phases—that is, the condition of the occurrence of a first-order phase transition between them (an analog of coexistence in a liquid–vapor system in condensed-matter theory).[3)] Quantitatively, it can be represented in the form (see [2])

$$m_{\rm dense} < \mu_c < m_{\rm vac}, \quad (2)$$

where μ_c is the critical chemical-potential value at which the two phases in question coexist, $m_{\rm vac}$ is the mass of a single-quark excitation of the true vacuum (this vacuum is not symmetric under chiral transformations), and $m_{\rm dense}$ is the quark mass in the phase where the baryon density is nonzero (that is, within a quark droplet). Relation (2) will be referred to as the condition of stability of quark matter. [The condition (2) of coexistence of the two phases can easily be understood if the chemical potential is interpreted as the lowest energy that a particle must have to escape from the system. If the two phases in question coexist at the chemical-potential value μ_c and if one of them (vacuum) does not contain quarks, then the inequality $\mu_c < m_{\rm vac}$ must hold (otherwise, quarks of energy about $m_{\rm vac}$ could not escape from the system, with the result that the baryon density in the vacuum would be nonzero). For the same reason, $\rho_B \neq 0$ in the dense phase merely because $m_{\rm dense} < \mu_c$, and the energy of quarks is insufficiently high for escaping from the system.] Thus, we see that, in the thermodynamical approach, the problem of stability reduces to solving the problem of the phase structure of the model and to finding first-order phase transitions occurring between the dense baryon phase and the vacuum and satisfying relation (2). We also note that, in this approach, we disregard surface effects, which are significant only for baryons consisting of a small number of quarks.

3. STABILITY AT $H = 0$

On the basis of the foregoing, we will first study the problem of stability at $H = 0$. In the leading order of a mean-field expansion,[4)] the thermodynamic potential Ω of the model has the form (see [2, 11])

$$\Omega(m;\mu) = \frac{m^2}{4G} - 2N_c \times \int \frac{d^3p}{(2\pi)^3}\Big\{E_p + \theta(\mu - E_p)(\mu - E_p)\Big\}, \quad (3)$$

where $E_p = \sqrt{m^2 + \mathbf{p}^2}$ and m is the order parameter for chiral symmetry. The point m_o at which the potential $\Omega(m;\mu)$ as a function of m reaches the global minimum is related to the vacuum expectation value for a quark–antiquark pair by the relation $m_o = -2G\langle\bar{\psi}\psi\rangle$. It follows that, if $m_o = 0$, then the ground state of the model is chiral-symmetric, but that, if $m_o \neq 0$, the chiral invariance of the model is spontaneously broken. Moreover, m_o is equal to the dynamical quark mass. By employing, in (3), the Lorentz-noninvariant regularization $\mathbf{p}^2 \leq \Lambda^2$ for the divergent integral, we can obtain

$$\Omega(m;\mu) = \frac{m^2}{4G} - \frac{3}{8\pi^2}\Big[\Lambda(2\Lambda^2 + m^2) \times \sqrt{m^2 + \Lambda^2} - m^4 \ln\left(\frac{\Lambda + \sqrt{m^2 + \Lambda^2}}{m}\right)\Big] - \frac{\theta(\mu - m)}{8\pi^2}\Big[\mu(2\mu^2 - 5m^2)\sqrt{\mu^2 - m^2} + 3m^4 \ln\left(\frac{\mu + \sqrt{\mu^2 - m^2}}{m}\right)\Big]. \quad (4)$$

At $\mu = 0$, it follows from (4) that, if $G \leq G_c \equiv \pi^2/(3\Lambda^2)$, the thermodynamic potential in question has the global minimum at $m = 0$, so that the vacuum is chiral-symmetric. If $G > G_c$, the chiral invariance of the model is spontaneously broken since the global minimum of the thermodynamic potential

[3)] This method is also used in some nuclear-physics models to describe the properties of dense nuclear matter (see, for example, [9]). In such models, a conventional nucleus of rather large charge number is identified with a droplet of a dense phase that coexists with the vacuum phase of the model.

[4)] In [10], a scheme for systematically going beyond the leading approximation in the mean-field expansion is given within the formalism of a bilocal source. We restrict our consideration here to the leading order of this expansion since this is sufficient for demonstrating effects associated with an external magnetic field.

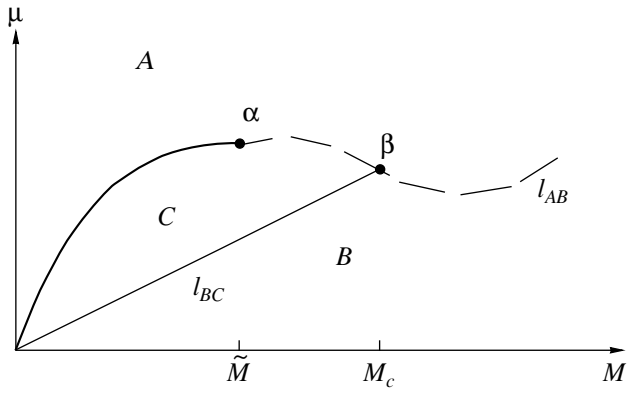

Fig. 1. Phase portrait of the model in the (M, μ) plane at $H = 0$. Points on the curve l_{AB} separating phases A and B satisfy the condition of stability.

$\Omega(m;0)$ occurs at a nonzero point M that satisfies the stationarity equation

$$\frac{\pi^2}{3G} = \Lambda\sqrt{M^2+\Lambda^2} - M^2 \ln\left(\frac{\Lambda+\sqrt{M^2+\Lambda^2}}{M}\right). \quad (5)$$

We consider predominantly the case of $G > G_c$, where, along with G, it is convenient to employ the parameter M, the dynamical quark mass in a vacuum whose chiral symmetry is broken. The quantities G and M are related by Eq. (5).

In [12], the phase structure of the model specified by the Lagrangian in (1) and regularized in a Lorentz-invariant way was already investigated for $\mu \neq 0$ (the problem of stability of quark matter was not considered there). By using the same methods as in [12] for the present case, we can obtain a phase portrait of the model. It is depicted in Fig. 1 in the (M, μ) parameter plane. In this figure, phase A is a dense chiral-invariant phase of the model, the quarks having zero mass there. Phase B, where chiral symmetry is spontaneously broken and where the quark mass is equal to M, corresponds to the true QCD vacuum. In this phase, $\rho_B = 0$. Finally, there is phase C, where the baryon density is nonzero ($\rho_B \neq 0$) and where the quark mass is also nonzero and depends on μ. The solid and dashed curves in the figure are the curves of, respectively, second- and first-order phase transitions. In particular, $l_{BC} = \{(M,\mu):\mu = M\}$, while the curve l_{AB}, which entirely lies below the straight line $\mu = M$, is determined by the equation

$$\Omega(M;\mu) = \Omega(0;\mu). \quad (6)$$

Solving Eq. (6), we obtain $l_{AB} = (M,\mu):\mu = \mu_c(M) < M, M \geq M_c = 0.56\Lambda$, where

$$2\mu_c^4(M) = 6\Lambda^3\sqrt{M^2+\Lambda^2} - 6\Lambda^4 - 3M^2F(M,\Lambda) \quad (7)$$

[the expression for $F(M,\Lambda)$ is the right-hand side of Eq. (5)]. In Fig. 1, there are in addition two tricritical points α and β whose coordinates are $\alpha = (\tilde{M}, \tilde{\mu})$ and $\beta = (M_c, M_c)$, where $\tilde{M} = 0.31\Lambda$ and $\tilde{\mu} = 0.37\Lambda$.

From the aforesaid, it follows that the relations $m_{\text{dense}} \equiv 0 < \mu_c(M) < M \equiv m_{\text{vac}}$, which are nothing but the stability condition (2), hold for points on the curve l_{AB} corresponding to the first-order phase transitions and separating the vacuum phase B from phase A, where the baryon density is nonzero. This means that only for $M \geq M_c = 0.56\Lambda$—that is, for $G > G_{\text{bag}} \equiv 1.37G_c$—can stable droplets of quark matter (quark droplets) arise within the original Nambu–Jona-Lasinio model. Quarks are massless within these droplets.

In should be recalled that, in [2], the problem of stability of quark droplets was already investigated within the Nambu–Jona-Lasinio model, but only for three values of the parameter M: $M_1 = 0.48\Lambda$, $M_2 = 0.67\Lambda$, and $M_3 = 0.88\Lambda$. The results reported in [2] confirm our more general conclusions: for the values $M_{2,3}$, quark droplets are stable, while, for M_1, there is no stability.

The baryon density ρ_{drop} within a stable quark droplet is calculated by the formula

$$\rho_{\text{drop}}(M) = -\frac{\partial\Omega(0;\mu)}{N_c\partial\mu}\bigg|_{\mu=\mu_c(M)} = \frac{1}{3\pi^2}\mu_c^3(M). \quad (8)$$

In particular, it follows from (8) that $\rho_{\text{drop}} = 1.43\rho_o$ at $M = M_2$ and $\Lambda = 600$ MeV and that $\rho_{\text{drop}} = 2.09\rho_o$ at $M = M_3$ and $\Lambda = 570$ MeV.

4. STABILITY FOR $H \neq 0$

The thermodynamic potential of the Nambu–Jona-Lasinio model in an external magnetic field has the form (the details of the derivation of this expression can be found in [13, 14])

$$\Omega(m;\mu,H) = \Omega(m;0,H) - \frac{3qH}{4\pi^2}\sum_{k=0}^{\infty}\alpha_k\theta(\mu - s_k) \times\left\{\mu\sqrt{\mu^2-s_k^2} - s_k^2\ln\left[\frac{\mu+\sqrt{\mu^2-s_k^2}}{s_k}\right]\right\}, \quad (9)$$

where

$$s_k = \sqrt{m^2+2qHk}, \quad \alpha_k = 2-\delta_{0k},$$

$$\Omega(m;0,H) = \Omega(m;0) - \frac{3(qH)^2}{2\pi^2} \quad (10)$$

$$\times\left\{\zeta'(-1,x)-\frac{1}{2}[x^2-x]\ln x+\frac{x^2}{4}\right\}.$$

Here, $\Omega(m;0)$ is the thermodynamic potential (4) at $\mu=0$, $x=m^2/(2qH)$, $\zeta(\nu,x)$ is a generalized Riemann zeta function [15], and $\zeta'(-1,x)=d\zeta(\nu,x)/d\nu|_{\nu=-1}$.

A few comments on the effect of a magnetic field on the vacuum of the model specified by the Lagrangian in (1) at $\mu=0$ are in order here. If $G\le G_c$, then, as was indicated above, the vacuum is chiral-invariant at $H=0$. However, the chiral invariance of the model is spontaneously broken at arbitrarily weak uniform and constant external magnetic fields, with the result that the quarks acquire a mass [16]. This is a manifestation of a universal effect of the magnetic catalysis of dynamical symmetry breaking (see the review articles quoted in [17])—for the first time, this effect was observed in the $(2+1)$-dimensional Nambu–Jona-Lasinio model [18]. If $G>G_c$, then, for $H\neq 0$, the potential $\Omega(m;0,H)$ reaches the global minimum at the point $m_o(H)$ that is also nonzero and which is associated with the dynamical quark mass $m_{\rm vac}$ from relation (2). Its value grows monotonically with increasing H, and $m_o(H)\to M$ for $H\to 0$.[5)] Thus, we can see that, at $\mu=0$ and $H\neq 0$, the chiral invariance of the model is spontaneously broken for all positive values of $G>0$.

In the case of $\mu\neq 0$ and $H\neq 0$, it is more difficult to study the phase structure of the model—that is, to find the global minimum of the thermodynamic potential (9); however, this problem is simplified considerably upon representing the (H,μ) plane as a unification of all regions ω_k $(k=0,1,\ldots,\infty)$:

$$\omega_k=\{(H,\mu):2qHk\le\mu^2\le 2qH(k+1)\}. \quad (11)$$

Indeed, only the first term $(k=0)$ of the infinite series in (9) does not vanish in the region ω_0, only the terms corresponding to $k=0$ and $k=1$ make a nonzero contribution in the region ω_1, etc. (It should be noted, however, that the smaller the value of H, the greater the number of regions ω_k that must be taken into account.) In the present study, the problem of stability of quark matter in an external magnetic field is considered in detail for the same values of the parameter M as in [2].

4.1. Magnetic Catalysis of Stability

In the case of $M=M_1$, we have investigated numerically the thermodynamic potential in (9) and constructed the phase portrait of the model. It is depicted in Fig. 2. On this portrait, one can see, among other things, phase B, which corresponds to the true QCD vacuum in an external magnetic field and in which the baryon density is nonzero, while the quarks have a nonzero mass $m_o(H)$, this mass being identified with $m_{\rm vac}$ from relation (2). In Fig. 2, the line $L=\{(H,\mu):\mu=m_o(H)\}$ represents an upper bound on the quantity μ_c from (2). Two dense phases—the chiral-invariant phase A involving massless quarks (in this phase, $m_{\rm dense}=0$) and phase C featuring massive quarks and broken chiral invariance—lie immediately below this curve. The boundaries between the phases in the figure are shown by the dashed and solid lines, which represent, respectively, first- and second-order phase transitions. The tricritical point α has the coordinates $\sqrt{2qH_\alpha}/\Lambda=0.59$ and $\mu_\alpha/\Lambda=0.44$; that is, it lies in the region ω_0 (11) ($H_\alpha\sim 10^{19}$ G).

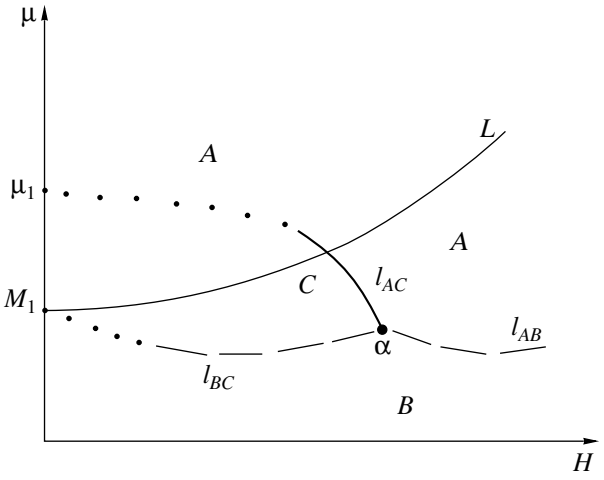

Fig. 2. Phase portrait of the model in the (H,μ) plane at $M=M_1\equiv 0.48\Lambda$ ($\tilde{M}<M_1<M_c$). Here, μ_1 is the chemical-potential value at which the point (M_1,μ_1) lies on the curve corresponding to the first-order phase transitions and connecting the tricritical points α and β in Fig. 1. Points on the curves l_{AB} and l_{BC} satisfy the stability condition.

We would like to emphasize one detail of paramount importance in Fig. 2: at nonzero values of H, a transition from the vacuum phase B to one of the dense baryon phases (A or C, depending on the value of H) is a discrete first-order transition, while, at $H=0$ and $M=M_1<M_c$, a transition from phase B to phase C is a second-order phase transition (see Fig. 1). (Thereby, we obtain, within the Nambu–Jona-Lasinio model, a corroboration of one the statements in the phenomenological theory of phase transitions—in external fields, second-order phase transitions transform into first-order phase transitions [20].) From Fig. 2, one can see that the stability relation (2) holds for points lying on the curve l_{AB}. For points on the curve l_{BC}, this relation

[5)] In different models of the QCD vacuum, the chiral condensate also grows with increasing magnetic field at $\mu=0$ [19].

is also valid (from the figure, it immediately follows that $\mu_c < m_{\rm vac} \equiv m_o(H)$; we skip the proof of the fact that $m_{\rm dense} < \mu_c$ in a dense phase C). This means that, within the model being considered, an external magnetic field stabilizes, at $M = M_1$, quark droplets, which were unstable at $H = 0$. We have verified that the curve l_{BC}, along which the vacuum (phase B) and phase C, where the baryon density is nonzero, coexist, traverses all regions ω_k for $k = 1, \ldots, 100$—that is, it extends to comparatively small values of $H \sim 10^{17}$ G. In all probability, it reaches the point M_1 (see Fig. 2, where the points show the extrapolations of the curves l_{AB} and l_{BC} to the region of small values of H). Depending on H values, stable multiquark droplets of matter are formed by massive ($H < H_\alpha \sim 10^{19}$ G) or massless ($H \geq H_\alpha$) quarks. A similar conclusion can also be drawn for arbitrary values of $M \in (\tilde{M}, M_c)$ (see Fig. 1).

It should be recalled that, in [13, 14], the phase structure of the model specified by the Lagrangian in Eq. (1) was considered at nonzero values of μ and H, but the problem of stability of quark matter was not addressed there. In [14], attention was focused on the case of $G < G_c$, while, in [13], the phase portrait of the model was obtained for values lying in the region $G > G_c$ and corresponding to $M < \tilde{M} < M_c$. In [13, 14], it was proven that, in an external magnetic field, there exists, at small values of μ, a chiral-noninvariant vacuum (phase B), which is separated by the critical curve of first-order phase transitions from phases where the baryon density is nonzero. It can easily be shown that the points of this curve also satisfy the stability condition in (2). Thus, we see that, while, at $H = 0$, quark droplets are unstable for $G \leq G_{\rm bag} \equiv 1.37 G_c$ within the model specified by the Lagrangian in Eq. (1), at $H \neq 0$, their stability is induced by an external magnetic field. We refer to this effect as the magnetic catalysis of stability of quark matter.

However, the following important feature of the effect is worthy of special note. From the formal point of view, the stability of quark droplets at $T = 0$ is induced by an arbitrarily weak external magnetic field. The binding energy E_b of one quark within such a droplet has the form $E_b = m_{\rm vac} - \mu_c$ [2]. Since, for $H \to 0$, the curve l_{BC} comes arbitrarily close to the line L (see Fig. 2), then E_b also approaches zero for $H \to 0$. In view of this, we admit that, at small values of H, the effect in question may not manifest itself under realistic conditions—that is, for $T \neq 0$—since rather strong thermal phenomena are obstacles for the formation of a loosely bound droplet of quark matter. However, we believe that the magnetic catalysis of stability of quark matter must be taken into account in studying neutron stars, within which the magnetic-field strength may be as great as 10^{18} G [4]. This is suggested by some estimates of the binding energy E_b. Indeed, the binding energy E_b is approximately equal to 6 keV in the region ω_{100}, where $H \sim 10^{17}$ G, whereas the temperature within compact stars may take much lower values (see, for example, the review article of Alford [21]) that are insufficient for a thermal destabilization of quark droplets whose binding energy is on this order of magnitude.

Yet another argument in favor of a true value of our effect is based on the results reported in [22], where it was shown that, for $qH < \Lambda^2_{\rm QCD}$, the dynamics in the nonperturbative QCD vacuum is in qualitative agreement with the predictions of the Nambu–Jona-Lasinio model ($\Lambda_{\rm QCD} \approx 250$ MeV). By means of a numerical analysis, we have found that quark droplets are stabilized in magnetic fields corresponding to $qH \sim 0.01\Lambda^2_{\rm QCD}$ (at such values of H, the curve l_{BC} in Fig. 2 traverses the region ω_{100}) and in stronger magnetic fields. In other words, the magnetic catalysis of stability of quark matter, an effect that was discovered within the Nambu–Jona-Lasinio model, has a direct bearing on QCD, a commonly accepted theory of strong interactions.

4.2. Case of $M = M_{2,3}$

It is well known that, at $H = 0$, stability is inherent in the model specified by Eq. (1) for $G > G_{\rm bag}$—that is, for $M > M_c = 0.56\Lambda$. Here, we will investigate the problem of the external-magnetic-field effect on the stability of quark droplets for the same values $M = M_{2,3} > M_c$, as in [2].

The phase portrait of the model at $M = M_2$ is schematically illustrated in Fig. 3, where use is made of the same notation as that which was adopted for Fig. 2. In contrast to what we have seen in Fig. 2, the region of the massive phase C is compact here; there appeared yet another tricritical point (β) and a triple point (γ) ($H_{\alpha,\beta,\gamma} \sim 10^{19}$ G). The first-order-phase-transition lines l_{AB} and l_{BC} of this figure satisfy the stability condition (2). It follows that, both at $H = 0$ and in an external magnetic field, the model in question predicts the existence of stable quark droplets formed by massive or massless quarks, depending on the value of the magnetic-field strength H. In the case of $M = M_3$, we have not found a massive phase C, the vacuum (phase B) coexisting with the dense chiral-invariant phase A at chemical-potential values that satisfy the stability condition (2). We then conclude that, at $M = M_3$ and $H \neq 0$, there can exist stable multiquark droplets consisting, as at $H = 0$, only of massless quarks.

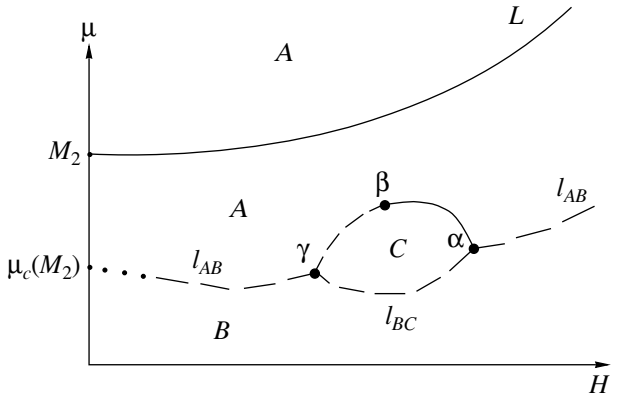

Fig. 3. Phase portrait of the model in the (H, μ) plane at $M = M_2 \equiv 0.67\Lambda$ ($M_c < M_2$), where $\mu_c(M_2) = 0.63\Lambda$. The points of the curves l_{AB} and l_{BC} satisfy the stability condition.

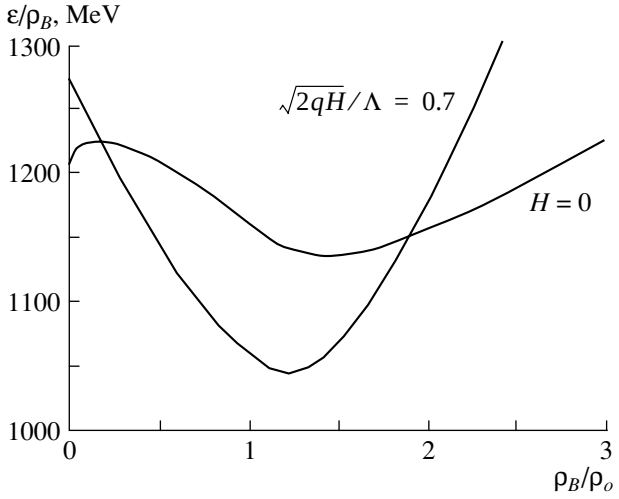

Fig. 4. Energy per baryon as a function of the baryon density at $H = 0$ and $\sqrt{2qH}/\Lambda = 0.7$.

In order to clarify the role of an external magnetic field in the very process of quark-droplet formation for $M > M_c$, we present, in Fig. 4, the energy ε/ρ_B per baryon as a function of the baryon density ρ_B at $H = 0$ and $H \neq 0$ ($M = M_2$). (As in [2], the energy density ε is given by

$$\varepsilon = \Omega(m; \mu, H) - \Omega(m_o(H); 0, H) + N_c \mu \rho_B, \quad (12)$$

where $\rho_B = -\partial\Omega/(N_c \partial\mu)$ and $m_o(H)$ is the dynamical quark mass in phase B.) In Fig. 4, the curve corresponding to $H = 0$ has a maximum at a point $\rho_{\max}$ and the global minimum at a point $\rho_{\text{drop}}(M_2)$ [see Eq. (8)]; there is also a local minimum at the point $\rho_B = 0$, and this point corresponds to the vacuum. We assume that fluctuations of the baryon density are possible in the vacuum. It is obvious that, if a quark droplet whose density is less than $\rho_{\max}$ appears in this state at $H = 0$ in one way or another, this droplet will be unstable, since it is energetically preferable to have an infinite volume where $\rho_B = 0$; that is, the droplet will actually disappear. But if the density in a droplet satisfies the condition $\rho_B > \rho_{\max}$, the droplet will be stable (it will not disappear); its volume will decrease or increase until the droplet occurs in the state of lowest energy, where $\rho_B = \rho_{\text{drop}}(M_2)$. Thus, we see that, at $H = 0$, the vacuum is a metastable state. This means that, for baryon-density fluctuations, there is a threshold $\rho_{\max}$ above which the vacuum disappears, with the result that the system goes over to a state where $\rho_B \neq 0$, this corresponding to the formation of one or a few baryon droplets.

The situation changes drastically in a rather strong magnetic field. Indeed, ε/ρ_B has a maximum in this case at $\rho_B = 0$ (see Fig. 4, where the magnetic-field strength is fixed by the condition $\sqrt{2qH}/\Lambda = 0.7$); therefore, it is energetically preferable for a drop of even an arbitrarily low density to contract to a finite volume (but not to disappear completely) at which the baryon density within it would correspond to a minimum of the function ε/ρ_B at $H \neq 0$. Our method of investigation is not very efficient at small nonzero values of the magnetic-field strength, in which case it is necessary to take into account contributions from a very large number of regions ω_k (11). Knowing the shape of the curve ε/ρ_B at $H = 0$ and $\sqrt{2qH}/\Lambda = 0.7$ (see Fig. 4), we can nevertheless make the natural assumption that, in response to variations in H, the curve ε/ρ_B changes shape in the following way: at $H = 0$, it has a local minimum at the point $\rho_B = 0$; with increasing H, this minimum gradually becomes shallower, with the result that, finally, the function ε/ρ_B develops a maximum at $\rho_B = 0$ from a rather high value of H. It follows that, with increasing H, the threshold above which rather strong fluctuations destroy the vacuum decreases, vanishing at sufficiently strong magnetic fields; that is, an external magnetic field facilitates the generation of stable droplets of quark matter for $G > G_{\text{bag}}$.

5. CONCLUSION

The problem of stability of quark matter in the presence of an external magnetic field has been considered within the simplest version of the Nambu–Jona-Lasinio model. It has been shown that (i) at $H = 0$, there exists a coupling-constant value ($G_{\text{bag}} \equiv 1.37 G_c$) such that quark droplets can be stable only for $G > G_{\text{bag}}$; (ii) if the magnetic field is nonzero, droplets of quark matter can be stable even for $0 < G \leq G_{\text{bag}}$ (magnetic catalysis of the stability of quark matter); (iii) in contrast to what we have in

the case of $H = 0$, stable quark droplets at $H \neq 0$ can be formed not only by massless but also by massive quarks; and (iv) from general energy considerations, it follows that, for $G > G_{\text{bag}}$, the formation of stable quark-matter droplets must occur more vigorously in an external magnetic field than at $H = 0$. This means that, in a rather strong magnetic field, arbitrarily small fluctuations of the baryon density lead to the generation of a quark droplet (in contrast, only rather strong fluctuations lead to the emergence of a quark droplet at $H = 0$).

It should also be noted that our results are also valid for values of the magnetic-field strength in the region $qH < \Lambda^2_{\text{QCD}}$, where QCD dynamics is in qualitative agreement with the predictions of the Nambu–Jona-Lasinio model [22]. One may therefore hope that the effects described above occur in QCD as well.

In the future, we are going to consider in more detail the region of low values of H and to take into account different structures of four-fermion interaction in the Lagrangian in (1); also, we plan to explore the role of the gluon condensate (which can be simulated by external chromomagnetic fields) in the stabilization of quark matter.

ACKNOWLEDGMENTS

This work was supported in part by Deutsche Forschungsgemeinschaft (project no. 436 RUS 113/477/0-2).

REFERENCES

1. Y. Nambu and G. Jona-Lasinio, Phys. Rev. **122**, 345 (1961).
2. M. Buballa, Nucl. Phys. A **611**, 393 (1996); M. Buballa and M. Oertel, Nucl. Phys. A **642**, 39 (1998).
3. M. Alford, K. Rajagopal, and F. Wilczek, Phys. Lett. B **422**, 247 (1998).
4. S. Ghosh, S. Ghosh, K. Goswami, *et al.*, astro-ph/0106153.
5. G. G. Likhachev and A. I. Studenikin, Zh. Éksp. Teor. Fiz. **108**, 769 (1995) [JETP **81**, 419 (1995)]; S. Chakrabarty, Phys. Rev. D **54**, 1306 (1996); T. C. Phukon, Phys. Rev. D **62**, 023002 (2000); V. R. Khalilov, Phys. Rev. D **65**, 056001 (2002); V. R. Khalilov, Teor. Mat. Fiz. **133**, 103 (2002).
6. T. Tatsumi, Phys. Lett. B **489**, 280 (2000); astro-ph/0004062.
7. M. Alford, J. Berges, and K. Rajagopal, Nucl. Phys. B **571**, 269 (2000).
8. D. M. Sedrakian, D. Blaschke, K. M. Shahabasyan, and D. N. Voskresensky, Astrofizika **44**, 443 (2001) [Astrophys. **44**, 359 (2001)].
9. J. I. Kapusta, *Finite-Temperature Field Theory* (Cambridge University Press, Cambridge, 1989).
10. V. E. Rochev and P. A. Saponov, Int. J. Mod. Phys. A **13**, 3649 (1998); R. K. Jafarov and V. E. Rochev, Preprint No. 2003-23, IFVÉ (Inst. of High Energy Phys., Protvino, 2003).
11. P. Zhuang, J. Hufner, and S. P. Klevansky, Nucl. Phys. A **576**, 525 (1994).
12. A. S. Vshyvtsev and K. G. Klimenko, Pis'ma Zh. Éksp. Teor. Fiz. **64**, 313 (1996) [JETP Lett. **64**, 338 (1996)]; A. S. Vshyvtsev, V. Ch. Zhukovskiĭ, and K. G. Klimenko, Zh. Éksp. Teor. Fiz. **111**, 1921 (1997) [JETP **84**, 1047 (1997)]; B. R. Zhou, hep-th/0308138.
13. D. Ebert, K. G. Klimenko, M. A. Vdovichenko, *et al.*, Phys. Rev. D **61**, 025005 (2000); M. A. Vdovichenko, K. G. Klimenko, and D. Ebert, Yad. Fiz. **64**, 386 (2001) [Phys. At. Nucl. **64**, 336 (2001)]; D. Ebert and K. G. Klimenko, nucl-th/9911073.
14. K. G. Klimenko, hep-ph/9809218; M. A. Vdovichenko, A. S. Vshyvtsev, and K. G. Klimenko, Yad. Fiz. **63**, 542 (2000) [Phys. At. Nucl. **63**, 470 (2000)].
15. A. Erdeyi, *Higher Transcendental Functions (Bateman Manuscript Project)* (McGraw-Hill, New York, 1953; Nauka, Moscow, 1965, 1966), Vols. 1, 2.
16. V. P. Gusynin, V. A. Miransky, and I. A. Shovkovy, Phys. Lett. B **349**, 477 (1995).
17. V. A. Miransky, Prog. Theor. Phys. Suppl. **123**, 49 (1996); A. S. Vshyvtsev, B. V. Magnitsky, V. Ch. Zhukovsky, and K. G. Klimenko, Fiz. Elem. Chastits At. Yadra **29**, 1259 (1998) [Phys. Part. Nucl. **29**, 523 (1998)]; V. P. Gusynin, Ukr. Phys. J. **45**, 603 (2000); Vivian de la Incera, hep-ph/0009303.
18. K. G. Klimenko, Z. Phys. C **54**, 323 (1992); Teor. Mat. Fiz. **89**, 211 (1991); **90**, 3 (1992); V. P. Gusynin, V. A. Miransky, and I. A. Shovkovy, Phys. Rev. Lett. **73**, 3499 (1994).
19. I. A. Shushpanov and A. V. Smilga, Phys. Lett. B **402**, 351 (1997); N. O. Agasyan, Yad. Fiz. **64**, 608 (2001) [Phys. At. Nucl. **64**, 554 (2001)]; D. Kabat, K. Lee, and E. Weinberg, Phys. Rev. D **66**, 014004 (2002).
20. L. D. Landau and E. M. Lifshits, *Statistical Physics*, 3rd ed. (Nauka, Moscow, 1976; Pergamon Press, Oxford, 1980).
21. M. Alford, Annu. Rev. Nucl. Part. Sci. **51**, 131 (2001).
22. V. A. Miransky, hep-ph/0208180; V. A. Miransky and I. A. Shovkovy, Phys. Rev. D **66**, 045006 (2002).

Translated by A. Isaakyan

Physics of Atomic Nuclei, Vol. 68, No. 1, 2005, pp. 131–143. Translated from Yadernaya Fizika, Vol. 68, No. 1, 2005, pp. 134–146.

ELEMENTARY PARTICLES AND FIELDS
Theory

Elastic Hadron Scattering on Li Isotopes at Intermediate Energies

M. A. Zhusupov[1)], E. T. Ibraeva[*], and O. Imambekov[1)]

Institute of Nuclear Physics, National Nuclear Center of the Republic of Kazakhstan, Almaty, 480082 Republic of Kazakhstan

Received September 30, 2003; in final form, January 23, 2004

Abstract—The elastic scattering of hadrons (protons, charged pions, and positively charged kaons) on ^{6,7,8}Li nuclei is analyzed on the basis of Glauber–Sitenko diffraction theory. A few nuclear-wave-function versions found within two- and three-particle potential cluster models are used in the calculations. It is shown that the application of these wave functions in diffraction theory makes it possible to describe adequately the experimental differential cross sections and analyzing powers in hadron scattering at intermediate energies. In this study, particular attention is given to a comparison of the scattering of different particles on the same target nucleus, as well as to a comparison of scattering of particles of the same sort on different target nuclei. © *2005 Pleiades Publishing, Inc.*

INTRODUCTION

Investigation of hadron interaction with nuclei is a key problem in the theory of the nucleus and of nuclear reactions. This is a test that makes it possible to study both the structure of nuclei and the nature of nuclear forces. The scattering of different particle species on the same target nuclei is of interest since particles of different nature interact differently with target nucleons, and this circumstance will manifest itself in observables. By way of example, we indicate that, in the region of intermediate energies (from 100 MeV to 1 GeV), the interaction of protons and positively charged kaons with target nucleons is of a nonresonance character, the range of positively charged kaons in a nuclear medium being 5 to 7 fm, which permits employing them as a probe for studying the interior of nuclei. Charged pions form, owing to the presence of antiquarks in their composition ($\bar{d}$ in π^+ and $\bar{u}$ in π^-), stable resonances and undergo a strong absorption in a nuclear medium (for the sake of comparison, we recall that their range is about 1 fm, which is less that the typical internucleon distance).

The cross sections for elastic and inelastic proton scattering on ^{6}Li nuclei were measured at the Gustav Werner Institute (Uppsala University, Sweden) [1] by using the 185-MeV synchrocyclotron and in Saclay (France) at the energies of 0.6 and 1.0 GeV [2]. The scattering of 0.2-GeV polarized protons on ^{6}Li and ^{7}Li nuclei was investigated at the cyclotron of Indiana University (USA) [3, 4]. The differential cross sections for the scattering of 0.1- to 0.24-GeV charged pions on ^{6}Li and ^{7}Li were measured at the Paul Scherrer Institute (PSI, Villigen, Switzerland) [5–7]. Experiments devoted to studying the scattering of positively charged kaons on ^{6}Li nuclei were performed in the Brookhaven National Laboratory (BNL AGS, USA) at $E_K = 0.375$ GeV [8–10].

The advent of the new technique that employs secondary radioactive beams permits performing experiments with unstable nuclei under conditions of so-called inverse kinematics, in which case a beam of radioactive nuclei is incident on a hydrogen target. A similar experiment for ^{8}Li nuclei is planned at the Petersburg Nuclear Physics Institute, as was claimed in [11].

Interest in $^{6-8}$Li nuclei is motivated by the fact that these few-nucleon systems are strongly clustered in some channels, so that they can be considered as a convenient testing ground for various model wave functions. These wave functions are calculated within potential cluster models, where the nucleus in question is represented as that which is formed by two (α and t in ^{7}Li) or three (α, n, and p in ^{6}Li and α, t, and n in ^{8}Li) fragments assigned the properties of the corresponding particles in a free state. These models take into account the Pauli exclusion principle and employ realistic potentials of intercluster interaction, this making it possible to describe the main features of nuclei, including their binding energies, the spectra of their low-lying levels, their root-mean-square radii, and their magnetic and quadrupole moments [12–19]. It was precisely these wave functions that provided a good description of direct and inverse reac-

[1)]Institute of Experimental and Theoretical Physics, Kazakh State University, ul. Timiryazeva 46, Almaty, 480121 Republic of Kazakhstan.

[*]e-mail: ibr@inp.kz

1063-7788/05/6801-0131$26.00

tions of photodisintegration through cluster channels [20, 21]. In the present study, multicluster wave functions are used to analyze the elastic scattering of protons, charged pions, and positively charged kaons on $^{6-8}$Li nuclei.

Glauber–Sitenko diffraction theory [22] is extensively used in the region of intermediate projectile energies. Apart from its relative simplicity, this theory is advantageous in that it involves a small number of input parameters to be extracted from data of independent experiments and employs elementary amplitudes whose parameters, having a rather simple physical meaning, are related to observables; moreover, the form of the multiple-scattering operator Ω in the Glauber–Sitenko diffraction theory is quite convenient for analysis. But in phenomenological approximations, such as the optical model, physical effects are masked by numerous adjustable parameters, whose meaning is not always clear.

The set of available experimental data and reliable computational methods make it possible to perform a detailed analysis of relevant processes, which includes a comparison of processes where particles of different species are scattered on the same target nuclei, a comparison of processes where particles of the same species are scattered on different lithium isotopes, and a comparison of our results with experimental data and with the results of other authors.

The scattering of protons, charged pions, and positively charged kaons on ^{6,7}Li nuclei was explored in a number of studies [1–10, 22–30] in the distorted-wave impulse approximation [1–4, 8–10, 23–25], within the coupled-channel method [6, 7], or within Glauber–Sitenko theory [5, 22, 26–30]. (Here, we have given references only to a small number of studies published thus far.) But only in some of those studies [5, 23, 27–29] was use made of wave functions that describe correctly the structure of nuclei both in their interior and at their periphery. None of them presents a comparison of processes involving the scattering of hadrons that belong to different species—that is, none covers the aspects of the problem that form the subject of the present study. At the same time, it was indicated in [3, 4, 24, 26] that an insufficiently accurate description of the structure of nuclei is one of the reasons for an inadequate description of the features of scattering (differential cross sections and analyzing powers A_y).

For example, the differential cross sections for p^6Li and p^7Li scattering and the analyzing power A_y for these processes were calculated in [3, 4] on the basis of the optical model with the standard Woods–Saxon potential in the first version and with a microscopic folding potential in the second version. These were the first studies where the purpose of deducing more justified conclusions on the shape of the ground-state densities and of the transition densities was pursued by simultaneously considering proton and electron scattering and by calculating the contributions of high multipoles ($J = 1, 2, 3$) to the observables in question. However, the authors of those studies themselves admitted that the failure of the distorted-wave impulse approximation to reproduce the scattering cross sections could be attributed to several factors, including the inadequacy of the single-scattering model, inaccuracy of the description of the nucleon–nucleon interaction in the transition matrix element, and a low quality of the transition density used in the calculations.

An attempt at taking into account quadrupole effects in π^7Li scattering was made in [24]. The calculations there were performed on the basis of the optical model with the ^{7}Li wave function found by the resonating-group method. The wave function obtained in this way for the ^{7}Li nucleus in the αt configuration describes the electromagnetic properties of the nucleus quite accurately. It was found that, in the elastic-scattering process, quadrupole effects are large, especially in the region of backward angles.

A complete microscopic analysis of the elastic scattering of 0.2-GeV protons on nuclei in the range from ^{6}Li to ^{208}Pb was given in [25]. The respective calculations were performed in the distorted-wave Born approximation (DWBA91 code) with fully antisymmetrized wave functions by using an effective approximation that includes central, tensor, and two-particle spin–orbit forces. The authors of that study achieved a good description of a vast body of experimental data—in particular, those on the binding energies of p- and sd-shell nuclei, root-mean-square charge radii, differential cross sections, and polarization observables (A_y and Q).

In [26], the calculation of the elastic and inelastic scattering of charged pions at $E_\pi = 0.16$–0.24 GeV was performed within Glauber–Sitenko diffraction theory, and it was shown there that, in the region of the Δ_{33} resonance, this theory provides, for these scattering processes, results that are not poorer than those within the generally accepted distorted-wave impulse approximation. However, the authors of that study considered predominantly the scattering on ^{12}C, ^{16}O, and ^{24}Mg nuclei, whose wave functions are taken in the shell model (only inelastic scattering was studied for ^{7}Li).

In connection with our investigation, we would also like to mention the study of Tag Eldin *et al.* [31], who used the Glauber–Sitenko diffraction theory to calculate elastic proton, antiproton, and pion scattering on ^{12}C nuclei. Some discrepancy between the

theoretical and experimental results for pion scattering on ^{12}C nuclei at $E = 0.18$ GeV was explained in [31] by several factors—in particular, by the need for choosing, for ^{12}C, a more realistic density, better than a Gaussian one, since, in the Δ-resonance region, pion interaction with ^{12}C nuclei occurs predominantly in the surface region. At such energies, it is therefore of importance to know the true shape of the nuclear density at the surface. In [31], attention was given primarily to exploring the possibility of applying the theory at not very high energies (from 50 MeV for antiprotons) and large scattering angles (up to 130° for pions). It was concluded that Glauber–Sitenko theory can be used throughout the region where the elementary amplitude has a strong forward peak.

The present analysis is a logical continuation of the preceding studies reported in [28, 29] and devoted to studying hadron scattering on ^{6,7}Li nuclei. However, the attention there was given predominantly to the application of Glauber–Sitenko theory to hadron scattering on individual nuclei, and no comparative analysis of the features of scattering was performed there. In addition to including one more nucleus in our consideration, ^{8}Li, we focus our attention primarily on a comparison of the calculated features of scattering on different lithium isotopes.

The ensuing exposition is organized as follows. In the next section, we briefly describe the formalism of Glauber–Sitenko theory and input parameters for which we take wave functions and elementary hadron–nucleon amplitudes. Further, we discuss the results that we obtain. In the last section, we formulate our basic conclusions.

BRIEF ACCOUNT OF THE FORMALISM OF DIFFRACTION THEORY AND DESCRIPTION OF INPUT PARAMETERS

Within diffraction theory, the amplitude for hadron–nucleus scattering can be represented in the form [22]

$$M_{if}(\mathbf{q}) = \frac{ik}{2\pi}\int d^2\rho \exp(i\mathbf{q}\cdot\boldsymbol{\rho})\langle\Psi_f^{JM_J}|\Omega|\Psi_i^{JM'_J}\rangle, \quad (1)$$

$$\langle\Psi_f^{JM_J}|\Omega|\Psi_i^{JM'_J}\rangle = \int\prod_{\nu=1}^{3} d\mathbf{r}_\nu \Psi_f^{JM_J}\Omega\Psi_i^{JM'_J}\delta(\mathbf{R}_A),$$

where $\boldsymbol{\rho}$ is the impact-parameter vector lying in the plane orthogonal to the axis of the incident-hadron beam; $\mathbf{r}_\nu$ stands for the nucleon coordinates; $\mathbf{R}_A$ is the c.m. coordinate of the target nucleus; $\Psi_i^{JM'_J}$ and $\Psi_f^{JM_J}$ are, respectively, the initial- and the final-state wave function for the target nucleus; and $\mathbf{q} = \mathbf{k}' - \mathbf{k}$ is the momentum transfer in the reaction being considered, $\mathbf{k}$ and $\mathbf{k}'$ being the c.m. momenta of, respectively, the incident and the scattered hadron. The absolute value of the momentum transfer is given by

$$q = 2k\sin\theta/2, \quad k = \sqrt{\varepsilon^2 - m^2}, \quad (2)$$

where m and ε are, respectively, the mass and the energy of the incident hadron and θ is the scattering angle (we use here the system of units where $\hbar = c = 1$).

We represent the multiple-scattering operator in the "factorized" form

$$\Omega = \Omega_\alpha + \Omega_b - \Omega_\alpha\Omega_b, \quad (3)$$

where b denotes an np pair in ^{6}Li, t in ^{7}Li, and a tn pair in ^{8}Li and

$$\Omega_b = 1 - \prod_{\nu=5}^{A}(1 - \omega_\nu(\boldsymbol{\rho} - \boldsymbol{\rho}_\nu)) \quad (4)$$

$$= 1 - \left[1 - \sum_{\nu=5}^{A}\omega_\nu + \sum_{\nu<\mu}\omega_\nu\omega_\mu - \ldots\right].$$

Here, $\boldsymbol{\rho}_\nu$ are the two-dimensional coordinates of intranuclear nucleons in the plane of the impact-parameter vector $\boldsymbol{\rho}$, and ω_ν is a profile function that is expressed in terms of the amplitude for xN scattering ($x \equiv p, \pi^\pm, K^+$) as

$$\omega_\nu(\boldsymbol{\rho} - \boldsymbol{\rho}_\nu) \quad (5)$$

$$= \frac{1}{2\pi ik}\int d^2q \exp(-i\mathbf{q}\cdot(\boldsymbol{\rho} - \boldsymbol{\rho}_\nu))f_{xN}(q),$$

where

$$f_{xN}(q) = f_{xN}^c(q) + \boldsymbol{\sigma}\cdot\mathbf{n}f_{xN}^s(q). \quad (6)$$

Here, $\boldsymbol{\sigma}$ is the spin Pauli matrix, and $\mathbf{n}$ is a unit vector orthogonal to the plane spanned by the vectors $\mathbf{k}$ and $\mathbf{k}'$. The expressions for the central elementary amplitude $f_{xN}^c(q)$ and the spin-orbit elementary amplitude $f_{xN}^s(q)$ are given below, while the fitted values of their parameters are quoted in Tables 1–3.

We write the operator of scattering on an alpha particle in the form of one profile function, $\Omega_\alpha = \omega_\alpha$, but we employ, in that case, the elementary amplitude $f_{\alpha N}$ instead of f_{xN}. This is because an alpha particle, which enters into the composition of all lithium isotopes, is treated as a structureless object within this approach, so that all special features of scattering on it are taken into account in the parameters of the elementary amplitude $f_{\alpha N}$. This approach has some obvious advantages since one can assume that some nontrivial effects, such as those that are associated with the spins of target nucleons, various nucleon–nucleon correlations, the Fermi motion of nucleons,

Table 1. Compendium of the parameters of the proton–nucleon amplitudes

E_p, GeV	Interaction	$\sigma_{pN}^{\mathrm{tot}}$, fm^2	ε_{pN}^c	β_{pN}^c, fm^2	D_s, fm^2	ε_{pN}^s	β_{pN}^s, fm^2	References
0.2	pp	2.36	1.15	0.65				[35]
	pn	4.20	0.71	0.68				
0.6	pp	3.7	−0.1	0.12	3.0	1.0	0.6	[33]
	pn	3.7	−0.1	0.12	3.0	1.0	0.6	
0.8	pp	4.73	0.06	0.34	7.3	1.18	0.11	[32]
	pn	3.79	0.2	0.46	11.3	0.35	0.12	
1.0	pp	4.75	−0.08	0.25	0.7	1.5	0.4	[34]
	pn	3.85	−0.41	0.25	0.7	1.5	0.4	

and multiparticle effects and which are difficult to take into account within the independent-particle model, are included in the $x\alpha$ amplitude fitted to experimental data. The question of the most convenient representation of the Glauber operator Ω and the question of which scattering effects are taken into account in the elementary amplitudes was discussed in detail elsewhere [29].

The operator Ω (3), which depends on the elementary $x\alpha$ and xN amplitudes, will be represented, in accordance with the partition of each of these into the central and the spin–orbit component [see Eq. (6)], in the form of the sum of two terms,

$$\Omega = \Omega^c + \Omega^s. \tag{7}$$

With allowance for the spin dependence, the scattering matrix element can be written in the form

$$M_{if}(\mathbf{q}) = M_{if}^c(\mathbf{q}) + M_{if}^s(\mathbf{q}). \tag{8}$$

The differential cross section is determined by the squared modulus of the matrix element; that is,

$$\frac{d\sigma}{d\Omega} = \frac{1}{2J+1}\sum_{M_J M_J'}\left[\left|M_{if}^c(\mathbf{q})\right|^2 + \left|M_{if}^s(\mathbf{q})\right|^2\right]. \tag{9}$$

The analyzing power is defined as

$$A_y = \frac{2\mathrm{Re}\left[M_{if}^c(\mathbf{q})M_{if}^{s^*}(\mathbf{q})\right]}{d\sigma/d\Omega}. \tag{10}$$

It is rather difficult to calculate the scattering amplitude (1). In order to accomplish this goal, we go over, in the wave functions and in the scattering operator, from single-particle coordinates to Jacobi coordinates and, after that, integrate the matrix element with respect to all variables. There are, however, a few difficulties along the way. First, the presence of the delta function of $\mathbf{R}_A$ in the amplitude given by Eq. (1) results in that this amplitude does not factorize into amplitudes for individual clusters and relative motion, since all of the variables are related to each other. Second, the coordinates of the nucleons involved are three-dimensional in the wave functions and two-dimensional in the operator Ω, since, in diffraction theory, scattering occurs in a plane orthogonal to the incident-beam axis; in view of this, one has to perform integration in the system of Cartesian coordinates rather than in the system of spherical coordinates, which would be simpler. However, the use of not only xN but also $x\alpha$ amplitudes for elementary amplitudes and the resort to the wave functions for relative motion in the form of expansions in terms of multidimensional Gaussian functions make it possible to integrate the relevant matrix elements analytically; as a result, there is no loss of accuracy in calculating the differential cross sections, since there do not arise here errors inevitable in a numerical calculation of multidimensional integrals.

The technique for calculating the matrix element (1) with multicluster wave functions is described in [29].

The elementary xN amplitudes [see formula (6)]

Table 2. Compendium of the parameters of the $\pi^{\pm}N$ amplitudes (data from [35])

E_π, GeV	Interaction	$\sigma_{\pi N}^{\mathrm{tot}}$, fm^2	$\varepsilon_{\pi N}^c$	$\beta_{\pi N}^c$, fm^2
0.15	$\pi^{\pm}N$	10.93	0.522	1.25
0.18	π^-p	6.0	0.18	0.570
	π^-n	7.6	−0.03	0.586
0.2	$\pi^{\pm}N$	11.90	−0.17	0.873

enter into the set of input parameters of Glauber–Sitenko theory. They describe phenomenologically the interaction of an incident hadron with target nucleons, the parameters of these amplitudes being extracted from data of independent experiments [32–35],

$$f^c_{xN} = \frac{k\sigma^{\rm tot}_{xN}}{4\pi}(i+\varepsilon^c_{xN})\exp(-\beta^c_{xN}q^2/2), \qquad (11)$$

$$f^s_{xN} = \frac{k\sigma^{\rm tot}_{xN}}{4\pi} i\sqrt{\frac{q^2}{4m^2}}D_s(i+\varepsilon^s_{xN})\exp(-\beta^s_{xN}q^2/2), \qquad (12)$$

where k and m are, respectively, the momentum and the mass of the incident hadron; $\sigma^{\rm tot}_{xN}$ is the total cross section for hadron–nucleon scattering; ε_{xN} is the ratio of the real part of the respective amplitude to its imaginary part; β_{xN} is the cone-slope parameter of the amplitude; and the indices c and s label, respectively, the central and the spin–orbit component of the amplitude.

The question of why protons, positively charged kaons, and charged pions are of interest as probes in studying the structure of nuclei is in order here. The answer is that this is due primarily to the mechanism of their interaction with bound nucleons that occur in nuclear matter. A positively charged kaon, whose strangeness is +1, cannot be entirely absorbed in a nucleus since there are no forces of one-pion exchange with a nucleon for it. Only elastic or inelastic scattering on a nucleon is possible for a positively charged kaon (as well as for a proton); therefore, it is the weakest of all hadronic probes. This mechanism is different from that which governs the interaction of charged pions, for which two-nucleon absorption is dominant. A strong perturbative interaction that has a complicated resonance structure (featuring a distinct forward maximum) is observed in $\pi^{\pm}N$ scattering; in this respect, $\pi^{\pm}N$ interaction more resembles K^-N interaction, since a negatively charged kaon can also be readily absorbed by a single nucleon.

The interaction of positively charged kaons with nucleons differs significantly from the interaction of other particles: at the same energy, the values of $\sigma^{\rm tot}_{xN}$ and β^c_{xN} for positively charged kaons are much less, while the value of $|\varepsilon^c_{xN}|$ is much greater (see Tables 1–3). The smallness of β^c_{xN} (it is one to two orders of magnitude smaller for K^+N interaction than for pN and $\pi^{\pm}N$ interactions), which characterizes the range of xN interaction, indicates that only the $l = 0$ and 1 partial waves are dominant in the K^+N amplitude. In simplicity, the interaction of positively charged kaons with nucleons can be compared with electron interaction, but the former is advantageous in that a positively charged kaon is sensitive to neutron interaction, this making it possible to realize processes involving high momentum transfers. The smallness of $\sigma^{\rm tot}_{xN}$ indicates that the imaginary part of the K^+N amplitude ($\sigma^{\rm tot}_{xN}$ is related to it by the optical theorem) is also small. The quantity $|\varepsilon^c_{xN}|$ is also indicative of this. That it is sometimes greater than unity means that the real part of the respective elementary amplitude is greater than its imaginary part, which is responsible for absorption; that is, the scattering process proceeds predominantly through the elastic channel. These circumstances explain why the interaction of positively charged kaons with nucleons is much weaker than the interaction of protons and charged pions and why the mean range of positively charged kaons in a nuclear medium is unusually long.

Table 3. Compendium of the parameters of the K^+N amplitudes (data from [30])

E_K, GeV	Interaction	$\sigma^{\rm tot}_{KN}$, fm^2	ε^c_{KN}	β^c_{KN}, fm^2
0.201	K^+p	1.29	−2.190	0.0134
	K^+n	1.31	−0.667	0.0013
0.23	K^+p	1.30	−1.964	0.0197
	K^+n	1.41	−0.575	0.0012
0.375	K^+p	1.32	−1.467	0.0114
	K^+n	1.67	−0.373	0.0015
0.468	K^+p	1.32	−1.258	0.0095
	K^+n	1.71	−0.305	0.0013
0.534	K^+p	1.39	−0.9074	0.0065
	K^+n	1.75	−0.105	0.0011

The total cross sections for the interaction of a proton, a positively charged kaon, and a negatively charged pion with a neutron are larger than their counterparts for interactions with a proton, as can be seen from a comparison of the corresponding values of $\sigma^{\rm tot}_{xN}$, and are determined by different isospin dependences. This is of importance in employing negatively charged pions as a probe of neutron and proton distributions in nuclei.

At the quark level, the elementary interactions of protons and charged pions and kaons with nucleons were considered in detail in [29].

The wave functions for target nuclei on which the scattering processes being considered occur form yet another element of the theory. The basic properties of these nuclei are rather well reproduced within the multiparticle shell model [36]. However, shell-model wave functions have an incorrect asymptotic

behavior; therefore, they describe poorly peripheral processes such as two-cluster photodisintegration through reactions of the $A(\gamma, b)B$ type or inverse reactions involving radiative cluster capture and belonging to the $B(b, \gamma)A$ type. The particular cluster models developed in [37, 38] are more adequate to such processes. Within these models, it is assumed that a nucleus A consists of two (sometimes three) composite particles and nucleons that are in the ground state each with respect to their internal motion, all excitations of the nucleus being associated exclusively with the relative motion of the fragments. As in the resonating-group method [39], the wave functions for a nucleus that consists, for example, of two fragments a and b, which can be either in a continuous or in a discrete spectrum, are written in the form

$$\Psi = \hat{A}(\Psi_a \Psi_b \Phi_\nu(\mathbf{R}_{ab})), \qquad (13)$$

where Ψ_a and Ψ_b are the intrinsic fragment wave functions, for which one usually employs known parametrizations that describe the properties of free particles. In contrast to what is done within the resonating-group method, antisymmetrization is not performed here explicitly, the Pauli exclusion principle being taken into account via a choice of interaction potential constraining the form of the relative-motion wave function, since it involves forbidden states in addition to allowed ones. The three-particle wave functions for ^{6}Li (in the αnp model) and for ^{8}Li (in the αtn model) can be symbolically represented in form similar to that in (13), since the intrinsic nucleon wave functions are not written explicitly, but all of their quantum numbers (spins, isospins, orbital angular momenta) are taken into account in the corresponding vector-composition coefficients. Thus, $\Psi_a = \Psi_\alpha$ for all lithium isotopes. We have $\Psi_b = \Psi_t$ for ^{7,8}Li and $\Psi_b = \text{const}$ for ^{6}Li, this implying the absence of the intrinsic nucleon wave functions in the representation in (13). The relative-motion wave functions $\Phi_\nu(\mathbf{R}_{ab})$ ($\nu = abN$) depend on the corresponding coordinates: for ^{6}Li, this is the radius vector between the alpha particle and the center of mass of the np pair, $\Phi_{abN}(\mathbf{R}_{ab}) = \Phi_{\alpha np}(\mathbf{R}_{\alpha-np})$; for ^{7}Li, this is the radius vector between the alpha particle and the triton, $\Phi_{abN}(\mathbf{R}_{ab}) = \Phi_{\alpha t}(\mathbf{R}_{\alpha-t})$; for ^{8}Li, this is the radius vector between the neutron and the center of mass of the αt pair, $\Phi_{abN}(\mathbf{R}_{ab}) = \Phi_{\alpha tn}(\mathbf{R}_{\alpha t-n})$. The structure of these states is determined by the correspondence of the relative-motion wave function to the shell-model wave function in the interior of the nucleus (the region where the fragments a and b overlap). We mean the correspondence of the internal node structure of the two functions (numbers of nodes and their positions). A shell-model wave function is an oscillator-type function featuring μ quanta. By way of example, we indicate that, for the ^{7}Li nucleus, which has the $(0s)^4(1p)^3$ shell configuration, three quanta are associated with the relative-motion wave function in the potential cluster model—that is, $\mu = 3$. Thus, we arrive at node wave functions for the ground state of the ^{7}Li nucleus in an αt model of the R_{3p} type. The R_{1p} state is forbidden. In order to obtain the relative-motion wave function for the ^{7}Li nucleus in the αt model, one has to solve the Schrödinger equation for the case where a central interaction in the form of a deep attractive potential of the Woods–Saxon [14] or the Gaussian [15] type is supplemented with spin–orbit and Coulomb terms. The parameters of two-cluster potentials are chosen on the basis of a fit to low-energy elastic-scattering phase shifts in all partial waves. In all models, relative-motion wave functions are sought in the form of an expansion in multidimensional Gaussian functions, this making it possible not only to find all matrix elements analytically but also to calculate wave functions for a broad basis with a large number of small components. We note that the number of Gaussian functions is chosen in such a way as to ensure a correct exponential asymptotic behavior of $\Phi_\nu(\mathbf{R}_{ab})$ for rather long distances. In the present study, we have performed calculations with two cluster wave functions for ^{7}Li that have the parameters borrowed from [14] (model 1) and from [16] (model 2).

In the literature, it is often indicated that the ^{6}Li nucleus is especially appealing for theorists: owing to a comparatively small number of nucleons in this nucleus, it may serve as a testing ground for constructing various model wave functions that, on one hand, are sensitive to multiparticle nuclear correlations and, on the other hand, make it possible to perform accurate calculations for such few-particle systems.

The wave functions obtained by Kukulin's group from the Institute of Nuclear Physics at Moscow State University [12, 13] were among the first wave functions for the ^{6}Li nucleus in the αnp model. The calculations performed with these functions for reactions featuring electrons [12, 13], protons [28, 29] and charged pions [5, 23, 27, 29] yielded reliable results. The wave functions for the ^{6}Li and ^{6}He nuclei in the dynamical multicluster model involving Pauli projection and full antisymmetrization were constructed in [40]. Also presented there are the most comprehensive calculations of all basic properties of these nuclei: the radius of the neutron halo in ^{6}He, the electromagnetic form factors, the features of the photomeson process $^6\text{Li}(\gamma, \pi^+)^6\text{He}$, and the cross sections for the elastic scattering of charged pions at 0.134 GeV.

Table 4. Form of intercluster interaction potentials used to calculate wave functions

Model	^{6}Li		^{7}Li	^{8}Li		
	αN	NN	αt	αn	tn	αt
1	SBB potential	Soft-core Reid potential	Buck potential	Split potential	Split potential	Buck potential
2	Split potential	Soft-core Reid potential	Woods–Saxon potential	Split potential	Split potential	Woods–Saxon potential

In our calculations, we employ the wave functions obtained in [12, 13].

Experimental data on the angular and energy dependences of observables for reactions like ^{7}Li$(\gamma, t)\alpha$, ^{6}Li$(\gamma, t)^3$He, and ^{6}Li$(\gamma, d)\alpha$ were explained on the basis of the above models for the ^{6}Li and ^{7}Li nuclei [20]. Moreover, a correct treatment of the structure of these nuclei within cluster models enabled one not only to describe available experimental data but also to make a number of successful predictions. For example, the data of the dedicated measurements of the asymmetry of the angular distribution of tritons from the polarized-photon-induced reactions ^{7}Li$(\gamma, t)\alpha$ and ^{6}Li$(\gamma, t)^3$He at the Kharkov Institute for Physics and Technology [41, 42] proved to be in perfect agreement with the results of the calculations performed earlier in [20, 21]. The same is true for the recently measured angular distributions of tritons in the reaction ^{7}Li$(\gamma, t)\alpha$ [43].

The ^{8}Li nucleus is of interest both for nuclear physics (as a one-neutron halo nucleus) and for nuclear astrophysics, since the radiative-capture reaction ^{7}Li$(n, \gamma)^8$Li provides one more channel in the chain of the thermonuclear fusion of C, N, and O elements in a nonstandard model of nucleosynthesis. The rate of this reaction may refine our ideas of the evolution of the Universe [44]. In view of this, the ^{8}Li nucleus has been vigorously studied so far [17–19].

As a rule, the wave functions for the ^{8}Li nucleus are calculated within three-particle αtn models with realistic potentials of intercluster interactions. In order to obtain deeper insight into the mechanism of the radiative-capture reaction in question, it is of importance to determine low-lying resonances precisely [18] and to consider simultaneously the effect of a strong deformation of the ^{7}Li nucleus, the dynamical polarization of its core, and its excitation [17]. In [19], the wave functions constructed there were used to calculate basic spectroscopic features (root-mean-square charge radius and quadrupole and magnetic moments) and to find the total cross section for the reaction ^{7}Li$(n, \gamma)^8$Li and its rate over the energy range between 10^{-5} keV and 1 MeV. We note that this energy range covers eight orders of magnitude of energy and that the calculated total cross sections agree with available experimental data throughout this range. In the present study, we will use precisely this wave function.

The wave-function configurations are determined by the quantum numbers λlLS, where l is the orbital angular momentum of the relative motion of the alpha-particle cluster and the center of mass of the remaining two clusters (or nucleons); λ is the orbital angular momentum of the relative motion of these two clusters (nucleons); and L and S are, respectively, the total orbital angular and the total spin momentum of the nucleus being considered.

In the ground-state wave function for the ^{6}Li nucleus ($J^\pi = 1^+$, $T = 0$) in the αnp model, we can retain only two leading configurations: $\lambda = l = L = 0$, $S = 1$ (S wave, its weight being greater than 90%) and $\lambda = 2$, $l = 0$, $L = 2$, $S = 1$ (D wave, its weight varying from 3 to 7% in the calculations with different interaction potentials). The total weight of the remaining components does not exceed a few percent. The contribution of the small D-wave component to the differential cross section and the role of this component in the filling of the diffraction minimum in the cross section were investigated in detail in [28, 29].

The ground state of the ^{7}Li nucleus is characterized by the following quantum numbers: $J^\pi = 3/2^-$, $T = 1/2$; $L = 1$. The dominant cluster αt configuration characterized by $\lambda = 1$ (its weight is greater than 95%) is assumed to be responsible for a significant quadrupole deformation of this nucleus. The effect from additional configurations in electromagnetic form factors was calculated in [45], and it was shown there that the αt component is dominant in the ground and in the first excited state, while other components contribute to higher excited states.

The model wave functions for the ^{8}Li nucleus were calculated in [19] with various αt potentials, since the αt interaction affects the ground-state properties of this nucleus more strongly than the αn and tn interactions do. The quantum numbers of the ground

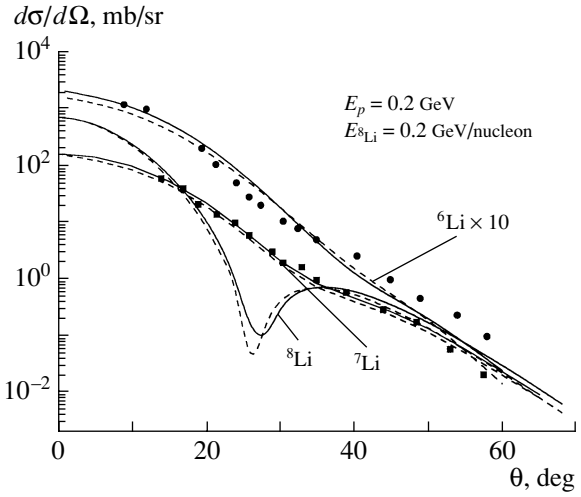

Fig. 1. Differential cross sections for elastic proton scattering on $^{6-8}$Li nuclei. The solid and dashed curves were calculated with wave functions based on models 1 and 2, respectively. The displayed points represent experimental data from [3, 4]. Here and in Fig. 2 below, the experimental data and the calculated curves for ^{6}Li were multiplied by 10 in order to avoid an overlap of the results.

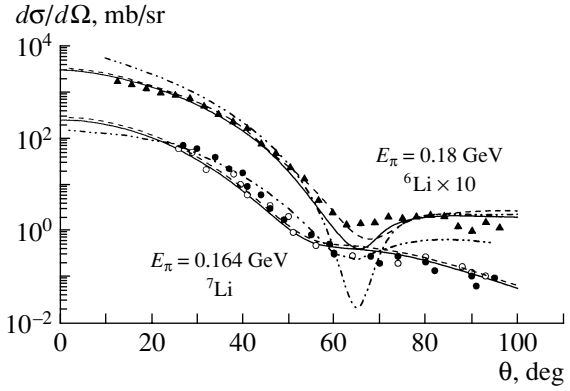

Fig. 2. Differential cross sections for the scattering of charged pions on ^{6}Li and ^{7}Li nuclei. The solid and dashed curves were calculated with wave functions based on models 1 and 2, respectively. The dash-dotted curves represent the results of the calculation in the distorted-wave impulse approximation for ^{6}Li from [23] and the results of the calculation with the oscillator wave function for ^{7}Li. The displayed experimental data were borrowed from (closed triangles, π^+) [5] and (closed circles, π^+ and open circles, π^-) [7].

state of this nucleus are the following: $J^\pi = 2^+$, $T = 1$; $\lambda = l = L = S = 1$.

Table 4 gives a compendium of the intercluster interaction potentials used to calculate the model wave functions. For the αN interaction, we took two potentials.

(i) Sack–Biedenharn–Breit (SBB in the table) [46] potential. Its central part has a Gaussian form. It also involves a spin–orbit and a Coulomb interaction. The Sack–Biedenharn–Breit potential describes quite accurately the main $P_{1/2}$ and $P_{3/2}$ phase shifts for elastic αN scattering and less accurately S-wave phase shifts up to an energy of 14 MeV. The main drawback of the Sack–Biedenharn–Breit potential is that it leads to a strong overestimation of the theoretical $D_{5/2}$ and $D_{3/2}$ phase shifts with respect to available experimental data.

(ii) Refined αN potential that involves the splitting of phase shifts in the parity of the orbital angular momentum [47] (split potential). It describes more precisely S-wave and especially $D_{5/2}$- and $D_{3/2}$-wave phase shifts than the Sack–Biedenharn–Breit potential.

For the αt interaction, we also chose two potentials.

(i) A deep attractive potential of the Woods–Saxon form [14] supplemented with a spin–orbit and a Coulomb term. The potential is rather deep, so that, in the p wave, it involves, in addition to the allowed $3p$ state, the forbidden $1p$ state. This potential provides an excellent description of known low-energy phase shifts for elastic αt scattering and, at the same time, reliably reproduces the binding energy of the ^{7}Li nucleus, as well as the spectrum of its low-lying states and its basic spectroscopic features. It is precisely the potential with which an adequate description of the two-particle-photodisintegration reaction $^7\mathrm{Li}\,(\gamma, t)\alpha$ was achieved in [20, 21]. We note that forbidden-state wave functions (of the type $R_{NL}(r) \equiv R_{1p}(r)$) are used in calculating projection operators in the three-particle model of the ^{8}Li nucleus [19].

(ii) Attractive Buck potential. Its radial part has a Gaussian form, contains two parameters, and includes a spin–orbit and a Coulomb term [15]. It reproduces known low-energy phase shifts for αt scattering, as well as the binding energy of the ^{7}Li nucleus, the spectrum of its low-lying levels, and its basic spectroscopic features. The respective radial function for the ground state of the ^{7}Li nucleus involves an internal node; that is, it has the form of the oscillatory function $R_{3p}(r)$. The Buck potential provides an adequate description of the total cross section for the radiative-capture reaction $\alpha t \to {}^7\mathrm{Li}\gamma$ and of the corresponding astrophysical S factor.

In the present study, we discuss precisely these two potentials, since they give nearly the same description of the spectroscopic features of the ^{7}Li nucleus. However, the potentials in question differ in asymptotic behavior, and this results in that the wave functions for the ground state of the ^{7}Li nucleus behave differently in the asymptotic region. This circumstance may be of importance in discussing the

elastic scattering of particles that penetrate differently into the interior of the target nucleus used.

DISCUSSION OF THE RESULTS

We have calculated the differential cross sections and analyzing powers for elastic proton scattering on $^{6-8}$Li nuclei and the differential cross sections for the elastic scattering of charged pions and positively charged kaons on ^{6,7}Li nuclei in the energy range between 0.164 and 1.0 GeV and have compared our results with experimental data from [1, 2–5, 7, 9] and with some results of other authors [3, 4, 10, 23].

Figures 1–4 display the differential cross sections (Figs. 1–3) and the asymmetry A_y (Fig. 4) calculated for $^{6-8}$Li nuclei. In all of these figures, the solid and dashed curves were calculated with wave functions determined within models 1 and 2, respectively. From Figs. 1–3, one can see that the differential cross sections depend only slightly on the model wave functions, which differ only in the form of the αN (for ^{6}Li) and αt (for ^{7}Li and ^{8}Li) potentials (see Table 4).

Let us first consider Fig. 1, which shows the differential cross sections for proton scattering at $E_p = 0.2$ GeV. The curves calculated with the wave functions in models 1 and 2 describe experimental data for ^{6,7}Li nuclei quite accurately. The calculation of the differential cross section for scattering on ^{8}Li nuclei under conditions of inverse kinematics was performed at two energy values of $E_{^8\mathrm{Li}} = 0.2$ (Fig. 1) and 1.0 GeV/nucleon (dash-dotted curve in Fig. 6 below) and is of a predictive character—there are presently no relevant experimental data. The distinction between the curves calculated for ^{8}Li is rather modest, although the minimum of the dashed curve in Fig. 1 is deeper and is shifted somewhat toward the region of small scattering angles. This brings about the question of how the distinction between the wave functions affects other properties of the ^{8}Li nucleus. From the results reported in [19], it follows that the static features of the nucleus (root-mean-square charge radius and quadrupole and magnetic moments) and the energy spectrum of low-lying excitations are better described within model 1 (with the wave function calculated in the Buck αt potential). The differential cross section for ^{8}Li has a deep minimum at $\theta = 26°–28°$, but there is no such minimum for ^{6,7}Li. As was shown in [28, 29], the minimum for ^{6}Li is filled by the contribution of the D-wave component of the wave function, while the minimum for ^{7}Li is filled by the contribution of the $\lambda = 1$ configuration, which is responsible for the large quadrupole deformation of this nucleus, and partly by the contribution from the transition to the first excited state of ^{7}Li ($J^\pi = 1/2^-$, $T = 1/2$)—it lies only 0.48 MeV above the ground state and is therefore indistinguishable from it experimentally. At zero scattering angle, the differential cross section for ^{8}Li is severalfold larger than those for the remaining nuclear species considered here, this reflecting the larger root-mean-square radius of this isotope.

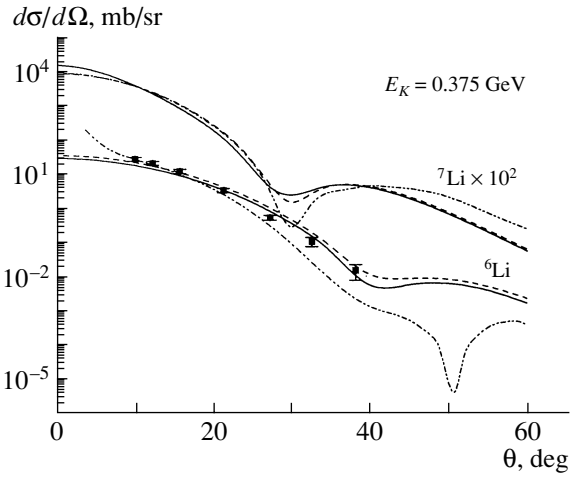

Fig. 3. Differential cross sections for the scattering of positively charged kaons on ^{6}Li and ^{7}Li nuclei. The solid and dashed curves were calculated with wave functions based on models 1 and 2, respectively. The dash-dotted curves represent the results of the calculation in the distorted-wave impulse approximation for ^{6}Li from [10] and the results of the calculation with the oscillator wave function for ^{7}Li. The displayed experimental data (points) were borrowed from [9, 10]. The results corresponding to the calculated curves for ^{7}Li were multiplied by 10^2 in order to avoid an overlap of the results.

Figure 2 shows the differential cross sections for the scattering of charged pions on ^{6,7}Li nuclei. Here, the pattern is similar to that which is observed in proton scattering—the calculations with the wave functions in models 1 and 2 adequately reproduce experimental data, and there is a distinction between the results of these calculations only for the ^{6}Li nucleus in the vicinity of the minimum, this being explained by different weights of the D wave in the wave functions: 3% in model 1 (solid curve) and 7% in model 2 (dashed curve) [12, 13]. The dash-dotted curve for ^{6}Li represents the results of the calculation in the distorted-wave impulse approximation from [23], where the authors employed, as we have done here, Kukulin's wave function, but they did not include the D-wave contribution. The role of the D wave in the filling of the minimum is clearly seen from a comparison of this dash-dotted curve with the solid and dashed curves.

For ^{7}Li, the dash-dotted curve represents the differential cross section obtained with the oscillator wave function. The oscillator wave function differs

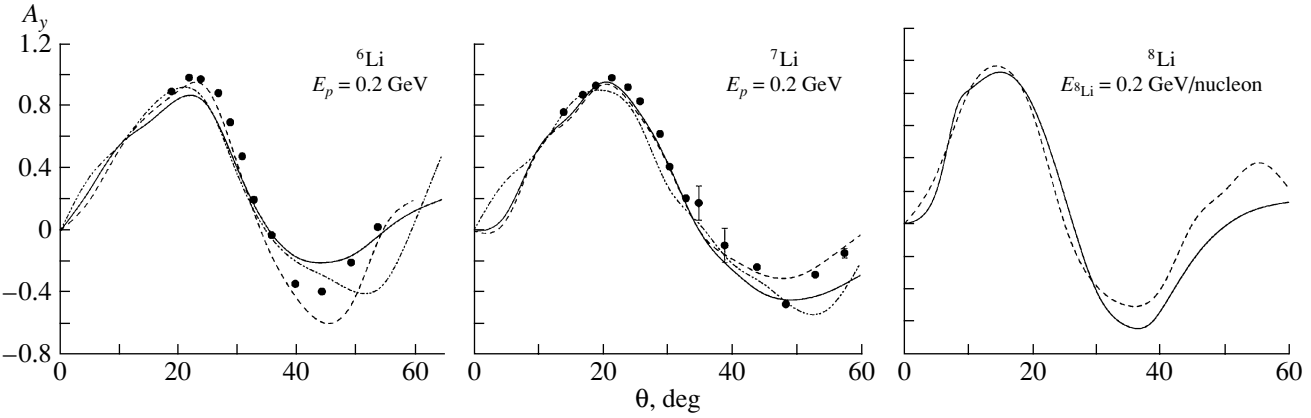

Fig. 4. Analyzing powers for proton scattering on ^{6}Li, ^{7}Li, and ^{8}Li nuclei. The solid and dashed curves represent the results of our calculation with wave functions based on models 1 and 2, respectively. The dash-dotted curves and points correspond to the calculation and experimental data from [3] for ^{6}Li and from [4] for ^{7}Li.

from its cluster counterparts both in the interior of the nucleus and at the periphery, although the position of the node is identical for all functions. The distinction between the results at small scattering angles, which correspond to low momentum transfers (at $E_\pi = 164$ MeV, $q < 0.09$ GeV/c for $\theta < 20°$), is due to the fact that the wave functions behave differently at large distances from the center of the nucleus (in the asymptotic region), where the cluster wave functions differ greatly from the oscillator wave function. At large scattering angles, which correspond to high momentum transfers (at $\theta = 80°$, $q = 0.33$ GeV/c), the behavior of the wave function in the interior of the nucleus is of importance, and the distinction there arises because of the disregard of correlation effects in the oscillator model.

Figure 3 gives the differential cross sections for the scattering of positively charged kaons. Here, the results of our calculation with the cluster wave functions are contrasted against the results of the calculation with the oscillator wave function (dash-dotted curve for ^{7}Li) and against the results of the calculation in the distorted-wave impulse approximation from [10] (dash-dotted curve for ^{6}Li). For ^{7}Li, the distinction between the solid and the dash-dotted curve is noticeable only for scattering angles of $\theta > 25°$ since a positively charged kaon, which is scattered in the interior of the nucleus, is less sensitive to the asymptotic region, so that the the difference in the behavior of the wave functions there does not affect the shape of the cross section. The scattering of positively charged kaons on ^{6}Li for $40° > \theta > 20°$ is better described by diffraction theory, although not only central but also quadrupole noncentral scattering was taken into account in [10], but the contribution of the latter proved to be overly small to affect the cross-section value. The distinction between the solid and the dash-dotted curve is especially large (three orders of magnitude) for $\theta = 50°$, but the correctness of the various model calculations cannot be confirmed by experimental data in this region.

It is noteworthy that, for protons and charged pions, the differential cross sections at $\theta = 0°$ for ^{6}Li are somewhat larger than those for ^{7}Li (see Figs. 1 and 2), but that, for positively charged kaons, the relationship between these cross sections is inverse. This inconsistency calls for a more detailed analysis, and it will be performed elsewhere.

It is well known that the polarization features are more sensitive to the structure of nuclei than differential cross sections. Bearing this in mind, we have calculated the analyzing powers for proton scattering on ^{6}Li, ^{7}Li, and ^{8}Li nuclei (see Fig. 4) with the same model wave functions for the lithium-isotope nuclei as those that were used in calculating the results displayed in Figs. 1–3. The dash-dotted curves represent the results of the calculations from [3] for ^{6}Li and from [4] for ^{7}Li. Here, the distinctions between the results of the calculations with the different wave functions are more pronounced. For ^{6,7}Li, our curves describe A_y at the first maximum almost identically, but there are significant distinctions for angles larger than 35°. None of the calculations performed here describes the minimum of A_y satisfactorily. The results of the calculations for A_y from [3, 4] are correct for $\theta < 35°$, but they fail to describe adequately the negative slope and the position of the minimum in the experimental data in the region $\theta > 35°$; in our opinion, this must be attributed to an insufficiently accurate determination of nuclear densities.

For scattering on ^{8}Li, the results of the calculations with the wave functions in models 1 and 2 differ over the entire region of angles. In the coordinate

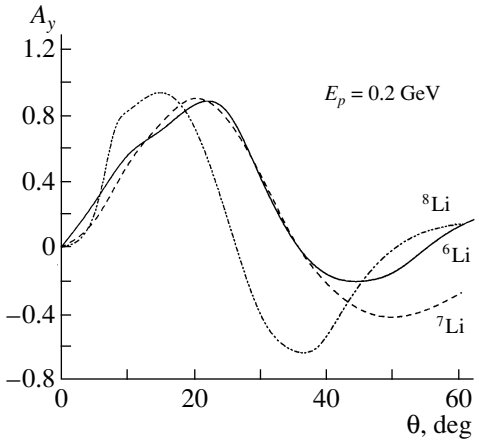

Fig. 5. Comparison of the analyzing powers for proton scattering on (solid curve) ^{6}Li, (dashed curve) ^{7}Li, and (dash-dotted curve) ^{8}Li nuclei according to calculations with the wave functions in model 1.

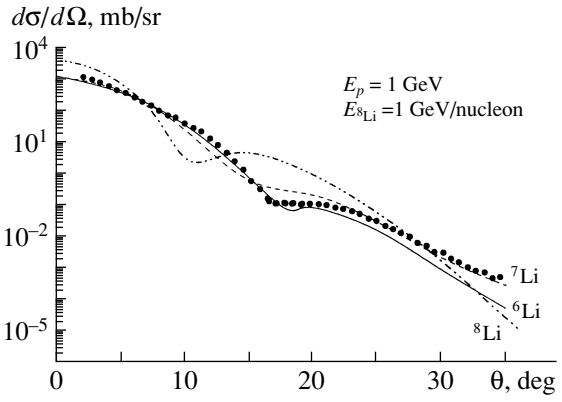

Fig. 6. Differential cross sections for elastic proton scattering on (solid curve) ^{6}Li, (dashed curve) ^{7}Li, and (dash-dotted curve) ^{8}Li nuclei at $E_p = 1$ GeV according to calculations with the wave functions based on model 1. The points represent experimental data from [2] for ^{6}Li.

space of wave functions, small scattering angles—that is, low momentum transfers [see Eq. (2)]—correspond to large relative distances lying in the asymptotic region of the wave functions. The discrepancies between the results of the calculations at these angles ($\theta < 30°$, $q < 0.28$ GeV/c) are indicative of the effect of the asymptotic behavior of the wave functions on A_y. But if there are discrepancies at large angles ($60° > \theta > 40°$, $0.55 > q > 0.37$ GeV/c), this suggests the effect of the high-momentum components of the wave functions on A_y. Thus, it has been shown that the analyzing power is a quantity that is sensitive to the behavior of the respective wave function both in the interior of the nucleus being considered and at its periphery.

From a comparison of the A_y values calculated with the wave functions found on the basis of model 1 for the various nuclear species (Fig. 5), one can see that the calculated curves for ^{6}Li and ^{7}Li are close to each other up to $\theta \leq 35°$ and that, for ^{8}Li, the zeros of A_y are shifted by approximately 10° toward the region of smaller angles, this being indicative of the presence of special features in the structure of this nucleus.

Thus, we can see that, even at not very high energies (below 1 GeV), in which case the applicability of Glauber–Sitenko theory may be questionable, it is not inferior in quality of the description of differential cross sections and A_y to the distorted-wave impulse approximation, possibly because of the use of realistic wave functions, which faithfully reproduce intermediate-energy processes involving modest momentum transfers.

In Fig. 6, the differential cross sections for proton scattering on lithium isotopes are given at yet another energy value, 1 GeV (results of the calculation with the wave function based on model 1). Experimental data at this energy are available only for ^{6}Li [2]. A comparison with these experimental data reveals that, for angles in the region $\theta < 25°$, the results of the calculation are in fairly good agreement with the data, but that slight discrepancies appear at larger angles. The differential cross sections for (solid curve) ^{6}Li, (dashed curve) ^{7}Li, and (dash-dotted curve) ^{8}Li nuclei have the following special features. The absolute value of the cross section for scattering in the forward direction is larger for ^{8}Li, this reflecting the fact that the nuclear-matter radius of this nucleus is larger than those of its counterparts. The diffraction minimum for large A is shifted toward the region of smaller scattering angles. The minimum in the cross section is more pronounced for the $A = 8$ nucleus than for the $A = 6$ and 7 nuclei. The deformation of nuclei (quantitatively, it is determined by the quadrupole moment) is the main reason for the filling of the minimum: the larger the deformation of a nucleus, the greater the extent to which the diffraction minimum is filled. The ^{7}Li nucleus has the greatest quadrupole moment among the lithium isotopes considered here ($Q = 40$ mb [48]); therefore, the cross section for this nuclear species does not have a distinct minimum, exhibiting only an inflection point. The minimum is filled by the quadrupole-component contribution. The ^{8}Li quadrupole moment calculated with the three-cluster wave function introduced in [19] and employed in the present study is 18.9 mb (the respective experimental value is 24 mb [48]), and the calculated minimum in the cross section for this nucleus is somewhat greater than that for ^{7}Li. The ^{6}Li quadrupole moment is close to zero, and the filling of the minimum in the respective cross section occurs owing to the D-wave contribution.

Finally, we will consider the behavior of the differential cross sections for the scattering of various particle species on the ^{6}Li nucleus versus momentum transfer squared at the fixed energy value of $E = 0.18$ GeV. Figure 7 demonstrate that the cross sections in question may differ in structure. Different symbols (points) correspond to the scattering of protons [1] and positively and negatively charged pions [5]. Since there are no experimental data at this energy value for the scattering of antiprotons and positively charged kaons on ^{6}Li nuclei, only the differential cross sections calculated in [29] are displayed in this figure. One can immediately see that there are a similarity in the structure of the cross sections for protons and positively charged kaons (curves *3*, *4*) and a similarity in the structure of the cross sections for antiprotons and charged pions (curves *1*, *2*). For protons and positively charged kaons, the cross section is a smoothly decreasing function, while, for antiprotons and charged pions, there is a minimum around $q^2 \approx 0.09$ (GeV/c)^2. A manifestation of the diffraction structure in the differential cross section at a relatively low energy—such as that which is now being discussed—is due to a special feature in the elementary amplitudes for antiprotons and charged pions: these amplitudes have a sharp anisotropy in the forward direction [this anisotropy is characterized by large values of $\beta^c_{\pi N}$ (see Table 2), which is 0.86 fm^2 for antiprotons at 0.18 GeV]; owing to this, the particles in question are predominantly scattered within a narrow forward cone, the eikonal approximation being valid for them to a high precision. This feature of the $\bar{p}N$ and $\pi^{\pm}N$ amplitudes extends the energy region where Glauber–Sitenko theory is applicable.

The total cross section calculated on the basis of the optical theorem is 838.9 mb for antiprotons and 327.3 mb for charged pions [29]. The diffraction structure in the cross sections for protons and positively charged kaons begins manifesting itself at energies higher than 0.18 GeV—specifically, at 0.6 GeV for protons and at 0.375 GeV for positively charged kaons [29].

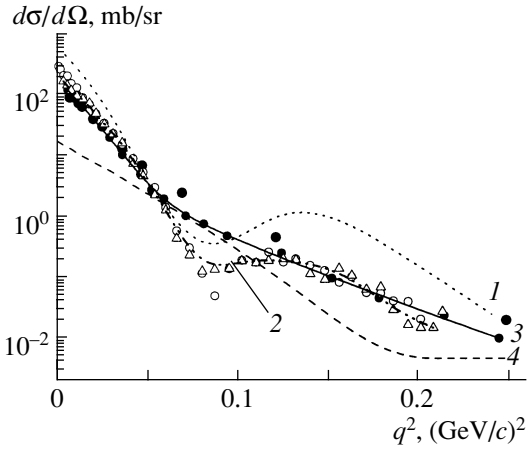

Fig. 7. Differential cross sections for elastic hadron scattering on ^{6}Li nuclei at 0.18 GeV versus momentum transfer squared. Points represent experimental data for (closed circles) protons [1] and (open circles and triangles) positively and negatively charged pions [5]. Curves *1*, *2*, *3*, and *4* depict the results of the calculations for, respectively, antiprotons, charged pions, protons, and positively charged kaons.

CONCLUSIONS

(i) For various hadron species, Glauber–Sitenko diffraction theory provides an adequate description of differential cross sections for scattering on $^{6-8}$Li nuclei over a wide range of projectile energies (between 0.1 and 1.0 GeV).

(ii) By using wave functions calculated on the basis of two- or three-particle cluster models with realistic interaction potentials, one can calculate reaction amplitudes analytically. As a result, the accuracy of the description of differential cross sections within diffraction theory is not inferior to or is even sometimes higher than the accuracy of the distorted-wave impulse approximation.

(iii) The differential cross sections for hadrons are only slightly dependent on the detailed structure of two- and three-particle wave functions, but they exhibit a significant dependence on their asymptotic behavior, since, in the interior of a nucleus, hadrons (especially antiprotons and charged pions) are strongly absorbed, so that the main contribution to elastic scattering comes from the surface region.

(iv) Analyzing powers are much more sensitive to wave functions calculated with different intercluster-interaction potentials than differential cross sections.

(v) A comparison of processes where particles of different species (protons, antiprotons, charged pions, and positively charged kaons) are scattered on ^{6}Li nuclei has revealed that, because of a strong absorption of antiprotons and charged pions in the interior of nuclei, the xN elementary amplitudes for them develop a special feature owing to which the diffraction structure in the differential cross sections for them is observed at energies lower than those for protons and positively charged kaons.

REFERENCES

1. R. M. Hutcheon, O. Sundberg, and G. Tibell, Nucl. Phys. A **154**, 261 (1970).
2. G. Bruge, J. Phys. (Paris) **40**, 635 (1979); E. Aslanides, T. Bauer, R. Bertini, *et al.*, Prog. Rep. Nucl. Phys. Dep. CEN, CEA-N-1861 (Saclay 1974/1975), p. 198.

3. C. W. Glower, C. C. Foster, P. Schwandt, *et al.*, Phys. Rev. C **41**, 2487 (1990).
4. C. W. Glower, C. C. Foster, P. Schwandt, *et al.*, Phys. Rev. C **43**, 1664 (1991).
5. L. E. Antonuk, D. Bovet, E. Bovet, *et al.*, Nucl. Phys. A **451**, 741 (1986).
6. S. Ritt, E. T. Boschitz, R. Meier, *et al.*, Phys. Rev. C **43**, 745 (1991).
7. R. Meier, E. T. Boschitz, B. Brinkmoller, *et al.*, Phys. Rev. C **49**, 320 (1994).
8. R. A. Michael, M. B. Barakat, S. Bart, *et al.*, Phys. Lett. B **382**, 29 (1996).
9. R. E. Chrien, R. Sawafta, R. J. Peterson, *et al.*, Nucl. Phys. A **625**, 251 (1997).
10. R. J. Peterson, A. A. Ebrahim, and H. C. Bhang, Nucl. Phys. A **625**, 261 (1997).
11. G. D. Alkhazov, in *Proceedings of the International Conference on the Properties of Excited Nuclear States and Nuclear Reactions Mechanism: LI Meeting on Nuclear Spectroscopy and Nuclear Structure*, *Sarov*, *Russia*, *2001*, p. 215 [in Russian].
12. V. T. Voronchev, V. M. Krasnopol'sky, and V. I. Kukulin, J. Phys. G **8**, 649 (1982); V. I. Kukulin, V. M. Krasnopol'sky, V. T. Voronchev, and P. B. Sazonov, Nucl. Phys. A **417**, 128 (1984); **453**, 365 (1986).
13. V. I. Kukulin, V. N. Pomerantsev, K. D. Razikov, *et al.*, Nucl. Phys. A **586**, 151 (1995).
14. S. B. Dubovichenko and M. A. Zhusupov, Izv. Akad. Nauk SSSR, Ser. Fiz. **48**, 935 (1984); Yad. Fiz. **39**, 1378 (1984) [Sov. J. Nucl. Phys. **39**, 870 (1984)].
15. B. Buck and A. C. Merchant, J. Phys. G **14**, L211 (1988).
16. S. B. Dubovichenko and A. V. Dzhazairov-Kakhramanov, Yad. Fiz. **57**, 784 (1994) [Phys. At. Nucl. **57**, 733 (1994)].
17. L. V. Grigorenko, B. V. Danilin, V. D. Efros, *et al.*, Phys. Rev. C **57**, R2099 (1998).
18. A. Csoto, nucl-th/9908081; nucl-th/9908082.
19. M. A. Zhusupov, Sh. Sh. Sagindykov, and S. K. Sakhiev, Izv. Akad. Nauk, Ser. Fiz. **65**, 714 (2001); M. A. Zhusupov and Sh. Sh. Sagindykov, Izv. Akad. Nauk, Ser. Fiz. **66**, 392 (2002).
20. N. A. Burkova and M. A. Zhusupov, Izv. Akad. Nauk SSSR, Ser. Fiz. **51,** 1, 182 (1987); Phys. Lett. B **223**, 136 (1989).
21. N. A. Burkova, M. A. Zhusupov, and R. A. Éramzhyan, Preprint No. P-0531, IYaI AN SSSR (Inst. Nucl. Res., USSR Acad. Sci., Moscow, 1987); Preprint No. P-055, IYaI AN SSSR (Inst. Nucl. Res., USSR Acad. Sci., Moscow, 1987).
22. R. G. Glauber, *Lectures of Theoretic Physics* (Interscience, New York; London, 1959), Vol. 1, p. 1; A. G. Sitenko, Ukr. Fiz. Zh. **4**, 152 (1959).
23. R. A. Eramzhyan, M. Gmitro, T. D. Kaipov, *et al.*, J. Phys. G **14**, 1511 (1988).
24. N. Nose, K. Kume, and S. Yamaguchi, Phys. Rev. C **50**, 321 (1994).
25. P. J. Dortmans, K. Amos, and S. Karataglidis, J. Phys. G **23**, 183 (1997).
26. E. Oset and D. Strottman, Nucl. Phys. A **377**, 297 (1982).
27. J. F. Germond, J. Phys. G **12**, 609 (1986).
28. M. A. Zhusupov, E. T. Ibraeva, V. I. Kukulin, and V. V. Peresypkin, Yad. Fiz. **57**, 2013 (1994) [Phys. At. Nucl. **57**, 1937 (1994)]; Izv. Akad. Nauk, Ser. Fiz. **58** (5), 71 (1994).
29. M. A. Zhusupov and E. T. Ibraeva, Fiz. Élem. Chastits At. Yadra **31**, 1427 (2000); **34**, 270 (2003); Yad. Fiz. **64**, 2003 (2001) [Phys. At. Nucl. **64**, 1917 (2001)].
30. K. Yamaguchi and Y. Sakamoto, Nuovo Cimento A **108,** 893 (1995).
31. I. M. A. Tag Eldin, E. H. Esmael, M. Y. M. Hassan, and M. N. H. Comsan, J. Phys. G **17**, 271 (1991).
32. L. Ray, Phys. Rev. C **19**, 1855 (1979); **20**, 1857 (1979).
33. J. P. Auger, J. Gillespie, and R. J. Lombard, Nucl. Phys. A **262**, 372 (1976).
34. J. P. Auger, C. Lazard, and R. J. Lombard, J. Phys. G **7**, 1627 (1981).
35. I. M. A. Tag Eldin, E. H. Esmael, M. Y. M. Hassan, *et al.*, J. Phys. G **16**, 1051 (1990).
36. A. N. Boyarkina, *Structure of 1p-Shell Nuclei* (MGU, Moscow, 1973) [in Russian].
37. B. Buck, C. B. Dover, and J. P. Vary, Phys. Rev. C **11**, 1803 (1975).
38. V. I. Kukulin, V. G. Neudatchin, and Yu. F. Smirnov, Fiz. Élem. Chastits At. Yadra **10**, 1236 (1979) [Sov. J. Part. Nucl. **10**, 492 (1979)].
39. K. Wildermuth and Y. C. Tang, *A Unified Theory of the Nucleus* (Vieveg, Braunschweig, 1977; Mir, Moscow, 1980).
40. R. A. Eramzhyan, G. G. Ryzhikh, and Yu. M. Tchuvil'sky, Yad. Fiz. **62**, 32 (1999) [Phys. At. Nucl. **62**, 37 (1999)].
41. Yu. V. Vladimirov *et al.,* Pis'ma Zh. Éksp. Teor. Fiz. **49**, 155 (1989) [JETP Lett. **49**, 155 (1989)].
42. N. A. Burkova, V. V. Denyak, R. A. Eramzhyan, *et al.*, Nucl. Phys. A **586**, 293 (1995).
43. V. P. Likhachev, M. N. Martins, M. T. F. da Cruz, *et al.*, Phys. Rev. C **59**, 525 (1999).
44. M. Weischer, R. Steininger, and F. Kappeler, Astrophys. J. **344**, 464 (1989).
45. M. Unkelbac and H. M. Hofmann, Phys. Lett. B **261**, 211 (1991).
46. S. Sack, L. C. Biedenharn, and G. Breit, Phys. Rev. **93**, 321 (1954).
47. V. I. Kukulin *et al.*, Preprints Nos. ANU-TP-1/92, ANU-TP-2/92 (Austral. Nat. Univ., Canberra, 1992); Nucl. Phys. A **586**, 151 (1995).
48. F. Ajzenberg-Selove, Nucl. Phys. A **490**, 1 (1988).

Translated by A. Isaakyan

Physics of Atomic Nuclei, Vol. 68, No. 1, 2005, pp. 144–159. From Yadernaya Fizika, Vol. 68, No. 1, 2005, pp. 147–162.

ELEMENTARY PARTICLES AND FIELDS
Theory

Application of the Hidden Local Symmetry Effective Chiral Lagrangian to Evaluation of the $\omega(782)$, $\phi(1020) \to 5\pi$ Decay Widths*

N. N. Achasov** **and A. A. Kozhevnikov*****

Sobolev Institute for Mathematics, Siberian Division, Russian Academy of Sciences, Novosibirsk, 630090 Russia

Received June 26, 2003; in final form, January 8, 2004

Abstract—The amplitudes obtained from the effective chiral Lagrangian with anomalous terms based on hidden local symmetry are applied to the evaluation of the partial widths of the decays $\omega \to 2\pi^+2\pi^-\pi^0$ and $\omega \to \pi^+\pi^-3\pi^0$. Combining the Okubo–Zweig–Iizuka rule, applied to the five-pion final state, with the Adler condition of vanishing of the amplitude at the vanishing of four-momentum of any final pion in the chiral limit, the $\phi \to 2\pi^+2\pi^-\pi^0$ and $\phi \to \pi^+\pi^-3\pi^0$ decay amplitudes are also calculated. The partial widths of the above decays are evaluated, and the resonance excitation curves in e^+e^- annihilation are obtained, assuming reasonable particular relations among the free parameters characterizing the anomalous terms of the Lagrangian. The evaluated branching ratios $\mathrm{Br}_{\phi\to\pi^+\pi^-3\pi^0} \approx 2\times10^{-7}$ and $\mathrm{Br}_{\phi\to2\pi^+2\pi^-\pi^0} \approx 5\times10^{-7}$ are such that with the luminosity $L = 500\ \mathrm{pb}^{-1}$, attained at the DAΦNE ϕ factory, one may already possess about 1340 events of the decays $\phi \to 5\pi$. © *2005 Pleiades Publishing, Inc.*

1. INTRODUCTION

The effective chiral Lagrangians describing the low-energy interactions of the ground-state octet of pseudoscalar mesons π, K, η are constructed upon treating these mesons as the Goldstone bosons of the spontaneously broken chiral $U_L(3)\times U_R(3)$ symmetry of the massless three-flavored QCD Lagrangian. The key point in this task is that the transformation properties of the Goldstone fields under the nonlinear realization of chiral symmetry are sufficient for establishing the most general form of the effective Lagrangian [1]. As far as vector mesons are concerned, the situation is not so clear, because the vector mesons, contrary to the pseudoscalar ones, cannot be considered as the Goldstone bosons of the spontaneously broken symmetry. For this reason, there exist different schemes of including these mesons in the effective chiral Lagrangians [2–4]. The scheme of [5, 6], where the vector mesons are treated as the dynamical gauge bosons of hidden local symmetry (HLS), incorporates these mesons into the effective chiral Lagrangian in a most elegant way. The fact is that the low-energy theorems for anomalous processes, such as, say, the decay $\pi^0 \to \gamma\gamma$, are fulfilled automatically in HLS. The general form of both nonanomalous and anomalous parts of the Lagrangian is given in original papers [5, 6]. Here, we restrict ourselves, first, by writing down only those pieces of the Lagrangian corresponding to the strong interaction processes, omitting the electroweak terms, and, second, by restricting the above Lagrangian to the subgroup $SU(2)\times U(1)$ with only isovector $\boldsymbol{\pi}$, $\boldsymbol{\rho}$, and isoscalar ω mesons. Taking into account the coupling of the $\phi(1020)$ meson with the mesons composed of nonstrange quarks demands additional assumptions to be discussed below.

The nonanomalous part of the HLS Lagrangian (with nickname "nan") obtained from the general expression found in [3, 5, 6] in the weak field limit is written as

$$\begin{aligned}\mathcal{L}^{\mathrm{nan}} = &-\frac{1}{4}\boldsymbol{\rho}_{\mu\nu}^2 - \frac{1}{4}\omega_{\mu\nu}^2 + \frac{1}{2}ag^2f_\pi^2(\boldsymbol{\rho}_\mu^2+\omega_\mu^2) \\ &+ \frac{1}{2}(\partial_\mu\boldsymbol{\pi})^2 - \frac{1}{2}m_\pi^2\boldsymbol{\pi}^2 + \frac{m_\pi^2}{24f_\pi^2}\boldsymbol{\pi}^4 \\ &+ \frac{1}{2f_\pi^2}\left(\frac{a}{4}-\frac{1}{3}\right)[\boldsymbol{\pi}\times\partial_\mu\boldsymbol{\pi}]^2 \\ &+ \frac{1}{2}ag\left(1-\frac{\boldsymbol{\pi}^2}{12f_\pi^2}\right)(\boldsymbol{\rho}_\mu\cdot[\boldsymbol{\pi}\times\partial_\mu\boldsymbol{\pi}]),\end{aligned} \tag{1}$$

where the dot $(\cdot)$ and cross $(\times)$ stand, respectively, for the scalar and vector products in the isotopic space;

$$\begin{aligned}\boldsymbol{\rho}_{\mu\nu} &= \partial_\mu\boldsymbol{\rho}_\nu - \partial_\nu\boldsymbol{\rho}_\mu + g[\boldsymbol{\rho}_\mu\times\boldsymbol{\rho}_\nu], \\ \omega_{\mu\nu} &= \partial_\mu\omega_\nu - \partial_\nu\omega_\mu\end{aligned} \tag{2}$$

are, respectively, the field strengths of the isovector field $\boldsymbol{\rho}_\mu$ and the isoscalar field ω_μ; g is the gauge coupling constant; $f_\pi = 92.4$ MeV is the pion decay

*This article was submitted by the authors in English.

**e-mail: achasov@math.nsc.ru

***e-mail: kozhev@math.nsc.ru

constant; and a is an HLS parameter. The boldface characters refer hereafter to the vectors in isotopic space. As is clear from Eq. (1),

$$g_{\rho\pi\pi} = \frac{1}{2}ag, \quad m_\rho^2 = ag^2 f_\pi^2 \tag{3}$$

are the coupling constant of the ρ with the pion pair and its mass squared, respectively. The $\omega(782)$ is degenerate with ρ in the present model. Note that $a = 2$ if one demands the universality condition $g = g_{\rho\pi\pi}$ to be satisfied. Then the so-called Kawarabayashi–Suzuki–Riazzuddin–Fayyazuddin (KSRF) relation [7] arises,

$$\frac{2g_{\rho\pi\pi}^2 f_\pi^2}{m_\rho^2} = 1, \tag{4}$$

which beautifully agrees with experiment. The $\rho\pi\pi$ coupling constant resulting from this relation is $g_{\rho\pi\pi} = 5.9$.

To include the decays of the ω meson in the many pion states, one should add the anomalous terms in the action (nicknamed "an"). They are given in [5, 6]. Using the formalism of the differential forms adopted in the literature on the subject, restricting the general expressions in [5, 6] to the ω, ρ, π-meson sector by writing $V = \frac{1}{2}\omega + \rho$, where ω and $\rho = (\boldsymbol{\tau}\cdot\boldsymbol{\rho})/2$ are, respectively, the scalar and matrix-valued 1-forms, $\boldsymbol{\tau}$ being three isospin Pauli matrices, one obtains

$$\Gamma^{\rm an} = \frac{in_c}{16\pi^2}\int\limits_{M_4} \omega \mathrm{Tr}[c_1\alpha_R^3 + id(\alpha_L\alpha_R) \tag{5}$$
$$\times (c_1/2 - c_2 - c_3) + i(c_1 + c_2 + c_3)\rho d(\alpha_L - \alpha_R)$$
$$- 2ic_3 d\rho(\alpha_L - \alpha_R) + (c_1 + c_2 - c_3)\rho^2(\alpha_L - \alpha_R)].$$

Here $n_c = 3$ is the number of colors and $c_{1,2,3}$ are arbitrary constants multiplying three independent structures in the solution [5, 6] of the Wess–Zumino anomaly equation [8]; the fourth constant c_4 multiplying the structure that includes electromagnetic field, as is explained above, is dropped. Our normalization of $c_{1,2,3}$ is in accord with [6]. In Eq. (5), it is implied that the gauge coupling constant is included in the fields ω and ρ as $\omega \to g\omega$, $\rho \to g\rho$; d is the symbol of exterior derivative; $\alpha_{L,R} = -id\xi_{L,R}\xi_{L,R}^+$; and the trace is over $SU(2)$ indices. In the unitary gauge to be used hereafter,

$$\xi_L^+ = \xi_R \equiv \xi = \exp\left[\frac{i}{2f_\pi}(\boldsymbol{\tau}\cdot\boldsymbol{\pi})\right],$$

one can rewrite Eq. (5) in the usual Minkowskian form as

$$\Gamma^{\rm an} = \frac{in_c g}{16\pi^2}\varepsilon_{\mu\nu\lambda\sigma}\mathrm{Tr}\int d^4x\{c_1\omega_\mu(\xi^+\partial_\nu\xi) \tag{6}$$
$$\times (\xi^+\partial_\lambda\xi)(\xi^+\partial_\sigma\xi) - (c_1/2 - c_2 - c_3)\omega_\mu[(\xi^+\partial_\nu\xi)$$
$$\times (\xi^+\partial_\lambda\xi)(\xi\partial_\sigma\xi^+) - (\xi\partial_\nu\xi^+)(\xi\partial_\lambda\xi^+)(\xi^+\partial_\sigma\xi)]$$
$$+ igc_3\omega_{\mu\nu}\rho_\lambda(\xi^+\partial_\sigma\xi - \xi\partial_\sigma\xi^+)$$
$$- ig(c_1 + c_2 - c_3)\omega_\mu\rho_\nu\partial_\lambda(\xi^+\partial_\sigma\xi - \xi\partial_\sigma\xi^+)$$
$$- g^2(c_1 + c_2 - c_3)\omega_\mu\rho_\nu\rho_\lambda(\xi^+\partial_\sigma\xi - \xi\partial_\sigma\xi^+)\},$$

with the convention $\varepsilon_{0123} = -1$. Using the following exact expression valid for the $SU(2)$ subgroup,

$$i\xi\partial_\mu\xi^+ = \frac{1}{2f_\pi}(\boldsymbol{\tau}\cdot\partial_\mu\boldsymbol{\pi})\left(\frac{\sin|\boldsymbol{\pi}|/f_\pi}{|\boldsymbol{\pi}|/f_\pi}\right) \tag{7}$$
$$+ \frac{(\boldsymbol{\tau}\cdot\boldsymbol{\pi})}{2f_\pi}\cos^2\frac{|\boldsymbol{\pi}|}{(2f_\pi)}\partial_\mu\left(\frac{\tan|\boldsymbol{\pi}|/(2f_\pi)}{|\boldsymbol{\pi}|/(2f_\pi)}\right)$$
$$- \frac{1}{4f_\pi^2}(\boldsymbol{\tau}\cdot[\boldsymbol{\pi}\times\partial_\mu\boldsymbol{\pi}])\left(\frac{\sin|\boldsymbol{\pi}|/(2f_\pi)}{|\boldsymbol{\pi}|/(2f_\pi)}\right)^2,$$

to expand in the weak field limit $|\boldsymbol{\pi}|/f_\pi \ll 1$ as

$$i\xi\partial_\mu\xi^+ \approx \frac{1}{2f_\pi}\boldsymbol{\tau}\cdot\left\{\partial_\mu\boldsymbol{\pi} - \frac{1}{2f_\pi}[\boldsymbol{\pi}\times\partial_\mu\boldsymbol{\pi}]\right. \tag{8}$$
$$\left. + \frac{1}{6f_\pi^2}[\boldsymbol{\pi}(\boldsymbol{\pi}\cdot\partial_\mu\boldsymbol{\pi}) - \boldsymbol{\pi}^2\partial_\mu\boldsymbol{\pi}]\right\},$$

and substituting this expansion into Eq. (6), one arrives at the expression for the anomalous part of the Lagrangian in the form

$$\mathcal{L}^{\rm an} = \frac{n_c g}{32\pi^2 f_\pi^3}(c_1 - c_2 - c_3)\varepsilon_{\mu\nu\lambda\sigma}\omega_\mu \tag{9}$$
$$\times (\partial_\nu\boldsymbol{\pi}\cdot[\partial_\lambda\boldsymbol{\pi}\times\partial_\sigma\boldsymbol{\pi}]) + \frac{n_c g}{128\pi^2 f_\pi^5}$$
$$\times\left[-c_1 + \frac{5}{3}(c_2 + c_3)\right]\varepsilon_{\mu\nu\lambda\sigma}\omega_\mu$$
$$\times (\partial_\nu\boldsymbol{\pi}\cdot[\partial_\lambda\boldsymbol{\pi}\times\partial_\sigma\boldsymbol{\pi}])\boldsymbol{\pi}^2 - \frac{n_c g^2 c_3}{8\pi^2 f_\pi}\varepsilon_{\mu\nu\lambda\sigma}\partial_\mu\omega_\nu$$
$$\times\left\{(\boldsymbol{\rho}_\lambda\cdot\partial_\sigma\boldsymbol{\pi}) + \frac{1}{6f_\pi^2}[(\boldsymbol{\rho}_\lambda\cdot\boldsymbol{\pi})(\boldsymbol{\pi}\cdot\partial_\sigma\boldsymbol{\pi})\right.$$
$$\left. - \boldsymbol{\pi}^2(\boldsymbol{\rho}_\lambda\cdot\partial_\sigma\boldsymbol{\pi})]\right\} - \frac{n_c g^2}{8\pi^2 f_\pi}(c_1 + c_2 - c_3)\varepsilon_{\mu\nu\lambda\sigma}\omega_\mu$$
$$\times\left\{\frac{1}{4f_\pi^2}(\partial_\nu\boldsymbol{\pi}\cdot\boldsymbol{\rho}_\lambda)(\boldsymbol{\pi}\cdot\partial_\sigma\boldsymbol{\pi}) - \frac{g}{4}([\boldsymbol{\rho}_\nu\times\boldsymbol{\rho}_\lambda]\cdot\partial_\sigma\boldsymbol{\pi})\right\}.$$

As is evident from the third term on the right-hand side of Eq. (9), the $\omega\rho\pi$ coupling constant is

$$g_{\omega\rho\pi} = -\frac{n_c g^2 c_3}{8\pi^2 f_\pi}. \tag{10}$$

Assuming

$$c_1 - c_2 - c_3 = 0, \tag{11}$$

i.e., the absence of the pointlike $\omega \to \pi^+\pi^-\pi^0$ amplitude, and using the $\omega \to \pi^+\pi^-\pi^0$ partial width to

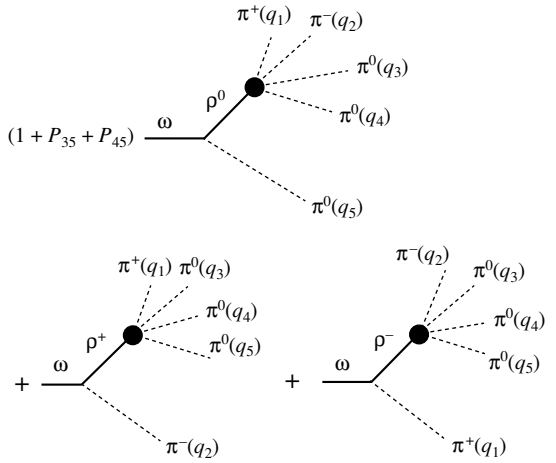

Fig. 1. The diagrams describing the amplitudes of the decay $\omega \to \pi^+\pi^-3\pi^0$ through the ρ intermediate state followed by the decay $\rho \to 4\pi$. The closed circles refer to the whole $\rho \to 4\pi$ amplitudes.

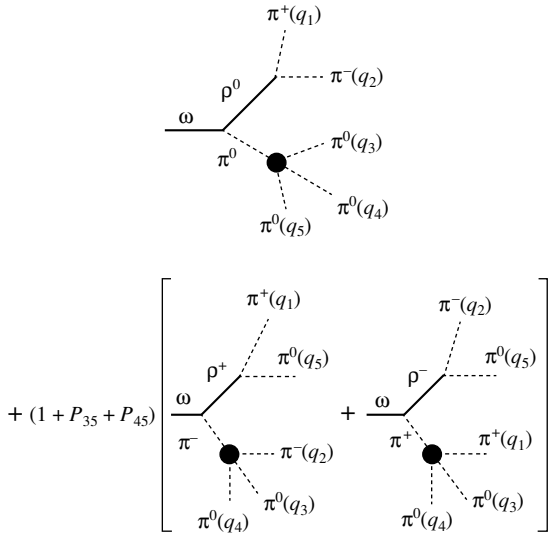

Fig. 2. The diagrams describing the amplitudes of the decay $\omega \to \pi^+\pi^-3\pi^0$ through the $\rho\pi$ intermediate state followed by the transitions $\rho \to 2\pi$ and $\pi \to 3\pi$. The closed circles refer to the effective $\pi \to 3\pi$ vertices given by Eq. (18). Note that the non-π-pole term is included in the diagrams in Fig. 4 below.

extract $g_{\omega\rho\pi}$, the $\rho \to \pi^+\pi^-$ partial width, and Eq. (3) to extract $g = g_{\rho\pi\pi} = 6.00 \pm 0.01$ (assuming $a = 2$), one finds

$$c_3 = 0.99 \pm 0.01, \tag{12}$$

where the errors come from the errors of the ω and ρ widths. Hereafter, we use the particle parameters (masses, full and partial widths, etc.) taken from [9].

The purpose of the present paper is to calculate the branching ratios of the decays

$$\omega \to \pi^+\pi^-3\pi^0, \tag{13}$$

$$\omega \to 2\pi^+2\pi^-\pi^0, \tag{14}$$

$$\phi \to \pi^+\pi^-3\pi^0, \tag{15}$$

and

$$\phi \to 2\pi^+2\pi^-\pi^0 \tag{16}$$

in the framework of chiral model for pseudoscalar and low-lying vector mesons based on HLS [see Eqs. (1) and (9)]. To this end, Section 2 is devoted to obtaining the $\omega \to \pi^+\pi^-3\pi^0$ and $\omega \to 2\pi^+2\pi^-\pi^0$ decay amplitudes from the Lagrangians given by Eqs. (1) and (9) and verifying the Adler condition for their expressions. The results of the evaluation of the branching ratios at the ω-pole position and the calculation of the excitation curves of the above decays in e^+e^- annihilation are given in Section 3, assuming some particular relations among the parameters $c_{1,2,3}$, which characterize various terms of the HLS Lagrangian [5, 6] [see Eq. (9)]. The reason for disagreement with our previous evaluations [10, 11] of the branching ratios for the decays (13) and (14) is explained. In Section 4, guided by the specific assumptions about how the OZI rule is violated in the decays of the ϕ meson into the states containing no particles with strangeness, the effective Lagrangian for the $\phi \to \pi^+\pi^-3\pi^0$ and $\phi \to 2\pi^+2\pi^-\pi^0$ decay amplitudes is written. Under the assumptions about the free parameters of this Lagrangian similar to $c_{1,2,3}$, the branching ratios and the e^+e^- annihilation excitation curves for the five-pion decays of the ϕ are given in the same section. The estimates of the number of events of the decays $\omega, \phi \to \pi^+\pi^-3\pi^0$ and $\omega, \phi \to 2\pi^+2\pi^-\pi^0$ at the respective ω and ϕ peak positions and the general conclusions about the possibilities of detecting the decays under consideration in e^+e^- annihilation are given in Section 5. The kinematical relations necessary for the phase-space integration, which express the Lorentz scalar products of the pion momenta through invariant Mandelstam-like variables, are given in the Appendix.

Our convention for the Lorentz scalar product of two different four-vectors a and b is $(a, b) = a_0b_0 - (\mathbf{a} \cdot \mathbf{b})$, while the Lorentz square is denoted as usual as a^2.

2. THE $\omega \to \pi^+\pi^-3\pi^0$ AND $\omega \to 2\pi^+2\pi^-\pi^0$ DECAY AMPLITUDES

The diagrams for the amplitude of the decay

$$\omega_q \to \pi^+_{q_1}\pi^-_{q_2}\pi^0_{q_3}\pi^0_{q_4}\pi^0_{q_5}, \tag{17}$$

where we explicitly label each particle in the reaction by its four-momentum, are shown in Figs. 1–4. Let

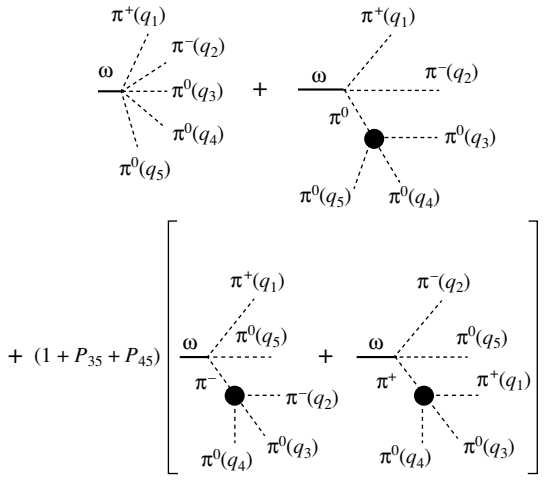

Fig. 3. The diagrams describing the contributions to the $\omega \to \pi^+\pi^-3\pi^0$ decay amplitude via pointlike vertices. The closed circles refer to the effective $\pi \to 3\pi$ vertices given by Eq. (18).

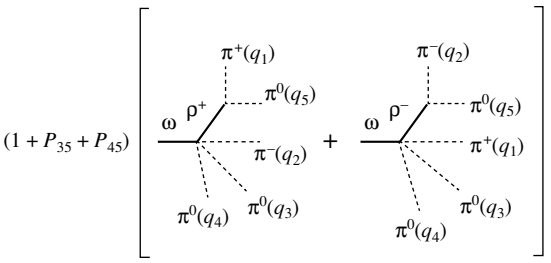

Fig. 4. The contributions to the $\omega \to \pi^+\pi^-3\pi^0$ decay amplitude arising due to the chiral vertex $\omega \to \rho 3\pi$.

us give the expressions corresponding to them. The amplitude in Fig. 1 includes the four-pion decay of the intermediate ρ meson, which was extensively discussed in, e.g., [10]. However, the so-called Weinberg Lagrangian [12] was used in [10] to find the expressions for the $\rho \to 4\pi$ decay amplitudes. This Lagrangian is different in coefficients as compared to Eq. (1) above. Yet one can show by direct computation that, as the result of the well-known parameter independence, the $\rho \to 4\pi$ amplitudes resulting from the above Lagrangians coincide. The reason is that the terms $\propto D_\pi(k)$ in the $\pi \to 3\pi$ amplitudes,

$$M(\pi_k^+ \to \pi_{q_1}^+\pi_{q_2}^+\pi_{q_3}^-) = \frac{1}{2f_\pi^2}(1+P_{12}) \qquad (18)$$
$$\times \left[-a(q_1,q_3) + (a-2)(q_1,q_2) + am_\rho^2 \frac{(q_2, q_3-q_1)}{D_\rho(q_1+q_3)} - \frac{1}{3}D_{\pi^+}(k)\right],$$
$$M(\pi_k^+ \to \pi_{q_1}^+\pi_{q_3}^0\pi_{q_4}^0) = \frac{1}{2f_\pi^2}(1+P_{34})$$
$$\times \left[-(a-1)(q_3,q_4) + (a-2)(q_1,q_3) + am_\rho^2 \frac{(q_4, q_3-q_1)}{D_\rho(q_1+q_3)} - \frac{1}{6}D_{\pi^+}(k)\right],$$
$$M(\pi_k^0 \to \pi_{q_1}^+\pi_{q_2}^-\pi_{q_5}^0) = \frac{1}{2f_\pi^2}(1+P_{12})$$
$$\times \left[-(a-1)(q_1,q_2) + (a-2)(q_1,q_5) + am_\rho^2 \frac{(q_2, q_1-q_5)}{D_\rho(q_1+q_5)} - \frac{1}{6}D_{\pi^0}(k)\right],$$
$$M(\pi^0 \to \pi_{q_3}^0\pi_{q_4}^0\pi_{q_5}^0) = \frac{m_{\pi^0}^2}{f_\pi^2},$$

which vanish on the pion mass shell, give the non-π-pole terms in the $\rho \to 2\pi \to 4\pi$ amplitude. When added to the pointlike $\rho \to 4\pi$ amplitude, they make their sum parameter independent. The same occurs with such terms in the expression derived from Fig. 2 below, which should be added to the expression derived from Fig. 4. The final expressions for the full $\omega \to \pi^+\pi^-3\pi^0$ decay amplitude will be given below. Hereafter, P_{ij} is the operator of permutation of the pion momenta q_i and q_j;

$$D_\rho(k) = m_\rho^2 - k^2 - i\sqrt{k^2}\Gamma_{\rho\to\pi^+\pi^-}(k^2), \qquad (19)$$
$$\Gamma_{\rho\to\pi^+\pi^-}(k^2) = \frac{g_{\rho\pi\pi}^2}{48\pi k^2}\left(k^2 - 4m_{\pi^+}^2\right)^{3/2}$$

are the inverse propagator of the ρ meson and its two-pion decay width, respectively; and

$$D_{\pi^{+,0}}(k) = m_{\pi^{+,0}}^2 - k^2 \qquad (20)$$

is the inverse propagator of the $\pi^{+,0}$ meson. Also, in view of the fact that the expressions for the ω, $\phi \to 5\pi$ amplitudes will appear to be rather long, the following shorthand notation for inverse propagators of the particle A will be used:

$$D_{Aab} \equiv D_A(q_a+q_b), \qquad (21)$$
$$D_{Aabc} \equiv D_A(q_a+q_b+q_c).$$

Let us give the expression for each diagram in Figs. 1–5. The upper index (n) (nickname of neutral, because three neutral pions are in the final state) will designate this particular isotopic state. Choosing q_μ, ϵ_μ for the four-momentum and four-vector of polarization of the ω, one obtains

$$M_1^{(n)} = \frac{g_{\omega\rho\pi}g_{\rho\pi\pi}}{f_\pi^2}\varepsilon_{\mu\nu\lambda\sigma}q_\mu\epsilon_\nu\Big[(1+P_{35} \qquad (22)$$
$$+ P_{45})\frac{q_{5\lambda}}{D_\rho(q-q_5)}J_\sigma(\rho^0 \to \pi_{q_1}^+\pi_{q_2}^-\pi_{q_3}^0\pi_{q_4}^0)$$
$$+ (1-P_{12})\frac{q_{2\lambda}}{D_\rho(q-q_2)}J_\sigma(\rho^+ \to \pi_{q_1}^+\pi_{q_3}^0\pi_{q_4}^0\pi_{q_5}^0)\Big]$$

for the diagrams in Fig. 1. The coupling constants $g_{\rho\pi\pi}$ and $g_{\omega\rho\pi}$ are given in Eqs. (3) and (10), respectively. The $\rho \to 4\pi$ decay currents standing in Eq. (22) are [10]

$$J_\sigma(\rho^0 \to \pi^+_{q_1}\pi^-_{q_2}\pi^0_{q_3}\pi^0_{q_4}) = (1 - P_{12}) \quad (23)$$
$$\times (1 + P_{34})\left\{q_{1\sigma}\left(-\frac{1}{4} + \frac{1}{D_{\pi^+234}}\left[(q_3, q_4 - 2q_2)\right.\right.\right.$$
$$\left.\left.\left. + a(q_3, q_2 - q_4)\left(\frac{m_\rho^2}{D_{\rho 24}} - 1\right)\right]\right) + \frac{m_\rho^2}{2D_{\rho 13}D_{\rho 24}}$$
$$\times [(q_3 + q_1)_\sigma(q_1 - q_3, q_2 - q_4) + 2(q_3 - q_1)_\sigma$$
$$\times (q_1 + q_3, q_2 - q_4)] + 2\left(\frac{n_c g^2 c_3}{8\pi^2}\right)^2 \frac{1}{D_{\omega 123}}$$
$$\times \left(\frac{1}{D_{\rho 12}} + \frac{1}{D_{\rho 13}} + \frac{1}{D_{\rho 23}} + 3\frac{c_1 - c_2 - c_3}{2c_3 m_\rho^2}\right)$$
$$\times [q_{1\sigma}((k, q_2)(q_3, q_4) - (k, q_3)(q_2, q_4))$$
$$\left. + q_{3\sigma}(k, q_1)(q_2, q_4)]\right\}$$

(with $k = q_1 + q_2 + q_3 + q_4$), where

$$D_{\omega abc} \equiv D_\omega(q_a + q_b + q_c) \quad (24)$$
$$= m_\omega^2 - (q_a + q_b + q_c)^2 - im_\omega\Gamma_\omega$$

is the inverse propagator of the ω (note that, because the ω resonance is narrow, we take the fixed width approximation for the ω meson), and

$$J_\sigma(\rho^+ \to \pi^+_{q_1}\pi^0_{q_3}\pi^0_{q_4}\pi^0_{q_5}) = (1 + P_{34} + P_{35}) \quad (25)$$
$$\times \left\{\frac{1}{3}q_{1\sigma}\left(1 - \frac{2m_{\pi^0}^2}{D_{\pi^0 345}}\right) + \frac{q_{3\sigma}}{D_{\pi^+145}}(1 + P_{45})\right.$$
$$\left. \times \left[(q_4, q_5 - 2q_1) + a(q_4, q_5 - q_1)\left(\frac{m_\rho^2}{D_{\rho 15}} - 1\right)\right]\right\}.$$

The expression for the diagrams in Fig. 2 is

$$M_2^{(n)} = -\frac{g_{\omega\rho\pi}g_{\rho\pi\pi}}{f_\pi^2}(1 - P_{12}) \quad (26)$$
$$\times (1 + P_{35} + P_{45})(1 + P_{34})\varepsilon_{\mu\nu\lambda\sigma}q_\mu\epsilon_\nu$$
$$\times \left\{\frac{q_{1\lambda}q_{5\sigma}}{D_{\rho 15}D_{\pi^+234}}\left[(q_3, q_4 - 2q_2) + a(q_3, q_2 - q_4)\right.\right.$$
$$\left.\left. \times \left(\frac{m_\rho^2}{D_{\rho 24}} - 1\right)\right] - \frac{q_{1\lambda}q_{2\sigma}m_{\pi^0}^2}{6D_{\rho 12}D_{\pi^0 345}}\right\}.$$

The expression for the diagrams in Fig. 3 is

$$M_3^{(n)} = \frac{n_c g}{32\pi^2 f_\pi^5}(1 - P_{12})(1 + P_{35} \quad (27)$$
$$+ P_{45})\varepsilon_{\mu\nu\lambda\sigma}q_\mu\epsilon_\nu\left\{\frac{4c_1 - 5(c_2 + c_3)}{3}q_{1\lambda}q_{2\sigma}\right.$$
$$\left. + 3(c_1 - c_2 - c_3)(1 + P_{34})\right.$$
$$\left.\times \left[\frac{q_{1\lambda}q_{5\sigma}}{D_{\pi^+234}}\left((q_3, q_4 - 2q_2) + a(q_3, q_2 - q_4)\right.\right.\right.$$
$$\left.\left.\left. \times \left(\frac{m_\rho^2}{D_{\rho 24}} - 1\right)\right) + \frac{q_{1\lambda}q_{2\sigma}}{3D_{\pi^0 345}}(q_3, q_4)\right]\right\}.$$

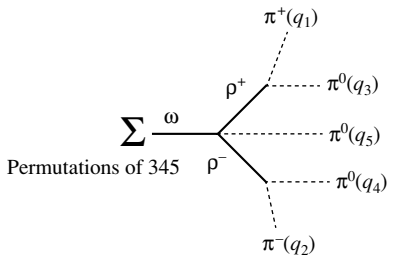

Fig. 5. The contributions to the $\omega \to \pi^+\pi^-3\pi^0$ decay amplitude via intermediate state with two ρ mesons. Total number of diagrams of this kind is $3! = 6$.

Notice the relation

$$\frac{n_c g}{32\pi^2 f_\pi^5} = -\frac{g_{\omega\rho\pi}g_{\rho\pi\pi}}{f_\pi^2}\frac{1}{2c_3 m_\rho^2}, \quad (28)$$

which is useful for an easier comparison of the present contribution with others. The expression for the diagrams in Figs. 4 and 5 are, respectively,

$$M_4^{(n)} = -\frac{g_{\omega\rho\pi}g_{\rho\pi\pi}}{f_\pi^2}(1 - P_{12})(1 + P_{35} \quad (29)$$
$$+ P_{45})\varepsilon_{\mu\nu\lambda\sigma}\frac{\epsilon_\nu(q_1 - q_5)_\lambda}{2D_{\rho 15}}$$
$$\times \left[q_\mu q_{2\sigma} - \frac{c_1 + c_2 - c_3}{2c_3}q_{2\mu}(q_3 + q_4)_\sigma\right]$$

and

$$M_5^{(n)} = \frac{g_{\omega\rho\pi}g_{\rho\pi\pi}m_\rho^2}{f_\pi^2}\frac{c_1 + c_2 - c_3}{4c_3}(1 - P_{12}) \quad (30)$$
$$\times (1 + P_{35} + P_{45})\varepsilon_{\mu\nu\lambda\sigma}\frac{\epsilon_\nu(q_1 - q_3)_\mu(q_2 - q_4)_\lambda q_{5\sigma}}{D_{\rho 13}D_{\rho 24}}.$$

The full $\omega \to \pi^+\pi^-3\pi^0$ decay amplitude is

$$M(\omega \to \pi^+\pi^-\pi^0\pi^0\pi^0) \quad (31)$$
$$= M_1^{(n)} + M_2^{(n)} + M_3^{(n)} + M_4^{(n)} + M_5^{(n)}.$$

Since the expressions for the amplitudes are very lengthy, one should invoke the method of control of the calculations. We take the Adler condition (see below) as the method of such a control.

Now, let us verify the Adler condition for the $\omega \to \pi^+\pi^-3\pi^0$ decay amplitude. This is the condition of vanishing of the amplitude of the process with soft pions, when the momentum of any pion is vanishing. Pions emitted in the decay $\omega \to 5\pi$ [10, 11] are truly soft, because they possess the typical momentum $|\mathbf{q}_\pi| \simeq 0.5m_\pi$. To verify the Adler condition, we,

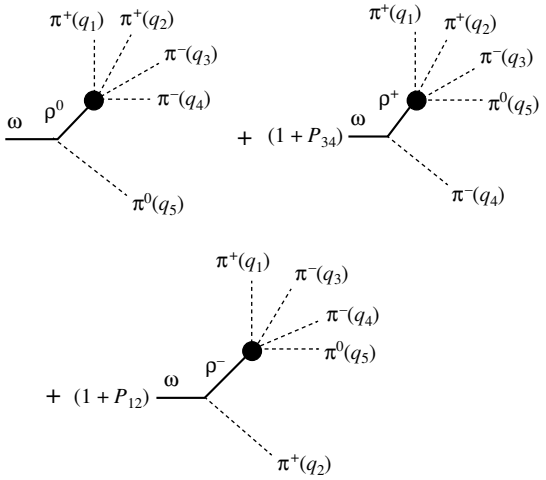

Fig. 6. The diagrams describing the amplitudes of the decay $\omega \to 2\pi^+2\pi^-\pi^0$ through the ρ intermediate state followed by the decay $\rho \to 4\pi$. The closed circles refer to the whole $\rho \to 4\pi$ amplitudes.

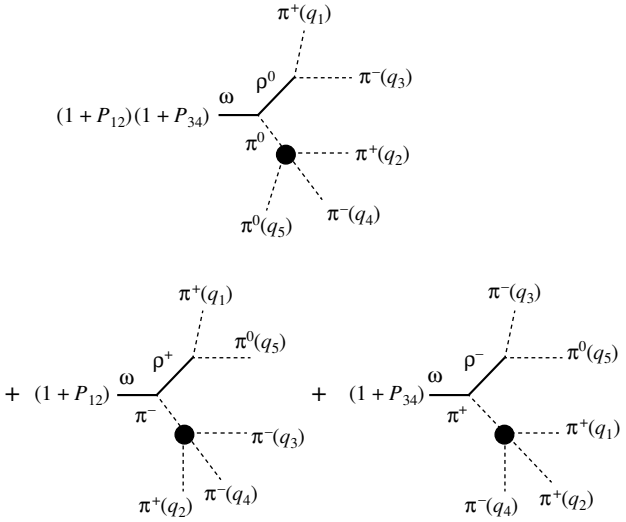

Fig. 7. The diagrams describing the amplitudes of the decay $\omega \to 2\pi^+2\pi^-\pi^0$ through the $\rho\pi$ intermediate state followed by the transitions $\rho \to 2\pi$ and $\pi \to 3\pi$. The closed circles refer to the effective $\pi \to 3\pi$ vertices given by Eq. (18). Note that the non-π-pole term is included in the first pair of diagrams in Fig. 9 below.

first, set any particular pion momentum to zero and, second, take the chiral limit, i.e., set the pion mass $m_\pi \to 0$. The correct expression should result in the vanishing of the amplitude in this limit.

(i) $q_1 = 0$. The contributions of the diagrams in Figs. 3–5 vanish; the contributions of the diagrams in Figs. 1 and 2 are equal in magnitude but opposite in sign, and hence they are canceled. The Adler condition is fulfilled. The case $q_2 = 0$ is obtained from the case of $q_1 = 0$ by the permutation property [see the operator $1 - P_{12}$ in front of each expression in Eqs. (22), (23), (26), (27), (29), and (30)].

(ii) $q_3 = 0$. Here, the situation is more subtle. Let us represent the amplitude at $q_3 = 0$ in the form

$$M(\omega \to \pi^+\pi^-\pi^0\pi^0\pi^0)\big|_{q_3=0}$$
$$= -\frac{g_{\omega\rho\pi}g_{\rho\pi\pi}}{f_\pi^2}(1 - P_{12})(1 + P_{45})\varepsilon_{\mu\nu\lambda\sigma}\epsilon_\nu T_{\mu\lambda\sigma}.$$

Then one obtains the following contributions to the tensor $T_{\mu\lambda\sigma}$ from Figs. 1–5, respectively:

$$T^{(1)}_{\mu\lambda\sigma} = \frac{q_\mu(q_1 - q_4)_\lambda q_{5\sigma}}{2D_{\rho 14}}, \qquad (32)$$

$$T^{(2)}_{\mu\lambda\sigma} = \frac{q_\mu q_{1\lambda} q_{4\sigma}}{D_{\rho 14}},$$

$$T^{(3)}_{\mu\lambda\sigma} = -\frac{1}{4m_\rho^2}\left(q_\mu q_{1\lambda} q_{2\sigma} + \frac{c_1 + c_2 - c_3}{c_3} q_{1\mu} q_{2\lambda} q_{4\sigma}\right),$$

$$T^{(4)}_{\mu\lambda\sigma} = \frac{1}{6} q_\mu \left[\frac{3q_{1\lambda}q_{2\sigma}}{2m_\rho^2} + \frac{(q_1 - q_4)_\lambda(2q_2 - q_5)_\sigma - 2q_{1\lambda}q_{4\sigma}}{D_{\rho 14}}\right]$$

$$- \frac{c_1 + c_2 - c_3}{4c_3}\left[\frac{q_{2\mu}(q_1 - q_4)_\lambda q_{5\sigma}}{D_{\rho 14}} - \frac{q_{1\mu}q_{2\lambda}q_{4\sigma}}{m_\rho^2}\right],$$

$$T^{(5)}_{\mu\lambda\sigma} = \frac{c_1 + c_2 - c_3}{4c_3}\frac{q_{2\mu}(q_1 - q_4)_\lambda q_{5\sigma}}{D_{\rho 14}}.$$

Note that, when obtaining the contribution $T^{(3)}_{\mu\lambda\sigma}$, Eq. (28) is essential. As is evident from Eq. (32), the terms with the factor $c_1 + c_2 - c_3$ and without such a factor are canceled separately in the sum. Hence, the Adler condition is satisfied in the case $q_3 = 0$ too. The cases $q_{4,5} = 0$ are obtained from this case by Bose symmetry.

The diagrams for the amplitude of the decay

$$\omega_q \to \pi^+_{q_1}\pi^+_{q_2}\pi^-_{q_3}\pi^-_{q_4}\pi^0_{q_5}, \qquad (33)$$

where the particles are labeled by their four-momenta, are shown in Figs. 6–10. Let us give the expressions corresponding to them. The upper index (c) (nickname of *charged*, because most pions in the final state are charged) will designate this particular isotopic state. The expression for the diagrams in Fig. 6 is written as

$$M^{(c)}_1 = \frac{g_{\omega\rho\pi}g_{\rho\pi\pi}}{f_\pi^2}\varepsilon_{\mu\nu\lambda\sigma}q_\mu\epsilon_\nu \qquad (34)$$

$$\times \left[\frac{q_{5\lambda}}{D_\rho(q - q_5)}J_\sigma(\rho^0 \to \pi^+_{q_1}\pi^+_{q_2}\pi^-_{q_3}\pi^-_{q_4})\right.$$
$$\left. + (1 + P_{34})\frac{q_{4\lambda}}{D_\rho(q - q_4)}J_\sigma(\rho^+ \to \pi^+_{q_1}\pi^+_{q_2}\pi^-_{q_3}\pi^0_{q_5})\right.$$

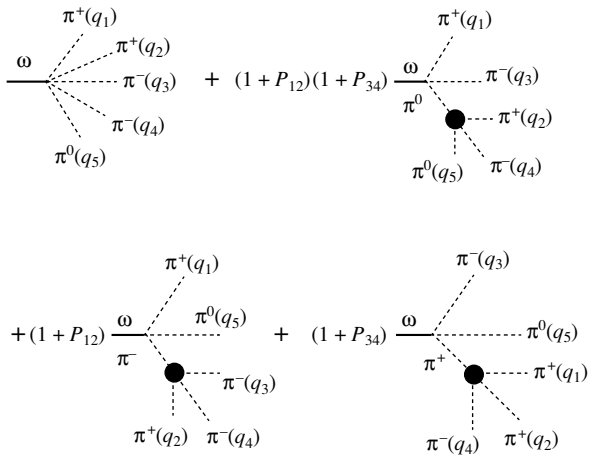

Fig. 8. The diagrams describing the contributions to the $\omega \to 2\pi^+2\pi^-\pi^0$ decay amplitude via pointlike vertices. The closed circles refer to the effective $\pi \to 3\pi$ vertices given by Eq. (18).

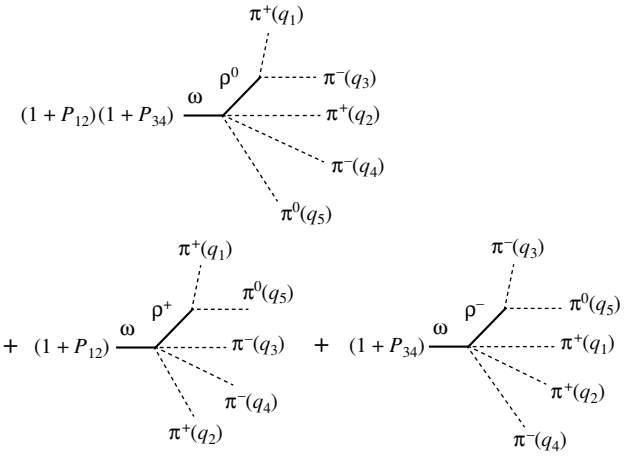

Fig. 9. The contributions to the $\omega \to 2\pi^+2\pi^-\pi^0$ decay amplitude arising due to the chiral $\omega \to \rho 3\pi$ vertex.

$$+ (1+P_{12})\frac{q_{2\lambda}}{D_\rho(q-q_2)}J_\sigma(\rho^- \to \pi^+_{q_1}\pi^-_{q_3}\pi^-_{q_4}\pi^0_{q_5})\Bigg].$$

Here, the currents responsible for the four-pion decay of the intermediate ρ meson are the following [10]:

$$J_\sigma(\rho^0 \to \pi^+_{q_1}\pi^+_{q_2}\pi^-_{q_3}\pi^-_{q_4}) = (1+P_{12}) \quad (35)$$
$$\times (1+P_{34})(1-P_{13}P_{24})\Bigg\{q_{1\sigma}\Bigg(-\frac{1}{2}+\frac{1}{D_{\pi^+234}}$$
$$\times\Bigg[a(q_3,q_2-q_4)\Bigg(\frac{m_\rho^2}{D_{\rho 24}}-1\Bigg)-2(q_3,q_4)\Bigg]\Bigg)\Bigg\}$$

and

$$J_\sigma(\rho^+ \to \pi^+_{q_1}\pi^+_{q_2}\pi^-_{q_3}\pi^0_{q_5}) = (1+P_{12}) \quad (36)$$
$$\times\Bigg\{\frac{1}{2}(q_1-q_5)_\sigma-(1+P_{23})\frac{q_{1\sigma}}{D_{\pi^0 135}}$$
$$\times\Bigg[(q_2,q_3-2q_5)+a(q_2,q_3-q_5)\Bigg(\frac{m_\rho^2}{D_{\rho 35}}-1\Bigg)\Bigg]$$
$$+\frac{q_{5\sigma}}{D_{\pi^+123}}\Bigg[-2(q_1,q_2)+a(q_1,q_3-q_2)$$
$$\times\Bigg(\frac{m_\rho^2}{D_{\rho 23}}-1\Bigg)\Bigg]+(1-P_{35})[2(q_1-q_5)_\sigma$$
$$\times(q_1+q_5,q_2-q_3)-(q_1+q_5)_\sigma$$
$$\times(q_1-q_5,q_2-q_3)]\frac{m_\rho^2}{2D_{\rho 15}D_{\rho 23}}+\frac{2}{D_{\omega 135}}$$
$$\times\Bigg(\frac{n_c g^2 c_3}{8\pi^2}\Bigg)^2[q_{1\sigma}(1-P_{35})(k,q_3)(q_2,q_5)$$
$$+q_{3\sigma}(1-P_{15})(k,q_5)(q_1,q_2)+q_{5\sigma}(1-P_{13})$$
$$\times(k,q_1)(q_2,q_3)]\Bigg(\frac{1}{D_{\rho 13}}+\frac{1}{D_{\rho 15}}+\frac{1}{D_{\rho 33}}$$
$$+\frac{c_1-c_2-c_3}{2c_3m_\rho^2}\Bigg)\Bigg\},$$

where $k = q_1+q_2+q_3+q_5$. The expression for $J_\sigma(\rho^- \to \pi^+_{q_1}\pi^-_{q_3}\pi^-_{q_4}\pi^0_{q_5})$ is obtained from Eq. (36) by the replacements $q_1 \leftrightarrow q_3$, $q_2 \to q_4$ and by inverting an overall sign. The expression for the contribution of the diagrams in Fig. 7 is

$$M_2^{(c)} = \frac{g_{\omega\rho\pi}g_{\rho\pi\pi}}{f_\pi^2}(1+P_{12}) \quad (37)$$
$$\times(1+P_{34})\varepsilon_{\mu\nu\lambda\sigma}q_\mu\epsilon_\nu\Bigg\{(1+P_{24})\frac{q_{1\lambda}q_{3\sigma}}{D_{\rho 13}D_{\pi^0 245}}$$
$$\times\Bigg[(q_2,q_4-2q_5)+a(q_2,q_4-q_5)\Bigg(\frac{m_\rho^2}{D_{\rho 45}}-1\Bigg)\Bigg]$$
$$-(1-P_{13}P_{24})\frac{q_{1\lambda}q_{5\sigma}}{D_{\rho 15}D_{\pi^+234}}$$
$$\times\Bigg[-2(q_3,q_4)+a(q_3,q_2-q_4)\Bigg(\frac{m_\rho^2}{D_{\rho 24}}-1\Bigg)\Bigg]\Bigg\}.$$

The expression for the contribution of the diagrams in Fig. 8 is written as

$$M_3^{(c)} = \frac{n_c g}{32\pi^2 f_\pi^5}(1+P_{12}) \quad (38)$$
$$\times(1+P_{34})\varepsilon_{\mu\nu\lambda\sigma}q_\mu\epsilon_\nu\Bigg\{\frac{4c_1-5(c_2+c_3)}{3}$$
$$\times q_{1\lambda}q_{3\sigma}+3(c_1-c_2-c_3)$$
$$\times\Bigg((1-P_{14}P_{23})\frac{q_{1\lambda}q_{5\sigma}}{D_{\pi^+234}}\Bigg[-2(q_3,q_4)$$
$$+a(q_3,q_2-q_4)\Bigg(\frac{m_\rho^2}{D_{\rho 24}}-1\Bigg)\Bigg]$$
$$-\frac{q_{1\lambda}q_{3\sigma}}{D_{\pi^0 245}}(1+P_{24})\Bigg[(q_2,q_4-2q_5)$$

$$+ a(q_2, q_4 - q_5)\left(\frac{m_\rho^2}{D_{\rho 45}} - 1\right)\Bigg]\Bigg)\Bigg\}.$$

Notice that Eq. (28) is necessary in verifying the Adler condition below. The expression for the contribution of the diagrams in Fig. 9 is

$$M_4^{(c)} = \frac{g_{\omega\rho\pi} g_{\rho\pi\pi}}{f_\pi^2}(1 + P_{12}) \tag{39}$$
$$\times (1 + P_{34})\varepsilon_{\mu\nu\lambda\sigma}\epsilon_\nu \Bigg\{\frac{1}{2}q_\mu\Bigg[\frac{(q_1 - q_3)_\lambda q_{5\sigma}}{D_{\rho 13}}$$
$$+ (1 - P_{13}P_{24})\frac{q_{1\lambda}q_{5\sigma} + \frac{1}{2}(q_1 - q_5)_\lambda q_{2\sigma}}{D_{\rho 15}}\Bigg]$$
$$- \frac{c_1 + c_2 - c_3}{4c_3}\Bigg[\frac{q_{5\mu}(q_1 - q_3)_\lambda (q_2 + q_4)_\sigma}{D_{\rho 13}}$$
$$+ (1 - P_{13}P_{24})\frac{q_{1\mu}(q_3 - q_5)_\lambda q_{4\sigma}}{D_{\rho 35}}\Bigg]\Bigg\}.$$

Finally, the amplitude resulting from the diagrams in Fig. 10 is

$$M_5^{(c)} = -\frac{g_{\omega\rho\pi} g_{\rho\pi\pi} m_\rho^2}{f_\pi^2} \tag{40}$$
$$\times \left(\frac{c_1 + c_2 - c_3}{4c_3}\right)(1 + P_{12})(1 + P_{34})$$
$$\times (1 + P_{24})\varepsilon_{\mu\nu\lambda\sigma}\epsilon_\nu \frac{(q_1 - q_3)_\mu q_{4\lambda}(q_2 - q_5)_\sigma}{D_{\rho 13} D_{\rho 25}}.$$

Notice that the product of the operators $(1 + P_{12})(1 + P_{34})$ [see (35) and (36)] makes evident the Bose symmetry of the full $\omega \to 2\pi^+2\pi^-\pi^0$ decay amplitude, which is

$$M(\omega_q \to \pi^+_{q_1}\pi^+_{q_2}\pi^-_{q_3}\pi^-_{q_4}\pi^0_{q_5}) \tag{41}$$
$$= M_1^{(c)} + M_2^{(c)} + M_3^{(c)} + M_4^{(c)} + M_5^{(c)}.$$

Let us verify the Adler condition for the $\omega \to 2\pi^+2\pi^-\pi^0$ decay amplitude and write down the Adler limits of all the above contributions to the $\omega \to 2\pi^+2\pi^-\pi^0$ decay amplitudes. As an example, the case $q_1 = 0$ is considered in detail. Representing the total amplitude Eq. (41) in this limit as

$$M(\omega_q \to \pi^+_{q_1}\pi^+_{q_2}\pi^-_{q_3}\pi^-_{q_4}\pi^0_{q_5})\big|_{q_1=0}$$
$$= \frac{g_{\omega\rho\pi} g_{\rho\pi\pi}}{f_\pi^2}(1 + P_{34})\varepsilon_{\mu\nu\lambda\sigma}\epsilon_\nu T_{\mu\lambda\sigma},$$

one has the following expressions for the diagrams in Figs. 6–10, respectively:

$$T^{(6)}_{\mu\lambda\sigma}(q_1 = 0) = \frac{1}{2}(1 - P_{35})q_\mu \tag{42}$$
$$\times \left[\frac{q_{4\lambda}(q_2 - q_5)_\sigma}{D_{\rho 25}} - \frac{q_{2\lambda}q_{3\sigma}}{D_{\rho 35}}\right],$$

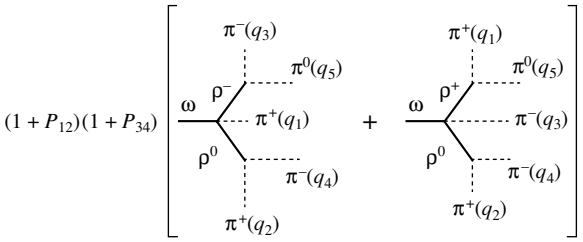

Fig. 10. The contributions to the $\omega \to 2\pi^+2\pi^-\pi^0$ decay amplitude via intermediate state with two ρ mesons.

$$T^{(7)}_{\mu\lambda\sigma}(q_1 = 0) = (1 - P_{35})\frac{q_\mu q_{2\lambda} q_{3\sigma}}{D_{\rho 23}},$$
$$T^{(8)}_{\mu\lambda\sigma}(q_1 = 0) = -\left(2 + \frac{c_1 + c_2 - c_3}{c_3}\right)\frac{q_\mu q_{2\lambda} q_{5\sigma}}{4m_\rho^2},$$
$$T^{(9)}_{\mu\lambda\sigma}(q_1 = 0) = \frac{1}{6}q_\mu$$
$$\times \Bigg[\frac{-2q_{2\lambda}q_{3\sigma} + (q_2 - q_3)_\lambda (2q_5 - q_4)_\sigma}{D_{\rho 23}}$$
$$- \frac{4q_{3\lambda}q_{5\sigma} + (q_3 - q_5)_\lambda (2q_4 - q_2)_\sigma}{D_{\rho 23}} + 3q_{2\lambda}q_{5\sigma}$$
$$\times \left(\frac{1}{D_{\rho 25}} + \frac{1}{m_\rho^2}\right)\Bigg] + \frac{c_1 + c_2 - c_3}{4c_3}$$
$$\times \left[\frac{q_\mu q_{2\lambda} q_{5\sigma}}{m_\rho^2} + (1 - P_{24}P_{35})\frac{q_{3\mu}(q_4 - q_5)_\lambda q_{2\sigma}}{D_{\rho 45}}\right],$$
$$T^{(10)}_{\mu\lambda\sigma}(q_1 = 0) = -\frac{c_1 + c_2 - c_3}{4c_3}$$
$$\times (1 - P_{24}P_{35})\frac{q_{3\mu}(q_4 - q_5)_\lambda q_{2\sigma}}{D_{\rho 45}}.$$

Again, when obtaining $T^{(8)}_{\mu\lambda\sigma}$, relation (28) is essential. The close inspection of Eq. (42) shows that, first, the ρ-pole terms in the sum of the diagrams in Figs. 6, 7, and 9 are canceled and, second, both the ρ-pole terms proportional to $c_1 + c_2 - c_3$ and the non-ρ-pole ones are canceled in the sum of the diagrams in Figs. 8–10. The cases of $q_{2,3,4} = 0$ are obtained from the present case by Bose symmetry and evident replacements of the pion momenta. In the case $q_5 = 0$, the contributions of the diagrams in Figs. 8–10 vanish in the chiral limit separately, while the contributions of the diagrams in Figs. 6 and 7 are equal in magnitude but opposite in sign, and hence they are canceled. The conditions of the vanishing of the amplitude in the Adler limit obtained here turn out to be of great importance in obtaining the $\phi \to 5\pi$ decay amplitudes.

3. THE $\omega \to \pi^+\pi^-3\pi^0$ AND $\omega \to 2\pi^+2\pi^-\pi^0$ BRANCHING RATIOS REVISITED

In our previous works [10, 11], the branching ratios of the $\omega \to \pi^+\pi^-3\pi^0$ and $\omega \to 2\pi^+\pi^-\pi^0$ decays were estimated. The basis of that evaluation was the expressions for the contributions of the diagrams shown in Figs. 1 and 6, added with the specific correction factor stemming from the diagrams shown in Figs. 2 and 7 of the present paper, respectively. This seemed to be justifiable because of the presence of the ρ pole. Moreover, the nonrelativistic limit $|\mathbf{q}_\pi| \ll m_\pi$ was essentially used, because the approximate nonrelativistic expressions gave almost the same numerical results for the $\rho \to 4\pi$ partial widths as exact ones, yet were much simpler. Those approximate amplitudes cannot satisfy the Adler condition that demands taking the massless pion limit, which is clearly opposite to the nonrelativistic limit. Finding the full decay amplitude undertaken in the present paper is essential in finding the $\phi \to 5\pi$ decay amplitudes (see Section 4). Having at hand the amplitudes satisfying the Adler condition, we evaluate here the above branching ratios using these amplitudes.

Strictly speaking, the HLS approach does not give the predictions even for the $\omega \to \pi^+\pi^-\pi^0$ decay rate, because arbitrary constants $c_{1,2,3}$ enter the expression for Lagrangian Eq. (9). As was pointed out in [5, 6], these constants should be determined from experiment. Nevertheless, HLS relates the contributions to the amplitudes [compare Figs. 1 and 2 to Figs. 3–5 (respectively, Figs. 6 and 7 to Figs. 8–10)], which otherwise appear unrelated. One can obtain reasonable predictions for the $\omega \to 5\pi$ decay rates upon assuming particular relations among $c_{1,2,3}$. First, there are no experimental indications on the pointlike $\omega \to \pi^+\pi^-\pi^0$ vertex; hence, one can take Eq. (11) for granted. Second, the constant c_3 [see Eq. (12)], extracted from the $\omega \to 3\pi$ branching ratio, is remarkably close to unity. Note that older chiral models [3] for the vector meson interactions, with the inclusion of the terms arising from the gauging of the anomalous Wess–Zumino action [8], predicted $c_3 = 1$. We fix c_3 from the $\omega \to 3\pi$ partial width [see Eqs. (10) and (12)]. After taking into account Eq. (11), the ratio c_1/c_3 remains arbitrary, and the magnitude of the $\omega \to 5\pi$ decay width depends on this parameter. We choose its value guided by the following considerations. The inspection of the expressions for the $\omega \to 5\pi$ decay amplitudes obtained in Section 2 shows that almost all the terms, except those proportional to $c_1 + c_2 - c_3$, have the tensor structure

$$M = \frac{g_{\omega\rho\pi}g_{\rho\pi\pi}}{f_\pi^2}\varepsilon_{\mu\nu\lambda\sigma}q_\mu\epsilon_\nu T_{\lambda\sigma}, \qquad (43)$$

where

$$T_{\lambda\sigma} = \sum_{a<b} G_{ab}q_{a\lambda}q_{(b)\sigma} \qquad (44)$$

is the tensor composed of pion four-momenta $q_{a\mu}$ (where $a = 1, \ldots, 5$ counts the final pions), and G_{ab} are invariant amplitudes, whose explicit form can be read off the expressions for the amplitudes obtained in Section 2 by gathering the coefficients in front of $q_{a\lambda}q_{(b)\sigma}$. They are very lengthy, so we do not give them here. In the rest frame system of the decaying ω, the Lorentz structure of Eq. (43) is reduced to the three-dimensional form $e_{ijk}\xi_i T_{jk}$, where $\boldsymbol{\xi}$ is the polarization vector of the ω in this frame and e_{ijk} is totally antisymmetric in $i, j, k = 1, 2, 3$. It enormously simplifies the calculation of the modulus squared of the amplitude. In the meantime, the terms proportional to $c_1 + c_2 - c_3$ have entirely the four-dimensional tensor structure $\varepsilon_{\mu\nu\lambda\sigma}\epsilon_\mu q_{a\nu}q_{(b)\lambda}q_{(c)\sigma}$. The resulting expression for the modulus squared of the full amplitude turns out to be extremely lengthy. Hence, for the sake of simplicity, we set

$$c_1 + c_2 - c_3 = 0 \qquad (45)$$

in what follows. Note that this means that the contributions of the diagrams in Figs. 5 and 10 together with the part of the contributions from the diagrams in Figs. 4 and 9 are dropped. Finally, our assumptions about HLS arbitrary constants $c_{1,2,3}$ and a are

$$c_1 = c_3, \quad c_2 = 0, \quad a = 2. \qquad (46)$$

Notice that the above relations among $c_{1,2,3}$ are the solutions of Eqs. (11) and (45). Of course, having the full expressions for the decay amplitude at hand, one can always loosen the constraint Eq. (45) and come back to the evaluation of the branching ratios at various values of c_1/c_3.

The expression for the partial width of the decays (13) and (14) is written as

$$\Gamma_{\omega\to5\pi}(s) = \frac{1}{2\sqrt{s}(2\pi)^{11}N_{\rm sym}}\int |M|^2 d\mathcal{D}_5, \qquad (47)$$

where $s = \left(\sum_{a=1}^5 q_a\right)^2$ is the total energy squared in the rest frame system of the decaying particle; the Bose symmetry factor $N_{\rm sym} = 6$ and 4 for the reaction (13) and (14), respectively; and $d\mathcal{D}_5$ given in [13] is the differential element of the phase-space volume of the five-pion final state. Note that we take into account the mass difference of the charged and neutral pions both in amplitude and in the phase-space volume. In the above formula,

$$|M|^2 = \frac{1}{3}\left(\frac{g_{\omega\rho\pi}g_{\rho\pi\pi}}{f_\pi^2}\right)^2 \frac{s}{2}\sum_{i,j=1}^3 |T_{ij} - T_{ji}|^2 \qquad (48)$$

is the modulus squared of the amplitude Eq. (43) averaged over three independent polarizations of the ω. When evaluating Eq. (47), eight Mandelstam-like invariant variables s_i, u_i, $i = 1, 2, 3$, and t_1, t_2 proposed by Kumar in [13] are suitable. They are given in the Appendix. All the scalar products of the pair of pion four-momenta are expressed via the Kumar variables by the expressions given in the Appendix. For the numerical evaluation of the eight-dimensional integral over Kumar variables, we use the method suggested in [14].

We evaluate both the branching ratios for the two aforementioned isotopic modes at the resonance mass,

$$\mathrm{Br}_{\omega\to 5\pi}(m_\omega^2) = \frac{\Gamma_{\omega\to 5\pi}(m_\omega^2)}{\Gamma_\omega}, \qquad (49)$$

and the branching ratios averaged over the resonance peak,

$$\mathrm{Br}^{\mathrm{aver}}_{\omega\to 5\pi} = \frac{2}{\pi}\int\limits_{m_\omega-\Gamma_\omega}^{m_\omega+\Gamma_\omega} d\sqrt{s}\frac{s\Gamma_{\omega\to 5\pi}(s)}{(s-m_\omega^2)^2+m_\omega^2\Gamma_\omega^2}. \quad (50)$$

The quantity $\mathrm{Br}^{\mathrm{aver}}_{\omega\to 5\pi}$ is useful in situations where the total energy of the five-pion state is not directly measured, as is the case in, e.g., photoproduction or peripheral production in πN collisions. The results of the evaluation are the following:

$$\mathrm{Br}_{\omega\to\pi^+\pi^-3\pi^0}(m_\omega^2) = 3.6\times 10^{-9}, \qquad (51)$$
$$\mathrm{Br}^{\mathrm{aver}}_{\omega\to\pi^+\pi^-3\pi^0} = 2.8\times 10^{-9},$$
$$\mathrm{Br}_{\omega\to 2\pi^+2\pi^-\pi^0}(m_\omega^2) = 3.3\times 10^{-9},$$
$$\mathrm{Br}^{\mathrm{aver}}_{\omega\to 2\pi^+2\pi^-\pi^0} = 2.5\times 10^{-9}.$$

These branching ratios for the $\omega\to 5\pi$ decay by a factor of more than 3 exceed those obtained in our previous papers [10, 11]. The reason of the disagreement is the following. As is mentioned at the beginning of the present section, the diagrams in Figs. 1 and 6 corrected with those in Figs. 2 and 7 were considered to be dominant in [10, 11]. Let us evaluate the contributions of the diagrams in Figs. 1 and 6 to the branching ratios of the decays $\omega\to\pi^+\pi^-3\pi^0$ and $\omega\to 2\pi^+2\pi^-\pi^0$, respectively. For a reason soon to become clear in the case of $\phi\to 5\pi$ decay, we call these contributions resonant. One obtains $\mathrm{Br}^{\mathrm{resonant}}_{\omega\to\pi^+\pi^-3\pi^0} = 1.54\times 10^{-9}$ and $\mathrm{Br}^{\mathrm{resonant}}_{\omega\to 2\pi^+2\pi^-\pi^0} = 1.3\times 10^{-9}$. These figures are close to $\mathrm{Br}_{\omega\to\pi^+\pi^-3\pi^0} \simeq \mathrm{Br}_{\omega\to 2\pi^+2\pi^-\pi^0} \simeq 1\times 10^{-9}$ obtained in [10, 11]. If one evaluates the net contribution of all the remaining diagrams called nonresonant, the following figures will be obtained: $\mathrm{Br}^{\mathrm{nonresonant}}_{\omega\to\pi^+\pi^-3\pi^0} = 0.47\times 10^{-9}$ and $\mathrm{Br}^{\mathrm{nonresonant}}_{\omega\to 2\pi^+2\pi^-\pi^0} = 0.50\times 10^{-9}$. The nonresonant contributions amount to 13–14% of the total [Eq. (51)]. However, the phase-space-averaged relative phase differences between the resonant and nonresonant contributions evaluated with the above numbers are $\delta = 21^\circ$ and 24°, respectively, for the reaction (13) and (14). These phase differences and the comparison with the total branching ratios [Eq. (51)] show that the aforementioned contributions to the decay amplitude are almost in phase. The neglect of seemingly small nonresonant contributions resulted in the underestimated magnitude of branching ratios in [10, 11].

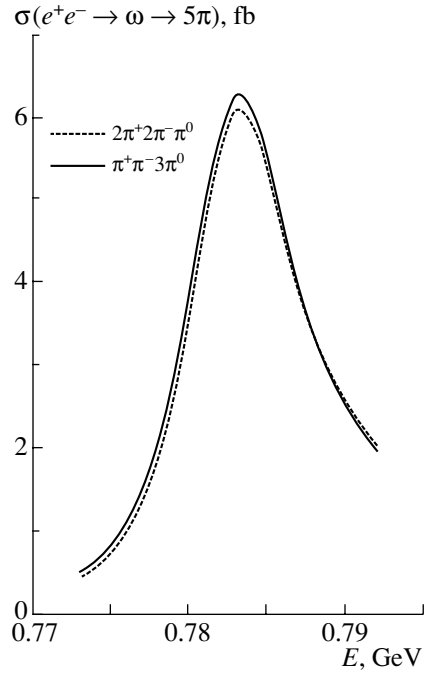

Fig. 11. The excitation curves of the decays $\omega\to 5\pi$ in e^+e^- annihilation.

The excitation curves for the $\omega\to 5\pi$ decays in e^+e^- annihilation,

$$\sigma_{\omega\to 5\pi}(s) = 12\pi\left(\frac{m_\omega}{\sqrt{s}}\right)^3\Gamma_{\omega\to e^+e^-}(m_\omega^2) \qquad (52)$$
$$\times\frac{s\Gamma_{\omega\to 5\pi}(s)}{(s-m_\omega^2)^2+m_\omega^2\Gamma_\omega^2},$$

are plotted in Fig. 11. The curves are asymmetric and shifted to higher values from the ω mass because of strong energy dependence of $\Gamma_{\omega\to 5\pi}(s)$ (see Figs. 12 and 13). As is seen, both isotopic channels have approximately equal branching ratios and almost coincident excitation curves in the ω-resonance region. This can be understood as follows. The matrix elements squared numerically are approximately the same in the near-to-threshold region, since the pion mass difference is smeared in the sum of various

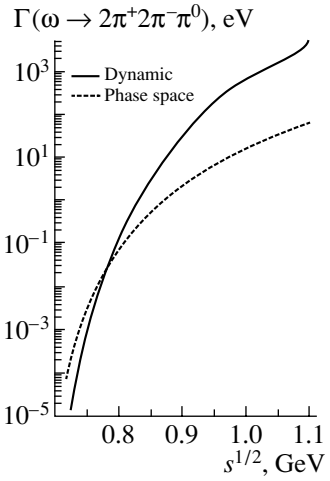

Fig. 12. The energy dependence of the $\omega \to 2\pi^+2\pi^-\pi^0$ partial width.

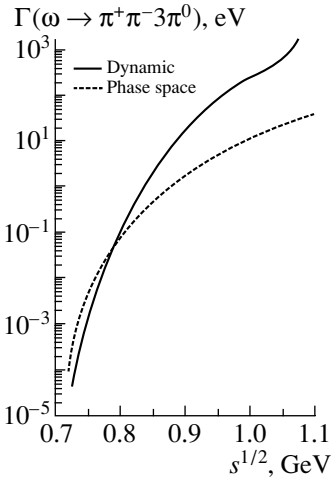

Fig. 13. The energy dependence of the $\omega \to \pi^+\pi^-3\pi^0$ partial width.

contributions. Hence, they are canceled in the ratio of two partial widths, leaving the ratio of the phase-space volumes. Using the nonrelativistic expression for the phase-space volume of the five-pion final state from [15], one obtains

$$\frac{\mathrm{Br}_{\omega\to 2\pi^+2\pi^-\pi^0}(m_\omega^2)}{\mathrm{Br}_{\omega\to\pi^+\pi^-3\pi^0}(m_\omega^2)} = \frac{3m_{\pi^+}}{2m_{\pi^0}}\left(\frac{2m_{\pi^+}+3m_{\pi^0}}{4m_{\pi^+}+m_{\pi^0}}\right)^{3/2} \times\left(\frac{m_\omega-4m_{\pi^+}-m_{\pi^0}}{m_\omega-2m_{\pi^+}-3m_{\pi^0}}\right)^5 = 0.93 \quad (53)$$

to be compared to 0.92 calculated from Eq. (51). The ratio of the Bose symmetry factors 3/2 compensates the smaller phase-space volume of the final state $2\pi^+2\pi^-\pi^0$, as compared to $\pi^+\pi^-3\pi^0$ one. In the meantime, the energy dependence of the $\omega \to 5\pi$ partial width in the dynamical model is drastically different from that in the model of the Lorentz-invariant phase space (lips). In the latter, one has the following expression for the $\omega \to 5\pi$ partial width:

$$\Gamma^{(\mathrm{lips})}_{\omega\to 5\pi}(s) = \Gamma_{\omega\to 5\pi}(m_\omega^2)\frac{W_{5\pi}(s)}{W_{5\pi}(m_\omega^2)}, \quad (54)$$

where $\Gamma_{\omega\to 5\pi}(m_\omega^2)$ is the partial width evaluated with the dynamical amplitudes given in Section 2, and the expression for the Lorentz-invariant phase-space volume is

$$W_{5\pi}(s) = \frac{\pi^4}{(2\pi)^{11}32s^{3/2}N_{\mathrm{sym}}} \times\int\limits_{(m_1+m_2+m_3+m_4)^2}^{(\sqrt{s}-m_5)^2}\frac{ds_1}{s_1}\lambda^{1/2}(s,s_1,m_5^2) \quad (55)$$

$$\times\int\limits_{(m_1+m_2+m_3)^2}^{(\sqrt{s_1}-m_4)^2}\frac{ds_2}{s_2}\lambda^{1/2}(s_1,s_2,m_4^2) \times\int\limits_{(m_1+m_2)^2}^{(\sqrt{s_2}-m_3)^2}\frac{ds_3}{s_3}\lambda^{1/2}(s_2,s_3,m_3^2)\lambda^{1/2}(s_3,m_1^2,m_2^2),$$

with m_i, $i = 1,\ldots,$ being the mass of the meson π_i and

$$\lambda(x,y,z) = x^2+y^2+z^2-2xy-2xz-2yz. \quad (56)$$

The predictions of both models for the energy dependence of $\Gamma_{\omega\to 2\pi^+2\pi^-\pi^0}(s)$ are plotted in Fig. 12. The corresponding plot for the $\pi^+\pi^-3\pi^0$ final state is shown in Fig. 13. The faster growth of the partial width in the dynamical model, as compared to the phase-space one, is due to the resonance enhancement arising from opening of the ρ production in the intermediate state.

There is one interesting limiting case of the $\omega \to 5\pi$ decay amplitudes. Since the pions in the five-pion decays are truly soft, the ρ meson can be considered as very heavy and hence can be integrated out, leaving an effective coupling of the ω meson to the five-pion state. This can be done at the Lagrangian level. But since we have the complete expressions for the amplitudes, one may keep in them only the leading terms in $1/m_\rho^2$. The resulting expressions are the following:

$$M(\omega_q \to \pi^+_{q_1}\pi^-_{q_2}\pi^0_{q_3}\pi^0_{q_4}\pi^0_{q_5}) \approx -\frac{3n_c g^2}{16\pi^2 f_\pi^5}(c_1-c_2+c_3)\varepsilon_{\mu\nu\lambda\sigma}\epsilon_\mu q_\nu(1-P_{12}) \quad (57)$$

$$\times (1+P_{53}+P_{54})\left[\frac{q_{1\lambda}q_{2\sigma}}{6}\left(1-\frac{m_{\pi^0}^2}{D_{\pi^0 345}}\right)\right.$$
$$\left.+\,q_{1\lambda}q_{5\sigma}\frac{(q_3,q_4)-(q_2,q_3+q_4)}{D_{\pi^+234}}\right],$$

$$M(\omega_q\to\pi^+_{q_1}\pi^+_{q_2}\pi^-_{q_3}\pi^-_{q_4}\pi^0_{q_5}) \qquad (58)$$
$$\approx\frac{3n_cg^2}{16\pi^2f_\pi^5}(c_1-c_2+c_3)\varepsilon_{\mu\nu\lambda\sigma}$$
$$\times\,\epsilon_\mu q_\nu(1+P_{12})(1+P_{34})$$
$$\times\left\{q_{1\lambda}q_{3\sigma}\left[\frac{(q_2,q_4)-(q_5,q_2+q_4)}{D_{\pi^0245}}-\frac{3}{2}\right]\right.$$
$$\left.+\,(1-P_{13}P_{24})q_{1\lambda}q_{5\sigma}\frac{(q_3,q_4)}{D_{\pi^+234}}\right\}.$$

One can convince oneself that the above expressions satisfy the Adler condition. Making the same assumptions about HLS parameters $c_{1,2,3}$, as earlier in this section, and evaluating the branching ratios with Eqs. (57) and (58) gives $\mathrm{Br}_{\omega\to\pi^+\pi^-3\pi^0}(m_\omega^2)=0.95\times10^{-9}$ and $\mathrm{Br}_{\omega\to2\pi^+2\pi^-\pi^0}(m_\omega^2)=1.04\times10^{-9}$, respectively, which fall short by a factor of 3 as compared to the evaluation with the full expressions. The reason is that the ρ pole in the full expressions is essential despite its nonresonant behavior in $\omega\to5\pi$ decay.

4. EVALUATION OF THE $\phi\to\pi^+\pi^-3\pi^0$ AND $\phi\to2\pi^+2\pi^-\pi^0$ BRANCHING RATIOS

As is known, chiral models, including HLS, do not possess terms responsible for the decays of the ϕ meson into final states containing nonstrange quarks only. However, one can guess the general form of such terms guided both by the way the OZI rule is broken in the decay $\phi\to\rho\pi\to\pi^+\pi^-\pi^0$ and by the condition of vanishing of the amplitude of the vector meson decays into the states consisting of many Nambu–Goldstone bosons.

There are two feasible models of the OZI-suppressed $\phi\to\rho\pi$ decay amplitude. The first one is the ϕ–ω-mixing model, where the above decay proceeds due to the small admixture of nonstrange quarks in the flavor wave function of the ϕ meson composed mostly of the pair of strange quarks. In the second model, ϕ goes to $\rho\pi$ directly, with the decay coupling constants originated from the OZI-rule-violating three-gluon state [16]. Earlier we pointed out that there are no particular reasons to prefer one model to another, and possible ways to resolve the issue were pointed out [16, 17]. Recent SND data [18] point to a sizable coupling constant of direct $\phi\to\rho\pi$ transition, assuming the dependence $|\psi(0,m_V)|^2\propto m_V^2$ [16] of the wave function of the vector $q\bar q$ bound state at the origin on the mass m_V of this state. It should be noted that the assumed dependence agrees remarkably well with the ratios of the measured leptonic widths of the vector quarkonia ρ, ω, ϕ, J/ψ, and $\Upsilon(1S)$.

The decays $\phi\to5\pi$ are treated slightly differently in the above models of OZI-rule violation. Let us consider them in turn. In the model of ϕ–ω mixing, ϕ goes to the off-mass-shell ω, which decays in a way considered in Section 2. Hence, one can immediately obtain

$$\Gamma_{\phi\to5\pi}(m_\phi^2)=|\varepsilon_{\phi-\omega}(m_\phi^2)|^2\Gamma_{\omega\to5\pi}(m_\phi^2), \qquad (59)$$

where $\varepsilon_{\phi-\omega}(m_\phi)$ is the complex parameter of ϕ–ω mixing taken at the ϕ mass. It can be evaluated as

$$|\varepsilon_{\phi-\omega}(m_\phi^2)|^2=\frac{\Gamma_{\phi\to3\pi}(m_\phi^2)}{\Gamma_{\omega\to3\pi}(m_\omega^2)}r=3.04\times10^{-3},$$

where $r=3.5\times10^{-2}$ is the ratio of the three-pion phase-space volumes at the ω and ϕ peaks.

If ϕ–ω mixing is negligible, one should introduce a number of new OZI-rule-violating parameters to quantify the $\phi\to5\pi$ decay amplitude. Guided by the condition of chiral symmetry expressed as the demand that the correct decay amplitude should fulfill the Adler condition, it is reasonable to expect that the effective Lagrangian, describing anomalous OZI-suppressed decays of the ϕ meson, looks similar to the Lagrangian Eq. (9),

$$\mathcal{L}^{\mathrm{an}}_{\phi,\rho,\pi}=\frac{1}{2f_\pi^3}(\beta_1-\beta_2-\beta_3)\varepsilon_{\mu\nu\lambda\sigma}\phi_\mu \qquad (60)$$
$$\times(\partial_\nu\boldsymbol{\pi}\cdot[\partial_\lambda\boldsymbol{\pi}\times\partial_\sigma\boldsymbol{\pi}])$$
$$+\frac{1}{8f_\pi^5}\left[-\beta_1+\frac{5}{3}(\beta_2+\beta_3)\right]\varepsilon_{\mu\nu\lambda\sigma}$$
$$\times\,\phi_\mu(\partial_\nu\boldsymbol{\pi}\cdot[\partial_\lambda\boldsymbol{\pi}\times\partial_\sigma\boldsymbol{\pi}])\boldsymbol{\pi}^2-\frac{2\beta_3g}{f_\pi}\varepsilon_{\mu\nu\lambda\sigma}\partial_\mu\phi_\nu$$
$$\times\left\{(\boldsymbol{\rho}_\lambda\cdot\partial_\sigma\boldsymbol{\pi})+\frac{1}{6f_\pi^2}[(\boldsymbol{\rho}_\lambda\cdot\boldsymbol{\pi})(\boldsymbol{\pi}\cdot\partial_\sigma\boldsymbol{\pi})\right.$$
$$\left.-\,\boldsymbol{\pi}^2(\boldsymbol{\rho}_\lambda\cdot\partial_\sigma\boldsymbol{\pi})]\right\}-\frac{2g}{f_\pi}(\beta_1+\beta_2-\beta_3)\varepsilon_{\mu\nu\lambda\sigma}\phi_\mu$$
$$\times\left\{\frac{1}{4f_\pi^2}(\partial_\nu\boldsymbol{\pi}\cdot\boldsymbol{\rho}_\lambda)(\boldsymbol{\pi}\cdot\partial_\sigma\boldsymbol{\pi})\right.$$
$$\left.-\,\frac{g}{4}([\boldsymbol{\rho}_\nu\times\boldsymbol{\rho}_\lambda]\cdot\partial_\sigma\boldsymbol{\pi})\right\},$$

where $\beta_{1,2,3}$ are the above-mentioned parameters responsible for the violation of the OZI rule in the $\phi\to5\pi$ decays of the ϕ meson. The analysis, similar to that presented in the case of the $\omega\to5\pi$ decay amplitudes, shows that the $\phi\to5\pi$ decay amplitudes obtained from the Lagrangian (60) satisfy the Adler condition.

As is evident from Eq. (60), one should identify the coupling constant of direct $\phi \to \rho\pi$ transition as

$$g_{\phi\rho\pi} = -\frac{2\beta_3 g}{f_\pi} = 0.8\ \text{GeV}^{-1}, \qquad (61)$$

where the magnitude of $g_{\phi\rho\pi}$ is obtained from the $\phi \to 3\pi$ partial widths, while the positive sign (relative to $g_{\omega\rho\pi}$ usually taken to be positive) is fixed by the ϕ–ω interference pattern observed in the energy dependence of the $e^+e^- \to \pi^+\pi^-\pi^0$ reaction cross section [19]. Note that we neglect the unitarity corrections to $g_{\phi\rho\pi}$ [20], because they are irrelevant in the context of the present work. Next, there seems to be no sizeable pointlike $\phi \to \pi^+\pi^-\pi^0$ contribution. Indeed, first, the existing upper limit to the branching ratio of the non-$\rho\pi$-intermediate-state direct transition $\phi \to \pi^+\pi^-\pi^0$, obtained by the SND group at VEPP-2M, is very small [21],

$$\text{Br}^{\text{direct}}(\phi \to \pi^+\pi^-\pi^0) < 6 \times 10^{-4} (90\%\ \text{C.L.}). \qquad (62)$$

Second, the KLOE Collaboration at DAΦNE gives the phase-space-averaged direct $\phi \to \pi^+\pi^-\pi^0$ contribution at the level of 1% [22], and this contribution is incoherent with the contribution of the intermediate resonant ρ meson. Hence, in a close analogy with the ω case, one can set

$$\beta_1 - \beta_2 - \beta_3 = 0. \qquad (63)$$

Then $\beta_3 = -0.006$ is fixed according to Eq. (61) by the $\phi \to 3\pi$ partial widths. After all, the ratio β_1/β_3 remains arbitrary. We set $\beta_1 + \beta_2 - \beta_3 = 0$; hence, $\beta_1 = \beta_3$, $\beta_2 = 0$, so that the $\phi \to 5\pi$ decay amplitudes are determined by only parameter β_3 and look like Eq. (43) for the $\omega \to 5\pi$ decay, with the replacement $g_{\omega\rho\pi} \to g_{\phi\rho\pi}$. The tensor $T_{\lambda\sigma}$ is the same as in the $\omega \to 5\pi$ decay amplitude. Under these assumptions, both aforementioned models for the OZI-rule-violating decay $\phi \to 3\pi$ give similar results for branching ratios of the decays $\phi \to 5\pi$. These are the following:

$$\begin{aligned} \text{Br}_{\phi\to\pi^+\pi^-3\pi^0}(m_\phi^2) &= 2.4 \times 10^{-7}, \qquad (64)\\ \text{Br}^{\text{aver}}_{\phi\to\pi^+\pi^-3\pi^0} &= 1.8 \times 10^{-7},\\ \text{Br}_{\phi\to2\pi^+2\pi^-\pi^0}(m_\phi^2) &= 5.0 \times 10^{-7},\\ \text{Br}^{\text{aver}}_{\phi\to2\pi^+2\pi^-\pi^0} &= 3.6 \times 10^{-7}, \end{aligned}$$

where Br^{aver}, useful for the reactions of peripheral production, stands for the branching ratio averaged over the $\pm\Gamma_\phi$ region around the ϕ peak [use Eq. (50) with replacement $\omega \to \phi$]. The evaluation of the excitation curve of the decays $\phi \to 5\pi$ in e^+e^- annihilation performed according to Eq. (52) (with the replacement $\omega \to \phi$) is plotted in Fig. 14. Notice that the ratio of

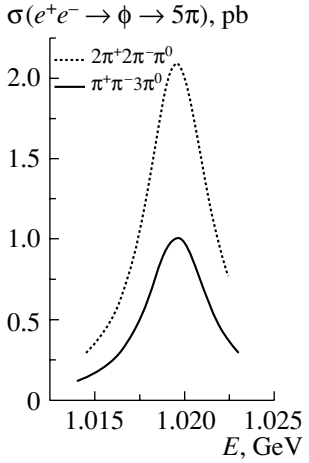

Fig. 14. The excitation curves of the decays $\phi \to 5\pi$ in e^+e^- annihilation.

the branching ratios of two isotopic modes at the ϕ peak is

$$\frac{\text{Br}_{\phi\to2\pi^+2\pi^-\pi^0}(m_\phi^2)}{\text{Br}_{\phi\to\pi^+\pi^-3\pi^0}(m_\phi^2)} = 2.1 \qquad (65)$$

to be compared to the number 1.3 obtained from the simple evaluation of the ratio of nonrelativistic phase space [see Eq. (53) with the replacement $m_\omega \to m_\phi$]. In the present case, the difference with the exact evaluation is sizable, because now the phase-space model is inadequate due to the strong ρ- and ω-resonance production in the intermediate states.

In this respect, it is interesting to look at the dynamical behavior of the specific contributions to the $\phi \to 5\pi$ decay amplitudes in another way. For this purpose, let us evaluate, at the ϕ mass, the contribution to $\text{Br}_{\phi\to\pi^+\pi^-3\pi^0}$ of the diagrams in Fig. 1 with the resonant ρ meson. (Notice that now ω in the initial state should be replaced with ϕ in all the diagrams, and the effective $g_{\phi\rho\pi}$ is understood at the corresponding expression, while other couplings are related to it, as is explained earlier in this section.) One obtains $\text{Br}^{\text{resonant}}_{\phi\to\pi^+\pi^-3\pi^0} = 2.1 \times 10^{-7}$. All the remaining contributions with the nonresonant intermediate ρ meson (see Figs. 2–4) amount to $\text{Br}^{\text{nonresonant}}_{\phi\to\pi^+\pi^-3\pi^0} = 0.34 \times 10^{-7}$. Notice that the seemingly resonant diagrams in Figs. 2 and 7 do not, in fact, possess this property, because three pions, produced from the transition $\pi \to 3\pi$, push the ρ meson away from the resonance. The phase-space-averaged relative phase between the resonant and nonresonant contributions calculated with the help of given branching ratios and that given in Eq. (64) is about $\delta = 91°$. Correspondingly, similar calculations for another isotopic state $2\pi^+2\pi^-\pi^0$ give $\text{Br}^{\text{resonant}}_{\phi\to2\pi^+2\pi^-\pi^0} =$

4.2×10^{-7} from Fig. 6, $\mathrm{Br}^{\mathrm{nonresonant}}_{\phi\to 2\pi^+2\pi^-\pi^0} = 0.70 \times 10^{-7}$ from Figs. 7–9, and $\delta = 96^\circ$. This clearly illustrates the dominance of the diagrams with the resonant ρ meson in the intermediate state in the decay $\phi \to 5\pi$, because the resonant and the smaller nonresonant contributions add incoherently in the case of $\phi \to 5\pi$ decay. For comparison, the opposite situation occurs in the case of $\omega \to 5\pi$ decay amplitudes (see the corresponding calculations in Section 3), where the smaller nonresonant contribution to the decay amplitude adds almost in phase with the resonant one and for this reason is essential. The above discussion shows that the branching ratios of the decays $\phi \to \pi^+\pi^-3\pi^0$ and $\phi \to 2\pi^+2\pi^-\pi^0$, determined within the conservatively estimated accuracy of 20% by the well-studied OZI-rule-violating coupling of the ϕ meson to the $\rho\pi$ state followed by the transition $\rho \to 4\pi$, are evaluated here in a model-independent way.

5. DISCUSSION AND CONCLUSION

In view of the fact that there are three (or even four, if one includes radiative decays—see [5, 6]) independent constants in the effective chiral Lagrangian describing anomalous decays of ω (and ϕ) mesons, one can only consider some scenarios of what may happen. We restrict ourselves by considering only the strong decays. In principle, the study of the Dalitz plot in the $\omega \to \pi^+\pi^-\pi^-$ decay allows one to extract c_3 and $(c_1 - c_2)/c_3$ by isolating the ρ-pole and non-ρ-pole contributions, because the density on this plot is proportional, omitting the ω–ρ interference term in the $\pi^+\pi^-$ mass spectrum, to the factor

$$\frac{d^2\sigma}{dm_+dm_-} \propto \left| \frac{1}{D_\rho(q_1+q_2)} + \frac{1}{D_\rho(q_1+q_3)} + \frac{1}{D_\rho(q_2+q_3)} + 3\frac{c_1-c_2-c_3}{2c_3m_\rho^2} \right|^2, \quad (66)$$

where $m_+^2 = (q_1+q_3)^2$, $m_-^2 = (q_2+q_3)^2$. Notice in this respect that the combination of parameters of the low-energy effective Lagrangian entering into the non-ρ-pole term in Eq. (66) should be treated as the low-energy limit of all possible contributions from the transitions $\omega \to \rho'\pi$, $\rho''\pi$, etc. If one assumes that the direct transitions are responsible for the decays of the ϕ meson to the states containing no strange quarks, the same will be true for the parameters $\beta_{1,2,3}$, characterizing the OZI-rule-violating decays $\phi \to 3\pi$ and $\phi \to 5\pi$. In the model of ϕ–ω mixing, the $\phi \to 5\pi$ decay amplitude contains no additional free parameters as compared to the case of $\omega \to 5\pi$ decay. It should be recalled that both models can be, in principle, discriminated either by the careful study of the ϕ–ω-interference minimum in the energy dependence of the $e^+e^- \to \pi^+\pi^-\pi^0$ reaction cross section or by the ratio of the leptonic widths of ω and ϕ mesons [16–18]. On the other hand, within an accuracy of 20%, the branching ratios of the $\phi \to 5\pi$ decays can be evaluated in a model-independent way (see the discussion at the end of Section 4).

The excitation curves of the decays $\omega \to 5\pi$ and $\phi \to 5\pi$ in e^+e^- annihilation can be used to evaluate the expected number of these decays at ω and ϕ peaks. With the luminosity $L = 10^{32}$ cm^{-2} s^{-1} at the ω peak, one may hope to observe three events of the decays $\omega \to \pi^+\pi^-3\pi^0$ and $2\pi^+2\pi^-\pi^0$ per each mode bimonthly. With the same luminosity at the ϕ peak, the observation of 540 (250) $\phi \to 2\pi^+2\pi^-\pi^0$ ($\phi \to \pi^+\pi^-3\pi^0$) decays per month is feasible. Note that the existing upper limit is $\mathrm{Br}_{\phi\to 2\pi^+2\pi^-\pi^0} < 4.6 \times 10^{-6}$ (90% C.L.) [23]. With the luminosity $L = 500$ pb^{-1} already attained at the ϕ factory DAΦNE [24], one could gain about 1340 events of the decay $\phi \to 5\pi$ proceeding via chiral mechanisms considered in the present paper. The possible nonchiral-model background from the dominant decay $\phi \to K_LK_S$, $K_L \to 3\pi$, $K_S \to 2\pi$ is well cut from the considered chiral mechanism because in the former mechanism kaons fly away by macroscopic distances. Rare decay $\phi \to \eta\pi^+\pi^-$, whose branching ratio was estimated [25, 26] at the level $\mathrm{Br}_{\phi\to\eta\pi^+\pi^-} \sim 3 \times 10^{-7}$, is cut by removing events in the vicinity of the η peak in the three-pion distribution observed in the five-pion events [23].

In the present work, we neglect the contribution of the $a_1(1260)$ meson. This is justifiable because both the $\omega(782)$ and $\phi(1020)$ peaks are deep under the threshold of $a_1\pi$ production. As is known, the approach to chiral dynamics based on HLS, allows one to take the axial vector mesons into account [5, 6]. This is the theme of future work.

ACKNOWLEDGMENTS

The present study was partially supported by the Russian Foundation for Basic Research, project no. RFFI-02-02-16061.

APPENDIX

Relations Expressing Lorentz Scalar Products through the Kumar Variables

The relations expressing the Lorentz scalar products (q_i, q_j) through Lorentz-invariant variables are presented. Given the pion momentum assignment according to

$$\omega_q \to \pi_{q_1}\pi_{q_2}\pi_{q_3}\pi_{q_4}\pi_{q_5}, \quad (A.1)$$

the eight Kumar variables [13] are defined as

$$\begin{aligned} s_1 &= (q-q_1)^2, \\ s_2 &= (q-q_1-q_2)^2, \\ s_3 &= (q-q_1-q_2-q_3)^2, \\ u_1 &= (q-q_2)^2, \\ u_2 &= (q-q_3)^2, \\ u_3 &= (q-q_4)^2, \\ t_2 &= (q-q_2-q_3)^2, \\ t_3 &= (q-q_2-q_3-q_4)^2. \end{aligned} \tag{A.2}$$

Associated with them, but not independent, are the following:

$$\begin{aligned} s_2' &= (q_1+q_2)^2, \\ s_3' &= (q_1+q_2+q_3)^2, \\ t_2' &= (q_2+q_3)^2, \\ t_3' &= (q_2+q_3+q_4)^2. \end{aligned} \tag{A.3}$$

Then all but two Lorentz scalar products of the pion momenta can be expressed through Eqs. (A.2) and (A.3):

$$\begin{aligned} (q_1,q_2) &= \frac{1}{2}(s_2' - m_1^2 - m_2^2), \\ (q_1,q_3) &= \frac{1}{2}(s_3' - s_2' - t_2' + m_2^2), \\ (q_1,q_4) &= \frac{1}{2}(t_2 - t_3 - s_3 + m_5^2), \\ (q_1,q_5) &= \frac{1}{2}(t_3 - m_1^2 - m_5^2), \\ (q_2,q_3) &= \frac{1}{2}(t_2' - m_2^2 - m_3^2), \\ (q_4,q_5) &= \frac{1}{2}(s_3 - m_4^2 - m_5^2). \end{aligned} \tag{A.4}$$

The remaining scalar products

$$\begin{aligned} (q_3,q_5) &= \frac{1}{2}(s_2 - s_3 - m_3^2) - (q_3,q_4), \\ (q_2,q_4) &= \frac{1}{2}(t_3' - t_2' - m_4^2) - (q_3,q_4) \end{aligned} \tag{A.5}$$

can be expressed through (q_3,q_4). The latter, using the method of invariant integration outlined in Appendix D of [13], can be found as

$$\begin{aligned} (q_3,q_4) = \frac{1}{2}[&\alpha(s - u_2 + m_3^2) \\ &+ \beta(u_1 - t_2 - m_3^2) + \gamma(s_2 - s_3 - m_3^2)], \end{aligned} \tag{A.6}$$

where

$$\begin{aligned} \alpha &= \frac{1}{\Delta_M}(Ft_2s_3 + BCG + ACH \\ &\quad - t_2BH - C^2F - As_3G), \\ \beta &= \frac{1}{\Delta_M}(ss_3G + ABH + BCF \\ &\quad - B^2G - sCH - As_3F), \\ \gamma &= \frac{1}{\Delta_M}(st_2H + ABG + ACF \\ &\quad - t_2BF - sCG - A^2H), \end{aligned} \tag{A.7}$$

and

$$\begin{aligned} A &= \frac{1}{2}(s + t_2 - t_2'), \\ B &= \frac{1}{2}(s + s_3 - s_3'), \\ C &= \frac{1}{2}(s_3 + t_2 - m_1^2), \\ F &= \frac{1}{2}(s - u_3 + m_4^2), \\ G &= \frac{1}{2}(t_2 - t_3 + m_4^2), \\ H &= \frac{1}{2}(s_3 + m_4^2 - m_5^2), \\ \Delta_M &= st_2s_3 + 2ABC - B^2t_2 - C^2s - A^2s_3. \end{aligned} \tag{A.8}$$

In the above formulas, m_i, $i = 1,\ldots,5$, are the masses of final pions.

REFERENCES

1. S. Weinberg, Physica A **96**, 327 (1979).
2. J. Schwinger, Phys. Lett. B **24B**, 473 (1967); J. Wess and B. B. Zumino, Phys. Rev. **163**, 1727 (1967); S. Gasiorowicz and D. A. Geffen, Rev. Mod. Phys. **41**, 531 (1969); U.-G. Meissner, Phys. Rep. **161**, 213 (1988).
3. Ö. Kaymakcalan, S. Rajeev, and J. Schechter, Phys. Rev. D **30**, 594 (1984).
4. M. C. Birse, Z. Phys. A **355**, 231 (1996).
5. M. Bando, T. Kugo, S. Uehara, *et al.*, Phys. Rev. Lett. **54**, 1215 (1985); M. Bando, T. Kugo, and K. Yamawaki, Nucl. Phys. B **259**, 493 (1985); Prog. Theor. Phys. **73**, 1541 (1985); Phys. Rep. **164**, 217 (1988).
6. M. Harada and K. Yamawaki, Phys. Rep. **381**, 1 (2003).
7. K. Kawarabayashi and M. Suzuki, Phys. Rev. Lett. **16**, 255 (1966); Riazuddin and Fayyazuddin, Phys. Rev. **147**, 1071 (1966).
8. J. Wess and B. B. Zumino, Phys. Lett. B **37B**, 95 (1971).
9. K. Hagiwara *et al.*, Phys. Rev. D **66**, 010001 (2002).
10. N. N. Achasov and A. A. Kozhevnikov, Phys. Rev. D **62**, 056011 (2000); Zh. Éksp. Teor. Fiz. **91**, 499 (2000) [JETP **64**, 433 (2000)].
11. N. N. Achasov and A. A. Kozhevnikov, Phys. Lett. B **480**, 257 (2000); Pis'ma Zh. Éksp. Teor. Fiz. **71**, 401 (2000) [JETP Lett. **71**, 277 (2000)].

12. S. Weinberg, Phys. Rev. **166**, 1568 (1968).
13. R. Kumar, Phys. Rev. **185**, 1865 (1969).
14. T. W. Sag and G. Szekeres, Math. Comput. **18**, 245 (1964).
15. E. Byckling and K. Kajantie, *Particle Kinematics* (Wiley, London, 1973).
16. N. N. Achasov and A. A. Kozhevnikov, Phys. Rev. D **52**, 3119 (1995); Yad. Fiz. **59**, 153 (1996) [Phys. At. Nucl. **59**, 144 (1996)].
17. N. N. Achasov and A. A. Kozhevnikov, Yad. Fiz. **55**, 3086 (1992) [Sov. J. Nucl. Phys. **55**, 1726 (1992)]; Part. World **3**, 125 (1993).
18. M. N. Achasov *et al.*, Phys. Rev. D **68**, 052006 (2003).
19. M. N. Achasov *et al.*, Phys. Rev. D **63**, 072002 (2001).
20. N. N. Achasov and A. A. Kozhevnikov, Phys. Rev. D **61**, 054005 (2000); Yad. Fiz. **63**, 2029 (2000) [Phys. At. Nucl. **63**, 1936 (2000)].
21. M. N. Achasov *et al.*, Phys. Rev. D **65**, 032002 (2002).
22. A. Aloisio *et al.* (KLOE Collab.), Phys. Lett. B **561**, 55 (2003).
23. R. R. Akhmetshin *et al.*, Phys. Lett. B **491**, 81 (2000).
24. KLOE Collab., hep-ex/0305108.
25. N. N. Achasov and V. A. Karnakov, Pis'ma Zh. Éksp. Teor. Fiz. **39**, 285 (1984) [JETP Lett. **39**, 342 (1984)].
26. N. N. Achasov and A. A. Kozhevnikov, Int. J. Mod. Phys. A **7**, 4825 (1992); Yad. Fiz. **55**, 809 (1992) [Sov. J. Nucl. Phys. **55**, 449 (1992)].

Physics of Atomic Nuclei, Vol. 68, No. 1, 2005, pp. 16–20. Translated from Yadernaya Fizika, Vol. 68, No. 1, 2005, pp. 17–22.

NUCLEI
Experiment

Energy Dependence of the Total Cross Section for the Reaction of ^{4}He Ions with Silicon Nuclei

V. Yu. Ugryumov[1)*], I. V. Kuznetsov[1)], E. Bialkowski[2)], A. Kugler[3)], K. A. Kuterbekov[4)], I. N. Kuhtina[1)], V. F. Kushniruk[1)], V. G. Lyapin[5)], V. A. Maslov[1)], Yu. E. Penionzhkevich[1)], Yu. G. Sobolev[1)], W. Trzaska[6)], G. P. Tjurin[5)], S. V. Khlebnikov[5)], and S. Yamaletdinov[1)]

Received September 26, 2003; in final form, May 17, 2004

Abstract—Directly measured data on the total cross section for the reaction of projectile ^{4}He ions with silicon nuclei at energies below 25 MeV/nucleon are presented. The energy dependence of the parameters of a semimicroscopic potential is determined from the measured values of this cross section. This investigation was performed at the Flerov Laboratory of Nuclear Reactions at the Joint Institute for Nuclear Research (Dubna, Russia) and at the Department of Physics at the University of Jyväskylä (Finland). © *2005 Pleiades Publishing, Inc.*

1. INTRODUCTION

Experimental data on the cross sections for reactions induced by nucleus–nucleus collisions permit us to evaluate the parameters of nuclear potentials and are supplementary to data on elastic scattering. The energy dependence of the total reaction cross section (σ_R) for ^{4}He ions incident on various targets was studied at intermediate energies ($E >$ 20 MeV/nucleon) in [1–6]. The cross section σ_R was found to change substantially with increasing atomic number of the target nucleus. For light nuclei ($A < 40$), the cross section decreases with increasing energy in accordance with the expected effect caused by the energy dependence of the cross section for nucleon–nucleon scattering. For medium-mass and heavy nuclei, the cross section remains independent of energy; in this region of nuclear masses, σ_R is determined primarily by the geometric size of the target nucleus.

In this study, we have measured the dependence of the total cross section for the reaction of ^{4}He ions with ^{28}Si at low energies ($E < 25$ MeV/nucleon). The choice of reaction and of energy range was motivated by the following considerations. In [7], our group measured the energy dependence of σ_R for the ^{6}He + ^{28}Si reaction in the range 10–28 MeV/nucleon, and the results exhibited an increase in the cross section in the energy range 10–17 MeV/nucleon. At low energies, a comparison of the excitation functions for the ^{4}He, ^{6}He, and ^{6}Li neighboring nuclei is of interest, because ^{4}He is the nuclear core of the neutron-halo nucleus ^{6}He and because ^{6}He and ^{6}Li are mirror nuclei. The distinction between the mechanisms of nuclear reactions can manifest itself most vividly in a comparison of low-energy excitation functions, because the respective collisions of nuclei are of a peripheral character in this case. Therefore, the objective of our study was to perform a detailed measurement of the low-energy excitation-function portion of σ_R in ^{4}He interaction with silicon nuclei.

2. EXPERIMENTAL PROCEDURE

The experiment was performed in 30-, 50-, 75-, 90-, and 115-MeV ^{4}He-ion beams from the K130 cyclotron of the Department of Physics at the University of Jyväskylä (Finland). The ^{4}He-beam intensity was 10 nA. The beam was extracted to a ^{208}Pb scattering target 4 mg/cm^2 thick, and elastically scattered ^{4}He ions were recorded by a telescope. The rate at which the particles hit the telescope was 500 s^{-1}. An assembly of detectors (Fig. 1) was located at a distance of 60 cm from the scattering target at an angle of 20° with respect to the beam axis inside a large scattering chamber. An aluminum diaphragm 5 mm thick having an inner diameter of 10 mm restricted the

[1)]Joint Institute for Nuclear Research, Dubna, Moscow oblast, 141980 Russia.
[2)]Institute of Nuclear Physics, ul. Kawiory 26a, PL-30-055 Kraków, Poland.
[3)]Nuclear Physics Institute, Academy of Sciences of the Czech Republic, CZ-250 68 Řež, Czech Republic.
[4)]Institute of Nuclear Physics, Almaty, 480082 Republic of Kazakhstan.
[5)]Khlopin Radium Institute, pr. Shvernika 28, St. Petersburg, 194021 Russia.
[6)]University of Jyväskylä, FIN-40351 Jyväskylä, Finland.
[*]e-mail: ugriumov@lnr.jinr.ru

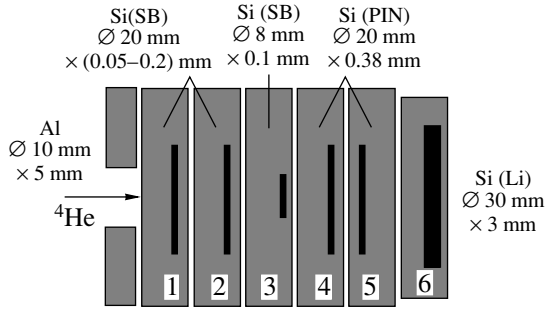

Fig. 1. Layout of the telescope detectors (the material, diameter, and thickness of the elements are also indicated).

angular spread of scattered particles to 1°. The energy spread of scattered ^{4}He ions that was measured by the telescope was approximately 400 keV for various beam energies.

Here, we give a brief account of the procedure used to measure σ_R, because it was described in detail elsewhere [7]. The telescope consisted of silicon detectors adjacent to one another; there were six detectors at $E_\alpha = 75$, 90, and 115 MeV and five of them at $E_\alpha = 30$ and 50 MeV. Alpha particles from elastic scattering on ^{208}Pb were extracted by means of cuts imposed on the energy depositions ΔE_1, ΔE_2, and ΔE_3 in the first three detectors (Figs. 2*a*, 2*b*). An active collimator (third detector) 8 mm in diameter was intended for extracting only those particles in the flux incident onto the telescope that hit the detector centers. The remaining particles either escaped detection in this detector or generated low responses that corresponded to hitting the boundary of the active layer. The target detector was placed behind the collimator detector. The extracted alpha particles could cause various nuclear reactions leading to a change in the typical ionization energy losses in the telescope detector being studied and in those that follow it. Reaction products were recorded by the energy depositions ΔE_4 and ΔE_5 in, respectively, the fourth and the fifth detector (Fig. 3). In the figure, events associated with reactions in the fourth detector are located predominantly above the energy distribution of alpha particles that did not initiate any reaction. If we denote by I_0 the number of alpha particles that hit the target and by I the number of events in which the energy deposition in this target corresponds to the elastic-scattering peak, then the total reaction cross section $\sigma_R(E_\alpha)$ can be determined from the relation

$$I = I_0 e^{-\sigma_R(E_\alpha)N}, \qquad (1)$$

where N is the number of target nuclei per unit surface.

The thickness of the ΔE detectors were between 50 and 380 μm, with the detectors of smaller thickness placed downstream of the target for the amount of nuclear reaction products produced inside them to be insignificant. The energy loss of the particles before the target was below 50%, and the energy dissipation in the target was below 20%.

The cross section $\sigma_R(E_\alpha)$ measured by means of the above procedure involves two main methodological uncertainties. First, nuclear-reaction events featuring particles that suffered scattering into the backward hemisphere and which moved from the target to the previous detector were not recorded as a reaction event, because the energy deposition in those events could not meet the constraints shown in Figs. 2*a* and 2*b*. The cross sections for these reaction channels were substantially smaller than the statistical uncertainties in the measured values of $\sigma_R(E_\alpha)$. Second, the elastic and the first inelastic channel of alpha-particle scattering on silicon nuclei were separated from each other. Excited levels in silicon were observed in the total energy distribution that was obtained by summing the energy depositions in all of the detectors; however, it was difficult to determine the detector in which the excitation occurred. Using data on the angular distributions in the reaction ^{28}Si(α, α*)^{28}Si for the 2^+ level in silicon at $E_\alpha =$ 104 MeV [8], we estimated the contribution of this reaction to the total cross section at 30 mb. This latter correction to $\sigma_R(E_\alpha)$ was taken into account by adding 30 mb to the statistical uncertainty.

3. RESULTS AND DISCUSSION

The experimental values of the total reaction cross sections σ_R are listed in Table 1, along with the mean alpha-particle energies E_α at which σ_R was measured. The widths of the energy intervals, $\pm\Delta E$, are determined by the energy losses in the detectors in which σ_R was measured and by the widths of the energy distributions. The uncertainties $\pm\Delta\sigma_R$ given in Table 1 include both statistical uncertainties and uncertainties associated with the procedure of event separation (Fig. 3).

Figure 4 shows the total-cross-section values listed in Table 1 (closed squares). The circles in this figure represent the σ_R values measured previously in [9], and the open squares correspond to data from [11]. The curve was calculated within the semimicroscopic folding model [10]. Figure 4 demonstrates that the reaction cross section reaches a maximum at $E \approx$ 20 MeV/nucleon. In order to follow carefully the behavior of σ_R over the whole energy range presented in Fig. 4, we invoke the strong-absorption model. It is well known that, within this model, the absorption cross section can be written as

$$\sigma_0 = \pi\lambda^2 \sum_L (2L+1)T_L, \qquad (2)$$

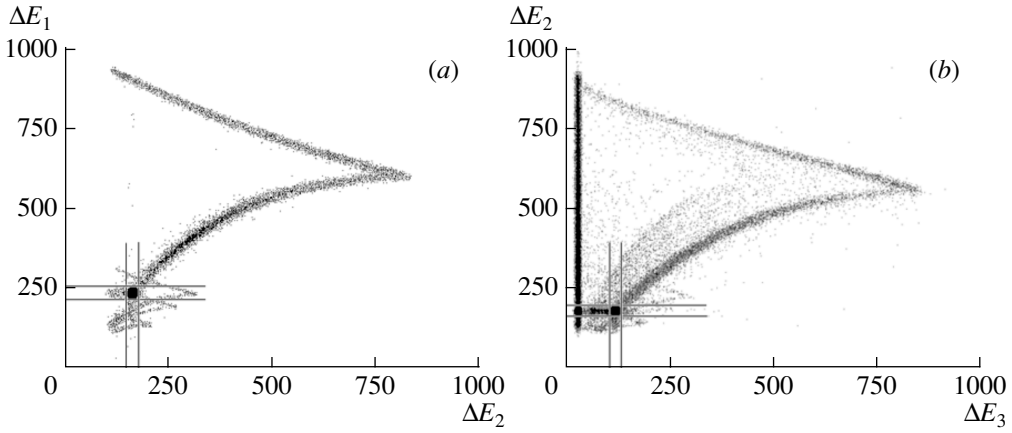

Fig. 2. Two-dimensional energy plots for detectors (*a*) 1 and 2 and (*b*) 2 and 3. The intersecting lines confine the contour containing events associated with elastic ^{4}He scattering on lead. The spectra are given in the ADC channels.

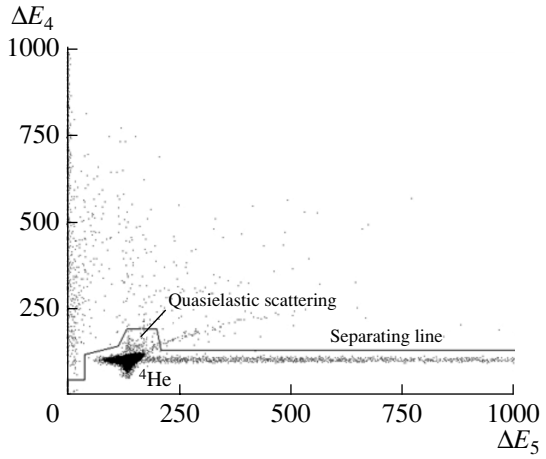

Fig. 3. Identification matrix of nuclear reaction products produced in detector 4 (events above the separating line) and in detector 5 (events to the right of the elastic-scattering peak). The spectra are given in the ADC channels.

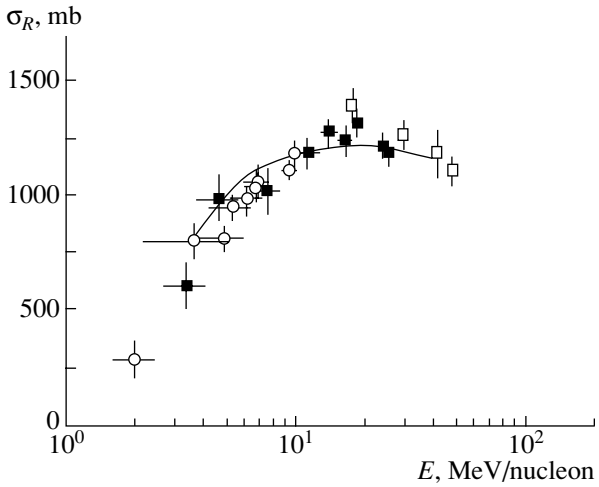

Fig. 4. Energy dependence of the total reaction cross section for alpha-particle interaction with ^{28}Si nuclei.

where $\lambda = h/\sqrt{2M(E-B)}$ is the de Broglie wavelength (M is the reduced mass of the projectile particle and the target nucleus, B is the height of the one-dimensional barrier, and E is the projectile energy), L is the orbital angular momentum of the nucleus, and T_L is the barrier penetrability. We can represent the data obtained here in the form of the ratio of the total reaction cross section to the absorption cross section, σ_R/σ_0, as a function of $E^{-1}_{\text{c.m.}}$. The cross section σ_0 is calculated as $\sigma_0 = \pi r_0^2(A_p^{1/3} + A_t^{1/3})^2$, where the parameter r_0 is taken to be 1.4 fm, as follows from the energy and mass dependences of this parameter [1], and A_p and A_t are the mass numbers of the projectile particle and the target nucleus, respectively. Figure 5 shows σ_R/σ_0 as a function of $E^{-1}_{\text{c.m.}}$. From this figure, one can see that there are actually two energy regions: the low-energy region, in which the relative cross section increases with increasing energy, and the high-energy region, in which it slowly decreases with increasing energy. This trend is usually observed in heavy-ion fusion reactions [11]. It is assumed that the maximum in the relative cross section must be associated with the threshold energy at which all inelastic channels of the reaction being considered become open; obviously, the position of the maximum depends strongly on the structural features of the target nucleus. The variation of σ_R/σ_0 with $E^{-1}_{\text{c.m.}}$ indicates that relation (2) cannot be interpreted unequivocally as penetration through a one-dimensional barrier. Indeed, a ^{4}He nucleus penetrates more deeply into the interaction region at high energies, the effective optical potential (the sum of the nuclear, centrifugal, and Coulomb potentials) acting at short distances within the barrier, where the

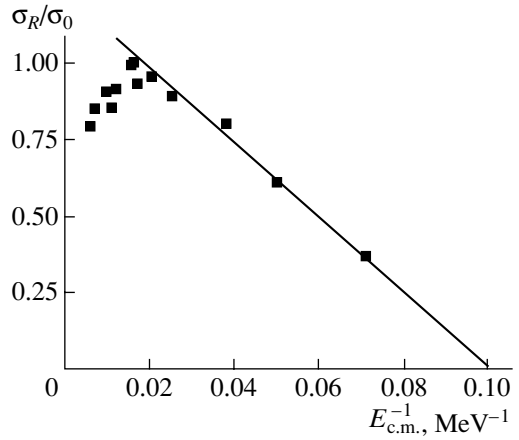

Fig. 5. Ratio of σ_R to the absorption cross section σ_0 as a function of the inverse energy.

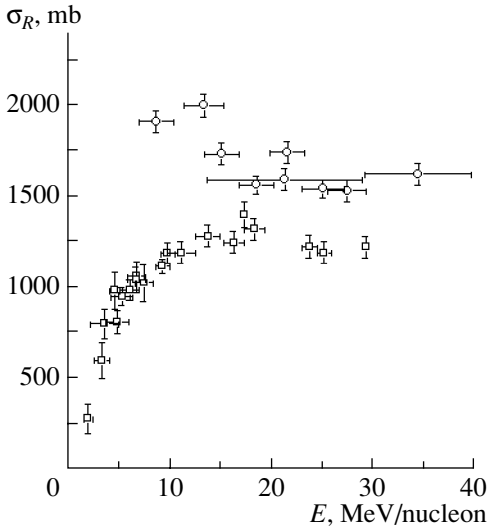

Fig. 6. Energy dependence of the total cross sections for the reactions of (□) ^{4}He and (○) ^{6}He ions with silicon nuclei.

barrier is determined by attractive nuclear forces. In this case, the energy dependence of the cross section is controlled by the energy dependence of the mean cross section for nucleon–nucleon interaction. In the low-energy region, we can assume that the barrier has the form

$$B = \frac{Ze^2}{R_{\text{Coul}}} = \frac{Ze^2}{r_{0\text{Coul}}A^{1/3}}. \qquad (3)$$

Using the slope of the curve in Fig. 5, we can determine the Coulomb interaction range $r_{0\text{Coul}}$, which differs from the actual interaction range. The barrier height B assessed in this way is 10 MeV, which is above the Coulomb barrier for the conventional parameter $r_{0\text{Coul}} = 1.3$ fm.

Figure 6 shows the energy dependences of the total cross sections for the ^{4}He + ^{28}Si and ^{6}He + ^{28}Si reactions according to the measurements in our experiment and according to [1, 6]. One can see from this figure that the cross sections σ_R behave differently for ^{4}He and ^{6}He at high energies. For ^{4}He, a decrease in the cross section with increasing energy is observed, while, for ^{6}He, the cross section is virtually independent of energy. The energy dependence of σ_R is still more contrasting for $E < 20$ MeV/nucleon: the ^{4}He cross section decreases sharply with decreasing energy, but the ^{6}He cross section increases, on the contrary, above $E \approx 20$ MeV/nucleon. This distinction between the energy dependences for ^{4}He and ^{6}He seems to suggest an additional reaction channel that opens for ^{6}He at 20 MeV/nucleon. The data on the cross section for ^{4}He production in ^{6}He(^{28}Si, ^{4}He)X reactions from [6, 7] cannot explain the observed jump of σ_R. In order to explain the observed phenomenon, one can assume that the ^{6}He + ^{28}Si reaction produces a nuclear system that decays via channels different from the entrance channel. In any case, it follows from Fig. 6 that the experimenters face the problem of identifying the reaction channel responsible for the increase in σ_R in the region $E <$ 20 MeV/nucleon.

The theoretical values of σ_R were calculated on the basis of the modified ECIS-88 code [12] by using the semimicroscopic potential

$$U_t(R) = U(R) - a_v\frac{dU(R)}{dR} + i\left(N_wU(R) - a_wR\frac{dU(R)}{dR}\right), \qquad (4)$$

where $U(R)$ is a microscopic real potential; a_v is the parameter of that part of the total potential which

Table 1. Measured values of the total cross sections for the ^{4}He + ^{28}Si reaction at various energies

E, MeV/nucleon	$\pm\Delta E$, MeV/nucleon	σ_R, mb	$\pm\Delta\sigma_R$, mb
3.4	0.70	600	60
4.6	0.75	982	60
7.5	0.96	1023	100
11.2	1.06	1191	60
13.8	1.21	1280	60
16.4	1.43	1247	60
18.4	0.88	1320	60
23.8	0.56	1223	55
25.3	0.71	1146	60

Table 2. Parameters of the semimicroscopic optical potential for elastic alpha-particle scattering on ^{28}Si at various energies

E, MeV	a_v	N_w	a_w
14.5	0.015	0.04	0
23.1	0.010	0.13	0
28.0	0.010	0.17	0
41.0	0.010	0.21	0
50.5	0.010	0.26	0
104.0	0	0.30	0.027
166.0	0	0.30	0.031

simulates dynamical polarization; and N_w and a_w are the parameters of, respectively, the volume and the surface imaginary potential [10]. For the alpha-particle energies at which the total cross sections were measured, we calculated the theoretical values of the total cross sections, fitting the values of a_v, a_w, and N_w. At energies below 50 MeV, the parameter a_w was set to zero, while the remaining two parameters were varied; above 50 MeV, the parameters a_v and N_w were fixed. In addition to the experimental data on the total reaction cross sections, there were some data on the differential cross sections for elastic scattering in the same range of energies E_α. Theoretical angular distributions were calculated for the data on elastic scattering. A global analysis of the data on the differential and total cross sections made it possible to calculate the parameters of the semimicroscopic potential (Table 2). The solid curve in Fig. 4 represents the energy dependence of the total reaction cross section corresponding to the calculated parameter values. As can be seen from Table 2, the parameter N_w of volume absorption is sensitive to the structure of both nuclei at $E_\alpha < 50$ MeV, whereas the parameter a_w of surface absorption becomes significant in the region $E_\alpha > 50$ MeV.

4. CONCLUSION

The energy dependence of the total cross section for the ^{4}He + ^{28}Si reaction has been measured in detail for the poorly studied region 4–25 MeV/nucleon. The results obtained in this way, together with other data available from the literature, have enabled us to trace the trend toward the variation of σ_R over a broad energy range and to find the inflection point of the function $\sigma_R(E)$ at $E = 20$ MeV/nucleon. The experimental values of σ_R at $E < 20$ MeV/nucleon cannot be described adequately on the basis of the semimicroscopic folding model with the parameters obtained in measurements of elastic ^{4}He scattering on a silicon target. With the aid of our experimental data on the total reaction cross section, new values were calculated for the parameters of the semimicroscopic folding potential.

We would also like to note that an increase in the total cross section for the ^{4}He + ^{28}Si reaction with increasing energy has been observed in the energy range 8–20 MeV/nucleon; at the same time, the cross section for the ^{6}He + ^{28}Si reaction decreases in this range [7]. Further experimental and theoretical studies of the total reaction cross section for ^{4,6}He and ^{6}Li ions at low energies ($E < 25$ MeV/nucleon) are required for understanding this phenomena.

ACKNOWLEDGMENTS

This work was supported in part by the Academies of Sciences of Finland and the Czech Republic, by INTAS (grant no. 00-00463), and by the Russian Foundation for Basic Research (project nos. 02-02-22001, 03-01-00657). I.V. Kuznetsov is grateful to the MDM bank for support during this experiment.

REFERENCES

1. A. Ingemarsson, J. Nyberg, P. U. Renberg, *et al.*, Nucl. Phys. A **676**, 3 (2000).
2. A. Auce *et al.*, Phys. Rev. C **50**, 871 (1994).
3. L. N. Govorenko *et al.*, Bull. Acad. Sci. USSR, Phys. Ser. **52**, 82 (1988).
4. V. N. Domnikov *et al.*, Bull. Acad. Sci. USSR, Phys. Ser. **52**, 62 (1988).
5. R. E. Warner *et al.*, Phys. Rev. C **40**, 2473 (1989).
6. R. E. Warner *et al.*, Phys. Rev. C **54**, 1700 (1996).
7. I. V. Kuznetsov, E. Byalkowski, M. P. Ivanov, *et al.*, Yad. Fiz. **65**, 1609 (2002) [Phys. At. Nucl. **65**, 1569 (2002)].
8. H. Rebel *et al.*, Phys. Rev. Lett. **26**, 1190 (1971).
9. M. K. Baktybaev, A. Duisebaev, B. A. Duisebaev, *et al.*, Yad. Fiz. **66**, 1662 (2003) [Phys. At. Nucl. **66**, 1615 (2003)].
10. O. M. Knyazkov, I. N. Kukhtina, and S. A. Fayans, Yad. Fiz. **61**, 827 (1998) [Phys. At. Nucl. **61**, 744 (1998)].
11. D. Glas and U. Mosel, Nucl. Phys. A **237**, 429 (1975).
12. J. Raynal, Phys. Lett. B **196**, 7 (1987).

Translated by E. Kozlovsky

Physics of Atomic Nuclei, Vol. 68, No. 1, 2005, pp. 160–167. Translated from Yadernaya Fizika, Vol. 68, No. 1, 2005, pp. 163–171.

ELEMENTARY PARTICLES AND FIELDS
Theory

Relativistic Description of Polarized-Deuteron Fragmentation Accompanied by the Emission of High-Transverse-Momentum Protons

L. S. Azhgirey[1)] and N. P. Yudin[2)]

Received July 18, 2003; in final form, November 17, 2003

Abstract—Available experimental data on the tensor analyzing power for nuclear relativistic-deuteron fragmentation accompanied by the emission of high-transverse-momentum protons are analyzed within light-front quantum mechanics. It is shown that, in contrast to calculations with standard wave functions, calculations employing the relativistic deuteron wave function obtained by V.A. Karmanov and his coauthors on the basis of light-front dynamics can explain the entire body of data without resort to additional degrees of freedom. © *2005 Pleiades Publishing, Inc.*

1. INTRODUCTION

Investigations of reactions involving a deuteron at intermediate and high energies receive constant attention. On one hand, the deuteron—the only known bound state of two nucleons—is quite appropriate for studying models in which nuclear interactions can be explained by meson exchange between baryons. On the other hand, it is a convenient object for testing the approaches that are used to describe relativistic bound states. Experiments performed with polarized-deuteron beams in Saclay [1–4] and in Dubna [5–10] resulted in understanding that, at short distances, the traditional ideas of the deuteron are invalid. For example, it was indicated in [10] that the analyzing power T_{20} for the pionless deuteron breakup $dp \to ppn$ in a kinematical region close to that of backward elastic deuteron–proton scattering in the c.m. frame depends on the primary deuteron momentum, the internal momentum k of nucleons in the deuteron (it is defined as a kinematical variable of light-front dynamics) being fixed. This gave sufficient grounds to assume that, in addition to k, one more variable is required for describing the bound state of two nucleons adequately.

Recent measurements of the tensor analyzing power A_{yy} in relativistic-deuteron fragmentation on nuclei that is accompanied by the emission of protons having high transverse momenta [11, 12] also favor this assumption. From available data, it follows that, at fixed values of the longitudinal momentum of protons, the quantity A_{yy} depends greatly on their transverse momentum; moreover, it turns out that the values of A_{yy} that are associated with fixed values of k exhibit a significant dependence on the angle between the vectors $\mathbf{k}$ and $\mathbf{n}$ (where $\mathbf{n}$ is a unit normal to the light-front surface).

The experimental data accumulated thus far for the spin features of $A(d,p)$ reactions at relativistic deuteron energies have not yet been interpreted theoretically at the ab initio level, since hadron physics is essentially nonperturbative, which hinders the formulation of basic concepts (within this framework) that would produce automatically, to a considerable extent, the whole diversity of hadron phenomena. In view of this, there remain many as-yet-unresolved problems in hadron physics, despite some advances such as the development of the concept of spontaneous chiral-symmetry breaking [13] or the development of effective field theory associated with this concept [14]. In particular, the way in which the relativistic invariance of hadron systems is realized has yet to be disclosed conclusively (that is, there is presently no answer to the question of which type of quantum mechanics is the most efficient in describing hadrons). Therefore, investigation of the polarization properties of deuteron-fragmentation reactions (d,p) is still one of the most important problems in relativistic hadron physics.

The results obtained by analyzing (d,p) reactions at relativistic energies of the deuterons involved are rather contradictory. On one hand, experimental data on the differential cross sections for inclusive deuteron breakup on nuclei [15, 16] are satisfactorily described within light-front dynamics in the approximation of the simple t-channel pole mechanism (Fig. 1) by using standard deuteron wave functions (see, for example, [17, 18]). On the other hand, calculations of polarization observables within this approach [19] do not reproduce experimental data,

[1)]Joint Institute for Nuclear Research, Dubna, Moscow oblast, 141980 Russia; e-mail: azhgirey@jinr.ru

[2)]Moscow State University, Vorob'evy gory, Moscow, 119899 Russia.

as a rule. The only exception in this respect was the analysis reported in [20], where data on deuteron fragmentation on nuclei that is accompanied by the emission of protons at zero angle were successfully described owing largely to taking into account the P wave in the ground state of the deuteron.

In the deuteron wave function, a P-wave state can be generated by various mechanisms. In [20], a P wave arises owing to the formation of a six-quark configuration, its fragmentation into baryons producing negative-parity resonances. In [21], a P wave appears as an essentially relativistic effect—on the basis of taking into account, in the deuteron ground state, an admixture of negative-energy nucleons (antiparticles). If, instead of phenomenologically considering mechanisms that generate a P wave in the deuteron wave function, one relies on calculations within the Bethe–Salpeter equation—for example, with a kernel (in the integral equation) that is constructed on the basis of the one-boson-exchange model—then the resulting admixture of the P wave would be overly small, insufficient for removing the discrepancy with experimental data [22]. It is interesting to note that, even within the approach developed in [23] and based on relativistic quantum mechanics—in this approach, nucleons interact via an instantaneous pair potential included in the Hamiltonian in such a way that the formalism proves to be Lorentz-invariant—the calculations fail to reproduce experimental data.

Thus, we have to admit that there is a theoretical crisis in describing polarization observables in relativistic-deuteron fragmentation on nuclei, so that further investigations are necessary. The simplest way would be to state that the discrepancy between theoretical and experimental results is due to the use of an overly simple reaction mechanism in the calculations. In our opinion, however, the potential of this simple (and very valuable for this reason) mechanism has not yet been exhausted in view of the currently achieved level of experimental accuracy. Bearing this in mind, we do not include new degrees of freedom (for example, mesonic ones) in our description of experimental data. Restricting ourselves to nucleonic degrees of freedom, we instead try to treat relativistic properties of deuteron–proton collisions more thoroughly.

In all of the preceding studies devoted to an analysis of polarization features of the reaction $A(d,p)X$, including those that used light-front quantum mechanics, a relativistic deuteron was taken in the form of a superposition of S and D waves that is known from nonrelativistic physics. This superposition presumes quite a specific relation between the transverse and the longitudinal component of the momentum of the internal motion of nucleons in a deuteron [19]. Within light-front dynamics, however, the dependence of the wave function on the transverse and longitudinal components of the internal momentum can differ considerably from that which is dictated by the combination of S and D waves. This possibility was first indicated in [24, 25], where the relativistic model of hard collisions of composite hadrons [26] was generalized to the case of relativistic nucleus–nucleus interactions.

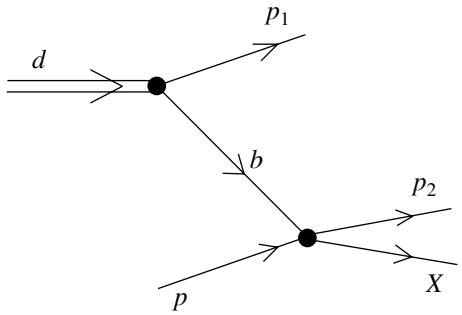

Fig. 1. Pole diagram for describing reactions induced by relativistic deuterons and accompanied by the emission of protons in the forward direction in the laboratory frame.

The objective of the present study was to investigate the aforementioned circumstance. The ensuing exposition is organized as follows. In Section 2, we describe assumptions concerning the application of light-front quantum mechanics. The relativistic deuteron wave function that is used in our calculations and which was obtained by Karmanov *et al.* [27] within light-front dynamics is described in Section 3. In Section 4, we present the formalism that we use to calculate the tensor analyzing power for deuteron fragmentation. The results of the calculations are given in Section 5, along with the corresponding discussion. Finally, the conclusions of the present study are formulated in Section 6.

2. LIGHT-FRONT QUANTUM MECHANICS

In the past years, various aspects of light-front dynamics were considered in a number of studies (see, for example, the review article of Miller [28] and references therein). However, we believe that a short discussion on the points relevant to our approach is appropriate.

It is well known that the dynamics of relativistic particles is determined by the shape of a fixed spacelike surface in four-dimensional spacetime—within quantum theory, it is the surface on which the Hilbert space of states is defined [29]. The choice of one or another version specifies the way in which ten generators of the Poincaré group, $P^\mu = (P^0, \mathbf{P}), M^{\mu\nu} = (\mathbf{J}, \mathbf{K})$, are partitioned into kinematical generators and dynamical ones (interaction-dependent Hamiltonians). Within conventional dynamics—that is,

instantaneous-form dynamics, where states are specified at the fixed time instants $t_0 = 0$—the momentum and angular-momentum operators ($\mathbf{P}$ and $\mathbf{J}$, respectively) are kinematical generators, while the energy operator P^0 and the Lorentz boost operator $\mathbf{K}$ are Hamiltonians. Within light-front quantum mechanics, where states are constructed on the fixed light-front surface $t^+ = t + z = 0$, the quantities $P_+ = P_0 + P_3$, P_1, P_2, $E_r = (K_r + \epsilon_{rs}J_s)/2$, K_3, and J_3 are kinematical operators, while $P_- = P_0 - P_3$ and $E_r = K_r - \epsilon_{rs}J_s$ (here, $r, s = 1, 2$ and ϵ_{rs} is an antisymmetric tensor: $\epsilon_{12} = -\epsilon_{21} = 1$) are Hamiltonians.

In relation to instantaneous-form dynamics, light-front dynamics possesses the advantage that particle–antiparticle pairs are not produced from a vacuum in this approach (here, the vacuum is "empty"). Owing to this, time-inverse diagrams must not be taken into account in describing the amplitudes for the processes being studied. However, this form of dynamics has the following disadvantages: First, one has to deal here with a specific direction—this is the direction of the z axis, with respect to which the generators of the Poincaré group are partitioned into kinematical and dynamical ones. Second, it turns out that the angular-momentum operators J_x and J_y, which are conventional kinematical quantities in instantaneous-form dynamics, become dynamical operators in light-front dynamics—that is, they prove to be interaction-dependent operators. To derive the result of the application of these operators to the wave function, it is necessary, in fact, to solve an additional Schrödinger-type equation—it is natural that, without doing this, there would arise difficulties in calculating the spin of a composite system. All of the aforesaid creates the impression that the results of the respective calculations are noncovariant. In fact, there must not be of course the dependence on the choice of direction for the z axis, since the original Lagrangian is Lorentz-invariant.

For the ensuing exposition to be clearer, we will now outline the scheme of a "correct" calculation of (d, p) reactions within light-front dynamics under the assumption of the pole mechanism displayed in Fig. 1. The relativistic-deuteron wave function, which is a function of the longitudinal (k_L) and transverse (k_T) components of the internal nucleon momentum,

$$\psi_d^M = \psi_d^M(k_L, k_T), \tag{1}$$

where $M = 0, \pm 1$ are the projections of the spin $\mathbf{J} = \mathbf{1}$ onto the quantization axis, is a key point in this calculation. We would like to highlight special features of this wave function.

First, we note that, although the functions ψ_d^M, which correspond to different values of M, are related, as in conventional instantaneous-form dynamics, to each other by the operators $J_x \pm iJ_y$, this relation is unusual in the sense that they are now "separated" by dynamics and can therefore differ from each other significantly. In view of this, it is difficult to introduce a conserved angular-momentum operator; that is, it is not straightforward, within light-front dynamics, to pinpoint the spin associated with a given state, and it is necessary, in general, to consider all three wave functions, which are related in quite an intricate way.

Second, the relation between the arguments k_L and k_T of the wave function (1) may differ significantly from that which is valid in the case where the state in question is described by a superposition of S and D waves. This circumstance may change qualitatively the situation in describing reactions that involve relativistic deuterons.

3. RELATIVISTIC DEUTERON WAVE FUNCTION

The difficulties in light-front dynamics that are associated with the particular role of the direction of the z axis and with the formation of the angular momentum were overcome to a considerable degree in [27, 30, 31] by extending the set of dynamical variables used to describe a composite system—namely, an additional variable was introduced there. This was the orientation of the spacelike quantization plane on which the Hilbert space of states was defined or the orientation of the plane on which the wave function was specified.

On one hand, the appearance of a variable that characterizes the orientation of the light-front plane complicates the situation because of an increase in the number of variables that are taken into account; on the other hand, this significantly simplifies the properties of the wave function with respect to rotations, making it possible to construct, irrespective of interaction (that is, in a purely geometric way), states of specific angular momentum. Problems associated with the introduction of an additional variable were solved in [27], and the relativistic deuteron wave function corresponding to a specific spin was found there within light-front dynamics. It is now a function of the spins of nucleons, their internal momentum, and the orientation of the quantization plane and has the form

$$\Psi^M_{\sigma_2\sigma_1} = w^*_{\sigma_2}\psi^M(\mathbf{k}, \mathbf{n})\sigma_y w_{\sigma_1}, \tag{2}$$

where σ_y is a Pauli matrix and

$$\boldsymbol{\psi}^M(\mathbf{k}, \mathbf{n}) = \frac{1}{\sqrt{2}}\boldsymbol{\sigma} f_1 \tag{3}$$
$$+ \frac{1}{2}\left[\frac{3}{k^2}\mathbf{k}(\mathbf{k}\cdot\boldsymbol{\sigma}) - \boldsymbol{\sigma}\right] f_2 + \frac{1}{2}\left[3\mathbf{n}(\mathbf{n}\cdot\boldsymbol{\sigma}) - \boldsymbol{\sigma}\right] f_3$$
$$+ \frac{1}{2k}[3\mathbf{k}(\mathbf{n}\cdot\boldsymbol{\sigma}) + 3\mathbf{n}(\mathbf{k}\cdot\boldsymbol{\sigma}) - 2\boldsymbol{\sigma}(\mathbf{k}\cdot\mathbf{n})] f_4$$

$$+\sqrt{\frac{3}{2}}\frac{i}{k}[\mathbf{k}\times\mathbf{n}]f_5+\frac{\sqrt{3}}{2k}[[\mathbf{k}\times\mathbf{n}]\times\boldsymbol{\sigma}]f_6.$$

Here, $\mathbf{k}$ is the nucleon momentum in the c.m. frame; $\mathbf{n}$ is a unit normal to the light-front plane; $\boldsymbol{\sigma}$ are the Pauli matrices; $w_{\sigma_1(\sigma_2)}$ are the nonrelativistic-nucleon spin functions; and $f_1,...,f_6$ are rotation-invariant functions of kinematical variables determining the deuteron state. We then have

$$k=\sqrt{\frac{m_p^2+\mathbf{p}_T^2}{4x(1-x)}-m_p^2}, \tag{4}$$

$$(\mathbf{n}\cdot\mathbf{k})=\left(\frac{1}{2}-x\right)\sqrt{\frac{m_p^2+\mathbf{p}_T^2}{x(1-x)}},$$

where x is the deuteron-longitudinal-momentum fraction taken away by the proton in the infinite-momentum frame [24, 25]. As in [19, 32], we choose the direction of the z axis to be antiparallel to the deuteron-beam axis, in which case $\mathbf{n}=(0,0,-1)$.

We take the normalization condition for the wave function (3) in the same form as previously in [17]; that is,

$$\int\frac{dxd\mathbf{k}_T}{(2\pi)^3 2x(1-x)}|\psi|^2=\int\frac{d\mathbf{k}}{(2\pi)^3\epsilon(k)}|\psi|^2=1, \tag{5}$$

where $\epsilon(k)=\sqrt{m^2+k^2}$ and m is the nucleon mass.

4. TENSOR ANALYZING POWER FOR THE DEUTERON-FRAGMENTATION PROCESS

For a binary reaction, the analyzing power $T_{\kappa q}$ is given by

$$T_{\kappa q}=\frac{\mathrm{tr}\{\mathcal{M}t_{\kappa q}\mathcal{M}^\dagger\}}{\mathrm{tr}\{\mathcal{M}\mathcal{M}^\dagger\}}, \tag{6}$$

where the operator $t_{\kappa q}$ is determined by the relation

$$\langle m|t_{\kappa q}|m'\rangle=(-1)^{1-m}\langle 1m1-m'|\kappa q\rangle,$$

with $\langle 1m1-m'|\kappa q\rangle$ being a Clebsch–Gordan coefficient; $\mathcal{M}$ is the reaction amplitude; $\mathcal{M}^\dagger$ is the Hermitian conjugate of the amplitude $\mathcal{M}$; and the symbol tr denotes summation over the diagonal elements of the spin matrices. We note that our definition of the averaged operator $t_{\kappa q}$ can differ by a factor from the operators used in other studies. For a more complicated reaction involving a greater number of particles in the final state—this is precisely our case—it is necessary to redefine $T_{\kappa q}$ as

$$T_{\kappa q}=\frac{\int d\tau\,\mathrm{tr}\{\mathcal{M}t_{\kappa q}\mathcal{M}^\dagger\}}{\int d\tau\,\mathrm{tr}\{\mathcal{M}\mathcal{M}^\dagger\}}, \tag{7}$$

where $d\tau$ is an element of phase space over which summation is performed. By way of example, we indicate that, in the case where two particles are emitted from the lower vertex of the diagram, it has the form

$$d\tau=\frac{1}{2(2\pi)^3}\delta^4(p_f-p_i)\frac{d^3p_2}{(2\pi)^3\cdot 2p_{20}}\frac{d^3p_3}{(2\pi)^3\cdot 2p_{30}}, \tag{8}$$

where $\delta^4(p_f-p_i)$ is the four-dimensional delta function of the difference of the total final and the total initial momentum. This definition of the phase space of summation corresponds to the invariant differential cross section $p_{10}d\sigma/d\mathbf{p}_1$ for the emission of particle 1. As a result, the expression for this cross section in the case of deuterons featuring a tensor polarization can be written in the form

$$\frac{p_{10}d\sigma}{d\mathbf{p}_1}=\left(\frac{p_{10}d\sigma}{d\mathbf{p}_1}\right)_{\mathrm{un}}\left(1+\sum\rho_{\kappa q}(2J+1)T_{\kappa q}\right). \tag{9}$$

Here, summation over dummy indices is implied, as usual; $(p_{10}d\sigma/d\mathbf{p}_1)_{\mathrm{un}}$ is the reaction cross section for the case where colliding particles are unpolarized; J is the deuteron spin; and $\rho_{\kappa q}$ are the initial-state spin–tensors, which transform, under rotations, according to the law

$$\rho_{\kappa q}=\sum D^\kappa_{qq'}(R)\rho'_{\kappa q'}, \tag{10}$$

where $\rho'_{\kappa q'}$ is the rank-κ spin–tensor in the coordinate system involving a new axis z' that is obtained from the original z axis upon the rotation R. The spin–tensors are defined in accordance with the following expansion of the spin density matrix:

$$\rho=\sum\rho_{\kappa q}t_{\kappa q}. \tag{11}$$

Within light-front dynamics, the amplitude for the process shown in Fig. 1 can be represented in the form

$$\mathcal{M}_a=\frac{\mathcal{M}(d\to p_1b)}{(1-x)(M_d^2-M^2(k))}\mathcal{M}(bp\to p_2X). \tag{12}$$

The expression

$$\psi(x,p_{1T})=\frac{\mathcal{M}(d\to p_1b)}{(M_d^2-M^2(k))} \tag{13}$$

is nothing but the deuteron wave function in the (b,N) channel. In formula (13), p_{1T} is that component of the momentum p_1 which is orthogonal to the z axis, while the quantity $M^2(k)$ is given by

$$M^2(k)=\frac{m^2+p_{1T}^2}{x}+\frac{b^2+p_{1T}^2}{1-x}, \tag{14}$$

where b^2 is the square of the invariant mass of the exchanged particle.

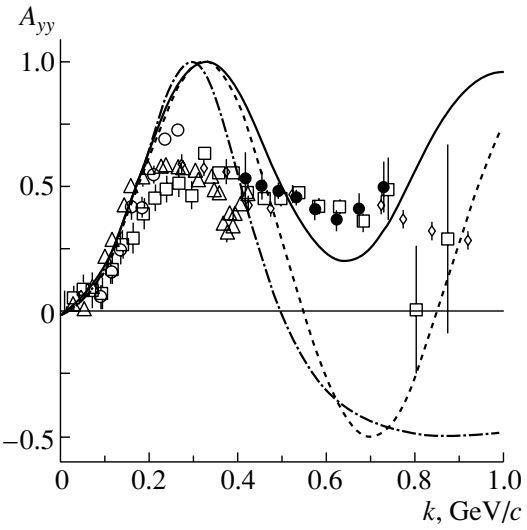

Fig. 2. Tensor analyzing power A_{yy} for deuteron fragmentation accompanied by the emission of protons at zero angle as a function of the internal momentum k. The displayed experimental data were borrowed from (triangles) [2], (boxes) [5], (diamonds) [6], and [7] for (open circles) a ^{1}H target and (closed circles) a ^{12}C target. The calculations were performed with the deuteron wave functions for the (dash-dotted curve) Paris [33] and (dashed curve) Bonn B [34] potentials. The solid curve was calculated with Karmanov's relativistic deuteron wave function [27].

For the ensuing calculations to be more compact, we introduce the matrix $\rho_{\mu\mu'}(\kappa, q)$ in the spin space of the nucleon b for the deuteron polarization characterized by the indices (κ, q),

$$\rho_{\mu\mu'}(\kappa,q) = \sum_{\nu,M,M'} \psi^M(\nu,\mu)(-1)^{1-M'} \times \langle 1M1-M'|\kappa q\rangle \psi^{*M'}(\nu,\mu'), \quad (15)$$

or, equivalently, in the symbolic form

$$\rho(\kappa,q) = \langle \psi t_{\kappa q}\psi^*\rangle. \quad (16)$$

It goes without saying that, like a conventional density matrix, this matrix can be represented in the form

$$\rho(\kappa,q) = \frac{1}{2}\rho_0(\kappa,q)(1+\mathbf{P}\cdot\boldsymbol{\sigma}), \quad (17)$$

where $\mathbf{P}$ is an analog of the polarization vector of a nucleon in the deuteron for a given deuteron polarization characterized by the indices (κ, q), $\boldsymbol{\sigma}$ are the Pauli matrices, and

$$\rho_0(\kappa,q) = \mathrm{tr}\{\rho(\kappa,q)\} = \sum \psi^M(\nu,\mu)\langle 1M1-M'|\kappa,q\rangle\psi^{*M'}(\nu,\mu'). \quad (18)$$

Formulas (15) and (16) are of a general character—one can substitute any spin–tensors into them. However, it is the tensor analyzing powers T_{20} and $A_{yy} = -T_{20}/\sqrt{2} - \sqrt{3}T_{22}$ that are usually measured in experiments. In view of this, it is assumed below that, in expressions (15) and (16), averaging is performed with the weights corresponding to T_{20} and A_{yy}.

Further, we denote by $\mathbf{p}_1$ the momentum of the detected proton, irrespective of the vertex from which it originates, and use the invariant differential cross section in the form

$$\frac{p_{10}d\sigma}{d\mathbf{p}_1} = \frac{(2\pi)^4}{4I(d,p)}\int \mathrm{tr}\{\mathcal{M}\rho_i\mathcal{M}^\dagger\}d\tau, \quad (19)$$

where ρ_i is the spin density matrix for the initial state and $I(d,p)$ is the invariant flux of deuterons incident on protons. As a result, we obtain

$$T_{2q}\left(\frac{p_{10}d\sigma}{d\mathbf{p}_1}\right)_{\mathrm{un}} = \frac{1}{2(2\pi)^3} \times \left\{\frac{I(b,p)}{I(d,p)(1-x)^2}\rho_0(2,q)\sigma(bp\to p_2X) + \int\frac{dyd\mathbf{p}_{2T}}{2y(1-y)}\frac{I(b,p)}{(1-y)I(d,p)}\rho_0(2,q) \times \frac{p_{20}d\sigma}{d\mathbf{p}_2}(bp\to p_2X)[1+\mathbf{P}\cdot\langle\boldsymbol{\sigma}\rangle]\right\}, \quad (20)$$

where $\langle\boldsymbol{\sigma}\rangle$ is the vector analyzing power for nucleon–nucleon scattering; $\sigma(bp\to p_2X)$ is the total cross section for nucleon–nucleon scattering (it is independent of polarization); and $\mathbf{P}$ is the polarization vector of a nucleon in the deuteron, its polarization being characterized by the indices (κ, q),

$$\mathbf{P} = \frac{\mathrm{tr}\{\boldsymbol{\sigma}\cdot\rho(\kappa,q)\}}{\rho_0(\kappa,q)}. \quad (21)$$

The first term in the braced expression on the right-hand side of (20) corresponds to the detection of a spectator proton, while the second term corresponds to the detection of a proton that underwent rescattering on a target proton.

The density matrices $\rho_0(\kappa, q)$ depend on the type of averaging in expression (15). For the analyzing powers T_{20} and T_{22}, they are given, respectively, by

$$\rho_0(2,0) = \frac{1}{\sqrt{6}}(\boldsymbol{\psi}\cdot\boldsymbol{\psi}^\dagger - 3\psi_z\cdot\psi_z) = -3f_3^2 - 12f_3f_4z + 3f_2^2z^2 - 12f_4^2z^2 - 6f_2^2z^4 - 1.5f_2^2(1-z^2) - 4.5f_4^2(1-z^2) + 3f_5^2(1-z^2) - 15.5885f_4f_6(1-z^2) - 1.5f_6^2(1-z^2) - 3f_2^2z^2(1-z^2) + 3f_2^2(1-z^2)^2 - 8.48528f_1f_3 - 16.9706f_1f_4z - 4.24264f_1f_2z^2 - 4.24264f_1f_2z^4 + 2.12132f_1f_2(1-z^2) - 2.12132f_1f_2z^2(1-z^2) + 2.12132f_1f_2(1-z^2)^2 \quad (22)$$

$$
\begin{aligned}
&- 6f_2f_3z^4 - 12f_2f_4z^5 + 4.5f_2f_3(1-z^2)\\
&+ 4.5f_2f_4z(1-z^2) - 7.79423f_2f_6z(1-z^2)\\
&- 7.5f_2f_3z^2(1-z^2) - 19.5f_2f_4z^3(1-z^2)\\
&- 7.79423f_2f_6z^3(1-z^2) - 1.5f_2f_3(1-z^2)^2\\
&- 7.5f_2f_4z(1-z^2)^2 - 7.79423f_2f_6z(1-z^2)^2
\end{aligned}
$$

and by

$$
\begin{aligned}
\rho_0(2,2) &= \frac{1}{2}(\psi_x\cdot\psi_x^\dagger - \psi_y\cdot\psi_y^\dagger) \qquad (23)\\
&= 1.06066f_1f_2(1-z^2) - 0.75f_2^2(1-z^2)\\
&+ 2.25f_4^2(1-z^2) - 1.5f_5^2(1-z^2)\\
&- 2.59808f_4f_6(1-z^2) + 0.75f_6^2(1-z^2)\\
&+ 1.06066f_1f_2z^2(1-z^2) + 1.5f_2^2z^2(1-z^2)\\
&+ 1.06066f_1f_2(1-z^2)^2 + 1.5f_2^2(1-z^2)^2\\
&- 0.75f_2f_3(1-z^2) + 0.75f_2f_4z(1-z^2)\\
&- 1.29904f_2f_6z(1-z^2) - 0.75f_2f_3z^2(1-z^2)\\
&+ 0.75f_2f_4z^3(1-z^2) - 1.29904f_2f_6z^3(1-z^2)\\
&- 0.75f_2f_3(1-z^2)^2 + 0.75f_2f_4z(1-z^2)^2\\
&- 1.29904f_2f_6z(1-z^2)^2.
\end{aligned}
$$

In order to calculate the analyzing power A_{yy}, the density matrix $\rho_0(y,y)$ can be derived from the relation

$$\rho_0(y,y) = -\frac{1}{\sqrt{2}}\rho_0(2,0) - \sqrt{3}\rho_0(2,2).$$

The invariant differential cross section for an unpolarized beam in formula (20) is given by

$$
\begin{aligned}
\left(\frac{p_{10}d\sigma}{d\mathbf{p}_1}\right)_{\text{un}} &= \frac{1}{2(2\pi)^3}\left\{\frac{I(b,p)}{I(d,p)(1-x)^2}\rho_0\right. \qquad (24)\\
&\times\sigma(bp\to p_2X) + \int\frac{dyd\mathbf{p}_{2T}}{2y(1-y)}\frac{I(b,p)}{(1-y)I(d,p)}\rho_0\\
&\left.\times\frac{p_{20}d\sigma}{d\mathbf{p}_2}(bp\to p_2X)\right\},
\end{aligned}
$$

where

$$
\begin{aligned}
\rho_0 &= 3[f_1^2 + f_2^2 + f_3^2 + f_2f_3(3z^2-1) \qquad (25)\\
&+ 4f_4(f_2+f_3)z + f_4^2(z^2+3) + (f_5^2+f_6^2)(1-z^2)].
\end{aligned}
$$

5. RESULTS OF THE CALCULATIONS AND DISCUSSION

In order to calculate the tensor analyzing power by formula (20), it is necessary to know the invariant differential cross sections $p_{20}d\sigma(bp\to p_2X)/d\mathbf{p}_2$ for processes proceeding in the lower vertex of the pole diagram. Moreover, it should be borne in mind that particle b is off the mass shell. In the calculations, this circumstance was taken into account through the use of analytic continuations of the parametrizations of $d\sigma(s',t')/dt'$ to s' and t' values defined for $b^2\neq m^2$. In doing this, we treated the contributions of the processes $pp\to pp$, $np\to pn$, $Np\to p\Delta$, and $Np\to pN\pi$ (up to $N\pi$ invariant masses of 1.5 GeV/c^2) in accordance with the parametrizations presented in [17].

The majority of the experiments with polarized deuteron beams in Saclay and Dubna were devoted to measuring the tensor analyzing power T_{20} in $A(d,p)X$ reactions accompanied by the emission of protons at zero angle. The results obtained by calculating the parameter $A_{yy}(0^\circ)$ for this process with Karmanov's wave function (3) are represented by the solid curve in Fig. 2 (it should be recalled that, at zero angle, $A_{yy} = -T_{20}/\sqrt{2}$).

One can see that, in contrast to what we have in the calculations with standard nonrelativistic deuteron wave functions [33, 34], the solid curve does not change sign and is in better agreement with experimental data in the region of k between 0.4 and 0.8 GeV/c. In all probability, the discrepancy between the results of the calculations and experimental data in the region of k around 0.3 GeV/c cannot be removed without going beyond the pole mechanism, this region corresponding precisely to those values of kinematical variables in backward elastic deuteron–proton scattering at which the cross section given for this process by the triangle diagram is expressed in terms of the cross section for the reaction $NN\to d\pi$ (the latter cross section has a resonance character here).

In Fig. 3, the results of the calculations are contrasted against experimental data on the tensor analyzing power in the reaction where the fragmentation of 4.5-GeV/c deuterons on beryllium nuclei is accompanied by the emission of protons at an angle of 80 mrad. One can see once again that the calculations with Karmanov's wave function provide a qualitatively correct picture of the general behavior of the parameter A_{yy} as a function of the detected-proton momentum, but that the curves calculated by using standard deuteron wave functions are in a sharp contradiction with experimental data, changing sign at a proton momentum of about 3.2 GeV/c.

Finally, Fig. 4 presents experimental data on the parameter A_{yy} in the inclusive breakup of 9-GeV/c deuterons on carbon nuclei for the case where the emitted protons are detected at an angle of 85 mrad. Also given in this figure are the results obtained by calculating this parameter with various deuteron wave functions.

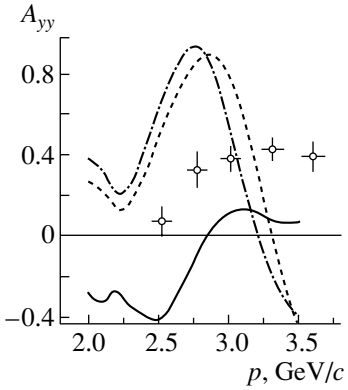

Fig. 3. Tensor analyzing power A_{yy} for the reaction where the fragmentation of 4.5-GeV/c deuterons is accompanied by the emission of protons at an angle of 80 mrad versus the detected-proton momentum. The displayed experimental data were borrowed from [12]. The notation for the curves is identical to that in Fig. 2.

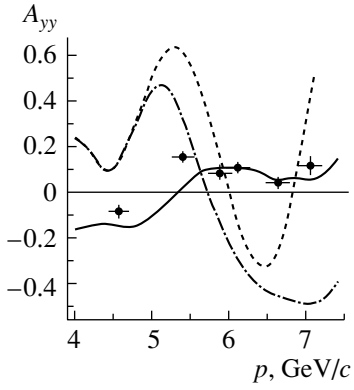

Fig. 4. Tensor analyzing power A_{yy} for the reaction where the fragmentation of 9-GeV/c deuterons is accompanied by the emission of protons at an angle of 85 mrad versus the detected-proton momentum. The displayed experimental data were borrowed from [11]. The notation for the curves is identical to that in Fig. 2.

It can be seen that the general trend revealed in discussing the data in Figs. 2 and 3 manifests itself here even more sharply: the momentum dependence calculated with the relativistic deuteron wave function from [27] is very close to the experimental values, whereas the calculations with the standard nonrelativistic wave functions lead to results that dramatically deviate from the experimental data.

Since the relativistic deuteron wave function from [27] has a rather complicated form, there arises the question of which terms in this function are crucial in qualitatively describing experimental data on the tensor analyzing power for relativistic-deuteron fragmentation on nuclei at high transverse momenta of protons. In order to answer this question, we have calculated the parameter A_{yy} for the reaction $^{12}\mathrm{C}(d,p)X$ at 9 GeV/c for the proton emission angle of 85 mrad, successively including in the calculation the terms $f_2,\ldots,f_6$ of the function in (3). The results are shown in Fig. 5.

From Fig. 5, one can see that the dominant contribution to the quantity A_{yy} comes from the first two terms of the function in (3); the remaining terms only lead to corrections, whose role becomes more pronounced with increasing momentum. It was shown in [27, 31] that, in the nonrelativistic limit, the functions f_1 and f_2 correspond to the S and D components of the deuteron wave function. It follows that, in a moving deuteron, the relationship between the longitudinal and transverse components of the internal momentum differs significantly from that which holds either in the nonrelativistic case or in the case where relativistic effects are taken into account in accordance with the approaches developed in [35, 19, 23]; in all probability, the method proposed in [27, 30, 31] for treating the region of relativistic momenta reflects this distinction correctly.

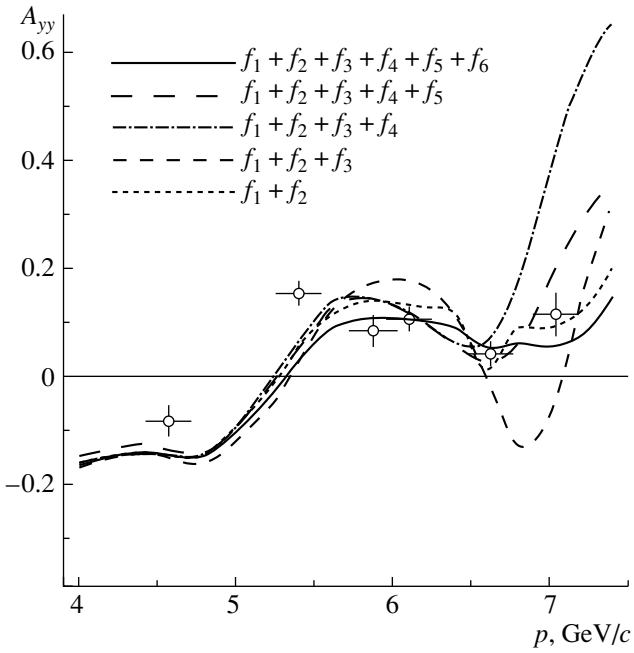

Fig. 5. Tensor analyzing power A_{yy} for the reaction $^{12}\mathrm{C}(d,p)X$ at a momentum of 9 GeV/c for the proton emission angle of 85 mrad versus the detected-proton momentum [11]. The different curves here correspond to the successive inclusion of the terms f_i of the relativistic deuteron wave function from [27] in the calculation.

6. CONCLUSION

The present investigation has provided sufficient grounds to conclude that, in contrast to standard nonrelativistic wave functions, the relativistic

deuteron wave function obtained in [27] within light-front dynamics makes it possible to reproduce basic features of experimental data even on the basis of the simple pole mechanism. In our opinion, this is due to the fact that, in the approach developed in [27, 30, 31], there arises a new relationship between the longitudinal and transverse components of the intranuclear-motion momentum, a relationship that is different from that which is dictated by a superposition of S and D waves in nonrelativistic deuteron wave functions. This effect was already discussed in [31] for the example of the Wick–Cutkosky model, and it was shown there that even a spherically symmetric S-wave system of two particles in light-front dynamics becomes dependent on angles. In all probability, this is a manifestation of a close relation in the relativistic region between the internal motion of a system and its motion as a discrete unit.

Our present results may have far-reaching consequences both for obtaining deeper insight into the structure of the deuteron at short distances and for interpreting mechanisms of relativistic-deuteron fragmentation. Indeed, it turns out, quite unexpectedly, that, within light-front quantum mechanics, the deuteron can be considered as a two-nucleon system up to short relative distances corresponding to internal-nucleon momenta of $k \sim 0.5$–0.8 GeV/c. A similar conclusion was also drawn in the studies reported in [16] and devoted to measuring the momentum spectra of 9-GeV/c deuterons in the region of proton transverse momenta between 0.5 and 1 GeV/c; it was indicated there that, in all probability, the nucleons of the deuteron preserve their individuality up to relative momenta of about 1 GeV/c.

The second important conclusion that can be drawn from the present investigation is that, in relativistic-deuteron fragmentation, relativistic effects become operative rather fast. Our results suggest that the simplest way to take them into account is to consider the reaction mechanism within light-front quantum mechanics without introducing additional degrees of freedom.

ACKNOWLEDGMENTS

This work was supported in part by the Russian Foundation for Basic Research (project no. 03-02-16224).

REFERENCES

1. J. Arvieux *et al.*, Phys. Rev. Lett. **50**, 19 (1983); Nucl. Phys. A **431**, 613 (1984).
2. C. F. Perdrisat *et al.*, Phys. Rev. Lett. **59**, 2840 (1987); V. Punjabi *et al.*, Phys. Rev. C **39**, 608 (1989).
3. E. Cheung *et al.*, Phys. Lett. B **284**, 210 (1992).
4. V. Punjabi *et al.*, Phys. Lett. B **350**, 178 (1995).
5. V. G. Ableev *et al.*, Pis'ma Zh. Éksp. Teor. Fiz. **47**, 558 (1988) [JETP Lett. **47**, 649 (1988)]; Kratk. Soobshch. OIYaI, No. 4[43]-90, 5 (1990).
6. T. Aono *et al.*, Phys. Rev. Lett. **74**, 4997 (1995).
7. L. S. Azhgirey *et al.*, Phys. Lett. B **387**, 37 (1996).
8. A. A. Nomofilov *et al.*, Phys. Lett. B **325**, 327 (1994).
9. B. Kuehn *et al.*, Phys. Lett. B **334**, 298 (1994); L. S. Azhgirey *et al.,* Kratk. Soobshch. OIYaI, No. 3[77]-96, 23 (1996).
10. L. S. Azhgirey *et al.*, Phys. Lett. B **391**, 22 (1997); Yad. Fiz. **61**, 494 (1998) [Phys. At. Nucl. **61**, 432 (1998)].
11. S. V. Afanasiev *et al.*, Phys. Lett. B **434**, 21 (1998).
12. V. P. Ladygin *et al.*, Few-Body Syst. **32**, 127 (2002); L. S. Azhgirey *et al.*, Yad. Fiz. **66**, 719 (2003) [Phys. At. Nucl. **66**, 690 (2003)].
13. Y. Nambu and G. Jona-Losinio, Phys. Rev. **122**, 345 (1961).
14. A. N. Manochar, hep-ph/9606222.
15. V. G. Ableev *et al.*, Nucl. Phys. A **393**, 491 (1983); **411**, 541(E) (1983); Pis'ma Zh. Éksp. Teor. Fiz. **37**, 233 (1983).
16. L. S. Azhgirey *et al.*, Nucl. Phys. A **528**, 621 (1991); L. S. Azhgireĭ *et al.*, Yad. Fiz. **46**, 1134 (1987) [Sov. J. Nucl. Phys. **46**, 661 (1987)]; **53**, 1591 (1991) [**53**, 977 (1991)].
17. L. S. Azhgireĭ, S. V. Razin, and N. P. Yudin, Yad. Fiz. **46**, 1657 (1987) [Sov. J. Nucl. Phys. **46**, 988 (1987)].
18. L. S. Azhgirey, M. A. Ignatenko, and N. P. Yudin, Z. Phys. A **343**, 35 (1992).
19. L. S. Azhgirey and N. P. Yudin, Yad. Fiz. **57**, 160 (1994) [Phys. At. Nucl. **57**, 151 (1994)].
20. A. P. Kobushkin, Phys. Lett. B **421**, 53 (1998).
21. F. Gross, Phys. Rev. D **10**, 223 (1974); W. W. Buck and F. Gross, Phys. Rev. D **20**, 2361 (1979).
22. L. Kaptari *et al.*, Phys. Lett. B **351**, 400 (1995).
23. Yu. N. Uzikov, Fiz. Élem. Chastits At. Yadra **29**, 1405 (1998).
24. I. A. Schmidt and R. Blankenbecler, Phys. Rev. D **15**, 3321 (1977).
25. Ch.-Y. Wong and R. Blankenbecler, Phys. Rev. C **22**, 2433 (1980).
26. D. Sivers, S. J. Brodsky, and R. Blankenbecler, Phys. Rep. **23**, 1 (1976).
27. J. Carbonell and V. A. Karmanov, Nucl. Phys. A **581**, 625 (1995).
28. G. Miller, Prog. Part. Nucl. Phys. **45**, 83 (2000).
29. P. A. M. Dirac, Rev. Mod. Phys. **21**, 392 (1949).
30. V. A. Karmanov and A. V. Smirnov, Nucl. Phys. A **575**, 520 (1994).
31. J. Carbonell *et al.*, Phys. Rep. **300**, 215 (1998).
32. L. S. Azhgirey and N. P. Yudin, Yad. Fiz. **63**, 2280 (2000) [Phys. At. Nucl. **63**, 2184 (2000)].
33. M. Lacombe *et al.*, Phys. Lett. B **101B**, 139 (1981).
34. R. Machleidt *et al.*, Phys. Rep. **149**, 1 (1987).
35. W. N. Polizou, Ann. Phys. (N.Y.) **193**, 367 (1989).

Translated by A. Isaakyan

Physics of Atomic Nuclei, Vol. 68, No. 1, 2005, pp. 168–170. Translated from Yadernaya Fizika, Vol. 68, No. 1, 2005, pp. 172–174.

FUTURE PUBLICATIONS

Inclusive Formation of π^0 Mesons in dC and dCu Interactions at a Momentum of 4.5 GeV/c per Nucleon

Kh. U. Abramyan, M. A. Kozhin, G. L. Melkumov, M. N. Khachaturyan, and A. G. Khudaverdyan

Cross sections for the inclusive production of π^0 mesons in $d + \mathrm{C} \to \pi^0 + x$ and $d + \mathrm{Cu} \to \pi^0 + x$ reactions at a momentum of 4.5 GeV/c per nucleon are measured for the kinematic region specified by the inequalities $\theta_\pi \leq 16^\circ$ and $E_\pi \geq 2$ GeV (in the laboratory frame). The dependence of the exponent n in the parametrization $Ed^3\sigma/d^3p \sim A^n$ on the cumulative numbers X in the interval of $0.6 \leq X \leq 1.8$ and on the square of the transverse momentum in the interval $0.04 \leq P_t^2 \leq 0.40$ $(\mathrm{GeV}/c)^2$ is obtained from the ratio of the cross sections for the generation of π^0 mesons on carbon and copper nuclei. The probabilities of the formation of six-quark configurations in ^{2}H, ^{4}He, and ^{12}C nuclei are estimated. On the basis of statistics including more than 40 000 π^0 mesons, the double-differential cross sections for the $d + \mathrm{C} \to \pi^0 + x$ reactions are determined for the first time.

Effects of Nuclear Deformations in Dinuclear Systems: Application to the Fission Process

A. V. Andreev, G. G. Adamyan, N. V. Antonenko, S. P. Ivanova, and W. Scheid

The relative yields of fission fragments and the mean values and variances of the distributions of the total kinetic energy of fragments are described on the basis of a refined scission-point model. It is shown that the potential energy of a prescission configuration as a function of fragment-deformation parameters has several minima at fixed charge and mass numbers of fragments. Fission from these minima results in a relative enhancement of the yield of fragments at the corresponding values of the total kinetic energy and in the appearance of a fine structure in the mass–energy distribution, this structure being different from the fine structure induced by the even–odd effect.

Inclusive Production of Deuterons in ^{16}Op Collisions at a Momentum of 3.25 GeV/c per Nucleon

E. Kh. Bazarov, V. V. Glagolev, K. G. Gulamov, M. Yu. Kratenko, S. L. Lutpullaev, K. Olimov, Kh. Sh. Khamidov, A. A. Yuldashev, and B. S. Yuldashev

For the first time, experimental data on the inclusive production of deuterons in ^{16}Op collisions at high energies are obtained under conditions of 4π geometry. In the deuteron-momentum spectrum in the oxygen-nucleus rest frame, an irregularity is found in the region $0.40 \leq p \leq 0.55$ GeV/c, and reasons that could be responsible for its appearance are discussed. The mean multiplicities of secondary fragments are correlated with the presence of a deuteron in an event, these correlations being positive for $z_f \leq 4$ fragments and negative for $5 \leq z_f \leq 7$ fragments (this is likely to be due to baryon-charge conservation).

Color Fluxes in the Process $gg \to B_c + c + \bar{b}$

A. V. Berezhnoy

The contributions of various color fluxes to the cross section for the gluonic production of B_c mesons are calculated, which is necessary for the simulation of events involving B_c mesons that is based on the PYTHIA package, since the method of hadronization of final partons and hadronic residues that is used in the PYTHIA code depends on the color-flux type. A modified method of partition into color fluxes is proposed.

1063-7788/05/6801-0168$26.00

Analysis of the Phase Time of Cold-Neutron Tunneling through a Neutron Interference Filter

A. K. Zaichenko and V. S. Olkhovsky

Explicit expressions for the energy dependence of the transmission factor for the tunneling of particles through two rectangular barriers and the respective tunneling phase time are obtained in the resonance region. The resonance half-width and the neutron-tunneling phase time at the resonance are calculated.

Quantum and Thermodynamic Features of Spontaneous and Low-Energy Induced Fission of Nuclei

S. G. Kadmensky

It is shown that the coordination of A. Bohr's concept of transition fission states with the properties of Coriolis interaction is possible if an axially symmetric fissile nucleus near the point of scission into fission products remains cold despite a nonadiabatic character of nuclear collective deformation motion. The quantum and thermodynamic properties of various stages of binary and ternary fission after the descent of a fissile nucleus from an external saddle point are investigated on the basis of the quantum theory of fission. The important role of superfluid and nucleon–nucleon correlations in the formation of fission products and in the classification of fission transitions is shown. The distributions of thermalized primary fission fragments with respect to spins and their projections onto the symmetry axis of the fissile nucleus and fission fragments are constructed, the properties of prompt neutrons and photons emitted by these fragments being determined by these distributions. A new nonevaporation mechanism of the formation of third particles in the ternary fission of nuclei is proposed. This mechanism is associated with the transitions of third particles from cluster states of the fissile-nucleus neck to high-energy states under shakeup effects, which are caused by a nonadiabatic character of nuclear collective deformation motion.

Alpha Particles Accompanying the Weak Decay of ${}^{10}_{\Lambda}$Be and ${}^{10}_{\Lambda}$B Hypernuclei

L. Majling, V. A. Kuzmin, and T. V. Tetereva

The possibilities of studying in detail weak ΛN interaction in ${}^{10}_{\Lambda}$Be and ${}^{10}_{\Lambda}$B hypernuclei, which stand out owing to their $\alpha\alpha N\Lambda$ cluster structure, are discussed. The detection of a few groups of correlated α-particle pairs furnishes information about decays to specific states of a final nucleus (^{8}Be*, ^{8}Li, ^{8}B), thereby opening the way to a phenomenological analysis of the weak decays of p-shell hypernuclei. The ratios of the intensities of individual groups—it is planned to measure them by using the JINR nuclotron—will become a useful criterion for selecting a suitable model of weak ΛN interaction. A brief review of the modern state of the physics of hypernuclei is given.

Decay $\phi(1020) \to \gamma f_0(980)$: Analysis within the Nonrelativistic-Quark-Model Approach

A. V. Anisovich, V. V. Anisovich, V. N. Markov, V. A. Nikonov, and A. V. Sarantsev

The possibility of adequately describing the processes $\phi(1020) \to \gamma\pi\pi$ and $\phi(1020) \to \gamma f_0(980)$ within the nonrelativistic quark model under the assumption that $f_0(980)$ is predominantly the quark–antiquark system is demonstrated. Various mechanisms of radiative decay—that is, the emission of a photon by a constituent quark (additive quark model) and a charge-exchange current—are considered. The status of the threshold theorem applied to the reactions being studied—namely, the behavior of the decay amplitude for $M_{\pi\pi} \to m_\phi$ and $m_{f_0} \to m_\phi$—is also discussed. In conclusion, arguments in favor of the $q\bar{q}$ origin of $f_0(980)$ are given.

Alpha-Cluster States in ^{18}O

V. Z. Goldberg, K.-M. Källman, T. Lönnroth, P. Manngård, and B. B. Skorodumov

The excitation function for elastic α-particle scattering on ^{14}C was measured in the laboratory-energy range 16.3–19.2 MeV by using a backscattering technique with a thick target. These data were analyzed, together with the old low-energy data of G.L. Morgan *et al.,* in the framework of the R-matrix formalism. Spin-parity assignments were made for 32 states in ^{18}O in the excitation range 9–20 MeV. The estimations

of the widths of the states are also presented. The 0^+ and 0^- α-cluster bands appeared to be well separated by 5.6 MeV (as in ^{16}O and ^{20}Ne). We did not find a confirmation of the existence of negative-parity molecular states proposed by M. Gai *et al.* We observed the effect of doubling of α-cluster levels in ^{18}O (it is similar to that found in ^{22}Ne).

Mass Splittings of Nuclear Isotopes within the Chiral Soliton Approach

V. B. Kopeliovich, A. M. Shunderuk, and G. K. Matushko

The differences in the masses of isotopes with atomic numbers between about 10 and about 30 can be described within the chiral soliton model in satisfactory agreement with data. The rescaling of the model is necessary for this purpose—the reduction of the Skyrme constant by about 30%, providing the nuclear variant of the model. The asymmetric term in Weizsäcker–Bethe–Bacher mass formula for nuclei can be obtained as the isospin-dependent quantum correction to the energy of a nucleus. Some predictions for the binding energies of neutron-rich isotopes are made in this way—for example, from ^{16}Be or ^{19}B to ^{31}Ne or ^{32}Na. Neutron-rich nuclides with high isospin values are unstable with respect to decay due to strong interactions. The $SK4$ (Skyrme) variant of the model, as well as the $SK6$ variant (sixth-order term in the Lagrangian as a soliton stabilizer), is considered, the rational-map approximation being used to describe multi-Skyrmions.

Subthreshold ϕ-Meson Production and Medium Effects in Proton–Nucleus Reactions

E. Ya. Paryev

Within the spectral-function approach, the direct production and decay are studied via the dikaon (dimuon) channel of ϕ mesons in the interactions of 2.4- and 2.7-GeV protons with light and medium-mass target nuclei. It is shown that the K^+K^- ($\mu^+\mu^-$) invariant-mass distribution consists of two components, which correspond to ϕ decays outside and inside the target nucleus. The first (narrow) component has the free ϕ width, while the second (broad) component is distorted by nuclear-matter effects due to resonance-nucleon scattering and a possible in-medium modification of kaons and ρ mesons at finite baryon density. The relative strength of the inside and outside components is analyzed within various scenarios for the ϕ width and momentum cut. It is demonstrated that the width of the resulting dimuon invariant mass distribution on medium nuclei is almost twice as broad as the free ϕ width if the total in-medium width of ϕ is used and if the respective cutoff for the ϕ 3-momentum is applied, whereas the resulting dikaon invariant-mass distribution has an insignificant sensitivity to the in-medium properties of ϕ owing to the strong absorption of the K^- in surrounding nuclear matter. On the other hand, because the K^+ and K^- are distorted on their paths out of the target nucleus mainly because of the hadronic kaon potential, the latter is broadened and shifted to higher invariant masses. This means that the measurement of such broadening would give an additional piece of evidence for the modification of kaon and antikaon properties in the nuclear medium.

Physics of Atomic Nuclei, Vol. 68, No. 1, 2005, pp. 21–32. Translated from Yadernaya Fizika, Vol. 68, No. 1, 2005, pp. 23–34.

NUCLEI
Experiment

Properties of Products Originating from the Interaction of 35-MeV/nucleon ^{7}Li Ions with Pb Nuclei

N. A. Demekhina*, G. S. Karapetyan[1)], S. M. Lukyanov[2)], Yu. E. Penionzhkevich[2)], N. K. Skobelev[2)], and A. B. Yakushev[2)]

Yerevan Physics Institute, ul. Brat'ev Alikhanian 2, Yerevan, 375036 Armenia

Received May 6, 2003

Abstract—The results are presented that were obtained by measuring and analyzing the yields and kinematical features of radioactive products of the reactions initiated in a lead target by lithium ions accelerated to an energy of 35 MeV per nucleon. The cross sections, charge and mass distributions, and kinematical and energy features of various reaction products associated with the fission and the evaporation channels of the decay of excited nuclei are determined. Quantities that are calculated in the present study include the momenta and kinetic energies of residual nuclei, as well as the momentum transfer and the excitation energy of intermediate nuclear systems formed upon complete and incomplete fusion. On the basis of an analysis of data obtained in our experiment, the total cross section for nuclear interaction and partial widths with respect to various channels of the decay of intermediate compound nuclei are determined in the energy range being investigated. © *2005 Pleiades Publishing, Inc.*

INTRODUCTION

Investigation of heavy-fragment production under the effect of accelerated ions is of great interest not only for exploring reaction mechanisms but also for obtaining deeper insights into the regularities of the formation of residual nuclei at intermediate energies. The results of such investigations can be used in considering a number of applied problems and in creating ion sources, as well as in exploring fundamental regularities of the formation of superheavy elements.

Previous investigations in the realms of ion–nucleus interaction revealed that, at low energies (less than 10 MeV per nucleon), the main interaction channel is characterized by the total fusion of nuclei and the formation of a compound nucleus. Its decay, dominated by the mean nuclear field, is adequately described on the basis of various statistical models [1–3]. The growth of the projectile-nucleus energy is accompanied by an increase in the probability of the formation of fast particles and light nuclei emitted in the direction of the incident-beam axis. This observation is interpreted by various authors as a manifestation of peripheral processes, incomplete fusion, preequilibrium emission, etc. A feature common to these products is that their production is of a spectator character, the projectile energy–momentum not being completely transferred to the target nucleus [4, 5]. At energies explored in the present study, the incomplete fusion of nuclei must occur with a high probability; however, data on the probability of the formation of intermediate nuclear systems, as well as on the properties of various decay channels and of the products originating from these channels, are scanty and fragmentary, this hindering the systematization of the data and the application of model concepts. The data reported in the literature for the scattering of ^{7}Li ions on Pb nuclei refer to the total interaction cross section measured by the beam-absorption method at energies in the range 30–60 MeV per nucleon [6].

Our present investigations of the probability of the formation of various products originating from the decay of intermediate excited states are of interest for understanding the mechanisms of relevant reactions and of energy dissipation in the processes of complete and incomplete fusion and for determining the probabilities of various deexcitation channels. For heavy nuclei, the fission of intermediate states, which are characterized by a broad distribution with respect to masses, excitation energies, and angular momenta, is the most probable decay channel in the energy range investigated here. An analysis of the charge and mass distributions of fission fragments makes it possible to draw conclusions on the properties of fissile nuclei. Spallation reactions accompanied by the evaporation of neutrons, charged particles, and light nuclei and

[1)]Yerevan State University, ul. A. Manukian 1, Yerevan, 375049 Armenia.
[2)]Joint Institute for Nuclear Research, Dubna, Moscow oblast, 141980 Russia.
*e-mail: nina@lx2.yerphi.am

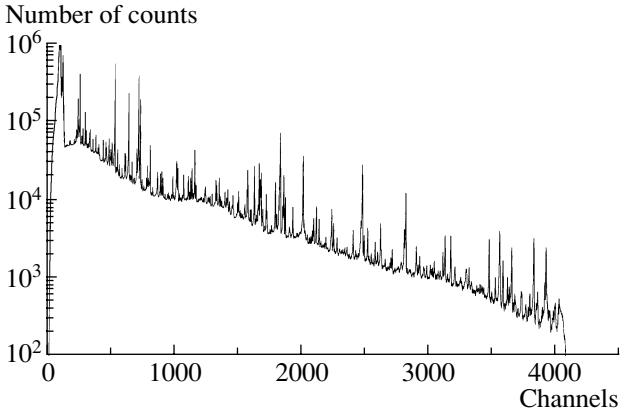

Fig. 1. Gamma spectrum of the activity induced in a ^{nat}Pb target (the time of the measurements was 4 hours, and the source–detector distance was 5 cm).

by the formation of products in the near-target mass region are competing processes at these energies. Therefore, information about processes proceeding at the nuclear surface in peripheral collisions can be obtained by measuring the yields of residual nuclei whose masses lie around the target mass.

Basic regularities of nucleus–nucleus reactions are investigated by analyzing the properties of both fast light products emitted from the target and heavy nuclear residues. In the latter case, measurement of an induced activity is the simplest and most informative method for separating interaction channels and for studying the charge, mass, and momentum distributions of nuclei produced in the target and recoiled into catch foils. The momentum and energy transfers are quantities that furnish information about the character of collisions. These data make it possible to estimate the relationship between complete- and incomplete-fusion processes and to explore conditions of the possible saturation of nuclear excitation [7, 8].

In the present study, the cross sections for the formation of heavy radioactive products were determined on the basis of a gamma-spectrometric analysis of an induced activity. Information about unmeasurable reaction products was extracted by using the approximations presented in the literature for the charge and mass distributions of residual nuclei. Data on the total and partial cross sections for the interaction in the energy region being studied were assessed via summation along the isobaric-distribution curve.

Relying on the measured fractions of radioactive products emitted into catch foils and employing the formalism of the two-step vector model, we determined the kinematical parameters of residual nuclei and the momentum features of intermediate nuclear systems [9–12]. The results of our calculations are discussed within the concept dealing with the probabilities of the complete and incomplete fusion of interacting nuclei in the energy region investigated here [13, 14].

EXPERIMENTAL PROCEDURE

A beam of ^{7}Li ions accelerated to an energy of 35 MeV per nucleon at the U-400M cyclotron of the Joint Institute for Nuclear Research (JINR, Dubna, Russia) was used to irradiate a target. The target was prepared in the form of an assembly of seven lead foils 12 μm thick having a natural isotopic composition (^{nat}Pb: 1.48% ^{204}Pb, 23.6% ^{206}Pb, 22.6% ^{207}Pb, and 52.3% ^{208}Pb). For catch foils, we took aluminum plates 20 μm thick arranged on the two sides of the target in the direction orthogonal to the beam axis. The whole system was placed within the vacuum chamber of the beam guide. The irradiation was performed for 40 min at a beam intensity of 30 nA (about 10^{10} nuclei per second).

The measurements of the spectra of gamma rays emitted in the decays of radioactive reaction products began 10 min after the completion of the irradiation and lasted five months. In the measurements, we used a detector from high-purity germanium, its resolution being 0.23% at an energy of 1330 keV. The dependence of the gamma-ray-detection efficiency on the energy and on the geometry of our experimental facility was measured with the aid of ^{57}Co, ^{60}Co, ^{154}Eu, ^{152}Eu, and ^{133}Ba reference sources.

In the process of our measurements, we were able to identify radioactive products in more than 20 spectra of ^{nat}Pb and in 40 spectra associated with recoil nuclei in the catch aluminum foils. Figures 1 and 2 display the spectra of the irradiated ^{nat}Pb foils and the spectra of recoiling nuclei in the catch aluminum foils. The main problem in identifying reaction products by the activation method stems from the fact that, in the presence of a heavy background caused primarily by induced activity and by a natural background, it is difficult to single out nuclear gamma transitions associated with a specific nucleus. The energies determined precisely for gamma lines associated with the same isotope, the ratios of their intensities, and the decay rates are basic observables that make it possible to separate radioactive reaction products and to determine the cross sections for their production. The number of photons recorded at the photopeak corresponding to a radioactive product of a specific reaction (independent yield, I) was calculated on the basis of the relation

$$S = \frac{N_n \Phi \kappa \varepsilon \omega \sigma (1 - e^{-\lambda t_1}) e^{-\lambda t_2} (1 - e^{-\lambda t_3})}{\lambda}, \quad (1)$$

where S is the area under the photopeak; σ is the cross section for the reaction leading to the formation of the product being studied; Φ is the beam intensity (in 1/s units); N_n is the number of target nuclei (in $1/\mathrm{cm}^2$ units); t_1 is the irradiation time; t_2 is the time interval between the termination of the irradiation and the commencement of the measurement; t_3 is the time of the measurement; λ is the decay constant; ω is the relative intensity of gamma transitions of given energy; κ is the coefficient of gamma-ray absorption in target and detector materials for a given energy; and ε is the detection efficiency for gamma rays from nuclear transitions. This case refers to isotope formation in the interaction of nuclei and concerns the independent yield (I). The presence of the contribution to the yield of a given isotope from the decays of neighboring unstable isotopes complicates the calculation of relevant cross sections [15, 16]. If the cross section for the production of a parent isotope has been determined experimentally or estimated on the basis of other sources, then the independent yields of daughter nuclei can be obtained from the relation

$$S = N_n\Phi\kappa\varepsilon\omega_d\left\{\sigma_p\omega_p\frac{\lambda_p-\lambda_d}{\lambda_d-\lambda_p}\left[\frac{1-e^{-\lambda_p t_1}}{\lambda_p^2}\times e^{-\lambda_p t_2}(1-e^{-\lambda_p t_3})\right.\right. \quad (2)$$
$$\left.\left. - \frac{1-e^{\lambda_d t_1}}{\lambda_d^2}e^{-\lambda_d t_2}(1-e^{-\lambda_d t_3})\right] + \sigma_d\frac{1-e^{-\lambda_d t_1}}{\lambda_d}e^{-\lambda_d t_2}(1-e^{-\lambda_d t_3})\right\},$$

where the symbols d and p label variables that refer to, respectively, the daughter and the parent isotope, while S determines the measured total area under the photopeak.

In some limiting cases, the precursor contribution can be disregarded if the parent-nucleus half-lives are very long or if the weight of the contribution is low.

In the case where parent and daughter isotopes could not be separated experimentally, the calculated cross sections are classified as cumulative ones (C).

In order to analyze the measured spectra, we employed the standard DEIMOS code [17]. The half-lives of identified isotopes were within the range between 15 min and 1 yr.

The error in determining cross sections depended on the following factors: the statistical significance of experimental results ($\leq 2-3\%$), the accuracy in measuring the target thickness and the accuracy of tabular data on nuclear constants ($\leq 3\%$), and the errors in determining the detector efficiency with allowance for the accuracy in calculating its energy dependence ($\leq 10\%$).

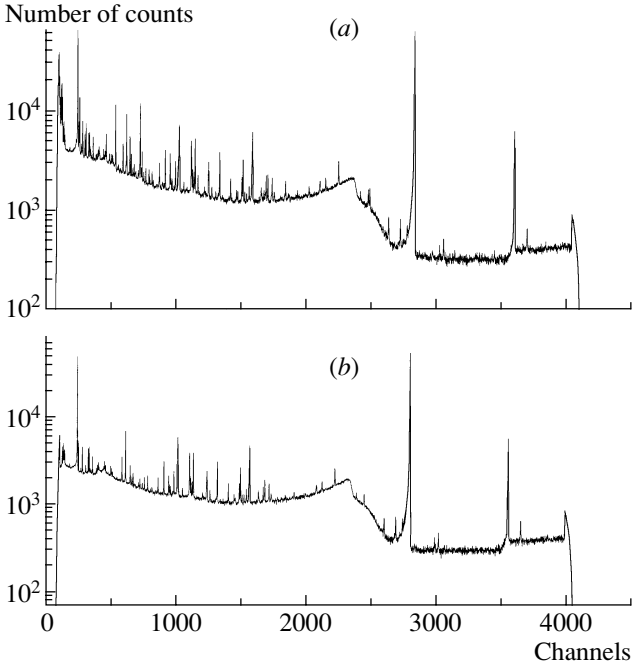

Fig. 2. Gamma spectrum of radioactive nuclei emitted into the catch aluminum foils: (*a*) data for forward catch foils and (*b*) data for backward catch foils.

Additional information about the reaction mechanism was obtained by measuring the properties of recoil nuclei with the aid of the catch-foil method. For a detailed account of the relevant experimental technique and of the mathematical formalism used in data processing, the interested reader is referred to [9–13]. The idea of the method consists in irradiating an assembly that contains target and catch foils and in recording, both in the target itself and in the catch foils, whose chemical composition rules out the formation of the nuclei under study in them under the effect of irradiation, the emerging products. Depending on the geometric and other experimental conditions and on the problem at hand, one measures the differential or integrated ranges of recoil nuclei and their angular distributions. If use is made of a *thick target–thick catch foil* system, as was done in the present experiment, the thicknesses of the targets and of the catch foils are severalfold larger than the ranges of the products being studied. The disposition of the catch foils in the immediate vicinity of the target makes it possible to capture nuclei emitted within a solid angle of about 2π, in the beam-axis direction (F) and in the direction opposite to it (B). Under such conditions, one measures the integrated ranges of radioactive reaction products and the anisotropy of their emission with respect to the beam axis.

As the results of the measurements, one obtains the relative amounts of radioactive products in the

forward (F) and backward (B) catch foils; that is,

$$F = S_F/(S_F + S_B + S_T), \quad (3)$$
$$B = S_B/(S_F + S_B + S_T),$$

where S_F, S_B, and S_T are the photopeak areas associated with the products under study in the catch foils and in the target. The resulting data were used to calculate the forward–backward (F/B) anisotropy of product emission and the ranges in the target material (R).

The results of such measurements are usually analyzed on the basis of the two-step vector model with the aid of the mathematical formalism developed in [9–12]. The gross features of the pattern being considered are consistent with the concept of compound-nucleus formation and decay within the cascade–evaporation model, but this pattern corresponds to a simplified version that makes it possible to estimate kinematical features of the reactions for a comparison with the measured parameters. According to [9–11], the first reaction stage involves the formation of a compound nucleus having an excitation energy E^* and a velocity $\mathbf{v}$ (or the momentum $\mathbf{p}$) along the beam axis. It is assumed that, at the second reaction stage, there occurs the evaporation of nucleons and light nuclei, with the result that the nucleus in question acquires an additional velocity $\mathbf{V}$. The velocity of the residual nucleus is given by the vector sum of the two velocities ($\mathbf{v} + \mathbf{V}$). That reaction fragments are emitted in the forward direction is due to the longitudinal velocity (v), which is acquired at the first stage of the interaction. In general, this velocity has a component along the beam axis and a component in an orthogonal direction, while the quantity V obeys an anisotropic distribution. However, the application of the procedure involving thick catch foils oriented orthogonally to the beam axis makes it possible to measure only the longitudinal component of the velocity transfer ($v_{||}$), not providing information about the angular distribution of the vector $\mathbf{V}$. In such experiments, an analysis of data is performed by introducing the following approximations:

(i) The quantity v is constant and has only one component $v_{||}$ directed along the beam axis.

(ii) The quantity V is isotropic.

(iii) The quantities v and V are independent of each other.

The mathematical formalism developed in [9, 11, 12] makes it possible to calculate, on the basis of experimental results for F and B, parameters that characterize the first ($v_{||}$, E^*) and the second (R and T, which are the fragment range and kinetic energy, respectively) stage of the interaction.

The longitudinal-momentum-transfer fraction $p_{||}/p_{\mathrm{CN}}$ with respect to the maximum possible value, which corresponds to the momentum of a hypothetical compound nucleus, enables one to calculate the excitation energy E^* and to determine the number of projectile nucleons transferred to the target.

DISCUSSION

Fission Products

Table 1 gives experimental data concerning the yields of products in the mass range 40–153 amu, which were interpreted as fission fragments. The application of the induced-activity procedure made it possible to determine the yields of radioactive products whose features are convenient for measurements. The yields of stable and short-lived nuclei, as well as the yields of other unmeasurable products, were estimated with the aid of the approximating functions known from [18]. Gaussian functions whose parameters were fitted to experimental results were employed to represent charge distributions.

The fission of nuclei in the region of lead is characterized by a symmetric mass distribution of products, which was described by a Gaussian distribution. A complete pattern of the charge and mass distribution of fission fragments was obtained with the aid of the expression [18]

$$\sigma(A,Z) = \theta_A \exp[-(A - M_A)^2/\Gamma_A^2] \quad (4)$$
$$\times \frac{1}{\sqrt{\pi}\Gamma_Z} \sum_i \exp[-(Z - i - Z_p)^2/\Gamma_Z^2],$$

where $\sigma(A,Z)$ is the cross section for the formation of a product that has a charge number Z and a mass number A, the remaining parameters that appear in this formula being determined from a fit to the measured yields. In performing our analysis, we assumed that Γ_A is a normalization factor. Further, M_A and θ_A are the mean values of, respectively, the mass and the width of the mass distribution of fission fragments; Z_p and Γ_Z are the most probable charge and width of the charge distribution; and the coefficient i determines the contribution of radioactive precursors (the value of $i = 0$ corresponds to the yield of an independent product, while positive and negative values of i specify the fractions of the β^- and β^+ branches of the decay of neighboring unstable isobars). The results of the analysis performed in [18] revealed that Z_p and Γ_Z can be represented as slowly varying linear functions of the mass numbers of fission fragments; that is,

$$Z_p = \mu_1 + \mu_2 A, \quad \Gamma_Z = \gamma_1 + \gamma_2 A, \quad (5)$$

where γ_1, γ_2, μ_1, and μ_2 are adjustable parameters. The values obtained here for the parameters are quoted in Table 2.

The total fission cross section was calculated by means of integration over the entire curve of the mass

Table 1. Cross sections for the formation of fission products

Nucleus	Reaction type	σ, mb	Nucleus	Reaction type	σ, mb
^{7}Be	I	27.70 ± 2.80	^{102m}Rh	I	0.42 ± 0.03
^{22}Na	C	7.40 ± 0.74	^{103}Ru	C	15.65 ± 1.51
^{24}Na	C	9.56 ± 1.00	^{105}Ru	C	7.70 ± 0.85
^{28}Mg	C	0.26 ± 0.03	$^{105(m+g)}$Rh	I	13.74 ± 1.37
^{38}S	I	≤ 0.40	$^{105(m+g)}$Ag	I	2.00 ± 0.22
^{43}Sc	C	0.21 ± 0.06	^{105}Cd	C	≤ 1.00
$^{44(m+g)}$Sc	I	0.37 ± 0.11	^{106}Ru	C	11.11 ± 1.11
$^{46(m+g)}$Sc	I	0.56 ± 0.07	^{106m}Rh	I	7.60 ± 0.91
^{47}Ca	C	≤ 0.03	^{110m}Ag	I	2.70 ± 0.40
^{54}Mn	I	≤ 0.02	^{111m}Pd	I	1.90 ± 0.19
^{55}Co	C	0.043 ± 0.008	$^{111(m+g)}$Ag	C	10.18 ± 1.02
^{56}Co	C	0.07 ± 0.009	^{111m}Cd	I	≤ 0.63
$^{58(m+g)}$Co	I	0.20 ± 0.03	^{111}In	C	2.50 ± 0.25
^{59}Fe	C	0.84 ± 0.09	^{111}Sn	C	≤ 1.91
^{67}Cu	C	7.40 ± 0.74	^{112}Pd	C	3.10 ± 0.31
^{69m}Zn	I	1.68 ± 0.17	^{112}Ag	I	2.10 ± 0.25
^{71m}Zn	I	1.32 ± 0.18	$^{113(m+g)}$Ag	C	2.45 ± 0.37
^{72}Zn	I	0.43 ± 0.04	$^{113(m+g)}$Sn	C	3.34 ± 0.50
^{72}Ga	I	6.80 ± 0.68	^{115}Cd	C	1.25 ± 0.13
^{73}Ga	C	1.23 ± 0.14	^{117g}Cd	C	1.26 ± 0.13
^{74}As	I	0.37 ± 0.04	^{117m}Cd	C	1.31 ± 0.16
^{75}Se	I	0.10 ± 0.01	^{117g}In	I	≤ 0.98
^{75}Br	C	≤ 0.17	^{117m}Sn	I	2.83 ± 0.28
^{76}As	I	4.13 ± 0.41	^{118m}Sb	I	1.90 ± 0.20
$^{77(m+g)}$Ge	I	2.00 ± 0.20	^{120m}Sb	I	3.80 ± 0.40
$^{77(m+g)}$Br	I	0.12 ± 0.01	^{121g}Te	I	4.60 ± 0.69
^{77}Kr	C	≤ 0.16	^{121m}Te	I	1.95 ± 0.29
^{78}Ge	C	≤ 0.11	^{121}I	I	≤ 0.14
^{78}As	I	≤ 1.45	^{121}Xe	C	≤ 0.79
^{81m}Se	C	≤ 0.77	$^{122(m+g)}$Sb	I	2.74 ± 0.30
$^{82(m+g)}$Br	I	1.67 ± 0.17	^{123m}Te	I	4.73 ± 0.50
^{83}Rb	C	2.25 ± 0.23	^{123}I	I	0.94 ± 0.10
^{84}Br	C	≤ 0.80	^{123}Xe	C	≤ 0.44
$^{84(m+g)}$Rb	I	5.22 ± 0.52	$^{124(m+g)}$Sb	I	0.88 ± 0.09
^{85g}Sr	C	2.70 ± 0.27	^{124}I	I	1.25 ± 0.13
^{85m}Sr	I	≤ 0.34	^{125}Sb	C	0.86 ± 0.09
^{85g}Y	C	0.35 ± 0.04	$^{126(m+g)}$Sb	I	≤ 0.07

Table 1. (Contd.)

Nucleus	Reaction type	σ, mb	Nucleus	Reaction type	σ, mb
^{85m}Y	C	5.29 ± 0.60	^{126}I	I	1.82 ± 0.19
$^{86(m+g)}$Rb	I	7.04 ± 1.05	^{127g}Sn	C	≤ 0.26
^{87}Kr	C	≤ 0.40	^{127}Sb	C	≤ 0.06
^{87g}Y	I	0.68 ± 0.07	$^{127(m+g)}$Xe	I	0.29 ± 0.03
^{87m}Y	C	2.00 ± 0.20	^{127}Cs	C	≤ 0.25
$^{87(m+g)}$Zr	C	≤ 7.40	^{128}Sb	C	0.38 ± 0.04
^{88}Y	C	1.12 ± 0.35	^{129}Sb	C	≤ 0.55
^{89}Rb	C	≤ 1.87	^{129m}Te	I	1.62 ± 0.17
$^{89(m+g)}$Zr	C	0.48 ± 0.05	^{129g}Ba	C	≤ 0.73
^{89m}Nb	I	≤ 0.45	^{129m}Ba	C	≤ 0.19
^{90m}Y	I	3.80 ± 0.40	$^{130(m+g)}$I	I	0.29 ± 0.03
^{91}Sr	C	4.94 ± 0.50	^{131m}Te	C	≤ 0.50
^{91m}Y	I	≤ 0.32	^{132}Te	C	≤ 0.02
^{92}Sr	C	1.34 ± 0.16	^{132}Cs	I	0.37 ± 0.04
^{92}Y	I	≤ 2.00	$^{133(m+g)}$I	C	≤ 1.00
^{92m}Nb	I	0.10 ± 0.01	^{133m}Ba	I	1.21 ± 0.15
^{93}Y	C	13.00 ± 1.30	^{133}La	C	≤ 1.60
^{94}Y	C	≤ 2.15	^{136}Cs	I	0.05 ± 0.005
^{95}Zr	C	8.40 ± 0.84	^{137m}Ce	I	≤ 0.10
$^{95(m+g)}$Nb	I	6.50 ± 0.65	^{139}Ba	C	≤ 0.45
^{95g}Tc	C	0.55 ± 0.06	$^{139(m+g)}$Ce	C	1.17 ± 0.12
^{95m}Tc	I	1.44 ± 0.14	^{140}Ba	C	≤ 0.06
^{95}Ru	C	≤ 0.30	^{140}La	I	0.18 ± 0.02
^{96}Nb	I	5.47 ± 0.55	^{141}La	C	≤ 0.30
$^{96(m+g)}$Tc	I	0.47 ± 0.05	^{141}Ce	I	0.57 ± 0.06
^{97}Zr	C	2.00 ± 0.22	^{147}Eu	I	≤ 0.24
$^{97(m+g)}$Nb	I	3.55 ± 0.36	^{147}Gd	C	≤ 0.03
^{97}Ru	C	≤ 0.20	^{148g}Pm	I	≤ 0.05
^{98m}Nb	I	1.50 ± 0.16	^{148m}Pm	I	≤ 0.68
^{99}Mo	C	10.72 ± 1.08	^{148}Eu	I	≤ 0.90
^{99m}Tc	I	0.26 ± 0.03	^{153}Gd	C	≤ 0.25
^{101m}Rh	I	0.78 ± 0.08	$^{182(m+g)}$Ta	C	≤ 0.01
^{101}Pd	C	1.50 ± 0.15			

distribution with allowance for the formation of two fragments in one fission event (by introducing a factor of 0.5). The result proved to be 2.85 ± 0.3 b. In the total isobaric distribution of interaction products (Fig. 3), the region of fission fragments is described by a curve that is calculated by using experimental data constituting about 60% of the total data set.

The calculation of the averaged properties of a fissile nuclear system revealed that the mass number of a nucleus undergoing fission is on average $\bar{A}_{\text{fiss}} =$

206 amu, the mean value of the charge being $\bar{Z}_{\text{fiss}} = 82$ ($Z^2_{\text{fiss}}/A_{\text{fiss}} = 32.64$). Thus, the nucleus undergoing fission does not differ from the target nucleus substantially, this being compatible with the concept that, in the energy region being considered, there occurs an incomplete fusion after the breakup of the projectile nucleus.

From Fig. 3, it can also be seen that light nuclei in the mass region $A < 40$ amu are produced with a high probability. The yields of such products are not discussed in the present study.

Our measurements of the properties of recoil nuclei made it possible to calculate kinematical parameters and single out data concerning fission fragments and the compound nucleus undergoing fission (see Table 3). For fission fragments, we obtained the mean value of $F/B = 1.23 \pm 0.25$ (see Table 3). A weak anisotropy of the divergence of these nuclei confirms the fission nature of their production. The ranges in question were calculated in the approximation where it is considered that the kinetic energies of fission fragments are due primarily to their Coulomb repulsion and are much higher than the energy of the moving compound nucleus. The use of the approximation $v/V < 1$ [9–11] makes it possible to calculate the ranges by the formula

$$R = 2W(F + B), \tag{6}$$

where W is the target thickness (in mg/cm^2). On the basis of the analysis performed in [9, 11, 12], one can also calculate the quantity

$$\eta = v_{\|}/V = [(F/B)^{1/2} - 1]/[(F/B)^{1/2} + 1] \tag{7}$$

and obtain values of the longitudinal velocity $v_{\|}$ and of the longitudinal-momentum transfer $p_{\|} = A_{\text{fiss}} v_{\|}$ in the primary interaction. The relative longitudinal-momentum (longitudinal-velocity) transfer $p_{\|}/p_{\text{CN}}$, where p_{CN} is the momentum of a hypothetical compound nucleus formed in a complete fusion, is the main feature that characterizes the probability of a complete or an incomplete fusion. Its mean value of 0.46 ± 0.09, which was obtained in the present study, supports the hypothesis that nuclei produced upon an incomplete fusion undergo fission. The mean excitation energy of the intermediate nucleus and the number of nucleons transferred from the projectile to the target nucleus can be estimated by using the relations [7, 8]

$$E^*/E_{\text{CN}} = 0.8 p_{\|}/p_{\text{CN}}, \tag{8}$$

$$v_{\|}/v_{\text{CN}} = \frac{(A_t + A_p)(A_p - \Delta m)}{A_p(A_t + A_p - \Delta m)}, \tag{9}$$

where A_t and A_p are the target and the projectile mass, respectively, and Δm is the number of nucleons emitted in the form of the projectile spectator. The quantity $(A_p - \Delta m)$ determines the number of nucleons that formed, together with a target nucleus, the compound nucleus.

Table 2. Fitted values of the parameters in (4) and (5)

Parameter	Value
θ_A	135.00 ± 5.80
M_A	103.00 ± 0.41
Γ_A	24.60 ± 0.39
γ_1	0.74 ± 0.10
γ_2	0.0042 ± 0.0008
μ_1	1.64 ± 0.23
μ_2	0.41 ± 0.008

In order to transform the ranges into the kinetic energy of fission fragments, we made use of the relation [9–11]

$$R = KT^{N/2}, \tag{10}$$

where K and N are constants that are determined on the basis of range–energy data from [19]. In order to obtain more precise values of these constants, we additionally performed a systematization of data presented in the literature for the ranges of ions.

The calculated energies of residual nuclei are given in Table 3. The total kinetic energy released in fission was determined by taking the sum of the energies of two presumed fission fragments. The result was 141.5 ± 12.7 MeV, on average. This value is in fairly good agreement with the estimate 142.67 MeV, which was obtained by using the statistical approximation [13].

Spallation Products

The results of investigations reveal that an incomplete fusion of interacting nuclei and, hence, only a partial transfer of the projectile-ion energy and momentum to the target nucleus manifest themselves even in the energy range 10–25 MeV/nucleon [9, 10]. As the limiting value of the projectile velocity at which one can still observe nuclear effects of complete fusion, the authors of [9, 10] presented $v/c \sim 0.19$. In the present experiment, the velocity of ^{7}Li ions was $v/c = 0.27$, in which case it was natural to expect that there is no complete fusion at all. In view of these considerations, searches for and separation of products in the near-target mass region are of special interest. Part of such nuclei are spallation or evaporation products, this being indicative of the presence of a nonfission mode in the decay of an excited nucleus. But

Table 3. Kinematical features of fission fragments

Nucleus	F/B	$2W(F+B)$, mg/cm^2	T, MeV	E^*, MeV	$p_{\|\|}/p_{\mathrm{CN}}$
^{72}Zn	1.11 ± 0.22	13.22 ± 2.64	107.41 ± 21.48	68.68 ± 11.64	0.33 ± 0.06
^{77}Br	1.16 ± 0.14	13.36 ± 1.60	100.17 ± 12.02	82.32 ± 11.52	0.42 ± 0.06
^{82}Br	1.17 ± 0.14	11.79 ± 1.41	96.25 ± 11.55	84.28 ± 11.79	0.43 ± 0.06
^{83}Rb	1.17 ± 0.08	10.25 ± 0.72	93.15 ± 6.52	80.36 ± 7.88	0.41 ± 0.04
^{84}Rb	1.14 ± 0.10	8.17 ± 0.74	89.56 ± 8.06	68.60 ± 7.82	0.35 ± 0.04
^{86}Rb	1.11 ± 0.08	9.81 ± 0.77	86.03 ± 6.42	54.88 ± 4.68	0.28 ± 0.04
^{87}Y	1.19 ± 0.06	10.50 ± 0.53	87.57 ± 4.38	86.24 ± 4.31	0.44 ± 0.02
^{91}Sr	1.18 ± 0.10	10.10 ± 0.81	79.05 ± 5.59	76.44 ± 7.64	0.39 ± 0.04
^{95}Zr	1.19 ± 0.16	11.41 ± 1.74	76.54 ± 11.51	78.40 ± 11.76	0.40 ± 0.06
^{95}Nb	1.23 ± 0.11	11.36 ± 1.02	77.22 ± 6.56	90.16 ± 7.84	0.46 ± 0.04
^{96}Tc	1.29 ± 0.14	10.09 ± 1.10	74.76 ± 8.22	99.47 ± 9.95	0.58 ± 0.06
^{99}Mo	1.22 ± 0.06	10.33 ± 0.52	71.86 ± 3.59	84.28 ± 4.21	0.43 ± 0.02
^{105}Rh	1.17 ± 0.09	10.07 ± 0.81	70.95 ± 5.65	66.64 ± 3.99	0.34 ± 0.02
^{111}Ag	1.22 ± 0.12	8.32 ± 0.83	65.69 ± 6.57	76.44 ± 7.64	0.39 ± 0.04
^{115}Cd	1.19 ± 0.12	10.77 ± 1.07	59.03 ± 5.90	64.68 ± 7.76	0.33 ± 0.04
^{117m}Sn	1.43 ± 0.17	7.69 ± 0.92	53.50 ± 6.42	119.56 ± 15.54	0.61 ± 0.08
^{120m}Sb	1.45 ± 0.06	4.29 ± 0.17	50.87 ± 2.03	119.56 ± 7.89	0.61 ± 0.04
^{124}I	1.65 ± 0.18	7.95 ± 0.87	46.47 ± 5.11	150.92 ± 15.09	0.77 ± 0.08

some of these products in the immediate vicinity of ^{215}At, the hypothetical compound nucleus A_{CN}, can be associated with the complete-fusion processes.

The radioactive products of mass number about A_p that were formed upon the emission of $\Delta A \geq 28$ nucleons from the hypothetical compound nucleus A_{CN} were associated with the region of near-target nuclei (see Table 4). The charge and mass distributions of these products are given in Fig. 4. The number of emitted nucleons is plotted along the abscissa in Fig. 4*b*. It can be seen that the respective cross sections decrease with increasing number of emitted nucleons, this being due to a modest excitation energy. The isotopes of At that are produced upon the addition of three protons to the target nucleus were considered here as products of the reactions where the complete fusion of Pb and ^{7}Li nuclei was followed by neutron evaporation. The potential of the procedure used was insufficient for measuring the yields of $^{212-215}$At, and only estimates could be obtained for the ^{205,206}At cross sections. By and large, the total yield of At isotopes was about 2 mb. This value can be interpreted as a lower limit on the cross section for complete fusion in the system being investigated. According to [20], the complete-fusion fraction decreases not only with increasing projectile energy but also with increasing mass asymmetry in the input channel.

The remaining heavy nuclei, whose cross sections are quoted in Table 4, were considered here as spallation products formed upon an incomplete fusion and a sequential emission of nucleons and light nuclei. The total yield of these products was 446.1 ± 52.9 mb, which, in view of the potential of the procedure used, can be treated as a lower limit for such reactions.

Energy and Momentum Features

From the results obtained by measuring kinematical features and displayed in Fig. 5, one can see that, for some nuclei, emission occurs predominantly in the forward direction ($F/B > 2$). This distinct anisotropy of the emission of nuclear fragments is indicative of their formation in nonequilibrium reactions that, in view of a high probability of an incomplete fission, are of a peripheral character. To a good approximation, the quantity F/B may be considered as the result of the motion of a compound nucleus along the beam axis and as an indication of

Table 4. Cross sections for the production of heavy products

Nucleus	Reaction type	σ, mb	Nucleus	Reaction type	σ, mb
^{188}Ir	I	3.85 ± 0.40	^{200m1}Bi	C	≤ 6.26
^{188}Pt	C	0.71 ± 0.07	^{201}Tl	I	40.08 ± 4.01
^{191}Pt	C	3.64 ± 0.40	$^{201(m+g)}$Pb	I	45.00 ± 4.50
$^{193(m+g)}$Tl	C	≤ 0.18	^{201g}Bi	C	4.24 ± 0.55
^{194g}Tl	C	≤ 0.83	^{201m}Bi	C	≤ 1.57
^{194m}Tl	I	≤ 0.35	^{202}Tl	I	3.18 ± 0.32
^{195g}Hg	I	0.64 ± 0.32	^{202m}Pb	I	13.26 ± 1.33
^{195m}Hg	I	1.80 ± 0.20	^{202}Bi	I	6.54 ± 0.65
$^{195(m+g)}$Tl	C	≤ 1.80	^{202}Po	C	1.11 ± 0.12
$^{196(m1+g)}$Au	I	0.22 ± 0.02	$^{203(m+g)}$Pb	I	44.80 ± 4.48
^{196g}Tl	I	≤ 1.35	^{203}Bi	I	13.89 ± 1.39
^{196m}Tl	I	2.43 ± 0.24	$^{203(m+g)}$Po	C	1.88 ± 0.28
^{196}Pb	C	1.63 ± 0.17	^{204m}Pb	I	2.67 ± 0.27
^{197m}Hg	I	1.00 ± 0.10	^{204}Bi	I	41.00 ± 4.10
$^{197(m+g)}$Tl	I	≤ 4.61	^{204}Po	C	6.35 ± 0.89
^{197g}Pb	C	1.72 ± 0.17	^{205}Bi	I	37.74 ± 3.77
^{197m}Pb	C	2.77 ± 0.30	^{205}Po	I	≤ 1.94
^{198g}Au	I	0.14 ± 0.02	^{205}At	I	≤ 0.33
^{198m}Au	I	0.34 ± 0.03	^{206}Bi	I	17.40 ± 1.74
^{198g}Tl	I	12.92 ± 1.50	^{206}Po	I	7.10 ± 0.71
^{198m}Tl	I	1.55 ± 0.23	^{206}At	I	≤ 0.37
^{198}Pb	C	27.00 ± 2.70	$^{207(m+g)}$Po	I	2.60 ± 0.99
^{199}Tl	I	32.87 ± 3.29	^{207}At	I	0.33 ± 0.04
$^{199(m+g)}$Pb	C	8.00 ± 0.80	^{208}At	I	0.17 ± 0.02
$^{199(m+g)}$Bi	C	3.10 ± 0.3	^{209}At	I	0.46 ± 0.05
^{200m}Au	I	1.33 ± 0.13	^{210}At	I	0.44 ± 0.04
^{200}Tl	I	13.13 ± 1.33	^{211}At	I	0.40 ± 0.04
^{200}Pb	I	15.56 ± 1.56	^{212}Bi	I	≤ 0.62
^{200g}Bi	C	4.33 ± 0.43			

a rather high value of the longitudinal component of the residual-nucleus velocity in relation to the velocity acquired upon evaporation, $v_{\|} > V$. In the case where the velocities in question satisfy this inequality, the ranges are calculated on the basis of the relation $R = WF$ [mg/cm^2] [9, 12]. The results of the calculations for the kinematical parameters are given in Table 5 and in Fig. 5. From these data, one can see that the mean relative longitudinal momentum $p_{\|}/p_{\mathrm{CN}}$ depends on the number of nucleons emitted from the hypothetical compound nucleus ^{215}At. With increasing ΔA, the relative momentum transfer to the nucleus grows, reaching a limiting value in the range $\Delta A = 18-27$ amu. In studying the longitudinal-momentum distribution of products originating from nonequilibrium processes, the authors of [5, 8, 14] explained a dependence of this type by the correlation of the longitudinal-momentum and energy transfer with the

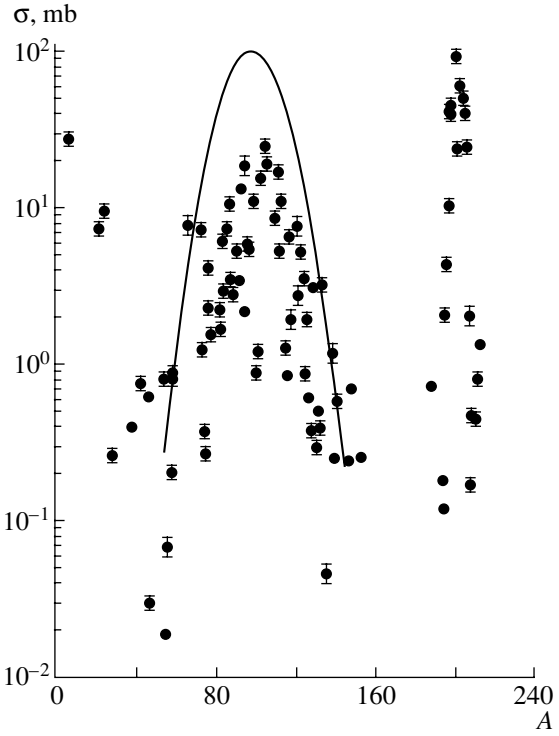

Fig. 3. Isobaric distribution of products originating from $^{7}\mathrm{Li} + {}^{\mathrm{nat}}\mathrm{Pb}$ interaction: (points) our experimental data and (curve) function approximating the yields of fission fragments in the form (4).

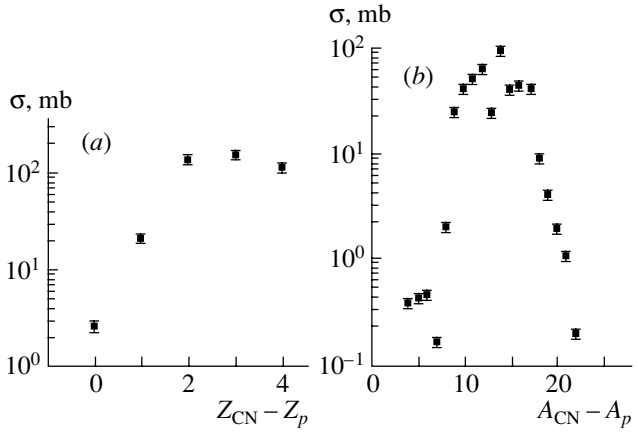

Fig. 4. Distributions of reaction products in the near-target region of mass numbers: (*a*) charge distribution and (*b*) mass distribution.

impact parameter. Those authors indicated that, with increasing projectile energy (above 10 MeV per nucleon) or with increasing impact parameter, the relative value of the linear-momentum transfer decreases, along with the excitation-energy transfer. If a relatively small number of nucleons are emitted in such processes, residual nuclei are characterized by a preferred emission in the forward direction—that is, by a large value of F/B.

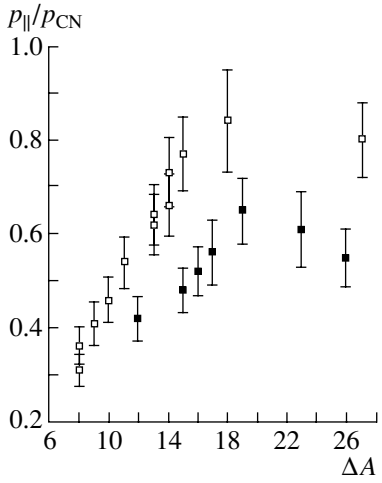

Fig. 5. Relative longitudinal momentum of the intermediate compound nucleus ($p_{||}$ is the intermediate-nucleus momentum, while p_{CN} is the momentum of the hypothetical compound nucleus formed upon complete fusion). The open and closed boxes correspond to different isotopic states of residual nuclei containing, respectively, a smaller and a larger number of neutrons.

Some authors explain the presence of a plateau at large values of $A \sim 18-28$ amu by a possible saturation in the energy–momentum transfer in a nuclear collision, this leading to specific decay channels [5, 20]. The value of 174 ± 18 MeV/c per nucleon, which we obtained for the momentum transfer in the plateau region, is in satisfactory agreement with the limiting momentum value of 180 MeV/c per nucleon from [20].

From Fig. 5, it can also be seen that, if use is made of momentum features not subjected to averaging, then the experimental points are distributed in the form of two curves referring approximately to different values of the longitudinal-momentum transfer. For the groups of nuclei being considered, the mean values of $p_{||}/p_{CN}$ within the plateau region were 0.55 ± 0.05 and 0.68 ± 0.06. The isotopes associated with these curves are characterized by different numbers of neutrons: neutron-rich nuclei are distributed below neutron-deficit nuclei. The resulting values of longitudinal-momentum transfer make it possible to calculate the excitation energies of intermediate nuclear systems, which are sources responsible for the production of these products. Estimations of the mean excitation energies on the basis of expression (8) revealed that isotopes enriched in neutrons are formed from states at an excitation energy of $E^* = 107.8 \pm 11$ MeV and that the sources responsible for the production of neutron-deficit products

Table 5. Kinematical features of heavy products

Nucleus	F/B	WF, mg/cm^2	T, MeV	E^*, MeV	$p_\parallel/p_{CN}$
^{188}Ir	2.90 ± 0.30	1.10 ± 0.11	5.14 ± 0.51	156.80 ± 20.38	0.80 ± 0.08
^{188}Pt	26.25 ± 3.41	0.32 ± 0.04	2.69 ± 0.35	108.00 ± 14.00	0.55 ± 0.05
^{191}Pt	7.24 ± 0.87	0.39 ± 0.06	3.21 ± 0.51	120.00 ± 15.60	0.61 ± 0.06
^{195m}Hg	3.02 ± 0.12	0.43 ± 0.05	3.59 ± 0.39	127.00 ± 10.16	0.65 ± 0.06
^{196}Au	2.00 ± 0.17	0.72 ± 0.09	6.00 ± 0.72	165.00 ± 24.75	0.84 ± 0.08
^{197m}Hg	4.69 ± 0.21	0.32 ± 0.03	2.66 ± 0.29	110.00 ± 9.90	0.56 ± 0.06
^{198}Au	3.96 ± 0.90	0.27 ± 0.03	2.27 ± 0.23	102.00 ± 5.10	0.52 ± 0.05
^{199}Tl	23.15 ± 0.60	0.59 ± 0.06	4.90 ± 0.49	151.00 ± 19.63	0.77 ± 0.08
^{200m}Au	22.77 ± 2.28	0.53 ± 0.05	2.33 ± 0.23	98.00 ± 12.74	0.50 ± 0.05
^{200}Tl	547.81 ± 3.29	0.53 ± 0.05	4.38 ± 0.44	143.00 ± 21.45	0.73 ± 0.07
^{200}Pb	112.37 ± 0.79	0.43 ± 0.04	3.59 ± 0.36	130.00 ± 19.50	0.66 ± 0.07
^{201}Tl	955.43 ± 13.93	0.38 ± 0.04	3.17 ± 0.32	122.00 ± 17.08	0.62 ± 0.06
^{201}Pb	80.81 ± 0.81	0.40 ± 0.04	3.35 ± 0.34	126.00 ± 12.6	0.64 ± 0.06
^{202}Tl	7.06 ± 0.42	0.18 ± 0.02	1.46 ± 0.18	82.40 ± 21.36	0.42 ± 0.04
^{203}Pb	257.61 ± 3.69	0.29 ± 0.03	2.39 ± 0.24	106.00 ± 11.34	0.54 ± 0.05
^{203}Bi	183.05 ± 5.49	0.28 ± 0.03	2.37 ± 0.24	106.00 ± 15.90	0.54 ± 0.05
^{204}Bi	38.07 ± 0.76	0.24 ± 0.02	1.96 ± 0.20	90.40 ± 10.85	0.43 ± 0.04
^{205}Bi	16.73 ± 0.90	0.16 ± 0.02	1.36 ± 0.23	80.40 ± 12.06	0.41 ± 0.04
^{206}Bi	4.32 ± 0.19	0.09 ± 0.01	0.79 ± 0.09	61.00 ± 6.34	0.31 ± 0.03

are characterized by an excitation energy of $E^* = 133.3 \pm 13$ MeV. To explain this pattern, one can assume that a few sources having different excitations can take part in the formation of residual nuclei [21, 22]. In a number of studies, the formation of various products is assumed to be distributed over the time scale of the development of the reaction.

Total and Partial Interaction Cross Sections

On the basis of the resulting pattern of the formation of various reaction products, we have calculated the total cross section for ^{7}Li + Pb interaction at the projectile energy of 245 MeV. By summing the yields from all of the reactions studied here, we obtained 3.318 ± 0.4 b. Upon adding, to this value, the cross section for the formation of light ($A < 40$ amu) nuclei, about 95 mb, the total interaction cross section becomes 3.413 ± 0.4 b, which is in good agreement with the results of calculations based on a microscopic model (3.19 b) and with experimental data (3.67 ± 0.12 b) determined by measuring the attenuation of a ^{7}Li beam in a Pb target [6].

The fissility of the product compound nucleus was 0.86, which is also compatible with the probability of nuclear fission in the mass region around 206 amu according to calculations within the liquid-drop model. The fraction of processes contributing to the probability of complete fusion was estimated here at a value below 0.1%. The contribution of nonfission reactions recorded in our experiment proved to be about 13.5% of the total cross section.

CONCLUSION

By investigating the interaction of lead with ^{7}Li ions at a projectile energy of 35 MeV per nucleon, we have obtained cross sections for various processes accompanying complete and incomplete fusion in a collision process. In the energy range investigated here, data on fission cross sections, as well as on the cross sections for spallation and for evaporation from intermediate compound nuclei, have been presented for the first time. On the basis of studying the kinematical features of reaction products, we have analyzed the properties of intermediate nuclear systems produced upon the incomplete fusion of interacting nuclei.

A comparison with estimates based on the statistical model has made it possible to determine the most probable number of projectile nucleons participating in reactions at the energy considered here.

REFERENCES

1. Sunita Gupta, B. P. Singh, M. M. Mustafa, *et al.*, Phys. Rev. C **61**, 064613 (2000).
2. A. Navin, A. Chatterjee, S. Kuilas, *et al.*, Phys. Rev. C **54**, 767 (1996).
3. T. Lund, D. Molzahn, R. Brandt, *et al.*, Phys. Lett. B **102B**, 239 (1981).
4. P. Vrgani, E. Gadioli, E. Vaciago, *et al.*, Phys. Rev. C **48**, 1815 (1993).
5. M. Blann, Nucl. Phys. A **235**, 211 (1974); **186**, 245 (1972).
6. R. E. Warner, M. H. McKinnon, N. C. Shaner, *et al.*, Phys. Rev. C **62**, 024608 (2000).
7. J. Jastrzebski, P. P. Singh, T. Mróz, *et al.*, Phys. Rev. C **34**, 60 (1986).
8. Wenxin Li, Tongyu Sun, Dingqing Wu, *et al.*, Radiochim. Acta **72**, 109 (1996).
9. L. Winsberg, Nucl. Instrum. Methods **150**, 465 (1978).
10. M. Lagarde-Simonoff and G. M. Simonoff, Phys. Rev. C **20**, 1498 (1979).
11. L. Winsberg, Phys. Rev. C **22**, 2116 (1980).
12. J. Alexander and L. Winsberg, Phys. Rev. **121**, 529 (1961).
13. V. E. Viola, K. Kwiatkowski, and M. Walker, Phys. Rev. C **31**, 1550 (1985).
14. W. Skulski and J. Jastrzebski, Phys. Rev. C **41**, 2605 (1990).
15. I. Adam, V. S. Pronskikh, A. R. Balabekyan, *et al.*, Preprint No. 10-2000-28, OIYaI (Joint Inst. Nucl. Res., Dubna, 2000).
16. H. Baba, J. Sanada, H. Araki, *et al.*, Nucl. Instrum. Methods Phys. Res. A **416**, 301 (1998).
17. J. Frana, Acta Politecnica **387**, 127 (1998).
18. M. C. Duijvestijn and A. J. Koning, Phys. Rev. C **59**, 779 (1999).
19. L. C. Northcliffe and R. E. Schilling, Nucl. Data, Sect. A **7**, 233 (1970).
20. M. Morgenstern, W. Bohen, W. Galster, *et al.*, Phys. Rev. Lett. **52**, 1104 (1984).
21. K. Akeklett, W. Loveland, T. Lund, *et al.*, Phys. Rev. C **33**, 885 (1986).
22. Y. W. Yu, C. H. Lee, and K. J. Moody, Phys. Rev. C **36**, 2396 (1987).

Translated by A. Isaakyan

Physics of Atomic Nuclei, Vol. 68, No. 1, 2005, pp. 3–15. Translated from Yadernaya Fizika, Vol. 68, No. 1, 2005, pp. 4–16.

NUCLEI
Experiment

Double-Differential Cross Sections for the Production of Neutrons from Pb, W, Zr, Cu, and Al Targets Irradiated with 0.8-, 1.0-, and 1.6-GeV Protons

Yu. V. Trebukhovsky, Yu. E. Titarenko*, V. F. Batyaev, R. D. Mulambetov, S. V. Mulambetova, G. N. Smirnov, K. A. Lipatov, A. B. Koldobsky, V. M. Zhivun, V. S. Barashenkov[1)], H. Kumawat[1)], S. G. Mashnik[2)], and R. E. Prael[2)]

Institute of Theoretical and Experimental Physics, Bol'shaya Cheremushkinskaya ul. 25, Moscow, 117259 Russia

Received April 28, 2003; in final form, December 9, 2003

Abstract—Experimental results obtained by determining the double-differential cross sections for neutron production in Pb, W, Zr, Cu, and Al targets irradiated with 0.8-, 1.0-, and 1.6-GeV protons are presented. The spectra of neutrons were measured at 15°, 30°, 60°, 90°, 120°, and 150° with a time-of-flight spectrometer by using a proton beam extracted from the 10-GeV synchrotron at the Institute of Theoretical and Experimental Physics (ITEP, Moscow). The neutrons are recorded with 5MAB-1F6BC501A/5L liquid scintillation detectors and NE110 solid-state scintillators. The experimental data in question are compared with the results of simulations based on the CEM97, LAHET, and CASCADE codes. © *2005 Pleiades Publishing, Inc.*

INTRODUCTION

The present-day strategy of the development of nuclear-power production is determined largely by the problem of annihilation of minor actinides and long-lived radioactive fission products in spent nuclear fuel.

One of the possible ways to resolve this problem is the transmutation of minor actinides and some long-lived fission products in ADS facilities constructed on the basis of a linear proton accelerator (characterized by a current of a few tens of mA and an energy of 1 to 3 GeV), a neutron-producing target, and a subcritical blanket. In turn, an optimal selection of the composition and design of the target and subcritical blanket requires data on particle yields from targets and on double-differential cross sections for particle production. The requirements for the uncertainty in data (about 10%) are defined by the accuracy in calculating the main blanket parameters—namely, neutron-breeding coefficient k_{eff}, the efficiency of the protection system control, the energy-deposition fields of fuel elements, the minor-actinide-transmutation rate, and the radiation resistance of materials.

The present-day data libraries [1, 2] include copious experimental data on various parameters, including particle yields and double-differential cross sections that characterize proton–nucleus interactions at low energies of protons. Recently, similar results were published for intermediate energy range, up to proton energies of about 3 GeV, and experimental data were compared with the results of simulations based on various codes. Table 1 presents all of the known experiments [3–17] aimed at measuring the double-differential cross sections and the spectra of neutrons emitted in intermediate-energy proton interactions with thin and thick targets made from various materials.

The analysis of the data published in [3–17] revealed that the double-differential cross sections for neutron emission from lead that were measured at the LANL, KEK, and SATURNE laboratories for primary proton energies of up to 0.8 GeV agree with one another and do not contradict the results of simulations on the basis of transport codes throughout the measured neutron-energy range. At the same time, the disagreement between experiment data and the results of simulations in this energy range may reach 100% for targets of low mass numbers.

As the primary proton energy increases to a few GeV, the experimental results become more and more different, and their agreement with the results of calculations deteriorates. This concerns tungsten, which

[1)]Joint Institute for Nuclear Research, Dubna, Moscow oblast, 141980 Russia.
[2)]Los Alamos National Laboratory, Los Alamos, NM 87545, USA.
*e-mail: Yury.Titarenko@itep.ru

Table 1. Experiments devoted to measuring the yields of neutrons from matter irradiated with intermediate-energy protons

No.	Proton energy, GeV	Target material	Neutron energy, MeV	Ejection angle in lab. frame	Research Center	Refs.
1*	0.585	C, Al, Fe, Nb, In, Ta, Pb, U	0.9–E_{max}	30, 90, 150	PSI	[3]
2*	0.12, 0.16	Al, Zr, Pb	≥ 30	0–145	IUCF	[4]
3*	0.113	Be, C, O, Al, Fe, W, Pb, U	0.5–E_{max}	7.5–150	LANL	[5]
4*	0.256	Be, C, O, Al, Fe, Pb, U	0.5–E_{max}	7.5–150	LANL	[6]
5*	0.256, 0.80	Li, Al, Zr, Pb	20–E_{max}	7.5–150	LANL	[7]
6*	0.318, 0.80	C, Al, Pb, U	5.0–E_{max}	7.5, 30	LANL	[8]
7*	0.597	Be, B, C, N, O, Al, Fe, Pb, U	0.5–E_{max}	30–150	LANL	[9]
8*	0.80	Be, B, C, N, O, Al, Fe, Cd, W, Pb, U	0.3–E_{max}	30–150	LANL	[10]
9*	0.8, 1.5, 3.0	C, Al, Fe, In, Pb	1–E_{max}	15–150	KEK	[11]
10	2.20	Cu	3.3–200	60	KEK	[12]
11	0.5, 0.8, 1.5	C, Pb	1–E_{max}	15–150	KEK	[13]
12	0.8, 1.2, 1.6	C, Al, Fe, Zr, W, Pb, Th	2–E_{max}	0–160	SATURNE	[14]
13	0.6, 1.2, 1.6	Al, Cu, Zr, Pb	3–200	15–150	ITEP	[15]
14	0.44–6.5	Be, C, Cu, Pb, U	7.5–190	119	ITEP	[16]
15	2.00, 2.55	Be, Al, Cu, Cd, Pb	0.2–E_{max}	30–120	JINR	[17]

Note. The tabulated data no. 1–9 (labeled with asterisks) were taken from the report of Yu.W. Watahable *et al.* in YAERI-Conf. 98-016 (1998), p. 24.

is proposed by some projects to be a material of an ADS multiplication target, and some other structural materials.

The optimal version of the ADS target composition and design can only be selected by using well-verified codes. Therefore, experiments aimed at obtaining reliable data still remain topical.

Taking into consideration all of the above and bearing in mind various materials that may be used as ADS targets, we measured, in the present study, the spectra and obtained double-differential cross sections for neutrons ejected at angles of 15°, 30°, 60°, 90°, 120°, and 150° from Pb targets irradiated with 0.8-, 1.0-, and 1.6-GeV protons and from W, Zr, Cu, and Al targets irradiated with 1.0- and 1.6-GeV protons. The experimental data are compared with the results of simulations based on the CEM97, LAHET, and CASCADE codes.

1. EXPERIMENTAL DESIGN

Our experiments aimed at determining the double-differential neutron production cross sections were performed by using a time-of-flight spectrometer and beam no. 512 from the 10-GeV proton synchrotron at the Institute of Experimental and Theoretical Physics (ITEP, Moscow). Figure 1 shows the layout of the beam optics and of the time-of-flight spectrometer in the experimental hall. Charged particles are ejected from the interactions of accelerated protons with nuclei of the inner Be foil target (TA) at an angle of 3.5° and are then focused by a magnetic dipole M_1 and quadrupoles Q_1–Q_4 into the intermediate focus F_1. After that, the charged particles are focused by a magnetic dipole M_2 and quadrupoles Q_5–Q_8 into the focus F_2, where the target is located. The inner target of the accelerator and the second focus F_2 were spaced 70 m apart. The particle beam of diameter about 2 cm was focused into the target center. The beam-pulse duration was about 0.3 s. The primary-beam intensity could be varied up to 10^5 protons per pulse.

Primary particles were recorded along the beam path by detectors C_0, C_1, and C_2 (C_1 is a scintillating NE-102A $10 \times 15 \times 1$ cm^3 plastic with an FEU-30 photomultiplier tube; C_0 and C_2 are NE-102A $\varnothing 4 \times 1$ cm^3 scintillating plastics with FEU XP-2020 amplitude–time photomultiplier tubes).

In dealing with a pure proton beam, the beam

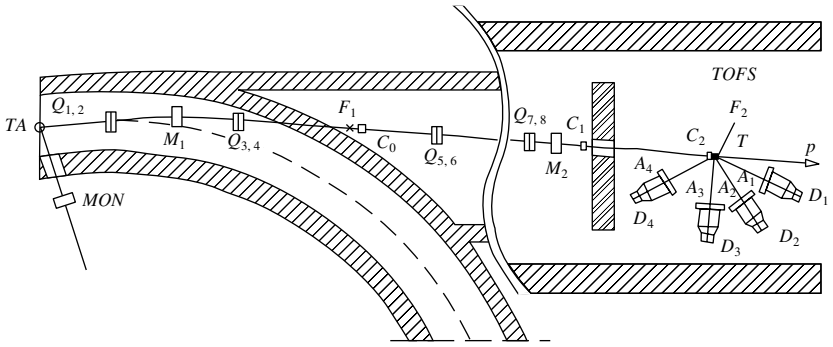

Fig. 1. The beam 512 layout showing the main spectrometer units: (TA) internal target of the ITEP synchrotron, (MON) beam monitor, ($Q_{1,2}$–$Q_{7,8}$) magnetooptic quadrupole lenses, (M_1, M_2) bending magnets, (F_1, F_2) first and second foci of the beam, (T) spectrometer target, (C_0, C_1, C_2) pilot detectors, (A_1–A_4) detectors of charged secondaries, (D_1–D_3) neutron detectors based on a BC501A liquid scintillator, and (D_4) neutron detector based on solid-state scintillating plastic.

path was tuned to the quasielastic peak of protons scattered by the inner Be target of the accelerator, while the protons were recorded by two pilot detectors C_1 and C_2 spaced 10 m apart. In dealing with a particle beam at high energies of accelerated protons, an additional thin plastic detector C_0 was placed at the intermediate focus F_1. The detectors C_0 and C_2 were spaced 34 m apart. In that case, the protons were separated from other particles by time-of-flight techniques at a 0.31-ns time resolution.

Secondary particles from the target were recorded by the following time-of-flight spectrometer detectors placed at various angles:

(a) the NE110 $1 \times 19 \times 19$ cm^3 scintillating plastics A_1, A_2, and A_3 placed at 2 cm from the neutron detectors D_1, D_2, and D_3 (the detectors A_{1-3} recorded charged particles that hit the neutron detectors);

(b) the detectors D_{1-3} (5MAB-1F6BC501A/5L $\varnothing 12.7 \times 15.2$ cm^3) with a liquid scintillator that are used in the main measurements to record neutrons, photons, and charged particles;

(c) the detector assemblies consisting of the NE110 $25 \times 25 \times 1$ cm^3 (A_4) and NE110 $20 \times 20 \times 11.5$ cm^3 (D_4) scintillating plastics, whose spectra were measured with a view to estimate and compare the γ-background contributions to various energy ranges of the neutron spectra measured in the liquid and large-volume plastic detectors of neutrons.

The detectors A_i and D_i were mounted and shifted at different angles by using a turning device placed at a distance of above 5 m from the ceiling and walls and a distance of 2.5 m from floor, without any additional shielding. The flight base from the target to the neutron detectors was 2.0 m (some of the measurements were made with a 3-m base). The results of the measurement were fixed in the separate particle-detection mode. Neutrons and photons were separated by techniques for discriminating pulse shapes, pulse durations, and the times of flight.

The functional logic of the operation of the time-of-flight spectrometer is as follows. The coincidence of a pulse from the telescope of the pilot detectors C_1 and C_2 (or C_0 and C_2) with a pulse from one of the neutron detectors D_i triggers the measurement circuit. The pulse from a detector (C_1 or C_0) is the stop signal of the circuit for time-of-flight measurements, while a pulse from one of the neutron detectors is the start signal (the inverse pattern). The time interval between the start and stop pulses was converted into a charge, which was then digitized by the charge-to digit converter (ChADC) to become the number of a channel. The ChADC was also used to measure some parameters that are necessary for separating neutrons and photons by their pulse shape. The data set from all the elements of time-of-flight spectrometer was fixed by the MES code [18]. Table 2 presents the dimensions and composition of the targets.

2. TECHNIQUES FOR RECORDING NEUTRONS

The neutron spectra were measured at angles of 15° to 150° with respect to the beam axis. The neutron detectors operated without evacuation of the flight base and without any additional shielding. Calculations and tentative measurements revealed that the contributions from neutrons scattered by the ceiling and walls to the main measurements are minor. The signals from the detectors A_i and D_i were recorded in the anticoincidence mode in measuring the neutron spectra and in the coincidence mode in measuring the charged-particle spectra. The energy calibration of the neutron detectors was made (a) with standard γ sources (^{137}Cs, ^{60}Co, ^{22}Na) at low energies (below

Table 2. Properties of the targets and of the proton beam

Target	Target dimensions (mm)	Composition, %	Density (g/cm^3)	Proton passage through the target (C_L)	Proton energy (GeV)	Proton energy loss (MeV)		
						0.8 GeV	1.0 GeV	1.6 GeV
Pb	∅50 × 10.0	99.9	11.3	0.97	1.0, 1.6		13	13
Pb	∅50 × 20.0	99.9	11.3	0.94	0.8	28		
W	∅50 × 5.1	97.5	18.8	0.97	1.0, 1.6		13	12
Zr	∅50 × 20.0	99.9	6.5	0.96	1.0, 1.6		18	17
Cu	∅50 × 10.0	99.9	8.9	0.97	1.0, 1.6		14	13
Al	∅50 × 50.0	99.9	2.7	0.94	1.0, 1.6		25	22

2.5 MeV) and (b) with proton beams at high energies (above some 30 MeV).

Since the differences in the neutron-detector-pulse amplitudes may reach a factor of 100 or be even higher, the recorded events were divided into two ranges in the following way to get a better separation of neutrons and photons:

(1) The method of amplitude–amplitude analysis of a recorded-particle pulse above the detection threshold, A_{FULL} (total-pulse charge) and A_{TAIL} (pulse-tail charge), was applied to the range of recoil proton energies between about 10 and about 30 MeV. The method is described in detail in [19]. Figure 2 shows the results obtained in this way.

(2) The method of measuring the total-pulse charge and the pulse duration above the detection threshold, A_{FULL} (total-pulse charge) at T_{DUR} (pulse duration), was applied to the range of recoil proton energies between about 10 and about 300 MeV. It should be recalled that the ADC used in the time-of-flight measurements (ChADC LeCroy 4300B) measures directly the pulse charge, which is an integral under the pulse. To illustrate the method, Fig. 3 shows the pulses of the same charge (area) from a neutron and a photon produced by a pulsed source of neutrons of energy about 14 MeV.

The pulses were recorded by a LeCroy LT-344 digital oscillograph. Figure 4 shows the results of applying the method of separation by pulse duration to the given energy range.

At the next stage, all neutron events from two energy ranges were combined, just as the respective sets of photon events. After that, the time-of-flight spectra were formed from the sets of neutron and photon events. Figure 5 gives an example of such a spectrum.

The γ-peak center was determined from the γ-spectrum maximum to within 0.79 ns, which is the same as the accuracy of determining the γ-peak half-width.

With our electronics, the particle time of flight is determined by measuring the charge of a calibrated rectangle pulse whose duration is the same as the measured time of flight and is equal to the time interval between the discriminator-formed and read-out timing signals. The difference between the instants of the occurrence of an analog pulse of a neutron detector and a formed timing pulse is determined by the analog-pulse amplitude. In such a manner, the particle time of flight measured by the electronics becomes somewhat dependent on the particle-pulse amplitude in the neutron detector. The dependence was taken into account by introducing an appropriate amplitude–time correction.

Upon the separation of charged particles and the removal of the amplitude–time dependence, the data-set files include only those events that result from the detection of neutral particles with a true time of flight, whereupon neutrons are separated from photons.

In such a way, neutrons were effectively separated, via the selection of an optimal situation with the amplitude–amplitude and amplitude–time separation, from photons emitted by the target.

An analysis of the solid-state scintillator data also demonstrates that neutron–photon separation via the amplitude–time separation is sufficiently efficient. Being dependent on the target material, the uncertainty in the photon contribution to the neutron spectra with a particle flight base of 3 m was 5–10% at emission angles smaller than 90° (at neutron energies of up to 200 MeV) and at least 5–15% at emission angles larger than 90° (at neutron energies of up to 100 MeV).

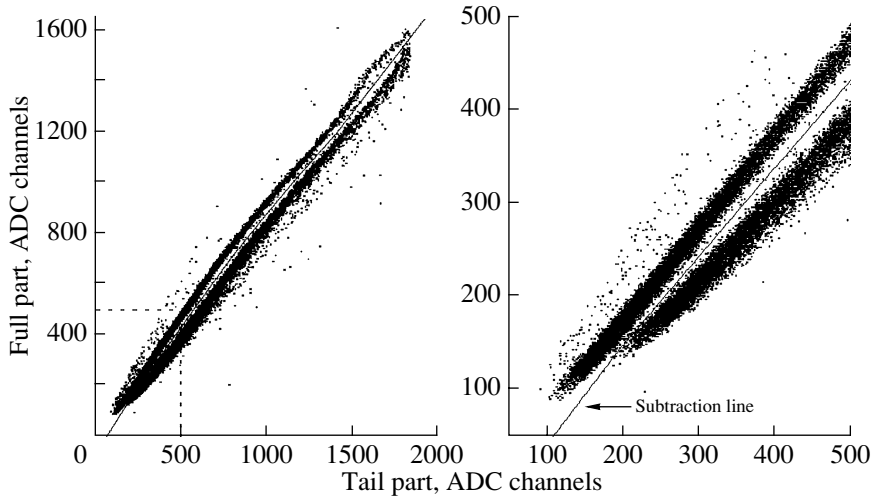

Fig. 2. Separation of neutrons from photons by an amplitude–amplitude analysis by the FULL-TAIL method (W target, $E_p = 1.0$ GeV, the angle is 120°).

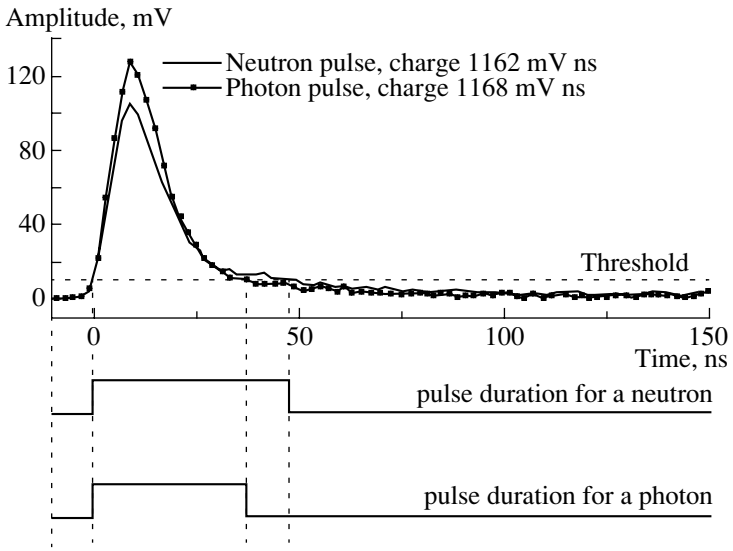

Fig. 3. Separation of neutrons from photons by the pulse-duration-measurement method.

3. DETERMINATION OF THE EFFICIENCY AND ENERGY RESOLUTION OF THE NEUTRON DETECTORS

(a) The neutron-detection efficiency for liquid and solid-state scintillators was calculated by the SCINFUL code [20] for $E_n < 80$ MeV and by the CECIL code [21] for $E_n > 80$ MeV at the discrimination threshold corresponding to $E_\gamma = 661.6$ keV (^{137}Cs). The CECIL data were normalized to get a smooth matching with the 80-MeV SCINFUL results. The relation between the photoelectron energy (corresponding to the total photon-energy transfer) and the energy of recoil protons that produce the same photoyield is [22]

$$E = 0.83E_p - 2.82(1 - e^{-0.25E_p^{0.93}}), \qquad (1)$$

where E_p is the proton energy (MeV) and E is the electron energy (MeV).

(b) The energy resolution is determined primarily by the following two factors that affect the accuracy in determining the detected-neutron velocities: (1) the spatial resolution (ΔL), which depends on the dimensions and relative position of the neutron counter and target; (2) the time resolution (ΔT), which is controlled by the speed of measuring equipment and by the fluctuations of the photoelectron flight time in a photomultiplier tube and of the time of flight of photons through a scintillator and through the detector

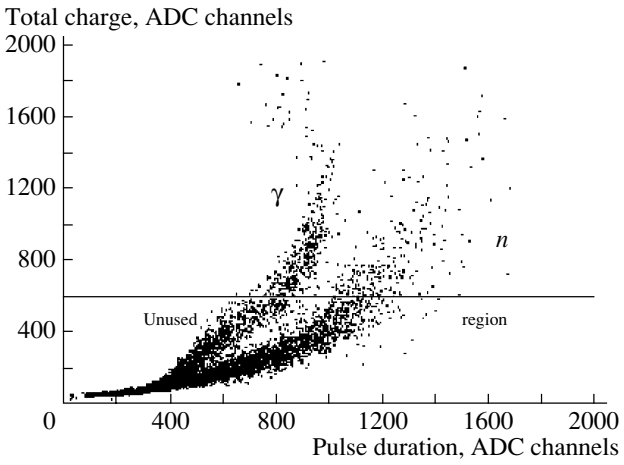

Fig. 4. Separation of neutrons from photons by the method of an amplitude–time analysis.

light guide. The time resolution was quantitatively estimated by the width of the peak associated with prompt photons from the Pb target. It proved to be 0.67 ns.

The energy resolution of the facility was determined as

$$\frac{\Delta E}{E} = \gamma(\gamma+1)\sqrt{\left(\frac{\Delta L}{L}\right)^2 + \left(\frac{\Delta T}{T}\right)^2}, \quad (2)$$

where γ is the relativistic Lorentz factor and L is the distance between the centers of the target and the detector.

When the target and the detector are spaced 2.0 m apart, the ultimate neutron energy at which the energy resolution is below 25% is 300 MeV.

4. EXPERIMENTAL RESULTS

The double-differential cross sections were determined from the time spectra of neutrons as

$$\frac{\partial^2\sigma}{\partial E\partial\Omega} = \frac{N_i A}{N_p C_L \varepsilon_i \Delta E_i \Delta\Omega \rho L_{\rm M} N_{\rm A}}, \quad (3)$$

where N_i is the number of neutron-induced signals fixed by the ith time channel, A is the atomic weight of the target material, N_p is the number of bombarding protons, C_L is a factor that takes into account the loss of protons in the target, ε_i is the neutron-detection efficiency corresponding to the middle of the ith time interval, ΔE_i is the energy width of the ith channel, $\Delta\Omega$ is the detector solid angle, ρ is the target-material density (g/cm^3), L_M is target thickness (cm), and $N_{\rm A}$ is Avogadro's number.

The neutron energy in the ith channel was determined as

$$E_i = m_n c^2 \left(1\Big/\sqrt{1-\frac{L^2}{(L+c(t_i-t_0))^2}} - 1\right), \quad (4)$$

where m_n is the neutron rest mass, c is the speed of light, and $t_i - t_0$ is the delay time between the instants at which a prompt photon and a neutron hit a detector (t_0 is determined in the middle of the prompt-photon peak, and t_i is determined in the middle of the ith time interval).

The errors in the above double-differential cross sections were mainly determined by the error in the neutron-detection efficiency. The error in calculating the detection efficiency was taken to be 10% at energies below 80 MeV and 15% at energies above 80 MeV. These are just the values recommended in [11] for neutron detectors based on liquid scintillators of a similar volume. The statistical errors fluctuated in the interval between about 1% and about 20%, depending on the neutron energy and emission angle. The systematic errors arising from scattered neutrons in the hall were estimated at less than 5% and were disregarded because of their smallness.

All of the data obtained for the double-differential cross sections were published in [23] in the form of figures and tables, supplemented with a complete description of the experimental setup. Table 3 makes it possible to compare our double-differential cross sections obtained for Pb at 0.8 GeV with similar data obtained elsewhere.

5. CODES USED TO SIMULATE EXPERIMENTAL DATA

The experimental data were simulated by using three codes—namely, (1) the CEM97 cascade–exciton code, (2) the LAHET cascade–evaporation–fission code, and (3) the CASCADE cascade–evaporation–fission code.

The models underlying the three codes are described in detail in [24–48]. We will only mention the fundamentals of the codes.

(i) In the CEM97 code [24], hadron–nucleus interactions are simulated by the Monte Carlo method in terms of the advanced version of the CEM cascade–exciton model for nuclear reactions [25]. The code deals with three-stage reactions. The first stage is an intranuclear cascade (INC) for primary and secondary particles to be multiply scattered until they are absorbed or emitted from a nucleus. The residual excited nucleus formed after cascade-particle emission specifies the particle–hole configuration, which is the initial state for the second (preequilibrium)

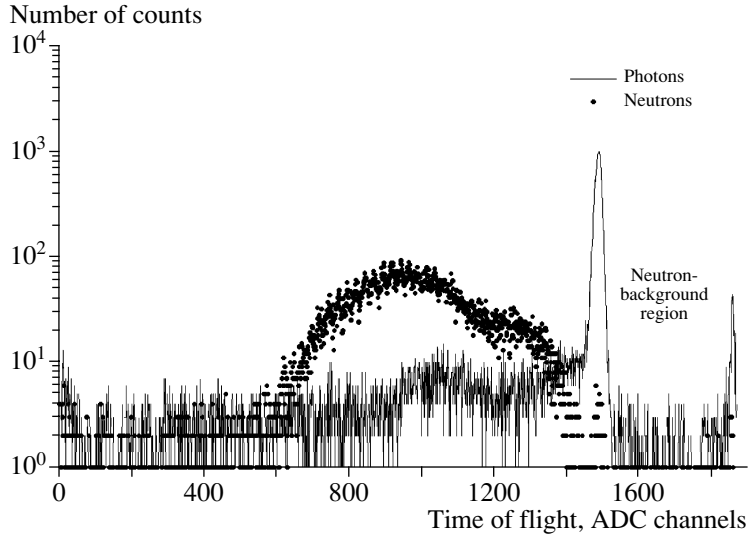

Fig. 5. Time-of-flight spectrum of neutrons and photons (W target, $E_p = 1.0$ GeV, the angle is 120°).

reaction stage. The subsequent relaxation of the nuclear excitation is simulated in terms of the exciton preequilibrium-decay model, which also describes the third (equilibrium) reaction stage. All three stages contribute to the measured secondary-particle spectrum.

The criterion of the transition from the intranuclear-cascade stage to the stage of preequilibrium evaporation is an important element of the CEM.

In conventional cascade–evaporation models (ISABEL [26] and BERTINI [27]) used in the LAHET code, fast particles are traced up to a certain minimum energy (cutoff energy T_{cut}), or the duration of the cascade reaction stage is compared with the cutoff time t_{cut}, which is usually taken at an energy of 7 to 10 MeV above the inner nuclear potential. Below the threshold, the particles are assumed to be absorbed by the nucleus (the so-called "temporal" cascade models of the type of Liege INC [28]).

The CEM code uses a criterion for the escape of a primary particle from the cascade stage via the introduction of the effective local optical potential $W_{\text{opt.mod}}(r)$ determined from the local interaction cross sections, including the blocking effects due to the Pauli exclusion principle. This imaginary potential is compared with the potential $W_{\text{opt.exp}}(r)$ determined in terms of the phenomenological global optical model by using data on elastic scattering by a nucleus. The convergence degree of imaginary potentials is determined via the parameter P,

$$P = |(W_{\text{opt.mod}}(r) - W_{\text{opt.exp}}(r))/W_{\text{opt.exp}}(r)|.$$

If P exceeds an empirically selected value, the particle escapes from the cascade stage of the process, becoming an exciton. In the CEM97 code, the parameter P is fixed at 0.3. This value was obtained from an analysis of data on proton– and pion–nucleus interactions at low and intermediate energies. With the selected P value, the cascade part of the code becomes shorter than in other cascade models.

The subsequent nuclear-reaction stages, which involve preequilibrium and equilibrium evaporation, are treated in terms of an improved modified exciton model (MEM) [29, 30]. At the preequilibrium stage, the CEM code takes into account all possible nuclear transitions leading to changes of $\Delta n = +2, -2$, and 0 in the exciton number n and all possible sequences of multiple emissions of n, p, d, t, ^{3}He, and ^{4}He. The set of equations for describing the behaviour of a nucleus at the preequilibrium stage is solved by the Monte Carlo technique [30].

The improved code CEM97 [24] makes use of new approximations of elementary interaction cross sections and of more accurate values of nuclear masses, Q, and binding and pairing energies. Also, it employs an updated systematics of the density-level parameters and improved approximations of pion binding energies. In addition, the code includes refined data on pion absorption on intranuclear quasideuteron pairs. Besides, the Pauli exclusion principle is taken into account in describing the preequilibrium stage.

(ii) The LAHET code, based on the Monte Carlo technique, is used to calculate the transport and interactions of nucleons, pions, muons, light ions, and antinucleons in extended objects. The code may also be employed without particle transport to generate cross sections for intranuclear interactions.

The LAHET code is a result of the LANL effort to develop a code system based on the HETC

Table 3. Double-differential cross sections for neutron generation, mb/(MeV sr), in a Pb target of dimensions ⌀50 × 20 mm^2 irradiated with 0.8-GeV protons

$E_{n-\Delta E}^{+\Delta E}$, MeV	Angle in lab. frame				
	30	60	90	120	150
330^{+136}_{-88}	0.497 ± 0.087	0.121 ± 0.024			
242^{+75}_{-54}	0.886 ± 0.14	0.278 ± 0.055	0.049 ± 0.022		
179^{+45}_{-35}	1.20 ± 0.19	0.554 ± 0.095	0.169 ± 0.041		
132^{+28}_{-23}	1.72 ± 0.28	0.926 ± 0.153	0.289 ± 0.057	0.176 ± 0.051	0.173 ± 0.079
99^{+18}_{-16}	2.51 ± 0.40	1.39 ± 0.23	0.513 ± 0.093	0.307 ± 0.076	0.280 ± 0.089
74^{+12}_{-11}	3.33 ± 0.40	1.96 ± 0.27	0.839 ± 0.11	0.456 ± 0.072	0.368 ± 0.084
$57.2^{+8.4}_{-7.6}$	4.13 ± 0.45	2.93 ± 0.33	1.29 ± 0.17	0.807 ± 0.12	0.638 ± 0.10
$44.8^{+6.0}_{-5.5}$	4.70 ± 0.56	3.45 ± 0.42	1.92 ± 0.23	1.17 ± 0.15	0.888 ± 0.14
$35.4^{+4.5}_{-4.1}$	6.94 ± 0.75	4.16 ± 0.52	3.31 ± 0.34	2.67 ± 0.27	2.06 ± 0.21
$28.4^{+3.4}_{-3.2}$	7.34 ± 0.79	5.63 ± 0.62	4.31 ± 0.44	3.88 ± 0.39	2.68 ± 0.28
$23.1^{+2.7}_{-2.6}$	8.00 ± 0.80	7.69 ± 0.77	5.02 ± 0.51	5.50 ± 0.56	4.12 ± 0.42
$18.9^{+2.1}_{-2.0}$	9.62 ± 0.97	8.96 ± 0.90	7.44 ± 0.75	7.89 ± 0.79	6.43 ± 0.64
$15.5^{+1.6}_{-1.6}$	13.4 ± 1.4	12.5 ± 1.3	11.8 ± 1.2	9.53 ± 0.96	8.61 ± 0.87
$12.8^{+1.3}_{-1.3}$	19.0 ± 1.9	19.8 ± 2.0	18.9 ± 1.9	17.0 ± 1.7	15.6 ± 1.6
$10.7^{+1.1}_{-1.0}$	24.5 ± 2.5	27.5 ± 2.8	23.4 ± 2.4	23.9 ± 2.4	20.1 ± 2.1
$8.88^{+0.90}_{-0.86}$	39.8 ± 4.0	39.2 ± 4.0	39.3 ± 4.0	35.6 ± 3.6	34.1 ± 3.5
$7.41^{+0.74}_{-0.71}$	52.6 ± 5.5	49.4 ± 5.2	49.8 ± 5.0	49.6 ± 5.0	45.2 ± 4.6
$6.20^{+0.61}_{-0.60}$	77.5 ± 8.0	63.1 ± 6.5	64.6 ± 6.5	64.1 ± 6.5	60.3 ± 6.1
$5.20^{+0.52}_{-0.50}$	105 ± 11	84.7 ± 8.8	76.0 ± 7.9	78.4 ± 7.9	70.4 ± 7.1
$4.37^{+0.43}_{-0.42}$	144 ± 15	110 ± 12	112 ± 12	86.2 ± 8.7	73.5 ± 7.8
$3.67^{+0.37}_{-0.36}$	186 ± 19	152 ± 16	147 ± 15	123 ± 13	110 ± 12
$3.10^{+0.31}_{-0.30}$	209 ± 22	170 ± 18	162 ± 17	158 ± 16	146 ± 15

code version intended for nucleon, pion, and muon transport and originally developed at the Oak Ridge Laboratory [31, 32]. Having been supplemented with copious amendments, the code system was named LAHET, and its associate code system was called the LAHET code system (LCS) [33]. The resultant code system can use the Bertini intranuclear-cascade models to describe the nucleon–nucleus interactions below 3.5 GeV [27].

Being an alternative to the Bertini model, the LCS also includes the intranuclear-cascade model from the ISABEL code [26], which is the Yariv–Frankel extension of the VEGAS code [34], and can simulate nucleus–nucleus and particle–nucleus interactions up to 1 GeV. The two models were used in the present study in the simulations via LCS.

The following LAHET code features are worth noting.

LCS makes it possible to calculate preequilibrium emission as an intermediate stage between the intranuclear cascade and evaporation/fission in terms of the multistage preequilibrium exciton model (MPM) [35]. As initially proposed in the multistage exciton model (MEM) [29, 30], the MPM uses the Monte Carlo technique to solve the set of master equations describing the equilibration of the excited residual nucleus that remains after the cascade reaction stage.

However, there are several important distinctions between the MPM and the MEM. First, the master equation of the MPM is simplified in relation to that of the MEM: the MPM takes into account only $\Delta n =$

+2 nuclear transitions, i.e., only in the direction of equilibration. The MEM considers all possible $\Delta n = +2, -2$, and 0 transitions, taking into account all possible positions of particle–hole pairs with respect to the Fermi level ($\Delta n = 0$ transitions). Second, the master equation of the MPM disregards the angular distributions of preequilibrium particles (note, however, that the MPM and, hence, the LAHET option allow one to calculate angular distributions of preequilibrium particles by using the phenomenological parametrization of Kalbach [34]). The MEM version used in CEM97 includes the conservation of momentum and the angular momentum of the nuclear system at the preequilibrium and equilibrium evaporation stages too. Therefore, the Monte Carlo algorithms are different when used in the MPM and the MEM to solve the respective equations.

There are several other distinctions between the MEM and the MPM, such as the use of different approximations for the cross sections describing inverse processes and for Coulomb barriers, for the level-density parameters, and for the nuclear-transition matrix elements (the details can be found in [29, 30, 35]).

There are also differences in interfaces between a portion of the intranuclear cascade and the preequilibrium emission in LAHET and CEM97. Besides, attention should be paid to the fact that LAHET invites the user to select between two fission models—namely, (a) the ORNL model [37] and (b) the Rutherford Appeleton Laboratory model (RAL) [38]. In fact, RAL consists of two parts (for actinides and preactinides separately), permits fission up to $Z = 71$, and is used in LAHET by default. The two fission models are used together with the Dresner evaporation model [36].

The LAHET code made use of the Bertini model at 1.6 GeV and of the ISABEL model at 0.8 and 1.0 GeV. The calculations were made without allowance for particle transport and the elastic scattering of neutrons for sufficiently thin Pb, W, Zr, Cu, and Al targets used at 1.0 and 1.6 GeV and with allowance for them for a 20-mm Pb target used at 0.8 GeV. The models included in LCS are described in detail in the references listed below and on some web sites [33].

(iii) The CASCADE Monte Carlo code system, which was developed at JINR (Dubna), has been used for many years to simulate ADS targets and the radiation damage of microelectronics, as well as to solve many other problems relevant to radiation transport in condensed and gaseous media [39, 40]. Like many other codes used to solve similar problems, the CASCADE code system is based on the cascade–evaporation intranuclear-cascade model. A feature peculiar to it is that the phenomenological angular and energy approximations are used in each interaction event to simulate the multiplicities and the parameters of particles produced in intranuclear hadron–nucleon interactions. Allowance is made in this case for the law of energy–momentum conservation and, sometimes, for the law of angular-momentum conservation [41]. The coordinates and momenta of all intranuclear nucleons are simulated for each intranuclear cascade in terms of a Gaussian distribution in light nuclei and of the Woods–Saxons distribution in the remaining nuclei. The decrease in the number of intranuclear nucleons due to knockout by fast cascade particles is also taken into account [42], just as the time coordinate, on assumption that an interaction event is determined by the particle that is the earliest in time [43]. This procedure also makes it possible to take into account the contribution from many-particle interactions, with a few cascade particles interacting simultaneously with an intranuclear nucleon within a time of 10^{-23} s [44].

The updated code developed by S. Mashnik and V. Toneev is used to calculate the emission of particles at the stage of relaxation of a strongly excited aftercascade nucleus [30]. The subsequent equilibrium decay of the after-cascade nucleus is calculated in terms of conventional Dostrovsky–Phong theory [41]. Allowance is also made for the dependence of the parameters of the density of levels in the decaying nucleus on its charge, mass, and excitation energy. The approximations of experimental cross sections are applied to the cross sections for hadron–nucleus interactions [45, 46].

6. COMPARISON OF EXPERIMENTAL DATA WITH THE RESULTS OF THE CALCULATIONS AND WITH DATA OBTAINED ELSEWHERE

In the present article, Fig. 6 shows only the double-differential cross sections for tungsten along with the results of simulations based on the LAHET, CEM97, and CASCADE codes.[3)]

A comparison of the experimental data with the results of the calculations leads to the following conclusions:

(1) An analysis of the spectra of the double-differential cross sections for neutrons emitted at angles of 15° to 150° for all of the incident proton energies has indicated fairly good agreement between the experimental data for Pb, W, and Zr with the results of the simulations on the basis of the LAHET, CEM97, and CASCADE codes throughout

[3)]The data for Pb, W, Zr, Cu, and Al in the form of tables and figures are given in [23].

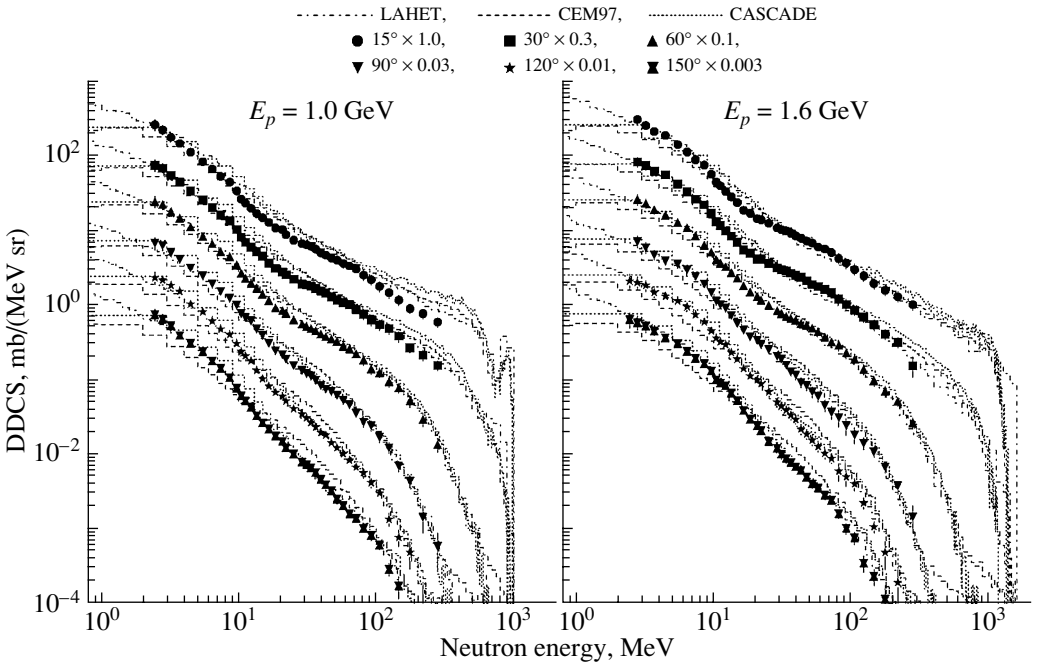

Fig. 6. Double-differential cross sections (DDCS) for the production of neutrons from a ^{nat}W target of dimensions 50 × 5.1 mm^2 irradiated with 1.0- and 1.6-GeV protons. Also shown are the results of the simulations based on the LAHET, CEM97, and CASCADE codes.

the neutron-energy range 3–300 MeV. A disagreement is observed only in the range between about 15 and 40 MeV, where the calculated values exceed the experimental data (by up to 50%) at neutron emission angles of 15° to 90°. The best agreement for Pb and W has been reached with LAHET. The CEM97 overestimation of the experimental data in the range 10–30 MeV is explained by the overestimated generation of preequilibrium neutrons. This conclusion is in good agreement with the results of a comparison of spallation-product yields calculated on the basis of CEM97 with the GSI (Darmstadt) data of the inverse-kinematics experiments [47]. The difficulty with the overestimated generation of preequilibrium neutrons is expected to be overcome by the updated CEM97 – CEM2k, CEM2k + GEM2, and LAQGSM + GEM2 code versions [48].

In the case of Zr and Cu, the experimental spectra for all angles are in the best agreement with the spectra simulated by using CEM97.

In the case of Al, the agreement between the experimental spectra and the spectra simulated by all of the codes is much poorer.

(2) Figure 7 shows the experimental spectra as integrated over all neutron emission angles within four energy ranges restricted at 3, 10, 30, 100, and 300 MeV. Also shown are the results of LAHET, CEM97, and CASCADE calculations. The energy groups presented are qualitatively resultant from three stages of proton–nucleus interaction process—namely, (i) the intranuclear-cascade stage (at neutron energies of 100–300 MeV), (ii) the preequilibrium-evaporation stage (energy ranges 10–30 MeV and, partly, 30–100 MeV), and (iii) the equilibrium-evaporation stage (energy ranges 3–10 MeV and, partly, 10–30 MeV).

An analysis of these spectra has revealed the following special features:

(a) In the case of Al, all codes simulate the region of cascade neutrons satisfactorily. The CASCADE code describes the evaporation and preevaporation stages quite properly at 1.0 GeV but leads to underestimated results at 1.6 GeV. The LAHET code is the best to predict the evaporated-neutron yield at 1.6 GeV.

(b) In the case of Zr and Cu, the CEM97 code simulates all interaction stages in good agreement with experimental data, the only reservation being that, for Zr, the evaporation-stage neutron yield is somewhat underestimated at two incident proton energies; this region is better described by the CASCADE code.

(c) In relation to the remaining targets, W and Pb are described much better by all codes (this is not so only in the range 10–30 MeV). The LAHET code is the best to agree with experimental data, especially in the case of Pb at 0.8 GeV and 1.0 GeV. The CASCADE code persistently overestimates the neutron yields at the evaporation and preequilibrium stages.

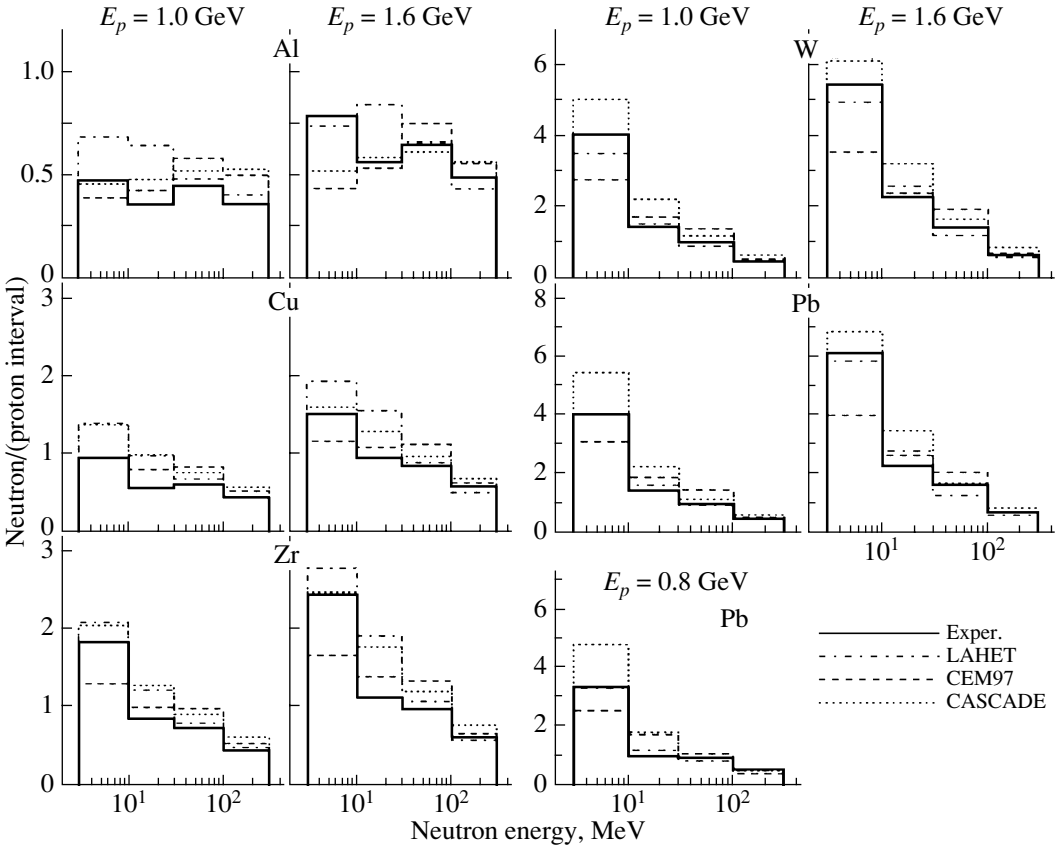

Fig. 7. Experimental neutron spectra integrated with respect to angles in four energy ranges with the boundaries at 3, 10, 30, 100, and 300 MeV. Also shown are the results of the simulations based on the LAHET, CEM97, and CASCADE codes.

The CEM97 code yields markedly underestimated results at energies below 5 MeV; this may result from the absence of simulations of neutron emission from fission products, as well as from the insufficiently correct description of the rotation energy and angular momentum of the nucleus at the evaporation reaction stage.

An analysis of the entire dataset leads to following conclusions:

(a) For the heavy nuclei Pb and W, the experimental data agree satisfactorily with the LAHET, CEM97, and CASCADE simulations. To achieve any better agreement, it is necessary to have a more accurate description of the point of inflection in spectra at the contact of the equilibrium and preequilibrium regions (about 10 to 30 MeV) for neutrons emitted into the forward hemisphere.

(b) For medium nuclei, the code CEM97 is the most adequate.

(c) For Al, all of the calculated spectra are markedly different from the experimental data in the case of equilibrium and preequilibrium evaporation. Traditionally, this is explained by the inadequacy of the intranuclear-cascade model to describing the case of light nuclei, where most of the nucleons are bound by shell effects, and by the increased probability for α-cluster emission in strongly excited light nuclei.

(d) For all of the measured nuclei and for all proton energies, all three codes describe the double-differential cross sections quite well at the intranuclear-cascade stage.

The following conclusion can be drawn from a comparison of our experimental data with the results obtained elsewhere:

At the incident proton energy of 1.0 GeV, our Pb and Al data are in good agreement with the results obtained earlier by using 0.8-GeV protons at LANL [7, 10] and KEK [11], while the Zr data show good agreement with the data from [7] within the intranuclear-cascade range (90–300 MeV).

At the incident proton energy of 1.6 GeV, our Pb data are in good agreement with KEK data from [11], but the Al data show a significant disagreement (up to 100%) at the equilibrium and preequilibrium evaporation stages.

ACKNOWLEDGMENTS

We are indebted to Dr. V.A. Korolev for his participation in the measurements, to Dr. A.V. Belkin for his assistance in dealing with computational software, and to Mrs. N.V. Belyavskaya for her invaluable help in preparing the manuscript.

This work was supported in part by the International Science and Technology Center and by the US Department of Energy.

REFERENCES

1. R. F. Rose, Report BNL-NCG-17541 (1991); K. Shibata, Report JAERI-1319 (1990).
2. M. Blann *et al.*, International Code Comparison for Intermediate Energy Nuclear Data, OECD/NEA (1994); D. Filges *et al.*, OECD Thick Target Benchmark, Report NSC/DOC(95)2 (1995).
3. S. Cierjacks *et al.,* Phys. Rev. C **36**, 1976 (1987); D. Filges *et al.*, Phys. Rev. C **36**, 1988 (1987); tabulated data available in the database EXFOR.
4. W. Scobel *et al.*, Phys. Rev. C **41**, 2010 (1990); tabulated data available in the database EXFOR.
5. M. M. Meier *et al.*, Nucl. Sci. Eng. **102**, 310 (1989); tabulated data available in the database EXFOR.
6. M. M. Meier *et al.*, Nucl. Sci. Eng. **110**, 299 (1992); tabulated data available in the database EXFOR.
7. S. Stamer *et al.*, Phys. Rev. C **47**, 1647 (1993); tabulated data available in the database EXFOR.
8. M. M. Meier *et al.*, Radiat. Eff. **96**, 73 (1986).
9. W. B. Amian *et al.*, Nucl. Sci. Eng. **115**, 1 (1993); tabulated data available in the database EXFOR.
10. W. B. Amian *et al.*, Nucl. Sci. Eng. **112**, 78 (1992); tabulated data available in the database EXFOR.
11. K. Ishibashi *et al.*, J. Nucl. Sci. Technol. **34**, 529 (1997).
12. T. A. Shibata *et al.*, Nucl. Phys. A **408**, 525 (1983).
13. T. Nakamoto *et al.*, J. Nucl. Sci. Technol. **32**, 827 (1995); S. Meigo *et al.*, in *Proceeding of 13th Meeting of the Int. Collaboration on Advanced Neutron Sources, PSI, Switzerland, Oct. 11–14, 1995*, pp. 442–453.
14. S. Leray *et al.*, Phys. Rev. C **65**, 044621 (2002); S. Meigo, in *Proceeding of the Third Specialists' Meeting on High Energy Nuclear Data, JAERI, Japan, March 30–31, 1998*, pp. 30–36; P. Pras *et al.*, in *Proceeding of the International Conference on Sub-Critical Accelerator Driven System, Moscow, October 11–15, 1999* (ITEP, Moscow, 1999), pp. 161–168.
15. I. A. Vorontsov *et al.*, Vopr. At. Nauki Tekh.: Ser. Fiz. Akt. Reakt., TIYAS-XI, 120 (1997); Yu. V. Trebukhovski, in *Proceeding of the International Conference on Sub-Critical Accelerator Driven System, Moscow, October 11–15, 1999* (ITEP, Moscow, 1999), pp. 212–217.
16. Yu. D. Bayukov *et al.*, Preprint No. ITEP-172-1983 (ITEP, Moscow, 1983).
17. A. V. Daniel *et al.*, JINR Communication E-1-92-174, Dubna (1992).
18. N. V. Gorbunov *et al.*, Preprint JINR, R-10-85-955, 954 (1985).
19. T. W. Armstrong *et al.*, Report CCC-178, ORNL (1977); Z. W. Bell, Nucl. Instrum. Methods Phys. Res. **188**, 105 (1981); F. M. Borne, THESES L'universite Bordeaux **36**, 107 (1998); H. Heltsley *et al.*, Nucl. Instrum. Methods Phys. Res. A **263**, 441 (1988).
20. J. K. Dickens, Report ORNL-6452 (1988).
21. R. A. Cecil *et al.*, Nucl. Instrum. Methods **161**, 439 (1979).
22. Bicron BC-501A, Liquid Scintillator, Properties, Saint-Gobain/Norton Industrial Ceramics Corporation.
23. Yu. V. Trebukhovsky *et al.*, Preprint No. 03-03 (Inst. Theor. Exp. Phys., Moscow); LANL Report No. LA-UR-03-6071 (Los Alamos, 2003).
24. S. G. Mashnik *et al.*, Nucl. Instrum. Methods Phys. Res. A **414**, 68 (1998); LANL Report LA-UR-97-2905 (1997); S. G. Mashnik and A. J. Sierk, LANL Report LA-UR-98-5999 (1998); nucl-th/9812069; in *Proceeding of Fourth International Workshop on Simulating Accelerator Radiation Environments (SARE-4), Knoxville, TN, September 13–16, 1998*, pp. 29–59.
25. K. K. Gudima, S. G. Mashnik, and V. D. Toneev, Nucl. Phys. A **401**, 329 (1983).
26. Y. Yariv and Z. Frankel, Phys. Rev. C **20**, 2227 (1979); **24**, 488 (1981).
27. H. W. Bertini, Phys. Rev. **131**, 1801 (1963); **138**, AB2 (1965); **188**, 1711 (1969); Phys. Rev. C **6**, 631 (1972); H. W. Bertini and M. P. Guthrie, Nucl. Phys. A **169**, 670 (1971).
28. J. Cugnon, C. Volant, and S. Vuillier, Nucl. Phys. A **620**, 475 (1997); A. Boudar, J. Cugnon, S. Leray, and C. Volant, Phys. Rev. C **66**, 044615 (2002).
29. K. K. Gudima, G. A. Osokov, V. D. Toneev, *et al.*, Yad. Fiz. **21**, 260 (1975) [Sov. J. Nucl. Phys. **21**, 138 (1975)].
30. S. G. Mashnik and V. D. Toneev, JINR Communication P4-8417, Dubna (1974).
31. Radiation Shielding Information Center, "HETC Monte Carlo High-Energy Nucleon-Meson Transport Code", Report CCC-178, Oak Ridge National Laboratory (August, 1977); http://www-rsicc.ornl.gov/codes/ccc/ccc0/ccc-017.html.
32. T. W. Armstrong and K. C. Chandler, Nucl. Sci. Eng. **49**, 110 (1972).
33. R. E. Prael and H. Lichtenstein, LANL Report LA-UR-89-3014, Los Alamos (1989); http://www-xdiv.lanl.gov/XCI/PROJECTS/LCS/index.html.
34. K. Chen *et al.*, Phys. Rev. **166**, 948 (1968); Phys. Rev. C **4**, 2234 (1971); G. D. Harp *et al.*, Phys. Rev. C **8**, 581 (1973).
35. R. E. Prael and M. Bozoian, Los Alamos National Laboratory Report LA-UR-88-3238 (1988).
36. L. Dresner, Oak Ridge National Laboratory Report ORNL-TM-196 (1962); P. Cloth *et al.*, Kernforschungsanlage Jülich Report Jül-Spez-196 (1983).

37. J. Barish *et al.*, Oak Ridge National Laboratory Report ORNL/TM-7882, Oak Ridge (1981); F. S. Alsmiller *et al.*, Nucl. Sci. Eng. **79**, 147 (1981); **79**, 166 (1981).
38. F. Atchinson, in *Proceeding of Meeting on Targets for Neutron Beam Spallation Sources, Jülich, June 11–12, 1979*, Jül-Conf-34, Kernforschungsanlage Jülich GmbH (January 1980), p. 17.
39. V. S. Barashenkov, *Programming and Mathematical Techniques* (World Sci., Singapore, 1994), p. 167.
40. V. S. Barashenkov, Comput. Phys. Commun. **126**, 28 (2000).
41. V. S. Barashenkov and V. D. Toneev, *Interactions of High-Energy Particles and Nuclei with Nuclei* (Atomizdat, Moscow, 1972) [in Russian].
42. V. S. Barashenkov *et al.*, Usp. Fiz. Nauk **109**, 91 (1973) [Sov. Phys. Usp. **16**, 31 (1973)].
43. V. S. Barashenkov, B. F. Kostenko, and A. M. Zadorogny, Nucl. Phys. A **338**, 413 (1980).
44. V. S. Barashenkov and B. F. Kostenko, JINR Communications P2-87-789 (Dubna, 1987).
45. V. S. Barashenkov, *Cross Sections for the Interaction of Particles and Nuclei with Nuclei* (JINR, Dubna, 1993) [in Russian].
46. V. S. Barashenkov *et al.*, JINR Preprint No. E-2-99-207 (Joint Inst. Nucl. Res., Dubna); *Paper No. Mo-O-C10 on the CD-ROM with Proc. of the 3rd Int. Conf. on Accelerator Driven Transmutation Technologies (ADTTA99), Praha (Pruhonice), Czech Republic, June 7–11, 1999* (http://www.fjfi.cvut.cz/con_adtt99).
47. S. G. Mashnik *et al.*, J. Nucl. Sci. Technol., Suppl. **2**, 785 (2002); nucl-th/0208075.
48. S. G. Mashnik *et al.*, Proc. SATIF-6, April 10–12, 2002, SLAC, CA 94025, USA; LANL Report LA-UR-03-2261 (Los Alamos, 2003); nucl-th/0304012; *Invited Talk Presented at the 12th Biennial Topical Meeting of the Radiation Protection and Shielding Division (RPSD) of the American Nuclear Society, Santa Fe, NM, April 14–17, 2002*; LANL Report LA-UR-02-5185, Los Alamos (2002); nucl-th/0208048.

Translated by Y. Trebukhovsky

Physics of Atomic Nuclei, Vol. 68, No. 1, 2005, pp. 33–41. Translated from Yadernaya Fizika, Vol. 68, No. 1, 2005, pp. 35–42.

NUCLEI
Theory

Diffractive Dissociation of Tritons by Incident Protons

V. K. Tartakovsky, A. V. Fursayev*, and B. I. Sidorenko

Bogolyubov Institute for Theoretical Physics, National Academy of Sciences of Ukraine, Metrologicheskaya ul. 14b, Kiev, 03143 Ukraine

Received March 14, 2003; in final form, November 14, 2003

Abstract—General expressions that are obtained in the present study for the differential cross sections describing the two- and three-body diffractive dissociation of tritons that is induced by intermediate-energy incident protons are used to calculate the energy distributions of neutrons and protons originating from this process and of scattered protons. The results are basically in satisfactory (but sometimes only qualitative) agreement with data from relevant coincidence experiments. © *2005 Pleiades Publishing, Inc.*

1. INTRODUCTION

The dissociation of the three-nucleon nuclei ^{3}H and ^{3}He that is induced by incident protons has been studied experimentally and theoretically for more than 30 years [1–7]. Among other things, these studies revealed that one can obtain additional and more detailed (than in the case of elastic nucleon scattering on three-nucleon nuclei) information both about the structure of three-nucleon systems and about the details of the nuclear interaction of nucleons with nucleons, deuterons, and ^{3}H and ^{3}He nuclei. Relevant coincidence experiments were performed at projectile-proton energies of about 10^2 MeV or higher. This suggests that the processes being considered appear to be predominantly of a quasifree-proton-scattering character, in which case momentum and energy are basically transferred to only one target nucleon, and that one can employ, in a theoretical investigation, various approximations that follow from the fact that the particles involved have rather high energies.

The diffraction approximation [8–10], which we employ in the present study in a theoretical consideration of the two- and three-particle dissociation of ^{3}H nuclei that is induced by incident protons of nonrelativistic kinetic energies E_0 around 70 MeV, is one of the most efficient approximations in describing the dissociation of nuclei at these energies. These were precisely the energies that protons that induced the dissociation of tritons had in the experiments reported in [5, 6], which have not yet received an adequate theoretical interpretation. In those experiments, the energy spectra of neutrons and protons originating from the dissociation of tritons and the coincidence spectra of inelastically scattered protons were measured in coplanar kinematics for the case where, after an interaction event, the proton momentum $\mathbf{p}_p$ and the neutron momentum $\mathbf{p}_n$ formed, respectively, the angle $\theta_p = 45^\circ$ and the angle $\theta_n = 45^\circ$ with the incident-proton momentum $\mathbf{p}_0$ in the triton rest frame and lay on different sides of the direction (z axis) of the vector $\mathbf{p}_0$ (that is, the angle θ_{pn} between the momenta $\mathbf{p}_p$ and $\mathbf{p}_n$ was 90°).

The kinematical conditions of the experiments that were reported in [5, 6] and which are treated here theoretically are at the applicability boundary usually indicated in the literature for the diffraction approximation. It will be seen below nevertheless that, in some cases, one can attain fairly good agreement between the calculated and measured differential cross sections, this indicating that, in fact, the applicability range of this approximation is much wider. It would be natural to expect at least qualitative agreement, since a qualitative description was obtained from calculations performed by other authors for a similar situation [3, 4]. Calculations show that, for smaller angles θ_p and θ_n—for example, those that fall within the range 10°–20°—and energies in the region $E_0 \geq 100$ MeV, differential cross sections would be much larger than those in [5, 6]; concurrently, the diffraction-approximation conditions would be satisfied much better, and better agreement between the results of the calculation with data from such experiments could be expected in this case. As will be seen from the ensuing consideration, it is possible to correct the traditional formalism of the diffraction nuclear model both for larger angles of incident-proton scattering and for larger angles of the emission of nucleons formed upon triton-dissociation reactions.

Our theoretical investigations of the processes $^3\mathrm{H}(p,pn)^2\mathrm{H}$ and $^3\mathrm{H}(p,pn)pn$ under the kinematical conditions of the experiments reported in [5, 6] reveal that the results here are much more sensitive to the nuclear structure and interaction than at smaller angles θ_p and θ_n and higher energies E_0, and this can

*e-mail: alya@ps.kiev.ua

be used in more precise experiments and calculations for extracting additional information.

In the present study, we aim at approximately solving the extremely difficult problem of four interacting and partly ($p + {}^3\mathrm{H}$, $p + n + {}^2\mathrm{H}$) or completely ($2p + 2n$) unbound nucleons in a specific range of energies of the system where one can use the diffraction approximation.

2. REACTION ${}^3\mathrm{H}(p, pn)^2\mathrm{H}$: FORMALISM

In experiments reported in [5, 6], neutrons originating from the dissociation of tritons could arise either in the two-particle breakup of tritons through the reaction ${}^3\mathrm{H}(p, pn)^2\mathrm{H}$ or in the complete (three-particle) dissociation of the ${}^3\mathrm{H}$ nucleus through the reaction ${}^3\mathrm{H}(p, pn)pn$. We will first consider the process ${}^3\mathrm{H}(p, pn)^2\mathrm{H}$, which is simpler from the point of view of a theoretical investigation.

In the diffraction approximation [4, 8–10], the amplitude $A_{\mathbf{f}}(\mathbf{q})$ for the reaction ${}^3\mathrm{H}(p, pn)^2\mathrm{H}$ can be represented in the form (use is made here of the system of units where $\hbar = c = 1$)

$$A_{\mathbf{f}}(\mathbf{q}) = -\int d^{(3)}\mathbf{r}\int d^{(3)}\mathbf{s} \times \int d^{(2)}\boldsymbol{\rho}\, e^{i\mathbf{q}\cdot\boldsymbol{\rho}}\varphi^*_{\mathbf{f}}(\mathbf{r})\varphi^*_d(\mathbf{s})\widehat{\omega}_{123}\psi(\mathbf{r},\mathbf{s}), \quad (1)$$

where $\psi(\mathbf{r},\mathbf{s})$ is the triton internal wave function; $\mathbf{r}$ is the radius vector between the first neutron and the center of mass of the remaining two nucleons in the triton being considered; $\mathbf{s}$ is the radius vector between these two nucleons, a neutron and a proton (respectively, the second and the third nucleon in the triton); $\varphi_d(\mathbf{s})$ is the wave function describing the internal state of the product deuteron; $\varphi_{\mathbf{f}}(\mathbf{r})$ is the wave function describing the relative motion (with a momentum $\mathbf{f}$) of the knock-on (first) neutron and this deuteron; and $\mathbf{q} = \mathbf{p}_0 - \mathbf{p}_p$ is the momentum-transfer vector. The wave functions in question are orthonormalized as follows (no account is taken of the particle spins here):

$$\int d^{(3)}\mathbf{s}\int d^{(3)}\mathbf{r}|\psi(\mathbf{r},\mathbf{s})|^2 = \int d^{(3)}\mathbf{s}|\varphi_d(\mathbf{s})|^2 = 1,$$
$$\int d^{(3)}\mathbf{s}\int d^{(3)}\mathbf{r}\varphi^*_{\mathbf{f}}(\mathbf{r})\varphi^*_d(\mathbf{s})\psi(\mathbf{r},\mathbf{s}) = 0. \quad (2)$$

As in [4, 7, 11], the diffraction operator $\widehat{\omega}_{123}$ (profile operator) in (1) is given by

$$\widehat{\omega}_{123} = \sum_{j=1}^{3}\omega_j e^{iq_z z_j}\prod_{k=j+1}^{3}(1-\omega_k), \quad (3)$$

where ω_j is the profile function for the incident proton and the jth nucleon in the triton ($j = 1, 2, 3$) and q_z and z_j are the z projections of, respectively, the vector $\mathbf{q}$ and the radius vector $\mathbf{r}_j$ between the incident proton and the jth nucleon of the triton. The value of q_z in (3) was taken to correspond to the momentum-conservation law. Integration with respect to $\boldsymbol{\rho}$ in (1) is performed in a plane that is orthogonal to the vector $\mathbf{p}_0 = 4\mathbf{k}/3$, where $\mathbf{k}$ is the momentum associated with incident-proton motion relative to the target nucleus ${}^3\mathrm{H}$ at rest, $\boldsymbol{\rho}$ being that component of the vector between the incident proton and the triton center of mass which lies in a plane that is orthogonal to the vector $\mathbf{k}$, so that $\boldsymbol{\rho}\cdot\mathbf{k} = 0$.

The profile operator $\widehat{\omega}_{123}$ defined in (3) is a generalization of the elastic-scattering profile operator [which is obtained from (3) upon discarding the exponential function $e^{iq_z z_j}$—that is, at $q_z = 0$] to the case of one deep-inelastic-collision event accompanied by nucleon knockout from the target nucleus. For angles of proton scattering and neutron emission from the triton (they are denoted by θ_p and θ_n, respectively) as large as those in the experiments reported in [5, 6], the value that is obtained for the longitudinal component $q_z = \mathbf{q}\cdot\mathbf{p}_0/p_0 = p_0 - p_{pz}$ of the momentum-transfer vector $\mathbf{q}$ upon taking correctly into account the momentum-conservation law is significant and cannot be disregarded, in contrast to what is done in the case of elastic scattering. This can also be seen from the theoretical results for the differential cross section at $q_z \neq 0$ and $q_z = 0$.

The physical reason behind the emergence of a significant longitudinal component q_z is that, prior to a collision with an incident proton, bound-state nucleons in the triton have relative-momentum distributions such that the most probable values of their relative momenta in ${}^3\mathrm{H}$ are not low. It is clear that, in addition to components orthogonal to $\mathbf{p}_0$, the momentum distribution in question features significant relative-momentum components aligned with $\mathbf{p}_0$, and this can lead to a considerable scatter of the values of p_{pz} and $q_z = p_0 - p_{pz}$.

The general expression for the differential cross section for the process $p + t \to p + n + d$ in terms of the transition amplitude $M^{(2)}_{i\to f}$ is [4, 7, 12]

$$d^9\sigma^{(2)} = (2\pi)^4|M^{(2)}_{i\to f}|^2\delta^{(4)}(p_0 + p_t - p_p - p_n - p_d)\frac{d^{(3)}\mathbf{p}_p}{(2\pi)^3}\frac{d^{(3)}\mathbf{p}_n}{(2\pi)^3}\frac{d^{(3)}\mathbf{p}_d}{(2\pi)^3}, \quad (4)$$

where the argument of the four-dimensional delta function involves the 4-momenta p_p, p_n, and p_d of, respectively, the proton, neutron, and deuteron after the scattering of an incident proton with a 4-momentum

p_0 on a triton with a 4-momentum p_t. All of the quantities on the right-hand side of (4) are defined in the laboratory frame, where the triton is at rest prior to the collision event ($\mathbf{p}_t = 0$), as in the experiments reported in [5, 6].

In order to relate the general transition amplitude $M^{(2)}_{i\to f}$ to the amplitude in (1) in the diffraction approximation (an insignificant phase factor being omitted there), it is sufficient to equate the differential cross section for the incident-proton-induced diffractive dissociation of a triton into a neutron and a deuteron [8–10],

$$d^5\sigma^{(2)}_{i\to f} = |A_{\mathbf{f}}(\mathbf{q})|^2 \frac{d^{(2)}\boldsymbol{\kappa} d^{(3)}\mathbf{f}}{(2\pi)^5}, \qquad (5)$$
$$d^{(2)}\boldsymbol{\kappa} = d^{(2)}\mathbf{q}_\perp,$$

to the differential cross section (4) integrated with respect to $\mathbf{p}_d$ and $q_z = p_0 - p_{pz}$ (with allowance for delta functions),

$$d^5\sigma^{(2)}_{i\to f} = \int\limits_{-\infty}^{\infty} dq_z \int d^{(3)}\mathbf{p}_d \left(\frac{d^9\sigma^{(2)}}{dq_z d^{(3)}\mathbf{p}_d}\right). \qquad (6)$$

Here, $\boldsymbol{\kappa} \equiv \mathbf{q}_\perp = -\mathbf{p}_{p\perp}$ is the momentum-transfer ($\mathbf{q}$) component orthogonal to $\mathbf{p}_0$ ($\boldsymbol{\kappa}$ is a two-dimensional vector) and $\mathbf{p}_{p\perp}$ is the scattered-proton-momentum ($\mathbf{p}_p$) component orthogonal to $\mathbf{p}_0$, so that $d^{(3)}\mathbf{p}_p \equiv dp_z d^{(2)}\mathbf{p}_{p\perp} = d^{(3)}\mathbf{q} = dq_z d^{(2)}\boldsymbol{\kappa}$. In performing integration in (6) and in reducing the result to (5), it is necessary to bear in mind that the element $d^{(3)}\mathbf{p}_p d^{(3)}\mathbf{p}_n$ of the six-dimensional volume in (4) can be replaced by $d^{(3)}\mathbf{q} d^{(3)}\mathbf{f}$ (the modulus of the transition Jacobian is equal to unity) owing to the relations $\mathbf{f} = \mathbf{p}_p/3 + \mathbf{p}_n - \mathbf{p}_0/3$ and $\mathbf{q} = \mathbf{p}_0 - \mathbf{p}_p$. In the diffraction approximation, only a term that is linear in q_z can be retained in the argument of the delta function

$$\delta(E_2) \equiv \delta\Big\{E_0 - \varepsilon_{dn} - \frac{1}{2M}[p_0^2 - 2p_0 q_z \qquad (7)$$
$$+ (4/3)(\kappa^2 + q_z^2) + (3/2)f^2]\Big\},$$

where $\varepsilon_{dn} \approx 6.26$ MeV is the energy required to detach a neutron (first nucleon) from the triton [13]. As a result, we arrive at the relation

$$M^{(2)}_{i\to f} = \sqrt{p_0/M}\, A_{\mathbf{f}}(\mathbf{q}) = \sqrt{4k/3M}\, A_{\mathbf{f}}(\mathbf{q}), \qquad (8)$$

where M is the nucleon mass. We now represent differential cross sections in the form of expressions that correspond to the differential cross sections measured in the experiments reported in [5, 6]. Integrating expression (4) with respect to the 3-momentum $\mathbf{p}_d$, we obtain

$$d^6\sigma^{(2)} = 2\pi \frac{p_0}{M} |A_{\mathbf{f}}(\mathbf{q})|^2 \delta(E_2) \frac{d^{(3)}\mathbf{p}_p}{(2\pi)^3} \frac{d^{(3)}\mathbf{p}_n}{(2\pi)^3}, \qquad (9)$$

$$E_2 = E_0 - \varepsilon_{dn} - E_p - E_n - E_d(\mathbf{p}_p, \mathbf{p}_n), \qquad (10)$$

$$E_0 = \frac{\mathbf{p}_0^2}{2M}, E_p = \frac{\mathbf{p}_p^2}{2M}, E_n = \frac{\mathbf{p}_n^2}{2M}, \qquad (11)$$

$$E_d(\mathbf{p}_p, \mathbf{p}_n) = \frac{\mathbf{p}_d^2}{4M} = \frac{1}{2}(E_0 + E_p + E_n) \qquad (12)$$
$$- \sqrt{E_0 E_p}\cos\theta_p - \sqrt{E_0 E_n}\cos\theta_n$$
$$+ \sqrt{E_p E_n}\cos\theta_{pn},$$

where $\mathbf{p}_d = \mathbf{p}_0 - \mathbf{p}_p - \mathbf{p}_n$. Taking into account (10)–(12), we now recast the differential cross section (9) into the form of an expression that has already been used in calculations (it contributed to the differential cross section measured in [5]). Specifically, we have

$$\frac{d^6\sigma^{(2)}_{i\to f}}{d\Omega_p d\Omega_n dE_p dE_n} = \frac{M^2 p_0 \sqrt{E_p E_n}}{8\pi^5} |A_{\mathbf{f}}(\mathbf{q})|^2 \delta(E_2), \qquad (13)$$

where we have replaced $\delta(E_2)$ by the function

$$\delta_\Delta(E_2) = \frac{1}{\sqrt{\pi\Delta^2}} \exp\left(-\frac{E_2^2}{\Delta^2}\right), \qquad (14)$$
$$\lim_{\Delta\to 0} \delta_\Delta(E_2) = \delta(E_2),$$

which involves a finite smearing parameter Δ. A numerical value of Δ reflects experimental errors associated with the particle energies and measured angles in (10)–(12). Since the two neutrons of the triton can be knocked out with equal probabilities, the ultimate expression for the differential cross section in (13) must be doubled. Integrating (9) with respect to the energy E_n of the knock-on neutron, we obtain [with allowance for relations (10)–(12) and doubling] a differential cross section that we have also directly used in our calculations (it made the main contribution to the differential cross section measured in [6]). Its specific form is

$$\frac{d^5\sigma^{(2)}_{i\to f}}{d\Omega_p d\Omega_n dE_p} = \frac{M p_0 \sqrt{2ME_p}}{8\pi^5 G} \qquad (15)$$
$$\times \Big\{[p_n^2 |A_{\mathbf{f}}(\mathbf{q})|^2]_{p_n = \frac{1}{3}(g+G)}$$
$$+ [p_n^2 |A_{\mathbf{f}}(\mathbf{q})|^2]_{p_n = \frac{1}{3}(g-G)}\Big\},$$

where

$$g = p_0\cos\theta_n - p_p\cos\theta_{pn}, \qquad (16)$$

$$G = [g^2 + 3(p_0^2 + 2p_0p_p\cos\theta_p - 3p_p^2 - 4M\varepsilon_{dn})]^{1/2}. \quad (17)$$

Over the kinematical region corresponding to the experimental conditions in [6], the contribution of the first term in the braced expression on the right-hand side of (15) is dominant.

Although nonrelativistic kinematics can be used in theoretically analyzing the reaction $^3\mathrm{H}(p,pn)^2\mathrm{H}$ at an energy of $E_0 \approx 70$ MeV, numerical estimations reveal that the Coulomb interaction effect is still modest; therefore, it can be disregarded. However, we will see that, at such moderate energies, the quasielastic-scattering approximation can prove to be inadequate numerically in some region (specifically, in the region where the differential cross section is small) because of a considerable value of ε_{dn}.

In calculating the differential cross sections (13) and (15) and differential cross sections that are given below, we use the model wave functions [14–16]

$$\psi(\mathbf{r},\mathbf{s}) = \frac{3^{3/4}\alpha^3}{\pi^{3/2}}\exp\Big[-\alpha^2\Big(r^2 + \frac{3}{4}s^2\Big)\Big], \quad (18)$$
$$\alpha = 0.375\ \mathrm{fm}^{-1};$$

$$\varphi_d(\mathbf{s}) = \left(\frac{2\lambda^2}{\pi}\right)^{3/4}\exp(-\lambda^2 s^2), \quad (19)$$
$$\lambda = 0.267\ \mathrm{fm}^{-1};$$

$$\varphi_{\mathbf{f}}(\mathbf{r}) = \exp(i\mathbf{f}\cdot\mathbf{r}) - \sqrt{8}\exp\left(-\frac{f^2}{4\alpha^2} - \alpha^2 r^2\right) \quad (20)$$

(their parameters were found in [14] from a fit to data on electron scattering from [17]) and the nucleon–nucleon profile functions [18, 19]

$$\omega_j(\boldsymbol{\rho}_j) = (a_1 - ia_2)\exp(-b\rho_j^2), j = 1,2,3, \quad (21)$$

where $\boldsymbol{\rho}_j$ is the component of the radius vector $\mathbf{r}_j$ in a plane orthogonal to the vector $\mathbf{k}$. The real-valued parameters a_1, a_2, and b appearing in (21) are functions of the relative energy of colliding nucleons. Their values were borrowed from [18, 19].

3. FORMALISM FOR THE REACTION $^3\mathrm{H}(p,pn)pn$: TOTAL CROSS SECTIONS

In the diffraction approximation, one can also describe quite straightforwardly the three-particle breakup of a triton undergoing a collision with a nonrelativistic incident proton, taking into account the final-state interactions between four unbound nucleons.

In the diffraction approximation, the amplitude $A_{\mathbf{f},\mathbf{u}}(\mathbf{q})$ for the reaction $t + p \to 2p + 2n$ can be represented in the form [8–10]

$$A_{\mathbf{f},\mathbf{u}}(\mathbf{q}) = -\int d^{(3)}\mathbf{r}\int d^{(3)}\mathbf{s} \quad (22)$$
$$\times \int d^{(2)}\boldsymbol{\rho}e^{i\mathbf{q}\cdot\boldsymbol{\rho}}\varphi_{\mathbf{f}}^*(\mathbf{r})\varphi_{\mathbf{u}}^*(\mathbf{s})\widehat{\omega}_{123}\psi(\mathbf{r},\mathbf{s}),$$

where $\varphi_{\mathbf{f}}(\mathbf{r})$ has the form (20) and is the wave function that describes the relative motion (with momentum $\mathbf{f}$) of the first neutron knocked out from the triton and the unbound system formed by the second neutron and the proton (third nucleon), which was released from the triton. We have

$$\varphi_{\mathbf{u}}(\mathbf{s}) = \exp(i\mathbf{u}\cdot\mathbf{s}) - \sqrt{8}\exp\left(-\frac{u^2}{3\alpha^2} - \frac{3}{4}\alpha^2 s^2\right), \quad (23)$$
$$\int d^{(3)}\mathbf{s}\int d^{(3)}\mathbf{r}\varphi_{\mathbf{f}}^*(\mathbf{r})\varphi_{\mathbf{u}}^*(\mathbf{s})\psi(\mathbf{r},\mathbf{s}) = 0,$$

where $\mathbf{u} = (\mathbf{p}_p' - \mathbf{p}_n')/2$ is the relative momentum of the second and the third nucleon, $\mathbf{p}_n'$ and $\mathbf{p}_p'$ being their momenta; the rest of the notation is identical to that in the preceding section.

The amplitude in (22) can be related to the transition amplitude $M_{i\to f}^{(3)}$ characterizing the process $^3\mathrm{H}(p,pn)pn$ and determining the differential cross section for complete triton dissociation induced by incident protons,

$$d^{12}\sigma_{i\to f}^{(3)} = (2\pi)^4|M_{i\to f}^{(3)}|^2\delta^{(4)}(p_0 + p_t \quad (24)$$
$$- p_p - p_n - p_{p'} - p_n')\frac{d^{(3)}\mathbf{p}_p}{(2\pi)^3}\frac{d^{(3)}\mathbf{p}_n}{(2\pi)^3}\frac{d^{(3)}\mathbf{p}_p'}{(2\pi)^3}\frac{d^{(3)}\mathbf{p}_n'}{(2\pi)^3},$$

where p_n' and p_p' are the 4-momenta of the second and the third nucleon (proton and neutron, respectively) released upon triton breakup [further, we assume, as in (4), that $\mathbf{p}_t = 0$]. Going over in (24) from the six-dimensional momentum-volume element $d^{(3)}\mathbf{p}_p'd^{(3)}\mathbf{p}_n'$ to the momentum-volume element $d^{(3)}\mathbf{u}d^{(3)}\mathbf{p}_d'$ (the absolute value of the transition Jacobian is equal to unity) and performing integration with respect to $\mathbf{p}_d'$ ($\mathbf{p}_d' = \mathbf{p}_n' + \mathbf{p}_p'$ is the total momentum of the unbound second and third nucleons), we obtain

$$d^9\sigma_{i\to f}^{(3)} = 2\pi|M_{i\to f}^{(3)}|^2\delta(E_3) \quad (25)$$
$$\times \frac{d^{(3)}\mathbf{p}_p}{(2\pi)^3}\frac{d^{(3)}\mathbf{p}_n}{(2\pi)^3}\frac{d^{(3)}\mathbf{u}}{(2\pi)^3},$$

$$E_3 = E_0 - \varepsilon - \frac{u^2}{M} \quad (26)$$

$$-\frac{1}{2M}\left[p_0^2+\frac{3}{2}f^2+\frac{4}{3}(\kappa^2+q_z^2)-2p_0q_z\right],$$

$$d^{(3)}\mathbf{u}=u^2dud\Omega_{\mathbf{u}}=u^2du\sin\theta_{\mathbf{u}}d\theta_{\mathbf{u}}d\varphi_{\mathbf{u}}, \quad (27)$$

where $\varepsilon\approx 8.5$ MeV is the triton binding energy [13].

Further, we go over in (25) from the variables $\mathbf{p}_p$ and $\mathbf{p}_n$ to the new variables $\mathbf{q}(q_z,\boldsymbol{\kappa})$ and $\mathbf{f}$ and perform integration with respect to q_z from $-\infty$ to $+\infty$, employing the delta function $\delta(E_3)$ and relation (26), where we disregard the q_z^2 term, which is small in the diffraction approximation. We then arrive at

$$d^8\sigma_{i\to f}^{(3)}=\frac{M}{p_0}|M_{i\to f}^{(3)}|^2\frac{d^{(2)}\boldsymbol{\kappa}}{(2\pi)^2}\frac{d^{(3)}\mathbf{f}}{(2\pi)^3}\frac{d^{(3)}\mathbf{u}}{(2\pi)^3}. \quad (28)$$

Comparing this expression with the corresponding differential cross section within the diffraction model [9, 10],

$$d^8\sigma_{i\to f}^{(3)}=|A_{\mathbf{f},\mathbf{u}}(\mathbf{q})|^2\frac{d^{(2)}\boldsymbol{\kappa}}{(2\pi)^2}\frac{d^{(3)}\mathbf{f}}{(2\pi)^3}\frac{d^{(3)}\mathbf{u}}{(2\pi)^3}, \quad (29)$$

we obtain the relation

$$|M_{i\to f}^{(3)}|^2=\frac{p_0}{M}|A_{\mathbf{f},\mathbf{u}}(\mathbf{q})|^2, \quad (30)$$

which is similar to that in (8) and which involves the well-known expression (22) for the amplitude of complete diffractive triton disassembly.

Let us now represent the differential cross section for three-particle triton breakup in a form that corresponds to the differential cross sections measured in [5, 6]. For this purpose, we substitute expression (30) into (25) and integrate the result with respect to the relative momentum $\mathbf{u}$, taking into account relations (26) and (27) [in doing this, it is not necessary at this stage to disregard the q_z^2 term in (26)]. As a result, we arrive at a differential cross section that was measured (partly) in [5]. Specifically, we have

$$\sigma_1^{(3)}\equiv\sigma_1^{(3)}(\theta_p,\theta_n,E_p,E_n) \quad (31)$$
$$=\frac{d^6\sigma_1^{(3)}}{d\Omega_pd\Omega_ndE_pdE_n}$$
$$=\frac{2M^3u_0p_0\sqrt{E_pE_n}}{(2\pi)^7}\overline{|A_{\mathbf{f},u_0}(\mathbf{q})|^2},$$

$$\overline{|A_{\mathbf{f},u_0}(\mathbf{q})|^2}=\frac{1}{4\pi}\int d\Omega_{\mathbf{u}}|A_{\mathbf{f},\mathbf{u}}(\mathbf{q})|^2, \quad (32)$$

where, on the right-hand side of (32), we must replace u by u_0,

$$u_0=\sqrt{M}[E_0-\varepsilon-E_p-E_n-E'_d(\mathbf{p}_p,\mathbf{p}_n)]^{1/2}, \quad (33)$$

$$E'_d(\mathbf{p}_p,\mathbf{p}_n)=\frac{1}{4M}[\mathbf{p}'_d(\mathbf{p}_p,\mathbf{p}_n)]^2, \quad (34)$$
$$\mathbf{p}'_d(\mathbf{p}_p,\mathbf{p}_n)=\mathbf{p}'_p+\mathbf{p}'_n=\mathbf{p}_0-\mathbf{p}_p-\mathbf{p}_n.$$

Thus, the differential cross section given by expression (31) depends on the momenta $\mathbf{p}_p$ and $\mathbf{p}_n$.

We will now take into account the identity of two protons and the identity of two neutrons in the final state of the process $^3\mathrm{H}+p\to 2p+2n$. Since, in [5], two nonidentical nucleons, a proton and a neutron, were recorded in coincidence in the reaction of complete triton dissociation, the differential cross section in (31) must be supplemented with three more terms (partial differential cross sections). Here, the situation is similar to that described in [20–23], and we will dwell on this analogy at some length later. Of these partial differential cross sections, one, $\sigma_2^{(3)}$, corresponds to recording the same neutron (first nucleon) as in (31) and the knock-on (not scattered) proton (third nucleon in the triton). The partial cross section $\sigma_2^{(3)}$ is obtained from the differential cross section (24) by integrating the latter with respect to the variables $\mathbf{p}_p$ and $\mathbf{p}'_n$. As a result, the partial differential cross section

$$\sigma_2^{(3)}\equiv\sigma_2^{(3)}(\theta'_p,\theta_n,E'_p,E_n)=\frac{d^6\sigma_2^{(3)}}{d\Omega'_pd\Omega_ndE'_pdE_n} \quad (35)$$

will depend on the momenta $\mathbf{p}'_p$ and $\mathbf{p}_n$.

Yet another partial differential cross section for complete triton dissociation, $\sigma_3^{(3)}$, is obtained upon integrating the differential cross section in (24) with respect to $\mathbf{p}_n$ and $\mathbf{p}'_p$, so that the differential cross section

$$\sigma_3^{(3)}=\sigma_3^{(3)}(\theta_p,\theta'_n,E_p,E'_n)=\frac{d^6\sigma_3^{(3)}}{d\Omega_pd\Omega'_ndE_pdE'_n} \quad (36)$$

will depend on $\mathbf{p}_p$ and $\mathbf{p}'_n$. It corresponds to recording the scattered proton [as in (31)] and the other neutron (second nucleon) escaping from the triton. The remaining partial differential cross section $\sigma_4^{(3)}$ is obtained by integrating (24) with respect to $\mathbf{p}_p$ and $\mathbf{p}_n$:

$$\sigma_4^{(3)}=\sigma_4^{(3)}(\theta'_p,\theta'_n,E'_p,E'_n)=\frac{d^6\sigma_4^{(3)}}{d\Omega'_pd\Omega'_ndE'_pdE'_n}. \quad (37)$$

Therefore, the differential cross section $\sigma_4^{(3)}$ depends on $\mathbf{p}'_p$ and $\mathbf{p}'_n$ and corresponds to recording the second and third nucleons of the dissociated triton.

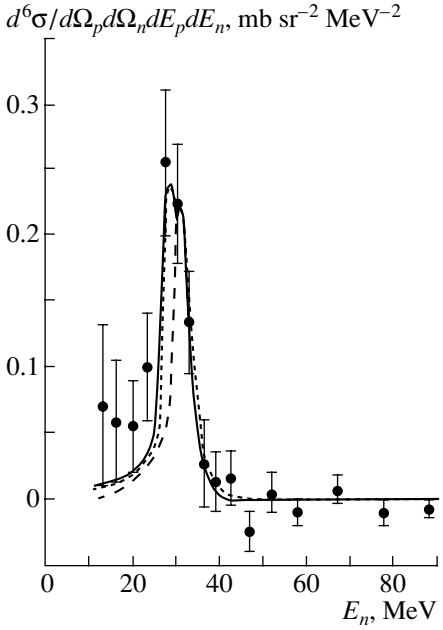

Fig. 1. Differential cross section $d^6\sigma_{i\to f}/d\Omega_p d\Omega_n dE_p dE_n$ for triton breakup in the scattering of $E_0 = 72$ MeV protons as a function of the energy E_n of knock-on neutrons for the case where the energy of knock-on protons is $E_p = 35$ MeV. The momenta $\mathbf{p}_p$ and $\mathbf{p}_n$ of the detected proton and neutron form angles of 45° with respect to the incident-proton momentum $\mathbf{p}_0$ in the rest frame of the ^{3}H nucleus and lie in the same plane with the vector $\mathbf{p}_0$ on different sides of it. The solid curve (total contribution of two- and three-particle triton breakup) and the dashed curve (contribution of two-particle breakup alone) were calculated with the triton wave function (18), while the dotted curve (which represents both the two- and the three-particle breakup of a ^{3}H nucleus) was calculated with the triton wave function (42).

Obviously, the differential cross section measured in [5] receives contributions from all four partial differential cross sections (31) and (35)–(37), which differ in structure; that is,

$$\frac{d^6\sigma^{(3)}_{i\to f}}{d\Omega_p d\Omega_n dE_p dE_n} = \sum_{k=1}^{4} \sigma^{(3)}_k(\theta_p, \theta_n, E_p, E_n). \quad (38)$$

Upon integration of (38) with respect to the energy E_n of the knock-on neutron (within the limits allowed by conservation laws), we obtain the differential cross section

$$\frac{d^5\sigma^{(3)}_{i\to f}}{d\Omega_p d\Omega_n dE_p} = \sum_{k=1}^{4} \int dE_n \sigma^{(3)}_k(\theta_p, \theta_n, E_p, E_n), \quad (39)$$

which will contribute to the differential cross section measured in [6].

Each of the cross sections measured in [5, 6] receives contributions both from the two- and from the three-particle breakup of a triton. It is clear that the sum of the differential cross sections given by (13) and (38) determines the differential cross section

$$\frac{d^6\sigma_{i\to f}}{d\Omega_p d\Omega_n dE_p dE_n} = \frac{d^6\sigma^{(2)}_{i\to f}}{d\Omega_p d\Omega_n dE_p dE_n} + \frac{d^6\sigma^{(3)}_{i\to f}}{d\Omega_p d\Omega_n dE_p dE_n}, \quad (40)$$

which, under respective kinematical conditions, must describe the differential cross section measured in [5], while the sum of the differential cross sections in (15) and (39), namely, the total cross section

$$\frac{d^5\sigma_{i\to f}}{d\Omega_p d\Omega_n dE_p} = \frac{d^5\sigma^{(2)}_{i\to f}}{d\Omega_p d\Omega_n dE_p} + \frac{d^5\sigma^{(3)}_{i\to f}}{d\Omega_p d\Omega_n dE_p}, \quad (41)$$

must describe the cross section observed in [6].

The following comments are in order here. It was indicated, for example, in [21] that, if the particles involved are quite widely separated in space (this is often so for short-range nuclear interactions) as clusters in some nuclei or as unbound diverging particles, the wave function used for the system being considered can be factorized to a good accuracy, as was done here for the final states in (1) and (22). Moreover, it is not necessary to perform symmetrization here with respect to identical particles in calculating the probabilities and differential cross sections in question, since the contributions from this symmetrization are quite small in this case [20–23]. The result then appears to be nearly identical to that in the case of a semiclassical consideration. The possibility of skipping symmetrization of the wave function for a system formed by widely spaced constituents is in fact the content of the "cluster law" [22], which was proven for a general case in [23]. The process considered here (as a matter of fact, it is a semiclassical process since the relevant wavelengths are short), which involves the diffractive dissociation of composite particles [8–10], falls within the applicability range of this law. Therefore, the identity of the scattered proton and the proton knocked out from a triton is taken here into account by means of a purely classical procedure—that is, by summation of the corresponding differential cross sections, since, in the experiments reported in [5, 6], these protons were not distinguished in detecting them. The identity of released neutrons in the case of complete triton dissociation was taken into account in a similar way. We would like to recall here that disappearance of interference upon going over to the classical limit takes place in collisions of identical particles in the case of long-range Coulomb interaction inclusive [24].

In accordance with the measurements described in [5, 6], we explore, in the present study, processes of coplanar kinematics, in which case the main contribution to the total differential cross sections (40) and (41) in the region of maxima comes from the two-particle dissociation of tritons. However, preliminary calculations revealed that, in a general (noncoplanar) case, there can arise kinematical situations where the contribution of the three-particle dissociation of tritons is dominant.

4. CALCULATION AND DISCUSSION OF THE RESULTS

Since the data obtained from experiments aimed at studying nucleon–nucleon scattering and employed in [18, 19] to determine the parameters a_1, a_2, and b appearing in (21) involved sizable errors and were incomplete, the resulting parameter values suffered from significant uncertainties. By using the corridors of possible values of these parameters for various nucleon energies, the differential cross sections calculated by formulas (40) and (41) were simultaneously fitted by the least squares method to experimental data from [5] and from [6] with allowance for both two- and three-particle triton dissociation induced by incident protons. Figures 1 and 2 display the results of such calculations (curves) and the corresponding experimental data from [5, 6] with errors (points), where $\Delta \approx 4$ MeV. With allowance for the two- and the three-particle dissociation of tritons, the solid curves were calculated with the triton wave function (18), while the dotted curves were calculated (for the sake of comparison) with the triton wave function represented in the clustered (factorized) form

$$\psi(\mathbf{r},\mathbf{s}) = \varphi_0(\mathbf{r})\varphi_d(\mathbf{s}), \qquad (42)$$

$$\varphi_0(\mathbf{r}) = \left(\frac{2\alpha^2}{\pi}\right)^{3/4} \exp(-\alpha^2 r^2),$$

where $\varphi_0(\mathbf{r})$ is the wave function describing the relative motion of the first (neutron) nucleon and the system of the other two triton nucleons in the bound state and $\varphi_d(\mathbf{s})$ is the deuteron wave function (19). The dashed curves represent the contribution from only two-particle triton breakup for the triton wave function (18).

Figure 1 displays the differential cross section $d^6\sigma_{i\to f}/d\Omega_p d\Omega_n dE_p dE_n$—that is, the differential cross section (40)—as a function of the energy E_n of knock-on neutrons at $E_p = 35$ MeV. It can be seen that, in the region of a maximum at $E_n \approx 30$ MeV, the main contribution to the differential cross section (40) comes from the differential cross section (13) for two-particle dissociation, but that, to the left of the maximum at $E_n \leq 25$ MeV, the differential cross section (38) for three-particle dissociation proves to be significant, so that its inclusion is necessary for attaining better agreement between the results of the calculations and experimental data from [5]. For $E_n \geq 28$ MeV, the contribution of three-particle triton breakup vanishes by virtue of conservation laws, and this is the reason why the dashed curve coincides with the solid curve for $E_n \geq 28$ MeV.

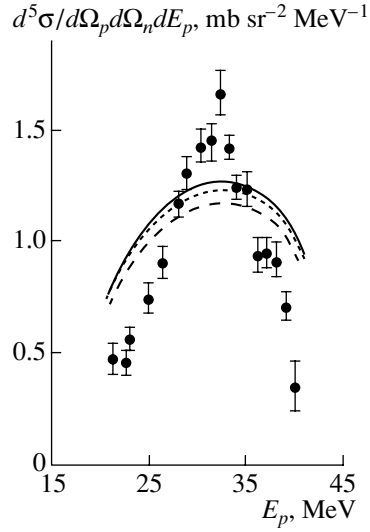

Fig. 2. Differential cross section $d^5\sigma_{i\to f}/d\Omega_p d\Omega_n dE_p$ for triton breakup in the scattering of $E_0 = 70$ MeV protons versus the energy E_p of knock-on protons (the calculations were performed for the same final-state kinematical parameters as those used for the differential cross section in Fig. 1). The notation for the curves is identical to that in Fig. 1.

The differential cross section calculated by formula (41)—namely, $d^5\sigma_{i\to f}/d\Omega_p d\Omega_n dE_p$—as a function of E_p is shown in Fig. 2, along with the corresponding experimental data from [6]. For all values of the detected-proton energy E_p, the contribution to (41) from the differential cross section (15) for the two-particle dissociation of tritons proved to be much greater than the contribution of the differential cross section (39) for the three-particle dissociation of ^{3}H nuclei in this case as well, the optimum values of the interaction parameters being

$$a_1 = 2.65, \quad a_2 = 1.95, \quad b = 0.372 \text{ fm}^{-2}. \qquad (43)$$

These values are close to those of the corresponding parameters in [18, 19], where the mean parameter values were determined on the basis of experimental data from [4, 19, 25, 26] on nucleon–nucleon scattering and were then varied within the aforementioned corridors of their values in order to achieve better agreement with the experimental results obtained in [5, 6].

We note that, among the four terms of the differential cross sections in (38) and (39) for complete triton

dissociation, the contributions of the two differential cross sections $\sigma_1^{(3)}$ and $\sigma_3^{(3)}$, which correspond to recording the scattered proton and one of the two released neutrons, proved to be, under the kinematical conditions of the experiments reported in [5, 6], two orders of magnitude smaller than the contributions of the remaining two differential cross sections $\sigma_2^{(3)}$ and $\sigma_4^{(3)}$, which are on the same order of magnitude.

From the figures, one can see that, within the diffraction approximation, the use of the model wave functions (18)–(20), (23), and (42) and the Gaussian-type profile functions (21) makes it possible to describe fairly well the experimental differential cross section from [5]; as to the experimental differential cross section from [6], its description within this framework is predominantly of only a qualitative character. Agreement with experimental data, especially with data from [6], can be improved by using more realistic dependences instead of the model wave functions (18)–(20) and (23). However, there will be a concurrent increase in computational difficulties associated with the growth of the multiplicity of integration to be performed numerically in that case. The agreement with the experimental data from [5, 6] can also be improved by calculating the differential cross sections in (40) and (41) without applying the procedure of simultaneous fitting, but this will lead to different sets of the interaction parameters a_1, a_2, and b in (21) for these two total differential cross sections. Finally, one can improve the agreement with the experimental data, especially in Fig. 2, by slightly changing (reducing) the numerical values of the structural parameters λ and α in (18)–(20), (23), and (42). However, we preferred the set of values in (43), which were obtained in our study simultaneously for the differential cross sections (40) and (41), and values that were derived previously in an independent way for the structural parameters λ and α.

In all probability, relatively small (within a few percent) distinctions between the final results for the two triton internal wave functions used [that in (18) and that in (42)]—that is, the proximity of the solid and dotted curves in the figures—can be explained by a partial clustering of the ^{3}H nucleus into a deuteron and a neutron. This conjecture is in accord with the conclusion drawn in [27], where it was shown that the probability P_d of an undistorted deuteron state in the triton is 0.448. Although this value is 1.5 times less than the value of $P_d = 0.65$ for the ^{6}Li nucleus [28], which is well known to be clustered into a deuteron and an alpha particle, it is indicative of the presence of some degree of clustering in the triton.

5. CONCLUSIONS

(i) In the diffraction approximation, analytic expressions have been obtained for differential cross sections describing two- and three-particle triton dissociation induced by intermediate-energy incident protons.

(ii) By and large, the differential cross sections for proton-induced triton dissociation that have been calculated by using model wave functions, profile functions, and one set of interaction parameters in (43) reproduce satisfactorily experimental data from [5], but they describe only qualitatively experimental data from [6].

(iii) It has been shown that, for the coplanar kinematical conditions of the experiments reported in [5, 6], the contribution of the two-particle dissociation of tritons to the differential cross section is dominant everywhere, but that, in order to attain better agreement with experimental data, it is necessary to take into account the three-particle dissociation of ^{3}H nuclei as well.

(iv) A comparison of the results obtained with the triton wave functions in (18) and in (42) indicates that, in accord with the data quoted in [27], the ^{3}H nucleus is partly clustered into a deuteron and a neutron.

REFERENCES

1. R. Frascaria, V. Comparat, N. Marty, *et al.*, Nucl. Phys. A **178**, 307 (1971).
2. P. Kitching, G. A. Moss, W. C. Olsen, *et al.*, Phys. Rev. C **6**, 769 (1972).
3. D. R. Lehman, Phys. Rev. C **6**, 2023 (1972).
4. E. B. Levshin and A. D. Fursa, Yad. Fiz. **24**, 1115 (1976) [Sov. J. Nucl. Phys. **24**, 585 (1976)].
5. M. V. Pasechnik, V. B. Shostak, V. P. Badovskiĭ, *et al.*, Izv. Akad. Nauk SSSR, Ser. Fiz. **47**, 28 (1983).
6. M. V. Pasechnik, V. B. Shostak, V. P. Badovskiĭ, *et al.*, Izv. Akad. Nauk SSSR, Ser. Fiz. **48**, 1950 (1984).
7. V. K. Tartakovskiĭ, A. V. Fursaev, and B. I. Sidorenko, Izv. Akad. Nauk, Ser. Fiz. **64**, 994 (2000).
8. A. I. Akhiezer and A. G. Sitenko, Zh. Éksp. Teor. Fiz. **32**, 794 (1957) [Sov. Phys. JETP **5**, 652 (1957)].
9. A. I. Akhiezer and A. G. Sitenko, Ukr. Fiz. Zh. **3**, 16 (1958).
10. V. K. Tartakovsky, M. A. Khassan, and I. S. Dotsenko, Preprint No. 77-84R, ITF (Inst. for Theor. Phys., Kiev, 1977).
11. J. S. Trefil, Phys. Rev. **180**, 1366 (1969).
12. V. I. Goldansky, Yu. P. Nikitin, and I. L. Rozental, *Kinematical Methods in High Energy Physics* (Nauka, Moscow, 1987) [in Russian].
13. V. A. Kravtsov, *Atomic Masses and Nuclear Binding Energies* (Atomizdat, Moscow, 1974) [in Russian].

14. A. G. Sitenko, I. V. Kozlovskiĭ, and V. K. Tartakovskiĭ, Yad. Fiz. **15**, 725 (1972) [Sov. J. Nucl. Phys. **15**, 406 (1972)].
15. E. Gerjuoy and J. Schwinger, Phys. Rev. **61**, 138 (1942).
16. A. G. Sitenko, E. Ismatov, and V. K. Tartakovskiĭ, Yad. Fiz. **5**, 573 (1966) [Sov. J. Nucl. Phys. **5**, 408 (1966)].
17. H. Collard, R. Hofstadter, E. B. Hughes, *et al.*, Phys. Rev. **138**, B57 (1965).
18. E. I. Ismatov, K. G. Sailer, V. K. Tartakovsky, and V. A. Cherednichenko, Vestn. Kiev. Univ., Fiz., No. 23, 53 (1982).
19. A. D. Fursa and N. I. Voloshin, in *Proceedings of the Annual Conference of Institute for Nuclear Research, 1997* (NTs Inst. Yad. Issled., Kiev, 1997), p. 4.
20. M. L. Goldberger and K. M. Watson, *Collision Theory* (Wiley, New York, 1964; Mir, Moscow, 1967).
21. K. Wildermuth and Y. C. Tang, *A Unified Theory of the Nucleus* (Vieweg, Braunschweig, 1977; Mir, Moscow, 1980).
22. J. R. Taylor, *Scattering Theory: The Quantum Theory of Nonrelativistic Collisions* (Wiley, New York, 1972; Mir, Moscow, 1975).
23. A. Messiah, *Quantum Mechanics* (North-Holland, Amsterdam, 1965; Nauka, Moscow, 1979), Vol. 2.
24. L. D. Landau and E. M. Lifshitz, *Quantum Mechanics: Non-Relativistic Theory* (Nauka, Moscow, 1989, Pergamon, Oxford, 1977).
25. R. Wilson, *The Nucleon-Nucleon Interaction* (Wiley, New York, 1963; Mir, Moscow, 1965).
26. V. S. Barashenkov, *Cross Sections for the Interaction of Elementary Particles* (Nauka, Moscow, 1966) [in Russian].
27. K. Miyagawa, H. Kamada, W. Glöckle, and V. Stoks, Phys. Rev. C **51**, 2905 (1995).
28. E. Hiyama, M. Kamimura, T. Motoba, *et al.*, Phys. Rev. C **53**, 2075 (1996).

Translated by A. Isaakyan

Physics of Atomic Nuclei, Vol. 68, No. 1, 2005, pp. 42–49. Translated from Yadernaya Fizika, Vol. 68, No. 1, 2005, pp. 43–50.

NUCLEI
Theory

Relativistic Inverse Scattering Problem for a Superposition of a Nonlocal Separable and a Local Quasipotential

Yu. D. Chernichenko

Pavel Sukhoi State Technical University of Gomel, pr. Oktyabrya 48, Gomel, 246746 Belarus

Received November 21, 2003; in final form, April 9, 2004

Abstract—Within the relativistic quasipotential approach to quantum field theory, the relativistic inverse scattering problem is solved for the case where the total quasipotential describing the interaction of two relativistic spinless particles having different masses is a superposition of a nonlocal separable and a local quasipotential. It is assumed that the local component of the total quasipotential is known and that there exist bound states in this local component. It is shown that the nonlocal separable component of the total interaction can be reconstructed provided that the local component, an increment of the phase shift, and the energies of bound states are known. © *2005 Pleiades Publishing, Inc.*

The inverse scattering problem has a long history [1–3]. A comprehensive review on this subject for the nonrelativistic case can be found in [4, 5]. For the most part, the interaction in this problem is reconstructed on the basis of the nonrelativistic Schrödinger equation [6–9], this being so in the case of separable potentials inclusive. Therefore, it would be of interest to solve the relativistic inverse scattering problem—in particular, within the quasipotential approach [10].

In the present study, the problem of reconstructing the nonlocal separable component of the total quasipotential describing the interaction of spinless particles that have different masses ($m_1 \neq m_2$) is considered within the relativistic quasipotential approach [11]. It is assumed that the local component $W(r)$ of the total interaction admits the existence of n_l bound states at energies satisfying the condition[1)]

$$0 \leq E_j = \cosh\chi_j < 1, \quad \chi_j = i\kappa_j, \qquad (1)$$
$$0 < \kappa_j \leqslant \pi/2, \quad j = 1, 2, \ldots, n_l.$$

Moreover, the local component is considered to be known. We will show that the nonlocal separable component $V_l(r)$ of the total potential can be reconstructed provided that the local component $W(r)$, the increment of the phase shift $\delta_l^V(\chi')$, and the energies of the bound states are known. Our starting point is the expression for the phase shift derived in [12] in the form

$$\tan\delta_l^V(\chi') = -\frac{\pi}{2}\sinh^{-1}\chi' A_l(\chi') \qquad (2)$$
$$\times \left[1 - \frac{\varepsilon_l}{2}\sum_{j=1}^{n_l} C_{lj}\frac{|\tilde{V}_l(\chi_j)|^2}{\cosh\chi' - \cosh\chi_j} + \frac{1}{2}\mathrm{P}\int_0^\infty d\chi \frac{A_l(\chi)}{\cosh\chi - \cosh\chi'}\right]^{-1},$$

$$A_l(\chi') = \frac{2}{\pi}\varepsilon_l |Q_l(\coth\chi')\tilde{V}_l(\chi')/F_l^W(\chi')|^2, \qquad (3)$$
$$\varepsilon_l = \pm 1,$$

where P symbolizes the principal-value prescription, $Q_l(z)$ is a Legendre function of the second order, $\tilde{V}_l(\chi)$ is the transform of the quasipotential $V_l(r)$, $F_l^W(\chi')$ is the Jost function, and C_{lj} are the normalization constants corresponding to the purely local quasipotential $W(r)$.[2)]

In order to reconstruct the separable component $V_l(r)$ of the total quasipotential on the basis of the increment of the phase shift $\delta_l^V(\chi')$, we will solve the integral Eq. (2) for the unknown function $A_l(\chi')$. In doing this, we will develop a relativistic generalization

[1)] Here and below, we use the system of units in which $\hbar = c = 1$.

[2)] We recall that the Jost function $F_l^W(\chi')$ is expressed in terms of the phase shift $\delta_l^W(\chi')$ as $F_l^W(\chi') = |F_l^W(\chi')|\exp[-i\delta_l^W(\chi')]$ and that the zeros of the Jost function, $\chi_j (j = 1, 2, \ldots, n_l)$, which determine the energies (1) of the bound states of the local quasipotential $W(r)$, are located on the positive part of the imaginary axis in the complex plane of the rapidity χ' (in the c.m. frame, the rapidity parametrizes the energy E'_q of an effective relativistic particle of mass $m' = \sqrt{m_1 m_2}$: $E' = E_{q'}/m' = \cosh\chi'$). The normalization constants C_{lj} for the bound-state eigenfunctions $\varphi_l(r, \chi_j)$ are also expressed in terms of the Jost function as $C_{lj}^{-1} = \int_0^\infty dr\varphi_l(r, \chi_j)\varphi_l^*(r, \chi_j) = \frac{i}{4}[Q_l(\coth\chi_j)]^{-2}F_l^W(-\chi_j)dF_l^W(\chi_j)/d\chi_j, j = 1, 2, \ldots, n_l$.

1063-7788/05/6801-0042$26.00

of the method proposed by Chadan [6] for solving the respective nonrelativistic inverse scattering problem. Making use of the Hilbert integral transformation, we will then find the function $\tilde{V}_l(\chi')$ from (3). After that, we will employ the generalized Hankel integral transformation [12][3)]

$$V_l(r) = \int_0^\infty d\rho_l(\cosh\chi)\tilde{V}_l(\chi)\varphi_l(r,\chi) \qquad (4)$$

$$= \sum_{j=1}^{n_l} C_{lj}\tilde{V}_l(\chi_j)\varphi_l(r,\chi_j) + \int_0^\infty d\chi\tau_l(\chi)\tilde{V}_l(\chi)\varphi_l(r,\chi),$$

$$\tau_l(\chi) = \frac{2}{\pi}|Q_l(\coth\chi)/F_l^W(\chi)|^2$$

to reconstruct the quasipotential $V_l(r)$.[4)]

For the resulting solution to the inverse scattering problem to be unique, we assume that the increment of the phase shift $\delta_l^V(\chi')$ in formula (2) is Hölder continuous with a positive value of the exponent and that, for $\chi' \to +\infty$, we have the estimate

$$\delta_l^V(\chi') = O(\chi'^{-\gamma}), \quad l \geq 0, \quad \gamma > 1. \qquad (5)$$

These requirements imply that the quasipotential $V_l(r)$ satisfies the condition

$$rV_l(r) \in L_1(0,\infty). \qquad (6)$$

Moreover, the Levinson theorem for the phase shift [12] states that

$$\delta_l^V(0) - \delta_l^V(\infty) = \delta_l^V(0) = \pi(\sigma_l - n_l + \nu_l) \qquad (7)$$

and

$$\delta_l^W(0) - \delta_l^W(\infty) = \delta_l^W(0) = \pi n_l.$$

Here, σ_l is the number of bound states corresponding to the total quasipotential and having energies that satisfy the conditions

$$0 \leq E_{tj'} = \cosh\chi_{tj'} < 1, \quad \chi_{tj'} = i\kappa_{tj'}, \quad 0 < \kappa_{tj'} \leq \pi/2, \qquad (8)$$

$$j' = 1,2,\ldots,\sigma_l, \quad \sigma_l = \begin{cases} n_l - 1 \quad (\Phi_l(1) < 0), \quad n_l \quad (\Phi_l(1) > 0) \quad \text{for} \quad \varepsilon_l = +1 \\ n_l \quad (\Phi_l(1) < 0), \quad n_l + 1 \quad (\Phi_l(1) > 0) \quad \text{for} \quad \varepsilon_l = -1, \end{cases}$$

where

$$\Phi_l(E') = \varepsilon_l \left[1 - \frac{\varepsilon_l}{2}\sum_{j=1}^{n_l}\frac{C_{lj}|\tilde{V}_l(\chi_j)|^2}{E' - E_j} + \frac{1}{2}\mathrm{P}\int_0^\infty d\chi\frac{A_l(\chi)}{\cosh\chi - E'}\right],$$

and ν_l is the number of spurious bound states whose energies satisfy the condition

$$E_{fk} = \cosh\chi_{fk} \geq 1, \quad k \qquad (9)$$

$$= \begin{cases} 0,1,\ldots,\nu_l - 1, \ \varepsilon_l = +1, \\ 1,2,\ldots,\nu_l, \ \varepsilon_l = -1. \end{cases}$$

As was demonstrated in [12], the energies (8) of true bound states for the total quasipotential are simple roots of the equation

$$\Phi_l(E_{tj'}) = \varepsilon_l \left[1 - \frac{\varepsilon_l}{2}\sum_{j=1}^{n_l}\frac{C_{lj}|\tilde{V}_l(\chi_j)|^2}{E_{tj'} - E_j} + \frac{1}{2}\int_0^\infty d\chi\frac{A_l(\chi)}{\cosh\chi - E_{tj'}}\right] = 0, \quad j' = 1,2,\ldots,\sigma_l, \qquad (10)$$

whereas the energies (9) of spurious bound states can be determined from the values of χ' at which the increment of the phase shift intersects the straight lines $\delta_l^V = \pi k$ (k is an integer) from above as χ' increases;

[3)] Note that, in the absence of the local interaction [$W(r) \equiv 0$], the integral transformation (4) is nothing but the Hankel integral transformation proposed in [13].

[4)] Here, $\varphi_l(r,\chi)$ is a regular solution to the finite-difference quasipotential equation for the local quasipotential $W(r)$ admitting the existence of n_l bound states whose energies are given by (1), while

$$\frac{d\rho_l(\cosh\chi)}{d(\cosh\chi)} = \begin{cases} \sinh^{-1}\chi\tau_l(\chi), \quad E = \cosh\chi \geq 1, \\ \sum_{j=1}^{n_l} C_{lj}\delta(\cosh\chi - \cosh\chi_j), \quad 0 \leq E = \cosh\chi < 1, \\ \chi = i\kappa, \quad \chi_j = i\kappa_j, \quad 0 < \kappa, \kappa_j \leq \pi/2, \end{cases}$$

is the spectral density associated with the local quasipotential $W(r)$.

that is,

$$\delta_l^V(\chi_{fk}) = \pi k, \quad k = \begin{cases} 0, 1, \ldots, \nu_l - 1, \ \varepsilon_l = +1, \\ 1, 2, \ldots, \nu_l, \ \varepsilon_l = -1. \end{cases} \tag{11}$$

Making the substitutions $x = \cosh\chi'$ and $t = \cosh\chi$ and introducing the notation

$$\Delta_l^V(x) = \delta_l^V(\operatorname{arcosh} x), \tag{12}$$
$$g_l(x) = -(2/\pi)(x^2-1)^{1/2}\tan\Delta_l^V(x),$$
$$\psi_l(x) = A_l(\operatorname{arcosh} x) g_l^{-1}(x)$$
$$\times [1 + i(\pi/2) g_l(x)(x^2-1)^{-1/2}],$$
$$h_l(x) = (\pi/2) g_l(x)(x^2-1)^{-1/2}$$
$$\times [1 - i(\pi/2) g_l(x)(x^2-1)^{-1/2}]^{-1}$$
$$= -\sin\Delta_l^V(x)\exp[-i\Delta_l^V(x)],$$

we recast the integral Eq. (2) into the form

$$\psi_l(x) = 1 - \frac{\varepsilon_l}{2}\sum_{j=1}^{n_l} C_{lj}\frac{|\tilde{V}_l(\chi_j)|^2}{x - E_j} + \frac{1}{\pi}\int_1^\infty dt \frac{\psi_l(t) h_l^*(t)}{t - x - i0}. \tag{13}$$

The integral Eq. (13) is a nonhomogeneous integral equation, in just the same way as in the case where the total quasipotential has no local part [$W(r) \equiv 0$] [13]. Moreover, this equation has the same form as the respective nonrelativistic equation obtained in [6]. In order to solve it, we introduce the function

$$H_l(z) = \mu_l(z) + \frac{1}{\pi}\int_1^\infty dt \frac{\psi_l(t) h_l^*(t)}{t - z}, \tag{14}$$

where

$$\mu_l(z) = 1 - \frac{\varepsilon_l}{2}\sum_{j=1}^{n_l} C_{lj}\frac{|\tilde{V}_l(\chi_j)|^2}{z - E_j}.$$

Obviously, the function $H_l(z)$ is an analytic function in the complex plane of the variable z with a cut from 1 to $+\infty$, with the exception of the points $z = E_j$ ($0 \le E_j < 1$, $j = 1, 2, \ldots, n_l$), where it has simple poles. Also, we have

$$\lim_{|z|\to\infty} H_l(z) = 1 \tag{15}$$

along any direction provided that the function $\psi_l(x)$ is Hölder continuous and that the integral in (14) converges. In terms of the function introduced above, the solution to the integral Eq. (13) has the form

$$\psi_l(x) = H_l(x_+) \equiv \lim_{\eta\to+0} H_l(x + i\eta), \quad 1 \le x \le \infty. \tag{16}$$

The function $H_l(z)$ can be represented in the form

$$H_l(z) = \mu_l(z) + G_l(z)\exp[\omega_l(z)], \tag{17}$$

where

$$\omega_l(z) = -\frac{1}{\pi}\int_1^\infty dt \frac{\Delta_l^V(t)}{t - z}. \tag{18}$$

From the above assumptions on the behavior of the increment of the phase shift and from conditions (5) and (15), it follows that

$$\lim_{|z|\to\infty}\omega_l(z) = 0, \quad \lim_{|z|\to\infty} G_l(z) = 0 \tag{19}$$

along all directions. Moreover, the function $G_l(z)$ must be analytic in the complex plane of the variable z with a cut from 1 to $+\infty$, while the function (18) is defined everywhere on the cut, with the exception of maybe the point $z = 1$, where its behavior is given by

$$\omega_l(z) = (1/\pi)\Delta_l^V(1)\ln|1 - z| + \Omega_l(z), \quad z \to 1. \tag{20}$$

The function $\Omega_l(z)$ is finite as $z \to 1$, and $\Delta_l^V(1) = \delta_l^V(0) = \pi(\sigma_l - n_l + \nu_l)$ according to the Levinson theorem (7). For this reason, the function $\exp[\omega_l(z)]$ either is finite at $\sigma_l - n_l + \nu_l = 0$ or has a zero of order $\sigma_l - n_l + \nu_l > 0$ at the point $z = 1$.[5)]

The discontinuity of the function $H_l(z)$ across the cut is given by

$$H_l(x_+) - H_l(x_-) = G_l(x_+)\exp[\omega_l(x_+)] - G_l(x_-)\exp[\omega_l(x_-)] = -2i\sin\Delta_l^V(x)\exp[i\Delta_l^V(x)]\psi_l(x). \tag{21}$$

Substituting the solution in (16) into expression (21) and taking into account the representation in (17), we arrive at the nonhomogeneous Riemann–Hilbert equation for the unknown function $G_l(z)$,

$$G_l(x_+)\exp[\omega_l(x_+) + 2i\Delta_l^V(x)] - G_l(x_-)\exp[\omega_l(x_-)] = \mu_l(x)\{1 - \exp[2i\Delta_l^V(x)]\}, \tag{22}$$

where

$$\omega_l(x_\pm) = \lim_{\eta\to+0}\omega_l(x \pm i\eta) = \alpha_l(x) \mp i\Delta_l^V(x), \tag{23}$$

$$\alpha_l(x) = -\frac{1}{\pi}\mathrm{P}\int_1^\infty dt \frac{\Delta_l^V(t)}{t - x}, \quad 1 \le x \le \infty. \tag{24}$$

[5)] In the case where $\delta_l^V(0) = -\pi$—that is, for $\sigma_l = n_l - 1$ ($n_l \ne 0$) and $\nu_l = 0$ ($\varepsilon_l = +1$), the function $H_l(z)$ and, hence, the function $\psi_l(x)$ are not finite at $z = 1$. For this reason, the inverse scattering problem for this case calls for a dedicated consideration.

Taking into account (23), we can recast Eq. (22) into the form

$$G_l(x_+) - G_l(x_-) = -\mu_l(x)\{\exp[-\omega_l(x_+)] - \exp[-\omega_l(x_-)]\}, \quad 1 \le x \le \infty. \tag{25}$$

A particular solution satisfying Eq. (25) and the conditions in (19) is given by

$$\tilde{G}_l(z) = 1 - \mu_l(z)\exp[-\omega_l(z)] - \frac{\varepsilon_l}{2}\sum_{j=1}^{n_l} C_{lj}\frac{|\tilde{V}_l(\chi_j)|^2}{z - E_j}\exp[-\omega_l(E_j)].$$

From this formula, we obtain a particular solution $\tilde{\psi}_l(x)$ to the nonhomogeneous integral Eq. (13). Taking expressions (16) and (17) into account, we arrive at

$$\tilde{\psi}_l(x) = \exp[\omega_l(x_+)] \times \left\{1 - \frac{\varepsilon_l}{2}\sum_{j=1}^{n_l} C_{lj}\frac{|\tilde{V}_l(\chi_j)|^2}{x - E_j}\exp[-\omega_l(E_j)]\right\}. \tag{26}$$

The function in (26) is regular at $x = 1$ (at this point, it either is finite at $\sigma_l - n_l + \nu_l = 0$ or has a zero of order $\sigma_l - n_l + \nu_l > 0$), Hölder continuous with an exponent equal to that for the increment of the phase shift, and bounded for $x \to +\infty$ in accord with a priori assumptions on its properties. Moreover, the function in (26) satisfies Eq. (13), because the residue theorem implies that

$$\lim_{\substack{R \to +\infty \\ \eta \to +0}} \frac{1}{2\pi i}\int_{\Gamma^+} dz \frac{\tilde{H}_l(z)}{z - x - i\eta} = \operatorname{res}\left[\frac{\tilde{H}_l(z)}{z - x - i\eta}, z = x + i\eta\right]\Bigg|_{\eta \to +0} + \sum_{j=1}^{n_l}\delta_{nj}\operatorname{res}\left[\frac{\tilde{H}_l(z)}{z - x - i\eta}, z = E_n\right]\Bigg|_{\eta \to +0},$$

where

$$\tilde{H}_l(z) = \left\{1 - \frac{\varepsilon_l}{2}\sum_{n=1}^{n_l} C_{ln}\frac{|\tilde{V}_l(\chi_n)|^2}{z - E_n}\exp[-\omega_l(E_n)]\right\} \times \exp[\omega_l(z)]$$

and Γ^+ is a closed contour consisting of the circumference C_R^+ of radius R centered at $z = 0$, the circumference C_η^- of radius η centered at $z = 1$, and the two edges of the cut from 1 to R, the direction of the contour along the upper edge being opposite to that along the lower edge. According to the asymptotic formula (19), the contribution of the integral along the circumference C_R^+ tends to unity as $R \to +\infty$, while, according to the estimate in (20) and the conclusions presented in footnote 5, the integral along the circumference C_η^- tends to zero as $\eta \to +0$. From the above and from expression (23), we obtain

$$1 + \frac{1}{\pi}\int_1^\infty dt \frac{\tilde{\psi}_l(t)h_l^*(t)}{t - x - i0} = \tilde{\psi}_l(x) + \frac{\varepsilon_l}{2}\sum_{j=1}^{n_l} C_{lj}\frac{|\tilde{V}_l(\chi_j)|^2}{x - E_j};$$

that is, the function $\tilde{\psi}_l(x)$ given by (26) is a particular solution to the nonhomogeneous integral Eq. (13).

A general solution to the homogeneous equation

$$\psi_{lo}(x) = \frac{1}{\pi}\int_1^\infty dt \frac{\psi_{lo}(t)h_l^*(t)}{t - x - i0} \tag{27}$$

has the form

$$\psi_{lo}(x) = H_{lo}(x_+) = \lim_{\eta \to +0} H_{lo}(x + i\eta), \quad 1 \le x \le \infty, \tag{28}$$

where the function

$$H_{lo}(z) = \frac{1}{\pi}\int_1^\infty dt \frac{\psi_{lo}(t)h_l^*(t)}{t - z} \tag{29}$$

is analytic in the complex plane of z with a cut from 1 to $+\infty$, the equation

$$\lim_{|z| \to \infty} H_{lo}(z) = 0 \tag{30}$$

being valid along any direction. Moreover, the function in (29) satisfies the Riemann–Hilbert homogeneous equation

$$H_{lo}(x_+)\exp[2i\Delta_l^V(x)] - H_{lo}(x_-) = 0, \quad 1 \le x \le \infty, \tag{31}$$

which follows from expression (21) for the discontinuity of the function $H_l(z) \equiv H_{lo}(z)$ across the cut and from the representation in (28). Therefore, we use the following ansatz for a general solution to Eq. (27):

$$H_{lo}(z) = \exp[\omega_l(z)]\sum_{k=0}^{m}\frac{A_k}{(z-1)^k}. \tag{32}$$

Under the condition that the function $H_{lo}(z)$ is finite at $z = 1$ (it either is finite at $\sigma_l - n_l + \nu_l = 0$ or has a zero of order $\sigma_l - n_l + \nu_l > 0$ at this point), the substitution of expression (32) into Eq. (31) gives

$$m = \begin{cases} \sigma_l - n_l + \nu_l > 0, \\ 0 \quad \text{at } \sigma_l - n_l + \nu_l = 0; \end{cases}$$

at $m = \sigma_l - n_l + \nu_l = 0$, $A_0 = 0$. Therefore, we have

$$\psi_{lo}(x) = H_{lo}(x_+) = \exp[\omega_l(x_+)] \begin{cases} \sum\limits_{k=1}^{\sigma_l - n_l + \nu_l} \dfrac{A_k}{(x-1)^k} & \text{at } \sigma_l - n_l + \nu_l > 0, \\ 0 & \text{at } \sigma_l - n_l + \nu_l = 0. \end{cases} \tag{33}$$

As in the case of a particular solution, integration along the contour Γ^+ leads to the conclusion that the function in (33) is a solution to Eq. (27) and possesses all the required properties.

According to relations (23), (24), (26), and (33), a general solution of the integral Eq. (13) is given by

$$\psi_l(x) = \tilde{\psi}_l(x) + \psi_{lo}(x) = \exp[\alpha_l(x) - i\Delta_l^V(x)] \times \left\{ 1 + \sum_{k=1}^{\sigma_l - n_l + \nu_l} \frac{A_k}{(x-1)^k} - \frac{\varepsilon_l}{2} \sum_{j=1}^{n_l} C_{lj} \frac{|\tilde{V}_l(\chi_j)|^2}{x - E_j} \exp[-\omega_l(E_j)] \right\}. \tag{34}$$

Making use of the notation in (12) and rearranging the sum into a product, one can recast the solution in (34) into either of the following two forms:

$$A_l(\chi') = -\frac{2}{\pi} \sinh\chi' \sin\delta_l^V(\chi') \exp[\alpha_l(\cosh\chi')] \times \left\{ 1 + \sum_{k=1}^{N_l} \frac{A_k}{(\cosh\chi' - 1)^k} - \sum_{j=1}^{n_l} \frac{B_j}{\cosh\chi' - E_j} \right\}, \tag{35}$$

$$A_l(\chi') = -\frac{2}{\pi} \sinh\chi' \sin\delta_l^V(\chi') \exp[\alpha_l(\cosh\chi')] \times \prod_{k=1-\delta}^{N_l - \delta} \left(1 + \frac{a_k}{\cosh\chi' - 1} \right) \prod_{j=1}^{n_l} \left(1 - \frac{b_j}{\cosh\chi' - E_j} \right), \tag{36}$$

where

$$\alpha_l(\cosh\chi') = -\frac{1}{\pi} \mathrm{P} \int_0^\infty d\chi \frac{\sinh\chi \delta_l^V(\chi)}{\cosh\chi - \cosh\chi'}, \tag{37}$$

$$B_j = \frac{\varepsilon_l}{2} C_{lj} |\tilde{V}_l(\chi_j)|^2 \exp[-\omega_l(E_j)], \tag{37a}$$

$$N_l = \sigma_l - n_l + \nu_l = \begin{cases} \nu_l - 1, \sigma_l = n_l - 1, \varepsilon_l = +1, \\ \nu_l, \sigma_l = n_l, \varepsilon_l = \pm 1, \\ \nu_l + 1, \sigma_l = n_l + 1, \varepsilon_l = -1, \end{cases} \tag{38}$$

$$\delta = \begin{cases} 1, \varepsilon_l = +1, \\ 0, \varepsilon_l = -1. \end{cases}$$

Obviously, the solutions in (35) and (36) depend on $N_l + n_l = \sigma_l + \nu_l$ parameters: the former depends on $\{A_k\}$ and $\{B_j\}$, while the latter depends on $\{a_k\}$ and $\{b_j\}$. The relations between these parameters are given by

$$1 + \sum_{k=1}^{N_l} \frac{A_k}{(\cosh\chi' - 1)^k} - \sum_{j=1}^{n_l} \frac{B_j}{\cosh\chi' - E_j} = \prod_{k=1-\delta}^{N_l - \delta} \left(1 + \frac{a_k}{\cosh\chi' - 1} \right) \times \prod_{j=1}^{n_l} \left(1 - \frac{b_j}{\cosh\chi' - E_j} \right). \tag{39}$$

In particular, we readily find from relation (39) that

$$B_j = b_j \prod_{\substack{n=1 \\ n \neq j}}^{n_l} \left(1 - \frac{b_n}{E_j - E_n} \right) \prod_{k=1-\delta}^{N_l - \delta} \left(1 - \frac{a_k}{1 - E_j} \right), \quad j = 1, 2, \ldots, n_l, \tag{40}$$

where N_l and δ are defined in (38).

It should be noted that, in the nonrelativistic limit ($\chi' \ll 1$), the solution in (35) coincides with the respective nonrelativistic solution obtained in [6]. At the same time, uniqueness of the parameter set for the nonrelativistic inverse scattering problem was not investigated there.

To determine the parameters $\{a_k\}$ and $\{b_j\}$, we first note that, by definition (3), the sign of the function $A_l(\chi')$ is identical for all values of χ', whereas the increment of the phase shift at the energies (9) of spurious bound states satisfies the condition in (11). Therefore, $\sin\delta_l^V(\chi')$ and the expression involving the products over k and j on the right-hand side of the solution in (36) must change sign at the same points χ_{fk} [see formula (9)]. This condition is satisfied if

$$a_k = 1 - \cosh\chi_{fk}, \tag{41}$$

$$k = \begin{cases} 0, 1, \ldots, N_l - 1, \ \varepsilon_l = +1, \\ 1, 2, \ldots, N_l, \ \sigma_l = n_l, \ \varepsilon_l = -1, \\ 1, 2, \ldots, N_l - 1, \ \sigma_l = n_l + 1, \ \varepsilon_l = -1, \end{cases}$$

$$b_{n_l} = \cosh\chi_{f(\nu_l - 1)} - \cosh\chi_{n_l}, \quad \sigma_l = n_l - 1, \ \varepsilon_l = +1.$$

The values of the remaining parameters $\{b_j\}$ and a_{ν_l+1} can be determined from σ_l in Eqs. (10) for the unknown energies in (8). Substituting the solution in (36) into Eqs. (10) for the unknown energies in (8) and taking into account relation (37a), we arrive at

$$1-\sum_{j=1}^{n_l}\frac{B_j\exp[\omega_l(E_j)]}{E_{tj'}-E_j} \tag{42}$$
$$-\frac{1}{\pi}\int_0^\infty d\chi\frac{\sinh\chi\sin\delta_l^V(\chi)\exp[\alpha_l(\cosh\chi)]}{\cosh\chi-E_{tj'}}$$
$$\times\prod_{k=1-\delta}^{N_l-\delta}(1+\frac{a_k}{\cosh\chi-1})\prod_{j=1}^{n_l}(1-\frac{b_j}{\cosh\chi-E_j})=0,$$
$$j'=1,2,\ldots,\sigma_l.$$

Making the change of variable $x=\cosh\chi$ in (42) and using relation (23), we recast expression (42) into the form

$$1-\sum_{j=1}^{n_l}\frac{B_j\exp[\omega_l(E_j)]}{E_{tj'}-E_j} \tag{43}$$
$$+\frac{1}{2\pi i}\int_1^\infty dx\frac{\exp[\omega_l(x_+)]-\exp[\omega_l(x_-)]}{x-E_{tj'}}$$
$$\times\prod_{k=1-\delta}^{N_l-\delta}\left(1+\frac{a_k}{x-1}\right)\prod_{j=1}^{n_l}\left(1-\frac{b_j}{x-E_j}\right)=0,$$
$$j'=1,2,\ldots,\sigma_l.$$

According the residue theorem, we can write

$$\lim_{\substack{R\to+\infty\\ \eta\to+0}}\frac{1}{2\pi i}\int_{\Gamma^+}\frac{dz\exp[\omega_l(z)]}{z-E_{tj'}}\prod_{k=1-\delta}^{N_l-\delta}\left(1+\frac{a_k}{z-1}\right)$$
$$\times\prod_{j=1}^{n_l}\left(1-\frac{b_j}{z-E_j}\right)$$
$$=1+\frac{1}{2\pi i}\int_1^\infty dx\frac{\exp[\omega_l(x_+)]-\exp[\omega_l(x_-)]}{x-E_{tj'}}$$
$$\times\prod_{k=1-\delta}^{N_l-\delta}\left(1+\frac{a_k}{x-1}\right)\prod_{j=1}^{n_l}\left(1-\frac{b_j}{x-E_j}\right)$$
$$=\mathrm{res}\left\{\frac{\exp[\omega_l(z)]}{z-E_{tj'}}\prod_{k=1-\delta}^{N_l-\delta}\left(1+\frac{a_k}{z-1}\right)\right.$$
$$\left.\times\prod_{j=1}^{n_l}\left(1-\frac{b_j}{z-E_j}\right),z=E_{tj'}\right\}$$
$$+\sum_{j=1}^{n_l}\mathrm{res}\left\{\frac{\exp[\omega_l(z)]}{z-E_{tj'}}\prod_{k=1-\delta}^{N_l-\delta}\left(1+\frac{a_k}{z-1}\right)\right.$$
$$\left.\times\prod_{n=1}^{n_l}\left(1-\frac{b_n}{z-E_n}\right),z=E_j\right\},\ j'=1,2,\ldots,\sigma_l,$$

where Γ^+ is the same closed contour as that used in integrating the function $\tilde{H}_l(z)$. In addition to the above, we have considered that, according to the asymptotic relation (19), the integral along the circumference C_R^+ tends to unity as $R\to+\infty$, while, according to the estimate in (20) and the conclusions presented in footnote 5, the integral along the circumference C_η^- tends to zero as $\eta\to+0$. As a consequence, Eqs. (43) take the form

$$\exp[\omega_l(E_{tj'})]\prod_{k=1-\delta}^{N_l-\delta}\left(1-\frac{a_k}{1-E_{tj'}}\right) \tag{44}$$
$$\times\prod_{j=1}^{n_l}\left(1-\frac{b_j}{E_{tj'}-E_j}\right)=0,\quad j'=1,2,\ldots,\sigma_l.$$

From this formula and from formula (41), we obtain

$$b_j=\cosh\chi_{tj'}-\cosh\chi_j, \tag{45}$$
$$j'=j=\begin{cases}1,2,\ldots,\sigma_l,\ \sigma_l=n_l-1\ (\Phi_l(1)<0),\ n_l\ (\Phi_l(1)>0),\ \varepsilon_l=+1,\\ 1,2,\ldots,n_l,\ \sigma_l=n_l\ (\Phi_l(1)<0),\ n_l+1\ (\Phi_l(1)>0),\ \varepsilon_l=-1,\end{cases}$$
$$a_{\nu_l+1}=1-\cosh\chi_{t(n_l+1)},\ \sigma_l=n_l+1\ (\Phi_l(1)>0),\ \varepsilon_l=-1.$$

Note that Eqs. (44) also admit solutions of the form

$$b_j=E_{tj}-E_j=0.$$

Thus, we arrive at a degeneracy of states at the energies E_j; since $E_{tj}=E_{t(j+1)}=E_j$, the degree of degeneracy for each eigenvalue E_j does not exceed two. Moreover, Eqs. (44) imply that at least one of the parameters $\{b_j\}$ is different from zero [12].

Thus, the coefficients $\{a_k\}$ and $\{b_j\}$ are determined unambiguously. Taking into account expressions (41) and (45), we can therefore recast the solu-

tion in (36) into the form

$$A_l(\chi') = -\frac{2}{\pi}\sinh\chi' \sin\delta_l^V(\chi')\exp[\alpha_l(\cosh\chi')] \quad (46)$$
$$\times [\sinh(\chi'/2)]^{-2N_l} \prod_{j'=1}^{\sigma_l}[\sinh^2(\chi'/2)+\sin^2(\kappa_{tj'}/2)]$$
$$\times \prod_{j=1}^{n_l}[\sinh^2(\chi'/2)+\sin^2(\kappa_j/2)]^{-1}$$
$$\times \prod_{k=1-\delta}^{\nu_l-\delta}[\sinh^2(\chi'/2)-\sinh^2(\chi_{fk}/2)],$$

where σ_l is defined in (8) and N_l and δ are defined in (38).

Thus, the solution in (46) is unambiguously determined by the energies (1) of the bound states of the local quasipotential $W(r)$, the energies (8) of the bound states of the total quasipotential, and the increment of the phase shift, since the values χ_{fk} are also determined by its behavior—that is, the condition in (11). Moreover, formulas (37) and (46) imply that the function $A_l(\chi')$ is Hölder continuous and that its asymptotic behavior for $|\chi'|\to\infty$ is

$$\cosh\chi'|\chi'|^{-\gamma}, \quad \gamma > 1,$$

provided that the increment of the phase shift satisfies the condition in (5), this in turn entailing fulfillment of the condition in (6) for the quasipotential $V_l(r)$.

In order to reconstruct the quasipotential $V_l(r)$ with the aid of the transformation in (4), we must find the function $\tilde{V}_l(\chi')$ (which is complex-valued, in contrast to what we have in the nonrelativistic case [6]) by using expression (46). For this purpose, we introduce the function

$$\hat{V}_l(\sinh(\chi'/2)) = \prod_{j'=1}^{\sigma_l}\left[\frac{\sinh(\chi'/2)+i\sin(\kappa_{tj'}/2)}{\sinh(\chi'/2)-i\sin(\kappa_{tj'}/2)}\right] \quad (47)$$
$$\times \prod_{j=1}^{n_l}\left[\frac{\sinh(\chi'/2)-i\sin(\kappa_j/2)}{\sinh(\chi'/2)+i\sin(\kappa_j/2)}\right]$$
$$\times |Q_l(\coth\chi')/F_l^W(\chi')|^2[\tilde{V}_l^{(-)}(\sinh(\chi'/2))]^2,$$

where

$$|\tilde{V}_l^{(-)}(\sinh(\chi'/2))| = |\tilde{V}_l(\chi')|, \quad (48)$$
$$\mathrm{Re}\tilde{V}_l^{(-)}(\sinh(\chi'/2)) = \mathrm{Re}\tilde{V}_l(\chi'),$$
$$\arg\tilde{V}_l^{(-)}(-\sinh(\chi'/2)) = -\arg\tilde{V}_l^{(-)}(\sinh(\chi'/2)).$$

With allowance for the conditions in (48), the relation $\arg\tilde{V}_l(-\chi') = \arg\tilde{V}_l(\chi')$ implies that

$$\arg\tilde{V}_l(\chi') = \mathrm{sgn}\chi'\cdot\arg\tilde{V}_l^{(-)}(\sinh(\chi'/2)). \quad (49)$$

The function $\hat{V}_l(\sinh(\chi'/2))$ is then analytic in the band $0<\mathrm{Im}\chi'\le\pi/2$ and is continuous for $0\le\mathrm{Im}\chi'\le\pi/2$. If the condition in (5) is met, then the estimate

$$\hat{V}_l(\sinh(\chi'/2)) = O(\sinh^2(\chi'/2)), \quad (50)$$
$$|\chi'|\to\infty, \quad 0\le\mathrm{Im}\chi'\le\pi/2$$

is valid for this function. Moreover, the function $\hat{V}_l(\sinh(\chi'/2))$ does not vanish anywhere in the band $0<\mathrm{Im}\chi'\le\pi/2$. Therefore, the function $\ln\hat{V}_l(\sinh(\chi'/2))$ is analytic in the band $0<\mathrm{Im}\chi'\le\pi/2$ and, according to the estimate in (50), behaves as $\ln\sinh^2(\chi'/2)$ when $|\chi'|\to\infty$. Therefore, the Hilbert integral transformation can be applied to both the real and the imaginary part of the function $\ln\hat{V}_l(\sinh(\chi'/2))$. For real values of χ', we then arrive at

$$\mathrm{Im}\ln\hat{V}_l(\sinh(\chi'/2))$$
$$= -\frac{1}{\pi}\mathrm{P}\int_{-\infty}^{\infty} d(\sinh(\chi/2))\frac{\mathrm{Re}\ln\hat{V}_l(\sinh(\chi/2))}{\sinh(\chi/2)-\sinh(\chi'/2)}$$
$$= -\frac{2\sinh(\chi'/2)}{\pi}\mathrm{P}\int_0^{\infty} d\chi\frac{\cosh(\chi/2)\ln[\pi\varepsilon_l A_l(\chi)/2]}{\cosh\chi-\cosh\chi'},$$

where we have considered that

$$\mathrm{Re}\ln\hat{V}_l(\sinh(\chi'/2)) = \ln[\pi\varepsilon_l A_l(\chi')/2].$$

From this formula and from expression (47), we obtain

$$|Q_l(\coth\chi')/F_l^W(\chi')|^2[\tilde{V}_l^{(-)}(\sinh(\chi'/2))]^2 = \frac{\pi}{2}\varepsilon_l A_l(\chi')\prod_{j'=1}^{\sigma_l}\left[\frac{\sinh(\chi'/2)-i\sin(\kappa_{tj'}/2)}{\sinh(\chi'/2)+i\sin(\kappa_{tj'}/2)}\right] \quad (51)$$
$$\times \prod_{j=1}^{n_l}\left[\frac{\sinh(\chi'/2)+i\sin(\kappa_j/2)}{\sinh(\chi'/2)-i\sin(\kappa_j/2)}\right]\exp\left[\frac{2\sinh(\chi'/2)}{i\pi}\mathrm{P}\int_0^{\infty} d\chi\frac{\cosh(\chi/2)\ln[\pi\varepsilon_l A_l(\chi)/2]}{\cosh\chi-\cosh\chi'}\right].$$

Taking into account relations (48) and (49), we finally arrive at

$$|Q_l(\coth\chi')/F_l^W(\chi')|\tilde{V}_l(\chi') = \sqrt{\pi\varepsilon_l A_l(\chi')/2} \quad (52)$$
$$\times \exp\left\{-i\mathrm{sgn}\chi'\left[\sum_{j'=1}^{\sigma_l}\arctan\frac{\sin(\kappa_{tj'}/2)}{\sinh(\chi'/2)}\right.\right.$$
$$-\sum_{j=1}^{n_l}\arctan\frac{\sin(\kappa_j/2)}{\sinh(\chi'/2)} + \frac{\sinh(\chi'/2)}{\pi}$$
$$\left.\left.\times \mathrm{P}\int_0^\infty d\chi\frac{\cosh(\chi/2)\ln[\pi\varepsilon_l A_l(\chi)/2]}{\cosh\chi - \cosh\chi'}\right]\right\}.$$

Thus, we have shown that, in the case considered here, a solution to the relativistic inverse scattering problem exists. It is unambiguously determined by the increment of the phase shift and by the energies of the bound states of the local and the total quasipotential. However, the particular case of $\sigma_l = n_l - 1$, $n_l \neq 0$, $\nu_l = 0$ must be excluded as in the nonrelativistic case [6] because formula (34) does not provide a regular solution at $x = 1$.

In conclusion, it should be emphasized that the method developed here for reconstructing the nonlocal separable component of the total interaction between two relativistic spinless particles having different masses is in fact equivalent to the one-body relativistic inverse scattering method. This equivalence stems from the fact that, within the relativistic quasipotential approach to quantum field theory, the total c.m. energy of two relativistic spinless particles having different masses can be represented in the form of an expression proportional to the energy of one effective relativistic particle of mass m' [14].

ACKNOWLEDGMENTS

I am grateful to V.V. Andreev, Yu.S. Vernov, A.M. Shirokov, I.L. Solovtsov, V.N. Kashpai, and Ya. Shnir for interest in this study, enlightening comments, and valuable discussions on the results presented in this article.

REFERENCES

1. I. M. Gelfand and B. M. Levitan, Dokl. Akad. Nauk SSSR **77**, 557 (1951); Izv. Akad. Nauk SSSR, Ser. Mat. **15**, 309 (1951).
2. V. A. Marchenko, Dokl. Akad. Nauk SSSR **104**, 695 (1955).
3. M. G. Kreĭn, Dokl. Akad. Nauk SSSR **76**, 21 (1951); **76**, 345 (1951).
4. K. Chadan and P. C. Sabatier, *Inverse Problems in Quantum Scattering Theory* (Springer-Verlag, New York, 1977; Mir, Moscow, 1980).
5. B. N. Zakhar'ev and A. A. Suz'ko, *Direct and Inverse Problems: Potentials in Quantum Scattering*, 2nd ed. (Énergoatomizdat, Moscow, 1985; Springer-Verlag, Berlin, 1990).
6. K. Chadan, Nuovo Cimento **10**, 892 (1958).
7. M. Bolsterli and J. MacKenzie, Physics **2**, 141 (1965).
8. F. Tabakin, Phys. Rev. **177**, 1443 (1969).
9. R. L. Mills and J. F. Reading, J. Math. Phys. (N.Y.) **10**, 321 (1969).
10. A. A. Logunov and A. N. Tavkhelidze, Nuovo Cimento **29**, 380 (1963).
11. V. G. Kadyshevsky, Nucl. Phys. B **6**, 125 (1968).
12. Yu. D. Chernichenko, Yad. Fiz. **67**, 433 (2004) [Phys. At. Nucl. **67**, 414 (2004)].
13. Yu. D. Chernichenko, Yad. Fiz. **63**, 2068 (2000) [Phys. At. Nucl. **63**, 1976 (2000)].
14. V. G. Kadyshevskiĭ, M. D. Mateev, and R. M. Mir-Kasimov, Yad. Fiz. **11**, 692 (1970) [Sov. J. Nucl. Phys. **11**, 388 (1970)].

Translated by R. Rogalyov

Physics of Atomic Nuclei, Vol. 68, No. 1, 2005, pp. 50–59. Translated from Yadernaya Fizika, Vol. 68, No. 1, 2005, pp. 51–60.

ELEMENTARY PARTICLES AND FIELDS
Experiment

Application of a Multivariate Statistical Technique to Interpreting Data from Multichannel Equipment for the Example of the KLEM Spectrometer

D. M. Podorozhnyi, E. B. Postnikov*, L. G. Sveshnikova, and A. N. Turundaevsky

Institute of Nuclear Physics,
Moscow State University, Vorob'evy gory, Moscow, 119899 Russia

Received November 25, 2003; in final form, February 20, 2004

Abstract—A multivariate statistical procedure for solving problems of estimating physical parameters on the basis of data from measurements with multichannel equipment is described. Within the multivariate procedure, an algorithm is constructed for estimating the energy of primary cosmic rays and the exponent in their power-law spectrum. They are investigated by using the KLEM spectrometer (NUCLEON project) as a specific example of measuring equipment. The results of computer experiments simulating the operation of the multivariate procedure for this equipment are given, the proposed approach being compared in these experiments with the one-parameter approach presently used in data processing.

INTRODUCTION

Highly precise measurements of energy are required in order to solve many important problems in cosmic-ray physics—for example, in order to localize the break in the power-law spectrum of primary cosmic rays. The smaller the error in measuring energy, the higher the probability of correctly interpreting these measurements and the higher the accuracy in determining the parameters of the break in the spectrum and other features of the energy spectrum in a given range. Requirements for the accuracy in measuring energy become especially stringent in the case of low statistics, since, among all statistical factors, it is the volume of statistics that has the strongest effect on the magnitude of errors in determining the parameters of the break [1].

With the aid of modern measuring equipment, one can obtain vast amounts of digitized information. For example, a strip silicon detector that is used in the KLEM spectrometer (NUCLEON project [2, 3]) to record the angular distribution of secondary particles makes it possible to measure simultaneously pulse heights in a few hundred channels, each of the channels carrying information about the primary-particle energy. In the present study, we propose, for the example of a computer model of the KLEM spectrometer, a multivariate procedure for processing data obtained by recording cosmic rays (it should be emphasized, however, that problems of this type admit a similar solution for any multichannel detector or any multiparameter measuring equipment).

The NUCLEON project is aimed at developing recording equipment that is intended for studying cosmic rays (protons and nuclei) over a broad energy range and which would be characterized by a relatively low weight and a high sensitivity. The KLEM measuring procedure essentially consists in determining the primary-particle energy from the lateral density distribution $\rho(x, y)$ of the flux of secondary particles produced in a thin target (first inelastic-interaction event) and bred in an ultrathin push-out device [4]. Two strip-detector matrices orthogonal to each other, the signal N_i from each of the strip detectors being proportional to the ionization loss in the ith strip, are used to measure $\rho(x, y)$. We will refer to the signal N_i or to any other data of multichannel measuring equipment as measured variables and to physical quantities (for example, primary-particle energy) to be determined on the basis of these measurements as estimated parameters.

We will consider two types of problems that can be solved optimally—that is, to the highest possible precision within a broad class of algorithms. These are problems of deriving estimates on the basis of multivariate data from multichannel equipment—first, one or a few physical quantities not measurable directly [5] (for example, primary energy, charge, etc.) and, second, the exponent of the power-law primary spectrum.

*e-mail: postn@rbcmail.ru

1063-7788/05/6801-0050$26.00

1. DETERMINATION OF PRIMARY ENERGY IN EACH INDIVIDUAL EVENT

The simplest multivariate method—this is the method of obtaining, for a random vector, a linear estimate that corresponds to the best (least) mean-square deviation—makes it possible to derive, for the problem of estimating, on the basis of data from measurements with multichannel equipment, one or a few physical parameters not measurable directly, a solution that would be more precise than that provided by any other linear algorithm for their determination [6]. For the KLEM spectrometer, this statement implies that, for any choice of coefficients of the measured variables N_i in an empirical or a speculated formula for estimating the primary energy,

$$E = \sum_i C_i N_i + C_0,$$

the estimated value of E would not be better than that which is obtained by applying the multivariate procedure.

Despite the linearity of the method in question, its multivariate character by far compensates for this restriction: although any of the physical quantities measured experimentally is only taken into account within a linear dependence, numerous relations between the measured variables and the estimated parameter, as well as the interplay of the measured variables themselves, are included in the procedure in the best possible way. In practice, this algorithm therefore works much better than any "simplified" procedure of data treatment via replacing all variables measured with the aid of expensive equipment by one variable representing their combination, whereupon one constructs a nonlinear dependence of an unknown quantity on this variable. By way of example, we indicate that, within the method developed previously by our group [4] for determining primary energy by means of the KLEM spectrometer, one replaces a few thousand variables N_i by only one variable

$$S = \sum_{i=1}^{m} \{\ln^2(2r_i/H)\} N_i, \qquad (1)$$

where r_i is the distance between the ith strip, which recorded the signal N_i, and the axis of a shower of secondary particles and H is the distance between the strip-detector plane and the interaction point. Moreover, there are various methods for taking nonlinearities into account even within multivariate strategies in the case where the importance of these nonlinearities is suggested by physical considerations.

In order to realize this method, the energy E is treated as a random variable, while all of the m measured variables (for example, signals from the detector strips) are treated as the coordinates of an m-dimensional random vector (it is denoted here by $\boldsymbol{\xi}$). After that, a linear estimate of the quantity E is formed on the basis of the entire body of information available from measurements; that is,

$$E_{\text{est}} = \sum_{i=1}^{m} b_i \xi_i + c, \qquad (2)$$

where the constant coefficients b_i and c are chosen in such a way as to minimize the mean-square deviation of the estimate of E from its true value (mean-square error):

$$\mathrm{M}(E_{\text{est}} - E)^2 = \left(\sum_{i=1}^{m} b_i \xi_i + c - E \right)^2 \sim \min \quad (3)$$

$$\{\text{in relation to any other linear estimate of } E\}.$$

Here, M symbolizes the expectation value.

The sought values of the coefficients appearing in the formula for estimating E are given by the theorem quoted in [6]; that is,

$$b_i = (\mathbf{S}_{E\xi} \cdot \mathbf{S}_{\xi}^{-1})_i, \quad c = \mathrm{M}E - \mathbf{S}_{E\xi} \cdot \mathbf{S}_{\xi}^{-1} \mathrm{M}\boldsymbol{\xi}, \quad (4)$$

where $\mathbf{S}_{\xi}$ is the autocovariance matrix for the random vector $\boldsymbol{\xi}$, $\mathbf{S}_{E\xi}$ is the mutual covariance matrix for E and $\boldsymbol{\xi}$, and the index i after a parenthesis labels the ith coordinate of a vector. Instead of unknown covariance matrices and expectation-value vectors, we use their unbiased estimates obtained on the basis of data from a learning sample (that is, a sample characterized by a rather large volume and specially simulated for estimating unknown coefficients), for example,

$$\mathrm{M}\xi \approx \langle \xi \rangle = \frac{1}{n_t} \sum_{i=1}^{n_t} \boldsymbol{\xi}_i, \qquad (5)$$

$$\mathbf{S}_{E\xi} = \frac{1}{n_t - 1} \sum_{i=1}^{n_t} (E_i - \langle E \rangle)(\boldsymbol{\xi}_i - \langle \boldsymbol{\xi} \rangle)^{\mathrm{T}},$$

where n_t is the volume of the learning sample; $\boldsymbol{\xi}_i$ and E_i are the ith realizations of the vector $\boldsymbol{\xi}$ and the energy E, respectively; angular brackets denote averaging; and T denotes transposition.

In general, the algorithm used to estimate energy involves the following steps:

(i) The response of the device to the passage of a beam of primary particles through the measuring equipment is simulated, their energy spectrum being preset; in other words, there occurs the formation of a learning sample.

(ii) The algorithm of estimation by formulas (2), (4), and (5) is formulated.

In addition, one can incorporate, into the procedure being developed, one or a few extra parameters that would describe our a priori ideas of the character

of the statistical relationship (more precisely, of the nonlinearity present in this relationship, since all of the linear correlations are estimated automatically) between measured and (or) estimated variables. The parameters themselves can be chosen on the basis of physical considerations, while their optimum values are fixed by using the results of a numerical (computer) experiment that simulates the operation of the procedure being developed. It follows that the formation of yet another random sample (a test one) is necessary, and this is the next step.

(iii) The test sample is formed by simulating the operation of the measuring device, and a computer testing of the procedure of estimation is performed on the basis of this new sample. After that, the error in the estimation on the basis of (3) is calculated, and the optimum values of all unknown parameters of the method are determined as those that minimize the error of the estimation.

As to the form of the energy spectrum of the learning and test samples, it must be determined by the special features of a concrete applied problem to be solved by means of the above algorithm for estimating the primary-particle energy. In order to improve the accuracy of the estimation, it is necessary to include a greater amount of various a priori information about the physical process being studied. Yet another important comment is in order. For a criterion that the procedure being developed must satisfy, one can take not only the condition in (3), which requires that the absolute error in estimating energy, $\mathrm{M}(E_{\mathrm{est}}-E)^2$, be minimized. The algorithm in question can be modified in such a way that it would minimize the dimensionless relative error $\mathrm{M}((E_{\mathrm{est}}-E)/E)^2$, which has a clearer meaning. The condition in (3) will then assume the form

$$\mathrm{M}((E_{\mathrm{est}}-E)/E)^2 \tag{6}$$
$$=\left(\left(\sum_{i=1}^{m} b_i\xi_i + c - E\right)/E\right)^2 \sim \min$$
$$\{\text{in relation to any other linear estimate of } E\}.$$

After some simple algebra, this problem reduces to the preceding one. The ingredients of the algorithm described in items (i)–(iii) and used to determine the primary-particle energy undergo no changes, with the exception of the formula for determining, on the basis of a simulated learning sample, the coefficients b_i and c in expression (2) for E_{est}; that is,

$$b_i = (\mathbf{\Sigma}_{\tilde{E}\tilde{\boldsymbol{\xi}}}\cdot\mathbf{\Sigma}_{\tilde{\xi}}^{-1})_i, \tag{7}$$
$$c = \{1/\mathrm{M}(1/E^2)\}\{\mathrm{M}(1/E) - \mathbf{\Sigma}_{\tilde{E}\tilde{\boldsymbol{\xi}}}\cdot\mathbf{\Sigma}_{\tilde{\boldsymbol{\xi}}}^{-1}\mathrm{M}(\boldsymbol{\xi}/E^2)\},$$

where $\tilde{\boldsymbol{\xi}} = \{1/E\}\{\boldsymbol{\xi} - \mathrm{M}(\boldsymbol{\xi}/E^2)/\mathrm{M}(1/E^2)\}$; $\tilde{E} = 1-(1/E)\mathrm{M}(1/E)/\mathrm{M}(1/E^2)$; and $\mathbf{\Sigma}_{\tilde{\boldsymbol{\xi}}}$ and $\mathbf{\Sigma}_{\tilde{E}\tilde{\boldsymbol{\xi}}}$ are correlation (that is, noncentered) matrices, whose sample estimates are obtained in a way similar to that in (5):

$$\mathbf{\Sigma}_{\tilde{\boldsymbol{\xi}}} = \frac{1}{n_t}\sum_{i=1}^{n_t}\tilde{\boldsymbol{\xi}}_i\cdot\tilde{\boldsymbol{\xi}}_i^{\mathrm{T}}, \quad \mathbf{\Sigma}_{\tilde{E}\tilde{\boldsymbol{\xi}}} = \frac{1}{n_t}\sum_{i=1}^{n_t}\tilde{E}_i\tilde{\boldsymbol{\xi}}_i^{\mathrm{T}}. \tag{8}$$

In contrast to what we have in (2) and (4), the estimate of energy, E_{est}, is no longer unbiased upon such a modification; that is, $\mathrm{M}E_{\mathrm{est}} \neq \mathrm{M}E$.

Finally, we would like to dwell at some length on the parameters that make it possible to take into account, within the chosen procedure, the nonlinearity of the physical processes being considered. First, we note that, even in the course of computer experiments that relied on a one-dimensional algorithm for estimating the primary-particle energy and which employed the artificial variable S (1), it was found that the tightest correlation is observed between E and N_i^a, where $a \approx 1.2$–1.4. This circumstance, as well as the case where the tightest correlation would take place between an unknown parameter (E) and any arbitrarily complicated known function of measured variables, can readily be taken into account within the multivariate algorithm for estimation as well. In order to include this a priori information, it is sufficient to modify appropriately, from the outset, the input database and to employ, in the following, data on N_i^a rather than on the recorded signals N_i themselves.

Yet another factor that enables one to take efficiently into account physical processes underlying the operation of the measuring equipment is inherent in the computational procedure of the multivariate method for estimation [7]. The point is that we realized the algorithm of pseudoinversion of the correlation matrix [8] with the aid of only a few maximal singular quantities whose number is determined in a computer experiment as that which minimizes the error in estimating energy. This algorithm implements some kind of "filtration" of small-scale, insignificant, and spurious interrelations stemming from insufficiently vast statistics and concurrently removes difficulties associated with addressing ill-posed problems.

As applied to the KLEM spectrometer, the algorithm for estimating energy is the following:

(i) The form of the cosmic-ray energy spectrum that is proposed to be recorded in a simulated or an actual experiment is chosen (for example, a power-law spectrum or a few monochromatic beams of fixed energy). The form of the learning and the test sample is chosen accordingly for a subsequent accumulation of computer statistics. The type of error—the absolute

error, as in (3), or the relative error, as in (6)—is chosen.

(ii) The beam of primary particles belonging to the sort in which we are interested and having the preset form of the energy spectrum (see the preceding item) is simulated at the input of the computer model of the detector. Preset values of the primary energy E and the measured values of the signal N_i are successively recorded in a file for each of the simulated events that involve the passage of beam particles through the device. The learning sample E, N_{i1}, E, N_{i2}, ..., E, N_{in} is formed, and all N_i are transformed into N_i^a, where the constant a is taken to be unknown for the time being.

(iii) The unknown constants of the algorithm are evaluated by formulas (4) and (5) or (7) and (8).

(iv) The testing sample is formed in a way similar to that described in item (i) of the algorithm, the energy of each particle from this sample is estimated, and the error in (3) or in (6) is calculated by means of averaging over the entire sample. The optimum value at which the error is minimal is determined for the parameter a. Formula (2) for estimating the primary energy has now been fully specified, since the values of all constants appearing in it have been determined.

(v) A test beam having the structure, spectral shape, and intensity in which were are interested is transferred to the input of the computer model of the measuring equipment (and, in the future, to the input of the actual device); the energy of each particle in the beam is estimated; and the error in these quantities is calculated.

We will now present the results obtained by applying the above procedure to solving two problems within one general problem of reconstructing the energy of primary particles. The first of these is that of determining the energy of each particle from a beam having a power-law energy spectrum, while the second is that of determining the energies of particles from a few beams of monochromatic energy between $E = 10^{11}$ and $E = 10^{15}$ eV.

Only protons incident orthogonally to the measuring-equipment plane were simulated in all of the cases considered here. This simulation was based on the GEANT 3.21 package [9]. High-energy interactions of hadrons were described with the aid of the QGSJET generator [10], while their low-energy interactions (up to 50 GeV) were treated by using the FLUKA generator [9]. The applicability of these models to describing hadron interactions was confirmed by a comparison with experimental data [10, 11].

Within the first problem, it is assumed that we know the shape of the actual energy spectrum. This is a power-law function, but it is not necessary that its exponent be known to a high precision. In order to take into account this a priori information, a random sample for learning our procedure must be taken precisely from a power-law distribution characterized by the presumed exponent value γ. For a criterion, we took the relative error. According to the results of the simulation, the mean-square error in estimating energy was 49%. The one-dimensional method that employs the variable S yields 56%. These values receive overwhelming contributions from low-energy events, since they result from averaging over a steeply descending power-law spectrum.

In the second problem, where monochromatic beams of energy ranging between 10^{11} and 10^{15} eV form the test sample, we are equally interested in energy values over the entire range on a logarithmic scale, from $E = 10^{11}$ to $E = 10^{15}$ eV; therefore, a random sample from an energy spectrum such that the logarithm of energy is uniformly distributed over the entire range that we chose must be taken to be learning. Such a sample was formed by about 500 events over the entire energy range covering five orders of magnitude. The volume of each of six test samples monochromatic in energy ranged between 100 and 500 events.

The results of estimating energy are given in Table 1 for several values of the parameter a, which characterizes nonlinearity. In order to compare these results with those that emerge from the application of the already existing procedure used within the KLEM–NUCLEON project to estimate energy, similar errors were calculated for the same test samples by means of the algorithm based on the single variable S in (1). We note that, in contrast to what was done previously in [4], we did not perform any low-energy truncation in calculating these errors—we took into account the entire body of statistics generated for test samples. Moreover, it is of importance that, as a matter of fact, the errors of the earlier procedure were calculated for the same data as those that were used in the algorithm itself to construct the calibration curve (thus, it was an a priori known energy that was subjected to reconstruction). This means that, within the earlier algorithm, it would be natural to expect even a poorer accuracy of reconstruction for different samples.

The last column of Table 1 gives the results obtained previously in [4] from computer experiments aimed at estimating the primary-particle energy with the KLEM spectrometer, where the error was calculated by using incomplete statistics, its part at the lowest energies being eliminated. Albeit being incorrect from the mathematical point of view, this procedure did not lead to loss of information significant for the ensuing data treatment, since the reconstructed energy values were further used directly to construct

Table 1. Relative error in reconstructing energy (in %)

E, eV	Multivariate method				One-dimensional method employing the parameter S	
	$a = 1.2$	$a = 1.3$	$a = 1.4$	$a = 1.5$	full statistics	result obtained in [4] without the low-energy part of statistics
10^{11}	46	43	37	33	92	72
10^{12}	58	59	62	64	103	69
10^{13}	61	61	62	64	101	61
10^{14}	60	62	63	65	95	55
10^{15}	63	66	69	73	83	56

the primary spectrum by means of histograms. The region of low energies is of no interest from this point of view, whereas the tail in the region of underestimated values of E_{est} makes a significant contribution to the total error, as is suggested by a comparison of the data in the last two columns of Table 1. The algorithm that will be proposed in the present study for reconstructing the exponent in the power-law spectrum employs only an estimate of $\langle \ln E \rangle$ rather than estimates of energy.

2. DETERMINATION OF THE EXPONENT IN THE PRIMARY POWER-LAW SPECTRUM

In order to reconstruct the exponent γ in the energy distribution of cosmic rays,

$$p(E) = \frac{\gamma - 1}{E_0} \left(\frac{E}{E_0} \right)^{-\gamma} \qquad (9)$$

(E_0 is the left boundary of the spectrum), and the shape of the spectrum, we previously used the traditional procedure for plotting histograms on the basis of reconstructed energy values [12, 13]. This procedure involves a large error, which is difficult to estimate, but it has long since become a conventional tool in these realms. Since the method proposed in Section 1 for estimating energy leads to unbiased results and involves a minimum mean-square error, it is quite natural to expect that even a direct application of the traditional algorithm of reconstructing the spectrum at energy values found by the new method, which is not in use at the present time, would lead to a higher precision in reconstructing the spectrum.

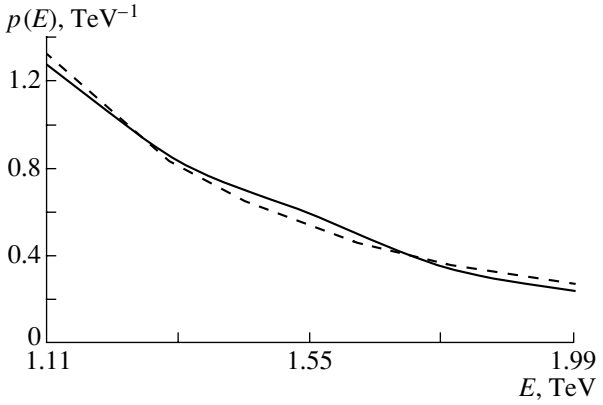

Fig. 1. Density of the primary energy distribution (solid curve, based on an analytic form) before and (dashed curve, constructed on the basis of a histogram) after the trigger.

One of the most serious difficulties in reconstructing the spectrum is that, in simulating the operation of the KLEM spectrometer, one performs a "multistep" selection of events that the detector used would record. As a result, the shape of the primary spectrum is severely distorted, so that even a perfectly precise measurement of energies of particles recorded by the detector would give no way to reconstruct their spectrum at the input of the measuring equipment (Fig. 1). The selection criterion results in that the exponent γ calculated by the maximum-likelihood method for the primary spectrum having the lower boundary at $E_0 = 1$ TeV is underestimated to become $\gamma_{\text{est}} = 2.58$ (in the case of a precise measurement of the energies of all particles that passed a triggering selection of particles) instead of $\gamma_0 = 2.70$, whereas, for the same volume of the sample, the statistical uncertainty in estimating γ can be determined as

$$\sigma_{\gamma_{\text{est}}} \sim \sigma\{1/\ln(E/E_0)\} = 0.017$$

[on the basis of formula (10) below, which provides a realization of the method in question in the case of precise measurements].

2.1. Spectrum Unbounded from the Right

In order to estimate the exponent γ in the power-law distribution by the maximum-likelihood method (MLM), one can make use of the formula

$$\gamma_{\text{est}} = 1 + 1/(\langle \ln E \rangle - \ln E_0). \qquad (10)$$

The quantity $\langle \ln E \rangle$ can be found by averaging the logarithms of the measured energy values only if the energy is measured without errors or if the errors in determining $\ln E$ do not depend on energy, but, in either case, this is an idealization—otherwise, the distribution of measured energies is the convolution of the primary spectrum with a function that describes distortions introduced by the measuring device. In the problem at hand, an additional distortion of the spectral shape arises even at the preliminary stage of event selection by instrumental triggers. Therefore, we applied a procedure that immediately yields the most precise estimate of $\ln E$—namely, a linear estimate that is constructed for $\ln E$ treated as a random variable and which is the best in the sense of the mean-square deviation. In contrast to the method employing the parameter S, this method yields unbiased results, guaranteeing that the respective estimate of $\langle \ln E \rangle$ will not suffer from systematic under- or overestimations.

The algorithm used to estimate the exponent of the primary power-law spectrum is the following:

(i) The "preliminary" step consists in choosing a few values of $\gamma = \gamma_0$ from the interval in which we are interested. In all, we employed three values of γ_0 in our numerical experiments (this was sufficient to ensure a fairly high precision).

(ii) For each of the chosen values of γ_0, two random samples are taken from the power-law spectrum that has this exponent. The use of precisely a power-law distribution for learning the method involves taking into account additional a priori information. In the procedure implemented further to reconstruct the logarithm of the energy for each γ_0, one sample will be used as a learning one, while the other is taken to be a test one.

(iii) For each individual event of the test sample, $\ln E$ is reconstructed by formulas (2), (4), and (5), where the random variable E is replaced by $\ln E$. For a learning sample, we employ that which features fixed γ_0 (beginning with the first one), while, for a test sample, we successively take samples involving each of the three values of γ_0 (including that which corresponds to the learning sample).

(iv) For each of the three sets of $\ln E$ that were determined at the preceding step, a preliminary estimate of γ is found by formula (10). These will be "preliminary" estimates of γ, the true values being equal to the first, the second, and the third of the γ_0 values, respectively; the learning of the procedure was performed by using one (initially, the first) of these γ_0 values.

(v) The procedures of steps (iii) and (iv) are repeated by using, for a learning sample, the sample that involves, first, the second and, then, the third value of γ_0. Thus, we performed the procedure for reconstructing $\ln E$ three times for each of the three γ_0 values, thereby deriving nine sets of reconstructed values of $\ln E$ and the corresponding "preliminary" estimates of γ_0: three estimates for the first value of γ_0, three estimates for the second one, and three estimates for the third one. The three estimates of the same value of γ_0 differ in that different learning samples (successively, the samples involving the first, the second, and the third value of γ_0) were used to obtain them.

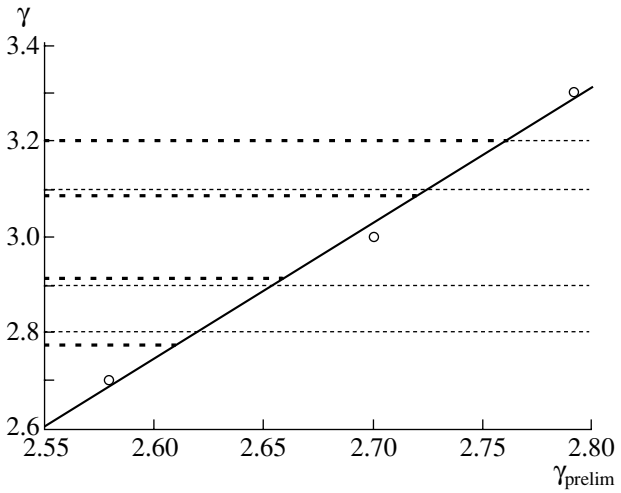

Fig. 2. Estimating γ on the basis of the linear dependence $\gamma(\gamma_{\text{prelim}})$: (open circles) "learning" points, (solid line) interpolation straight line corresponding to the least squares method, (thick dashed lines) ultimate estimates of the parameter γ, and (dotted lines) true values of the estimated γ.

(vi) An interpolation curve representing the dependence of the true value of γ on its "preliminary" estimate is constructed on the basis of the points found at the preceding step (in our case of three points, we use a linear function). For each of the three values of γ_0, we construct an individual interpolation dependence. For cases like that in which the estimated value is much greater or much less than the known one, we thereby obtain the possibility of comparing the quality of the developed procedure for different values of γ_0 preassigned for learning this procedure.

(vii) The "ultimate step" consists in finding the estimates of the exponent γ that are corrected with the aid of the three interpolation dependences constructed at the preceding step. An example of how the procedure outlined here is represented graphically is given in Fig. 2.

We have performed computer experiments aimed at estimating the exponent of a power-law proton spectrum (for a vertical incidence of the beam to the detector plane). In order to compare our multivariate

Table 2. Estimates of the exponent γ in the form $\langle\gamma_{\text{est}}\rangle \pm \Delta_\gamma$

True values of γ	$N = 100$, $\sigma_{\text{MLM}} = 0.18$				$N = 200$, $\sigma_{\text{MLM}} = 0.12$		$N = 300$, $\sigma_{\text{MLM}} = 0.10$		$N = 400$, $\sigma_{\text{MLM}} = 0.09$	
	One-dimensional method involving the parameter S	Multivariate method			One-dimensional method involving the parameter S	Multivariate method, $\gamma_0 = 2.7$	One-dimensional method involving the parameter S	Multivariate method, $\gamma_0 = 2.7$	One-dimensional method involving the parameter S	Multivariate method, $\gamma_0 = 2.7$
		$\gamma_0 = 2.7$	$\gamma_0 = 3.0$	$\gamma_0 = 3.3$						
2.8	2.81 ± **0.29**	2.81 ± **0.30**	2.81 ± **0.31**	2.81 ± **0.30**	2.80 ± **0.21**	2.80 ± **0.22**	2.81 ± **0.15**	2.79 ± **0.17**	2.78 ± **0.13**	2.79 ± **0.15**
2.85	2.90 ± **0.33**	2.83 ± **0.32**	2.85 ± **0.31**	2.85 ± **0.30**	2.88 ± **0.22**	2.84 ± **0.22**	2.84 ± **0.13**	2.83 ± **0.18**	2.86 ± **0.13**	2.84 ± **0.16**
2.9	2.90 ± **0.31**	2.89 ± **0.30**	2.91 ± **0.29**	2.91 ± **0.30**	2.92 ± **0.24**	2.89 ± **0.21**	2.88 ± **0.16**	2.89 ± **0.17**	2.87 ± **0.14**	2.89 ± **0.16**
3.1	3.19 ± **0.46**	3.14 ± **0.27**	3.16 ± **0.26**	3.13 ± **0.27**	3.11 ± **0.29**	3.14 ± **0.19**	3.13 ± **0.20**	3.13 ± **0.15**	3.15 ± **0.19**	3.13 ± **0.13**
3.15	3.24 ± **0.44**	3.17 ± **0.26**	3.17 ± **0.25**	3.17 ± **0.24**	3.22 ± **0.34**	3.18 ± **0.18**	3.20 ± **0.25**	3.17 ± **0.15**	3.16 ± **0.19**	3.18 ± **0.13**
3.2	3.20 ± **0.43**	3.16 ± **0.26**	3.16 ± **0.25**	3.17 ± **0.26**	3.13 ± **0.25**	3.15 ± **0.18**	3.09 ± **0.21**	3.16 ± **0.15**	3.13 ± **0.19**	3.15 ± **0.14**

procedure with that which employs one parameter, the exponent γ was estimated by the two methods as applied to the same simulated data—that is, by the algorithm that employs a multivariate statistical estimation of the logarithm of energy and by the method that reconstructs energy on the basis of the parameter S (1).

The learning of the multivariate method was performed by using three proton beams having a power-law energy spectrum whose exponent γ_0 takes the values of 2.7, 3.0, and 3.3. The exponent was estimated for beams characterized by a set of γ values in the range between 2.8 and 3.2. The number of events in each of the learning beams was quite large (a few thousand), but this imposed no constraints on the implementation of the tested procedure in practice, since the learning samples can be accumulated via a computer simulation rather than in an actual experiment. The test samples were taken to have a volume of 100 to 400 events—such numbers of primary protons can be recorded by the KLEM facility on board a cosmic vehicle.

The results of the estimation are given in Table 2. For the purposes of visualization, the data in the column corresponding to $N = 100$ and $\gamma_0 = 2.7$ are represented graphically in Fig. 3. Since the estimates of γ that were obtained for each of the three learning samples specified by the values of $\gamma_0 = 2.7$, 3.0, and 3.3 proved to be close to one another, only estimates at $\gamma_0 = 2.7$ are given in all parts of the table, with the exception of the first one.

On the basis of the data in Table 2, one can assess the strength of the effect that the volume of accumulated data has on the accuracy of estimation. As was indicated above, the statistical uncertainty of an estimate due exclusively to the finiteness of a sample (the energy is known precisely) can be obtained by using the maximum-likelihood-method formula (10). This uncertainty is "irremovable"; therefore, it is of paramount importance to get an idea of the order of its magnitude playing the role of the "limiting resolution" (which corresponds to the case of perfectly accurate measurements) of the procedure (or facility) for reconstructing the exponent γ. A graph that represents this "irremovable" uncertainty as a function of the volume of statistics, N, is given in Fig. 4 for an interval covering a few hundred events, which is of interest to us.

We note that, although each estimation of γ by formula (10) involves only data associated with N (from 100 to 400) events in Table 2, the estimates of γ are averaged over a few N-event samples from the entire body of available data in order to suppress random "outliers" and to verify an unbiased character of the results given by this procedure and the absence of a systematic bias. However, we will have modest statistics in an actual experiment, and this will prevent averaging results over a few samples. Therefore,

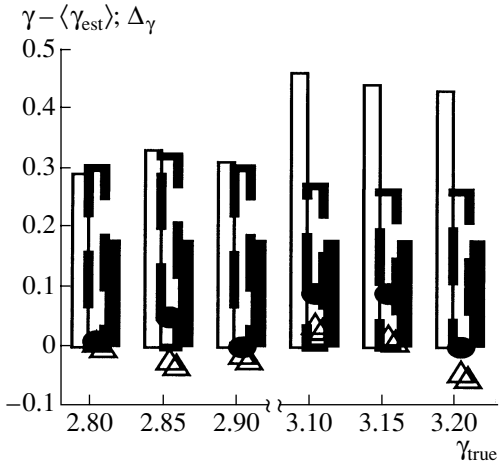

Fig. 3. Deviations from the mean value, $\gamma - \langle\gamma_{\rm est}\rangle$, and mean-square errors, Δ_γ, for estimates of the exponent γ (here, $N = 100$ and $\sigma_{\rm MLM} = 0.18$; for the multivariate method, $\gamma_0 = 2.7$): (thin-solid-line histogram) Δ_γ within the one-dimensional method, (thick-dashed-line histogram) Δ_γ within the multivariate method, (closed histogram) $\sigma_{\rm MLM}$, (closed circles) $(\gamma - \langle\gamma_{\rm est}\rangle)$ within the one-dimensional method, and (double triangles) $(\gamma - \langle\gamma_{\rm est}\rangle)$ within the multivariate method.

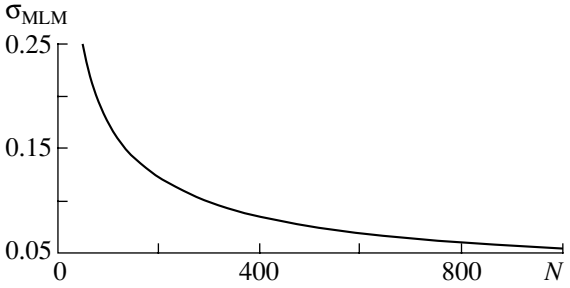

Fig. 4. Error in estimating γ by the maximum-likelihood method for a precisely known primary energy versus the volume of statistics.

the errors Δ_γ (printed in boldface type in Tables 2–4), which can be used to assess the degree of deviations from the averaged value that are expected in performing a single experiment for statistics involving N events, carry information of no less importance. The smaller the factor by which this error exceeds the "irremovable" error $\sigma_{\rm MLM}$, which is displayed in Table 2 and in Fig. 4, the higher the quality of estimation.

It should be noted that the above comparison of the two procedures, the one-dimensional and the multivariate one, involves some degree of arbitrariness, since no generally accepted algorithm for reconstructing the exponent of the power-law spectrum in processing data simulated for the KLEM equipment exists at the present time, and this was one of the reasons for developing a new universal algorithm. In our case, the values of E (or $\ln E$) that were obtained for each of the primary particles from simulated beams by the multivariate method and by the one-dimensional method employing the parameter S were merely subjected to identical treatment. It follows that, as a matter of fact, the same complicated algorithm of treatment was applied to the results of energy measurements by both procedures.

In order to render the conditions of our numerical experiment closer to those that will be prevalent in a live experiment, where the left boundary of the spectrum of recorded particles will not be known, the estimation of γ for an unknown left boundary of the spectrum was simulated in an independent run of the calculations. We took only those events that were selected according to the criterion $E_{\rm est} > E_0$, where E_0 is a known preset value (more rigorously, one does not determine the energy itself within the multivariate procedure of estimation; therefore, the selection criterion has the form $(\ln E)_{\rm est} > \ln E_0$ within this algorithm). The value for the left boundary of the spectrum was chosen, first, with allowance for the possibility of estimating it to a fairly high degree of precision and, second, with allowance for the volume of data that is necessary for the present purposes. On the basis of these considerations, we choose a few values of E_0 in the range between 2 and 4 TeV. Table 3 displays the results obtained by estimating γ for some values of E_0.

From a comparison of these results with the data in Table 2, it can be seen that the exponent of the spectrum whose left boundary is a priori unknown and is reconstructed on the basis of results of measurements performed with recording equipment can be estimated to a precision not poorer than that attained in estimating the exponent of the spectrum characterized by a fixed value of E_0.

2.2. Spectrum within the (E_1, E_2) Segment

In the case where one is interested in the value of the exponent γ only within some segment of the energy spectrum of primary cosmic rays, it is advisable to consider the spectrum in a form different from that in (9),

$$p(E) = \frac{\gamma - 1}{E_1^{1-\gamma} - E_2^{1-\gamma}} E^{-\gamma}, \quad \text{if} \quad E \in (E_1, E_2);$$

$$p(E) = 0, \quad \text{if} \quad E \notin (E_1, E_2).$$

This form of the spectrum is more complicated from the point of view of estimating γ, since, in this case, the maximum-likelihood method yields, instead of the direct formula (10), a nonlinear equation for γ,

$$\gamma = 1 + (E_1^{1-\gamma} - E_2^{1-\gamma})/(E_1^{1-\gamma}\{\langle\ln E\rangle - \ln E_1\} \tag{11}$$

Table 3. Estimates of the exponent γ in the form $\langle\gamma_{\text{est}}\rangle \pm \Delta_\gamma$ at a fixed left boundary E_0 of the spectrum for $\gamma_0 = 2.7$, 3.0, and 3.3 (here, $N = 100$ and $\sigma_{\text{MLM}} = 0.18$)

True values of γ	$E_0 = 2$ TeV			$E_0 = 2.5$ TeV			$E_0 = 3$ TeV		
	2.7	3.0	3.3	2.7	3.0	3.3	2.7	3.0	3.3
2.8	$2.84 \pm \mathbf{0.23}$	$2.82 \pm \mathbf{0.23}$	$2.83 \pm \mathbf{0.22}$	$2.85 \pm \mathbf{0.25}$	$2.86 \pm \mathbf{0.24}$	$2.86 \pm \mathbf{0.27}$	$2.83 \pm \mathbf{0.22}$	$2.83 \pm \mathbf{0.19}$	$2.80 \pm \mathbf{0.21}$
2.85	$2.83 \pm \mathbf{0.23}$	$2.83 \pm \mathbf{0.24}$	$2.80 \pm \mathbf{0.23}$	$2.81 \pm \mathbf{0.24}$	$2.79 \pm \mathbf{0.23}$	$2.76 \pm \mathbf{0.25}$	$2.80 \pm \mathbf{0.22}$	$2.77 \pm \mathbf{0.20}$	$2.80 \pm \mathbf{0.21}$
2.9	$2.91 \pm \mathbf{0.24}$	$2.91 \pm \mathbf{0.23}$	$2.88 \pm \mathbf{0.22}$	$2.90 \pm \mathbf{0.24}$	$2.91 \pm \mathbf{0.24}$	$2.92 \pm \mathbf{0.25}$	$2.93 \pm \mathbf{0.23}$	$2.93 \pm \mathbf{0.21}$	$2.93 \pm \mathbf{0.21}$
3.1	$3.11 \pm \mathbf{0.23}$	$3.10 \pm \mathbf{0.24}$	$3.08 \pm \mathbf{0.24}$	$3.14 \pm \mathbf{0.25}$	$3.10 \pm \mathbf{0.23}$	$3.11 \pm \mathbf{0.24}$	$2.97 \pm \mathbf{0.22}$	$2.97 \pm \mathbf{0.20}$	$3.02 \pm \mathbf{0.18}$
3.15	$3.25 \pm \mathbf{0.28}$	$3.24 \pm \mathbf{0.26}$	$3.22 \pm \mathbf{0.25}$	$3.27 \pm \mathbf{0.30}$	$3.26 \pm \mathbf{0.29}$	$3.33 \pm \mathbf{0.33}$	$3.26 \pm \mathbf{0.27}$	$3.23 \pm \mathbf{0.23}$	$3.27 \pm \mathbf{0.27}$
3.2	$3.19 \pm \mathbf{0.24}$	$3.17 \pm \mathbf{0.23}$	$3.16 \pm \mathbf{0.23}$	$3.26 \pm \mathbf{0.26}$	$3.30 \pm \mathbf{0.27}$	$3.30 \pm \mathbf{0.28}$	$3.26 \pm \mathbf{0.23}$	$3.20 \pm \mathbf{0.19}$	$3.20 \pm \mathbf{0.19}$

$$- E_2^{1-\gamma}\{\langle \ln E\rangle - \ln E_2\}).$$

The algorithm of estimation exactly reproduces that which was described above for the case of an unbounded spectrum, the only exception being that the maximum-likelihood method, which underlies both algorithms, is now realized through Eq. (11) rather than through formula (10).

As in the case of an unbounded spectrum, the vertical incidence of a proton beam to the detector plane was considered in computer experiments aimed at estimating the exponent γ within various energy ranges. All of the parameters of the simulation were identical to those in the preceding case. The values for both the left and the right boundary of the spectrum were not considered to be known and were reconstructed on the basis of simulated data, as is described in the preceding subsection.

For statistics including 100 events, Table 4 shows the results for an energy interval of width 2 TeV. It can be seen that, even for so small a volume of data, the exponent γ can be estimated within an energy range of small width by using the proposed procedure, albeit the uncertainty is somewhat greater than for an unbounded spectrum. This is because the irremovable error inherent in the maximum-likelihood method is greater in this case. This error now depends not only on the volume of statistics but also on the width of the energy interval. The relationship between the actual and the minimum possible error remains approximately identical to that in estimating the exponent γ of an unbounded spectrum.

Table 4. Estimates of the exponent γ in the form $\langle\gamma_{\text{est}}\rangle \pm \Delta_\gamma$ for the interval $2 < E < 4$ TeV (here, $N = 100$ and $\sigma_{\text{MLM}} = 0.29$)

True values of γ	One-dimensional method involving the parameter S	Multivariate method		
		$\gamma_0 = 2.7$	$\gamma_0 = 3.0$	$\gamma_0 = 3.3$
2.8	$2.94 \pm \mathbf{0.50}$	$2.78 \pm \mathbf{0.37}$	$2.72 \pm \mathbf{0.36}$	$2.70 \pm \mathbf{0.35}$
2.85	$2.93 \pm \mathbf{0.45}$	$2.85 \pm \mathbf{0.39}$	$2.94 \pm \mathbf{0.37}$	$2.77 \pm \mathbf{0.36}$
2.9	$2.86 \pm \mathbf{0.46}$	$2.82 \pm \mathbf{0.41}$	$2.87 \pm \mathbf{0.37}$	$2.74 \pm \mathbf{0.39}$
3.1	$2.94 \pm \mathbf{0.48}$	$3.18 \pm \mathbf{0.40}$	$3.14 \pm \mathbf{0.36}$	$3.04 \pm \mathbf{0.37}$
3.15	$3.10 \pm \mathbf{0.48}$	$3.19 \pm \mathbf{0.41}$	$3.15 \pm \mathbf{0.36}$	$3.07 \pm \mathbf{0.38}$
3.2	$2.95 \pm \mathbf{0.52}$	$3.18 \pm \mathbf{0.40}$	$3.11 \pm \mathbf{0.37}$	$3.00 \pm \mathbf{0.41}$

CONCLUSION

Multivariate procedures for processing the results of measurements with multichannel equipment have been developed, implemented, and tested in computer experiments. These procedures, which are optimal within a broad class of algorithms in the sense that they are characterized by the highest sensitivity, are intended for estimating (i) physical parameters inaccessible to direct measurements (such as the primary energy and other features of the primary particle) and (ii) the exponent of the primary spectrum of cosmic rays.

The multivariate procedures for estimation have been studied in computer experiments employing a mathematical model for the KLEM measuring equipment from the NUCLEON project. The following conclusions have been drawn from the results of these experiments:

(a) In estimating the primary-particle energy, the multivariate procedure yields a much smaller error (by a factor of 1.5) in relation to the one-dimensional algorithm used previously by our group.

(b) In estimating the exponent of the spectrum of primary cosmic rays, the multivariate procedure works at least no poorer than the algorithm based on a one-dimensional estimation of the energy of each

individual event. At the same time, the new procedure in question, in contrast to algorithms that are aimed at determining the exponent of the spectrum from histograms on the basis of a one-dimensional estimation of energy and which were previously applied in the KLEM–NUCLEON project and in other investigations, is optimal in a rigorous mathematical sense, is universal, and makes it possible to employ codes of a single type in processing multiparameter data of any kind.

ACKNOWLEDGMENTS

This work was supported by the Russian Foundation for Basic Research (project no. 03-02-16660).

REFERENCES

1. L. W. Howell, Nucl. Instrum. Methods Phys. Res. A **480**, 741 (2001).
2. G. L. Bashindzhagyan *et al.*, Preprint No. 99-13/571, NIIYaF MGU (Inst. Nucl. Phys., Moscow State Univ., Moscow, 1999).
3. J. Adams, G. L. Bashindzhagyan, P. G. Bashindzhagyan, *et al.*, Izv. Akad. Nauk, Ser. Fiz. **65**, 430 (2001).
4. N. A. Korotkova, D. M. Podorozhnyi, E. B. Postnikov, *et al.*, Yad. Fiz. **65**, 884 (2002) [Phys. At. Nucl. **65**, 852 (2002)].
5. E. B. Postnikov, G. L. Bashindzhagyan, N. A. Korotkova, *et al.*, Izv. Acad. Nauk, Ser. Fiz. **66**, 1634 (2002).
6. Yu. P. Pyt'ev, *Methods for Analyzing and Interpreting Experimental Results* (Mosk. Gos. Univ., Moscow, 1990), pp. 15, 16 [in Russian].
7. E. B. Postnikov, Candidate's Dissertation in Mathematics and Physics (Mosk. Gos. Univ., Moscow, 1999).
8. Yu. P. Pyt'ev, *Mathematical Methods for Interpreting Experiments* (Vysshaya Shkola, Moscow, 1989) [in Russian].
9. GEANT User's Guide, CERN DD/EE/83/1 (Geneva, 1983).
10. N. N. Kalmykov *et al.*, Preprint No. 98-36/537, NIIYaF MGU (Inst. Nucl. Phys., Moscow State Univ., Moscow, 1998).
11. I. D. Rapoport, A. N. Turundaevsky, and V. Ya. Shestoperov, Yad. Fiz. **65**, 176 (2002) [Phys. At. Nucl. **65**, 170 (2002)].
12. A. V. Apanasenko, V. A. Sukhadolskaya, V. A. Derbina, *et al.*, Astropart. Phys. **16**, 13 (2001).
13. I. P. Ivanenko *et al.*, in *Proceedings of the 23rd ICRC, Calgary, 1993* (*Contributed Papers*), Vol. 2, p. 17.

Translated by A. Isaakyan

Physics of Atomic Nuclei, Vol. 68, No. 1, 2005, pp. 60–68. Translated from Yadernaya Fizika, Vol. 68, No. 1, 2005, pp. 61–69.

ELEMENTARY PARTICLES AND FIELDS
Experiment

Cosmic-Ray Studies with an Alpha Magnetic Spectrometer (AMS Detector) on the International Space Station

V. V. Plyaskin

Institute of Theoretical and Experimental Physics,
Bol'shaya Cheremushkinskaya ul. 25, Moscow, 117259 Russia

Received December 10, 2003; in final form, March 1, 2004

Abstract—A brief description of the physics research program implemented with an alpha magnetic spectrometer (AMS detector) by a large-scale international collaboration on board the International Space Station is presented. The features of the experimental facility under construction are given, along with some results obtained during the test flight of the prototype spectrometer on board a space shuttle.

INTRODUCTION

The detection of cosmic-ray particles at the beginning of the 20th century initiated research that resulted in fundamental discoveries. In order to assess the impact of these discoveries on the formation of modern ideas of our world, it would suffice to recall that the first antiparticles (positrons), as well as muons and pions, were first observed in cosmic-ray experiments. Up to the early 1950s, when the first powerful accelerators were created, cosmic rays had been the single source of particles used in investigations into the area later called high-energy physics.

To a great extent, cosmic-ray studies have given impetus to the development of various detecting devices. Almost all detectors used in modern experiments were invented for investigations associated with cosmic rays.

Since the time of the Aragatz expeditions, A.I. Alikhanov, who headed these expeditions, had given much attention to cosmic-ray studies. Thus, it was not merely a matter of accident that there was a laboratory for cosmic-ray studies at the Institute of Theoretical and Experimental Physics (ITEP, Moscow) organized by Alikhanov. Up to the early 1960s, when a strong-focusing accelerator—the first one in the Soviet Union—was commissioned at ITEP, the institute carried out intensive investigations into the properties of cosmic rays. For example, the helicity of cosmic-ray muons was measured under the supervision of Alikhanov [1].

Since the advent of accelerators, cosmic-ray studies have been related, to a greater extent, to astrophysics and cosmology rather than to elementary-particle physics. Nevertheless, these two realms of physics have always been interrelated [2]. For example, the modern understanding of baryogenesis is based, among other things, on the ideas elaborated as the result of studying the dynamical and static properties of elementary particles in accelerator experiments. At the same time, astrophysics investigations—predominantly, measurements of cosmic microwave background radiation [3]—indicate that the total baryon mass is not greater than 5% of the total Universe mass, the visible component (that which emits or absorbs electromagnetic waves) being only 1/10 of this fraction. The remaining 95% of the Universe mass is due to dark matter and dark energy. Although the existence of these dominant components of the Universe is an experimental fact, the nature of dark matter and dark energy has not yet been established.

In efforts to explain this picture, theorists have ever more often discussed processes that occur in the energy region beyond the capabilities of present-day accelerators. At the same time, some processes accompanying the evolution of stars result in the production of particles whose energy exceeds that of modern accelerators by several orders of magnitude. A nonfixed energy and a nonfixed "beam" content, as well as a fast decrease in the beam intensity with energy, are the main problems associated with the use of this natural accelerator in investigations. In addition, arrays deployed on the Earth's surface and used in experiments with cosmic-ray particles are beneath the atmosphere, with the result that they detect predominantly secondary particles produced in air showers. For this reason, terrestrial experiments furnish only indirect information about the fluxes of primary protons and nuclei and are unable to

1063-7788/05/6801-0060$26.00

study the fluxes of electrons, positrons, and gamma rays.

Balloon-borne experiments solve in part the problem of interaction between primary cosmic rays and the atmosphere. However, the relatively short duration of flight of balloons, and small area and acceptance of the detectors used prevent obtaining sufficiently large data samples for the flux of charged particles at energies above a few tens of GeV.

The emerging possibility of studying cosmic rays for a long time with rather large facilities by installing them on board a space vehicle significantly extends the region of investigations. The application of detectors and methods developed for accelerator experiments in these facilities would provide a radical solution to the problem of measuring the flux of primary particles up to energies of several TeV.

An alpha magnetic spectrometer (AMS) is one of the first large-scale facilities intended for a long-term study of primary cosmic rays with a device located in a near-Earth orbit.

The idea to create an AMS detector was put forth in 1994 by physicists from the Massachusetts Institute of Technology (MIT) (S. Ting's laboratory) and from ITEP (Yu.V. Galaktionov's laboratory) [4]. The idea is based on the desire to use the vast experience gained by accelerator experimentalists to solve problems that lie at the meeting point of two areas of physics (elementary-particle physics and astrophysics) rapidly developing over the past decades.

The search for antimatter in the Universe through a potential discovery of antinuclei in cosmic rays [5], searches for dark matter, and measurement of the spectra for various types of cosmic radiation are the main points of the AMS research program. The program is officially supported by the Russian Academy of Sciences.

The implementation of such an ambitious project would be impossible without a space platform suitable for deploying the experimental facility. This opportunity is offered by the International Space Station (ISS), which, at the moment, is under construction in a near-Earth orbit.

It is worth noting that the AMS experiment is the first project supported both by NASA and by US DOE, which provides financial support to experiments in elementary-particle physics, mainly accelerator experiments.

In Russia, the experiment is supported by the Ministry of Atomic Energy and the Ministry of Industry, Science, and Technology.

At the moment, over 200 physicists and engineers from more than 30 countries of Europe, Asia, and America, including, in addition to researchers from ITEP, colleagues from the Kurchatov Institute and the Institute of Nuclear Physics at Moscow State University, are involved in the project.

COSMIC RADIATION

For several decades, the problem of baryogenesis—that is, the problem of explaining the fact that the observable world consists of matter, while, according to theory, the Universe upon the Big Bang contained equal amounts of matter and antimatter—has been one of the fundamental problems in cosmology.

In principle, a baryon-asymmetric universe—that is, that which contains only matter—can be obtained if three conditions for the appearance of baryon asymmetry (nonconservation of the baryon charge, C and CP violation, thermodynamic nonequilibrium of the system) that were formulated by A.D. Sakharov in [6] are valid.

It seems that the validity of all three conditions is confirmed experimentally. For example, the Universe expansion observed through the redshift of spectra is indicative of its thermodynamic nonequilibrium. Investigation of muon and kaon decays revealed C and CP violation in weak interactions. Finally, the very existence of our world as a phase of the evolution from a baryon-symmetric state can be considered as an indication of baryon-charge nonconservation. However, it turns out that the degree of CP violation observed so far only in kaon decay is clearly insufficient for explaining the existing ratio of the number of baryons to the number of cosmic-microwave-background photons in the Universe. As for the baryon charge, no experimental manifestations of its nonconservation, apart from the aforementioned fact of our existence, have been obtained thus far.

In view of this, there are numerous theoretical models of baryogenesis that are based on commonly accepted (albeit not yet experimentally confirmed) theories, like supersymmetric extensions of the Standard Model or Grand Unification Theory, or on new hypotheses (equally not based on any experimental observations). The universe predicted by various models may contain or not contain antimatter. If, in turn, a model predicts the existence of antimatter, this antimatter may appear in the form of rather distant galaxy clusters entirely consisting of antimatter or in the form of objects that have dimensions on the order of star dimensions and which may occur within a galaxy of ordinary matter like ours [7]. Since the production of antinuclei in the interaction of ordinary matter is virtually impossible, the observation of a single nucleus of antihelium or any heavier element in cosmic rays would be an indisputable confirmation of

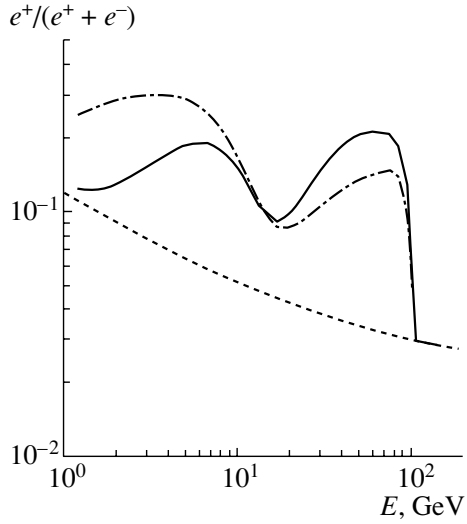

Fig. 1. Energy (E) dependence of the ratio of the positron flux to the sum of the electron and positron fluxes for the case of the annihilation of neutralinos having a mass of 120 GeV [9]. The displayed dependences correspond to two different models of the propagation of cosmic rays in the interstellar space of our Galaxy. The dashed curve represents the fluxes from ordinary sources.

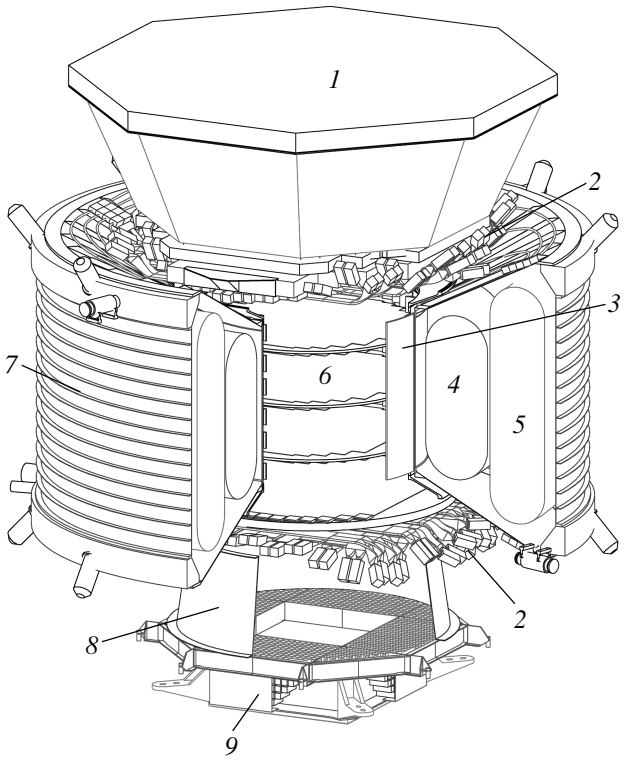

Fig. 2. AMS detector: (*1*) detector of transition radiation, (*2*) scintillation counters of the time-of-flight system, (*3*) anticoincidence counters, (*4*) magnet windings, (*5*) vessel with liquid helium, (*6*) planes of microstrip silicon detectors, (*7*) superconductor magnet, (*8*) Cherenkov counter, and (*9*) calorimeter.

the existence of large (on an astronomic scale) objects that consist of antimatter.

Charged cosmic-ray particles detected in near-Earth space are predominantly produced inside our Galaxy. Primary particles, dominated by protons and helium nuclei, are assumed to appear and gain energy in the process of a diffuse acceleration in the shock wave generated by the divergence of supernova-explosion remnants [8]. Accelerated charged particles are scattered by intragalactic interstellar magnetic fields. As a result, they reach the vicinity of the solar system in the form of isotropic radiation.

Near the Earth, the flux of particles with a rigidity of up to several GV/c is reduced owing to the effect of solar modulation. The reduction level clearly depends on solar activity. Information about the content and the energy spectra of various components of cosmic rays makes it possible to draw conclusions about occurring astrophysical processes.

At the moment, the measured spectra of primary cosmic rays are in good agreement with the theoretically predicted power-law dependence of the particle flux on energy. However, the accuracy of these measurements is rather poor, especially at high energies. For fluxes decreasing with energy, deviations for various particles from a universal spectral index may be indicative of the presence of new-physics processes. If we assume that dark matter in the invisible halo of galaxies consists of neutralinos predicted by supersymmetry, one can expect an increase in the cosmic-ray flux due to neutralino annihilation. Figure 1 shows how the neutralino-annihilation process in the halo of our Galaxy might reveal itself in the positron spectrum [10]. Similar deviations from the power-law dependence in the proton spectra could indicate the presence of cosmic-ray-acceleration mechanisms other than those that are the commonly accepted [11].

It is worth noting that theoretically predicted deviations are usually very small and manifest themselves in a bounded energy region [12]. Therefore, their detection requires a high detector resolution and long exposures. In addition, the detector used must feature a high efficiency of particle identification. We emphasize that the flux of high-energy cosmic-ray protons exceeds the corresponding positron flux by four orders of magnitude; therefore, the corresponding suppression of the proton background is necessary for measuring the positron spectrum.

The absence of the background from secondary particles is an important factor in measuring fluxes of primary cosmic rays; therefore, the detecting devices must be in outer space.

The AMS experiment satisfies all of the aforementioned conditions.

AMS DETECTOR

The AMS detector (Fig. 2) is a wide-aperture magnetic spectrometer. The inner diameter and length of the cylindrical superconductor magnet of the spectrometer (*7*) are approximately 1 m. Twenty-two specially oriented magnet coils (*4*) placed along its perimeter produce a field directed orthogonally to the cylinder axis. The maximum field strength is 0.85 T.

Eight planes of double-sided microstrip silicon detectors (*6*) located inside, above, and below the cylinder are used to measure the track coordinates of particles traversing the spectrometer. The precision of the track-coordinate measurement is 10 μm in the plane of the trajectory-curvature measurement and 30 μm in the plane orthogonal to it. The amplitudes of the signals from the detectors are used to measure the charges of particles by ionization losses.

The combination of the high deflecting power of the magnet and a high precision in determining the points where a particle traverses the microstrip detectors provides a high resolution of the spectrometer (2 to 3%) in the particle rigidity ($R = p/Z$) over a broad interval ($1 < R < 50$ GV/c). The maximum rigidity detectable with the spectrometer ($\sigma_R/R = 100\%$) is 2.5 TV/c.

A transition-radiation detector is located (*1*) in the upper part of the facility. It contains 20 layers, each being a radiator made from plastic fibers, which is followed by a layer of thin-wall drift tubes of small diameter filled with a Xe/CO_2 gas mixture. The detector is intended for the separation of positrons from protons with a suppression factor of 10^3 to 10^2 in the energy range between 1.5 and 300 GeV. Individual groups of drift tubes are located in mutually orthogonal directions, this making it possible to trace the direction along which particles enter the detector. In addition to determining the coordinates of particle tracks, the gas detectors permit estimating the particle charge by ionization losses on the basis of the amplitudes of signals from 20 layers of tubes.

The same method is used to measure the charge in four planes of scintillation counters. The counter pairs placed above and below the magnetic spectrometer (*2*) measure the time of flight. Another set of scintillation counters (*3*) is located at the inner cylindrical surface of the magnet, suppressing the background from particles that interacted with the magnet.

A Cherenkov detector (*8*) and a calorimeter (*9*) are arranged in the lower part of the spectrometer. The Cherenkov detector consists of a radiator manufactured from aerogel and a matrix of photomultiplier tubes intended for detecting photons. Providing the possibility of reconstructing the radius of the Cherenkov radiation ring by the coordinates of detected photons, the detector permits measuring particle velocities to a precision of 0.1% up to an energy of about 10 GeV. The number of detected photons enables one to determine the particle charge. In order to improve the detection efficiency, the detector is equipped with a conic mirror. Information from the Cherenkov detector, together with the rigidity measured in the magnetic spectrometer, makes it possible to determine directly the masses of particles and nuclei.

The calorimeter is made from 18 lead layers arranged in two projections, with scintillating plastic fibers being uniformly distributed within each layer. The calorimeter has a thickness of 15 radiation-length units. It is intended for measuring energy and for determining the shape of a shower produced in the interaction of a particle with the calorimeter. The calorimeter ensures a precision of a few percent in measuring energy. Knowing the shape of a shower in two projections, one can distinguish electrons and positrons from hadrons in the energy range between 1.5 GeV and 1 TeV, the hadron-suppression factor being about 10^4. Measurement of hadron energies up to a few TeV is yet another important function of the calorimeter.

In order to suppress the background from secondary particles to the maximum possible degree and to reduce the impact of multiple scattering on the precision of rigidity measurements, the general layout of the AMS detector was implemented in such a way as to ensure the minimum amount of matter at the inlet of the spectrometer and within it.

The AMS facility is essentially a classical magnetic spectrometer, such as those that are extensively used in high-energy-physics experiments. The significant distinction between the AMS and similar spectrometers is that this complicated apparatus, consisting of technologically ultramodern detectors, should permanently operate without failures for a few years under conditions of outer space.

None of the facilities deployed on the Earth's surface operates under such harmful external conditions as those experienced by a facility in outer space. During its flight in a near-Earth orbit, the facility periodically moves from the zone of direct solar-light impact into the shadow region, the surface temperature of the detector concurrently changing from $+50^\circ$ to -180°C. In addition, the detectors themselves and the readout electronics are permanently exposed to cosmic radiation, which is able, especially during magnetic storms caused by solar flares, to disturb the operation of the detector or even to destroy it. In addition, there are vibrations and overloads amounting to a few g and affecting the facility during the launch of the vehicle carrying it.

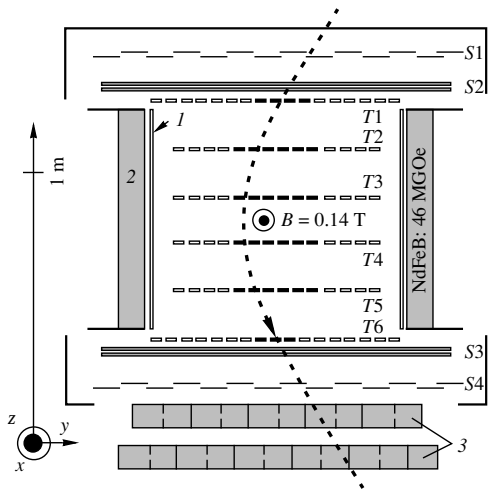

Fig. 3. Layout of the AMS-01 detector: ($S1-S4$) scintillation counters of the time-of-flight system, ($T1-T6$) planes of the microstrip silicon detectors, (*1*) anticoincidence counters, (*2*) permanent magnet, and (*3*) Cherenkov counters. The dashed curve shows the particle trajectory.

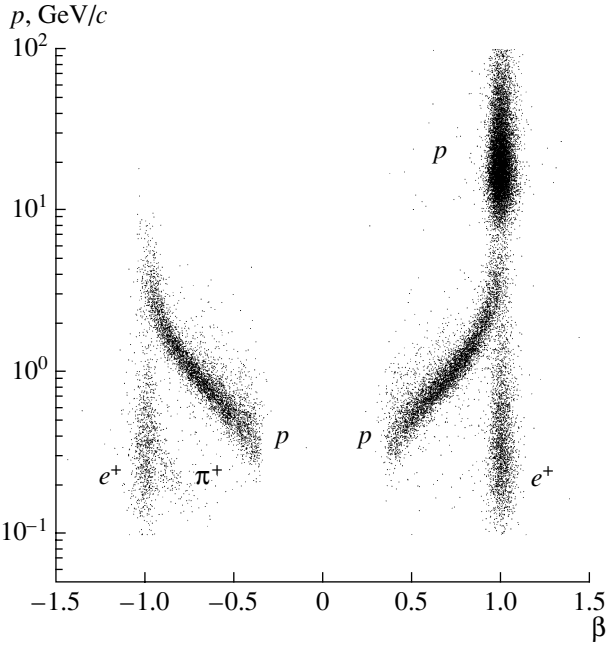

Fig. 4. Measured dependence of the momentum of particles carrying a positive charge of unity on their velocity ($\beta = v/c$). Presented are data obtained over one period of the flight when the shuttle traversed the equator. Particles traversing the spectrometer in the direction from the Earth ($\beta < 0$) include, in addition to positrons, pions produced in the interaction of secondary subthreshold protons with the shuttle casing.

In order to ensure a successful launch and the ensuing reliable operation of the detector for a few years, it is therefore necessary to solve numerous technological problems. In particular, silicon detectors are known to be very sensitive to temperature variations, so that there arises the problem of thermal protection and thermal stabilization of the elements of the microstrip detector. In turn, the refrigerators of the magnet cooling system should uninterruptedly supply the facility with superfluid helium at a temperature of 1.8 K. Further, the presence of the gas detectors operating in a vacuum imposes stringent requirements on the gas-supply system and on the gas tightness of the detector. All of these problems, which are quite readily solved in facilities deployed on the Earth's surface, become virtually the most important consideration in designing a facility intended for operation in outer space. In addition, there are stringent restrictions on the total weight of the equipment (6 t in the case of the AMS), its dimensions and power consumption (2 kW for this detector), the radiation resistance of the materials and electronics, and the safety of the detector for astronauts and for the station. These conditions require the application of state-of-the-art and, as a rule, very expensive technologies.

In order to gain experience in constructing a complicated apparatus and employing it under conditions of outer space, NASA required that a prototype spectrometer be developed and operated in a test flight. The device known as AMS-01 was constructed and tested.

RESULTS OF THE FLIGHT OF THE AMS-01 DETECTOR

Figure 3 shows the layout of the AMS-01 detector. A permanent magnet was used as an analyzing element of the spectrometer. A modern magnetic material (NdFeB) ensured a magnetic induction of about 0.15 T over a rather large volume. The magnet had the shape of a cylinder 80 cm long. The magnetic field was nearly uniform and was orthogonal to the cylinder axis, ensuring an efficient deflection of particles traveling along the cylinder axis. The particle rigidity was measured by the curvature of tracks detected in six layers of the microstrip silicon detectors; within the interval 1–10 GV/c, the precision of this measurement was 10%. The maximum detectable rigidity was 400 GV/c.

Entering the magnet and leaving it, a particle traverses the scintillation hodoscopic counters of the time-of-flight system ($S1-S4$). The precision in measuring the time of flight over a base of about 1 m was approximately 100 ps, and this permitted measuring the particle velocity to a precision of $\sigma_\beta/\beta \simeq 2.4\%$, whereby one could distinguish protons (antiprotons) from (e^-) e^+ for momentum values of up to 1.5 or 2 GeV/c (see Fig. 4). The aerogel

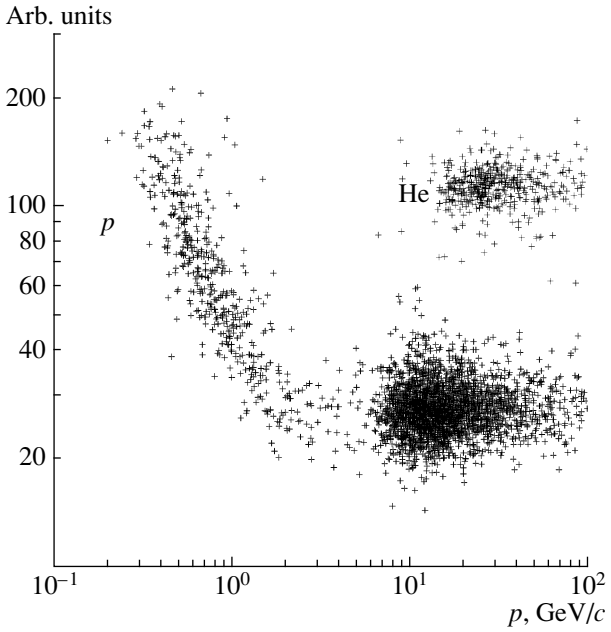

Fig. 5. Ionization losses (in arbitrary units) of particles versus their momentum according to measurements in the silicon detectors. Presented are data obtained over one period of the flight when the shuttle traversed the equator. The figure clearly demonstrates the presence of secondary subthreshold particles.

Cherenkov counter situated in the lower part of the spectrometer extended the region where protons were distinguished from leptons to 3.5 GeV/c. The particle charge was determined by ionization losses in the scintillation counters of the system for time-of-flight measurements and in the silicon microstrip detectors independently. The inner surface of the magnet was covered with anticoincidence scintillation counters.

Since the detector should operate in the vacuum of outer space, all of the detector elements were carefully tested at the thermovacuum test bench at the stage of construction and assembly. The detector was also tested at the vibration table in order to investigate the stability of the AMS-01 structure against strong vibrations that arise during the operation of the shuttle jet engines. Successful preflight tests guaranteed a reliable operation of the detector during the flight.

The test flight of the AMS-01 detector occurred in June 1998, on the Discovery space shuttle [13]. The detector operated in a virtually circular orbit 400 km from the Earth, with the orbit-plane inclination being 51.8°. The flight lasted 10 days; for a significant part of this period, the shuttle was docked to the MIR station. Throughout the flight in the orbit, the detector accumulated experimental data. Approximately 10^8 cosmic-ray particles traversing the facility were detected over the flight time. The most interesting part of the total statistics included data collected for 100 hours of independent flight of the shuttle; for about 24 hours of this independent flight, the AMS-01 detector was oriented toward the zenith. Figures 4 and 5 display the distributions of the parameters of particles detected over a few minutes of such a flight of the detector in the equator region.

Figure 4, which displays the dependence of the momentum of a particle carrying a positive charge of unity (the particle momentum was determined by the track curvature) on its velocity in units of the speed of light (β), demonstrates the potential of AMS-01 for discriminating between positrons and protons. In the figure, positive and negative values of β correspond to particles moving toward and from the Earth, respectively. From Fig. 5, which shows the dependence of the ionization losses measured by the silicon detectors on the measured particle momentum, one can see that the detector provides a reliable determination of the particle charge. Similarly, the charge is determined by the counters of the system for measuring the time of flight.

The data obtained from measurements and presented in Figs. 4 and 5 are merely a raw material for a physical analysis. Nevertheless, some conclusions can be drawn directly from the displayed distributions. For example, it is clear from Fig. 4 that, along with the expected flux of protons having momentum values above the geomagnetic threshold (which is about 10 GeV/c near the equator) and moving toward the Earth, there are particles of momenta substantially below the geomagnetic-cutoff threshold. Moreover, the subthreshold fluxes of particles (protons and positrons) toward the Earth and away from it are equal to each other. Subthreshold electrons were also detected. A data analysis revealed that subthreshold particles are present not only in the equator region but at all latitudes covered by the orbit of the AMS-01 flight. The presence of particles in the Earth's radiation fields referred to as Van Allen belts had been known before the AMS-01 flight. However, protons in the Van Allen belts have energies within the interval 10–100 MeV and occur at distances of a few thousand kilometers from the Earth. In the AMS-01 case, we are dealing with protons present at a distance of 400 km from the Earth that have energies exceeding the energy of protons in external radiation belts by one or two orders of magnitude. The back tracking of subthreshold particles in the Earth's magnetic field showed that they are particles that are produced in hadronic showers caused by the interaction of primary cosmic rays with the atmosphere [14]. In the course of their motion in the magnetic field, these particles can repeatedly traverse the surface of the sphere at the

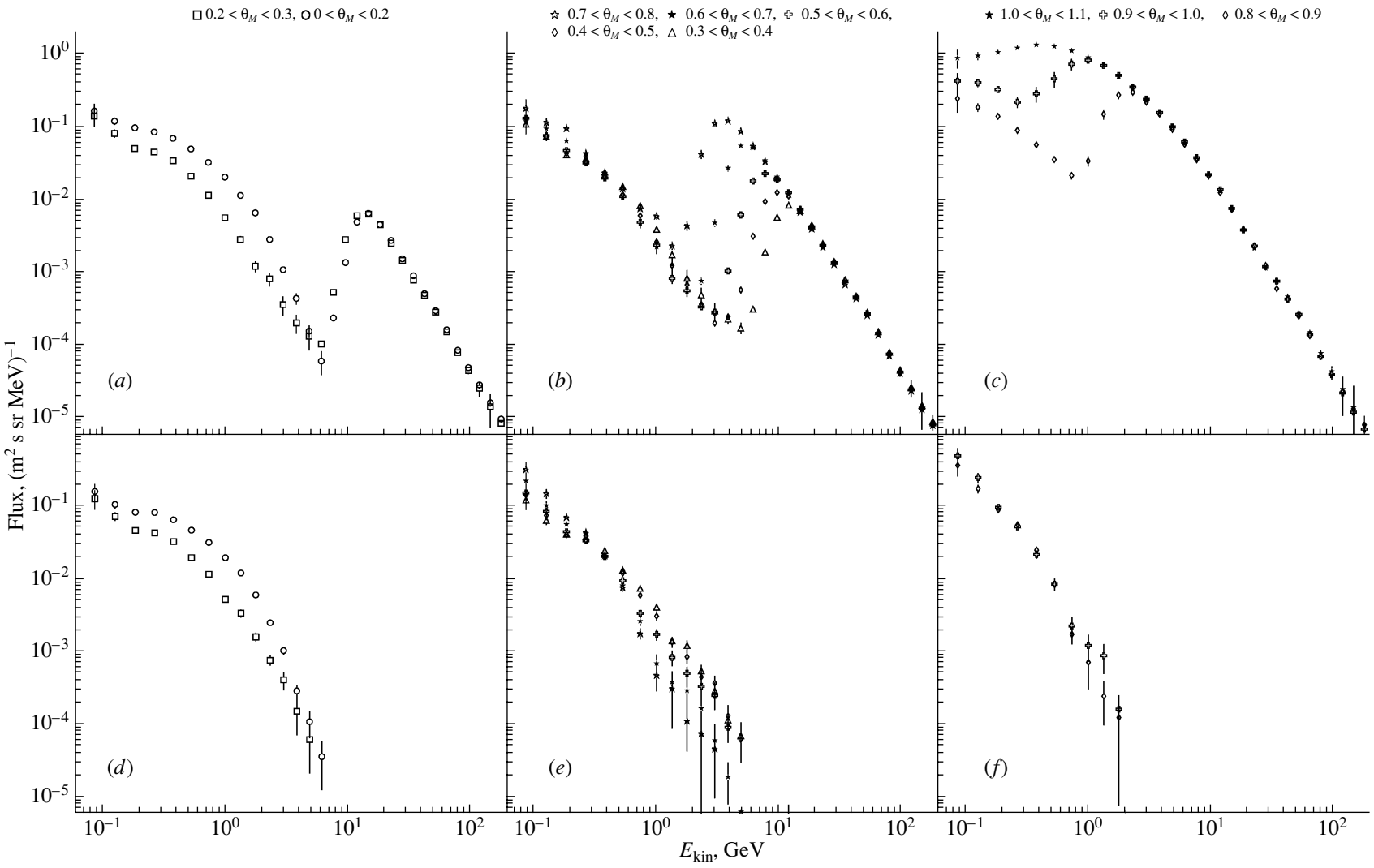

Fig. 6. Energy spectra of protons for various values of the magnetic latitude θ_M: (a, b, c) data for protons moving toward the Earth and (d, e, f) data for protons moving away from the Earth.

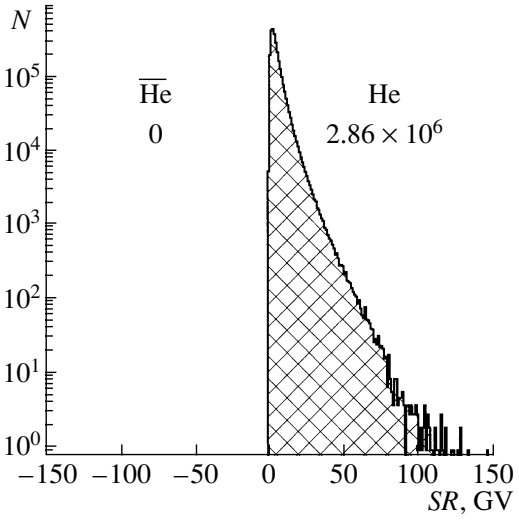

Fig. 7. Number of detected A = 4 nuclei (N) versus the product of the charge sign (S) and rigidity (R).

altitude of the space-shuttle flight in both directions, toward or away from the Earth. In view of this circumstance, the ascending and descending fluxes prove to be equal.

A precise measurement of the fluxes of primary and secondary particles is of paramount importance. In particular, knowledge of the fluxes of various particles entering the atmosphere and of the character of the development of air showers is crucial for interpreting results for atmospheric neutrinos [15]. The results obtained in the test flight substantially improved the accuracy of information about the primary fluxes of cosmic rays. In addition, information about the spectra of secondary particles (p, e^+, e^-) produced in air showers together with neutrinos provides very important data for validating hadronic-shower models that are used to calculate the fluxes of atmospheric neutrinos.

Throughout the AMS-01 flight, 2.86×10^6 He nuclei of rigidity up to 140 GV/c were detected, but no signal from anti-He nuclei was found (Fig. 7). Assuming the same He and anti-He spectra in the interval $1 < R < 140$ GV/c, we arrive at the following limit on the ratio of antihelium and helium fluxes: $N_{\overline{\text{He}}}/N_{\text{He}} < 1.1 \times 10^{-6}$. In addition, the data on the fluxes of nuclei heavier than helium make it possible to set a limit of 2×10^{-5} on the antimatter-to-matter ratio for heavy antinuclei.

The limits derived for the fluxes of antinuclei in cosmic rays from the data obtained over a few tens of hours of the test flight proved to be more stringent than those from many years of searches for antimatter that had been performed before the AMS-01 flight.

CONCLUSION

The test flight described above resulted not only in obtaining interesting physics results but also in gaining experience in operating the facility under conditions of an actual space flight. On the basis of this experience, the spectrometer design was significantly changed and supplemented in order to improve the accuracy of measurements and to extend the physics potential of the facility. At the moment, the changes in question are being implemented in the AMS detector under construction. The replacement of the permanent magnet used in the AMS-01 detector by a superconductor magnet is worthy of special note. A sixfold increase in the deflecting power of the magnet due to this replacement would enable a reliable determination of the sign of the charge of particles traversing the spectrometer up to an energy of a few hundred GeV per nucleon. This would be of paramount importance in searches for antinuclei if one considers that, during the main mission, the spectrometer would detect approximately 2×10^9 helium nuclei, including more than 2×10^5 nuclei of energy above 2 TeV.

Within the next few years, the AMS detector will be installed on board the International Space Station Alpha. It is planned to collect data for 3 to 5 years. Evidently, information obtained within this period would contribute to improving our knowledge of processes occurring in the Universe both in the astrophysical and cosmological aspects and at the level of elementary-particle interactions.

ACKNOWLEDGMENTS

I would like to thank Yu.G. Abov, who proposed to write this article, and Yu.V. Galaktionov for enlightening comments.

REFERENCES

1. A. I. Alikhanov *et al.*, in *Proceedings of the 1960 Annual International Conference on High Energy Physics at Rochester* (Intersci., New York, 1960), Vol. 1, p. 539.
2. Ya. B. Zel'dovich, Usp. Fiz. Nauk **95**, 209 (1968) [Sov. Phys. Usp. **11**, 2381 (1968)].
3. D. N. Spergel *et al.*, Astrophys. J. Suppl. **148**, 175 (2003); astro-ph/0302209; C. L. Bennett *et al.*, Astrophys. J. Suppl. **148**, 1 (2003); astro-ph/0302207.
4. S. P. Ahlen *et al.*, Nucl. Instrum. Methods Phys. Res. A **350**, 351 (1994).
5. Yu. V. Galaktionov, Rep. Prog. Phys. **65**, 1243 (2002).
6. A. D. Sakharov, Pis'ma Zh. Éksp. Teor. Fiz. **5**, 32 (1967) [JETP Lett. **24**, 21 (1967)].
7. A. D. Dolgov, in *Proceedings of 14th Rencontres de Blois: Matter—Antimatter Asymmetry, Chateau de Blois*, *France*, *2002*; hep-ph/0211260.

8. R. Blandford and D. Eichler, Phys. Rep. **154**, 1 (1987).
9. M. Kamionkowski and M. S. Turner, Phys. Rev. D **43**, 1774 (1991).
10. G. Jungman, M. Kamionkowski, and K. Griest, Phys. Rep. **267**, 195 (1996); hep-ph/9506380.
11. S. Heinz and R. A. Sunyaev, astro-ph/0204183.
12. J. L. Feng, K. T. Matchev, and F. Wilczek, Phys. Rev. D **63**, 045024 (2001); astro-ph/0008115.
13. AMS Collab. (M. Aguilar *et al.*), Phys. Rep. **366**, 331 (2002).
14. V. Plyaskin, Phys. Lett. B **516**, 213 (2001); hep-ph/0103286v3.
15. T. K. Gaisser, Nucl. Phys. B (Proc. Suppl.) **118**, 109 (2003); hep-ph/0209195.

Translated by M. Kobrinsky

Physics of Atomic Nuclei, Vol. 68, No. 1, 2005, pp. 69–72. From Yadernaya Fizika, Vol. 68, No. 1, 2005, pp. 70–73.

ELEMENTARY PARTICLES AND FIELDS
Experiment

Neutrino Geophysics at Baksan I: Possible Detection of Georeactor Antineutrinos*

G. V. Domogatsky[1)], V. I. Kopeikin, L. A. Mikaelyan, and V. V. Sinev**

Russian Research Centre Kurchatov Institute, pl. Kurchatova 1, Moscow, 123182 Russia

Received February 16, 2004

Abstract—J.M. Herndon in the 1990s proposed a natural nuclear fission georeactor at the center of the Earth with a power output of 3–10 TW as an energy source to sustain the Earth magnetic field. R.S. Raghavan in 2002 pointed out that, under certain conditions, antineutrinos generated in such a georeactor can be detected using massive scintillation detectors. We consider the underground Baksan Neutrino Observatory (4800 m w.e.) as a possible site for developments in geoneutrino physics. Here, the intrinsic background level of less than 1 event/yr in a liquid scintillation ~1000-t target detector can be achieved and the main source of background is the antineutrino flux from power reactors. We find that this flux is ~10 times lower than at the KamLAND detector site and two times lower than at the Gran Sasso laboratory and thus at Baksan the georeactor hypothesis can be conclusively tested. We also discuss possible searches for the composition of georeactor burning nuclear fuel by analysis of the antineutrino energy spectrum. © *2005 Pleiades Publishing, Inc.*

INTRODUCTION

In this paper, we consider possibilities of detecting at BNO (Baksan Neutrino Observatory of the Institute for Nuclear Research, RAS) antineutrinos from a georeactor using a liquid scintillation spectrometer of ~1000-t target mass. The same spectrometer can detect $\bar{\nu}_e$ coming from terrestrial ^{238}U and ^{232}Th decays; the latter problem will be considered in the next publication. We mention also that here searches for the astrophysical antineutrino flux can be done.

The Earth's magnetic field varies in intensity and irregularly reverses polarity with an average interval between reversals of about 200 000 yr. This requires some variable or intermittent energy source. This source is understood as a georeactor, i.e., as naturally varying self-sustaining nuclear chain reaction burning at the center of the Earth. The georeactor started ~4.5 billion years ago when ^{235}U/^{238}U enrichment was about 30%. In the georeactor, ^{239}Pu is formed by neutron capture in ^{238}U followed by two short-lived beta decays: $^{238}\mathrm{U}(n,\gamma) \rightarrow {}^{239}\mathrm{U}(\beta^-) \rightarrow {}^{239}\mathrm{Np}(\beta^-) \rightarrow {}^{239}\mathrm{Pu}$. The neutron flux in the reactor is extremely low and, in contrast with man-made high-flux power reactors, ^{239}Pu does not contribute to the fission power and decays to ^{235}U: $^{239}\mathrm{Pu}(\alpha, T_{1/2} = 2.4 \times 10^4 \text{ yr}) \rightarrow {}^{235}\mathrm{U}$. Thus, the georeactor operates in a breeder regime and reproduces ^{235}U through the $^{238}\mathrm{U} \rightarrow {}^{239}\mathrm{Pu} \rightarrow {}^{235}\mathrm{U}$ cycle. An average thermal power output of the uranium-based reactor is assumed to amount to 3–6 TW. Had thorium been included, the power could be higher. Variations of georeactor power originate from self-poisoning due to accumulation of fission products and subsequent removal of these products by diffusion or some other mechanism. This is a short and very schematic summary of the georeactor concept proposed in a number of publications by Herndon [1].

A nuclear fission chain reaction can occur in nature. In 1956, Kuroda [2] showed that thick seams of uranium ore, 2 billion years ago, might have been able to support chain reactions and function as a natural nuclear reactor. Sixteen years later, remains of a natural nuclear fission reactor were actually found in a mine at Oklo in the Republic of Gabon in Africa [3].

Herndon's idea about a georeactor located at the center of the Earth, if validated, will open a new era in planetary physics. However, it is not clear whether further geophysical, chemical, etc., studies can in the foreseeable future give a decisive confirmation (or disproof) of this reactor. Particle physics can give another approach to the problem. In 2002, Raghavan [4] pointed out that, under certain conditions, a direct and conclusive test could be obtained by detection of antineutrinos from such a georeactor.

Below, we consider a georeactor: expected $\bar{\nu}_e$ rate

*This article was submitted by the authors in English.

[1)]Institute for Nuclear Research, Russian Academy of Sciences, Moscow, Russia.

**e-mail: sinev@polyn.kiae.su

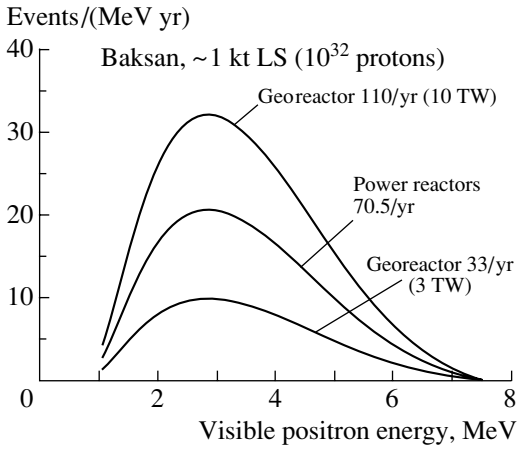

Fig. 1. Positron spectra for georeactor power $W = 3$ TW, 10 TW, and power reactor background at BNO (no oscillation; 100% efficiency is assumed).

and spectrum (Section 1), and detector design and backgrounds (Section 2).

In Section 3, we compare $\bar{\nu}_e$ energy spectra emitted in ^{235}U, ^{238}U, and ^{233}U fission and discuss possibilities of searches for georeactor fuel composition using $\bar{\nu}_e$ spectroscopy.

1. GEOREACTOR: EXPECTED $\bar{\nu}_e$ RATE AND SPECTRUM

Georeactor antineutrinos are detected in a liquid scintillation spectrometer via the inverse beta-decay reaction

$$\bar{\nu}_e + p \to n + e^+. \quad (1)$$

The visible positron energy E_e is related to the $\bar{\nu}_e$ energy as

$$E_e = E - 1.80 + E_{\text{annihil}} - r_n \approx E - 0.8\ [\text{MeV}], \quad (2)$$

where 1.80 MeV is the threshold of the reaction and r_n is the neutron recoil energy. The signature of a neutrino event is e^+ and 2.2-MeV neutron signals correlated in time and space.

The calculated antineutrino interaction rate for georeactor power $W = 3{-}10$ TW and $N_p = 10^{32}$ target protons $N_{\nu\text{GR}} = (33{-}110)$/yr is found for the no-oscillation case and detection efficiency $\epsilon = 100\%$, the Earth's radius $R_{\text{Earth}} = 6370$ km, and typical PWR parameters:

$$N_{\nu\text{GR}} \approx (33{-}110)/\text{yr with } 10^{32} \text{ protons, } 3{-}10 \text{ TW}, \quad (3)$$
$$\epsilon = 100\% \text{ and no oscillation},$$

which is exactly what has been found in [4]. Had ^{235}U neutrino fission parameters been used, the rate would be ~10% higher.

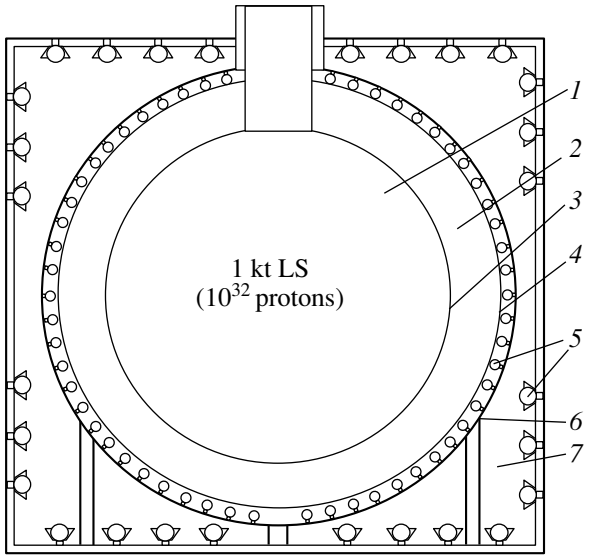

Fig. 2. Detector (schematic): *1*—10^{32} p LS target, *2*—buffer zone (oil), *3*—balloon, *4*—Rn protector, *5*—PMTs, *6*—vessel, *7*—outer water Cherenkov detector.

The positron visible energy spectrum is shown in Fig. 1.

2. DETECTOR DESIGN AND BACKGROUNDS

The sensitivity of low-energy antineutrino detection depends on detector size and level of background. In the past ten years, the sensitivity has been increased, in two steps (CHOOZ, KamLAND), by a factor of ~10^8 and approaches ~1 event per year per ~1000-t LS target.

The main features of future BNO detector design and location can be the following:

(a) Three-concentric zone detector design (Fig. 2). The central ~14-m-diameter zone one is a 10^{32} H atom liquid scintillator target contained in a spherical transparent balloon. Zone two is a buffer of nonscintillation oil contained in a ~19-m-diameter stainless steel vessel; on the inner surface of the vessel are mounted PMTs with ~30% photocathode coverage. A transparent acrylic barrier protects radon emanations from penetrating in the LS of zone one. Zone three is ~22-m-diameter water Cherenkov detector which gives veto signals for cosmic muons and, as passive shielding, protects the inner parts from neutrons and γ rays coming from the surrounding rock.

(b) Deep underground position of the detector to reduce muon-induced backgrounds. BNO is located at a site with 4800 m w.e. rock overburden, which is much deeper than KamLAND's 2700 m w.e. position.

Antineutrino backgrounds at BAKSAN from power reactors

Country or plant	Number of cores	Thermal power, GW	Distance from BNO, km	Energy flux*, $J/cm^2/yr$	Rate*, 10^{32} $p\ yr^{-1}$
Rostov	1	3	463	2.99	5.34
Kursk	4	12.8	1070	2.38	4.26
Smolensk	3	9.6	1500	0.91	1.6
Balakovo	4	12	1035	2.37	4.27
Tver	2	6	1600	0.5	0.89
Novovoronezh	3	5.75	945	1.37	2.46
Rovno	3	5.75	1550	0.51	0.9
Khmelnitsky	1	3	1395	0.33	0.59
Chernobyl	1	3.2	1278	0.39	0.7
Zaporozhie	6	18	612	10.3	18.33
Yuzhnoukrainskaya	3	9	1035	1.79	3.2
Great Britain	35	38.5	3390	0.71	1.28
France	58	204.8	2940	5.05	9.04
Germany	19	69.5	2550	2.28	4.07
Baltic countries	26	69.7	2355	2.68	4.79
Nearest European countries	25	62.4	2250	2.63	4.7
Armenia	1	1.375	400	1.83	3.28
Bucher**	1	3	1760	0.21	0.37
Pakistan	1	0.375	3130	0.01	0.017
India	10	5.8	4320	0.08	0.14
Total				39.35	70.5

* Average power is assumed to be 0.85 of its maximal value.

** Bucher Power Plant is under construction now.

(c) Highest purification of zone *1* (LS) and zone *2* (oil) (U, Th, and K concentrations as low as 10^{-17} g/g).

Experience accumulated in the KamLAND experiment [5] shows that with conditions (a)–(c), an intrinsic detector background at BNO of less than 1/yr in an LS target with 10^{32} H atoms can be achieved.

The most important condition for successful detection of georeactor antineutrinos is not too high an antineutrino flux coming from power reactors. Using data from [6], the $\bar{\nu}_e$ interaction no-oscillation rate $N_{\nu\mathrm{PWR}}$ is (see table)

$$N_{\nu\mathrm{PWR}} = 70.5/\mathrm{yr\ with}\ 10^{32}\ \mathrm{protons}, \quad (4)$$
$$\epsilon = 100\%\ \mathrm{and\ no\ oscillation}.$$

This rate is ∼10 times smaller than at Kamioka site and two times smaller than at Gran Sasso (for KamLAND and Gran Sasso data see [4]). Using known PWR powers and their distances from BNO, this rate can be calculated with ∼3% systematic uncertainty.

Antineutrino interaction rates (3), (4) are obtained for the no-oscillation case and 100% detection efficiency. With realistic $\epsilon = 80\%$ and LMA oscillation parameters, the detection rates are two times lower. Nevertheless, in ∼2 yr of data taking, a 3-TW georeactor can be conclusively confirmed.

3. ON ANALYSIS OF FUEL COMPOSITION IN GEOREACTOR

Imagine that the georeactor hypothesis is confirmed. The next step could be efforts to obtain direct information on composition of the nuclear fuel, which, no doubt, would be of primary geophysical importance.

The shape of the reactor $\bar{\nu}_e$ energy spectrum depends on contributions of fissile isotopes to the total chain reaction rate. Thus measurement of the $\bar{\nu}_e$ spectrum provides information on the nuclear fuel composition. This idea was first proposed years ago [7] and later was confirmed in experiments at reactors [8].

In water-cooled thermal neutron power reactors with (initial) $^{235}U/^{238}U$ enrichment ∼4%, fast neutron fission of ^{238}U contributes typically 7.5% to the total reactor fission rate. In the fast neutron georeactor, the ^{238}U contribution can be expected to be much higher (no information on this subject is given in [1]). The calculated ratio of reaction (1) positron spectra induced by ^{238}U and ^{235}U fission antineutrinos (Fig. 3) considerably departs from unity. Thus, using shape analysis and with larger statistics, the contribution of ^{238}U fission can be estimated.

We continue speculations on the georeactor nuclear fuel composition. Suppose that, initially (∼4.5 billion years ago), a large amount of ^{232}Th was present in the georeactor core. Then ^{233}U is formed through neutron capture and two beta decays: $^{232}\mathrm{Th}(n,\gamma) \rightarrow {}^{233}\mathrm{Th}(\beta) \rightarrow {}^{233}\mathrm{Pa}(\beta) \rightarrow {}^{233}\mathrm{U}$. ^{233}U with its large fission cross section would contribute greatly to the total georeactor fission rate.

We have calculated the ^{233}U fission $\bar{\nu}_e$ energy spectrum (V. Kopeikin *et al.*, to be published) and

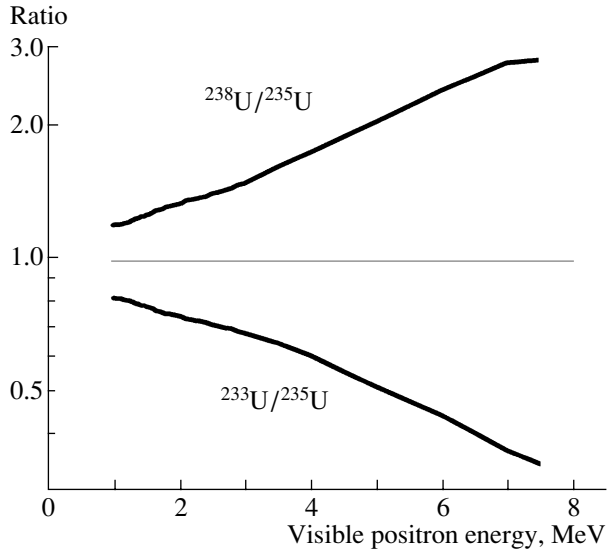

Fig. 3. Ratios of ^{238}U/^{235}U and ^{233}U/^{235}U antineutrino-induced positron spectra.

found that it is much softer than the ^{235}U fission $\bar{\nu}_e$ energy spectrum (Fig. 3). Thus, if the contribution of ^{233}U fission is sufficiently large, this can be found in experiments considered here. We note also that, if ^{233}U and ^{238}U contribute equally to georeactor fission power, the resulting positron spectrum can look very much like that of ^{235}U.

CONCLUSIONS

The hypothesis of a 3-TW georeactor burning inside the Earth can be conclusively tested at Baksan with a few years of data taking using an ~1000-t target liquid scintillation detector. With longer time/larger LS mass, a search for the dominant nuclear fuel components can be done. The same spectrometer can detect $\bar{\nu}_e$ coming from terrestrial ^{238}U and ^{232}Th decays; the latter problem will be considered in the next publication. We mention also that here searches for the astrophysical antineutrino flux can be done.

ACKNOWLEDGMENTS

We are grateful to Prof. O.G. Ryazhskaya, Prof. J.M. Herndon, and Prof. Yu. Kamyshkov for fruitful discussions. This study is supported by the Russian Foundation for Basic Research, project no. 03-02-16055, and Russian Federation President's grant no. 1246.2003.2.

REFERENCES

1. J. M. Herndon, Proc. Natl. Acad. Sci. USA **100**, 3047 (2003); D. F. Hollenbach and J. M. Herndon, Proc. Natl. Acad. Sci. USA **98**, 11085 (2001); J. M. Herndon, J. Geomagn. Geoelectr. **45**, 423 (1993).
2. P. K. Kuroda, J. Chem. Phys. **25**, 781 (1956).
3. M. Neuilly *et al.*, C. R. Acad. Ser. D **275**, 1847 (1972).
4. R. S. Raghavan, hep-ex/0208038.
5. KamLAND Collab., Phys. Rev. Lett. **90**, 021802 (2003).
6. http://www.insc.anl.gov/
7. L. A. Mikaelyan, in *Proceedings of International Conference NEUTRINO'77, Baksan, 1977* (Nauka, Moscow, 1978), Vol. 2, p. 383.
8. Yu. V. Klimov *et al.*, At. Énerg. **76**, 123 (1994); V. I. Kopeikin, L. A. Mikaelyan, and V. V. Sinev, Yad. Fiz. **60**, 230 (1997) [Phys. At. Nucl. **60**, 172 (1997)].

Physics of Atomic Nuclei, Vol. 68, No. 1, 2005, pp. 73–87. Translated from Yadernaya Fizika, Vol. 68, No. 1, 2005, pp. 74–88.

ELEMENTARY PARTICLES AND FIELDS
Experiment

Investigation of the Structure of a Muon Disk for $E_0 \geq 5 \times 10^{16}$ eV according to Data of the Yakutsk Array for Studying Extensive Air Showers

A. V. Glushkov*, L. G. Dedenko[1)], and I. E. Sleptsov

Institute of Cosmophysical Research and Aeronomy, Yakutsk Research Center, Siberian Division, Russian Academy of Sciences, pr. Lenina 31, Yakutsk, 677891 Russia

Received October 29, 2003

Abstract—The results are presented that were obtained at the Yakutsk array by investigating the time structure of a muon disk in extensive air showers of primary energy in the region $E_0 \geq 5 \times 10^{16}$ eV at distances of 250 to 1500 m from the shower core. The measurements were performed with a large muon detector that has an area of 184 m^2 and a detection threshold of $E_\mu \approx 0.5\sec\theta$ GeV and which began operating in November 1995. Two components having different muon-disk thicknesses were discovered, and this requires strong modifications in the currently prevalent idea of the development of extensive air showers. The problem of the existence of $E_0 \geq 10^{20}$ eV events is considered. © *2005 Pleiades Publishing, Inc.*

1. INTRODUCTION

Muons of energy in the range between about 0.5 and 1.0 GeV are an important component of extensive air showers generated by cosmic rays of ultrahigh energy ($E_0 \geq 10^{15}$ GeV). They are weakly absorbed in the atmosphere and are sensitive to the properties of nuclear interactions in the process of the development of extensive air showers and to the chemical composition of primary cosmic rays.

There exists the opinion that the composition of primary cosmic radiation is significantly enriched in heavy nuclei at energies in the range $3 \times 10^{15} < E_0 \leq 10^{17}$ eV (see, for example, [1, 2]), but that, at energies in the range $10^{17} < E_0 \leq 10^{18}$ eV, it again changes fast, approaching a proton-dominated composition [3]. The heaviest composition corresponds to $E_0 \approx 10^{17}$ eV. These results can be explained within the diffusion model [4].

Muons of energy in the region $E_\mu \geq 1.0$ GeV have been unceasingly investigated at the Yakutsk array since 1974. In [5–8], it was shown that the development of showers at $E_0 \geq (3–5) \times 10^{18}$ eV is different from their development in the region of lower energies. In the opinion of the authors of [9–19], this may be associated with new primary-cosmic-ray particles of an extragalactic origin.

In November 1995, a large muon detector that has a detection threshold of $E_\mu \approx 0.5 \sec\theta$ GeV began operating at the Yakutsk array. A preliminary analysis of the results obtained with the large muon detector revealed that it has a high additional potential for studying the development of extensive air showers [20, 21]. Below, we present some results obtained by studying the time structure of a muon disk. We also compare the results of the measurements with their counterparts calculated on the basis of the model of quark–gluon strings (QGS) [22].

2. LARGE MUON DETECTOR

The large muon detector consists of 92 scintillation counters of area 2 m^2 that are similar to those in the Yakutsk array stations deployed on the Earth's surface. They are arranged in six rows in an underground hall having dimensions of 26×12 m^2 and occurring at a distance of 180 m from the center of the array. The main part of the electronics used was manufactured in the CAMAC standard and was positioned within the same hall, while the controlling computer IBM PC 486 was in the laboratory house. The computer ensures the monitoring of the operation of this electronic equipment and performs the calibration of the detectors and the recording and storage of information. The exchange of information between the computer and the electronics in the underground hall is implemented by means of two drivers connected in series that involve six communication lines each.

The electronic equipment was developed in such a way that the height of a pulse and the time of its arrival

[1)]Institute of Nuclear Physics, Moscow State University, Vorob'evy gory, Moscow, 119899 Russia.
*e-mail: a.v.glushkov@ikfia.ysn.ru

in a shower is measured independently of the actuation of other detectors. An amplitude-time-channel block mounted on each scintillation counter was created for such measurements. This block consists of the amplitude channel for measuring the number of muons and the time channel for measuring the time of the arrival of the first particle. All amplitude–time channels are concentrated in 11 crates, and signals to the input of each amplitude–time signal are transferred from a photomultiplier tube through a PK-75 cable of length 20 to 70 m.

An amplitude channel, which has a dynamical range of about 10^3, operates with a follower threshold (of 1 mV to 2 V) in the mode of background loading, whose intensity ranges between 100 and 1000 events per second. An analogous signal at the amplitude-channel input is preliminarily delayed for about 100 ns (this corresponds to 20 m of the PK-75 cable) in order that the respective time channel have time to generate, at the controlling amplitude-channel input, a rectangular pulse of duration 2 μs for integrating the charge q from the photomultiplier tube. After 2 μs, the linear transformation $q \to T$ and the recording of this duration in the memory by a 10-MHz clock generator begins. In the memory of an amplitude–time channel, pulse-height information is stored up to the arrival of the successive pulse or up to the completion of the interrogation of the large muon detector by the central recorder (see below).

The time channel belonging to an amplitude–time channel and consisting of two synchronized channels is used to perform an accurate measurement of the time interval between the instant of counter actuation ("start") and a signal from the receiver of synchropulses of the master array for studying extensive air showers ("stop"). The "start" signal triggers the precise time channel measuring the interval up to the beginning of the successive cycle of the 10-MHz reference generator common to all amplitude–time channels. In turn, the "stop" of the precise time channel serves as the start of the rough time channel counting the number of cycles of the reference generator before the generation of the main "stop" signal for the large muon detector by the receiver of a synchropulse of the array. The "stop" signal for the large muon detector is synchronized with the beginning of a successive 10-MHz cycle, and this guarantees that the rough time channels of all counters actuated in a shower are stopped simultaneously. In a precise time channel, a short time interval (from 0 to 100 ns) is extended by a factor of about 100 by means of a "time–time" transformer, and the same 10-MHz clock generator is used to obtain a digital code. This scheme makes it possible to measure the whole interval up to the internal "stop" signal for the large muon detector to a precision of about 5 ns and to have a relative precision of about 5 ns between different counters arranged in the underground hall.

A signal is fed to a time channel after a preliminary amplification and a high-frequency pulse-edge correction for a discriminator that has a follower threshold; being actuated at a specific phase of the leading edge of a pulse, this discriminator renders the actuation of a time channel independent of the height of an input pulse. The synchropulses of the array are fed by a transmitter with a frequency of 10 kHz.

The total time of actuation of the time channel of an individual counter is determined as the sum of the readings of the rough and precise time channels with allowance for the delay of signal propagation along the cable from the photomultiplier tube to the amplitude-time channel and an additional instrumental delay.

As soon as the processing of a signal that has arrived begins, the amplitude–time channels are blocked from repeated actuations up to the completion of processing in each channel (this time can range between 5 and 250 μs). If, within 100 μs since the arrival of a signal, the Yakutsk array selects an extensive air shower or a local actuation of the large muon detector occurs, then the actuated amplitude–time channels are blocked to save information and to transfer data to the controlling computer.

Information about the last selected event is always stored in the memory of amplitude–time channels. Only after the arrival of a new event (if the unit is not blocked by a special command) is the memory cleared. Amplitude–time channels involve a special trigger for recalling counters that were actuated in a given shower. This trigger is set in a special position in the presence of a signal at the input of amplitude–time channels at the instant of shower selection with a resolution time of 100 μs (bit of involvement) and is then interrogated in reading off information.

The block of master selection serves for synchronizing the operation of all amplitude–time channels, obtaining the master of the main array for studying extensive air showers, selecting local events, and developing an interruption signal for the computer used. A signal associated with a shower that is recorded by the main array for studying extensive air showers is transferred from the central recorder to the block of master selection along a special cable, and the block of master selection develops interruption for the computer operating with the large muon detector and transmits pulses to all amplitude–time channels for generating a bit of involvement. Such an event is always recorded irrespective of whether the counters of the large muon detector were actuated.

Moreover, the block of master selection itself selects local showers of energy $E_0 \sim 10^{15}$ eV if several

counters are actuated simultaneously within 2 μs. The number and the arrangement of counters are determined by the tuning of summing schemes in each crate and in the block of master selection itself. The permission or prohibition of a given type of selection can be implemented in a computer-controlled way. Also, a controlling code can imitate an artificial shower upon operator's command. This code is used to test the equipment involved and the coupling between the computer and remote electronics.

The block of master selection has a memory that can contain 32 16-digit words. This memory is used to save permanently the times of arrival of individual events. A special 10-digit counter (clock) counts the number of cycles of the 10-MHz generator from a successive pulse of synchronization of the array. At the instant of arrival of such a signal, the readings of this counter are annihilated. As soon as the signal of an allowed event arrives, data of this counter are recorded in the successive cell of the memory of the block of master selection. One employs ten digits to record times and the remaining six digits to indicate a feature of an event. Such events include (i) instants of arrival of a synchropulse of the array, in which case the recording in the memory occurs before clearing the time counter (feature 0); (ii) actuation of any detector in each row of 14 to 16 counters, in which case the feature is determined by the number of a row and is indicated in the first to the sixth digit; and (iii) the instant of the completion of a pulse formed in a large muon detector in shower events for developing a bit of involvement in amplitude–time channels, in which case a further recording is blocked up to interrogation and a subsequent unblocking by the controlling code (feature 0). This scheme makes it possible to obtain a time development of events over several periods of 100 μs up to the selection of a shower and to monitor the operation of the time channels of individual amplitude–time channels.

An individual computer is used to record and accumulate data from the large muon detector. In showers, the block of master selection produces an interruption signal according to which an event is recorded in a file on the hard disk of the computer. Each recording of this file refers to one shower and has a structure that makes it possible to store information from all counters of the large muon detector. In order to identify and combine straightforwardly data from the large muon detector and from the main array in common showers, both recorders save the time of an event according to unified clocks of world time (UT). For this, an input register to which a code from an external UT clock is transferred is arranged in a special crate connected to one of the lines of a series driver; concurrently, the same code is advanced to the input register of the main recorder of the Yakutsk array.

In between the showers, the recording code of the large muon detector accumulates testing and calibration information. With the aid of this code, the background and the amplitude spectra from all counters are measured continuously, and these spectra are recorded in individual files on the hard disk and are used for the pulse-height calibration of the counters.

3. PROPERTIES UNDER STUDY

For zenith angles satisfying the condition $\cos\theta \geq 0.7$, we have investigated the time structure of a muon disk in extensive air showers of energy in the region $E_0 \geq 5 \times 10^{16}$ eV . By way of example, the distribution of delays of the arrival of muons (T) for a threshold energy of $E_\mu \approx 0.5 \sec\theta$ GeV with respect to a plane front (plane orthogonal to the extensive-air-shower axis at the point of its intersection with the array plane) is shown by curve *1* in Fig. 1 according to calculations on the basis of the QGS model for primary photons of energy $E_0 = 10^{18}$ eV for $\cos\theta \geq 0.9$ at the distance of $R = 630$ m from the shower core. The mean density of muons at this distance is $\rho_\mu(630) = 0.35$ m^{-2}, whereas the mean delay time is $\langle T\rangle = 156$ ns, the respective standard deviation being $\sigma_T = 114.2$ ns. The FWHM value of this pulse is $T_{1/2} = 107$ ns, while its width at a relative height of 0.01 from the base is 475 ns. This is the time of full integration (99%) of all muons in a specific event.

Curve *2* represents the distribution obtained by integrating curve *1*. As a matter of fact, it reflects the pulse shape that would be developed by an oscilloscope at the output of an ideal detector. The width of this distribution at a level of 10 to 50% is $T15 = 62$ ns. This quantity is often measured in experiments and is used to characterize the thickness of the disk in an extensive air shower.

Of practical interest in measuring particle densities are not the values of T but the relative delay times

$$t_i = T_i - T_1 \qquad (1)$$

(where T_1 is the time of arrival of the fastest muon among n actuated counters of the large muon collider in each individual shower and T_i is the time of arrival of the first muon to the ith counter), since the latter reflect the real time necessary for collecting the preset fraction of all particles at the chosen distance from the shower core.

The distribution of the delays defined by (1) has an exponential form,

$$P(t) \approx \exp(-t/\lambda). \qquad (2)$$

One can state with confidence that it depends unambiguously on the mean density of recorded muons,

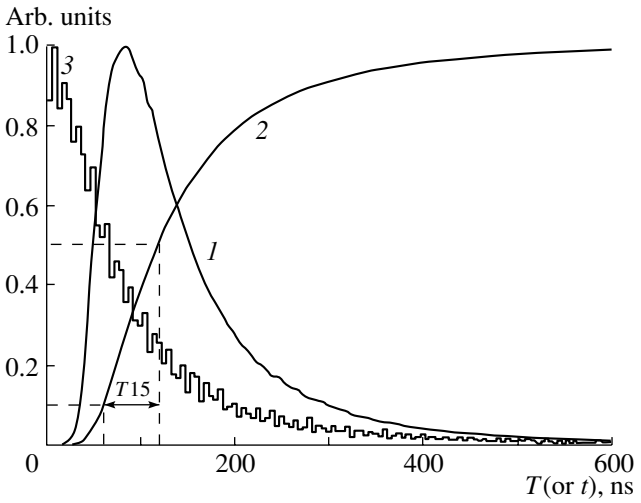

Fig. 1. Distribution of delays of the arrival of muons for the threshold energy of $E_\mu \approx 0.5 \sec\theta$ GeV at the observation level of $X = 1020 \sec\theta$ g cm^{-2} at the distance of $R = 630$ m from the shower core according to calculations on the basis of the QGS model for primary protons of energy $E_0 = 10^{18}$ eV for zenith angles satisfying the condition $\cos\theta \geq 0.9$: (*1*) delays with respect to a plane front and (*3*) delays with respect to the first muon for densities of $\rho_\mu \leq 0.35$ m^{-2} in the case of the actuation of two counters (2 m^2 in area) in each of 5000 showers; $T15$ is the rise time for curve *2* (which was obtained by integrating curve *1*) at a level of 10 to 50%.

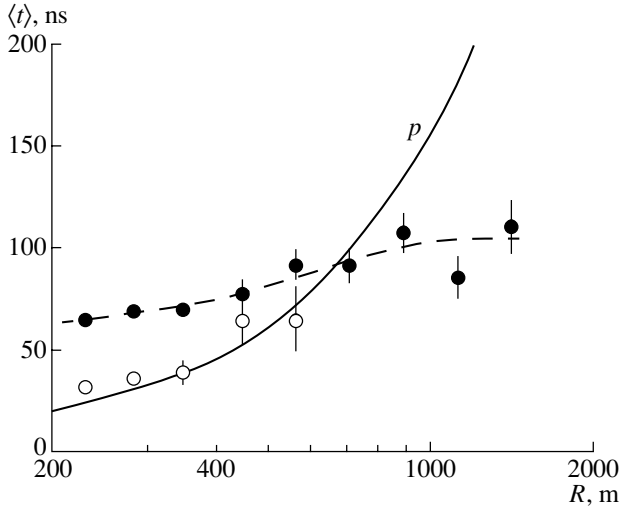

Fig. 2. Delays $\langle t\rangle$ with respect to the fastest muons at various distances from the shower core in each shower for showers characterized by $\langle E_0\rangle \approx 3 \times 10^{17}$ eV and $\langle\cos\theta\rangle \approx 0.95$: (closed circles) $\langle\rho_\mu\rangle \approx 0.45$ m^{-2}, (open circles) $\rho_\mu \geq 2.5$ m^{-2}, (dashed curve) behavior on average, and (solid curve) results of the calculation on the basis of the QGS model for primary protons.

$\langle\rho_\mu(R)\rangle$—more precisely, on the number m of muons that traversed the area S (in our case, $S = 2$ m^2), which, at the mean value of $\langle m\rangle = \langle\rho_\mu(R)\rangle S$, obey the Poisson distribution

$$P_m(\langle m\rangle) = \langle m\rangle^m/m!\exp(-\langle m\rangle). \quad (3)$$

Histogram *3* in Fig. 1 represents the distribution of delays (1) that was obtained with the aid of the Monte Carlo method by rescaling curve *1* for $\langle m\rangle = 0.7$ in the case of the actuation of two counters. The delay corresponding to this histogram is $\langle t\rangle = 99$ ns, whereas the respective standard deviation is $\sigma_t = 115.8$ ns. The quantities $\langle t\rangle$ and $T15$ are related by the equation

$$\langle t\rangle \approx 1.6T15, \quad (4)$$

which may prove to be of use in estimating the time of integration of signals at the input of pulse-height transformers in measuring the number of particles at various distances from the extensive-air-shower core.

An analysis has revealed that, in our case, the distributions of delays for $\rho_\mu \leq 1$ m^{-2} have the exponential form (2), where the parameters λ and $\langle t\rangle$ are close to each other. On this basis, one can readily derive a relation for estimating the time T_η that is required for recording the fraction η of all muons. Specifically, we have

$$T_\eta = -\langle t\rangle \ln(1-\eta). \quad (5)$$

From (5) and from the distribution represented by curve *2* in Fig. 1, it follows that the effective thickness of a muon disk (95% of all particles) in showers of energy in the region $E_0 \leq 10^{18}$ eV does not exceed 300 ns for distances R from the shower core not larger than 630 m and that 99.7% of all muons will be recorded within the time $T_\eta = 600$ ns.

4. RESULTS

The data sample subjected to the present analysis includes showers recorded over the period between 1995 and 2002 at the Yakutsk array with the aid of the large muon detector. The primary-particle energy E_0 was determined from the relations

$$E_0 = (4.8 \pm 1.6) \times 10^{17}(\rho_{s,600}(0^\circ))^{1.0\pm0.02}\,[\text{eV}], \quad (6)$$

$$\rho_{s,600}(0^\circ) = \rho_{s,600}(\theta)\exp((\sec\theta - 1) \times 1020/\lambda_\rho)\,[\text{m}^{-2}], \quad (7)$$

$$\lambda_\rho = (450 \pm 44) + (32 \pm 15)\log(\rho_{s,600}(0^\circ))\,[\text{g/cm}^2], \quad (8)$$

where $\rho_{s,600}(\theta)$ is the charged-particle density measured by scintillation detectors at the distance of $R =$

600 m from the shower core that are deployed on the Earth's surface.

Below, we will consider only the mean delay times obtained from the quantities in (1). For showers characterized by energies in the range $10^{17} \le E_0 \le 10^{18}$ eV and zenith angles satisfying the condition $\cos\theta \ge 0.9$, Fig. 2 shows the values of $\langle t\rangle$ at distances from the extensive-air-shower core in the range $R = 250$–1500 m. The closed circles correspond to $\langle t\rangle$ in the case where two counters of the large muon detectors were actuated if $m \le 2$ ($\langle m\rangle \approx 0.9$) muons traversed them. The dashed curve reflects the behavior of $\langle t\rangle$ on average. The solid curve (p) shows $\langle t\rangle$ values expected in this case on the basis of the QGS model for primary protons. The open circles represent $\langle t\rangle$ values obtained by selecting $\rho_\mu \ge 2.5$ m^{-2} events, which correspond to the case where $m \ge 5$ muons traverse the counters.

One can see that the variation represented by the closed circles is more gently sloping than the prediction of the QGS model. The disagreement for $R <$ 500 m stems from taking, in the calculations, muon densities at any values of m (that is, without imposing the constraint $m \le 2$), this leading to a significant decrease in the "looseness" of the muon disk and, hence, to a decrease in $\langle t\rangle$. The above distinction disappears in the case where $m \ge 5$ muons traverse the counters of the large muon detector (open circles). As to disagreement for $R > 800$ m, it eludes all attempts at explanation presently.

In the following, our attention will be given primarily to studying the thickness of the muon disk at distances from the shower core in the range $R \approx$ 500–800 m. This choice was motivated by a few factors. First, data from the large muon collider versus E_0 and θ are the most extensive in this range of distances. Second, the muon density $\rho_{\mu,600}$ measured at a distance of 600 m from the shower core is weakly dependent on the zenith angle for $E_0 \le (3$–$5) \times 10^{18}$ eV [7, 8]; therefore, it is yet another parameter, along with that in (5), convenient for estimating the energy of primary particles. For muons of threshold energy $E_\mu \ge 1.0$ GeV, the respective dependence obtained at the Yakutsk array in vertical showers has the form [8]

$$E_0 = 2.4 \times 10^{18} (\rho_{\mu,600}(0^\circ))^{1.08\pm0.01}\ [\text{eV}]. \qquad (9)$$

Third, model results and experimental data are consistent to some extent at distances from the shower core in the range $R \approx 500$–800 m (see Fig. 2), and this gives sufficient grounds to employ the results of the calculations in interpreting results presented below.

For a standard distance, we have chosen $R =$ 630 m and have rescaled all results to it. In Figs. 3 and 4, the lines represent the delays $\langle t\rangle$ expected at this distance according to the calculation on the basis of the QGS model for primary (p) protons or (Fe) iron nuclei in the case of the actuation of two large-muon-detector counters traversed by $m \le 2$ muons (Figs. 3 and 4 show these results, respectively, versus E_0 for showers characterized by $\cos\theta \ge 0.8$ and versus $\sec\theta$ for showers of energy in the range $10^{17} \le E_0 \le 10^{18}$ eV). For primary particles of atomic weight A, the results of the calculations can be accurately approximated by the dependence

$$\langle t\rangle \approx 104 + 5(\log(E_0/18) - \log(A)) \qquad (10)$$
$$- 140(\sec\theta - 1) + 0.194(R - 630)$$

for $10^{16.7} \le E_0 \le 10^{18.3}$ eV and $\theta \le 45^\circ$ in the range $500 \le R \le 1000$ m of distances from the shower core. The experimental data in question were obtained under the same selection conditions as those used in the calculation. The dashed lines reflect the behavior of experimental data on average. One can see that the measured and calculated values of $\langle t\rangle$ in Fig. 3 are compatible with the hypothesis that the composition of primary cosmic rays is mixed for $E_0 \le 10^{18}$ eV. In the region around $E_0 \approx 10^{17}$ eV, this composition is enriched in iron nuclei to a considerable extent, while, at $E_0 \approx 10^{18}$ eV, it becomes close to a purely protonic composition. At first glance, it seems that this conclusion is in fairly good agreement with the results obtained by many other researchers (see Introduction). However, we would like to attract the attention of the reader to the zenith-angle dependence of the experimental data in Fig. 4, which are in much poorer

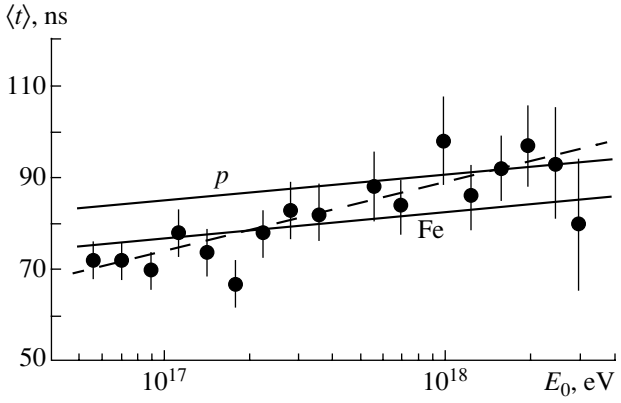

Fig. 3. Mean delay time $\langle t\rangle$ as a function of E_0 at the distance of $R = 630$ m from the shower core for extensive air showers whose zenith angles satisfy the condition $\cos\theta \ge 0.8$: (closed circles) experimental data for $\langle\rho_\mu\rangle \approx 0.45$ m^{-2} in the case of the actuation of two showers of the large muon detector in each shower, (dashed line) behavior of $\langle t\rangle$ on average, and (solid lines) results of the calculation on the basis of the QGS model for primary (p) protons or (Fe) iron nuclei.

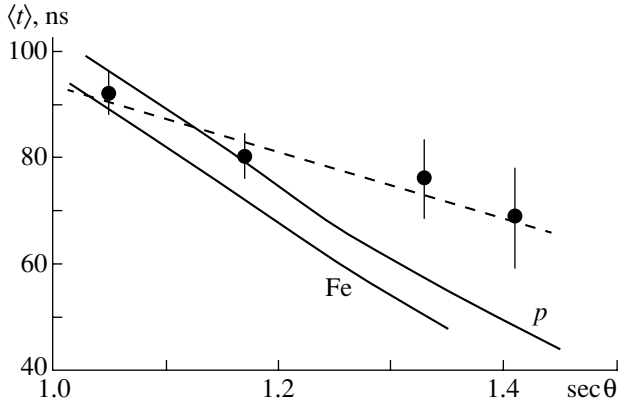

Fig. 4. Mean delay time $\langle t\rangle$ as a function of $\sec\theta$ at a distance of $R = 630$ m from the shower core for extensive air showers characterized by $\langle E_0\rangle \approx 3\times 10^{17}$ eV. The notation here is similar to that in Fig. 3.

agreement with the results of the calculations for inclined extensive air showers ($\theta > 35^\circ$–40°), where the mean thickness of the muon disk proved to be much larger than that predicted by the QGS model.

In order to disentangle this situation and to clarify the reasons behind the aforementioned disagreement between the theory and experiment in Fig. 2, we have studied the measured delay times (1) in greater detail. It turned out that their distribution for $E_0 \leq (3$–$5)\times 10^{17}$ eV differs considerably from the purely exponential distribution in (2). This can clearly be seen from the example in Fig. 5*a*, which, for the case of the actuation of two large-muon-detector counters traversed by $m \leq 2$ muons, shows experimental results for a sample of 477 showers characterized by $10^{16.7} \leq E_0 \leq 10^{17.0}$ eV and $\cos\theta \geq 0.8$. The points there correspond to an integrated distribution that can be represented in the form

$$N(\geq t) = N_1\exp(-t/\lambda_1) + N_2\exp(-t/\lambda_2). \quad (11)$$

The first term in this sum (solid straight line) at $\lambda_1 \approx 105$ ns includes about 50% of all events. It is not due to methodological factors associated with the operation of the large muon detector but reflects the fact that the sample being considered involves part of the showers in which the distribution of muons at the distance of $R = 630$ m from the shower core is broader than that predicted by model calculations. If these events are subtracted from the total distribution, there remains the second term (dashed curve) at $\lambda_2 \approx 52$ ns. For $E_0 > (5$–$7)\times 10^{17}$ eV, the pattern is different—here, the delay times (1) are of a purely exponential form over the entire range where they are measured. One can clearly see this in Fig. 5*b*, which, for the case of the actuation of two large-muon-detector counters traversed by $m \leq 2$ muons, shows experimental results for a sample of 154 showers

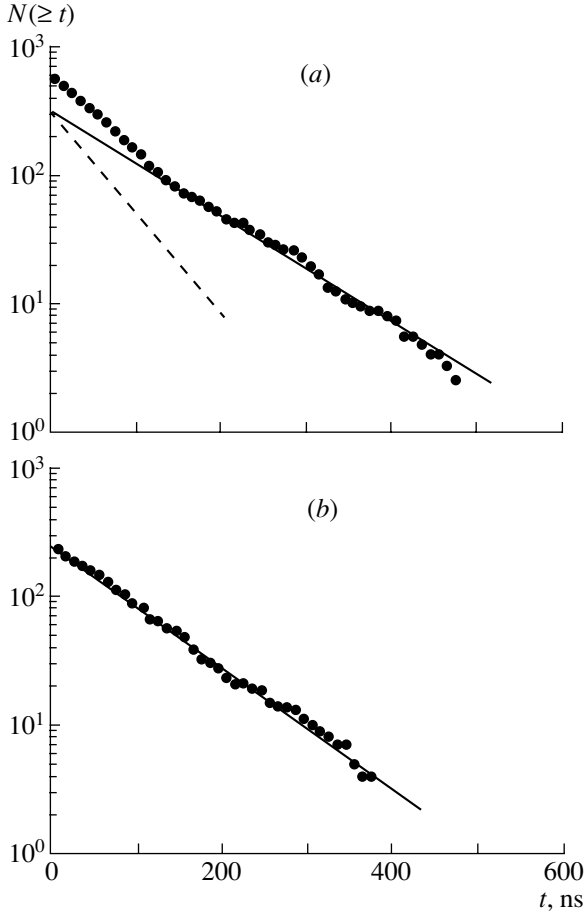

Fig. 5. Integrated distributions of the delay times (1) at the distance of $R = 630$ m from the shower core in $\langle\cos\theta\rangle \approx 0.9$ extensive air showers for the case of the actuation of two counters of the large muon detector at $\langle\rho_\mu\rangle \approx 0.45$ m^{-2} in each shower for the (*a*) $10^{16.7} \leq E_0 \leq 10^{17.0}$ eV and (*b*) $10^{17.9} \leq E_0 \leq 10^{18.2}$ eV samples: (solid straight line) first term in (11) at $\lambda_1 \approx 105$ ns and (dashed straight line) second term in (11) at $\lambda_2 \approx 52$ ns.

characterized by $10^{17.9} \leq E_0 \leq 10^{18.2}$ eV and $\cos\theta \geq 0.8$. The straight line there corresponds to the distribution $N(\geq t) = N_1\exp(-t/105)$.

5. DISCUSSION

Figure 6 displays the variations in the structural parameters of the delay spectrum in (11) versus the energy of an extensive air shower in the intervals $\Delta\log E_0 = 0.3$. For $E_0 \leq (5$–$7)\times 10^{17}$ eV, the delay times as defined in (1) are characterized by a stable two-component distribution that has the form given in (11) and which involves substantially different parameters λ_1 and λ_2 (closed and open circles, respectively). One can see this in Fig. 6*a*, where, for the sake of comparison, we also show the results of our model

calculations and the averaged dependence of experimental data (dashed line) from Fig. 3. In Fig. 6*b*, we give the fraction of either component. All of the results refer to $R \approx 630$ m and showers characterized by $\langle \cos\theta \rangle \approx 0.9$.

Before proceeding to interpret the results, we will consider the gross pattern of the formation of mean delay times $\langle t \rangle$. The calculations reveal that they are determined primarily by muons arriving from altitudes in the vicinity of the maximum of the development of extensive air showers. A decrease in $\langle t \rangle$ with decreasing primary energy E_0 is due to an increase in the distance between the depth of the shower maximum, X_m, and the observation level X (for Yakutsk, $X = 1020 \sec\theta$). One can clearly see this from the illustrative Fig. 7, which shows the relative delay times $t_a < t_b$ because of a deteriorating geometric factor of the collection of muons. At a fixed energy E_0, the growth of the zenith angle leads to an increase in $X - X_m$, with the result that the difference of the delays for muons decreases (see Fig. 4).

Let us now revisit data in Fig. 6 and try to understand their meaning from the physical point of view. Taking into account the above mechanism of the formation of delay times in (1), we can assume that they are associated with different shapes of cascade curves characterized by radically different values of X_m. One of these is peculiar to showers for which the depth of the maximum is much higher in the atmosphere than what is predicted by the QGS model, this being so for any composition of primary particles, from protons to iron nuclei. The fraction of such showers decreases fast in the energy range $E_0 \approx (4\text{–}10) \times 10^{17}$ eV (see Fig. 6*b*).

We can assume that these events are generated by primary particles of some unknown nature. The results obtained by analyzing the arrival directions for cosmic rays of energy in the range $E_0 \approx 10^{16.9}$–$10^{17.2}$ eV are presented in [19]. It was revealed there that a considerable part of such rays (about 50%) have a small-scale cellular structure and, in all probability, stem from neutral particles of an extragalactic origin. It was also shown in [19] that the range of these particles up to the first nuclear interaction is very short ($\Lambda_1 \approx 3.3 \times 10^{-2}$ g cm^{-2}). They are likely to disappear after the first interaction, giving way, in the development of extensive air showers, to a standard cascade of secondary particles; otherwise, showers generated by them would differ strongly from ordinary showers and would be readily identifiable. Because of so short a range—we denote it by Λ_1—these mysterious neutral particles are expected to cause an enhanced development of extensive air showers with a cascade-curve maximum at a higher altitude than in the case of primary protons. Possibly, one of

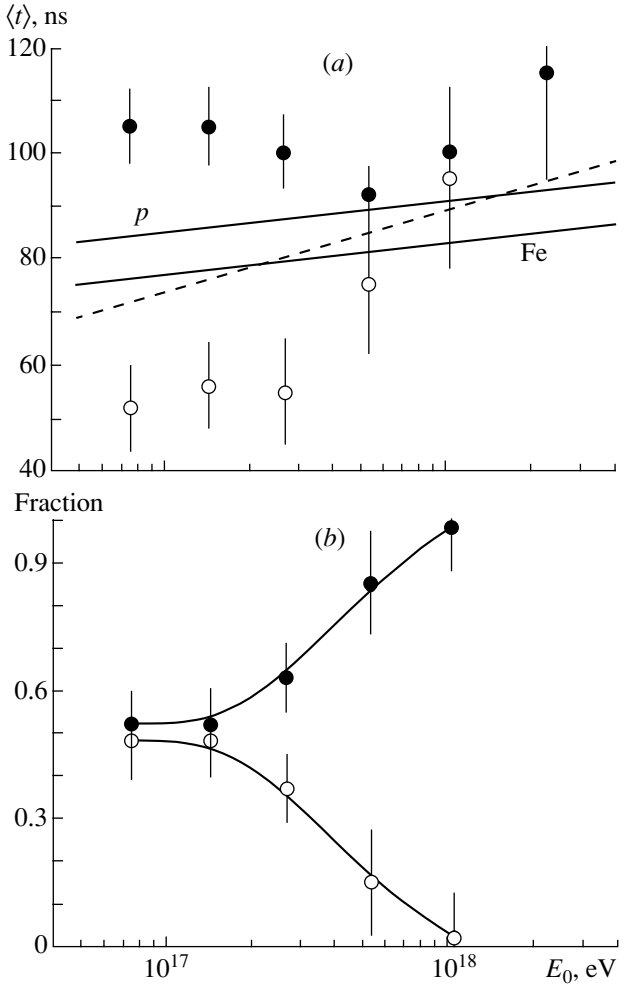

Fig. 6. Variations in (*a*) the structural parameters (closed circles) λ_1 and (open circles) λ_2 of the integrated distribution of delay times in (11) and (*b*) the fraction of these components versus the energy of an extensive air shower (in the intervals $\Delta \log E_0 = 0.3$). The solid and dashed lines represent the data from Fig. 3.

the components represented by open circles in Fig. 6 reflects roughly the contribution of such particles.

Any specific conclusions on the neutral particles in question are still premature. We cannot rule out the possibility that these are neutrinos. The calculations reported in [23] show that, if the growth of the cross section for neutrino–nucleon interaction ($\sigma_{\nu N}$) in the region of ultrahigh energies satisfies some specific conditions, the resulting extensive air showers can be similar in many respects to showers originating from the standard composition of primary cosmic rays. Fargion *et al.* [24] and Weiler [25] considered the hypothesis of ultrahigh-energy neutrinos, which interact with relic neutrinos, producing "Z-boson" showers.

According to [26], neutral pions can also play the role of the presumed neutral particles of primary

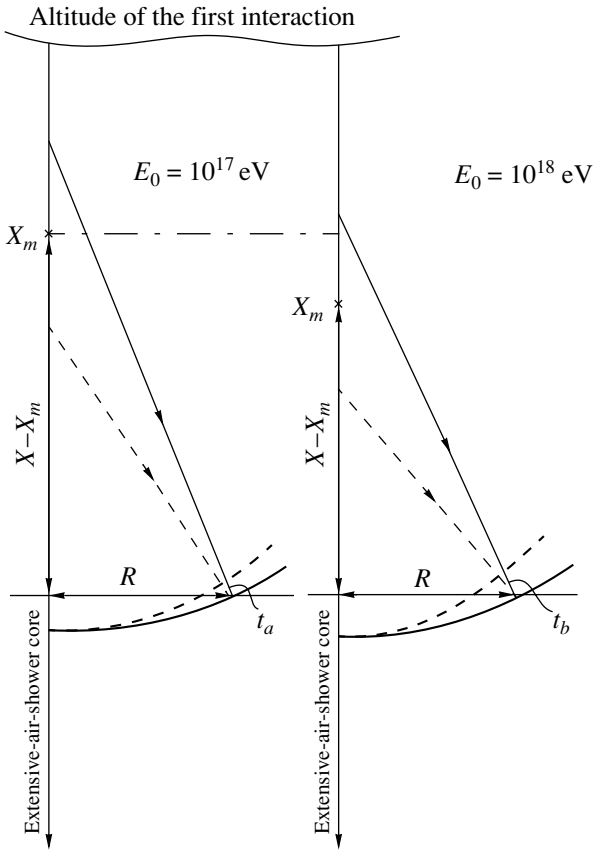

Fig. 7. Scheme of formation of relative delays in extensive air showers of various primary energies.

cosmic rays. In [26], it was shown that stable pions can exist in the composition of ultrahigh-energy cosmic rays. The calculations there were performed on the basis of the QGS model [22] with allowance for the Landau–Pomeranchuk–Migdal effect [27] within the Coleman–Glashow hypothesis of a very weak violation of Lorentz invariance. That the interaction of pions with photons of cosmic microwave background radiation is kinematically forbidden is of particular importance here, since this makes it possible to resolve the Greisen–Zatsepin–Kuz'min paradox [28, 29].

The second group of data in Fig. 6 (closed circles) refers to showers for which the depth of the maximum is likely to be much lower in the atmosphere than what is expected according to the predictions of the QGS model in the case of primary protons; the fraction of these events increases fast in the energy region $E_0 \approx (4–10) \times 10^{17}$ eV (see Fig. 6*b*). The reason behind this disagreement between the theory and experiment is not yet clear. Possibly, it is due to imperfections of the QGS model used here, but we cannot rule out the possibility that these events are associated with "long-range" showers, for which the depth of the maximum "sinks" significantly deep into the atmosphere in relation to what we have for ordinary extensive air showers. Such showers were experimentally observed at the Tien Shan array for $E_0 > 2 \times 10^{16}$ eV [30]. Their appearance is explained by the formation of a sizable fraction of charmed particles during the development of extensive air showers; penetrating deep into matter without interaction, charmed particles thereby shift significantly the maximum of the cascade curve toward the observation level.

In my opinion, the results in Figs. 3 and 6 are quite instructive. On one hand, they are not (in Fig. 3) in a glaring contradiction with the hypothesis of a mixed composition of primary cosmic rays in the energy region being considered, where there occurs a rapid variation from the predominance of iron nuclei at $E_0 \approx 10^{17}$ eV to a purely protonic composition at $E_0 \approx 10^{18}$ eV. On the other hand, the same experimental data subjected to a more thorough analysis lead to the results displayed in Fig. 6, which suggest a totally different pattern of the development of extensive air showers. Here, we cannot rule out the situation where a superposition of two components in Fig. 6 can "mimic" showers generated by a mixed composition of primary cosmic rays. Probably, this could explain the as-yet-unresolved problem of the origin of the first break in the spectrum of cosmic rays for $E_0 \geq 3 \times 10^{15}$ eV (it was discovered more than 40 years ago by a group of researchers from Moscow State University [31])—the point is that, being based on a comparison of various observed features of extensive air showers with their counterparts calculated on the basis of model concepts of the development of extensive air showers with one presumed composition of primary cosmic rays or another, the majority of the methods for determining the composition of primary cosmic rays are indirect.

Many experiments have been performed over the past years, but there is still no unambiguous understanding of this phenomenon. Disclosing its nature would greatly contribute to solving the problem of the origin of cosmic rays having ultrahigh energies up to about 10^{20} eV. In [9–19], it is shown that, for $E_0 > 5 \times 10^{16}$ eV, some part of primary cosmic rays have a small-scale ordered structure associated with the distribution of extragalactic pointlike primary-cosmic-ray sources that, in all probability, generate neutral particles. These results are consistent with our present results—and precisely in what is concerned with the possible existence of neutral particles of extragalactic origin. Massive efforts of theoretical astrophysics that are aimed at investigating the phenomenon in question beyond the traditional ideas of the composition of primary cosmic rays and to

the level of experimentally measured nuclear-physics features of the development of extensive air showers are required here.

6. ON $E_0 \sim 10^{20}$ eV EVENTS

Event the first observations of extensive air showers at large arrays worldwide, like Volcano Ranch (USA) [32], Haverah Park (England) [33], SUGAR (Sydney University Giant Airshower Recorder, Australia) [34] and Yakutsk [35], made it possible to discover giant air showers of energy in the region $E_0 > 10^{19}$ eV. Following the discovery of cosmic microwave background radiation, it was shown that, because of the interaction of primary protons and nuclei with this radiation, their flux for $E_0 > 3 \times 10^{19}$ eV should decrease sharply owing to the Greisen–Zatsepin–Kuz'min cutoff [28, 29]. However, this prediction is at odds with observations of giant air showers at various arrays [36–39], where their energies were estimated at values of up to about $(1–3) \times 10^{20}$ eV. Arrays that are still larger than those mentioned above are being now created in order to investigate the problem of the "upper endpoint" of the energy spectrum of giant air showers. The AGASA (Akeno Giant Air Shower Array) facility of area about 100 km^2 [40] is operative at the present time. Giant arrays of area about 1000 to 5000 km^2, where the detectors to be used are spaced by a distance of 1 to 1.5 km are being designed or are under construction at present [41, 42].

Even at this moment, however, there is a sharp contradiction in the observed changes in the energy spectrum of primary cosmic rays in the vicinity of $E_0 \sim 10^{20}$ eV. On one hand, only one giant air shower of energy $E_0 \approx 1.5 \times 10^{20}$ eV was recorded at the Yakutsk array [37], which has been in use for more than 30 years (exposure of about 825 km^2 yr sr). On the other hand, 11 events characterized by $E_0 > 10^{20}$ eV were recorded at the AGASA array [43], where the exposure is only twice as large (1649 km^2 yr sr) as that in Yakutsk. This fact was used by Watson [44] to criticize the detection methods at the Yakutsk array and estimations of the energy of giant air showers there. We note that, previously, a group of researchers including Watson recorded six giant air showers of energy $E_0 \geq 10^{20}$ eV at the Haverah Park array [36], but that none of such events survived upon revisiting these data and reducing the estimate of energy by about 30% [45]. A recent reanalysis of data from the Fly's Eye and Hires arrays also reduced the number of recorded giant air showers of energy $E_0 \geq 10^{20}$ eV from eight to one [46]. Thus, all arrays worldwide (with the exception of the AGASA) find a sharp cutoff in the spectrum of giant air showers at $E_0 \approx 10^{20}$ eV.

6.1. Measurements at the Yakutsk Array

Let us now dwell on the essence of the criticism in [44]. In the opinion of Watson, the miscounts of the master system of the Yakutsk array in detecting giant air showers of energy in the region $E_0 \geq 10^{20}$ eV was one of the main reasons for underestimating their number. However, this is an erroneous opinion. First, the time of coincidence between two scintillation detectors (of area 2 m^2 each) at all stations was 2 μs and not 1.2 μs, as was reported in [44]. Second, the Yakutsk array has a rather dense network of stations that form equilateral triangles of side length 500 m at the center and 1000 m at the periphery. Since 1995, all stations are within a circle of radius 2 km and form a triangular network, the side length in its cell being 500 m.

Each station, together with any two of its neighbors, is included in the master system selecting showers. In recording giant air showers whose cores fall within the perimeter of the array, not less than two master triangles are actuated in the majority of cases. Therefore, the core of such a shower is always within a distance of 1000 m from three to four stations at the highest densities of particles.

By way of example, the mean lateral distributions of all charged particles and muons for a muon threshold energy of $E_\mu \geq 1$ GeV are shown in Fig. 8 (closed and open circles, respectively) for giant air showers of energy $E_0 = 2 \times 10^{19}$ eV that are characterized by $\langle \cos\theta \rangle = 0.98$, 0.78, or 0.58 [7]. In this figure, curves *1* and *2* represent the approximations

$$f_s(R) = \rho_{s,600}(R/600)^{-1.3}((R + R_M)/(600 + R_M))^{1.3-b_s}((R + 2000)/2600)^{-3.5} \quad (12)$$

with $b_s = 3.19$, 2.67, 2.15 and

$$f_\mu(R) = \rho_{\mu,600}(R/600)^{-0.75}((R + 280)/880)^{0.75-b_\mu}((R + 2000)/2600)^{-8.0}, \quad (13)$$

where the fitted parameter values of $b_\mu = 1.92$, 2.07, and 1.32 correspond to the above three zenith angles and R_M is the Molière radius (for the Yakutsk array, $R_M = 70$ m).

From Fig. 8*a*, one can see that, in giant air showers close to the vertical direction, the densities of charged particles at a distance of $R \approx 1000$ m are about 10 m^{-2}. Accordingly, about 20 particles traverse each detector. The probability that, at this particle density, two detectors of the station will not yield a coincidence signal within 2 μs does not exceed 10^{-6}. In showers of energy $E_0 \approx 10^{20}$ eV, the particle densities at the distance indicated above is five times higher—that is, it is about 50 m^{-2}. This rules out completely a miscount of the master system of the Yakutsk array.

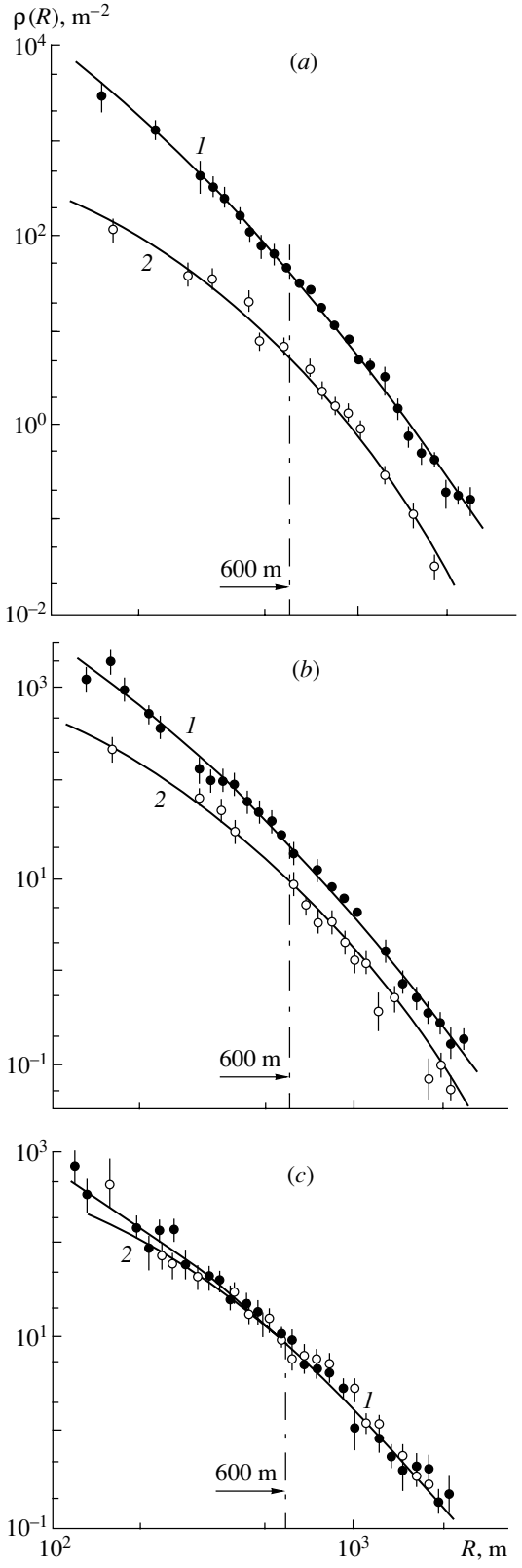

Fig. 8. Lateral distributions of (closed circles) all charged particles and (open circles) muons for a threshold energy of $E_\mu \approx 1.0 \cdot \sec\theta$ GeV in showers of energy $E_0 = 2 \times 10^{19}$ eV for $\langle \cos\theta \rangle =$ (*a*) 0.98, (*b*) 0.78, and (*c*) 0.58. Curves *1* and *2* represent the approximations of the experimental data in the form (12) and (13), respectively.

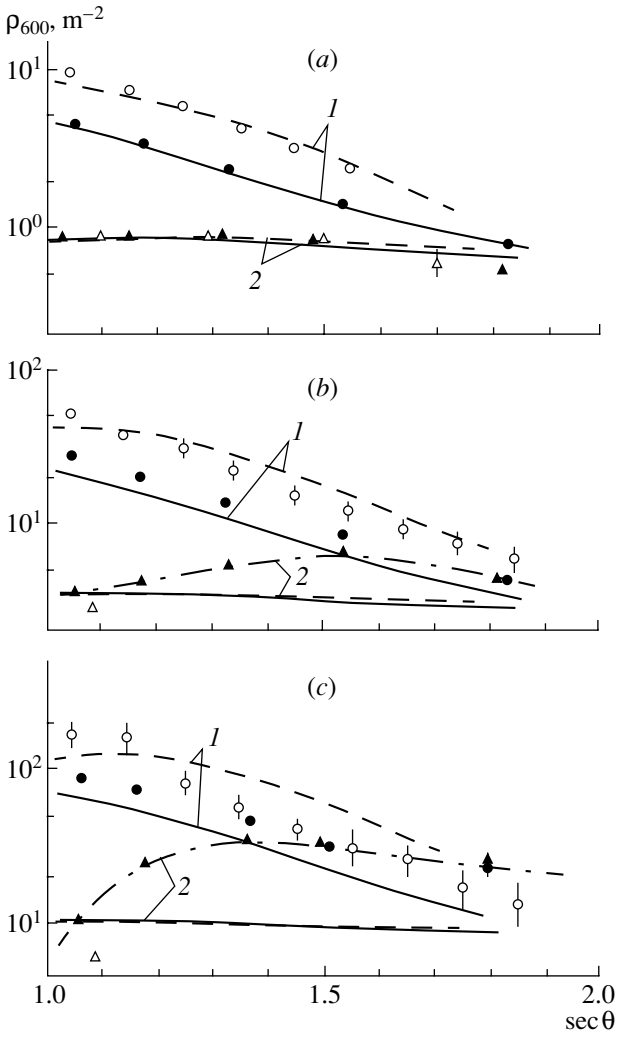

Fig. 9. Densities ρ_{600} of (*1*) all charged particles and (*2*) muons versus $\sec\theta$ at $E_0 =$ (*a*) 2×10^{18}, (*b*) 10^{19}, and (*c*) 3×10^{19} eV according to data from (closed circles and triangles) the Yakutsk array and (open circles [52] and open triangles [53]) AGASA. The solid and dashed curves represent the results of the calculations on the basis of the QGSJET model that were performed for the case of primary protons for, respectively, the Yakutsk array and AGASA.

Watson asserts [44] that an insufficiently long time of integration of signals by pulse-height transformers at the stations is the second reason for underestimating, at the Yakutsk array, the number of giant air showers of energy in the region $E_0 \geq 10^{20}$ eV. In his opinion, this leads to underestimating the quantity $\rho_{s,600}(\theta)$ by about 25% and, accordingly, the energy E_0 by a factor of 1.25 [see relation (6)].

This opinion is also erroneous. The largest giant air shower was recorded at the Yakutsk array at an angle of $\theta = 58.7°$ [37]. It consisted of muons almost completely. The shape of a pulse at a distance of

$R = 930$ m from the shower core was measured at the output of one of the standard scintillation detectors deployed on the Earth's surface. Its FWHM value proved to be $T_{1/2} \approx 200$ ns. This result is consistent with measurements of the pulse shape at the Pierre Auger Observatory array [47], where, in a giant air shower characterized by $E_0 \approx (2–3) \times 10^{19}$ eV and $\theta = 54°$, the signal at half maximum at the output of a water Cherenkov tank had a duration of $T_{1/2} \approx$ 200 ns at a distance of $R = 977$ m from the shower core. The total width of the signal was about 400 ns. Upon going over from inclined to vertical showers, the disk thickness at distances of $R \approx 1000–2000$ m increases, according to AGASA data [48] and according to the results of the calculations reported in [49], by a factor of about 2 owing to the addition of electrons to muons. It follows that, at sea level, the effective disk thickness (95% of all particles) in giant air showers of energy $E_0 \approx 10^{20}$ eV is $T_{0.95} \approx 800$ ns at a distance of $R \approx 1000$ m from the shower core.

We note that the investigations of the time structure of the giant-air-shower disk at the Haverah Park array [50] lead to the same conclusion. This array and that in Yakutsk are situated at approximately the same altitude above sea level. The time $T15 \approx 260$ ns measured experimentally in a giant air shower of energy $E_0 = 6 \times 10^{19}$ eV and zenith angle $\theta = 30°$ at the distance of $R = 1029$ m from the shower core is quoted in [50]. From relations (4) and (5), we obtain $\langle t \rangle \approx 416$ ns at an effective disk thickness of $T_{0.95} \approx$ 1250 ns. From the above data, one can see that the thickness of the shower disk of all particles in a giant air shower of energy in the range $E_0 \approx (2–6) \times 10^{19}$ eV is 0.8–1.2 μs (about 1 μs on average) at a distance of $R \approx 1000$ m from the shower core.

Logarithmic RC transformers (R and C are, respectively, the resistance and the capacitance of the input circuit) characterized by the time constant $\tau = RC \approx 10–12$ μs of integration of the input signal U,

$$U \sim \exp(-t/\tau), \qquad (14)$$

are used at the Yakutsk array to measure pulse heights. Calculations revealed [51] that, if the number of particles hitting the detector is not less than ten, the coefficient of the input-signal transfer is $k = U/U_0 \approx 1 + d/\tau$, where U_0 is the height of an undistorted pulse and d is the half-width of the shower disk. In our case, $d \approx 0.5$ μs, so that $k \leq 1.05$. Therefore, the density of charged particles can hardly be underestimated at distances in the region $R \leq 1000$ m—the more so in measuring $\rho_{s,600}$.

6.2. Measurements at AGASA

Thus, we can state with confidence that virtually no giant air showers of energy in the region $E_0 \geq 10^{20}$ eV have been recorded at the Yakutsk array and at other arrays worldwide In this connection, we will critically reconsider the method used at AGASA to determine the energies of giant air showers. Previously, we repeatedly indicated that, in the energy range $E_0 \geq (3–5) \times 10^{18}$ eV, the development of showers differs from their development at lower energies [5–8]; this especially concerns giant air showers of extremely high energy—their lateral structure changes significantly.

In order to obtain deeper insight into the essence of the problem, we will perform a comparative analysis of lateral distributions measured at the Yakutsk array and at AGASA. We will first consider the zenith-angle dependences of the parameters $\rho_{s,600}(\theta)$ and $\rho_{\mu,600}(\theta)$, which are used at both arrays to estimate the energy E_0. In Fig. 9, these dependences are shown for $E_0 =$ (*a*) 2×10^{18}, (*b*) 10^{19}, and (*c*) 3×10^{19} events by closed and open symbols for all charged particles and muons, respectively. The curves there represent theoretical lateral distributions referring to both arrays for (*1*) all charged particles and (*2*) muons. The calculations were performed on the basis of the QGSJET model for primary protons [8]. The data from the Yakutsk array and all calculated values were obtained from the averaged lateral distributions. At AGASA, the experimental values of $\rho_{s,600}(\theta)$ were deduced by the method of intensity isolines [52], while the $\rho_{\mu,600}(\theta)$ values for muons there were obtained with the threshold of $E_\mu \approx 1.0 \cdot \sec\theta$ GeV [53]. One can see that, at $E_0 = 2 \times 10^{18}$ eV (see Fig. 9*a*), all experimental data agree with the results of the calculations. There is no such agreement for giant air showers. At $E_0 = 10^{19}$ eV, the energies determined according to data from the Yakutsk array are greater than their calculated counterparts by a factor of about 1.25 (see Fig. 9*b*). The values of $\rho_{\mu,600}(\theta)$ undergo more pronounced changes (dash-dotted curve); for inclined showers ($\theta \geq 52°$), they coincide with $\rho_{s,600}(\theta)$. On the contrary, there is a trend in the AGASA data toward underestimating the experimental values of $\rho_{s,600}(\theta)$ by a factor of about 1.25 in the zenith-angle range 35°–50°.

The above anomaly in the development of giant air showers is fast enhanced with increasing energy of primary cosmic radiation. One can clearly see this in Fig. 9*c* for showers of energy $E_0 = 3 \times 10^{19}$ eV, in which case all experimental data are in a glaring contradiction with the predictions of the QGSJET model. This contradiction is not due to relatively low statistics of events. A trend toward a change in $\rho_{\mu,600}(\theta)$ in the data from the Yakutsk array (dash-dotted curve) becomes ever more pronounced, reaching a nearly threefold enhancement in relation to the results of the calculations for $\theta \geq 35°$. The experimental values of

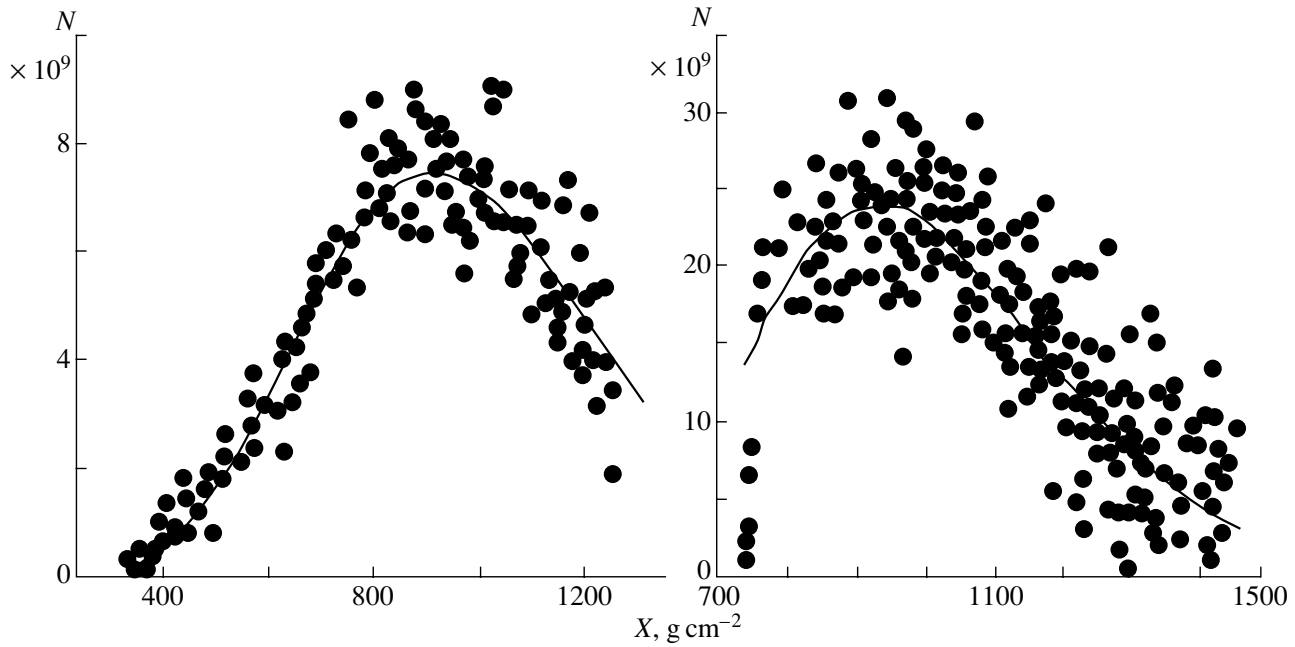

Fig. 10. Cascade curves of giant air showers of energy $E_0 = (a)\ 1.3 \times 10^{19}$ and $(b)\ 3.3 \times 10^{19}$ eV according to data from the Pierre Auger Observatory array [54].

$\rho_{s,600}(\theta)$ in giant air showers whose arrival directions are close to the vertical direction are greater than their calculated counterparts by a factor of about 1.4 and coincide with $\rho_{\mu,600}(\theta)$ for $\theta \geq 45°$. The $\rho_{s,600}(\theta)$ values measured by AGASA for $\theta \leq 30°$ are also larger than the calculated values by a factor of about 1.4 and decrease fast in more inclined showers: they are less than the results of the calculations for $\theta \geq 37°$ by a factor of about 1.4 and become commensurate with the data from the Yakutsk array for $\theta \geq 45°$.

It follows that, in these showers, only muons of energy in the region $E_\mu \geq 1.5$ GeV are recorded at the above distance from the shower core for $\theta \geq 45°$. There are no "softer" muons here and the more so electrons. In all probability, the above trend will be still more enhanced as soon as the energy of giant air showers approaches the limiting value. The disregard of this circumstance may lead to large errors in estimating E_0.

We will now pay special attention to some important details in Fig. 9*c*. For $\sec\theta \leq 1.2$, the $\rho_{s,600}(\theta)$ values measured at the two arrays in question proved to be greater than their theoretical counterparts by a factor of about 1.5, while the $\rho_{\mu,600}(\theta)$ values according to the AGASA data are 1.7 times less than the theoretical values. From the point of view of the longitudinal development of giant air showers, this may imply an anomalously deep position of the cascade-curve maximum. This assumption is confirmed experimentally by the data in Fig. 10 from the Pierre Auger Observatory array [54] for giant air showers of energy $E_0 = (a)\ 1.3 \times 10^{19}$ and $(b)\ 3.3 \times 10^{19}$ eV. One can see that the measured value of $X_m \approx 950$ g cm^{-2} is indeed larger by $\Delta X_m \approx 160$ g cm^{-2} than a value ($X_m \approx 790$ g cm^{-2}) that is expected on the basis of the QGSJET model for primary protons. This situation may prove to be dramatic for AGASA, which is situated at an altitude of 920 g cm^{-2}, since the depth of the maximum of the development of giant air showers at $E_0 \approx 10^{20}$ eV lies directly in the array plane (or below it). Here, calculations other than those used previously in the region of lower energies of extensive air showers are required for interpreting experimental data.

We would like to note yet another interesting feature of the data in Fig. 9*c*. One can see that, albeit lying higher than theoretical results, all experimental densities $\rho_{s,600}(\theta)$ measured at the Yakutsk array (closed circles) are parallel to them. As to the AGASA data (open circles), they behave differently—in particular, these data intersect the dashed theoretical curve *1*, an increase in $\rho_{s,600}(\theta)$ in giant air showers whose arrival directions are close to the vertical direction (that is, for $\sec\theta \leq 1.2$) in relation to inclined showers with respect to the results of the calculations being about 2.5. The data in Fig. 9*a* do not exhibit this feature. We assume that there can be a methodological experimental error here. Within the intensity-isoline method, which was used at AGASA to obtain the aforementioned data, this probably oc-

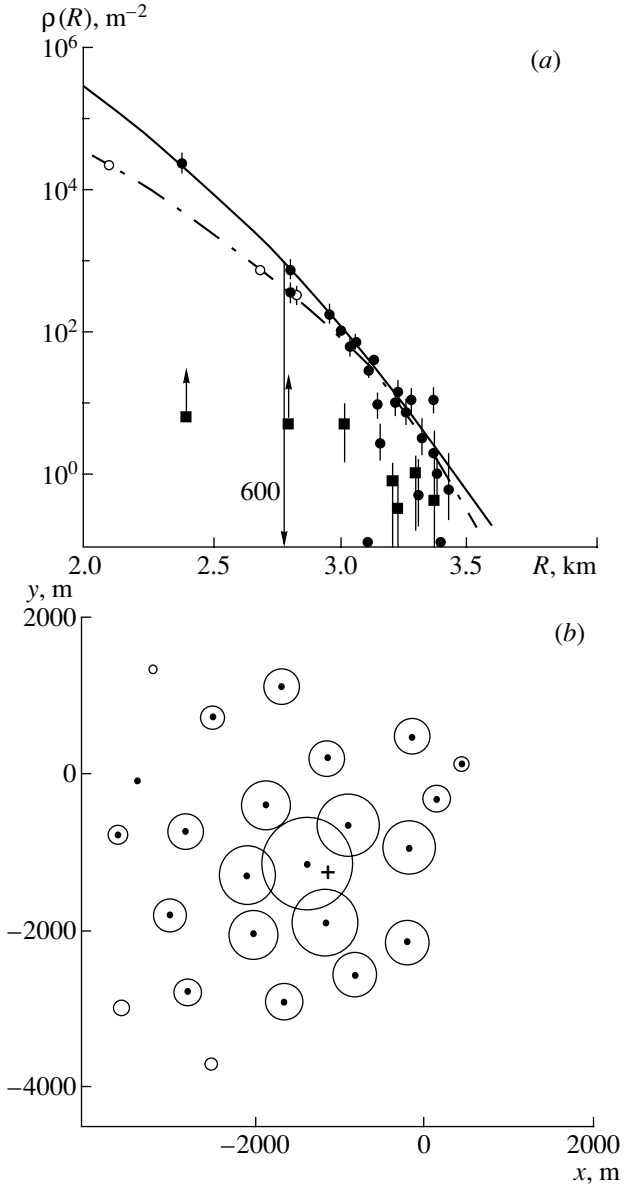

Fig. 11. One of the largest showers recorded by AGASA and characterized by $E_0 \approx (1.7–2.6) \times 10^{20}$ eV and $\theta \approx 23^\circ$ [55]: (a) lateral distribution of (closed circles) all charged particles and (closed boxes) muons for a threshold of $E_\mu \approx 1.0 \cdot \sec\theta$ GeV in the latter case, along with the approximations according to (15) and our supposition (solid and dash-dotted curve, respectively); (b) chart of the densities in the array plane (the radii of the circles are proportional to the logarithm of the density in each detector, and the symbol + indicates the position of the shower core according to [55]).

curred because of an uncontrolled growth of $\rho_{s,600}(\theta)$ upon going over from inclined to vertical events.

We will show how this could happen by considering the example of one of the largest showers recorded by AGASA. In Fig. 11a, the closed symbols represent the lateral distribution of all charged particles in

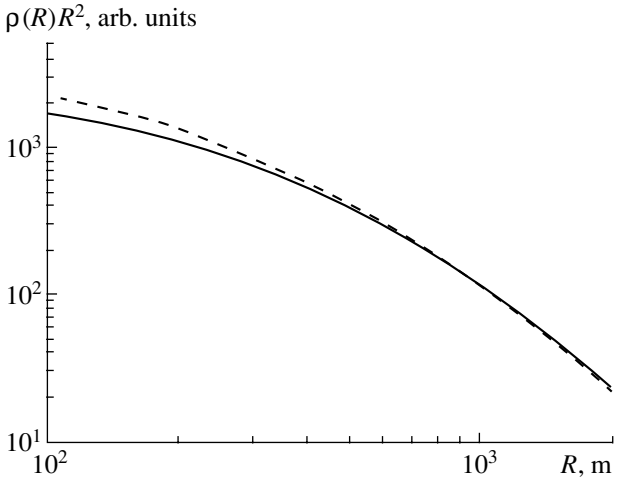

Fig. 12. Lateral distribution of all charged particles in a giant air shower of energy $E_0 = 2 \times 10^{19}$ eV at a depth of $X = 1040$ g cm^{-2} in the atmosphere: (solid curve) approximation in the form (12) with $b_s = 3.19$, $\cos\theta = 0.98$, and $R_M = 91.6$ m and (dashed curve) approximation in the form (15) with $\eta = 3.74$ ($\sec\theta = 1.13$).

giant air showers characterized by $E_0 \approx (1.7–2.6) \times 10^{20}$ eV and $\theta \approx 23^\circ$ [55]. The solid curve corresponds to the approximation

$$\rho_s(R) \sim (R/R_M)^{-1.2}(1 + R/R_M)^{1.2-\eta}(1 + (R/1000)^2)^{-0.6} \quad (15)$$

with $R_M = 91.6$ m and with the parameter value

$$\eta = 3.97 - 1.79(\sec\theta - 1). \quad (16)$$

This approximation was used to find the shower-core coordinates (cross in Fig. 11b). The closed boxes indicate the densities of muons for a threshold of $E_\mu \approx 1.0 \cdot \sec\theta$ GeV. The arrows indicate the saturation of the detectors. The depth of the atmosphere for this event is $X = 920 \sec\theta \approx 1000$ g cm^{-2}.

We will now address the question of what will occur if one treats the data with the aid of another, more "humped" lateral distribution (dash-dotted curve in Fig. 11a). As a result, the giant-air-shower axis will approach significantly the detectors with the highest particle densities: the first detector with the maximum particle density (23 682) will become closer to the new axis by about 120 m (left open circle), the second detector (687 particles) will approach it by about 100 m, and the third detector (357 particles) will move away by about 30 m; this shift of the axis coordinates has virtually no effect on the remaining points in Fig. 11a. This leads to a decrease in the value of $\rho_{s,600}(\theta) = 892$ m^{-2}, which was found at AGASA, by a factor of 2.5. Accordingly, E_0 will decrease in the same proportion.

The dash-dotted curve in Fig. 11*a* is not more than our assumption, which is rough but quite feasible since the overwhelming majority of the densities in giant air showers were measured by AGASA at distances in the region $R > 600$ m. As was shown previously in [7, 8] and as can be seen in Fig. 9, the lateral distribution of charged particles in giant air showers changes significantly according to data of the Yakutsk array. We will now consider the consequences of this in the case of AGASA. We will make use of the lateral distribution in Fig. 8*a* (for the depth of $X = 1040$ g cm^{-2} in the atmosphere) and change, in the approximation of the form (12), the Molière radius $R_M = 70$ m by 91.6 m. The result is shown in Fig. 12 by the solid curve. In the same figure, the dashed curve represents the approximation in the form (15) for the same depth in the atmosphere [with the parameter value of $\eta = 3.74$, which corresponds to (16) for $\sec\theta = 1.13 = 1040/920$]. The two curves in question are matched at $R = 1000$ m.

It can be seen that the shapes of the lateral distributions in Fig. 12 are virtually indistinguishable at distances of about 600 to 2000 m. This is yet another argument in favor of the statement that there were no distortions in the measurements of the charged-particle densities by the Yakutsk array at the periphery of giant air showers. However, the approximation of the form (12) is more gently sloping than the approximation of the form (15) as one approaches the shower core; in all probability, this trend becomes more pronounced as the energy of a giant air shower tends to the limiting value. The situation is aggravated by the circumstance that the cascade-curve maximum proves to be nearly at the same level as the array itself. Here, many particles traverse scintillation detectors at distances in excess of 1000 m at very small angles with respect to their surface. Under such conditions, detector responses to particle fluxes may be substantially different from those that are observed in the region of much lower energies of extensive air showers.

7. CONCLUSION

From the data quoted above, one can see that the structure of the muon disk in extensive air showers of energy in the range $5 \times 10^{16} < E_0 \leq 10^{18}$ eV is rather complicated. On one hand, the results presented in Fig. 3 do not exhibit strong inconsistencies with the hypothesis of a mixed composition of primary cosmic rays in the energy region being considered, where this composition changes fast, from the dominance of iron nuclei at $E_0 \approx 10^{17}$ eV to a purely protonic composition at $E_0 \approx 10^{18}$ eV. On the other hand, the same experimental data—if subjected to a more thorough analysis—lead to results shown in Fig. 6, which offer a totally different pattern of the development of extensive air showers. Here, one cannot rule out the possibility that the superposition of two components in Fig. 6 can mimic showers initiated by a mixed composition of primary cosmic rays. Possibly, this underlies the explanation of the as-yet-unresolved problem of the origin of the first break in the spectrum of cosmic rays at $E_0 \geq 3 \times 10^{15}$ eV.

As to the criticism expressed in [44] in connection with the detection methods at the Yakutsk array and the methods for estimating the energies of giant air showers there, it is hardly sober. Possibly, this was due to a lack of publicity of the technical features of the Yakutsk array in the widespread scientific literature. In our opinion, it cannot be stated with confidence that an increase in the number of events at energies of $E_0 \sim 10^{20}$ eV at presently operating arrays or the construction of arrays having enormous areas (about 1000 to 5000 km^2) and employing detectors spaced by a distance of 1 to 1.5 km [41, 42] would contribute to solving the problem of the limiting energies of giant air showers. We believe that it is illegitimate to extrapolate, to this region, any calculated [at energies in the range $E_0 \leq (2\text{–}3) \times 10^{18}$ eV] or experimental dependence. Such extrapolations could lead to large errors in estimating the energies of primary particles. Dedicated investigations of the lateral distributions of all charged particles and muons at arrays where the detectors used are spaced by a distance not longer than 200 or 300 m are required here.

ACKNOWLEDGMENTS

The financial support extended by the Ministry for Science of the Russian Federation to the Yakutsk multipurpose array for studying extensive air showers (grant no. 01-30) is gratefully acknowledged. This work was also supported within the state contract no. 40.014.11.1110.

REFERENCES

1. V. I. Vishnevskaya, N. N. Kalmykov, G. V. Kulikov, *et al.*, Yad. Fiz. **62**, 300 (1999) [Phys. At. Nucl. **62**, 265 (1999)].
2. H. Ulrich, T. Antoni, W. D. Apel, *et al.*, in *Proceedings of 27th ICRC, Hamburg, 2001*, Vol. 2, p. 97.
3. T. Abu-Zayyad, K. Belov, D. J. Clay, *et al.*, astro-ph/0010652.
4. V. S. Ptuskin *et al.*, Astron. Astrophys. **268**, 726 (1993).
5. A. V. Glushkov, I. T. Makarov, E. S. Nikiforova, *et al.*, Yad. Fiz. **58**, 1265 (1995) [Phys. At. Nucl. **58**, 1186 (1995)].
6. A. V. Glushkov, I. T. Makarov, M. I. Pravdin, *et al.*, Pis'ma Zh. Éksp. Teor. Fiz. **71**, 145 (2000) [JETP Lett. **71**, 97 (2000)].

7. A. V. Glushkov, M. I. Pravdin, I. E. Sleptsov, *et al.*, Yad. Fiz. **63**, 1557 (2000) [Phys. At. Nucl. **63**, 1477 (2000)].
8. A. V. Glushkov, M. I. Pravdin, I. E. Sleptsov, *et al.*, Yad. Fiz. **65**, 1346 (2002) [Phys. At. Nucl. **65**, 1313 (2002)].
9. A. V. Glushkov, Pis'ma Zh. Éksp. Teor. Fiz. **48**, 513 (1988) [JETP Lett. **48**, 555 (1988)].
10. A. V. Glushkov, Pis'ma Zh. Éksp. Teor. Fiz. **73**, 355 (2001) [JETP Lett. **73**, 313 (2001)].
11. A. V. Glushkov and I. E. Sleptsov, Izv. Akad. Nauk, Ser. Fiz. **65**, 437 (2001).
12. A. V. Glushkov and M. I. Pravdin, Zh. Éksp. Teor. Fiz. **119**, 1029 (2001) [JETP **92**, 887 (2001)].
13. A. V. Glushkov and M. I. Pravdin, Pis'ma Astron. Zh. **27**, 577 (2001) [Astron. Lett. **27**, 493 (2001)].
14. A. V. Glushkov, Pis'ma Zh. Éksp. Teor. Fiz. **75**, 3 (2002) [JETP Lett. **75**, 1 (2002)].
15. A. V. Glushkov, Izv. Akad. Nauk, Ser. Fiz. **66**, 1599 (2002).
16. A. V. Glushkov and M. I. Pravdin, Pis'ma Astron. Zh. **28**, 341 (2002) [Astron. Lett. **28**, 296 (2002)].
17. A. V. Glushkov, Pis'ma Astron. Zh. **29**, 172 (2003) [Astron. Lett. **29**, 142 (2003)].
18. A. V. Glushkov and M. I. Pravdin, Yad. Fiz. **66**, 886 (2003) [Phys. At. Nucl. **66**, 854 (2003)].
19. A. V. Glushkov, Yad. Fiz. **66**, 1292 (2003) [Phys. At. Nucl. **66**, 1252 (2003)].
20. A. V. Glushkov, V. B. Kosarev, I. T. Makarov, *et al.*, Pis'ma Zh. Éksp. Teor. Fiz. **67**, 361 (1998) [JETP Lett. **67**, 383 (1998)].
21. A. V. Glushkov, L. G. Dedenko, V. B. Kosarev, *et al.*, in *Proceedings of 26th ICRC*, *Salt Lake City*, *1999*, Vol. 1, p. 387.
22. A. B. Kaĭdalov, K. A. Ter-Martirosyan, and Yu. M. Shabel'skiĭ, Yad. Fiz. **43**, 1282 (1986) [Sov. J. Nucl. Phys. **43**, 822 (1986)].
23. L. Anchordoqui, H. Golgberg, T. McCauley, *et al.*, hep-ph/0011097.
24. D. Fargion, B. Mele, and A. Salis, Astrophys. J. **517**, 725 (1999).
25. T. J. Weiler, Astropart. Phys. **11**, 303 (1999).
26. L. G. Dedenko, T. M. Roganova, G. F. Fedorova, *et al.*, Pis'ma Zh. Éksp. Teor. Fiz. **78**, 131 (2003) [JETP Lett. **78**, 101 (2003)].
27. A. B. Migdal, Phys. Rev. **103,** 1811 (1956).
28. K. Greisen, Phys. Rev. Lett. **16,** 748 (1966).
29. G. T. Zatsepin and V. A. Kuz'min, Pis'ma Zh. Éksp. Teor. Fiz. **4**, 78 (1966) [JETP Lett. **4**, 53 (1966)].
30. P. F. Bejl, R. U. Bejsembaev, N. G. Vildanov, *et al.,* in *Proc. 28th ICRC*, *Tsukuba*, *2003*, Vol. 1, p. 9.
31. G. V. Kulikov and G. B. Khristiansen, Zh. Éksp. Teor. Fiz. **35**, 635 (1958) [Sov. Phys. JETP **8**, 441 (1958)].
32. J. Linsley, Phys. Rev. Lett. **10**, 146 (1963).
33. D. M. Edge, A. C. Evans, H. J. Garmston, *et al.*, J. Phys. A **6**, 1612 (1973).
34. C. J. Bell *et al.*, J. Phys. A **7**, 990 (1974).
35. D. D. Krasilnikov, A. I. Kuzmin, J. Linsley, *et al.*, J. Phys. A **7**, 176 (1974).
36. *Catalog of Highest Energy Cosmic Rays: Giant Extensive Air Showers* (World Data Center C2 for Cosmic Rays, Mito, Japan, 1980), No. 1.
37. N. N. Efimov, T. A. Egorov, A. V. Glushkov, *et al.*, in *Proceedings of International Workshop of Astrophysical Aspects of the Most Energetic Cosmic Rays* (Kofu, 1990), p. 20.
38. N. Hayashida, K. Honda, M. Honda, *et al.*, ICRR Report 324-94-19 (Tokyo, 1994).
39. D. J. Bird, S. C. Corbato, H. Y. Dai, *et al.*, Astrophys. J. **424**, 491 (1994).
40. N. Chiba, K. Hashimoto, N. Hayashida, *et al.*, Nucl. Instrum. Methods Phys. Res. A **311**, 338 (1992).
41. J. C. Cronin *et al.*, Preprint EHI 92-08 (University of Chicago, Chicago, 1992).
42. M. Teshima, M. Bessho, H. Y. Dai, *et al.*, *Proc. of RIKEN*, *International Workshop on Electromagnetic and Nuclear Cascade Phenomena at High and Extremely High Energies* (1993), p. 135.
43. M. Takeda, N. Sakaki, K. Honda, *et al.*, in *Proc. 28th ICRC, Tsukuba*, *2003*, Vol. 1, p. 381.
44. A. A. Watson, in *Proc. 28th ICRC*, *Tsukuba*, *2003*, Vol. 1, p. 373.
45. M. Ave, J. A. Hinton, J. Knapp, *et al.*, in *Proceedings of 27th ICRC*, *Hamburg*, *2001*, Vol. 1, p. 381.
46. T. Abu-Zayyad, G. Archbold, J. A. Bellido, *et al.*, astro-ph/0208243.
47. J. Bluemer *et al.*, in *Proceedings of 28th ICRC*, *Tsukuba*, *2003*, Vol. 1, p. 445.
48. K. Honda, K. Hashimoto, N. Kawasumi, *et al.*, in *Proceedings of 28th ICRC*, *Tsukuba*, *2003*, Vol. 1, p. 361.
49. T. Suomijarvi *et al.*, in *Proceedings of 28th ICRC*, *Tsukuba*, *2003*, Vol. 1, p. 473.
50. M. Ave, J. Knapp, M. Marchesini, *et al.*, in *Proceedings of 28th ICRC*, *Tsukuba*, *2003*, Vol. 1, p. 349.
51. A. N. Gadalov, A. V. Glushkov, T. A. Egorov, *et al.*, in *Experimental Methods of Investigations into Ultrahigh Energy Cosmic Rays* (Yakutsk, 1974), p. 30 [in Russian].
52. M. Nagano, D. Heck, S. Shinozaki, *et al.*, Preprint No. 6191, FZKA (Karlsruhe, 1998).
53. S. Yoshida, N. Hayashida, K. Honda, *et al.*, J. Phys. G **20**, 651 (1994).
54. S. Argiro *et al.*, in *Proc. of 28th ICRC*, *Tsukuba*, *2003*, Vol. 1, p. 457.
55. N. Hayashida, K. Honda, M. Honda, *et al.*, Phys. Rev. Lett. **73**, 3491 (1994).

Translated by A. Isaakyan

Physics of Atomic Nuclei, Vol. 68, No. 1, 2005, pp. 88–93. From Yadernaya Fizika, Vol. 68, No. 1, 2005, pp. 89–94.

ELEMENTARY PARTICLES AND FIELDS
Theory

On CP-Odd Effects in $K_L \to 2\pi$ and $K^\pm \to \pi^\pm\pi^\pm\pi^\mp$ Decays Generated by Direct CP Violation*

E. P. Shabalin**

Institute for Theoretical and Experimental Physics,
Bol'shaya Cheremushkinskaya ul. 25, Moscow, 117259 Russia

Received January 22, 2004; in final form, May 13, 2004

Abstract—The amplitudes of the $K^\pm \to 3\pi$ and $K \to 2\pi$ decays are expressed in terms of different combinations of one and the same set of CP-conserving and CP-odd parameters. Extracting the magnitudes of these parameters from the data on $K \to 2\pi$ decays, we estimate an expected CP-odd difference between the values of the slope parameters g^+ and g^- of the energy distributions of "odd" pions in $K^+ \to \pi^+\pi^+\pi^-$ and $K^- \to \pi^-\pi^-\pi^+$ decays. © *2005 Pleiades Publishing, Inc.*

1. INTRODUCTION

The observation of CP effects in $K^\pm \to 3\pi$ decays would allow one to understand better how the mechanisms of CP violation work.

Now the Collaboration NA48/2 has begun a search for such an effect with accuracy $\delta\left(\frac{g^+-g^-}{g^++g^-}\right) \le 2\times 10^{-4}$.

Contrary to the case of $K_L \to 2\pi$ decay, where CP is violated in both $\Delta S = 2$ and $\Delta S = 1$ transitions, in the $K^\pm \to 3\pi$ decays, only the latter (so-called direct) CP violation takes place. Experimentally, the existence of direct CP violation in $K_L \to 2\pi$ decays, predicted by the Standard Model (SM) and characterized by the parameter ε', is established: $\varepsilon'/\varepsilon = (1.66 \pm 0.16)\times 10^{-3}$.

What is expected for CP effects in $K^+ \to \pi^\pm\pi^\pm\pi^\mp$ decay? To give an answer, it is necessary to understand the role of the electroweak penguin (EWP) operators in both decays and get rid of the large uncertainties usual for the theoretical calculations. The real scale of these uncertainties is characterized by the following predictions obtained before the above experimental result:

$$\frac{\varepsilon'}{\varepsilon} = (17^{+14}_{-10})\times 10^{-4} \quad [1],$$
$$\frac{\varepsilon'}{\varepsilon} = (1.5\text{–}31.6)\times 10^{-4} \quad [2].$$

To avoid the uncertainties arising in the theoretical calculation of the ingredients of the theory, we use the following procedure. We express the amplitudes of $K \to 2\pi$ and $K^\pm \to 3\pi$ decays in terms of one and the same set of parameters, and calculating $g^+ - g^-$, we use the magnitudes of these parameters extracted from data on $K \to 2\pi$ decays.

2. THE SCHEME OF CALCULATION

A theory of $\Delta S = 1$ nonleptonic decays is based on the effective Lagrangian [3]

$$L(\Delta S = 1) = \sqrt{2}G_F \sin\theta_C \cos\theta_C \sum_i c_i O_i, \quad (1)$$

where

$$O_1 = \bar{s}_L\gamma_\mu d_L \cdot \bar{u}_L\gamma_\mu u_L - \bar{s}_L\gamma_\mu u_L \cdot \bar{u}_L\gamma_\mu d_L \quad (2)$$
$$(\{8_f\}, \Delta I = 1/2);$$

$$O_2 = \bar{s}_L\gamma_\mu d_L \cdot \bar{u}_L\gamma_\mu u_L + \bar{s}_L\gamma_\mu u_L \cdot \bar{u}_L\gamma_\mu d_L \quad (3)$$
$$+ 2\bar{s}_L\gamma_\mu d_L \cdot \bar{d}_L\gamma_\mu d_L + 2\bar{s}_L\gamma_\mu d_L \cdot \bar{s}_L\gamma_\mu s_L$$
$$(\{8_d\}, \Delta I = 1/2);$$

$$O_3 = \bar{s}_L\gamma_\mu d_L \cdot \bar{u}\gamma_\mu u_L + \bar{s}\gamma_\mu u_L \cdot \bar{u}\gamma_\mu d_L \quad (4)$$
$$+ 2\bar{s}_L\gamma_\mu d_L \cdot \bar{d}_L\gamma_\mu d_L - 3\bar{s}_L\gamma_\mu d_L \cdot \bar{s}_L\gamma_\mu s_L$$
$$(\{27\}, \Delta I = 1/2);$$

$$O_4 = \bar{s}_L\gamma_\mu d_L \cdot \bar{u}\gamma_\mu u_L + \bar{s}_L\gamma_\mu u_L \cdot \bar{u}_L\gamma_\mu d_L \quad (5)$$
$$- \bar{s}_L\gamma_\mu d_L \cdot \bar{d}_L\gamma_\mu d_L$$
$$(\{27\}, \Delta I = 3/2);$$

$$O_5 = \bar{s}_L\gamma_\mu\lambda^a d_L\left(\sum_{q=u,d,s}\bar{q}_R\gamma_\mu\lambda^a q_R\right) \quad (6)$$
$$(\{8\}, \Delta I = 1/2);$$

*This article was submitted by the author in English.

**e-mail: shabalin@heron.itep.ru

$$O_6 = \bar{s}_L\gamma_\mu d_L\Big(\sum_{q=u,d,s}\bar{q}_R\gamma_\mu q_R\Big) \quad (7)$$
$$(\{8\}, \Delta I = 1/2).$$

This set is sufficient for calculation of the CP-even parts of the amplitudes under consideration. To calculate the CP-odd parts, it is necessary to add the so-called electroweak contributions originated by the operators O_7, O_8:

$$O_7 = \frac{3}{2}\bar{s}\gamma_\mu(1+\gamma_5)d\Big(\sum_{q=u,d,s}e_q\bar{q}\gamma_\mu(1-\gamma_5)q\Big) \quad (8)$$
$$(\Delta I = 1/2, 3/2);$$

$$O_8 = -12\sum_{q=u,d,s}e_q(\bar{s}_L q_R)(\bar{q}_R d_L), \quad (9)$$
$$e_q = \left(\frac{2}{3}, -\frac{1}{3}, -\frac{1}{3}\right) \quad (\Delta I = 1/2, 3/2).$$

The coefficients c_{5-8} have the imaginary parts necessary for CP violation.

In the case of nonlinear realization of chiral symmetry, the bosonization of these operators can be done using the relations [4]

$$\bar{q}_j(1+\gamma_5)q_k = -\frac{1}{\sqrt{2}}F_\pi r\left(U - \frac{1}{\Lambda^2}\partial^2 U\right)_{kj}, \quad (10)$$

$$\bar{q}_j\gamma_\mu(1+\gamma_5)q_k = i[(\partial_\mu U)U^\dagger - U(\partial_\mu U^\dagger) \quad (11)$$
$$-\frac{rF_\pi}{\sqrt{2}\Lambda^2}(m(\partial_\mu U^\dagger) - (\partial_\mu U)m)]_{kj}.$$

Here

$$F_\pi \approx 93\ \text{MeV}, \quad \Lambda \approx 1\ \text{GeV},$$
$$r = 2m_\pi^2/(m_u + m_d), \quad m = \text{diag}(m_u, m_d, m_s),$$

$$U = \frac{F_\pi}{\sqrt{2}}\left(1 + \frac{i\sqrt{2}\hat{\pi}}{F_\pi} - \frac{\hat{\pi}^2}{F_\pi^2}\right. \quad (12)$$
$$\left. + a_3\left(\frac{i\hat{\pi}}{\sqrt{2}F_\pi}\right)^3 + 2(a_3-1)\left(\frac{i\hat{\pi}}{\sqrt{2}F_\pi}\right)^4 + \ldots\right),$$

where a_3 is an arbitrary number and

$$\hat{\pi} = \begin{pmatrix} \frac{\pi_0}{\sqrt{3}} + \frac{\pi_8}{\sqrt{6}} + \frac{\pi_3}{\sqrt{2}} & \pi^+ & K^+ \\ \pi^- & \frac{\pi_0}{\sqrt{3}} + \frac{\pi_8}{\sqrt{6}} - \frac{\pi_3}{\sqrt{2}} & K^0 \\ K^- & \bar{K}^0 & \frac{\pi_0}{\sqrt{3}} - \frac{2\pi_8}{\sqrt{6}} \end{pmatrix}. \quad (13)$$

The PCAC condition demands $a_3 = 0$ [5] and we adopt this condition, bearing in mind that, on the mass shell, the values of the mesonic amplitudes are independent of a_3.

Using also the relations between matrices in the color space

$$\delta^\alpha_\beta\delta^\gamma_\delta = \frac{1}{3}\delta^\alpha_\delta\delta^\gamma_\beta + \frac{1}{2}\lambda^\alpha_\delta\lambda^\gamma_\beta,$$
$$\lambda^\alpha_\beta\lambda^\gamma_\delta = \frac{16}{9}\delta^\alpha_\delta\delta^\gamma_\beta - \frac{1}{3}\lambda^\alpha_\delta\lambda^\gamma_\beta$$

and the Fierz transformation relation

$$\bar{s}\gamma_\mu(1+\gamma_5)d\cdot\bar{q}\gamma_\mu(1-\gamma_5)q$$
$$= -2\bar{s}(1-\gamma_5)q\cdot\bar{q}(1+\gamma_5)d$$

and representing $M(K \to 2\pi)$ in the form

$$M(K_1^0 \to \pi^+\pi^-) = A_0 e^{i\delta_0} - A_2 e^{i\delta_2}, \quad (14)$$
$$M(K_1^0 \to \pi^0\pi^0) = A_0 e^{i\delta_0} + 2A_2 e^{i\delta_2}, \quad (15)$$
$$M(K^+ \to \pi^+\pi^0) = -\frac{3}{2}A_2 e^{i\delta_2}, \quad (16)$$

where δ_0 and δ_2 are the S-wave shifts of $\pi\pi$ scattering in the isotopic spin $I = 0, 2$ channels, we obtain

$$A_0 = G_F F_\pi \sin\theta_C\cos\theta_C\frac{m_K^2 - m_\pi^2}{\sqrt{2}} \quad (17)$$
$$\times\left[c_1 - c_2 - c_3 + \frac{32}{9}\beta(\text{Re}\tilde{c}_5 + i\text{Im}\tilde{c}_5)\right];$$

$$A_2 = G_F F_\pi \sin\theta_C\cos\theta_C\frac{m_K^2 - m_\pi^2}{\sqrt{2}} \quad (18)$$
$$\times\left[c_4 + i\frac{2}{3}\beta\Lambda^2\text{Im}\tilde{c}_7(m_K^2 - m_\pi^2)^{-1}\right],$$

where

$$\tilde{c}_5 = c_5 + \frac{3}{16}c_6, \quad \tilde{c}_7 = c_7 + 3c_8, \quad (19)$$

$$\beta = \frac{2m_\pi^4}{\Lambda^2(m_u + m_d)^2}.$$

The contributions from $\tilde{c}_7 O_7$ to $\text{Re}A_0$ and $\text{Im}A_0$ are small because $\tilde{c}_7/\tilde{c}_5$ is proportional to the electromagnetic constant α and we neglected these corrections. From data on widths of $K \to 2\pi$ decays, we

obtain

$$c_4 = 0.328; \tag{20}$$
$$c_1 - c_2 - c_3 + \frac{32}{9}\beta \mathrm{Re}\tilde{c}_5 = -10.13.$$

At $c_1 - c_2 - c_3 = -2.89$ [3, 6], we obtain

$$\frac{32}{9}\beta \mathrm{Re}\tilde{c}_5 = -7.24. \tag{21}$$

From the expression for A_2, it is seen that the contribution of the operators $O_{7,8}$ is enlarged by the factor Λ^2/m_K^2 in comparison with the other operator contribution. The reason is discussed in the Appendix.

Using the general relation

$$\varepsilon' = ie^{i(\delta_2-\delta_0)}\left[-\frac{\mathrm{Im}A_0}{\mathrm{Re}A_0} + \frac{\mathrm{Im}A_2}{\mathrm{Re}A_2}\right]\left|\frac{A_2}{A_0}\right| \tag{22}$$

and the experimental value $\varepsilon' = (3.78 \pm 0.38) \times 10^{-6}$, we come to the relation

$$-\frac{\mathrm{Im}\tilde{c}_5}{\mathrm{Re}\tilde{c}_5}\left(1 - \Omega_{\eta,\eta'} + 24.36\frac{\mathrm{Im}\tilde{c}_7}{\mathrm{Im}\tilde{c}_5}\right) \tag{23}$$
$$= (1.63 \pm 0.16) \times 10^{-4},$$

where $\Omega_{\eta,\eta'}$ takes into account the effects of $K^0 \to \pi^0\eta(\eta') \to \pi^0\pi^0$ transitions.

Introducing the notation

$$-\frac{\mathrm{Im}\tilde{c}_5}{\mathrm{Re}\tilde{c}_5} = x\frac{\mathrm{Im}\lambda_t}{s_1}, \quad \frac{24.36}{1-\Omega_{\eta,\eta'}}\frac{\mathrm{Im}\tilde{c}_7}{\mathrm{Im}\tilde{c}_5} = -y \tag{24}$$

and using

$$(\mathrm{Im}\lambda_t)/s_1 \approx s_2 s_3 \sin\delta = \frac{(1.2 \pm 0.2) \times 10^{-4}}{0.223} \quad [7], \tag{25}$$

we can write Eq. (23) for $\Omega_{\eta,\eta'} = 0.25 \pm 0.08$ in the form

$$x(1-y) = 0.40 \times (1 \pm 0.22). \tag{26}$$

In the last two equations, s_i and δ are the parameters of the CKM matrix. Equation (26) depends on the variables x and y representing the contribution of the QCD penguin and relative contribution of EWP, respectively. To move further, we are forced to apply to existing theoretical estimates of one of these variables.

In terms of notation in [8–10],

$$y = \frac{\Pi_2}{\omega}/\Pi_0(1 - \Omega_{\eta,\eta'}). \tag{27}$$

According to [8], $y \approx 0.3$ and, hence, $x = 0.57 \pm 0.12$. But $\varepsilon'/\varepsilon = 2.2 \times 10^{-3}$, or is 30% larger than the experimental value.

In [10], the central value of y is $y \approx 0.5$ and, consequently, $x = 0.80 \pm 0.18$. This result looks like a reliable one. A very close result $x = 0.71 \pm 0.27$ can be derived from the result $(\varepsilon'/\varepsilon)_{\mathrm{EWP}} = (-12 \pm 3) \times 10^{-4}$ [11], compared to the experimental value $(\varepsilon'/\varepsilon)_{\mathrm{exp}} = (16.6 \pm 1.6) \times 10^{-4}$. But it should be noted that the previous estimates of x were rather different. In particular, according to [12], $x = 1.4 \pm 0.28$. An estimate of x can be extracted also from [13–15] operating with a different set of four-quark operators Q_i, where the combination C_6Q_6 corresponds to our c_5O_5. From the general representation

$$C_6(\mu) = z_6(\mu) + \left(s_2^2 + s_2 s_3 \frac{c_2}{c_1 c_3}\cos\delta\right) y_6(\mu)$$
$$- is_2 s_3 \frac{c_2}{c_1 c_3} y_6(\mu)\sin\delta$$

and the calculated magnitudes of y_6 and z_6, we find for $x \approx y_6/z_6$

$$x \approx 2 \text{ at } \Lambda^{(4)}_{\mathrm{QCD}} = 0.35 \text{ GeV}, \quad \mu = 0.8 \text{ GeV}, \tag{28}$$
$$m_t = 176 \text{ GeV} \quad [13];$$

$$x = 2.8 \text{ at } \Lambda_{\overline{MS}} = 0.3 \text{ GeV}, \quad \mu = 1 \text{ GeV}, \tag{29}$$
$$m_t = 130 \text{ GeV} \quad [14];$$

$$x = 5.5 \text{ at } \Lambda^{(4)}_{\mathrm{QCD}} = 0.3 \text{ GeV}, \quad \mu = 1 \text{ GeV}, \tag{30}$$
$$m_t = 170 \text{ GeV} \quad [15].$$

Such a difference of the theoretical estimates of x makes very desirable an investigation of CP effects in $K^\pm \to \pi^\pm\pi^\pm\pi^\mp$ decays, where, contrary to $K_L \to 2\pi$ decays, the EWP contributions increase CP effects.

3. DECAY $K^\pm \to \pi^\pm\pi^\pm\pi^\mp$

To the leading p^2 approximation,

$$M(K^+ \to \pi^+(p_1)\pi^+(p_2)\pi^-(p_3)) \tag{31}$$
$$= \kappa\left[1 + ia_{\mathrm{KM}} + \frac{1}{2}gY(1 + ib_{\mathrm{KM}}) + \ldots\right],$$

where

$$\kappa = G_{\mathrm{F}}\sin\theta_{\mathrm{C}}\cos\theta_{\mathrm{C}} m_K^2 c_0 (3\sqrt{2})^{-1}, \tag{32}$$

$$a_{\mathrm{KM}} = \left[\frac{32}{9}\beta\mathrm{Im}\tilde{c}_5 + 4\beta\mathrm{Im}\tilde{c}_7\left(\frac{3\Lambda^2}{2m_K^2} + 2\right)\right]\Big/ c_0, \tag{33}$$

$$b_{\mathrm{KM}} = \left[\frac{32}{9}\beta\mathrm{Im}\tilde{c}_5 + 8\beta\mathrm{Im}\tilde{c}_7\right]\Big/(c_0 + 9c_4). \tag{34}$$

The last two quantities represent the imaginary parts produced by the Kobayashi–Maskawa phase δ,

$$\frac{1}{2}g = -\frac{3m_\pi^2}{2m_K^2}\left(1 + \frac{9c_4}{c_0}\right), \quad Y = \frac{s_3 - s_0}{m_\pi^2}, \tag{35}$$

$$c_0 = c_1 - c_2 - c_3 - c_4 + \frac{32}{9}\beta \mathrm{Re}\tilde{c}_5 = -10.46. \quad (36)$$

As the field K^+ is complex and its phase is arbitrary, we can replace K^+ by $K^+(1+ia_{\mathrm{KM}}) \times (\sqrt{1+a_{\mathrm{KM}}^2})^{-1}$. Then

$$M(K^+ \to \pi^+(p_1)\pi^+(p_2)\pi^-(p_3)) \quad (37)$$
$$= \kappa\left[1 + \frac{1}{2}gY(1 + i(b_{\mathrm{KM}} - a_{\mathrm{KM}})) + \dots\right].$$

Though this expression contains the imaginary CP-odd part, it does not lead to observable CP effects. Such effects arise due to interference between the CP-odd imaginary part and the CP-even imaginary part produced by rescattering of the final pions. Then

$$M(K^+ \to \pi^+\pi^+\pi^-) \quad (38)$$
$$= \kappa\left[1 + ia + \frac{1}{2}gY(1 + ib + i(b_{\mathrm{KM}} - a_{\mathrm{KM}}) + \dots\right],$$

where a and b are the corresponding CP-even imaginary parts of the amplitude. These parts can be estimated to the leading approximation in momenta by calculating the imaginary part of the two-pion loop diagrams with

$$M(\pi^+(r_2)\pi^-(r_3) \to \pi^+(p_2)\pi^-(p_3))$$
$$= F_\pi^{-2}[(p_2+p_3)^2 + (r_2-p_2)^2 - 2m_\pi^2],$$
$$M(\pi^0(r_2)\pi^0(r_3) \to \pi^+(p_2)\pi^-(p_3))$$
$$= F_\pi^{-2}[(p_2+p_3)^2 - m_\pi^2],$$
$$M(\pi^+(r_1)\pi^+(r_2) \to \pi^+(p_1)\pi^+(p_2))$$
$$= F_\pi^{-2}[(r_1-p_1)^2 + (r_1-p_2)^2 - 2m_\pi^2].$$

Then we find

$$a = 0.12065, \qquad b = 0.714. \quad (39)$$

Using the definition

$$|M(K^\pm \to \pi^\pm(p_1)\pi^\pm(p_2)\pi^\mp(p_3))|^2$$
$$\sim [1 + g^\pm Y + \dots]$$

and the results of our calculation

$$|M(K^\pm \to \pi^\pm(p_1)\pi^\pm(p_2)\pi^\mp(p_3))|^2 \quad (40)$$
$$\sim \left[1 + \frac{g}{1+a^2}Y\,(1 + ab \pm a(b_{\mathrm{KM}} - a_{\mathrm{KM}})) + \dots\right],$$

we find

$$R_g \equiv \frac{g^+ - g^-}{g^+ + g^-} = \frac{a(b_{\mathrm{KM}} - a_{\mathrm{KM}})}{1+ab}. \quad (41)$$

At the numerical values of the parameters fixed above and $\Omega_{\eta,\eta'} = 0.25$, we obtain to the leading p^2 approximation

$$(R_g)_{p^2} = 0.030\frac{\mathrm{Im}\tilde{c}_5}{\mathrm{Re}\tilde{c}_5}\left(1 - 14.9\frac{\mathrm{Im}\tilde{c}_7}{\mathrm{Im}\tilde{c}_5}\right) \quad (42)$$
$$= -(2.44 \pm 0.44) \times 10^{-5} x\left(1 - \frac{0.13 \pm 0.03}{x}\right).$$

4. THE ROLE OF p^4 AND OTHER CORRECTIONS

The corrections to the result obtained in the conventional chiral theory up to the leading p^2 approximation are of two kinds. The corrections of the first kind are connected with a necessity to explain the observed enlargement of the S-wave $I = 0$ $\pi\pi$ amplitude. The corrections of the second kind are the p^4 corrections. As was argued in [16, 17], the corrections of both kinds must be properly estimated in the framework of a special linear $U(3)_L \otimes U(3)_R$ σ model with broken chiral symmetry. The above-mentioned enlargement of the S wave in this model is originated by mixing between the $\bar{q}q$ state and the gluonic state $(G^a_{\mu\nu})^2$ states. In such a model,

$$U = \hat{\sigma} + i\hat{\pi},$$

where $\hat{\sigma}$ is a 3×3 matrix of scalar partners of the mesons of the pseudoscalar nonet. The relations between diquark combinations and spinless fields are as given by Eqs. (10) and (11), but without the terms proportional to Λ^{-2}. Such contributions in the σ model appear from an expansion of the propagators of the intermediate scalar mesons. The parameter Λ^2 in this model is equal to the difference $m^2_{a_0(980)} - m^2_\pi$. The strength of mixing between the isosinglet σ meson and the corresponding gluonic state is characterized by the parameter ξ.

If the p^2 approximation gives

$$(\kappa)_{p^2} = 1.495 \times 10^{-6}, \quad (g)_{p^2} = -0.172, \quad (43)$$

instead of

$$(\kappa)_{\mathrm{exp}} = 1.92 \times 10^{-6}, \quad (44)$$
$$(g)_{\mathrm{exp}} = -0.2154 \pm 0.0035,$$

the corrected values of these CP-even parameters of the $K^+ \to \pi^+\pi^+\pi^-$ amplitude are closer or practically equal to the experimental ones [16]:

$$(\kappa)_{(p^2+p^4;\xi=-0.225)} = 1.73 \times 10^{-6}, \quad (45)$$
$$(g)_{(p^2+p^4;\xi=-0.225)} = -0.21.$$

More information on the parameter ξ can be found in [16, 17]. The expressions for the corrected $\pi\pi \to \pi\pi$ amplitudes are presented in [17].

Calculating the CP-even imaginary part of the $K^\pm \to \pi^\pm\pi^\pm\pi^\mp$ amplitude originated by two-pion intermediate states, we obtain

$$a(p^2 + p^4; \xi = -0.225) = 0.16265, \quad (46)$$

$$b(p^2+p^4;\xi=-0.225)=0.762. \quad (47)$$

An estimate of the parameter a can also be obtained without any calculations using the experimental data on the phase shifts of $\pi\pi$ scattering δ_0^0, δ_0^2, δ_1^1. According to definition (38), a is a phase at $s_3=s_0$. The mean value of the squared energy of the $\pi^+\pi^-$ system is

$$\frac{1}{2}[(p_1+p_3)^2+(p_2+p_3)^2]=s_0+\frac{s_0-s_3}{2}.$$

Consequently, a is a phase shift of $\pi^+\pi^-$ scattering at $\sqrt{s}=\sqrt{s_0}$. But the only significant phase shift at $\sqrt{s}=\sqrt{s_0}$ is δ_0^0. The remaining phase shifts are very small: $|\delta_0^2(s_0)|<1.8^\circ$ and $\delta_1^1(s_0)<0.3^\circ$ [18]. Then, according to Eq. (38), $a\approx\tan\delta_0^0(s_0)$, or $a=0.13\pm0.05$, if $\delta_0^0(s_0)=(7.50\pm2.85)^\circ$ [19] and $a=0.148\pm0.018$ if $\delta_0^0(s_0)=(8.4\pm1.0)^\circ$ [20]. These results coincide inside the error bars with the result (46). The corrected magnitude of R_g is

$$(R_g)_{(p^2+p^4;\xi=-0.225)} \quad (48)$$
$$=0.039\frac{\mathrm{Im}\tilde{c}_5}{\mathrm{Re}\tilde{c}_5}\left(1-11.95\frac{\mathrm{Im}\tilde{c}_7}{\mathrm{Im}\tilde{c}_5}\right)$$
$$=-(3.0\pm0.5)\times10^{-5}x\left(1-\frac{0.11\pm0.025}{x}\right).$$

This result is 23% larger in absolute magnitude than that calculated in the leading approximation. Therefore, we come to the conclusion that the corrections to the result obtained in the framework of conventional chiral theory to the leading approximation are not negligible (23%), but not so large, as was declared in [21].

5. CONCLUSION

From Eqs. (22), (26), and (48), it follows that EWP contributions diminish ε'/ε and increase R_g. The EWP corrections cancel one-half of the QCD penguin contribution to ε'/ε at $x=0.8$ and cancel 80% of the QCD penguin contribution at $x=2$. In both cases, ε'/ε is the same.

In the case of $K^\pm\to3\pi$ decays, the direct influence of EWP corrections themselves on CP effects is not so crucial as in $K_L\to2\pi$ decays. But if a cancellation between the contribution of QCD and EWPs in ε'/ε is large, the factor x in Eq. (48) is also larger than 1. So, for $x=2$, the predicted R_g must be 2.5 times larger than that at $x=0.8$.

Therefore, measuring R_g, one obtains a possibility to determine the true relation between QCD and EWP contributions to CP violation in kaon decays.

ACKNOWLEDGMENTS

This work is supported in part by the Federal Program of the Russian Ministry of Industry, Science, and Technology no. 40.052.1.1.1112.

APPENDIX

Here, we explain why an expansion of the amplitudes originated by EWP diagrams begins from the term independent of momenta and masses of the pseudoscalar mesons.

The operators $O_{7,8}$ can be expressed in terms of colorless diquark combinations in the form

$$O_7=-\bar{s}(1-\gamma_5)u\cdot\bar{u}(1+\gamma_5)d-\frac{3}{8}O_5, \quad (A.1)$$
$$O_8=3O_7.$$

Using Eq. (10), we find

$$O_7=-\frac{F_\pi^2r^2}{2}U_{21}U_{13}^* \quad (A.2)$$
$$+(\text{terms proportional to}\quad p_i^2(m_i^2)).$$

Omitting the terms proportional to derivatives of U and taking in Eq. (12) $a_3=0$, we find for the parity-even transitions

$$(O_7)^{P\text{-even}}=-\frac{F_\pi^2r^2}{2}\left\{\pi^-K^+\right. \quad (A.3)$$
$$+\frac{1}{2F_\pi^2}\times\left[\pi^-\left(\frac{2\pi_0}{\sqrt{3}}+\frac{2\pi_8}{\sqrt{6}}\right)+K^0K^-\right]$$
$$\left.\times\left[K^+\left(\frac{2\pi^0}{\sqrt{3}}-\frac{\pi_8}{\sqrt{6}}+\frac{\pi_3}{\sqrt{2}}\right)+\pi^+K^0\right]+\dots\right\}.$$

This expression does not contain a direct contribution to $K^+\to3\pi$ decays, but thanks to the term π^-K^+, the part of the $K^+\to3\pi$ amplitude independent of $p_i^2(m_i^2)$ arises. In the p^2 approximation,

$$\langle\pi^+(p_1)\pi^+(p_2)\pi^-(p_3)|O_7|K^+(k)\rangle \quad (A.4)$$
$$=-\frac{F_\pi^2r^2}{2(m_K^2-m_\pi^2)}\left[\frac{s_1+s_2-2m_\pi^2}{F_\pi^2}\right.$$
$$\left.-\frac{s_1+s_2-m_\pi^2-m_K^2}{F_\pi^2}\right]=-\frac{r^2}{2},$$

where $s_i=(k-p_i)^2$ and the first term in brackets describes the $\pi^+(k)\to\pi^+(p_1)\pi^+(p_2)\pi^-(p_3)$ transition. The second term describes the transitions $K^+(k)\to K^+(p_{1,2})\pi^+(p_{2,1})\pi^-(p_3)$.

Therefore, the operator O_7 violates the rule according to which an expansion of the mesonic amplitudes begins from the terms proportional to $p_i^2(m_i^2)$.

It may seem that, by removing the nondiagonal term $-\frac{r^2}{2}\pi^-K^+$ from the effective Lagrangian by redefinition of K^+ and π^- fields [22], the problem with

the constant contribution could be solved. But this is not so.

In our case, the mass part of the effective Lagrangian contains, in particular, the combination

$$-m_\pi^2\pi^+\pi^- - m_K^2K^+K^- \qquad (A.5)$$
$$-\frac{F_\pi^2 r^2}{2}(\gamma K^+\pi^- + \gamma^* K^-\pi^+),$$

where $\gamma = \sqrt{2}G_F \sin\theta_C \cos\theta_C c_7$. The transformations

$$\pi^- \to \pi^- + \beta K^-, \quad K^+ \to K^+ - \beta\pi^+, \qquad (A.6)$$
$$\pi^+ \to \pi^+ + \beta^* K^+, \quad K^- \to K^- - \beta^*\pi^-$$

with

$$\beta = \gamma^* F_\pi^2 r^2/[2(m_K^2 - m_\pi^2)] \qquad (A.7)$$

remove the nondiagonal terms in the linear in γ approximation. But the effective Lagrangian of strong interaction generates the sum of the amplitudes

$$\langle\pi^+(p_1)\pi^+(p_2)\pi^-(p_3)|\pi^+(k)\rangle \qquad (A.8)$$
$$+\langle K^+(p_1)\pi^+(p_2)\pi^-(p_3)|K^+(k)\rangle$$
$$+\langle K^+(p_2)\pi^+(p_1)\pi^-(p_3)|K^+(k)\rangle,$$

which after the transformation (A.6) generates the amplitude

$$\langle\pi^+(p_1)\pi^+(p_2)\pi^-(p_3)|O_7|K^+(k)\rangle = -\frac{\beta}{\gamma^*} \qquad (A.9)$$
$$\times\left[\frac{s_1+s_2-2m_\pi^2}{F_\pi^2} - \frac{s_1+s_2-m_\pi^2-m_K^2}{F_\pi^2}\right] = -\frac{r^2}{2}.$$

We have reproduced the result (A.4). The contribution of the operators $O_{7,8}$ to the leading approximation does not depend on $p_i^2(m_i^2)$.

REFERENCES

1. S. Bertolini *et al.*, Nucl. Phys. B **514**, 93 (1998).
2. T. Hambye *et al.*, Nucl. Phys. B **564**, 391 (2000).
3. M. A. Shifman, A. I. Vainshtein, and V. I. Zakharov, Zh. Éksp. Teor. Fiz. **72**, 1277 (1977) [Sov. Phys. JETP **45**, 670 (1977)].
4. W. A. Bardeen, A. J. Buras, and J.-M. Gerard, Nucl. Phys. B **293**, 787 (1987).
5. J. Cronin, Phys. Rev. **161**, 1483 (1967).
6. L. B. Okun, *Leptons and Quarks* (North-Holland, Amsterdam, 1982), pp. 315, 323.
7. A. Ali and D. London, Eur. Phys. J. C **18**, 665 (2001).
8. S. Bertolini, J. O. Eeg, and M. Fabbrichesi, Phys. Rev. D **63**, 056009 (2001).
9. A. J. Buras and J.-M. Gerard, Phys. Lett. B **517**, 129 (2001).
10. T. Hambye, S. Peris, and E. de Rafael, hep-ph/0305104 v. 2.
11. J. F. Donoghue and E. Golovich, Phys. Lett. B **478**, 172 (2000).
12. M. B. Voloshin, Preprint No. ITEP-22 (Moscow, 1981).
13. S. Bertolini *et al.*, Preprint SISSA 102/95/EP.
14. A. J. Buras, M. Jamin, and M. Lautenbacher, Nucl. Phys. B **408**, 209 (1993).
15. S. Bertolini, J. O. Eeg, and M. Fabbrichesi, Nucl. Phys. B **449**, 197 (1995).
16. E. P. Shabalin, Nucl. Phys. B **409**, 87 (1993).
17. E. P. Shabalin, Yad. Fiz. **61**, 1478 (1998) [Phys. At. Nucl. **61**, 1372 (1998)].
18. E. P. Shabalin, Yad. Fiz. **63**, 659 (2000) [Phys. At. Nucl. **63**, 594 (2000)].
19. L. Rosselet *et al.*, Phys. Rev. D **15**, 574 (1977).
20. S. Pislak *et al.*, Phys. Rev. Lett. **87**, 221801 (2001).
21. A. A. Bel'kov *et al.*, Phys. Lett. B **300**, 283 (1993).
22. G. Feinberg, P. K. Kabir, and S. Weinberg, Phys. Rev. Lett. **3**, 527 (1959).

Physics of Atomic Nuclei, Vol. 68, No. 1, 2005, pp. 94–103. Translated from Yadernaya Fizika, Vol. 68, No. 1, 2005, pp. 95–105.

ELEMENTARY PARTICLES AND FIELDS
Theory

Hadroproduction of Direct J/ψ and ψ' Mesons in the Fragmentation of Gluons and c Quarks at High Energies

V. A. Saleev* **and D. V. Vasin****

Samara State University, ul. Akademika Pavlova 1, Samara, 443011 Russia

Received December 3, 2003; in final form, April 26, 2004

Abstract—The transverse-momentum spectra of direct J/ψ and ψ' mesons in pp interactions at the Tevatron collider energy of $\sqrt{s} = 1.8$ TeV are calculated on the basis of nonrelativistic QCD, the fragmentation model, the k_T-factorization approach, and the standard parton model. The contribution of gluon fragmentation is shown to exceed the contribution of c-quark fragmentation both within the parton model and within the k_T-factorization approach. Experimental data of the CDF Collaboration agree with the assumption that gluon fragmentation plays a dominant role in the $Q\bar{Q}[^3S_1, 8]$ octet state, with the nonperturbative matrix element taking approximately equal values in the parton model and in the k_T-factorization approach. © *2005 Pleiades Publishing, Inc.*

1. INTRODUCTION

The phenomenology and the theory of processes involving the production of heavy quarkonia have been vigorously developed for several years following the measurement of the transverse-momentum (p_T) spectra and polarizations of J/ψ and ψ' mesons by the CDF Collaboration at the Tevatron collider [1, 2]. At the moment, it is clear that the production of heavy quarkonia has a complicated physical nature and requires new physical ideas for their description. The color-singlet model [3] previously proposed to describe a nonperturbative transition of a $Q\bar{Q}$ pair to final-state quarkonium was extended in a natural way within the formalism of nonrelativistic QCD (NRQCD) [4]. The extended model takes into account $Q\bar{Q}$-pair production not only in the color-singlet state [3] but also in the color-octet state. Moreover, it turned out that the octet-production mechanism is dominant in some processes.

The NRQCD formalism makes it possible to calculate consistently, by perturbation theory in two small parameters (strong coupling constant α_s at the scale of the heavy-quark mass and the relative velocity v of quarks in quarkonium), not only the parton cross sections for quarkonium-production processes through the fusion of Q and $\bar{Q}$ quarks but also the universal functions for parton fragmentation into various quarkonium states [5–10].

It is natural to assume that, in the region of high quarkonium transverse momenta ($p_T \gg M_{Q\bar{Q}}$), the contribution of the fragmentation production mechanism is greater in the k_T-factorization approach—in just the same way as in the parton model [6, 11]—than the contribution of the mechanism associated with the fusion of a heavy quark and a heavy antiquark produced in a hard subprocess.

In the Tevatron energy region ($\sqrt{s} = 1.8$ TeV), the main contribution to the cross sections for the production of heavy quarks comes from gluon–gluon fusion at small values of the argument x of the gluon distribution function and large values of the QCD-evolution scale parameter $\mu^2 \simeq M^2_{Q\bar{Q}} + p^2_T$. In this kinematical region, the collinear parton model can be generalized within the k_T-factorization approach [12–14], which takes into account, in the evolution equation for the transverse-momentum-dependent noncollinear distribution of gluons in the proton, corrections of the form $(\alpha_s \log(1/x))^n$ along with large logarithmic corrections of the form $(\alpha_s \log\mu^2)^n$. As a result, interesting observable effects appear in the production of heavy quarkonia, as was first shown 10 years ago in [15] and more recently in [16–19].

In the present study, the p_T spectra of direct J/ψ and ψ' mesons in pp interactions at the Tevatron energy are calculated in the fragmentation approximation. The results differ considerably from those obtained in [17–19] by using the k_T-factorization approach as well but within the model of gluon–gluon fusion. We consider the possible reasons for the disagreement between these results.

The term "direct" refers to J/ψ and ψ' mesons originating immediately from the hard parton subprocess. Of course, they do not include J/ψ mesons

*e-mail: Saleev@ssu.samara.ru
**e-mail: Vasin@ssu.samara.ru

produced in the cascade decays of the P-wave charmonium states χ_{cJ} and ψ' or B mesons. Since the ψ'-meson mass exceeds the masses of P-wave charmonium states, direct ψ' mesons do not contain contributions from the decays of B mesons. The present-day technique of vertex detectors makes it possible to separate experimentally direct J/ψ mesons, J/ψ mesons produced in the radiative decays of χ_{cJ}, and J/ψ mesons from the weak decays of B mesons.

Within NRQCD, it is shown that the main contribution to the production of J/ψ and ψ' mesons may come from the fragmentation of gluons through the $Q\bar{Q}[^3S_1, 8]$ octet state and the fragmentation of c ($\bar{c}$) quarks through the $Q\bar{Q}[^3S_1, 1]$ color-singlet state. The contribution of the singlet state for gluons and the contribution of the octet state for c ($\bar{c}$) quarks are suppressed within the expansion in α_s and v [5–10].

Below, we will compare the predictions obtained for the p_T spectra of direct J/ψ and ψ' mesons in the collinear parton model and in the k_T-factorization approach. In both cases, we perform calculations with hard amplitudes in the leading order of perturbative QCD. In the parton model, we take into account the following main subprocesses:

$$g + g \to g + g, \tag{1}$$

$$c(\bar{c}) + g \to c(\bar{c}) + g. \tag{2}$$

It was shown in [20] that, at high transverse momenta, $p_T \gg m_c$, the contribution of the parton subprocess (2) to the cross section for the hadroproduction of J/ψ or ψ' mesons is an order of magnitude greater than the contribution of the subprocess

$$g + g \to c + \bar{c}. \tag{3}$$

In the k_T-factorization approach, our calculations take into account the following parton subprocesses:

$$g^* + g^* \to g, \tag{4}$$

$$c(\bar{c}) + g^* \to c(\bar{c}). \tag{5}$$

As in the parton model, the contribution of subprocess (5) in the region $p_T \gg m_c$ exceeds significantly the contribution of the subprocess

$$g^* + g^* \to c + \bar{c}, \tag{6}$$

which we disregard.

2. NRQCD FORMALISM

Within the NRQCD approach, the cross section for the production of heavy quarkonium H and the $a \to H$ fragmentation function, where a stands for a parton, can be represented as sums of terms where coefficients determined by hard-interaction physics and the matrix elements that describe the effects of long-distance physics factorize [4]:

$$d\sigma(H) = \sum_n d\hat{\sigma}(Q\bar{Q}[n])\langle \mathcal{O}^H[n]\rangle, \tag{7}$$

$$D(a \to H) = \sum_n D(a \to Q\bar{Q}[n])\langle \mathcal{O}^H[n]\rangle. \tag{8}$$

Here, n stands for the set of color, spin, and orbital quantum numbers of the $Q\bar{Q}$ pair, $d\hat{\sigma}(Q\bar{Q}[n])$ is its production cross section, and $D(a \to Q\bar{Q}[n])$ is the respective fragmentation function. The last two quantities can be calculated by perturbation theory in the strong coupling constant α_s. For the production of quarkonium H in pp interaction, one must take the convolution of the cross section $d\hat{\sigma}$ with the parton distribution in the proton. The nonperturbative transition of a $Q\bar{Q}$ pair to final quarkonium H is described by the matrix element $\langle \mathcal{O}^H[n]\rangle$, which can be calculated by the nonperturbative QCD methods or can be extracted from experimental data. Fits to the experimental p_T spectra obtained for J/ψ, χ_c, and ψ' mesons by the CDF Collaboration [1, 2] were constructed by various authors within the collinear parton model (for an overview, see [21]).

In [22, 23], it was shown that, at high transverse momenta ($p_T > 17$ GeV), gluon fragmentation to the color-octet state,

$$g^* \to Q\bar{Q}[^3S_1, 8], \tag{9}$$

makes the main contribution to the direct production of J/ψ and ψ' mesons. According to [23], the values of the nonperturbative matrix elements that describe the transition in (9) are $\langle \mathcal{O}^{J/\psi}[^3S_1, 8]\rangle = 4.4 \times 10^{-3}$ GeV^3 and $\langle \mathcal{O}^{\psi'}[^3S_1, 8]\rangle = 4.2 \times 10^{-3}$ GeV^3. We note that a fit to data within the model of gluon–gluon fusion and within the collinear parton model give a different value of the matrix element, $\langle \mathcal{O}^{J/\psi}[^3S_1, 8]\rangle = 1.2 \times 10^{-2}$ GeV^3 [24]. This is of importance for a comparison of the results obtained within the k_T-factorization approach on the basis of the fusion model and on the basis of the fragmentation-production model.

3. FRAGMENTATION FUNCTIONS

Gluon fragmentation to the $^3S_1$ charmonium state depends on the probability of the transition of a $c\bar{c}$ pair to the color-singlet (Fig. 1*a*) or the color-octet (Fig. 1*b*) state. In [8, 9], it was shown that the contribution of the octet production mechanism considerably exceeds the contribution of the singlet mechanism and that, in the leading order in α_s, the fragmentation functions that describe the transition in (9) to

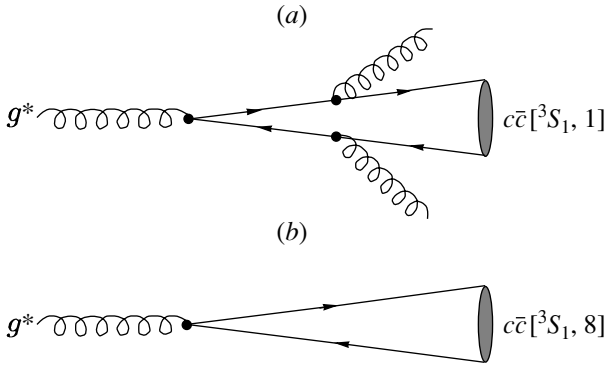

Fig. 1. Diagrams that describe the fragmentation processes $g^* \to J/\psi + g + g$ [color-singlet state; (a)] and $g^* \to J/\psi$ [color-octet state; (b)] in the leading order in the coupling constant α_s.

transversely and longitudinally polarized J/ψ mesons can be calculated at $\mu^2 = \mu_0^2 = 4m_c^2$; that is,

$$D^T_{g\to J/\psi(\psi')}(z,\mu_0^2) = 2d^T(z,\mu_0^2)\langle \mathcal{O}^{J/\psi(\psi')}[^3S_1,8]\rangle, \tag{10}$$

$$D^L_{g\to J/\psi(\psi')}(z,\mu_0^2) = d^L(z,\mu_0^2)\langle \mathcal{O}^{J/\psi(\psi')}[^3S_1,8]\rangle, \tag{11}$$

where

$$d^T(z,\mu_0^2) = \frac{\pi\alpha_s(\mu_0^2)}{48m_c^3}\delta(1-z), \tag{12}$$

$$d^L(z,\mu_0^2) = \frac{\alpha_s^2(\mu_0^2)}{8m_c^3}\frac{(1-z)}{z}. \tag{13}$$

It is clear that the probability of gluon fragmentation to a longitudinally polarized J/ψ (ψ') meson is negligible; therefore, the product J/ψ (ψ') meson is transversely polarized.

In the first approximation, the QCD evolution of the fragmentation functions (10) and (11) is described by the standard Dokshitzer–Gribov–Lipatov–Altarelli–Parisi equation [25]

$$\mu^2\frac{\partial D_g}{\partial\mu^2}(z,\mu^2) = \frac{\alpha_s(\mu^2)}{2\pi}\int\limits_z^1\frac{dx}{x}P_{gg}\left(\frac{x}{z}\right)D_g(x,\mu^2), \tag{14}$$

where $P_{gg}(x)$ is the gluon–gluon splitting function in the leading order in α_s. We solved Eq. (14) by using the well-known method based on the Mellin transformation. It can easily be shown that the Mellin moment of the fragmentation function for an arbitrary value of μ^2 can be expressed in terms of the moment at $\mu^2 = \mu_0^2$; that is,

$$D_g(n,\mu^2) = D_g(n,\mu_0^2)\exp\left[\frac{P_{gg}(n)}{2\pi}\int\limits_{\mu_0^2}^{\mu^2}\frac{d\mu^2}{\mu^2}\alpha_s(\mu^2)\right], \tag{15}$$

where

$$P_{gg}(n) = 3\left[-2S_1(n) + \frac{11}{6} + \frac{2}{n(n-1)} + \frac{2}{(n+1)(n+2)}\right] - 1, \tag{16}$$

$$S_1(n) = \sum_{j=1}^{n}\frac{1}{j}. \tag{17}$$

In the one-loop approximation, the running strong coupling constant $\alpha_s(\mu^2)$ is

$$\alpha_s(\mu^2) = \frac{4\pi}{b_0\log(\mu^2/\Lambda^2)}, \tag{18}$$

where $b_0 = 11 - (2/3)N_F$, N_F being the number of active flavors. Taking into account (18), we can represent Eq. (15) in the form

$$D_g(n,\mu^2) = D_g(n,\mu_0^2)\exp\left[\frac{2}{b_0}P_{gg}(n)\log\left(\frac{\log(\mu^2/\Lambda^2)}{\log(\mu_0^2/\Lambda^2)}\right)\right], \tag{19}$$

where

$$D_g(n,\mu_0^2) \approx D_g^T(n,\mu_0^2) = \frac{\pi\alpha_s(\mu_0^2)}{24m_c^3}\langle \mathcal{O}^{J/\psi(\psi')}[^3S_1,8]\rangle. \tag{20}$$

In order to obtain the fragmentation function in z space, it is necessary to perform the inverse transformation

$$D_g(z,\mu^2) \approx D_g^T(z,\mu^2) = \int\limits_C dn z^{-n}D_g^T(n,\mu^2). \tag{21}$$

The integration contour C can be transformed in such a way that

$$D_g(z,\mu^2) = \frac{1}{\pi}\int\limits_0^\infty dt\ \mathrm{Im}\left[e^{i\phi}z^{-n}D_g^T(n,\mu^2)\right], \tag{22}$$

where $n = c + te^{i\phi}$, $c \approx 2$, and $\phi = \pi/2$. Figure 2 shows the resulting $gluon \to J/\psi$ fragmentation function multiplied by 10^4 at $\mu^2 = 30, 100$, and 300 GeV^2. We emphasize that the curve corresponding to $\mu^2 = 300$ GeV^2 is in good agreement with the result previously obtained in [26].

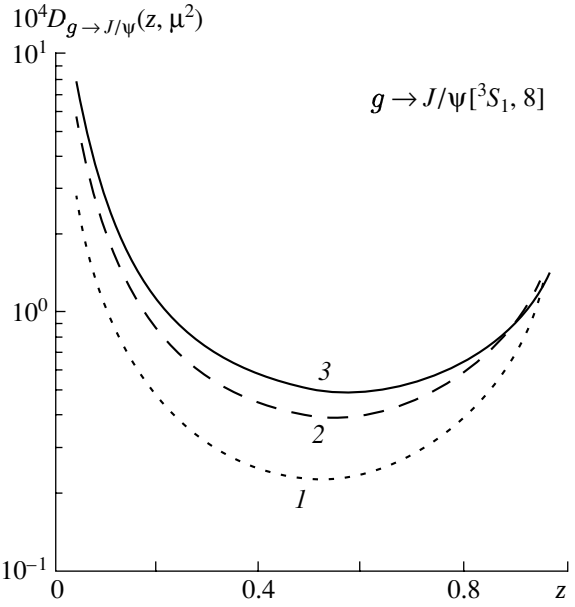

Fig. 2. Fragmentation function $D_{g\to J/\psi}(z,\mu^2)$ versus z for $\mu^2 = (1)\,30, (2)\,100$, and $(3)\,300$ GeV^2.

The c-$quark \to J/\psi\ (\psi')$ fragmentation function corresponding to the diagram in Fig. 3 was first obtained in [5] at $\mu^2 = \mu_0^2$ and can be represented in the form

$$D_{c\to J/\psi(\psi')}(z,\mu_0^2) = \frac{\alpha_s^2(\mu_0^2)}{m_c^3}\langle \mathcal{O}^{J/\psi(\psi')}[^3S_1,1]\rangle \times \left(\frac{16z(1-z)^2}{243(2-z)^6}(16-32z+72z^2-32z^3+5z^4)\right), \quad (23)$$

where the color-octet contribution is negligible and is therefore disregarded. The evolution of the fragmentation function $D_{c\to J/\psi(\psi')}(z,\mu^2)$ is described by the equation

$$\mu^2\frac{\partial D_c}{\partial \mu^2}(z,\mu^2) = \frac{\alpha_s(\mu^2)}{2\pi}\int\limits_z^1 \frac{dx}{x}P_{cc}\left(\frac{x}{z}\right)D_c(x,\mu^2), \quad (24)$$

where $P_{cc}(x)$ is the quark $\to$ quark splitting function in the leading order in α_s.

The Mellin moment of the splitting function $P_{cc}(x)$ is

$$P_{cc}(n) = \frac{4}{3}\left[-2S_1(n) + \frac{3}{2} + \frac{1}{n(n+1)}\right]. \quad (25)$$

Owing to fast convergence of the hypergeometric series for ${}_2F_1(\alpha,\beta,\gamma,z)$ at $z = 1/2$, the moment of the fragmentation function at $\mu^2 = \mu_0^2$ can be represented in a form convenient for a numerical calculation,

$$D_c(n,\mu_0^2) = \frac{16}{243}\frac{\alpha_s^2(\mu_0^2)}{m_c^3}\langle \mathcal{O}^{J/\psi(\psi')}[^3S_1,1]\rangle \times \left[\frac{1}{2}\frac{{}_2F_1\left(6,n+1,n+4,\frac{1}{2}\right)}{(n+1)(n+2)(n+3)} - \frac{{}_2F_1\left(6,n+2,n+5,\frac{1}{2}\right)}{(n+2)(n+3)(n+4)} + \frac{9}{4}\frac{{}_2F_1\left(6,n+3,n+6,\frac{1}{2}\right)}{(n+3)(n+4)(n+5)} - \frac{{}_2F_1\left(6,n+4,n+7,\frac{1}{2}\right)}{(n+4)(n+5)(n+6)} + \frac{5}{32}\frac{{}_2F_1\left(6,n+5,n+8,\frac{1}{2}\right)}{(n+5)(n+6)(n+7)}\right]. \quad (26)$$

A transition to arbitrary $\mu^2 > \mu_0^2$ is performed just as in (19):

$$D_c(n,\mu^2) = D_c(n,\mu_0^2)\exp\left[\frac{2}{b_0}P_{cc}(n)\log\left(\frac{\log(\mu^2/\Lambda^2)}{\log(\mu_0^2/\Lambda^2)}\right)\right]. \quad (27)$$

A numerical transition to z space is performed according to an expression similar to (22),

$$D_c(z,\mu^2) = \frac{1}{\pi}\int\limits_0^\infty dt\ \mathrm{Im}\left[e^{i\phi}z^{-n}D_c(n,\mu^2)\right]. \quad (28)$$

Figure 4 shows the resulting c-$quark \to J/\psi$ fragmentation function multiplied by 10^4 at $\mu^2 = 30$, 100, and 300 GeV^2.

In evaluating the convolutions of the fragmentation functions with the parton-production cross sections, we define the argument of the fragmentation

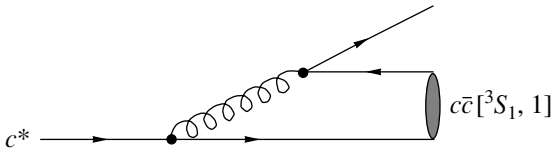

Fig. 3. Diagram that describes the fragmentation process $c^* \to J/\psi + c$ (color-singlet state) in the leading order in the coupling constant α_s.

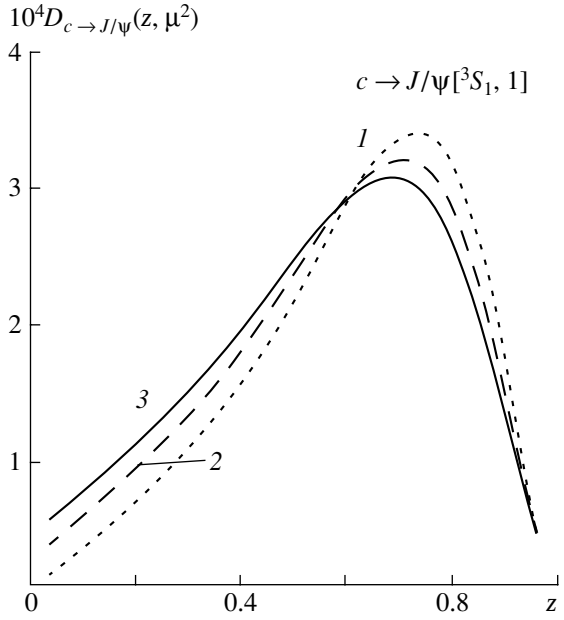

Fig. 4. Fragmentation function $D_{c\to J/\psi}(\mu^2)$ versus z at $\mu^2 = (1)\,30, (2)\,100$, and $(3)\,300$ GeV^2.

function as

$$z = \frac{E_{J/\psi(\psi')} + |\mathbf{p}_{J/\psi(\psi')}|}{E_{c,g} + |\mathbf{p}_{c,g}|} \tag{29}$$

and assume that the product J/ψ (ψ') meson has a low transverse momentum with respect to the axis of the gluon or c-quark jet, so that, in the laboratory frame, the pseudorapidity of the meson is approximately equal to that of the parton:

$$\eta_{J/\psi(\psi')} = \eta_{g,c}. \tag{30}$$

Within the fragmentation model, the cross section for the production of a J/ψ (ψ') meson and the cross section for gluon (or c-quark) production are related by the equations

$$\hat{\sigma}(gg \to J/\psi(\psi')X) \tag{31}$$
$$= \int dz D_{g\to J/\psi(\psi')}(z, \mu^2)\hat{\sigma}(gg \to gg),$$
$$\hat{\sigma}(cg \to J/\psi(\psi')X) \tag{32}$$
$$= \int dz D_{c\to J/\psi(\psi')}(z, \mu^2)\hat{\sigma}(cg \to cg)$$

in the collinear parton model and by the equations

$$\hat{\sigma}(g^*g^* \to J/\psi(\psi')X) \tag{33}$$
$$= \int dz D_{g\to J/\psi(\psi')}(z, \mu^2)\hat{\sigma}(g^*g^* \to g),$$
$$\hat{\sigma}(cg^* \to J/\psi(\psi')X) \tag{34}$$
$$= \int dz D_{c\to J/\psi(\psi')}(z, \mu^2)\hat{\sigma}(cg^* \to g)$$

in the k_T-factorization approach.

4. AMPLITUDES OF PARTON SUBPROCESSES

The squared amplitudes of the parton subprocesses (1) and (2) are well known and can be represented as functions of the Mandelstam variables ($\hat{s}$, $\hat{t}$, $\hat{u}$); that is,

$$\overline{|M(gg \to gg)|^2} \tag{35}$$
$$= 18\pi^2\alpha_s^2 \frac{(\hat{s}^4 + \hat{t}^4 + \hat{u}^4)(\hat{s}^2 + \hat{t}^2 + \hat{u}^2)}{(\hat{s}\hat{t}\hat{u})^2},$$
$$\overline{|M(cg \to cg)|^2} \tag{36}$$
$$= 16\pi^2\alpha_s^2 \left[\frac{\hat{s}^2 + \hat{u}^2}{\hat{t}^2} - \frac{4}{9}\left(\frac{\hat{u}}{\hat{s}} + \frac{\hat{s}}{\hat{u}}\right)\right].$$

At the moment, there are two methods for calculating the parton amplitudes for processes (4) and (5) within the k_T-factorization approach. Effective Feynman rules for processes involving virtual gluons were proposed in [13]. A feature peculiar to these rules is a special choice of the initial-gluon polarization vector,

$$\varepsilon^\mu(k_T) = k_T^\mu/|\mathbf{k}_T|, \tag{37}$$

where $k_T = (0, \mathbf{k}_T, 0)$ is the gluon transverse 4-momentum. Fadin and Lipatov [27] considered initial gluons as Reggeons (or Reggeized gluons) and defined the effective Reggeon–Reggeon–gluon vertex as

$$C^\lambda(k_1, k_2) = -(k_1 - k_2)^\lambda \tag{38}$$
$$+ P_1^\lambda\left(\frac{k_1^2}{(kP_1)} + 2\frac{(kP_2)}{(P_1P_2)}\right)$$
$$- P_2^\lambda\left(\frac{k_2^2}{(kP_2)} + 2\frac{(kP_1)}{(P_1P_2)}\right),$$

where

$$P_1 = \frac{\sqrt{s}}{2}(1, 0, 0, 1) \quad \text{and} \quad P_2 = \frac{\sqrt{s}}{2}(1, 0, 0, -1)$$

are the 4-momenta of colliding protons, $k_1 = x_1P_1 + k_{1T}$ and $k_2 = x_2P_2 + k_{2T}$ are the 4-momenta of initial virtual gluons, $k_T = (0, \mathbf{k}_T, 0)$, $k = k_1 + k_2$ is the 4-momentum of the final real gluon, and s is the squared energy of proton–proton interaction.

It can easily be shown that the vertex function $C^\lambda(k_1, k_2)$ satisfies the gauge-invariance requirement; that is, $(k_1 + k_2)_\lambda C^\lambda(k_1, k_2) = 0$. Omitting the color factor f^{abc} and using the Feynman rules formulated in [13], we can represent the amplitude of process (4) in the form

$$\mathcal{M} = -g\varepsilon^\lambda(k)\frac{k_{1T}^\mu k_{2T}^\nu}{|\mathbf{k}_{1T}||\mathbf{k}_{2T}|}[(k + k_1)_\nu g_{\lambda\mu} \tag{39}$$

$$+ (-k_1 + k_2)_\lambda g_{\mu\nu} + (-k_1 - k)_\mu g_{\nu\lambda}],$$

where $g^2 = 4\pi\alpha_s$ and $g_{\mu\nu}$ is the metric tensor.

Upon simple transformations, the amplitude in (39) assumes the form

$$\mathcal{M} = -\frac{g\varepsilon^\lambda(k)}{2|\mathbf{k}_{1T}||\mathbf{k}_{2T}|} x_1 x_2 s \tilde{C}_\lambda(k_1, k_2), \qquad (40)$$

where

$$\tilde{C^\lambda}(k_1, k_2) = -(k_1 - k_2)^\lambda \qquad (41)$$
$$+ \frac{2P_1^\lambda}{x_2 s}\left(k_1^2 + x_1 x_2 s\right) - \frac{2P_2^\lambda}{x_1 s}\left(k_2^2 + x_1 x_2 s\right)$$
$$= C^\lambda(k_1, k_2).$$

Thus, the approaches developed in [13] and [27] are equivalent and yield identical results for the squared modulus of the vertex function and the amplitude; that is,

$$C^\lambda(k_1, k_2) C_\lambda(k_1, k_2) = -\frac{4k_1^2 k_2^2}{x_1 x_2 s} \qquad (42)$$

and

$$\overline{|M(g^* g^* \to g)|^2} = \frac{3}{2}\pi\alpha_s \mathbf{p}_T^2, \qquad (43)$$

where $\mathbf{p}_T^2 = (\mathbf{k}_{1T} + \mathbf{k}_{2T})^2 = x_1 x_2 s$, $\mathbf{p}_T$ being the transverse momentum of the final gluon.

Disregarding the c-quark mass (we study the region $p_T \gg m_c$), we similarly find for the process in (5) that

$$\overline{|M(cg^* \to c)|^2} = \frac{2}{3}\pi\alpha_s \mathbf{p}_T^2, \qquad (44)$$

where $\mathbf{p}_T$ is the transverse momentum of the final c quark.

5. CROSS SECTION FOR THE PROCESS $p + p \to J/\psi(\psi') + X$

Within the collinear parton model, it is assumed that the cross section for a hadronic process—in our case, $\sigma^{\mathrm{PM}}(pp \to J/\psi(\psi')X, s)$—and the cross section for the corresponding parton subprocess—for example, $\hat{\sigma}(gg \to J/\psi(\psi')X, \hat{s})$—are related by the equation

$$\sigma^{\mathrm{PM}}(pp \to J/\psi(\psi')X, s) \qquad (45)$$
$$= \int dx_1 \int dx_2 G(x_1, \mu^2) G(x_2, \mu^2)$$
$$\times \hat{\sigma}(gg \to J/\psi(\psi')X, \hat{s}),$$

where $\hat{s} = x_1 x_2 s$, $G(x, \mu^2)$ is the collinear distribution of gluons in the proton, $x_{1,2}$ are the proton-momentum fractions carried by gluons, and μ^2 is a typical scale of the hard-scattering process. The QCD evolution of the gluon distribution is described by the Dokshitzer–Gribov–Lipatov–Altarelli–Parisi equation [25].

Within the k_T-factorization approach, the hadronic and the partonic cross sections are related as

$$\sigma^{\mathrm{KT}}(pp \to J/\psi(\psi')X, s) \qquad (46)$$
$$= \int \frac{dx_1}{x_1} \int d\mathbf{k}_{1T}^2 \int \frac{d\phi_1}{2\pi} \Phi(x_1, \mathbf{k}_{1T}^2, \mu^2)$$
$$\times \int \frac{dx_2}{x_2} \int d\mathbf{k}_{2T}^2 \int \frac{d\phi_2}{2\pi} \Phi(x_2, \mathbf{k}_{2T}^2, \mu^2)$$
$$\times \hat{\sigma}(g^* g^* \to J/\psi(\psi')X, \hat{s}),$$

where $\sigma(g^* g^* \to J/\psi(\psi')X, \hat{s})$ is the cross section for the production of a J/ψ (ψ') meson by two Reggeized gluons, $k_1^2 = k_{1T}^2 = -\mathbf{k}_{1T}^2$, $k_2^2 = k_{2T}^2 = -\mathbf{k}_{2T}^2$, $\hat{s} = x_1 x_2 s - (\mathbf{k}_{1T} + \mathbf{k}_{2T})^2$, and $\phi_{1,2}$ are the azimuthal angles in the xy plane between the vectors $\mathbf{k}_{1T}$ and $\mathbf{k}_{2T}$ and the fixed x axis ($\mathbf{p}_{J/\psi(\psi')} \in xz$). The unintegrated distributions of gluons in the proton satisfy the Balitsky–Fadin–Kuraev–Lipatov [28] or Ciafaloni–Catani–Fiorani–Marchesini [29] evolution equations.

In our parton-model calculations, we used the GRV LO [30] and CTEQ5L [31] parametrizations of the gluon distributions in the proton. In the calculations within the k_T-factorization approach, we relied on the following parametrizations of the unintegrated gluon distributions $\Phi(x_1, \mathbf{k}_{1T}^2, \mu^2)$ in the proton: JB from the Blumlein article [32]; JS from the article of Jung and Salam [33]; and KMR from the article of Kimber, Martin, and Ryskin [34].

In Figs. 5 and 6, we present the unintegrated gluon distributions in the proton versus x at constant $\mathbf{k}_T^2$ (Fig. 5) and versus $\mathbf{k}_T^2$ at constant x (Fig. 6). It is clear that, in the transverse-momentum region under consideration ($\mathbf{k}_T^2 \approx 100\ \mathrm{GeV}^2$), the parametrizations differ by more than an order of magnitude.

Taking into account relations (31), (33), (45), and (46), we can represent the double-differential cross section for the process $p + p \to J/\psi(\psi') + X$ in the parton model and in the k_T-factorization approach in the form

$$\frac{d\sigma^{\mathrm{PM}}}{d\eta_\psi dp_{\psi T}} = \int dx_1 \int dz G(x_1, \mu^2) \qquad (47)$$
$$\times G(x_2, \mu^2) D_{g\to J/\psi(\psi')}(z, \mu^2) \frac{p_{gT} E_g}{E_\psi}$$
$$\times \frac{\overline{|M(gg \to gg)|^2}}{8\pi x_1 x_2 s(u + x_1 s)},$$

where

$$u = -\sqrt{s}(E_g - p_{gz}), \quad t = -\sqrt{s}(E_g + p_{gz}),$$

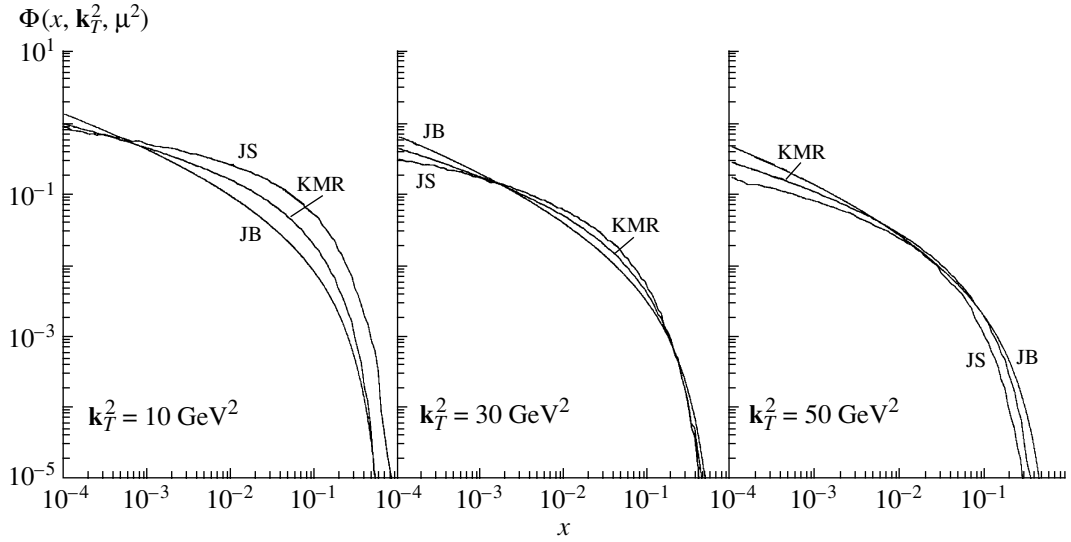

Fig. 5. Unintegrated distribution of gluons in the proton, $\Phi(x, \mathbf{k}_T^2, \mu^2)$, versus x at $\mathbf{k}_T^2 = 10, 30$, and 50 GeV^2 for $\mu = 10$ GeV.

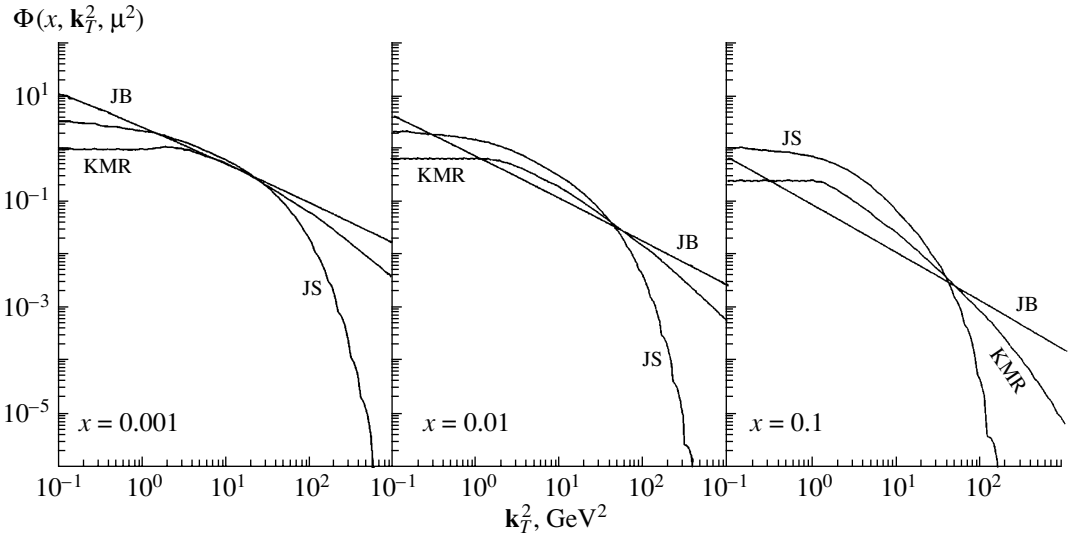

Fig. 6. Unintegrated distribution of gluons in the proton, $\Phi(x, \mathbf{k}_T^2, \mu^2)$, versus $\mathbf{k}_T^2$ at $x = 0.001$, 0.01, and 0.1 for $\mu = 10$ GeV.

$$x_2 = -\frac{x_1 t}{u + x_1 s}, \quad x_{1,\min} = -\frac{u}{s+t},$$
$$\hat{t} = x_1 t, \quad \hat{u} = x_2 u, \quad \hat{s} = x_1 x_2 s;$$

$$\frac{d\sigma^{\mathrm{KT}}}{d\eta_\psi dp_{\psi T}} = \int dz \int d\phi_1 \int d\mathbf{k}_{1T}^2 \qquad (48)$$
$$\times \Phi(x_1, \mathbf{k}_{1T}^2, \mu^2)\Phi(x_2, \mathbf{k}_{2T}^2, \mu^2) D_{g\to J/\psi(\psi')}(z, \mu^2)$$
$$\times \frac{E_g}{p_{gT} E_\psi} \frac{\overline{|M(g^* g^* \to g)|^2}}{x_1 x_2 s}.$$

Here, we have used the notation

$$\mathbf{k}_{2T} = \mathbf{p}_{gT} - \mathbf{k}_{1T}, \quad x_1 = \frac{E_g + p_{gz}}{\sqrt{s}}, \qquad (49)$$

$$x_2 = \frac{E_g - p_{gz}}{\sqrt{s}}.$$

Expressions (47) and (48) for the partonic processes $cg \to cg$ and $cg^* \to c$ can be written in a similar form upon trivial substitutions. The pseudorapidity of the product J/ψ (ψ') meson is determined by the J/ψ (ψ') emission angle in the laboratory frame,

$$\eta_{J/\psi(\psi')} = -\ln\tan(\theta_{J/\psi(\psi')}/2). \qquad (50)$$

In our calculations, the typical hard-interaction scale is

$$\mu^2 = m_{J/\psi(\psi')}^2 + p_{J/\psi(\psi')T}^2. \qquad (51)$$

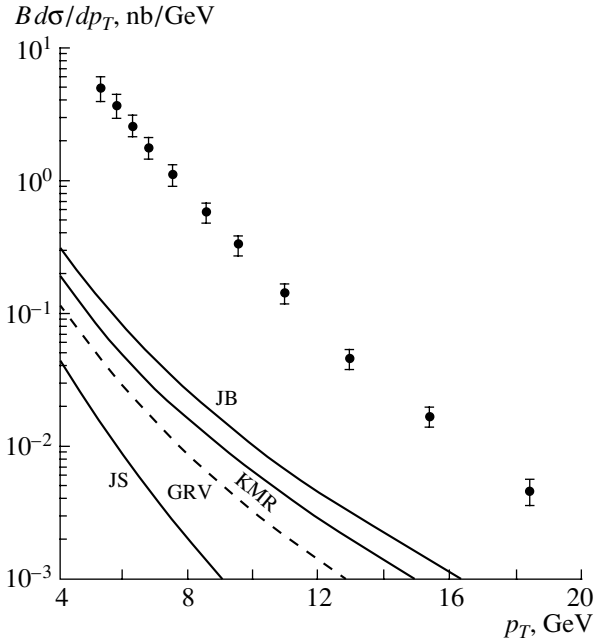

Fig. 7. Production spectrum of direct J/ψ mesons with respect to p_T for $\sqrt{s} = 1800$ GeV and $|\eta_{J/\psi}| < 0.6$ (only the contribution of c-quark fragmentation to the color-singlet state of the J/ψ meson is taken into account; $\langle \mathcal{O}^{J/\psi}[^3S_1, 1]\rangle = 1.13$ GeV^3). The experimental data displayed here and in Figs. 8–10 were taken from [2]. The quantity B is the branching ratio for the decay $J/\psi \to \mu^+\mu^-$.

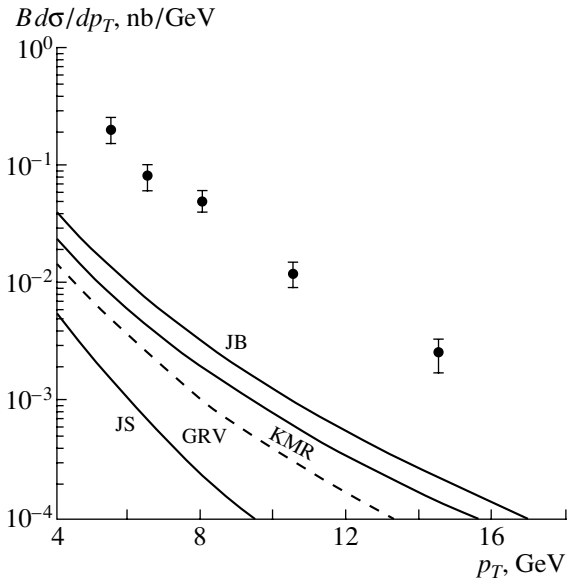

Fig. 8. Production spectrum of direct ψ' mesons with respect to p_T at $\sqrt{s} = 1800$ GeV and $|\eta_{\psi'}| < 0.6$ (only the contribution of c-quark fragmentation to the color-singlet state of the ψ' meson is taken into account; $\langle \mathcal{O}^{\psi'}[^3S_1, 1]\rangle = 0.573$ GeV^3). The quantity B is the branching ratio for the decay $\psi' \to \mu^+\mu^-$.

6. RESULTS OF THE CALCULATIONS

In this section, we present our results and compare them with experimental data of the CDF Collaboration [1, 2] for the p_T spectra of direct J/ψ and ψ' mesons in pp interactions at $\sqrt{s} = 1.8$ TeV. The cross section for the production of direct J/ψ mesons does not include the contribution from the decays of B and ψ' mesons to J/ψ mesons or the contribution from the radiative decays of P-wave charmonia ($\chi_{cJ} \to J/\psi\gamma$). The cross section for the production of direct ψ' mesons does not include the contribution from the decay $B \to \psi' X$. Our results obtained in the collinear parton model do not depend, within 10 to 20%, on the parametrization of the gluon distribution and agree with the results obtained previously in [20, 23] by using a similar approach.

Let us first consider the contribution from c-quark fragmentation to the cross section for the production of direct J/ψ and ψ' mesons. Since, in these fragmentation processes, the contribution of the color-singlet production mechanism is dominant, the fragmentation function $D_{c\to J/\psi(\psi')}(z, \mu^2)$ is determined by the nonperturbative matrix element $\langle \mathcal{O}^{J/\psi(\psi')}[^3S_1, 1]\rangle$, which is related to the value of the nonrelativistic $J/\psi\,(\psi')$ wave function at the origin as

$$\langle \mathcal{O}^{J/\psi(\psi')}[^3S_1, 1]\rangle = 2N_c(2J+1)|\Psi_{JLS}(0)|^2. \quad (52)$$

Thus, the matrix element $\langle \mathcal{O}^{J/\psi(\psi')}[^3S_1, 1]\rangle$ can be either theoretically calculated within the nonrelativistic potential approach (see the results presented in [35] for various types of the quark–quark interaction potential) or unambiguously extracted from experimental data on the leptonic-decay width of the $J/\psi\,(\psi')$ meson.

Figures 7 and 8 display the results of our calculations for the p_T spectra of J/ψ and ψ' mesons with allowance for only the contributions from the fragmentation of $c\,(\bar{c})$ quarks to J/ψ and ψ' mesons. One can see that the curves calculated within the k_T-factorization approach lie higher (by a factor of 2 to 3) than the predictions of the collinear parton model, with the exception of the curve obtained with the JB parametrization [33] for the unintegrated gluon distribution.

Figures 9 and 10 show the results of our calculations for the p_T spectra of J/ψ and ψ' mesons with allowance for only the contribution of gluon fragmentation to J/ψ and ψ' mesons. We see that the curves lie higher by more than an order of magnitude than the curves obtained by taking into account only the fragmentation of $c\,(\bar{c})$ quarks to J/ψ and ψ' mesons. It is also clear from Figs. 9 and 10 that the curves labeled with GRV and obtained on the basis of the

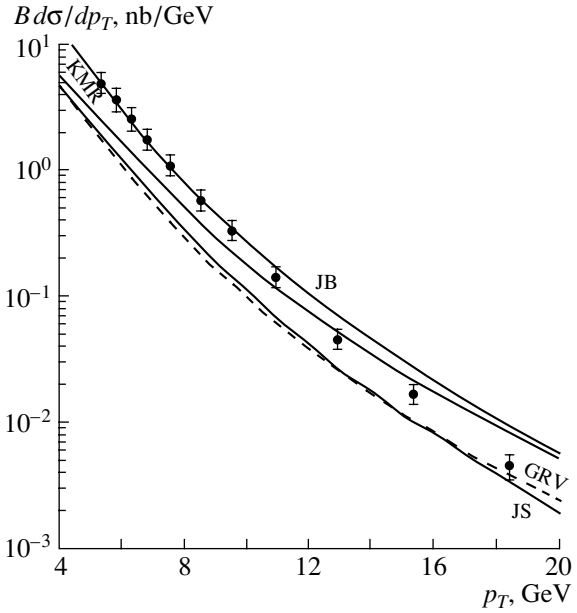

Fig. 9. Production spectrum of direct J/ψ mesons with respect to p_T for $\sqrt{s} = 1800$ GeV and $|\eta_{J/\psi}| < 0.6$ (only the contribution of gluon fragmentation to the color-octet state of the J/ψ meson is taken into account; $\langle \mathcal{O}^{J/\psi}[^3S_1, 8]\rangle = 4.4 \times 10^{-3}$ GeV^3). The quantity B is the branching ratio for the decay $J/\psi \to \mu^+\mu^-$.

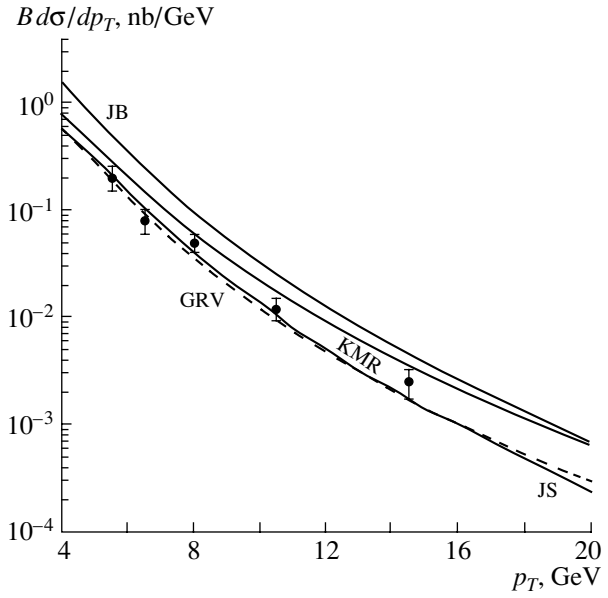

Fig. 10. Production spectrum of direct ψ' mesons with respect to p_T at $\sqrt{s} = 1800$ GeV and $|\eta_{\psi'}| < 0.6$ (only the contribution of gluon fragmentation to the color-octet state of the ψ' meson is taken into account; $\langle \mathcal{O}^{\psi'}[^3S_1, 8]\rangle = 4.2 \times 10^{-3}$ GeV^3). The quantity B is the branching ratio for the decay $\psi' \to \mu^+\mu^-$.

parton model are below the experimental points, especially in the region of low p_T, where the contribution of gluon–gluon fusion to the color-octet states $^1S_0$ and $^3P_0$ is dominant [23, 24]. The results obtained within the k_T-factorization approach depend strongly on the choice of parametrization for the unintegrated gluon distribution. In the region $p_T \gg m_c$, where the application of the fragmentation model is well justified, the results obtained with the JB [32] and KMR [34] parametrizations are close. However, the parametrization JS [33] predicts cross-section values that are approximately two times smaller and which are closer to the values obtained on the basis of the collinear parton model with the GRV parametrization [30]. Thus, the p_T spectra of direct J/ψ and ψ' mesons within the collinear parton model and within the k_T-factorization approach agree within a factor of 2. We emphasize that our result contradicts the results obtained previously in [17–19], where the calculations were performed within the model of gluon–gluon fusion. In contrast to our results, the fit to data of the CDF Collaboration [1, 2] according to [17–19] requires a strong suppression (by a factor of 10 to 30) of the contribution from the octet nonperturbative matrix element $\langle \mathcal{O}^{J/\psi(\psi')}[^3S_1, 8]\rangle$ in relation to the values obtained within the parton model.

We can indicate a few reasons for the discrepancies between our results and those reported in [17–19].

First, we have employed the fragmentation model, which effectively takes into account higher order corrections in the strong coupling constant α_s through the Dokshitzer–Gribov–Lipatov–Altarelli–Parisi evolution equation [25].

Second, the authors of [17–19] chose the argument μ^2 of the running coupling constant $\alpha_s(\mu^2)$ to be $\mu^2 = \mathbf{k}_{1T}^2$ or $\mu^2 = \mathbf{k}_{2T}^2$, while we took it in the form $\mu^2 = m^2_{J/\psi(\psi')} + p^2_{J/\psi(\psi')T}$. The choice of argument in the constant $\alpha_s(\mathbf{k}_T^2)$ increases the cross section by a factor of 2 to 3 [19].

Third, the authors of [17, 18] used the KMS parametrization for the unintegrated gluon distribution in the proton [36]. It is clear from Figs. 9 and 10 that the difference in the p_T spectra obtained with different parametrizations can also reach a factor of 2 to 3.

The results of the present study for direct J/ψ and ψ' mesons produced in pp interactions, along with our previous results for the photoproduction of J/ψ mesons at the HERA energy [16], show that the predictions for the p_T spectra of J/ψ and ψ' mesons within the k_T-factorization approach with hard amplitudes in the leading order in α_s are in good agreement with the predictions of the parton model in

the next order in the coupling constant α_s. The calculation of the cross section for the photoproduction of J/ψ mesons in the next order in α_s on the basis of the collinear parton model was performed in [37].

It is clear that the hard subprocess in the next order in α_s for gluon production in the k_T-factorization approach coincides with the Born subprocess of gluon production in the collinear parton model:

$$g^* + g^* \to g + g. \tag{53}$$

The amplitude of the process in (53) has an infrared divergence even at high values of the transverse momentum of the final gluon, which later fragments into a J/ψ (ψ') meson. On the contrary, both final gluons must be hard in a similar process within the parton model but with real gluons in the initial state. A method for calculating the amplitude of (53) was proposed in [27], where the initial gluons were treated as Reggeons and where the infrared divergences in question are removed. Calculations of the spectra of J/ψ and ψ' mesons with allowance for the subprocess in (53) are of considerable interest and are close to completion at the moment.

ACKNOWLEDGMENTS

We are grateful to H. Jung for placing information about the parametrizations of unintegrated gluon distributions at our disposal and to B. Kniehl, O. Teryaev, and L. Smizanovskii for enlightening discussions on the results obtained in this study.

D.V. Vasin is grateful to the Dynasty Foundation and the International Center for Fundamental Physics in Moscow for financial support.

REFERENCES

1. CDF Collab. (F. Abe *et al.*), Phys. Rev. Lett. **79**, 572 (1997).
2. CDF Collab. (T. Affolder *et al.*), Phys. Rev. Lett. **85**, 2886 (2000).
3. E. L. Berger and D. Jones, Phys. Rev. D **23**, 1521 (1981); R. Baier and R. Rückl, Phys. Lett. B **102B**, 364 (1981); S. S. Gershtein, A. K. Likhoded, and S. R. Slabospitskiĭ, Yad. Fiz. **34**, 227 (1981) [Sov. J. Nucl. Phys. **34**, 128 (1981)]; V. G. Kartvelishvili, A. K. Likhoded, and S. R. Slabospitskiĭ, Yad. Fiz. **28**, 1315 (1978) [Sov. J. Nucl. Phys. **28**, 678 (1978)].
4. G. T. Bodwin, E. Braaten, and G. P. Lepage, Phys. Rev. D **51**, 1125 (1995).
5. E. Braaten and T. C. Yuan, Phys. Rev. D **50**, 3176 (1994).
6. E. Braaten and T. C. Yuan, Phys. Rev. D **52**, 6627 (1995).
7. E. Braaten, K. Cheung, and T. C. Yuan, Phys. Rev. D **48**, 4230 (1993).
8. E. Braaten and J. Lee, Nucl. Phys. B **586**, 427 (2000).
9. J. P. Ma, Nucl. Phys. B **447**, 405 (1995).
10. A. P. Martynenko and V. A. Saleev, Phys. Rev. D **53**, 6666 (1996).
11. E. Braaten and T. C. Yuan, Phys. Rev. Lett. **71**, 1673 (1993).
12. L. V. Gribov, E. M. Levin, and M. G. Ryskin, Phys. Rep. **100**, 1 (1983).
13. J. C. Collins and R. K. Ellis, Nucl. Phys. B **360**, 3 (1991).
14. S. Catani, M. Ciafaloni, and F. Hautmann, Nucl. Phys. B **366**, 135 (1991).
15. V. A. Saleev and N. P. Zotov, Mod. Phys. Lett. A **9**, 151 (1994).
16. V. A. Saleev, Phys. Rev. D **65**, 054041 (2002); V. A. Saleev and D. V. Vasin, Phys. Lett. B **548**, 161 (2002).
17. P. Hagler *et al.*, Phys. Rev. D **62**, 071502 (2000); Phys. Rev. Lett. **86**, 1446 (2001).
18. F. Yuan and K.-T. Chao, Phys. Rev. D **63**, 034006 (2001); Phys. Rev. Lett. **87**, 022002 (2001).
19. S. P. Baranov, Phys. Rev. D **66**, 114003 (2002).
20. C.-F. Qiao, J. Phys. G **29**, 1075 (2003).
21. G. T. Bodwin, Preprint ANL-HEP-CP-02-114 (2002); hep-ph/0212203.
22. E. Braaten and S. Fleming, Phys. Rev. Lett. **74**, 3327 (1995).
23. E. Braaten, B. A. Kniehl, and J. Lee, Phys. Rev. D **62**, 094005 (2000).
24. M. Kramer, Prog. Part. Nucl. Phys. **47**, 141 (2001).
25. V. N. Gribov and L. N. Lipatov, Yad. Fiz. **15**, 781 (1972) [Sov. J. Nucl. Phys. **15**, 438 (1972)]; Y. L. Dokshitser, Zh. Éksp. Teor. Fiz. **73**, 1216 (1977) [Sov. Phys. JETP **46**, 641 (1977)]; G. Altarelli and G. Parisi, Nucl. Phys. B **126**, 298 (1977).
26. B. A. Kniehl and L. Zwirner, Phys. Lett. B **468**, 294 (1999).
27. V. S. Fadin and L. N. Lipatov, Nucl. Phys. B **477**, 767 (1996).
28. E. A. Kuraev, L. N. Lipatov, and V. S. Fadin, Zh. Éksp. Teor. Fiz. **71**, 840 (1976) [Sov. Phys. JETP **44**, 443 (1976)]; Ya. Ya. Balitskiĭ and L. N. Lipatov, Yad. Fiz. **28**, 1597 (1978) [Sov. J. Nucl. Phys. **28**, 822 (1978)].
29. M. Ciafaloni, Nucl. Phys. B **296**, 49 (1988); S. Catani, F. Fiorani, and G. Marchesini, Phys. Lett. B **234**, 339 (1990); G. Marchesini, Nucl. Phys. B **445**, 49 (1995).
30. M. Glück, E. Reya, and A. Vogt, Z. Phys. C **67**, 433 (1995).
31. CTEQ Collab. (H. L. Lai *et al.*), Eur. Phys. J. C **12**, 375 (2000).
32. J. Blumlein, DESY 95-121 (1995).
33. H. Jung and G. Salam, Eur. Phys. J. C **19**, 351 (2001).
34. M. A. Kimber, A. D. Martin, and M. G. Ryskin, Phys. Rev. D **63**, 114027 (2001).
35. E. J. Eichten and C. Quigg, Phys. Rev. D **52**, 1726 (1995).
36. J. Kwiecinski, A. Martin, and A. Stasto, Phys. Rev. D **56**, 3991 (1997).
37. M. Kramer, Nucl. Phys. B **459**, 3 (1996).

Translated by M. Kobrinsky